A modular platform for growth of hybrid and polymer membrane systems by vesicle fusion

Dissertation

zur Erlangung des akademischen Grades

doctor rerum naturalium

(Dr. rer. nat.)

von: **M. Sc. Nika Otrin (geb. Marušič)**

geb. am 11.07.1988 in Koper, Slowenien

genehmigt durch die Fakultät für Verfahrens- und Systemtechnik der Otto-von-Guericke-Universität Magdeburg

Promotionskommission: Prof. Dr. rer. nat. Nora Kulak (Vorsitz)

Prof. Dr.-Ing. Kai Sundmacher (Gutachter)

Prof. Dr. Sébastien Lecommandoux (Gutachter)

Prof. Dr. Katarzyna Adamala (Gutachter)

eingereicht am: 3.5.2022

Promotionskolloquium am: 04.07.2022

Summary

The MaxSynBio research project aims to construct artificial cells through mimicking predefined cell functions by a bottom-up approach via the assembly of functional parts and modules. Together with energy, metabolism, division, signaling and motility, growth represents one of the essential cell functions. This thesis was focused on the development of a growth module for artificial cells by achieving membrane expansion via vesicle fusion. Four different growth strategies were explored based on electrostatic interactions between the membranes, physicochemical factors (mechanical stress or dehydration) or fusogenic (soluble NSF-attachment protein receptor, SNARE) proteins. Relevant protocols, such as giant unilamellar vesicles (GUVs) and proteoGUVs formation, were developed, and the efficiency of each growth mechanism was analyzed through size distribution, membrane and content mixing.

The membrane-bound compartments were formed from the copolymer poly(dimethylsiloxane)-*graft*-poly(ethylene oxide) (PDMS-*g*-PEO) or its blends with lipids. Prior to exploring growth mechanisms, their biophysical characteristics (bending rigidity, lateral diffusion, membrane disorder, proton permeability, durability and chemical stability) were analyzed and compared to pure lipid compartments. Furthermore, a model membrane protein bo_3 oxidase was reconstituted in GUVs and its interplay with polymer and hybrid membrane was studied. The investigated membranes interacted differently with the reconstituted protein: while insertion of bo_3 oxidase in soy phosphatidylcholine (PC) decreased the fluidity, it exercised the opposite effect on the polymer by loosening its structure. Characteristics of hybrid membranes were shown to be not always intermediate between lipid and polymer ones – blending the membrane led to overall increased proton permeability, but after proton pump insertion the compartments were surprisingly resealed, which was attributed to beneficial hybrid membrane rearrangement. Another example of non-intermediate characteristic of hybrid membranes was the bending rigidity, whereby the prevailing component (i.e., the polymer) dictated the membrane softness. Both hybrid and polymer membranes were shown to further soften upon insertion of largely hydrophobic membrane proteins. Furthermore, PDMS-*g*-PEO appears to increase the functional lifetime of membrane proteins and their resistance to reactive oxygen species (ROS).

The first growth mechanism investigated in the thesis was based on electrostatic attraction between the membranes. Utilizing natural anionic and synthetic cationic lipids, oppositely charged vesicles, containing predominatly PDMS-*g*-PEO were formed and their fusion was explored. Partially replacing lipids with synthetic polymer PDMS-*g*-PEO led to significantly increased fusion efficiency. Furthermore, the results

revealed that charged lipids are not required in both of the fusion-intended vesicle populations; neutral hybrids could be utilized instead of anionic ones, which also led to higher content mixing.

Second growth mechanism was induced by mechanical stress in presence of salt and was limited to polymersomes. The approach was shown to be compatible with essential artificial cell functions, such as encapsulation of cytosolic components and the reconstitution of membrane machinery. Furthermore, the type of salt dictated the type of newly grown polymer structures upon agitation (GUVs in KCl and long tubes and polymer beads in NaCl), while the presence of dUTP caused the formation of tightly connected PDMS-*g*-PEO GUVs, similar to tissues.

The third growth mechanism explored here was fusion/electroformation – a two-step mechanism. In the first step, LUVs were fused by partial dehydration, and in the second step GUVs were grown via electroformation. The approach was tuned for each type of tested membranes: PDMS-*g*-PEO, PDMS-*g*-PEO/soy PC and soy PC, and protein-functionalized microcompartments were successfully grown. Moreover, this work demonstrated that the optimized approach could be utilized for different types of membrane proteins – transmembrane peptides or complex mostly hydrophobic or asymmetric proteins. The method resulted in active enzymes – tested via proton pumping for *bo*$_3$ oxidase, ATP synthesis for F_1F_O-ATPase, and fusion for SNAREs. Finally, the approach was extended to the growth of multicompartmentalized microcompartments, which platform will enable the integration of artificial organelles into artificial cells.

The last, fourth, growth approach studied in this work utilized SNARE proteins, which are key components driving membrane fusion in nature. Utilizing know-how for the formation of protein-functionalized microcompartments (obtained by optimizing the fusion/electroformation approach), 2–40 μm SNARE-functionalized GUVs were formed. Interestingly, SNAREs had an opposite effect on membrane bending rigidity than the hydrophobic membrane protein (*bo*$_3$ oxidase) – SNAREs rigidified both polymer and hybrid membranes. Fusion of SNARE-functionalized microcompartments was arrested in hemifusion, meanwhile, micro- and nanocompartments proceeded into pore opening and full fusion.

Zusammenfassung

Die Nachahmung vordefinierter, klar abegrenzter Zellfunktionen mit Hilfe biomolekularer Teile und funktionaler Module beschreibt den Bottom-Up Ansatz in der synthetischen Biologie. Dieser Ansatz wurde in dem Forschungsprojekt MaxSynBio der Max-Planck-Gesellschaft (2014-2020) mit dem Ziel genutzt, erste Prototypen für künstliche Zellen zu erzeugen. Energieversorgung, Metabolismus, Zellwachstum, Zellteilung, Signalübertragung und Fortbewegung repräsentieren diese essentiellen Zellfunktionen. Der Fokus der vorliegenden Arbeit lag in diesem Kontext auf der Entwicklung von Wachstumsmodulen für zukünftige künstliche Zellkonstrukte, welche mittels Membranerweiterung auf dem Weg der Vesikelfusion erreicht werden sollte. Dazu wurden vier verschiedene Wachstumsstrategien, basierend auf elektrostatischen Interaktionen zwischen Membranen, externen Faktoren (mechanischer Stress oder Dehydration) und Fusionsproteinen (SNARE-soluble NSF-attachement protein receptor), entwickelt. Die zur Herstellung von großen unilamellaren Vesikeln (GUVs giant unilamellar vesicles) und proteinhaltigen großen unilamellaren Vesikeln (proteoGUVs) notwendigen Vorschriften wurden in dieser Arbeit entwickelt und die Effizienz des Wachstums durch Ermittlung der Größenverteilung, der Membranvermischung und der Vermischung des Vesikelinhaltes analysiert.

Die membrangebundenen Kompartimente wurden mit dem Copolymer Poly(dimethylsiloxane)-*graft*-poly(ethylene oxide) (PDMS-*g*-PEO) oder aus ihrer Verbindung mit Lipiden gebildet. Deren biophysikalische Eigenschaften (Krümmungs-Steifheit, laterale Diffusion, Membranverteilung, Protonenpermeabilität, Haltbarkeit und chemische Stabilität) mussten vor der Entwicklung der Wachstumsmechanismen bestimmt werden und mit reinen Lipid-Kompartimenten verglichen werden. Weiterhin wurde ein größtenteils hydrophobes Membranprotein, die Protonenpumpe bo_3-Oxidase, in GUVs rekonstituiert und sein Verhalten in Polymer- und Hybridmembranen studiert. Die untersuchten Membranen verhielten sich nach der Rekonstitution des Proteins unterschiedlich: Während der Einbau des Proteins die Fluidität von Membranen aus Soja-basierten Phosphatidycholinen (PC) herabsetzte, hatte es den entgegengesetzten Effekt auf Polymermembranen, deren Struktur durch die Rekonstitution gelockert wurde. Im Falle von hybriden Membranstrukturen hat sich gezeigt, dass deren Eigenschaften nicht immer zwischen denen der Lipid- und der Polymermembranen liegen. Eine Vermischung dieser beiden Membranarten führt zu einer erhöhten Protonenpermeabilität und zu einer breiteren Verteilung; jedoch waren nach der Rekonstitution des Proteins die Kompartimente erstaunlicherweise nahezu verschlossen. Dies ist zurückzuführen auf die vorteilhafte Neuanordnung der Makromoleküle in der hybriden Membran. Ein weiteres Beispiel dafür ist die Krümmungs-Steifheit von hybriden Membranen, in denen die vorherrschende Komponente, das polymere Makromolekül, die Weichheit der Membran vorgibt. Für beide

Membranarten, Hybride und Polymere, konnte gezeigt werden, dass sie durch die Einbau von größtenteils hydrophoben Membranproteinen weicher werden. Zudem scheint das synthetische Polymer PDMS-*g*-PEO die funktionale Lebensdauer von Membranproteinen zu verlängern und deren Resistenz gegenüber reaktiven Sauerstoffspezies (ROS) zu erhöhen.

Die ersten in dieser Arbeit untersuchten Wachstumsmechanismen basieren auf elektrostatischen Interaktionen zwischen Membranen. Unter Verwendung natürlicher anionischer und synthetischer kationischer Lipide wurden entgegengesetzt geladene Vesikel, die hauptsächlich PDMS-*g*-PEO enthielten, gebildet und untersucht. Das partielle Ersetzen von Lipiden durch das synthetische Polymer PDMS-*g*-PEO erhöhte die Fusionseffizienz. Ferner wurde herausgefunden, dass geladene Lipide in beiden fusions-gesteuerten Vesikelpopulationen während der hybriden Membranfusion nicht notwendig sind, denn neutrale Hybride können statt anionischer verwendet werden, was ebenfalls zu einer höheren Durchmischung führte.

Der zweite Wachstumsmechanismus wird durch mechanischen Stress in Vorhandensein von Salz ausgelöst und ist auf Polymersome beschränkt. Es zeigte sich, dass dieser Ansatz kompatibel mit essentiellen Funktionen der künstlichen Zellen ist, wie z. B. die Enkapsulierung zytosolischer Komponenten und die Rekonstitution von membrangebundenen Prozessen. Zudem bestimmt die Art der durch das Salz hervorgerufenen Formen von neu gewachsenen, durch aktive Durhmischung entstandenen polymeren Strukturen (lange Röhren bei GUVs in KCl und Polymerkugeln in NaCl) und die Anwesenheit des Enzyms dUTP (Deoxyuridine triphosphate) bewirkt die Formierung fest verbundener PDMS-*g*-PEO GUVs, die wiederum gewebeähnliche Strukturen ausbilden.

Der dritte in der Arbeit erforschte Wachstumsmechanismus ist die Fusion/Elektroformation - ein zweistufiger Prozess: Im ersten Schritt wurden LUVs durch partielle Dehydration fusioniert und im zweiten Schritt zu GUVs durch Elektroformation heranwachsen gelassen. Dieser Ansatz wurde genauestens für jeden Membrantyp abgestimmt: PDMS-*g*-PEO, PDMS-*g*-PEO/PC (Soja) und PC (Soja). Als Resultat konnten erfolgreich Protein-funktionale Mikrokompartimente erzeugt werden. Dabei zeigte sich, dass der gewählte Ansatz für verschiedene Arten von Membranproteinen, transmembrane Peptide oder komplexe, größtenteils hydrophobe oder asymmetrische Proteine, verwendet werden kann. Die Methode resultierte in aktiven Enzymen, wie für die Protonenpumpe *bo*$_3$-Oxidase, die Synthese von ATP mit der F_1F_O-ATPase und die Fusion von Vesikeln durch SNARE-Proteine nachgewiesen. Letztendlich wurde der Ansatz auch auf Multi-Mikrokompartimente erweitert. In der längerfristigen Perspektive könnte die entwickelte Plattform für die Integration künstlicher Organellen in künstliche Zellen nutzbar gemacht werden.

Der letzte, vierte Ansatz, der in dieser Arbeit untersucht wurde, beschäftigte sich mit SNARE-Proteinen, welche in der Natur als der Schlüsselproteinkomplex für Membranfusionen bekannt sind. Die Anwendung des in der Optimierung des Fusions-/Elektroformation-Wachstumsansatzes erworbenen Knowhows zum Aufbau Protein-funktionalisierter Mikrokompartimente führte zur Entwicklung von 2-40 µm großen SNARE-funktionalisierten GUVs. Interessanterweise hatten die SNAREs einen entgegengesetzten Effekt auf die Membran-Krümmungs-Steifheit als die größtenteils hydrophoben Membranproteine (bo_3 Oxidase). Durch die SNAREs wurden sowohl die polymeren, als auch die hybriden Membransysteme steifer. Die Fusion der SNARE-funktionalisierten Mikrokompartimente verharrte in einer Hemifusion, während es bei der Fusion zwischen Mikro- und Nanokompartimenten zur Porenöffnung und vollständigen Fusion kam.

Table of Contents

Abbreviations

ADP	Adenosine-5’-diphosphate
ATP	Adenosine-5’-triphosphate
bR	Bacteriorhodopsin
DOPC	1,2-dioleoyl-sn-glycero-3-phosphocholine
DOTAP	1,2-dioleoyl-3-trimethylammonium-propane
DLS	Dynamic light scattering
DTT	Dithiothreitol
dUTP	Deoxyuridine triphosphate
FITC-12-dUTP	Fluorescein-5(6)-carboxaminocaproyl-[5-(3-aminoallyl)-2'-desoxyuridin-5-triphosphat]
FRAP	Fluorescence recovery after photobleaching
FRET	Fluorescence resonance energy transfer
GUV	Giant unilamellar vesicle
LUV	Large unilamellar vesicle
OG	n-octyl-β-D-glucoside, octyl glucoside
PC	Phosphatidylcholine
PDMS-*g*-PEO	Poly(dimethylsiloxane)-*graft*-poly(ethylene oxide)
PDMS-*g*-PEO-FITC	Poly(dimethylsiloxane)-*graft*-poly(ethylene oxide)-fluorescein
PDMS-*g*-PEO-Rho	Poly(dimethylsiloxane)-*graft*-poly(ethylene oxide)-rhodamine
PE-NBD	1,2-dioleoyl-sn-glycero-3-phosphoethanolamine-N-(7-nitro-2-1,3-benzoxadiazol-4-yl) (ammonium salt)

PE-Rho	1,2-dioleoyl-sn-glycero-3-phosphoethanolamine-N-(lissamine rhodamine B sulfonyl) (ammonium salt)
PS	Phosphatidylserine
ROS	Reactive oxygen species
R_{sat}	Saturation point
R_{sol}	Solubilization point
SC	Sodium cholate
SNARE	Soluble *N*-ethylmaleimide-sensitive factor (NSF)-attachment protein receptor
SUVs	Small unilamellar vesicles
TTX	Triton X-100
Q_1	Ubiquinone 1

1 Introduction

Chapter 1.3.1, paragraph 3, Chapter 1.3.3.1, paragraph 2, Chapter 1.3.5.1, paragraph 1 and Chapter 1.3.5.2, first part of paragraph 2 were reprinted (adapted) from Marušič et al., Constructing artificial respiratory chain in polymer compartments: Insights into the interplay between bo_3 oxidase and the membrane. *Proceedings of the National Academy of Sciences* 117 (26): 15006-15017 (2020) (1), licensed under CC BY 4.0 (https://creativecommons.org).

Chapter 1.3.4.1 was reprinted (adapted) with permission from Marušič et al., Increased efficiency of charge-mediated fusion in polymer/lipid hybrid membranes. *Proceedings of the National Academy of Sciences* 119 (20): e2122468119 (2022) (2) licensed under CC BY 4.0 (https://creativecommons.org).

Chapter 1.3.4.2, paragraph 4 was reprinted (adapted) with permission from Marušič et al., Fusion-induced growth of biomimetic polymersomes: Behavior of poly(dimethylsiloxane)-poly(ethylene oxide) vesicles in saline solutions under high agitation. *Macromolecular Rapid Communications* 43 (5): 2100712 (2022) (3), licensed under CC BY 4.0 license (https://creativecommons.org).

1.1 Bottom-up synthetic biology

Similarly as artists find their inspiration in the beauty of nature and their admiration is expressed in paintings, scientists are intrigued by the mystery of nature and their never-ending curiosity pushes them to understand the miracles of biology and to attempt to mimic them. This curiosity in combination with a worldwide need for production of novel substances or of existing ones in a more efficient way, such as pharmaceuticals or fuels, launched a new field of science, i.e., synthetic biology. Synthetic biology tackles tasks beyond the production of novel substances, such as redesigning organisms by engineering them to obtain new abilities, for example sensing a pathogen in the environment. One approach of synthetic biology that uses metabolic and genetic engineering techniques to impart new functions to existing living cells is known as the top-down approach. Meanwhile, the creation of new biological systems, in particular artificial cells, by the step-wise assembly of functional parts and modules is called the bottom-up approach. The latter approach on one side enables further understanding of the smallest biological units that in the top-down approach are too integrated inside the living cell, and on the other side it is an opportunity to not just mimic cells, but to introduce synthetic materials that can lead to novel functions that may expand or surpass the natural ones. In this regard, the enrichment of the library of building blocks with synthetic alternatives holds also in the case of cell membranes, where scaffold phospholipids can be replaced with other amphiphilic molecules like synthetic polymers or blended with them in hybrid systems into a form of chemical prosthetics (4).

Although consensus partially exists about some of the main cell functions that the artificial cell should have (such as self-replication, growth, division, etc.), the hierarchical nomenclature (e.g., parts/module/systems) is used inconsistently among laboratories. Furthermore, a wide range from simple (nanoreactors with encapsulated water-soluble enzymes (5)) to complex (mutlicompartentlized systems (6)) systems have been named artificial organelles, and compartments with single-functionality have been addressed as artificial cells (7, 8). The highly interdisciplinary field of bottom-up synthetic biology requires input from various fields, such as molecular biology, biochemistry, biophysics, engineering and modeling. To work toward a common goal, i.e., construction of artificial cell with minimal functions, researchers from those various fields are stepping together and establishing consortiums, where different tools and know-how from various labs are available for the whole consortium. The first consortium in bottom-up synthetic biology started in 2014 and was coordinated by Prof. Dr.-Ing. Kai Sundmacher (MPI for Dynamics of Complex Technical Systems, Magdeburg) and Prof. Dr. Petra Schwille (MPI for Biochemistry, Martinsried). The project was supported by the Max Planck Society and the Federal Ministry of Education and Research and involved research groups from nine Max Planck Institutes across Germany, as well as the Department of Theology of the Friedrich Alexander University Erlangen-Nuremberg. The consortium was concentrating on the synthesis of selected life processes, which are of fundamental importance for the proliferation of living cells: energy, metabolism, growth, division, signaling and motility. The entirety of those life processes is summarized under the term “proliferome”, which is based on two major prerequisites: compartmentalization and protein expression. The modular bottom-up approach is based on four hierarchical levels, namely systems, modules, parts and molecular entities. The major focus of the current thesis is growth (increase in the area and volume of a single cell), while accompanying and underlying research topics (such as compartmentalization) are discussed too.

1.2 Strategies to achieve membrane expansion

1.2.1 Natural growth

Cell growth is the process by which cells accumulate mass and increase in size. There are different examples in nature how cells can grow. For example, animal cells can increase in size by continued DNA replication in absence of cell division (endoreplication of megakaryoblasts), by accumulating intracellular lipids (adipocytes), or by increasing their macromolecule content without increasing their DNA content (neurons and cardiac muscle cells) (9). Increase in cell size can be from 1.4 to 5× in diameter (from 20 to 100 μm and from 85 to 120 μm for megakaryoblasts and adipocytes, respectfully (9)).

For growth of the cell membrane, newly synthetized lipids have to be transferred to the outer membrane. In eukaryotic cells, endoplasmic reticulum is the main site for lipid synthesis. Because of their hydrophobic

nature, most lipids cannot be effectively transferred by free diffusion from one compartment to another and must therefore rely on active mechanisms to facilitate intercompartmental transport (Figure 1). There are three basic mechanisms: 1) membrane transport that involves the budding of vesicles or tubules from donor membranes and subsequent fusion with acceptor membrane, 2) cytosolic carrier proteins for transferring lipids between the compartments, 3) bringing of donor and acceptor membranes into close proximity and transfer of lipids via membrane contact sites (10).

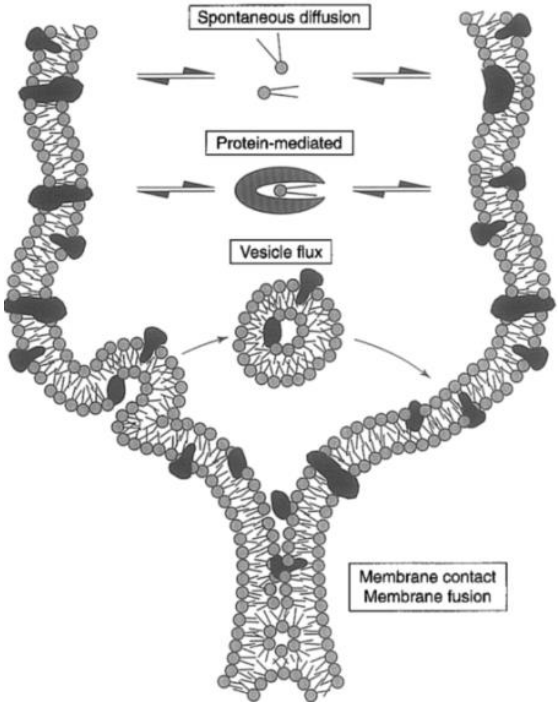

Figure 1. Transfer of phospholipids between membranes. Spontaneous migration of lipids through the aqueous compartment is only effective when the respective lipid is sufficiently water soluble, which is rarely the case (e.g., for lysophosphatidic acid). Protein-catalysed lipid transfer, vesicle-driven transport of lipids and lipid migration via membrane contact are possible mechanisms for transfer of glycerophospholipids. As an example of the latter, a subfraction of the endoplasmic reticulum (membrane fraction associated with mitochondria) appears to interact specifically with the mitochondrial outer membrane. Figure adopted with permission from ref. (11).

1.2.2 Synthetic growth

According to Gánti's chemoton model, life should fundamentally and essentially have three properties: metabolism, self-replication, and a bilipid membrane (12). The metabolic and replication functions together form an autocatalytic subsystem necessary for the basic functions of life, and a membrane encloses this subsystem to separate it from the surrounding environment (12). The model includes an amphiphilic molecule that is spontaneously produced and is incorporated into the structure. Roughly following those principles, researchers have experimentaly tackled separate or combined propreties of the chemoton. Below

are discussed examples of incorporation of membrane building blocks uptaken from the environment or synthetized by the system alone.

Growth of artificial compartments, indicating volume increase and membrane expansion, has initially been approached by the uptake of fatty acids into phospholipid compartments (liposomes) in alkaline solution (13). The drawback of such a growth approach is that such compartments lose their chemical identity, stability (fatty acid membranes are only stable within a narrow pH range, i.e., ~ 7–9) and have increased permeability. Nevertheless, this approach has a relevance in mimicking the prokaryotic world, where fatty acids, synthetized in cytosol, are uptaken by the cell membrane for coupling to the glycerol backbone and the head group. Later studies focused on achieving phospholipid synthesis followed by their uptake into liposomes, but encountered uptake difficulties. Such an example is the development of an *in vitro* phospholipid biosynthesis pathway based on a cascade of eight enzymes, starting from fatty acid building blocks and glycerol 3-phosphate, whereby the expansion of liposomes was not attributed to phospholipids uptake, but rather to the partitioning of the oleic acid into the membrane (14). The spontaneous incorporation of lipids is unlikely because phospholipid membranes are stable over wide range of amphiphilic concentrations, pH, and temperature. The latter was resolved recently by Blanken et al. (2020) by direct synthesis of phospholipids inside the membrane. In the latter study, acyl chain precursors are converted via five-enzyme pathway into newly synthesized membrane-bound phospholipids (15).

Vesicle fusion has been nearly the only rewarding method to observe visible growth of liposomes with natural chemistry (16), and next to proteins, has been induced by physicochemical triggers like charge (17) or osmotic tension (18). Moreover, regardless of the precise biological blueprint, the uptake of preformed membrane building blocks is conceptually equivalent to the uptake of membrane precursors and thus fully valid synthetic approach. Various fusion mechanisms of liposomes have been explored based on charge-charge interactions, charge naturalization, dehydration of membrane surface, and destabilization of lipid bilayer (discussed in Chapter 1.3.4.2). By charge-mediated fusion between anionic GUVs and cationic LUVs (17) increase in membrane surface was observed, whereby growth was limited by charge neutralization. Recently, growth of lipid GUVs, up to doubling its volume, was achieved by multiple membrane tension-mediated fusion events with SUVs (18). Another GUVs-SUVs fusion and consequent 16 % growth in diameter was achieved by combination of oppositely charged membranes, protein zein reconstituted in GUVs and detergent to destabilize the SUV (19). Membrane expansion via vesicle fusion is limited by rounds of fusion. The mean diameter expected after binary fusion could be calculated according to $d = ({d_1}^2 + {d_2}^2)^{\frac{1}{2}}$ for the area constraint. This expression assumes that if two vesicles fuse, the size of the fused vesicle will be defined by a sphere with the sum of the two vesicle areas. Nevertheless,

due to volume constraint imposed by the osmolarity, the volume is the one that defines the final size, and therefore the expected mean diameter should be $d = ({d_1}^3 + {d_2}^3)^{\frac{1}{3}}$. This means, for example, that two 100 nm vesicles would have after fusion a mean diameter of 126 nm; and 1.3× increase in size being below increase observed during growth of natural cells (see 1.2.1). Therefore, for more pronounced vesicle growth, multiple fusion rounds are required.

Thus far, growth has been predominantly studied and realized in liposomes due to the biological relevance of the membrane building blocks and the resulting natural environment for membrane proteins. However, those phospholipid compartments have limited stability (20); they are prone to aggregation, oxidation and hydrolysis, which shortcoming is relevant in the creative context of synthetic biology and biotechnology. To increase the stability and functional lifetime, while potentially introducing entirely novel functionalities, lipids have been completely or partially substituted with synthetic polymers (21-23). Growth of polymer compartments via uptake of polymer molecules was tackled in a single study so far and is limited to the specific polymer chemistry; meanwhile, growth via vesicle fusion holds a great promise and the existing examples are mentioned in Section 1.3.4.2. The example of the former mechanism is polymersome growth via polymerization-induced self-assembly (24). Polymerization was an activator of growth in another study performed on neither lipid nor polymer vesicles: sodium bis-(2-ethylhexyl) sulfosuccinate (AOT) molecules in the external solution were selectively incorporated into the membrane of AOT-emeraldine salt vesicles during enzymatic polymerization occurring on the surface of the vesicles, leading to vesicle growth (25).

1.3 Membrane-enclosed compartments

1.3.1 Biomimetic membranes

Glycerophospholipids represent the most abundant class of lipids in mammalian cells. The most common head group in mammalian cells is choline and the respective phospholipid class, phosphatidylcholines, makes up approximately half of the total cellular phospholipids (10). Phosphatidylethanolamines, -serines and -inositols are other common mammalian glycerophospholipid classes. A single cell may contain thousands of different phospholipid molecules and the functional significance of this complexity is only slowly revealing itself. Man-made vesicles exhibit much lower complexity – typically, membranous systems are limited to one (26), two (27) or three components (28).

By far the most commonly utilized vesicles in bottom-up synthetic biology are vesicles made completely of lipids (liposomes). But as mentioned above, bottom-up synthetic biology offers unique possibility to introduce new materials from the beginning (starting with compartmentalization) and lately vesicles made

of polymer/lipid mixtures, polymers, or even mixtures of two different types of polymer have been frequently used for biomedical studies (29, 30) or construction of artificial organelles (21, 31, 32). Polymer vesicles (polymersomes) have a similar structure to liposomes and result from the self-assembly of polymers into monolayers (triblock copolymers) or bilayers (graft or diblock copolymers) (20) (Figure 2). Polymersomes have been mainly used in the context of drug delivery (33, 34) including showcases like stimuli-responsive release (35) and cell targeting (36). The covalent bonds in polymers are generally more difficult to break than the ester bonds in phospholipids and degradation of repeating units would have a lower impact on the overall stability (20). In addition to chemical stability (37, 38), synthetic polymers offer increased resistance against aggregation (37, 39), broader chemical versatility (20), and increased tunability (40, 41). It is also possible to modify the size and morphology of the compartments by changing the hydrophilic/hydrophobic ratio (37, 42) or to functionalize the surface, e.g., for adhesion (43).

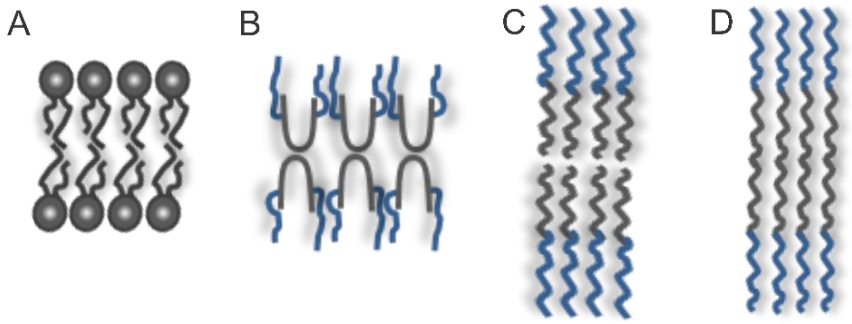

Figure 2. Structure of the membranes with different composition. (**A**) Lipid bilayer, (**B**) graft copolymer bilayer, (**C**) diblock copolymer bilayer, (**D**) triblock copolymer monolayer.

Amphiphilic assemblies serve another key role beyond compartmentalization; they act as interfaces for interactions with peripheral membrane proteins, and accommodate integral membrane proteins. The latter take part in essential cellular processes such as selective transport and energy conversion, e.g., oxidative phosphorylation, in which electron transport chain (ETC) proteins pump protons across the membrane and the resulting proton-motive force (PMF) drives the synthesis of adenosine triphosphate (ATP). High PMF and reduced ETC have been linked to increased production of reactive oxygen species (ROS) in mitochondria (44, 45). ROS can induce peroxidation of lipids (unsaturated fatty acids) or cleave ester bonds and thus disrupt the bilayer arrangement, which may in turn inactivate membrane proteins and increase the permeability (46, 47). With respect to this, partially or completely replacing the phospholipids with synthetic polymers, which are less prone to oxidation and hydrolysis, would increase the overall system stability.

Polymersomes and hybrid vesicles used in this thesis were made of poly(dimethylsiloxane)-*graft*-poly(ethylene oxide) (PDMS-*g*-PEO). PDMS-*g*-PEO is an amphiphilic copolymer, where PDMS has hydrophobic and PEO hydrophilic character. The incorporation of both hydrophobic and hydrophilic groups into a synthetic polymer is a potent way of controlling its surface and interfacial properties. PDMS-*g*-PEO copolymers form micelles in water with PDMS as the core and PEO as the corona (48). The polymer can also form vesicular structure with a membrane thickness of 5 nm (49), very close to that of liposomes (and natural membranes). As component of hybrid vesicles it has been previously studied in correlation to fluidity and thickness of the hybrid bilayers (49). This polymer has in the past been shown to have biomedical application – it was investigated as surface modifying agents for pacifying hydrophobic polymer surfaces in blood contacting applications (50).

1.3.2 Formation of nano- and microcompartments

Cell size is highly variable among organisms, with some algae such as *Caulerpa taxifolia* being a single cell several meters in length (51) and microalgae *Micromonas pusilla* only 1–2 μm long (52). Plant cells are much larger than animal cells, and protists such as *Paramecium* can be 330 μm long, while a typical human cell might be 10 μm. The size of bacteria ranges from ~ 0.3 μm for obligate intracellular photogenic members of the genus *Mycoplasma*, to ~ 600 μm for *Epulopiscium fishelsoni*, a Gram-positive commensal inhabitant of Surgeonfish guts, and 750 μm for *Thiomargarita namibiensis*, a chemilithotropic Gram-negative bacterium (53). Hence various techniques were developed to mimic cell membranes and form artificial vesicles in various sizes, ranging from a few nanometers to hundreds of micrometers. Small unilamellar vesicles (SUV, < 100 nm) or large unilamellar vesicles (LUV, 100–1000 nm) are largely developed for medical purposes (54, 55), but lately also for construction of artificial organelles (21, 32). In cell mimicking technologies, giant unilamellar vesicles (GUVs, > 1 μm) are arguably of the highest interest as eukaryotic cells are typically 10–100 μm in diameter.

SUVs and LUVs are typically formed via freeze-thaw cycles of resuspended amphiphiles (lipids/polymers) film to reduce vesicle multilamellarity, followed by extrusion through membranes with various pore sizes (50–800 nm) to unify their size. Meanwhile, various methodologies were developed for formation of GUVs and can be categorized as 1) emulsion-based techniques and 2) solvent-free techniques. The first category may be used in to microfluidics (56) which enables encapsulation of complex entities, control over each leaflet of the vesicle to achieve membrane asymmetry and high throughput of monodispersed vesicles. Another technique from the first category is emulsion-phase transfer, which has been also used to establish complex protocellular systems (8, 57). The major drawback of those solvent-displacement methods is the contamination of the artificial membrane with solvents and other additives (58). Microfluidic setups use mixtures of different components (surfactant, sugar, polyelectrolytes, nonamphiphilic polymers, etc.) for

stability, formation and dewetting, which remains in the membrane or in the vesicular lumen. The presence of those additives alters the physiochemical properties of the membrane and compromises the quality and reproducibility of the results, as they might interfere for example with a reaction that should take place inside the GUV or hinder the activity of membrane proteins. To achieve better biocompatibility, solvent- and additivies-free methodologies for the formation of GUVs are preferred. Nevertheless, they also have drawbacks, such as lower controllability, thus generating polydisperse GUVs with broader size distributiona compared to e.g., microfluidics. Furthermore, generation of asymmetric membranes is more challenging, although some progress has been made in this direction (27). In the solvent-free techniques, amphiphiles dissolved in organic solvent (chloroform or chloroform/methanol mixture) are applied onto a surface (glass, Teflon, electrodes), dried under nitrogen stream or in desiccator to form a thin film free of solvent, and then immersed in aqueous media. Hydration without any extra input is called gentle hydration and requires long swelling times (typically several hours to days) for GUVs formation. Another type of solvent-free hydration involves a water-soluble polymeric (agarose or polyvinyl alcohol) support, the so called gel-assisted hydration, which requires typically shorter swelling times (up to 1 h) but the gel contaminates the membrane, which alters its physical proprieties (59, 60). Lately, most commonly used solvent-free method in bottom-up synthetic biology is electroformation, where hydration involves electric current. The latter is more commonly utilized than gentle hydration not just due to the shorter swelling times, but also due to the formation of a lower amount of multilamellar deformed vesicles (61).

Some techniques from both categories were applied for the formation of not just lipid, but also polymer and hybrid GUVs. For example, microfluidics was utilized to form purely polymer GUVs (62), meanwhile, electroformation was applied for the formation of polymer and polymer/lipid hybrid GUVs (49); the latter technique was utilized also in this thesis. Each research group designs their own home-made electrochamber, whereby properties, such as the volume of the hydration chamber, the dimension of the electrodes, etc. can highly vary. This makes the adoption of previously published protocols almost non-realistic, in particular when not just chamber parameters change, but also membrane and media composition. Hence protocol optimization for successful electroformation can be lengthy and cumbersome, as many different combinations of conditions have to be tested.

1.3.3 Reconstitution of membrane proteins

1.3.3.1 Reconstitution of membrane proteins in nanocompartments

While there are three main approaches for insertion of membrane proteins into LUVs, i.e., organic solvent-mediated reconstitution, direct incorporation into preformed liposomes and detergent-mediated reconstitution, the last one is most commonly used, in particular for energy-transducing membrane proteins,

because of its high efficiency and retention of protein activity. The reconstitution is performed in presence of detergent at concentrations of the vesicle saturation point or higher, i.e., above the vesicle to micelle transition (63). The fluid membranes of the liposomes are comparatively easy to solubilize (low detergent concentrations are needed), while the degree of solubilization for reconstitution is determined for the individual membrane protein. On the other hand, in the case of the more rigid membranes of polymersomes, the solubilization requires higher detergent concentrations. For example, for efficient micellization of PBD-*b*-PEO polymer/lipid mixture with sodium cholate, 8.6 times higher concentrations were used than for reconstitution of bo_3 oxidase in PC and PDMS-*g*-PEO:PC vesicles (21, 64). In case of octyl glucoside, 16 times higher concentration was needed for reconstitution in block copolymer LUVs than for reconstitution of bo_3 oxidase in graft copolymer LUVs (21, 64). In cases when micellization of block polymer/lipid mixture is possible, the transition to vesicles after detergent removal is difficult to achieve (64). For PDMS-*g*-PEO graft copolymer various detergents (including mild ones as sodium cholate, which do not damage sensitive proteins) can be used and only very low concentration are needed, even much lower than for solubilization of liposomes (21). This is most likely possible due to the intrinsic surfactant proprieties of PDMS-*g*-PEO (65).

To obtain detergent-free proteoLUVs, dialysis, size exclusion chromatography, absorption by polystyrene beads (Bio-Beads), or cyclic sugar oligomers (cyclodexytrins) can be utilized. In 2021 novel reconstitution method was presented – gradient reconstitution (GRecon) (66) where detergent removal, lipid reconstitution, and gradient centrifugation is combined in one single step. While method shows great promise, proteins activity retention has yet to be demonstrated. Regardless to the chosen protocol, the reconstitution process, in which detergent is replaced by lipid (or polymer), must be carefully controlled, as otherwise the proteins tend to denature and aggregate (67).

1.3.3.2 Reconstitution of membrane proteins in microcompartments

To assess the functionality of membrane proteins, the latter are predominantly integrated in SUVs and LUVs. However, the easer manipulation and optical access to vesicles in the micrometer range significantly expands the analytical possibilities and allows for studying membrane effects at cellular dimensions and in greater detail. Thus, protein-functionalized GUVs serve as superior model systems from both fundamentally biological and cell-mimicking perspective.

There are two common techniques for reconstitution of membrane proteins into microcompartments: emulsion-transfer method and electroformation or its modification dehydration/electroformation (also named fusion/electroformation). Due to potential membrane impurities when GUVs are prepared by emulsion-based techniques (mentioned in 1.3.2), fusion/electroformation is typically preferred.

Nevertheless, high protein orientation control has been demonstrated for the former technique (90 % of photosynthetic reaction centers retained the physiological orientation (68)). Meanwhile, different membrane proteins have been incorporated into GUVs via fusion/electroformation, such as voltage-gated ion channels (69), mechanosensitive channels (70), transporters (70), photoconverters (bacteriorhodopsin (bR) (71), proteorhodopsin (72), plant-derived photosystem II (72)), ATPases (71), and SNARE proteins (73-75). Those protein-functionalized GUVs were formed by electroformation by rehydrating partially dried (and fused) proteoSUVs, as a substitute for the lipid/polymer film. Membrane proteins can be reconstituted also directly into GUVs containing detergent, such GUVs are grown via electroformation from lipid/detergent film (e.g., reconstitution of F_1F_O-ATPase (76), Cu-ATPase (77), bR (78)). A simplification of the later approach is reconstitution by detergent dilution, where membrane proteins in detergent micells are added to preformed detergent-free GUVs (79). The latter approach has low control over protein orientation and often insertion efficiency is limited. A different approach to obtain GUVs with membrane proteins is to utilize membrane fusion as delivery mechanism; for example, bo_3 oxidase and F_1F_O-ATPase were previously delivered into lipid GUVs via charge-mediated fusion (80). Until now, various membrane proteins of the respiratory and photosynthetic ETC have been reconstituted in phospholipid microcompartments, meanwhile, membrane proteins reconstitution in polymer membranes is still rare and usually limited to nano-sized compartments and less pretentious porins and channels (reviewed in (81)). In most cases, block copolymer membranes are too thick (2–10 fold thicker than the lipid bilayer), viscous and rigid for the functional insertion of large and complex membrane proteins (22, 81, 82). While in some cases the functional reconstitution was transparently demonstrated (proteorhodopsin in PMOXA-PDMS-PMOXA vesicles (83)), for other attempts the protein functionality may require further confirmation (31, 84). The latter example is co-reconstitution of bR and F_1F_O-ATPase in PEtOz-PDMS-PEtOz vesicles, where bR was incorporated in the form of purple membrane (31): due to the high lipid content of purple membranes (10 lipids per bR (85)), it is likely that F_1F_O-ATPase was incorporated into lipid portion of these lipid/polymer hybrid vesicles instead of polymer one. Further analysis would also be required in the case of reported reconstitution of complex I in PMOXA-PDMS-PMOXA vesicles (84); while electron transfer was clearly demonstrated, proton pumping activity of complex I was not.

1.3.4 Fusion of biomimetic compartments

1.3.4.1 Natural fusion mediators

In eukaryotic cells, membrane fusion mediated by N-ethylmaleimide-sensitive factor (NSF)-attachment protein receptors (SNAREs) (86) plays a crucial role in various cell functions, such as exo- and endocytosis, membrane remodeling, expansion, cell division, signal transduction and intracellular trafficking. Three

SNARE proteins, target membrane proteins, SNAP-25 and synthaxin (t-SNARE) and secretory vesicle-associated membrane proteins (v-SNARE) or VAMP were discovered in the 1990's and suggested to be the minimal fusion machinery (87, 88). The 2013 Nobel prize in Physiology and Medicine was awarded to James Rothman, Randy Schekman, and Thomas Südhof for their discoveries of a machinery regulating vesicle traffic. In addition to fusogenic proteins, Ca^{2+} is another important mediator and usually participates in fusion events together with SNAREs (e.g., Ca^{2+} triggers neurotransmitter release by synaptic vesicle exocytosis (89)). Primarily due to the polar phosphate head groups, native vesicles exhibit a significant negative surface charge, which produce a repulsive force, preventing aggregation and fusion of apposing vesicles. SNAREs bring opposing bilayers close to within a distance of 2-3 Å, thus allowing Ca^{2+} to interact with the phospholipid head groups, and bridging them (90). The bound Ca^{2+} then leads to the exclusion of water between the bilayers at the bridging site, allowing lipid mixing and membrane fusion. An accompanying actor in charge-related mechanisms are anionic phospholipids such as phosphatidylinositols and phosphatidylserine (PS) (90); for example, redistribution of PS in the outer leaflet is required during apoptosis and syncytial fusion (91). In addition to fusion occurring inside the same organism, viruses developed their own mechanisms to insert their genetic material into the host cell (92). All those natural fusion facilitators offer a diverse toolbox, which can be utilized in bottom-up synthetic biology to engineer artificial cells and mimic living features. The mechanisms behind salt (93-96), charge (17, 97, 98) (Figure 3A), SNARE (99, 100) (Figure 3D) and viral (101, 102) fusion of phospholipid compartments are well characterized and have been employed for the construction of life-like functional systems: integral membrane proteins have been co-reconstituted by SNAREs (103) and delivered to vesicles via charge interactions (80, 104), while Mg^{2+} facilitated the formation of droplet-stabilized protocells (105). On the other side, fusion of polymer or polymer/lipid hybrid compartments mediated by natural fusion mediators has not been yet well explored. Recently, a breakthrough was achieved, where we demonstrated that polymer and hybrid LUVs can undergo SNARE-mediated fusion (106), meanwhile GUV-LUV or GUV-GUV fusion of those compartments was not tackled prior to this work.

1.3.4.2 Non-natural fusion mediators

To overcome the energy barrier of the different fusion intermediate steps, structural reorganization of large molecules like proteins/peptides supplies the required driving force. On the other side, small molecules/ions do not share this advantage and hence fusion is expected to be different from that induced by proteins/peptides. Apart from protein and peptides, there are lipids, small organic ligands, metal ions, polymers, and drugs that can act as fusogens (107). In addition to Ca^{2+}, a natural fusion mediator, Mg^{2+} was also found to induce membrane fusion effectively (95, 108). Both Ca^{2+} and Mg^{2+} can induce fusion of anionic PS vesicles or PS:PC mixed vesicles (Figure 3B). In addition to increased membrane surface tension

resulting in lateral compressibility and structural defects, PS headgroup readily absorbs divalent cations, forming covalent bond through the carboxylate oxygen of the PS headgroup (107).

Isolating, purifying and reconstituting active SNARE machinery requires skills from protein purification to membrane protein reconstitution. Furthemore, assembly and fusion kinetics in these systems are highly complex; and it is difficult to differentiate between parameters affecting nucleation and zippering of the helix bundle and the downstream events of membrane contact, hemifusion, and fusion. Simpler model systems aim at reducing complexity in membrane fusion, and can often present a more convenient option. A minimal SNARE mimetic system for membrane fusion are coiled-coil forming peptides 'K' enriched in lysine and 'E' enriched in glutamic acid (109, 110). They form heterodimer coiled-coils, with a hydrophobic core surrounded by pairs of oppositely charged residues on either side (109). Although, the peptides E and K have been shown to produce vesicle fusion, the fraction of successful fusion events is typically low compared to fusion induced by SNARE complexes. Another SNARE-mimetic system consists of hybrids between the transmembrane domain/linker segments from natural membrane-bound SNARE proteins and peptide nucleic acid (PNA) recognition motifs (111, 112). A simpler model system is also complementary lipid-anchored DNA oligonucleotides, which allow sequence-specific hybridization to bring membrane surfaces into close proximity (113, 114) (Figure 3D). Action of fusion proteins has been mimicked also by synthetic ligand molecules that are connected to lipid-like membrane anchors; for example, amphiphilic ligands with a β-diketone head group that can be cross-linked by Eu^{3+} ions (115), lipids containing complementary hydrogen bonding head groups (barbituric acid (BAR) and 2,4,6-triaminopyrimidine (TAP)) (116), and synthetic bipyridine lipoligands Bn bearing a bipyridine unit as head group that form complexes MBn and MBn_2 in presence of Ni^{2+} or Co^{2+} metal ions (117).

On a different note, fusion of lipid membranes can be also photoinduced. Such example is fusion of lipid vesicles through the use of a photosensitive surfactant containing an azobenzene moiety (AzoTAB) (118). Fusion can be also triggered by the application of a strong DC pulse (115) (Figure 3C), via ligand-mediated ion interactions (115), or through localized nanoparticle-mediated (119) or laser-mediated heating (120).

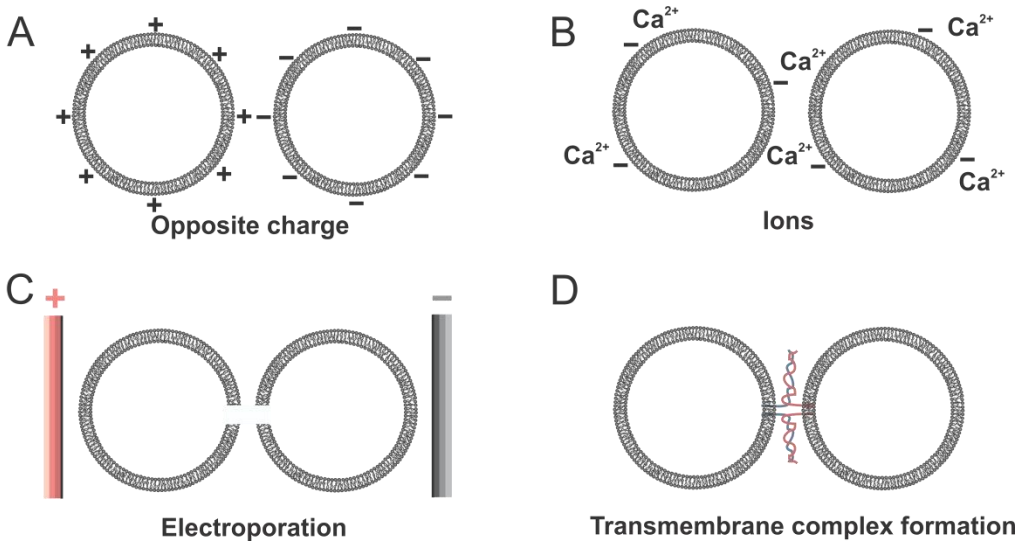

Figure 3. Some of the commonly utilized fusion mechanisms. (**A**) Fusion of oppositivly charged vesicles. Commonly utilized cationic lipid is 1,2-dioleoyl-3-trimethylammonium-propane (DOTAP), and anionic one 1,2-dioleoyl-sn-glycero-3-phospho-L-serine (DOPS) or 1,2-dioleoyl-sn-glycero-3-phospho-(1'-rac-glycerol) (DOPG). (**B**) Fusion of vesicles containing anionic lipids (e.g., PS) in presence of divalent cations (Ca^{2+} or Mg^{2+}). The negative PS headgroup readily absorb the positive divalent ions, forming a covalent bond through the carboxylate oxygen of the PS headgroup (107). (**C**) Electrofusion relies on poration of two opposing membranes exposed to strong electric fields. (**D**) Fusion can be mediated by the formation of transmembrane complex: SNAREs complex or zipper-like DNA-based mimics of SNAREs proteins (sequence-programmable base-pairing of DNA). While in the former case SNAREs are reconstituted into membrane with their hydrophobic part, in the latter case DNA is tagged by cholesterol or tocopherol (121) in order to self-assemble into the membrane.

Polymersomes can be morphed in various shapes, including stomatocytes (122), and undergo orchestrated events of SNARE-mediated fusion (106). Yet the fusion of polymersomes by simpler physicochemical cues is heavily underexplored. One of the few existing examples reported fusing poly(trimethylene carbonate)-poly(L-glutamic acid) vesicles below the melting temperature of the hydrophobic block and ascribed it to conformational change and variation of membrane packing (123). In this regard, freeze-thaw cycling of lipid protocells was also investigated as an environmental driver for exchange of nucleic acids (124). Upon irradiation, fusion of poly(N-isopropylacrylamide)-*b*-poly(6-[4-(4-methylphenyl-azo) phenoxy] hexylacrylate) (PNIPAM-*b*-PAzoM) giant vesicles was observed (125), caused by the increased polarity of the isomerized azobenzene units on the hydrophobic block (125). In parallel, LUVs of poly(ethylene oxide)-poly(butadiene) blocks (PBd-*b*-PEO) were shown to form giant vesicles upon agitation in presence of NaCl solutions (126). At time of writing the thesis, there was no existing example of protein-free fusion of polymer/lipid hybrids vesicles.

1.3.4.3 Fusion intermediates

Protein-mediated and protein-free pathway for fusion of lipid membranes involves two important intermediates: hemifusion structures and fusion pores (127, 128). Hemifusion is characterized by connected

outer leaflets of apposed membranes, the inner leaflets remaining separate (Figure 4Aiv) (127). This transient state can either dissociate, leaving two separate membranes, or proceed to a fusion pore (129, 130), the latter being a connection involving both outer and inner leaflets (Figure 4Av) (127). In other words, the fusion pore establishes an aqueous connection between the two inner volumes of the fusing vesicles (127).

The lipid composition, which determines the spontaneous curvature of membrane monolayers (Figure 4B), plays a role in the propensity of lipid bilayers to hemifuse and develop fusion pores (to bend into fusion intermediates) (131). Lipids of nonzero spontaneous curvature can either promote or inhibit formation of a particular fusion intermediate, depending on its net curvature (131). Another fusion condition is the establishment of a sufficiently close inter-bilayer contact (trans-bilayer distance of less than 1 nm), which can be achieved by a direct dehydration (132). There is also dependence of fusion on liposome size, with the smallest liposomes being the most fusogenic (133), where membrane tension plays an important role (in particular, in driving the evolution of hemifusion structures toward fusion pore formation and expansion) (134).

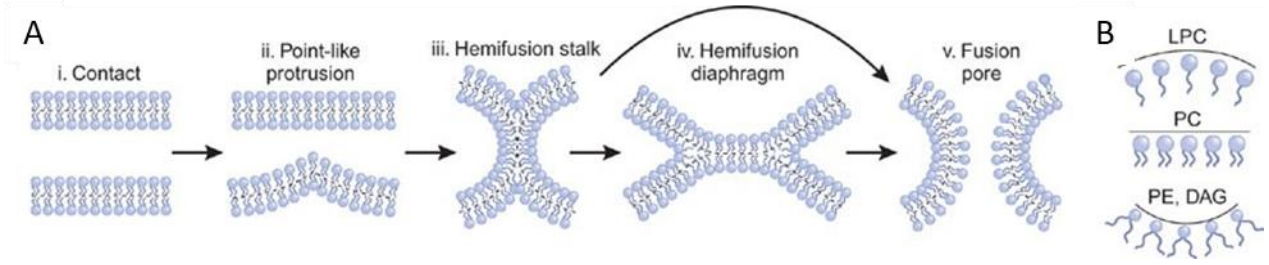

Figure 4. Fusion-through hemifusion pathway of lipid bilayer fusion. (**A**) (i) Pre-fusion contact. (ii) A point-like membrane protrusion minimizes the energy of the hydration repulsion between the proximal leaflets of the membranes coming into immediate contact. (iii) A hemifusion stalk with proximal leaflets fused and distal leaflets unfused. (iv) Stalk expansion yields the hemifusion diaphragm. (v) A fusion pore forms either in the hemifusion diaphragm bilayer or directly from the stalk. Dashed lines show the boundaries of the hydrophobic surfaces of monolayers. (**B**) Different lipids spontaneously form monolayers of different curvatures and, thus, demonstrate different effective molecular shapes. Monolayers formed by inverted cone–shaped lysophosphatidylcholine (LPC) and by cone-shaped phosphatidylethanolamine (PE) and diacylglycerol (DAG) bulge in the direction of the polar heads and in the direction of the hydrocarbon chains, respectively. Cylindrical phosphatidylcholine (PC) forms an almost flat monolayer. Figure adopted with permission from ref. (127).

Due to the distinct structural difference between the copolymers and the lipid molecule, it is anticipated that triblock copolymer vesicles (with monolayer membrane, Figure 2B) and even diblock or graft copolymer vesicles (with bilayered membrane, Figure 2B,C) may exhibit different fusion behavior when compared with liposomes. While fusion intermediates for lipid membranes have been well studied, progression of polymer and polymer/lipid hybrid vesicle fusion is widely unexplored. Recently, we proposed a SNARE-mediated fusion pathway for PDMS-*g*-PEO and PDMS-*g*-PEO:PC membranes (106).

Interestingly, the pathway differed for polymer and hybrid membranes: in the first case, vesicle docking proceeded into point contact, narrow hemifusion, diaphragm expansion, membrane thinning at the juncture, followed by pore opening, while in the second case we observed long contact between the lipid-rich domain of one fusing vesicle and polymer-rich domain of another, which proceeded into crosswise membrane mixing ("hybrid zippering"), hemifusion, and pore opening in the more central region of the juncture (106). Similarly, by examining a large number of TEM micrographs, the intermediate structures in the fusion process of poly(styrene)-*b*-poly(acrylic acid) (PS-*b*-PAA) polymersomes have been obtained (135). In the latter study, the center wall between the two adhering polymersomes was destabilized and resulted in an asymmetric detachment, followed by retraction of the thickened part of the center wall into the outer wall, and finally smoothing of the outer wall to give uniform vesicles (135). Interestingly, pore opening at the juncture, instead in the center, seems to be common to graft and diblock copolymer vesicles. Fusion progression of triblock copolymer ($C_1R_5C_2$) vesicles has so far been addressed only via simulations (136) and was divided in four stages: kissing, adhesion, hemifusion, and fusion, whereby each stage had specific characteristics differing to the ones for diblock copolymer (R_5C_2) vesicles (137).

1.3.4.4 Monitoring membrane fusion

Initial intermediate formation of vesicle fusion, i.e. docking, can be monitored via absorption at 272 nm (104). Vesicle aggregation increases the absorption, which indicates vesicle docking. The following steps, such as stock formation and hemifusion diaphragm expansion are typically monitored via fluorescence resonance energy transfer (FRET) between two lipid dyes (typically donor 1,2-dioleoyl-sn-glycero-3-phosphoethanolamine-N-(7-nitro-2-1,3-benzoxadiazol-4-yl) (ammonium salt) (PE-NBD) and acceptor 1,2-dioleoyl-sn-glycero-3-phosphoethanolamine-N-(lissamine rhodamine B sulfonyl) (ammonium salt) (PE-Rho) (17, 80, 138)), hydrophobic dye dequenching (e.g., 1,1′-dioctadecyl-3,3,3′,3′-tetramethylindotricarbocyanine iodide (DiR) (139) or Marina Blue-labeled lipids (140)), or by the fluorescence lifetime of a membrane-located probe (e.g., 1-palmitoyl-2-[2-[4-(6-phenyl-trans-1,3,5-hexatrienyl)phenyl]ethyl)carbonyl)-3-sn-phosphatidylcholine (DPHpPC) (133)), where total membrane mixing is obtained by vesicle solubilization.

To determine if fusion pore opening and complete vesicle fusion occurs, various content mixing assays have been used in literature based on either fluorescence complex formation or dye dequenching. For instance, study of content mixing during SNARE-mediated LUV-LUV fusion was performed by monitoring FRET between PhycoE-Biotin and Cy5-Streptavidin (140) and for GUV/LUV-LUV fusion via calcein (138) or sulforhodamine B (SRB) dequenching (141). For lipid-anchored DNA oligonuceleotides-mediated SUV-SUV fusion content mixing was determined with Tb^{3+}/dipicolinic acid (DPA) assay (113).

Meanwhile, for charge-mediated fusion Co^{2+}-calcein/EDTA assay for LUV-LUV fusion (98, 104) and calcein dequenching for GUV-GUV fusion (142) was applied.

Finally, increase in vesicle size upon fusion of LUVs can be determined via dynamic light scattering (DLS) (106, 126), quasi-elastic light scattering (QELS) (133), tunable resistive pulse sensing (TRPS) (80) or cryo-TEM (106, 133). Furthermore, cryo-TEM is applied to reveal fusion intermediates (106). Meanwhile, increase in GUVs size upon fusion with LUVs or GUVs can be directly observed with confocal (17) or epifluorescence microscopy (118, 123).

1.3.5 Biophysical parameters of membranes relevant for growth

1.3.5.1 Bending rigidity

The bending rigidity (κ), given in units of k_BT (product of the Boltzmann's constant and the absolute temperature, 4×10^{-21} J), is an important membrane characteristic with implications on cellular mimics as it reflects the resistance to deformation (143), which vesicles may experience during division, fusion or osmotic shock. Furthermore, there is a common notion that increased rigidity impedes the reconstitution and most importantly the activity of complex membrane proteins. Therefore, bending rigidity and its change upon membrane protein insertion is important characteristic for bottom-up construction of artificial cell, from integration of modules via fusion and compartment growth to functionalization of compartments with membrane proteins (formation of functional parts and modules). The bending rigidity of fluid lipid membranes is typically in the order of 10–20 k_BT (144), while polymersomes can exhibit various stiffness (up to 400 k_BT (20)), depending on the membrane thickness. Commonly used block polymersomes have usually higher rigidity, for example PEO-PBD (35 ± 6 k_BT (40)), but there are also block copolymers that form much softer membranes such as Pluronic L121 (PEO_5-PPO_{68}-PEO_5, ~ 3 k_BT (40)).

During the prefusion stage, merger of the contacting membrane surfaces requires the formation of some transient membrane discontinuities. The energy price of this stage includes the local membrane approach to almost zero distance against strong intermembrane repulsion, the energy of rupture of the merging monolayers, and the deformation energy of the monolayers accompanying their local approach and rupture (131). The latter parameter is partially determined by membrane bending rigidity – the bending energy F_{bend} as a function of deformation is $F_{bend} = \frac{1}{2}A\kappa(J - J_s)^2$, where A is the membrane area, J is total curvature ($J = \frac{2}{R}$) and J_s is the spontaneous curvature (131). This indicates that softer membranes will require lower bending energy and easier undergo prefusion stages, such as pointlike protrusion (Figure 4Aii). Meanwhile, the first intermembrane lipid connection, i.e., fusion stalk (Figure 4Aiii), combines deformation of bending, tilt, and splay of the monolayers. For the membranes of 1,2-dioleoyl-sn-glycero-3-phosphocholine (DOPC)

the predicted stalk energy is ~ 45 $\kappa_B T$, which exceeds by ~ 5 $\kappa_B T$ the characteristic thermal energy $F_{therm} \approx 40\kappa_B T$. In such case, the energy required for membrane rearrangements has to be delivered by the proteins (SNAREs exercise at the conclusive stage of fusion 5 $\kappa_B T$ (145) of mechanical work).

The approaches for determining bending rigidity can be classified in four categories: (i) methods based on the analysis of thermal fluctuations of the membrane of giant vesicles; (ii) techniques relying on measuring the force to actively bend their membrane typically employing micropipettes, optical tweezers, electric or magnetic fields, and light; (iii) approaches based on scattering techniques; and iv) molecular dynamic simulations (144). The most common method for measuring the membrane bending rigidity, which was also utilized in this thesis, is fluctuation analysis. It relies on time sequences of snapshots, obtained by optical microscopy, which are used to determine the mean square values of shape deviations around an equilibrium form (144). The latter provide the fluctuation spectrum of a membrane: $\langle u_q^2 \rangle = \frac{k_B T}{\kappa q_\perp^4 + \sigma q_\perp^2}$, where u(r) is the local displacement in the normal direction to the membrane with respect to its mean position, and $q_\perp$ is the wave vector corresponding to r, the projection of the position of a point of the membrane on the mean-plane (146). In membranes of protein-functionalized vesicles, the amplitude of height fluctuations can be dependent on non-thermal forces (147). Such example are nonequilibruium or active membranes: by light-activation of bR the height fluctuations were enhanced (147, 148), and F_1F_O-ATPase (in presence of K^+ gradient and K^+ transporter valinomycin) (76) and Ca^{2+}-ATPase (in the presence of ATP) (149) have been shown to modify the effective membrane bending rigidity.

1.3.5.2 Lateral diffusion

Diffusion is a fundamental process that is relevant over all scales of biology. How rapidly diffusion occurs is characterized by the diffusion coefficient D, a parameter that provides a measure of the mean squared displacement per unit time of the diffusing species (150). At the cellular level, measurements of D can provide important insights into how proteins and lipids interact with their environment, such as the binding of transcription factors with DNA and of proteins and lipids with membrane domains (151, 152). Lateral diffusion of lipids and proteins gives rise to what we call membrane fluidity, which refers to the membrane viscosity (η_m). The latter parameter can be calculated from the diffusion coefficient with the Saffman-Delbrück equation (diffusion molecules have to be simplified to cylinders with radius R): $D = \frac{k_B T}{4\pi d \eta_m}\left[ln\frac{\eta_m d}{\eta_s R} - \gamma\right]$, where k_B is Boltzmann's constant, T is the absolute temperature, d is the membrane thickness, η_s is the viscosity of the surrounding media, and $\gamma = 0.5772$ is Euler's constant (153).

Compartments for the artificial cell have to offer a suitable environment for membrane proteins, i.e., fluid and flexible membrane and thickness in the natural range (to avoid size mismatches, which may

compromise protein folding). Commonly used block copolymer membranes have significantly lower fluidity compared to lipid membranes (e.g., diffusion coefficients of 0.22 ± 0.06 $\mu m^2 s^{-1}$ for PBd_{46}-*b*-PEO_3 (154) vs. 10.0 ± 0.4 $\mu m^2 s^{-1}$ for DOPC (155)), which appears to be one of the main reasons for the hindered functionality of membrane proteins. Lateral diffusion has direct implications also on other potential scenarios in bottom-up synthetic biology, such as the assembly of protein monomers and clusters, fission and fusion for trafficking, as well as equal distribution of membrane constituents upon division. Furthermore, diffusion of membrane proteins leads to source of force fluctuations (156), which has an effect on membrane bending rigidity, and consequently on efficiency of first fusion stage (see 1.3.5.1). In the context of membrane fusion in nature, proteins provide specificity of fusion, but lipids are the one that confer the fluidity necessary for membranes to deform into configurations that lead to fusion (during fusion, lipids must temporarily leave the bilayer arrangement for a non-bilayer configuration). Increased membrane fluidity by oleic acid and other substances that mobilize the structure of the liposome membrane may induce erythrocytes to fuse (157). In contrast, myoblasts undergo a sharp decrease in membrane microviscosity, and shortly afterwards fuse rapidly to form multinucleated myotubes (158). Dramatic membrane fluidity changes are present also during cell differentiation (neurons tend to have the highest membrane fluidity at early time points emphasizing its correlation with plasticity and the need for this malleability during differentiation (159)).

Currently, biologists have at their disposal a wide range of fluorescence-based techniques to monitor the diffusion of biomolecules in cells, including single-particle tracking (SPT), fluorescence correlation spectroscopy (FCS), photoactivation and fluorescence recovery after photobleaching (FRAP) (160). Of these approaches, many require specialized equipment, analytical tools or probes. In contrast, confocal FRAP is one of the most accessible methods to measure apparent diffusion (or effective diffusion). In FRAP, the diffusion of a population of fluorescently labeled molecules can be studied by photobleaching the molecules contained within a user-defined region of interest (ROI), and then monitoring fluorescence recovery due to the exchange of bleached molecules within the bleach ROI with the surrounding reservoir of unbleached molecules (150).

Lipid packing can influence the fluidity of the membrane. Membrane disorder, a parameter describing lipid packing, is typically determined with amphiphilic fluorescent probes. A probe extensively used to determine the structural and dynamical features of lipid bilayers is 1,6-diphenyl-1,3,5-hexatriene (DPH). In particular, DPH fluorescence anisotropy is a parameter interpreted as a membrane microviscosity (viscosity in the bilayer interior) or fluidity (161). Interpretation of the fluorescence anisotropy is not straightforward as it provides information about the orientation and dynamics of the probe in the lipid bilayer. Laurdan is another common probe used to determine membrane fluidity (through Laurdan

aniosotropy) and membrane disorder (through generalized polarization, GP) (162). Its sensitivity to excitation and emission spectra to the physical state of the membrane arises from dipolar relaxation processes in the membrane region surrounding the Laurdan molecules. A low GP value corresponds to a higher fluidity and a higher GP value is associated with a more rigid membrane.

1.3.5.3 Surface charge

The surface charge of cell membranes differs between species, and is crucial for creation of lipid rafts, where the charge of the lipid head groups is important for protein uptake and cell signaling. Artificial membranes can be formed with lipids exhibiting different electrostatic charge. In general, if membrane constituents are not electroneutral, they will contribute to the surface charge of the membrane.

Zeta potential (ζ) is a popular method to measure the surface potential of extracellular vesicles, as well as artificial nano-sized vesicles, while used as an indicator of surface charge and colloidal stability. It is determined from measurements of electrophoretic mobility in a suspension, and its value depends on the nanomaterial properties (surface chemistry), the solution conditions (ionic strength and composition), and the theoretical model applied (163). The zeta potential of vesicles changes inversely with the buffer concentration and becomes less negative at acidic pH, and *vice versa* (164).

The net surface charge of vesicles, as indicated by the zeta potential, determines the stability of vesicle-vesicle and vesicle-medium interactions, including the tendency of the vesicles to aggregate. Typically, vesicle suspensions with zeta potential above ± 30 mV have good stability and are not prone to aggregation. Tuning the surface charge of artificial vesicles can be exploited to control their aggregation and their association with cells (165). Furthermore, vesicles surface charge is a key player in fusion of oppositely charged vesicles, and has an important role in prefusion stage (establishing contact, Figure 4Ai) during non-charge mediated fusion mechanisms. The bilayers, which do not carry an electric charge, tend to approach each other spontaneously up to the equilibrium distance of 2–3 nm (131). The initial distances between biological membranes are much larger, 10–20 nm, because of the electrostatic repulsion between the bilayers and the steric interaction of membrane proteins (131). In order to decrease electrostatic repulsion between same-charged artificial vesicles, salt can be added to the media, which neutralizes surface charge of the vesicles (106). Meanwhile, addition of salt would have due to decrease in electrostatic driving force an opposite effect on charge-mediated vesicle fusion (decrease in fusion efficiency (104)). On a different note, increase in membrane surface charge is associated with increase in bending rigidity (144). The latter occurs due to stronger repulsion in the bilayer plane, which effectively suppresses the membrane undulations and thus increases the membrane rigidity (144). Increased bending rigidty has a hindering effect on prefusion stage and stalk formation, as discussed in 1.3.5.1.

1.3.5.4 Passive proton permeability

Compartments involved in growth process are meant to be integrated with other functional modules, where membrane proteins are involved, and encapsulated artificial organelles and metabolic cascades should not leak uncontrollably from the compartment. There can be significant differences in water permeability of compartments, which plays an important role in adaptation to osmotic shock and regulation of concentration of encapsulated substances; for example, block copolymer vesicles have significantly lower permeability then lipid ones (1–10 vs. 10–100 μm s^{-1} (166)). Meanwhile, for reconstitution of the energy machinery, it is crucial that the compartments have limited proton permeability in order to sustain a gradient. Passive proton permeability partially determines the range of attainable electrochemical proton gradient values and it is specific to vesicle system used since it depends upon the nature of other ions present, the internal volume of the vesicles, membrane thickness (167), and the presence of incorporated protein (168). In vesicles with reconstituted proton pumps, active (determined by the number of pumping units) and passive (determined by membrane constituents) proton movement is present. Complex IV and a bacterial homologue, cytochrome *bo_3* oxidase from *Escherichia coli*, typically pump one proton per electron, therefore four protons per dioxygen molecule (169). The reduction of dioxygen is further coupled to the uptake/release of four charges (proton and/or electrons), adding up to a total of eight charges transported across the membrane for each dioxygen that is reduced (169). Upon establishment of ΔpH, transient membrane pores can randomly form (170), leading to increased passive proton permeability. However, steady-state proton electrochemical potential is only partially determined by the number of pumping units and proton passive permeability – retroinhibition of the pump by the proton gradient (back-pressure effect of ΔpH) also appears to be strong regulating factor (171). In order to synthetize ATP, a driving force for numerous cell reactions, proton pumps can be coupled in artificial vesicles to a ΔpH consumer, i.e., F_1F_O-ATP synthases (172). ADP is phosphorylated to ATP via the F_1F_O-ATPase reaction: $H^+ + ADP + Pi + n_A\,\Delta H^+ \rightleftharpoons ATP$, where $n_A \approx 3$ is the number of protons transported each time this reaction turns over (173). Maximal rates for ATP synthesis and hydrolysis have been described to be around 50 to 250 ATP s^{-1}, corresponding to a maximal H^+-translocation rate of 150–1200 $H^+ \times s^{-1} \times$ enzyme^{-1} (174). An example of a proton pump/F_1F_O-ATPase coupled system is co-reconstituted *bo_3* oxidase with F_1F_O-ATPase in liposomes, where ATP synthesis rates up to 90 ATP $\times$ s^{-1} $\times$ enzyme^{-1} were observed after addition of an electron source to initiate proton pumping by the oxidase. Due to ΔpH being partially determined by passive proton permeability of the membrane (discussed above), final ATP synthesis rate is also partially dictated by it. Another factor playing a role in passive proton permeability and consequently range of obtained proton gradients is the surface-to-volume ratio of vesicles. The latter is low for GUVs (e.g. for a 10 μm GUV it is 0.6 μm^{-1}) and high for LUVs (e.g. for a 100 nm LUV it is 60 μm^{-1}), comparing to mitochondrial one, which is estimated to be 5.99 μm^{-1} (173).

To determine passive proton permeability of artificial compartments, a pH-sensitive fluorescent probe can be encapsulated and via its fluorescence intravesicular pH can be determined. To obtain membrane proton permeability (P_H^+) values fluorescence data is fitted to a single (175) or double (170) exponential curve and fitted parameters are used to solve the equation for the proton permeability: $P_H^+ = \frac{\Delta pH}{t}\frac{BCV}{SA\ \Delta C}$ (175), where SA is the surface area of the vesicle, ΔC is the initial difference in concentration of protons between inside and outside of the vesicle, ΔpH is the excursion in pH when time equals 1/*t*, *t* is the time constant of exponential curve describing the change in fluorescence as a function of time, and BVC is the buffer capacity of an individual vesicle. One commonly used water-soluble fluorescent probe is pyranine (8-hydroxy-1,3,6-pyrenetrisulfonic acid, HPTS) (176, 177). pH determination is based on ratiometric measurements between two fluorescence excitations: one at 458 nm, which is pH dependent, and the other at 405 nm, which is a pH-independent isosbestic point. Ratiometric measurement bypass any artifacts occurring from dye bleaching. Pyranine has three sulfonate groups and an 8-hydroxyl group. At a pH higher than 1, the three sulfonate groups are completely ionized (pKa ≈ 0–1), whereas in the ground state the 8-hydroxyl group is ionized at alkaline pH (pKa = 7.2–7.3). Consequently, over a wide pH range and depending on the degree of ionization of the OH group, this molecule can exist as a trivalent or tetravalent anion. Pyranine proved to have considerably better stability, greater dynamic range, and lower toxicity than other pH-sensitive dyes (178). The sulfonate groups of pyranine do not become protonated at or near the physiological pH, ensuring that the dye will remain in the polyanionic, impermeant form throughout. This property ensures retention of the dye. All those combination makes it one of the most commonly used pH-sensitive fluorescent probes to monitor pH and pH changes in biochemical and biophysical research. Pyranine has been extensively employed for determining of H^+ permeability of synthetic vesicles (1, 168, 170, 175, 177, 179) and monitoring pH changes in lumen of artificial organelles, whereby pH difference was obtained by activated proton pumps (1) or F_1F_O-ATPase (76). Furthermore, pyranine is not utilized merely in bottom-up synthetic biology, but for cell studies as well, such us measurement of cytosolic pH (178, 180, 181), or pH changes in *E. coli* membrane vesicles (182).

1.4 Overview

1.4.1 Aim of the thesis

This PhD thesis emerged from the MaxSynBio research project that aimed at constructing an artificial cell by mimicking predefined cellular functionalities. More specifically, this work focuses on the development of a growth module for an artificial cell. The MaxSynBio roadmap was to achieve the expansion of cellular microcompartments via fusion with other compartments in the proximate environment. The latter can be tackled via fusion of nanocompartments to achieve larger nano- or even microcomparments or asymmetric

fusion between micro- and nanocompartments (Figure 5: Step I). The membrane-bound nanocompartments used in this study were large unilamellar vesicles (LUVs) and the micrompartments were giant unilamellar vesicles (GUVs). PDMS-*g*-PEO polymersomes and PDMS-*g*-PEO:lipid hybrid vesicles were shown as highly promising compartments for the artificial cell (1, 21, 32, 183) and were therefore chosen to be investigated in the context of growth. Lipid compartments were used only as a benchmark for the behavior of (semi-)synthetic hybrid and polymer compartments.

A crucial aspect in constructing an artificial cell is the compatibility of functional parts and modules (Figure 5: Step II), while having in mind their individual optimal environment (membrane and media composition). For example, while high osmolarity increases the stability of membrane proteins, it reduces the membrane fusion rate, and while a polymer can potentially increase the stability and durability of the system and perhaps the fusion potential, complete absence of lipids can impede the membrane protein functionality. Therefore, having one universal growth mechanism, while integrating all other desired functions of artificial cell, is likely not realistic. Therefore, different growth mechanisms were considered, that are compatible with specific requirements, which in the end led to the identification of the most promising growth mechanism with regard to the possibility of integration with multiple functional modules toward the construction of an artificial cell.

Since fusion is not only important for the growth module, but it is involved in various other cell processes, such as exo- and endocytosis, signal transduction, intracellular trafficking, division, etc., and in particular utilized in bottom-up synthetic biology for the stepwise integration of functional parts and modules, the studied fusion mechanisms are discussed in a broader context and their application is demonstrated also outside the growth module.

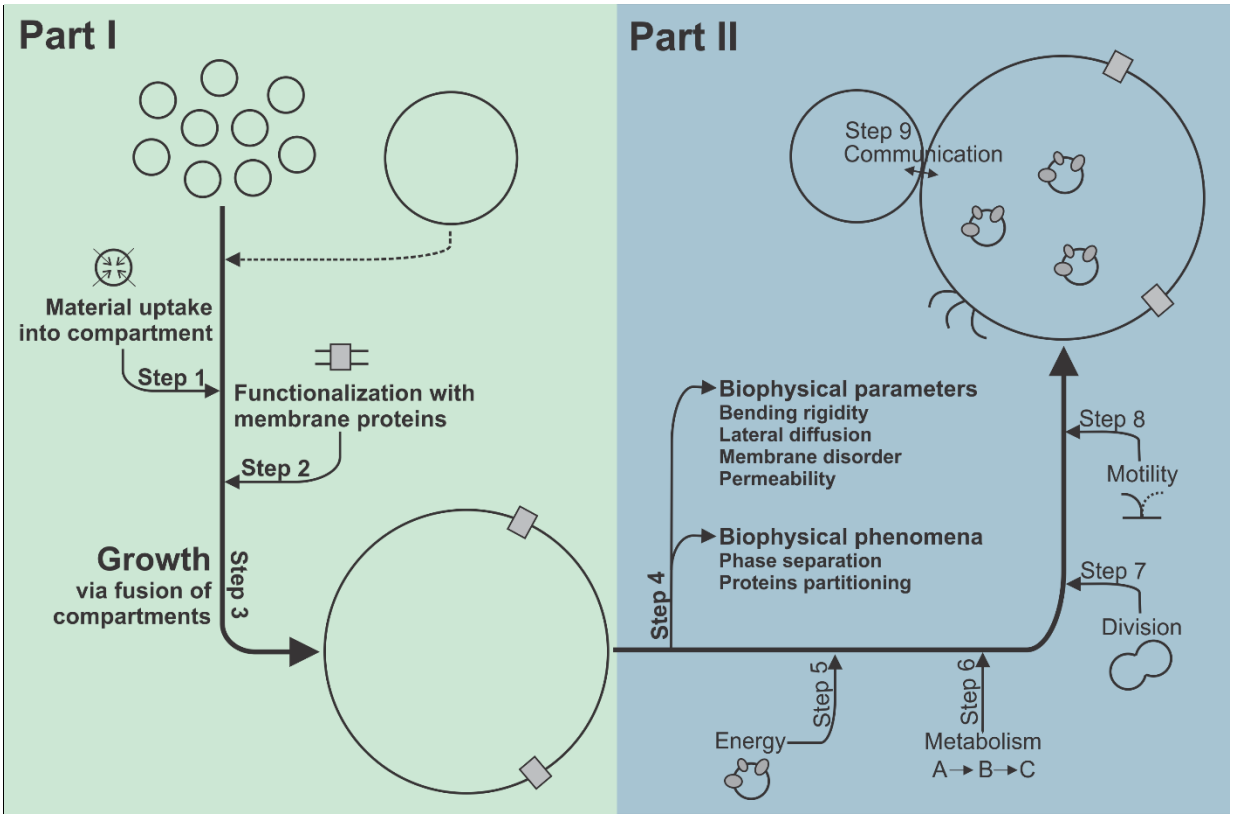

Figure 5. A modular platform for step-wise assembly of multi-component membranous systems by vesicle fusion. Part I: Growth of microcompartments via fusion of nanocompartments or via fusion of nano and microcompartments. Fueling the synthetic cell - material uptake into compartments during growth process (RNA/DNA, substrates for metabolism, etc.). Functionalization of newly grown compartments with membrane proteins (porins, transporters, proteins of photophosphorylation or oxidative phosphorylation, SNARE proteins). **Part II**: Biophysical study of compartment composition, control and application of phase separated membranes. Integration of growth with energy module and metabolism by their encapsulation in growing compartments. Integration of growth and division via dynamic membrane remodeling. Integration of growth and motility by coupling with cilia. Intercellular communication via membrane hemifusion/fusion. Steps in bold were tackled in the thesis.

Especially five key research questions were raised in this study, namely:

1. Can hybrids/polymersomes mimic their natural counterparts in fusion processes? – This question was addressed by studying polymersome/hybrid fusion in presence of different mediators:
    a. electrostatic interactions between the membranes (Section 3.2),
    b. external factors (mechanical stress (Section 3.3), dehydration (Section 3.4)),
    c. fusogenic proteins (SNAREs) (Section 3.5).

2. Where do the differences in fusion efficiency between liposomes, hybrids and polymersomes arise from? – This question was addressed by studying the biophysical properties of membranes.

3. Can visible growth of polymer or hybrid compartments be observed? – In order to evaluate newly grown vesicles, their size distribution was analyzed by epifluorescence microscopy.

4. Is this minimal growth mechanism compatible with other cell functions and do the growth conditions allow to successfully mimic those functions? – For each growth mechanism, integration with at least one other cell function (material uptake or/and energy regeneration) was shown.

5. Which phenomena can be observed during the growth of multi-component hybrid membranous systems? – Focus was given on study offing the conditions that induce phase separation of lipid/polymer in presence or absence of membrane proteins.

These questions were addressed by the following concrete investigations:

Biophysical characterization of compartments:

- Analysis of vesicle surface charge.
- Analysis of bending rigidity and changes upon membrane protein insertion.
- Analysis of lateral diffusion of membrane constituents and proteins.
- Analysis of membrane disorder and changes upon membrane protein insertion.
- Analysis of proton permeability and changes upon membrane protein insertion.
- Analysis of membrane resistance against ROS.
- Analysis of compartment durability in the context of membrane protein functional stability.

Development of tools for growth of membranous systems:

- Preparation of charged hybrid GUVs and analysis of charge-mediated fusion.
- Optimization and evaluation of mechanically-induced growth.
- Optimization of fusion/electroformation approach for growth of protein-functionalized GUVs.
- Preparation of SNARE-GUVs and analysis of SNARE-mediated fusion.

Analysis of fusion/growth efficiency:

- Analysis of vesicle size distribution before and after fusion via dynamic light scattering (DLS) and epifluorescence microscopy.
- Analysis of membrane mixing via dye dequenching and/or FRET.
- Analysis of content mixing via functional coupling of two membrane proteins (*bo*$_3$ oxidase and F_1F_O-ATPase).

1.4.2 Structure of the thesis

This thesis is structured into introduction, wherein the background of bottom-up synthetic biology and the envisaged growth module (Chapter 1.1 and 1.2) is provided, followed by an overview of biomimetic

compartments used in bottom-up synthetic biology, their preparation, fusion, functionalization and biophysical properties (Chapter 1.3). The experimental work conducted for this thesis on growth of biomimetic polymer and hybrids membrane systems is presented in Chapter 3 (for schematic representation see Figure 6), and the methodology supporting it can be found in Chapter 2. Chapter 3.1 includes results that identified some important biophysical characteristics of compartments used in this thesis and the rationale for their use as compartments for the growth module. The following Chapters 3.2–3.5 include studies of four different growth mechanisms, focusing on development of growth protocols, fusion and growth efficiency analysis, investigation of novel biophysical phenomena, and integration with at least one functional part or cell function. General conclusions identifying important aspects of each growth mechanism, with an outlook for their use in an ongoing bottom-up SynBio project is given in Chapter 4.

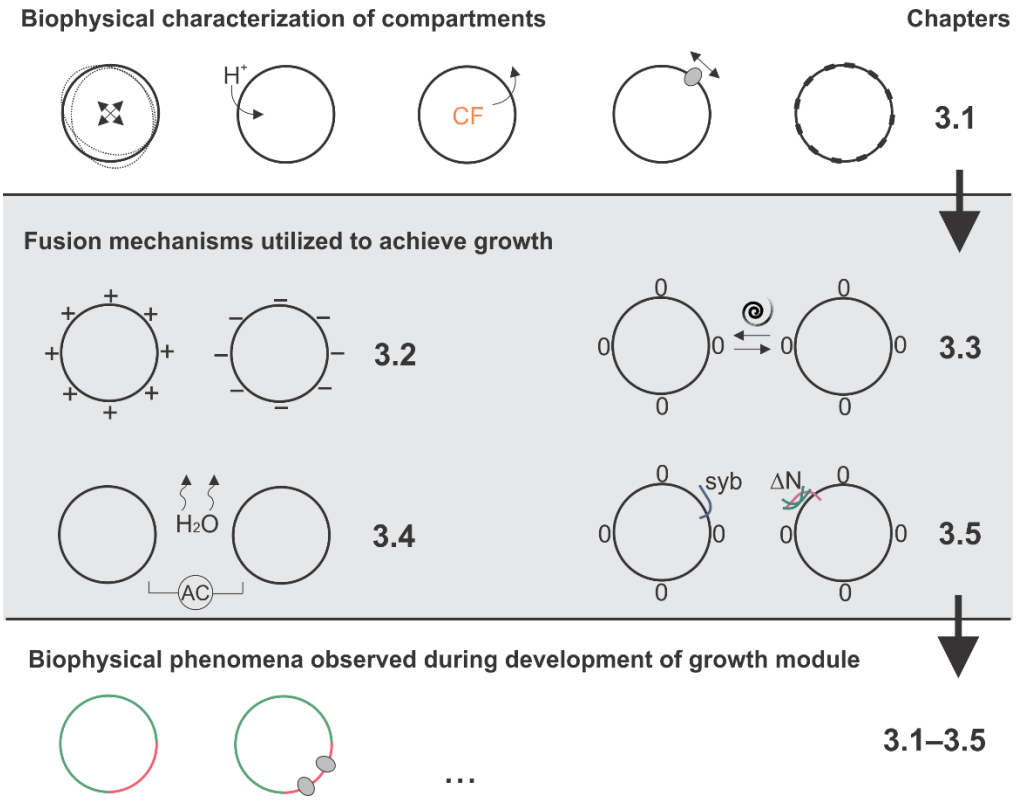

Figure 6. Scheme representing a summary of the main topics reported in the chapter "Results". Results starts with biophysical characterization of polymer and polymer/lipid hybrid compartments and demonstrating rational for their use as compartments for growth module (Chapter 3.1). Each of the following four chapters focuses on one growth mechanism: charge-mediated growth (Chapter 3.2), mechanically-induced salt-mediated growth (Chapter 3.3), dehydration/ or fusion/electroformation-mediated growth (Chapter 3.4) and SNARE-mediated growth (Chapter 3.5). During the development of the growth module various biophysical phenomena were observed and investigated.

2 Materials and Methods

Chapters 2.2, 2.4, 2.9.6.1, 2.9.6.2, 2.10.4, 2.10.5, 2.10.7.1, 2.10.8, 2.10.9 and 2.10.10 were reprinted (adapted) from Marušič et al., Constructing artificial respiratory chain in polymer compartments: Insights into the interplay between bo_3 oxidase and the membrane. *Proceedings of the National Academy of Sciences* 117 (26): 15006-15017 (2020) (1), licensed under CC BY 4.0 (https://creativecommons.org).

Chapters 2.9.2, 2.9.3.4 and 2.10.7.3 were reprinted (adapted) from Otrin, Marušič et al., En route to dynamic life processes by SNARE-mediated fusion of polymer and hybrid membranes. *Nature Communications* 12, 4972 (2021) (106), licensed under CC BY 4.0 (https://creativecommons.org).

Chapters 2.8, 2.10.6, 2.11.1.1, 2.11.3.1 and 2.11.3.2 were reprinted (adapted) with permission from Marušič et al., Increased efficiency of charge-mediated fusion in polymer/lipid hybrid membranes. *Proceedings of the National Academy of Sciences* 119 (20): e2122468119 (2022) (2) licensed under CC BY 4.0 (https://creativecommons.org).

Chapters 2.11.1.2, 2.11.2 and 2.12.3 were reprinted (adapted) with permission from Marušič et al., Fusion-induced growth of biomimetic polymersomes: Behavior of poly(dimethylsiloxane)-poly(ethylene oxide) vesicles in saline solutions under high agitation. *Macromolecular Rapid Communications* 43 (5): 2100712 (2022) (3), licensed under CC BY 4.0 license (https://creativecommons.org).

2.1 Chemicals

1,2-dioleoyl-sn-glycero-3-phosphocholine (DOPC), 1,2-dioleoyl-3-trimethylammonium-propane (18:1 TAP (DOTAP)), L-α-phosphatidylserine (soy, 99%) (soy PS), L-α-phosphatidylcholine (soy, 95%) (soy PC), 1,2-dipalmitoyl-sn-glycero-3-phosphoethanolamine-N-(7-nitro-2-1,3-benzoxadiazol-4-yl) (PE-NBD), 1,2-dioleoyl-sn-glycero-3-phosphoethanolamine-N-(lissamine rhodamine B sulfonyl) (PE-Rho), L-α-Phosphatidylethanolamine-N-(lissamine rhodamine B sulfonyl) (ammonium salt) (egg PE-Rho), 1-myristoyl-2-(6-[(7-nitro-2-1,3-benzoxadiazol-4-yl)amino]hexanoyl)-sn-glycero-3-phosphoethanolamine (14:0-06:0 NBD PE (M-NBD-PE)) and 1-myristoyl-2-(6-[(7-nitro-2-1,3-benzoxadiazol-4-yl)amino]hexanoyl)-sn-glycero-3-phosphocholine (14:0-06:0 NBD PC (M-NBD-PC) were purchased from Avanti Polar Lipids. NHS-rhodamine, NHS-fluorescein, sulforhodamin B, calcein, Laurdan (6-dodecanoyl-2-dimethylaminonaphthalene) and 1,1'-dioctadecyl-3,3,3',3'-tetramethylindotricarbocyanine iodide (DiR) were purchased from Thermo Fisher Scientific. Fluorescein isothiocyanate-dextran (FITC-dextran; MW 20,000 g mol^{-1}), fluorescein-12-dUTP (FITC-12-dUTP) and luciferin/luciferase assay (CLSII) were purchased from Merck. All ATTO NHS-esters were purchased from ATTO-TEC. $PDMS_{26}$-*g*-$(PEO_{12})_2$

(Scheme 1) was a kind gift from Dow Corning. The viscosity-average molecular weight of 3000 g mol^{-1}, the 47% weight fraction of ethylene oxide (2 arms of PEO per PDMS chain, on average) and the average degree of polymerization of 12 are reported in the data provided by the supplier. PDMS-*g*-PEO labeled with fluorescein (PDMS-*g*-PEO-FITC) or rhodamine (PDMS-*g*-PEO-Rho) were synthesized by Dr. Lado Otrin following a previously described procedure (49) and was used as a fluorescent polymer marker for the visualization of polymer membrane in epifluorescence and confocal microscopy and for fluorescence resonance energy transfer (FRET) measurements in fluorescent spectrophotometer. All other chemicals, including adenosine triphosphate (ATP), dithiothreitol (DTT) and ubiquinol 1 (Q_1) were of analytical grade and purchased from Merck.

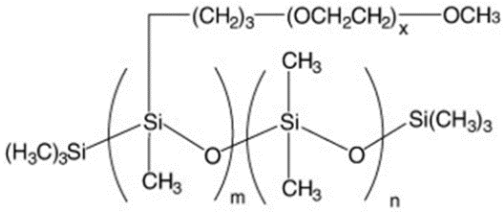

Scheme 1. Chemical structure of $PDMS_{26}$-*g*-$(PEO_{12})_2$. n = 26, m = 2, x = 12.

2.2 Microfluidic chip preparation

Wafer design and fabrication. The pattern on the wafer was designed with AutoCAD 2017 by Dr. Ziliang Zhao in the Dimova lab. The wafers were produced with the conventional soft lithography method (184). Typically a desired thickness of SU 8-3050 was spin coated onto a 4 inch silicon wafer and pre-baked at different temperatures, then a mask aligner (EVG-620) was employed for writing the desired pattern onto the coated wafer, and the wafer was immediately post-baked. SU-8 developer was used for dissolving the unwanted portion of photoresist in order to obtain the final pattern on the wafer.

Chip fabrication. Microfluidic chips were produced by pouring degassed PDMS precursor and curing agent (Sylgard 184, Dow Corning GmbH) onto the wafer at a weight ratio of 10:1 and baked at 80 °C for 2 hours. The PDMS block was peeled off from the wafer, cut into pieces with a razor, inlet and outlet holes were punched by a biopsy punch. Glass coverslips were cleaned by detergent, water and ethanol, then blow dried with nitrogen gas. The PDMS device and coverslip were then exposed to oxygen plasma for 1 min and the two parts were immediately bonded after plasma treatment, followed by further baking at 80 °C to accelerate the process. The microfluidic chips were stored in a closed box until using. Each post in the trap has a dimension of 40 μm by 40 μm, and a height of ~ 70 μm, the gap distance between two posts was 5 μm.

Chip coating. The microchannels of the device were filled with 2 % (w/v) bovine serum albumin (BSA) solution by centrifugation (10 min at 900 × g, Rotina 420R, Hettich) and incubated for 30 min at room temperature. (Filling the chip without centrifugation, using syringe pump instead, introduced air bubbles into the chip.) This avoids unwanted GUV surface adhesion and rupture. After incubation, BSA solution was replaced with 100 µl of ~ 500 mM sucrose using a syringe pump in withdraw mode at 10 µl min^{-1}.

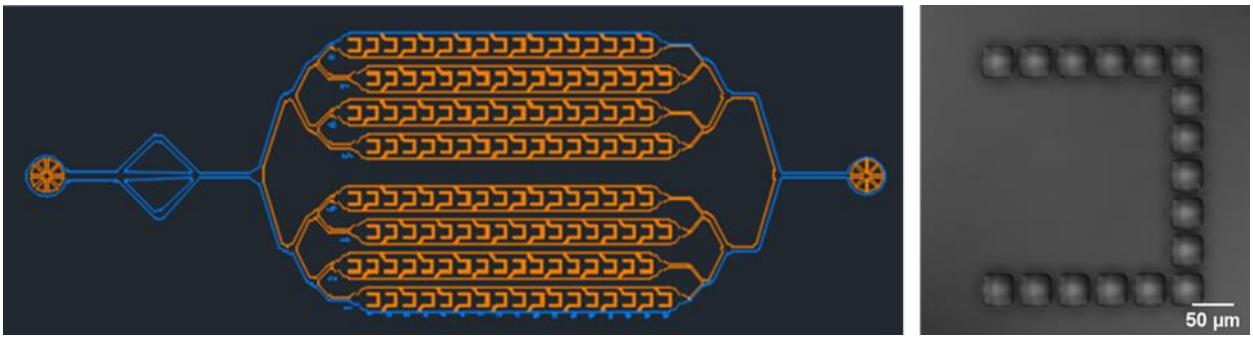

Scheme 2. Network design of the microfluidic chip (185) (left) used for trapping GUVs in proton pumping and proton permeability experiments. The channels split into 8 separate lines, each with 17 traps totaling 136 per device. Bright filed image of one trap with posts of dimensions 40 × 40 µm (right).

All microfluidic chips used for experiments in this work were prepared by Dr. Ziliang Zhao in Dr. Rumiana Dimova's group at Max Planck Institute of Colloids and Interfaces in Potsdam/Golm.

2.3 Protein purification

2.3.1 Purification of *bo₃* oxidase and F_1F_O-ATPase

The *E. coli bo₃* oxidase was expressed from plasmid pETcyo in *E. coli* strain C43 (DE3)(ΔcyoABCDE) and purified as described (186). The *E. coli* F_1F_O ATP synthase was expressed from plasmid pBWU13-βHis in *E. coli* strain DK8 (ΔuncBEFHAGDC) and purified as previously described (187).

bo₃ oxidase and F_1F_O-ATPase plasmids were a kind gift from Prof. Christoph von Ballmoos, University of Bern, Switzerland. *bo₃* oxidase and F_1F_O-ATPase were isolated and purified by Claudia Bednarz in our lab.

2.3.2 Purification of SNAREs

Synaptobrevin-2 (1-116) (188), truncated synaptobrevin-2 (49-96) (189), syntaxin-1A (183-288) (190) and SNAP-25a (1-206) (191) all originating from *Rattus norvegicus* were overexpressed in *E. coli* strain BL21(DE3) and purified as described previously (73, 192) with Ni^{2+}-NTA affinity followed by ion-exchange chromatography on Äkta system (GE Healthcare). The ΔN complex comprising truncated synaptobrevin-2, syntaxin-1A and SNAP-25a was preassembled as described previously (189, 193) by

mixing mentioned constituent at the 1.5:1:1 molar ratio, respectively. Said mixture was then incubated at 4 °C overnight and purified by ion-exchange chromatography on the following day.

SNAREs plasmids were a kind gift from Prof. Reinhard Jahn, Max Planck Institute for Biophysical Chemistry, Göttingen. SNAREs were isolated and purified by Claudia Bednarz in our lab.

2.4 Protein labeling

2.4.1 Labeling of largely hydrophobic model protein with ATTO dyes

bo₃ oxidase was labeled with the amine-reactive ATTO 425 N-hydroxysuccinimidyl(NHS)-ester, ATTO 514 NHS-ester, ATTO 520 NHS-ester or ATTO 532 NHS-ester. The enzyme was dissolved to 2.2 mg ml^{-1} in 20 mM HEPES, containing 0.05% DDM at pH = 8.2, which ensured sufficient concentration of unprotonated (and thus reactive) amino groups. Eightfold molar access of ATTO 425 NHS, ATTO 514 NHS, ATTO 520 NHS or ATTO 532 NHS, dissolved to 2 mg ml^{-1} in anhydrous DMSO, was added to the enzyme solution and the reaction mixture was incubated for 1.5 h at room temperature, under agitation (300 rpm). Unbound dye was removed from the conjugate solution via size exclusion chromatography on a column filled with Sephadex G-25 resin, equilibrated with 20 mM HEPES (pH = 7.5), containing 0.05% DDM. The average number of dye molecules coupled to the enzyme (degree of labeling, DOL), was estimated via absorption spectroscopy, and can be described with the equation, provided by the manufacturer:

$$DOL = \frac{A_{max} \times \varepsilon_{prot}}{(A_{280} - A_{max} \times CF_{280}) \times \varepsilon_{max}}$$

where A_{max} is the absorbance of conjugate at the absorption maximum λ_{abs} (for ATTO 425 λ_{abs} = 439 nm, for ATTO 514 λ_{abs} = 511 nm, for ATTO 520 λ_{abs} = 517 nm, for ATTO 532 λ_{abs} = 532 nm), ε_{prot} is the molar extinction coefficient of enzyme (ε_{bo3} = 184720 M^{-1} cm^{-1}, denatured, ExPASy/ProtParam), A_{280} is the absorbance of conjugate at the absorption maximum of proteins (280 nm), CF_{280} is the correction factor for the dye ($CF_{280\,(ATTO\,425)}$ = 0.17, $CF_{280\,(ATTO\,514)}$ = 0.07, $CF_{280\,(ATTO\,520)}$ = 0.20, $CF_{280\,(ATTO\,532)}$ = 0.09) and ε_{max} is the extinction coefficient of the dye at the absorption maximum λ_{abs} ($\varepsilon_{max\,(ATTO\,425)}$ = 45000 M^{-1} cm^{-1}, $\varepsilon_{max\,(ATTO\,514)}$ = 115000 M^{-1} cm^{-1}, $\varepsilon_{max\,(ATTO\,520)}$ = 110000 M^{-1} cm^{-1}, $\varepsilon_{max\,(ATTO\,532)}$ = 115000 M^{-1} cm^{-1}). The DOL was determined to be 2.8 molecules of ATTO 425 per enzyme, 1.1 molecules of ATTO 514 per enzyme, 1.2 molecules of ATTO 520 per enzyme, and 1.1 molecules of ATTO 532 per enzyme. The net charge increase of protein on coupling with ATTO 425 NHS-ester is 0, ATTO 514 NHS-ester is −1, with ATTO 520 NHS-ester +1, and with ATTO 532 −1.

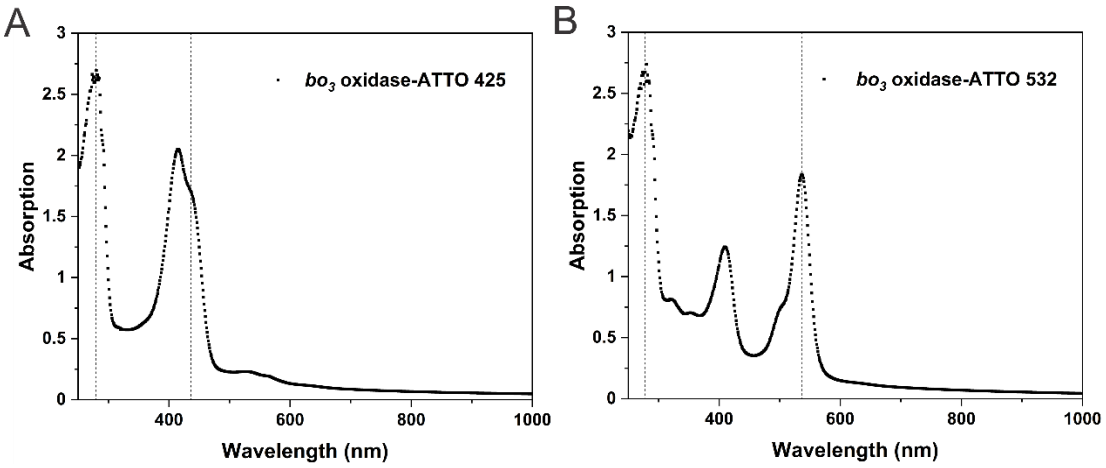

Figure 7. Absorption spectra of *bo*$_3$ oxidase labeled with ATTO dyes. (**A**) *bo*$_3$ oxidase labeled with ATTO 425 NHS; (**B**) *bo*$_3$ oxidase labeled with ATTO 532 NHS. Dotted lines indicate absorption at 280 nm (maximum absorption for the protein) and maximum absorption of ATTO dyes.

2.4.2 Labeling of asymmetric model protein with ATTO dyes

Purified F_1F_O-ATPase was labeled with the fluorescent dye ATTO 620 NHS or ATTO 655 NHS via conjugation to the primary amino groups of the enzyme. Towards this end, the F_1F_O-ATPase was first diluted to 2 mg ml^{-1} in 50 mM HEPES (pH = 8.3) containing 100 mM KCl, 250 mM sucrose, 5 mM $MgCl_2$, 0.1 mM EDTA, 0.2 mM DTT, 2.5 % glycerol, 0.5 % sodium cholate, 0.8 % phosphatidylcholine, 1.5 % octyl glucoside and 0.5 % sodium deoxycholate. Next, ATTO 620 NHS or ATTO 655 NHS dissolved at 1 mg ml^{-1} in DMSO was added to the enzyme at 8-fold molar excess and the conjugation mixture was thoroughly but gently mixed. The enzyme and the dye were incubated for 1.5 h at 4 ºC under agitation (shaking at 600 rpm). Following incubation, nonconjugated dye was removed via size exclusion chromatography (G-25 Sephadex resin, column length 10 cm) with gravity protocol. The net charge increase of protein on coupling with ATTO 620 NHS-ester is +1 and ATTO 655 NHS-ester is 0. For ATTO 620 λ_{abs} = 620 nm, $CF_{280\ (ATTO\ 620)}$ = 0.06 and $\varepsilon_{max\ (ATTO\ 620)}$ = 120,000 M^{-1} cm^{-1}, and for ATTO 655 λ_{abs} = 663 nm, $CF_{280\ (ATTO\ 655)}$ = 0.08 and $\varepsilon_{max\ (ATTO\ 655)}$ = 125,000 M^{-1} cm^{-1}. $\varepsilon_{(F_1F_O\text{-}ATPase)}$ = 340,000 M^{-1} cm^{-1}. The DOL was determined to be 0.75 molecules of ATTO 620 per enzyme, 0.72 molecules of ATTO 655 per enzyme.

2.5 Compartments composition

Compartments studied in this thesis were formed from only from lipids, PDMS-*g*-PEO or a mixture of PDMS-*g*-PEO and lipids. The latter, were varied depending on the fusion mechanism and compatibility with membrane proteins. When studying attractive interaction between membranes, DOTAP was used as cationic lipid and soy PS as anionic one. In case where external factors were investigated a zwitterionic

(also referred here as neutral) lipid DOPC or soy PC were utilized. To visualize the membrane of microcompartments and for membrane mixing experiments, lipids PE-Rho and PE-NBD or polymer dyes PDMS-*g*-PEO-Rho and PDMS-*g*-PEO-FITC were used. Table 1 represents composition of compartments used in different growth approaches.

Table 1. Composition of vesicles used in different growth approached. For charge-mediated fusion composition of vesicles used for negative controls are not mentions; those vesicles contained DOPC instead of soy PS or DOTAP. For mechanically-induced fusion control with DOPC and PDMS-*g*-PEO:DOPC was performed.

	Charge-mediated growth	**Mechanically-induced growth**	**Fusion/electroformation-mediated growth**	**SNARE-mediated growth**
Liposomes	DOPC:soy PS		Soy PC	Soy PC
	DOPC:DOTAP			
Hybrids	PDMS-*g*-PEO:soy PS		PDMS-*g*-PEO: soy PC	PDMS-*g*-PEO: soy PC
	PDMS-*g*-PEO: DOTAP			
Polymersomes		PDMS-*g*-PEO	PDMS-*g*-PEO	PDMS-*g*-PEO

2.6 Preparation of protein-free microcompartments

2.6.1 Preparation of monocompartmentalized GUVs

Protein-free microcomparments, i.e., lipid, hybrid and polymer GUVs, were formed via dehydration of lipid, polymer/lipid or polymer film in presence of electrical filed (electroformation). By regulating ratio between lipid and polymer, homogenous or heterogeneous (phase-separated) hybrid GUVs could be formed (Figure 8). All the experiments in this thesis were performed with homogenous hybrids (≥ 70 mol% PDMS-*g*-PEO), if not otherwise stated.

Hybrid GUVs were obtained with electroformation at room temperature. 1 mg of PDMS-*g*-PEO:soy PC, PDMS-*g*-PEO:DOPC, PDMS-*g*-PEO:DOTAP or PDMS-*g*-PEO:soy PS mixture (50:50, 70:30 or 80:20), containing 0.05 mol% PDMS-*g*-PEO-FITC, 0.05 mol% PDMS-*g*-PEO-Rho or 0.5 mol% PE-NBD or/and 0.5 mol% PE-Rho was dissolved in 1 ml of 2:1 chloroform:MeOH (v/v). 25 µl of this solution were spread on each of both glass slides of a homemade electroformation device composed of two electrodes (glass slides coated with indium tin oxide with resistivity of 55 Ω) and a silicone spacer (1.81 mm thick). Solvent was evaporated under a gentle stream of nitrogen and the electroformation chamber was filled with 200 mM sucrose or weak buffer solution. For neutral hybrids a sine wave (2 V, 10 Hz) was applied for 40 min followed by squared wave (1 V, 2 Hz) for 15 min. For anionic and cationic hybrids next protocol was used:

1.6 V, 10 Hz for 8 h, followed by 2 V, 4 Hz for 30 min. For the GUVs analysis by the epifluorescent microscopy, 10 µl of GUVs suspension was deposited onto poly-L-lysine coated glass slides (Sigma-Aldrich).

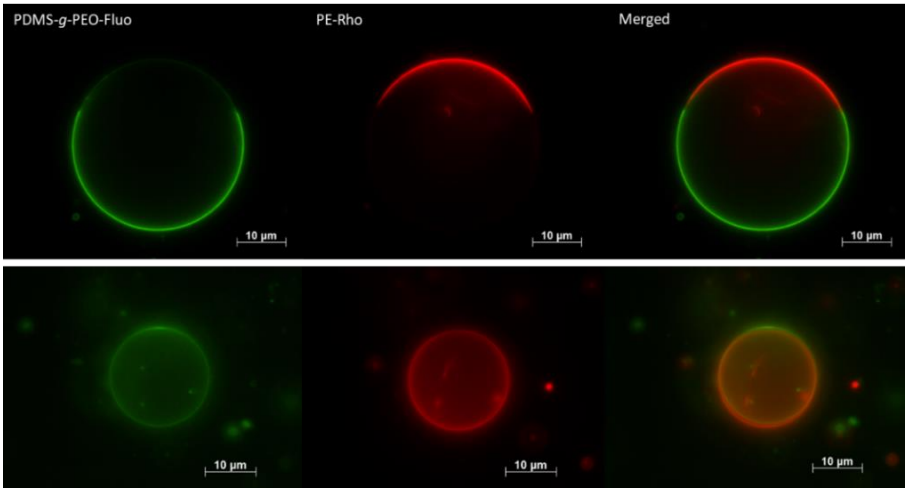

Figure 8. Hybrid GUVs formed via electroformation. Phase-separated (domain formation) (above) and homogenous hybrids (below) formed by rehydration of hybrid film, from polymer/lipid (PDMS-*g*-PEO:soy PC) solution in chloroform:MeOH (2:1, v/v), under AC in 100 mM sucrose. Images were taken by epifluorescence microscopy.

2.6.2 Preparation of multicompartmentalized GUVs

2.6.2.1 Growth of multicompartmentalized microcompartments via electroformation

First, 1 mg of PDMS-*g*-PEO, containing 0.05 mol% PDMS-*g*-PEO-FITC, was dissolved in 1 ml of 2:1 chloroform:MeOH(v/v). Next, 25 µl of this solution were spread on each of ITO-coated glass slides and solvent was evaporated under a gentle stream of nitrogen. Electroformation chamber was filled with LUVs/SUVs suspension (1–3 mg ml^{-1}) in 200 mM sucrose or weak buffer solution. LUVs (100 nm) and SUVs (50 nm) composition was DOPC:DOPE:TOCL:PE-Rho (82.85:11.4:5.7:0.05, mol%) or DOPC:DOTAP:PE-Rho (79.95:20:0.05, mol%) and were prepared as described in 2.7. Three different electroformation protocols were tested: a) 2 V, 10 Hz for 40 min (sine wave); 1 V, 2 Hz for 15 min (square wave); b) 1.2 V, 10 Hz for 8 h; 2 V, 4 Hz for 30 min (sine wave); and c) 50, 100, 200, 500, 700, 900, 1100 mV, 50 Hz – 6 min steps; 1.1 V, 50 Hz for 8 h; 2 V, 4 Hz for 30 min (sine wave).

2.6.2.2 Growth of multicompartmentalized microcompartments via fusion/electroformation

Seven 2 µl-droplets of 5 mg ml^{-1} polymer LUVs (PDMS-*g*-PEO:PDMS-*g*-PEO-FITC = 99.92:0.08, mol%) in 200 mM sucrose were deposited on each of the two ITO-coated glass slides and partially dehydrated for ~ 40 min at room temperature. LUVs were prepared as described in 2.7. Before use, ITO-coated glass slides

were plasma cleaned for 1 min in Plasma cleaner PDC-32G-2 (Harrick Plasma). Plasma treatment causes better surface wettability, which increases hydrophilic properties of the surface. The latter decreased the droplets contact angle and facililated dehydration. Next, electroformation chamber was filled with 0.5 or 1 mg ml^{-1} lipid LUVs (DOPC:DOPE:TOCL:PE-Rho = 82.85:11.4:5.7:0.05, mol%) in 200 mM sucrose and alternative current was applied. The electroformation protocol used was: 10 Hz, 1.2 V for 24 h, following with detachment step 4 Hz, 2 V for 30 min.

2.7 Preparation of nanocompartments

Nanocompartments, i.e., SUVs and LUVs, used in this work were formed by rehydration of lipid, polymer or lipid/polymer film, followed by freeze-thaw cycles and extrusion through 50 (for SUVs), 100 or 200 (for LUVs) nm pore-size membrane. Liposomes were prepared from soy PC (95 %), DOPC, DOPC:soy PS (70:30, mol%) or DOPC:DOTAP (70:30, mol%), polymer/lipid hybrid vesicles were prepared from PDMS-*g*-PEO:soy PC (70:30, mol%), PDMS-*g*-PEO:DOPC (70:30, mol%), PDMS-*g*-PEO:soy PS (70:30, mol%) or PDMS-*g*-PEO:DOTAP (70:30, mol%), and polymersomes were prepared from PDMS-*g*-PEO. For epifluorescent and confocal microscopy, FRAP, passive proton permeability and proton pumping experiments liposomes were supplemented with 0.016–0.05 mol% PE-Rho or PE-NBD, while hybrids and polymersomes were supplemented with 0.05–0.5 mol% PDMS-*g*-PEO-Rho or PDMS-*g*-PEO-FITC.

5/10/30 mg of polymer/lipid mixture (for hybrids), 5/10 mg of polymer (for polymersomes) or 5/10 mg of lipid (for liposomes) in chloroform:MeOH (2:1, v/v) were deposited in a glass vial and the solvent was removed by evaporation under a gentle stream of nitrogen for ~ 30 min. The thin lipid, lipid/polymer or polymer film was rehydrated with 200 mM sucrose, 250 mM KCl, 250 mM NaCl, 125/250 mM $MgCl_2$ or different buffered solutions (1 mM Tris-HCl (pH 7.5), 250 mM KCl; 1 mM Tris-HCl (pH 7.5), 100 mM sucrose; 20 mM Tris-PO4 (pH 8.0)) and resuspended to a final lipid concentration of 5/10/30 mg ml^{-1} by vortexing. PDMS-*g*-PEO is liquid at room temperature, leading to facile re-suspension of polymer or lipid/polymer film in comparison to lipid (PC) film (only 2–3 min of vortexing) and much more unlabored than block copolymer film (which requires heating of the media to facilitate the process or mixing for 1–2 days (64)). If polymersomes were used for reconstitution, the rehydration buffer was supplemented with 0.1 % sodium cholate (for bo_3 oxidase) or 0.05 % octyl glucoside (for F_1F_O-ATPase). The suspension of multilamellar vesicles (MLVs) was subjected to 5 freeze-thaw cycles (1 min lN_2, then water bath at 35 °C until thawed completely, followed by 30 s vortexing). The freeze-thaw step was skipped for polymersomes. For liposomes and hybrids freeze-thaw cycles were needed to obtain unilamellar vesicles with a single peak observed in dynamic light scattering (DLS) after extrusion, but for polymersomes freeze-thaw cycles could be skipped – polymer prefers to organize in single monolayer than forming multilayers (observed by cryo-

TEM (1)). Finally, the size and lamellarity of vesicles was unified by extrusion (21 times) through a 50, 100 or 200 nm pore (polycarbonate membrane, Mini Extruder). Because of the liquid state of PDMS-*g*-PEO room temperature (22 °C) was sufficient when extruding hybrids or polymersomes (60 °C is needed for PBD-*b*-PEO (64)). Furthermore, for extruding PDMS-*g*-PEO polymersomes lower mechanical force was needed than for liposomes with the same mass concentration. The latter might be due to lower vesicle concentration (Figure 9). After polymer film rehydration, polymersomes had a maximum diameter of 300 nm (verified by DLS) and were extruded through a membrane with 100 or 200 nm sized-pores without difficulty.

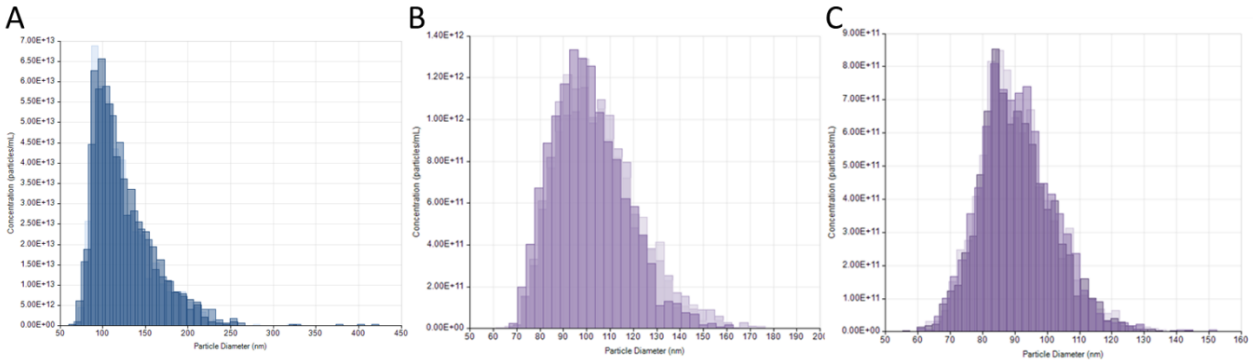

Figure 9. Size distribution by vesicle concentration (TRPS): liposomes (**A**) hybrids (**B**) and polymersomes (**C**), extruded through 100 nm-pore size membrane. Mean size of liposomes was 124 nm and concentration 4.49×10^{14} particles ml^{-1}; mean size of hybrids was 94 nm and concentration 5.60×10^{13} particles ml^{-1}; mean size of polymersomes was 91 nm and concentration was 8.42×10^{12} particles ml^{-1}. Each sample was measured three times (three overlapping histograms).

2.8 Nanocompartments solubilization by detergents

Solubilization of 100 nm vesicles upon step-wise addition of detergent was monitored via absorbance at 540 nm. First, 100 µl hybrids (30 mg ml^{-1}) or 100 µl liposomes (10 mg ml^{-1}) in 20 mM Tris-PO_4 (pH 8.0) was transferred into 100-µl quartz cuvette and initial absorbance was measured. Next, sodium cholate, sodium deoxycholate or Triton X-100 was added vesicles, followed by 1-min incubation at room temperature and absorbance measurement. This step was repeated 30–40 times such that the vesicles were completely solubilized. The vesicles size distribution was analyzed by DLS before solubilization, at saturation point (R_{sat}) and at solubilization point (R_{sol}).

2.9 Reconstitution of membrane proteins into compartments

2.9.1 Reconstitution of respiratory enzymes into LUVs: detergent-mediated reconstitution

2.9.1.1 Reconstitution of largely hydrophobic model membrane protein into LUVs

bo$_3$ oxidase was reconstituted at lipid/polymer to protein molar ratio of 4,800/2,400/1,200 (for preparation of *bo*$_3$-GUVs) or 31,000 (for charged fusion experiments) or 9,000:1 (for mechanical fusion experiments) in 100 nm LUVs. For reconstitution in soy PC liposomes, 0.4 % sodium cholate was added to the vesicle suspension (10 mg ml^{-1}), and to PDMS-*g*-PEO:soy PC hybrids (5 mg ml^{-1}) 0.1 % sodium cholate. Polymersomes (5 or 20 mg ml^{-1} for *bo*$_3$-GUVs formation or mechanical fusion experiments, respectively) already contained sodium cholate (0.1 or 0.4 %), therefore detergent was not added in this step. For reconstitution in DOPC, DOPC:soy PS, DOPC:DOTAP, PDMS-*g*-PEO:DOPC, PDMS-*g*-PEO:soy PS or PDMS-*g*-PEO:DOTAP sodium cholate, sodium deoxycholate, Triton X-100 or octyl glucoside were added at R_{sat} or R_{sol}. Next, *bo*$_3$ oxidase was gently added to LUVs at different final concentrations 0.35–5.40 μM. The reconstitution mixture was incubated at 4 °C for 30 min with mild agitation, followed by detergent removal via Bio-Beads SN-2 (Bio-Rad). For preparation of proteoliposomes, for 200 μl of reconstitution mixture 90 mg was added at once and incubated for 1.5 h at room temperature on a rocking platform. Meanwhile, for preparation of 200 μl of proteohybrids and protopolymersomes suspension, the beads were added in 3 subsequent additions, 30 mg of beads each, followed by 30 min incubation period, at room temperature on a rocking platform. After that, beads were pelleted and the supernatant (proteovesicles) was collected and stored on 4 °C. For experiment on protein-functionalized nanocompartments, proteoLUVs were always used fresh (daily prepared). If the proteoLUVs were used for preparation of protein-functionalized microcompartments (proteoGUVs) and were not used the same day, the proteoLUVs suspension was frozen in lN_2 and aliquots of 20 μl were stored at −80 °C. The size distributions of LUVs and proteoLUVs (Figure 10) were analyzed by DLS (see 2.10.1).

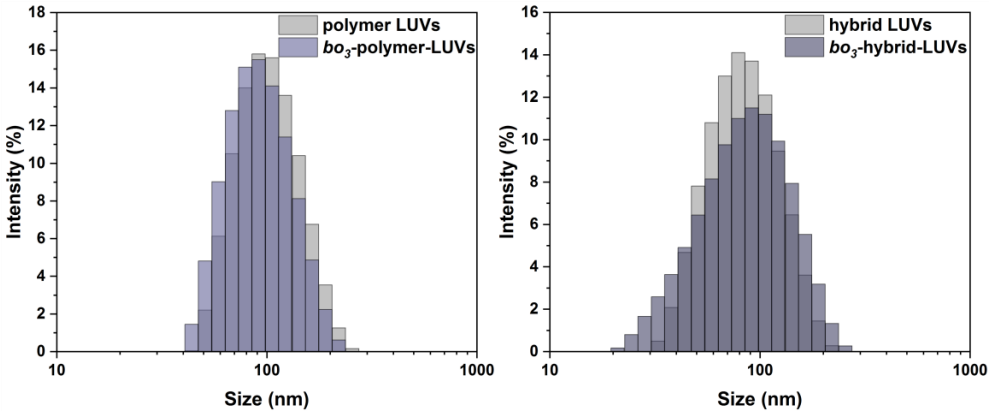

Figure 10. Size distribution of LUVs and *bo*$_3$-LUVs by DLS intensity. Vesicles were extruded through 100 nm pore-sized membrane. *bo*$_3$ oxidase was reconstituted into LUVs via detergent-mediated reconstitution. *Left*: polymersomes and proteopolymersomes; *right*: hybrids and proteohybrids.

To obtain aggregated *bo*$_3$ oxidase, all the steps were repeated as for the reconstitution, with the exception that the vesicle suspension was replaced by a buffer (1 mM Tris-HCl (pH 7.5), 250 mM KCl or 1 mM Tris-HCl (pH 7.5), 100 mM sucrose).

2.9.1.2 Reconstitution of asymmetric model membrane protein into LUVs

For reconstituting F_1F_O-ATPase, sodium cholate was added to the liposomes (10 mg ml^{-1} LUVs, final concentration of sodium cholate 0.6 %) or octyl glucoside to the hybrids (5 mg ml^{-1} LUVs, final concentration of octyl glucoside 0.05 %). The polymersome suspensions (5 mg ml^{-1}) already contained the detergent, therefore it was not added in this step. Next, F_1F_O-ATPase was gently added to the liposomes, hybrids and polymersomes at the final concentration 2.70 µM, 0.675/0.975/0.7 µM, and 0.525 µM, respectively. The reconstitution mixture was incubated at 4 °C for 30 min with mild agitation, followed by detergent removal via Bio-Beads SN-2 (Bio-Rad), as described in 2.9.1.1.

2.9.1.3 Co-reconstitution of membrane proteins with coupled activity

For co-reconstitution of *bo*$_3$ oxidase and F_1F_O-ATPase oxidase sodium cholate was added to liposomes (10 mg ml^{-1} LUVs, final concentration of sodium cholate 0.6 %) or octyl glucoside to hybrids (5 mg ml^{-1} LUVs, final concentration of octyl glucoside 0.05 %). The polymersome suspensions (5 mg ml^{-1}) already contained a detergent, therefore it was not added in this step. The final concentration of *bo*$_3$ oxidase in the reconstitution mixture was 2.70 µM, 0.90/1.95 µM, and 0.70 µM and the final concentration of F_1F_O-ATPase 1.35 µM, 0.45 µM, and 0.35 µM for liposomes, hybrids and polymersomes, respectively. For the co-reconstitution in polymersomes F_1F_O-ATPase was added first and after 20 min of incubation, *bo*$_3$ oxidase was added and incubated for another 15 min. The reconstitution mixture was incubated at 4 °C for 30 min

under mild agitation, followed by detergent removal by use of Bio-Beads SN-2 (Bio-Rad), as described in 2.9.1.1.

2.9.2 Reconstitution of fusogenic proteins into LUVs: co-micelization

2.9.2.1 SNARE-LUVs used for preparation of SNARE-GUVs for size distribution, bending rigidty and membrane mixing analysis

The SNARE proteins were reconstituted in LUVs via a co-micellization technique. First, 5 mg of polymer or 3.9 mg polymer/lipid mixture in chloroform:MeOH (2:1, v/v) were deposited in a glass vial and the solvent was removed by evaporation under a gentle stream of nitrogen for ~ 30 min. The thin polymer or polymer/lipid film was rehydrated with 100 µl SNARE rehydration buffer (20 mM HEPES-KOH (pH 7.4, 150 mM KCl, 5 % sodium cholate) and resuspended to a final polymer or polymer/lipid concentration of 50 or 39 mg ml^{-1} by vortexing. Next, synaptobrevin or ΔN complex was added at molar ratio polymer/lipid-to-protein 500:1 or 1000:1, respectfully. The suspension was mixed by vortexing (three short bursts) and incubated for 5 min at room temperature. To remove sodium cholate and form proteoLUVs, suspension was applied on size exclusion column with Sephadex G-25 resin (prepacked). For column equilibration and elution SNARE rehydration buffer without sodium cholate was used. Collected syb-polymer-LUVs and ΔN-polymer-LUVs had estimated concentration of ~ 10 mg ml^{-1}, and syb-hybrid-LUVs and ΔN-hybrid-LUVs of ~ 7.8 mg ml^{-1} (taking into account column dilution).

2.9.2.2 SNARE-LUVs used for preparation of SNARE-GUVs for content mixing analysis

SNARE-LUVs and SNARE-bo_3/F_1F_O-LUVs for content mixing analysis were prepared similarly as in 2.9.2.1 with some modification. ΔN-LUVs were prepared in a SNARE rehydration buffer (20 mM HEPES-KOH (pH 7.4, 150 mM KCl, 5 % sodium cholate), meanwhile, syb-bo_3/F_1F_O-LUVs were prepared in reaction buffer (20 mM HEPES (pH 8.0/KOH), 5 mM KCl, 20 mM KH_2PO_4; 103 mOsmol kg^{-1}). After addition of synaptobrevin to the resuspended polymer film, three short vortex bursts and 5 min, bo_3 oxidase or F_1F_O-ATPase were added at a polymer-to protein molar ratio 27,000:1 and 81,000:1, respectively. After addition of respiratory enzymes, the mixture was vortexed again in three short bursts and incubated for 5 min at room temperature. Sodium cholate was removed with Sephadex-25 resin (prepacked), equilibrated with reaction buffer.

2.9.3 Reconstitution of membrane proteins into GUVs: fusion/electroformation

In a broader sense, formation of GUVs from preformed SUVs can be considered as “synthetic growth”. In this context (proteo)GUVs were formed via swelling of fused (proteo)LUVs film in the presence of an

electric field. Similar as for other growth approaches studied in this thesis, here, growth was achieved via fusion of LUVs, induced by vesicles dehydration.

2.9.3.1 Preparation of GUVs with reconstituted largely hydrophobic membrane protein

Dehydration conditions. For the successful fusion of LUV membranes and formation of > 20 μm polymer and hybrid GUVs, it was crucial to deposit on ITO-coated glass slides a layer of LUVs with optimal thickness. Various vesicle concentrations (0.1–10 mg ml^{-1}) and different deposition procedures were tested (spreading 2–20 μl of vesicle suspension on plasma cleaned ITO slides or depositing 0.2–2 μl droplets of vesicle suspension). For all types of vesicles, deposition of the LUV suspension in droplets was more efficient for vesicle fusion (the DLS peak intensity at 100 nm decreased substantially or even disappeared). For hybrids and polymersomes, large droplets of relatively highly concentrated vesicles had to be deposited; this can be explained by the lower amount of hybrid and polymer particles (i.e., LUVs) shown by TRPS and DLS, compared to the lipid ones for the same mass concentration (Figure 9). Spreading the droplets or depositing smaller (< 1 μl) droplets decreased the fusion efficiency (large amount of LUVs was left in the samples after electroformation). The previous deposition parameters (< 0.2 μl droplets of 3 mg ml^{-1} (194)) for lipid LUVs were shown to be insufficient for fusion of soy PC lipid membranes in buffer with low salt concentration (1 mM Tris-HCl (pH 7.5), 100 mM sucrose). Therefore, to facilitate the water evaporation and to increase the fusion efficiency by increasing the proximity of the membranes, higher liposome concentrations was deposited. To retain the reconstitution conditions in LUVs, I did not reconstitute bo_3 oxidase into higher amount of vesicles, but instead concentrated the bo_3-lipid-LUVs by ultracentrifugation. In addition, various dehydration procedures were tested: 2 h and overnight in desiccator (at room temperature and 4 °C) in presence and absence of saturated NaCl (71), and 30–60 min at room temperature. The water removal from polymer and hybrid LUVs films was facilitated in comparison to lipid LUV film. This is most likely associated to the different concentration of deposited vesicles. The hybrid LUV film behaved similarly to the polymer film because of the high molar percent of polymer in hybrids (70 mol%).

Electroformation protocol. Various electroformation protocols were tested aiming at obtaining a high yield of > 10 μm GUVs. With most commonly used protocols for the preparation of lipid GUVs in low (10 Hz, 1.1 V, 1–3 h) and high salt buffers (500 Hz, 1.1 V, 1–3 h), hybrid and polymer bo_3-GUVs were formed with maximum diameter of around 1 μm. With the protocol that we previously used for the preparation of hybrid and polymer GUVs (typical electroformation from lipid/polymer film, i.e., sine wave for 40 min (2 V, 10 Hz), followed by square wave for 15 min (1 V, 2 Hz) (21)), larger (> 5 μm) protein-free hybrid and polymer GUVs were formed, but the size of bo_3-GUVs was still around 1 μm. Assuming the need of slower initial swelling to prevent the early LUVs film detachment, I applied a protocol consisting of three subsequent steps: first, the voltage was slowly increased for 42 min (starting with 50 mV and increasing in

6 min-steps to 1.1 V), in which the fused membranes film started to swell. Second, swelling and growing continued at constant voltage and third, the GUVs detached at an elevated voltage and decreased frequency. Comparison of polymer GUVs prepared with the two different electroformation protocols is shown in Chapter 3.4.1., Figure 73. Extending the second part from 2 h to overnight (ca. 12 h) led to increased yield of 20–30 μm GUVs. For the most experiments, the yield was high enough with shorter second swelling part, and to retain protein activity (which was decreasing faster at room temperature), the shorter, 2 h swelling step was preferred. For the overnight protocol, during the first electroformation step chamber was at room temperature, while for next two steps chamber was transferred to an ice box (to avoid moisture contact, chamber was protected with plastic bag).

Factors determining the size of proteoGUVs. The effect of the buffer, in which the proteoGUVs are being electroswollen cannot be neglected. As demonstrated previously (194), electroformation from lipid films in high salt buffers demands higher AC frequency (e.g., 500 Hz instead of 10 Hz). In sucrose, high yields of GUVs with size 30–40 μm were obtained, while in a low salt buffer, the vesicles had diameters of only 13–20 μm. When the low salt buffer was supplemented with water-soluble dye (pH-sensitive dye pyranine), the AC frequency had to be further increased. In addition, the dye should be used at lowest possible concentration, otherwise it might interact with charged lipid/polymer dyes or labeled proteins, which in turn caused aggregates and much smaller proteoGUVs.

Preparation of bo_3-polymer-GUVs and bo_3-hybrid-GUVs. Droplets (2 μl) of 100 nm proteohybrids or proteopolymersomes (5 mg ml^{-1}) mixed with 100 nm hybrids or polymersomes (5 mg ml^{-1}; usually containing 0.05 mol% PDMS-*g*-PEO-Rho) in volume ratio 1:10, 1:1, 2:1, 4:1, 2:1 or 4:1 were deposited on ITO-coated glass slides (55 Ω) (Figure 11, step 1). The LUV film was partially dehydrated for ~ 40 min at room temperature. Afterwards, an electroformation chamber (consisting of two sandwiched ITO-coated glass slides separated by a 1.81-mm-thick silicone spacer) was assembled and filled with 1 mM Tris-HCl (pH 7.5), 100 mM sucrose (Figure 11, step 2). For pH experiments buffer was supplemented with 10 μM pyranine. Electroformation (Figure 11, step 3) in buffer without pyranine was performed by applying the following sinusoidal electric field: 50 Hz, 50, 100, 200, 300, 500, 700, and 900 mV for 6 min each; 50 Hz, 1.1 V for 2 h; and 4 Hz, 2 V for 30 min; when the buffer was supplemented with 10 μM pyranine, the AC frequency was increased to 500 Hz for the first two steps. These bo_3 oxidase-GUVs could be kept on ice for 48 h without losing activity; all the experiments, in which protein activity was essential, were done in this time frame.

Preparation of bo_3-lipid-GUVs. A sample with 400 μl volume of 100 nm proteoliposomes (10 mg ml^{-1}) was pelleted at 200,000 ×*g* for 2 h at 4 °C and resuspended in 40 μl of buffer (1 mM Tris-HCl (pH 7.5),

100 mM sucrose). Droplets (0.2 µl) of highly concentrated proteoliposomes were deposited on ITO slides. The LUV film was partially dehydrated overnight in desiccator in saturated NaCl environment at 4 °C. Afterwards, the electroformation chamber was assembled and filled with 1 mM Tris-HCl (pH 7.5), 100 mM sucrose and the same electroformation protocol as for proteopolymersomes and proteohybrids was applied.

Preparation of GUVs. All protein-free GUVs studied for proton permeability and FRAP were prepared by fusion/electroformation from partially dehydrated film of protein-free LUVs. The dehydration and electroformation protocols were the same as for *bo*$_3$-GUVs.

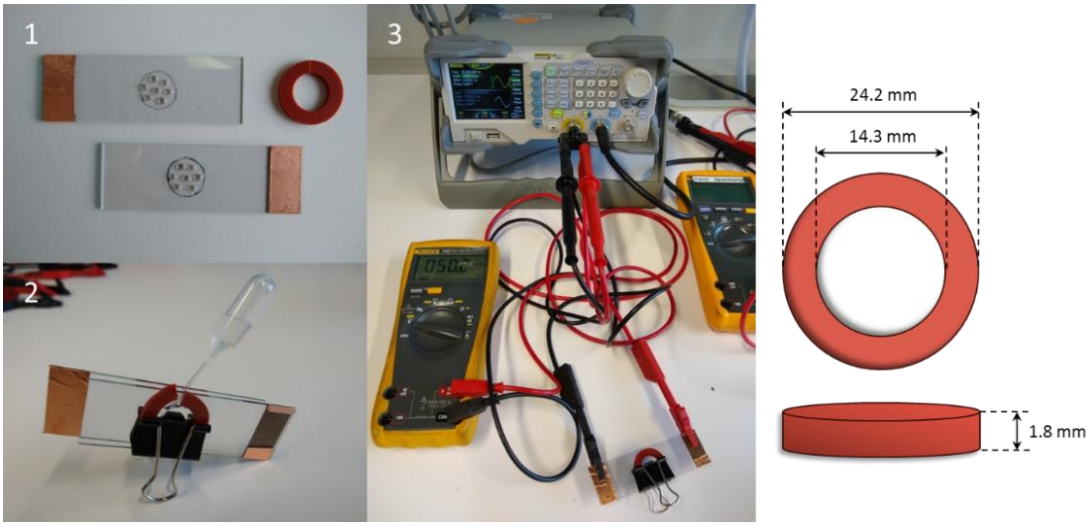

Figure 11. Setup for fusion/electroformation. *Left*: Preparation of proteoGUVs via fusion/electroformation. 1) Seven 2 µl droplets of proteoLUVs (5 mg ml^{-1}) deposited on ITO-coated glass slides, followed by dehydration for ~ 40 min at room temperature. 2) Filling of the electroformation chamber with buffer. 3) Electroformation chamber connected to voltage generator. *Right*: Dimension of electroformation spacer.

Quality (size, unilamellarity, intravesicular structures) of bo*$_3$*-GUVs. The drawback of working with sensitive membrane proteins is that during reconstitution, the protein can be deactivated (by aggregation, denaturation, or loss of cofactors). To retain the activity of *bo*$_3$ oxidase, the dehydration step had to be strictly controlled. Longer dehydration steps caused complete fusion of 100 nm vesicles but at the expense of protein activity. Therefore, for the goal to largely retain protein activity, the dehydration period was shortened, and *bo*$_3$-LUVs were only partially dried, which caused their incomplete fusion and the appearance of ~ 700–1000 nm vesicles in the final sample. Furthermore, all hybrid and polymer GUVs were unilamellar. In contrast, *bo*$_3$-lipid-GUVs, as well as protein-free lipid GUVs sample always contained a portion of multilamellar vesicles. Also, a small portion of the GUVs contained internalized vesicles; again, this was hardly observed for synthetic vesicles. In addition, a portion of the liposomes was aggregated, which occasionally caused blockage of the microfluidic channel, while no aggregation was observed for hybrids and polymersomes.

2.9.3.2 Preparation of GUVs with reconstituted asymmetric membrane protein

Hybrid GUVs with reconstituted F_1F_O-ATPase were prepared via fusion/electroformation similarly as *bo*$_3$-GUVs. Shortly, droplets (2 µl) of 100 nm F_1F_O-hybrid-LUVs (5 mg ml^{-1}) mixed with 100 nm protein-free hybrid LUVs (5 mg ml^{-1}; containing 0.05 mol% PDMS-g-PEO-Rho) in volume ratio 4:1 were deposited on ITO-coated glass slides (55 Ω). After ~ 40 min of partialy dehydration, electroformation chamber was filled with with buffer (1 mM Tris-HCl (pH 7.5), 1 mM KCl, 200 mM sucrose) supplemented with 10 µM pyranine (232 mOsmol kg^{-1}). Electroformation was performed by applying the following sinusoidal AC electric field: 50 Hz, at average voltage levels of 50, 100, 200, 300, 500, 700, and 900 mV for 6 min each; 50 Hz, 1.1 V for 2 h; and 4 Hz, 2 V for 30 min.

2.9.3.3 Preparation of GUVs with two types of membrane proteins

Droplets (2 µl) of 100 nm proteohybrids or proteopolymersomes (5 mg ml^{-1}) mixed with 100 nm hybrids or polymersomes (5 mg ml^{-1}; usually containing 0.05 mol% PDMS-*g*-PEO-Rho) in volume ratio 1:1:2 and 1:1:0 (for approach I) or 1:1 or 1:0 (for approach II) were deposited on ITO-coated glass slides (55 Ω). The LUV film was partially dehydrated for ~ 40 min at room temperature. Afterwards, an electroformation chamber (consisting of two sandwiched ITO-coated glass slides separated by 1.8-mm-thick silicone spacer) was assembled and filled with 1 mM Tris-HCl (pH 7.5), 100 mM sucrose. Electroformation was performed by applying the following sinusoidal AC electric fields: 50 Hz, at voltage levels of 50, 100, 200, 300, 500, 700, and 900 mV for 6 min each; 50 Hz, 1.1 V for 2 h; and 4 Hz, 2 V for 30 min.

2.9.3.4 Preparation of SNARE-GUVs

Synaptobrevin-GUVs (syb-GUVs) and ΔN-GUVs were prepared via fusion/electroformation approach, where an optimized protocol was used for the reconstitution of *bo*$_3$ oxidase in PDMS-*g*-PEO vesicles and modified for SNARE proteins. First, syb-LUVs or ΔN-LUVs (10 or 7.8 mg ml^{-1}), prepared by co-micellization and gel filtration (Chapter 2.9.2), were deposited on ITO-coated glass slides (7 × 2 µl droplets), followed by partial dehydration for ~ 30 min. Next, an electroformation chamber (consisting of two sandwiched ITO-coated glass slides separated by a 1.81-mm-thick silicone spacer) was assembled and filled with 5 mM HEPES (pH 7.4), 5 mM KCl and 30 mM sucrose (for bending rigidty analysis); 100 mM sucrose (for size distribution analysis); 5 mM HEPES (pH 7.4), 5 mM KCl and 100 mM sucrose (for size distribution analysis and memrbane mixing); 20 mM HEPES (pH 7.4), 150 mM KCl and 100 mM sucrose (for size distribution analysis); 5 mM HEPES (pH 8.0), 5 mM KCl, 85 mM sucrose (for content mixing analysis). Electroformation was performed by applying the following sinusoidal AC electric fields: 500 Hz, at voltage levels of 0.05, 0.1, 0.2, 0.3, 0.5, 0.7, 0.9, 1.1, 1.3, 1.5, 1.7 and 2.0 V for 6 min each; 500 Hz, 2 V for 20 h; and 4 Hz, 0.5 V for 30 min.

2.9.4 Monitoring protein incorporation and size distribution of proteoGUVs

The incorporation of ATTO 514-labeled *bo₃* oxidase and ATTO 620-labeled F_1F_O-ATPase in GUVs was analyzed by a Leica TCS SP8 confocal laser scanning microscopy (Wetzlar, Germany) equipped with a water immersion 63× (NA 1.2) objective. The commercial software (Leica) LAS X was used for image analysis. The protein distribution was assessed from the images by averaging two segments of the vesicle contour. For statistical evaluation of the size distribution of GUVs, 60–100 images were taken per sample with Axio Images.M1 Zeiss (100×/1.3 oil Ph3) and the size of 100–250 GUVs was evaluated in Axio-Vision Rel. 4.8 software.

2.9.5 Determination of protein concentration in GUV membrane

The concentration of *bo₃* oxidase-ATTO 514 in the GUV membrane was determined as described by Aimon et al. (2011) (69). The protein concentration in GUVs membranes was determined by measuring fluorescence intensity of the membrane in confocal images of the vesicle equatorial plane. The fluorescence signal was calibrated with DOPE-ATTO 520, as a reference fluorophore that could be incorporated into the membrane at a known concentration. LUVs with reconstituted *bo₃* oxidase-ATTO 514 and LUVs with different mol% of DOPE-ATTO 520 were then used to account for the relative intensity per fluorophore. To determine membrane intensity, confocal images of GUVs were analyzed by use of the software (Leica) LAS X.

The measured membrane fluorescence intensity of reference GUVs was proportional to fluorescent lipid concentration for both hybrid and polymer GUVs (Figure 12). Thus, the slope of this calibration curve, M_{ref}, could be used to convert fluorescence intensity of *bo₃* oxidase-ATTO 514-GUVs membrane to fluorophore (ATTO 514) concentration.

The protein concentration in *bo₃*-GUVs, *C*, could be deduced from the intensity of *bo₃*-GUVs membrane, *I*, using the following equation:

$$C = \frac{I}{M_{ref} \times F \times N_f}$$

where N_f is the number of fluorophores (ATTO 514) per protein, and *F* is the fluorescence intensity of a molecule ATTO 514 linked to *bo₃* oxidase (Figure 13).

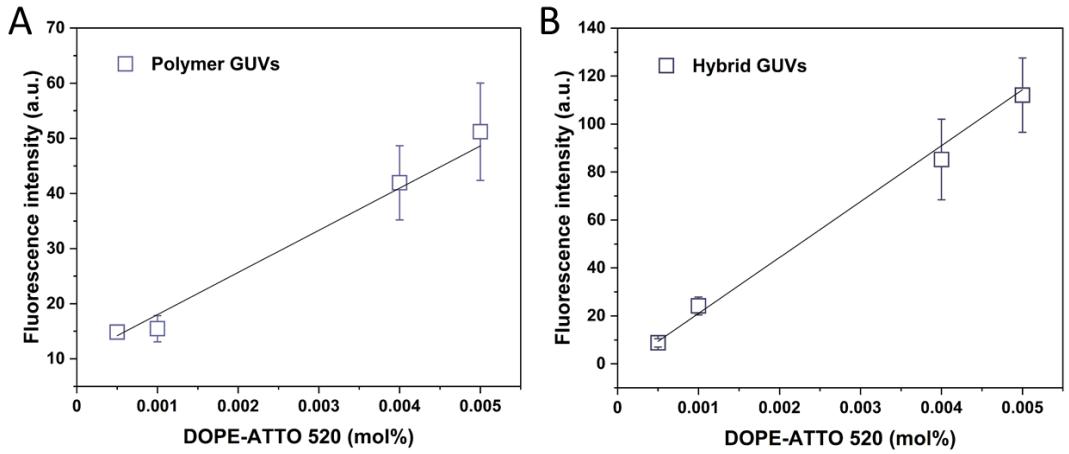

Figure 12. Calibration of GUV confocal fluorescence. Membrane fluorescence intensity of polymer (**A**) and hybrid (**B**) GUVs as a function of DOPE-ATTO 520 concentration. Each point represents an average of 10–20 vesicles with their standard deviation. The slopes of those calibration curves, M_{ref}, relate the membrane fluorescence intensity to the fluorophore concentration.

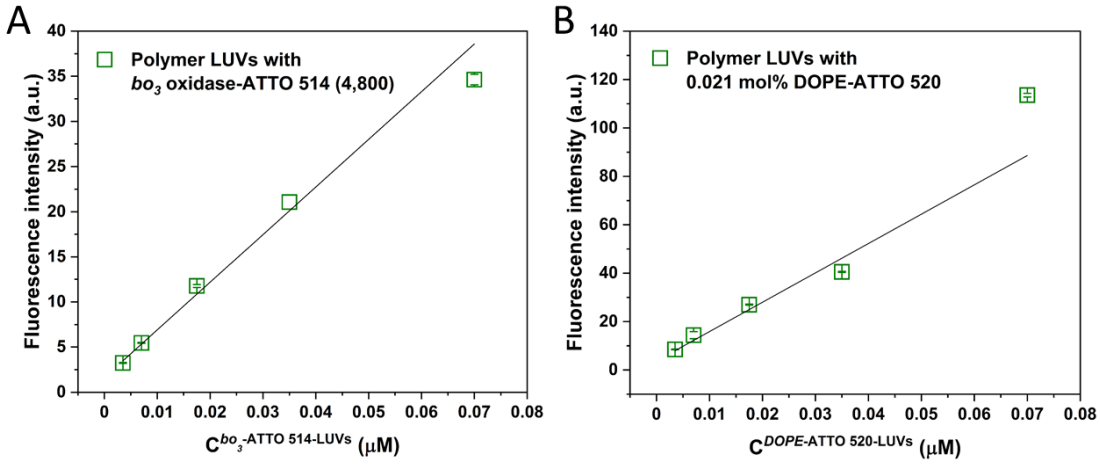

Figure 13. Fluorescence measured in bulk using LUVs, as a function of the volume concentration of fluorophore. The fluorescence in bulk was measured 5–6 times for each LUVs concentration. (**A**) bo_3 oxidase-ATTO 514 was reconstituted in polymer LUVs at polymer-to-protein molar ratio 4,800:1. Linear fit to $I^{bo_3\text{-ATTO 514}} = a^{bo_3\text{-ATTO 514}} \times C^{bo_3\text{-ATTO 514}}$ gives $a^{bo_3\text{-ATTO 514}}$ 527.7 ± 40.7. (**B**) Polymer LUVs were prepared with 0.021 mol% DOPE-ATTO 520. Linear fit to $I^{\text{DOPE-ATTO 520}} = a^{\text{DOPE-ATTO 520}} \times C^{\text{DOPE-ATTO 520}}$ gives $a^{bo_3\text{-ATTO 514}}$ 1212.6 ± 175.6. The efficiency ratio is defined as $F = \frac{a^{bo3-\text{ATTO 514}}}{a^{\text{DOPE-ATTO 520}}}$ = 0.44. All the data presented in this figure and in Figure 12 were acquired using the same excitation/acquisition conditions.

2.9.6 Proteovesicles functional characterization

2.9.6.1 Oxygen consumption measurements

The activity of bo_3-LUVs and bo_3-GUVs was determined via the oxygen consumption of bo_3 oxidase in bulk samples. Oxygen consumption measurements were performed with the Oxytherm system (Hansatech

Instruments). It consists of the S1/MINI oxygen electrode disc, Oxytherm control unit, Oxytherm electrode chamber and the OxyTrace software. The principle of oxygen detection is described in Scheme 3.

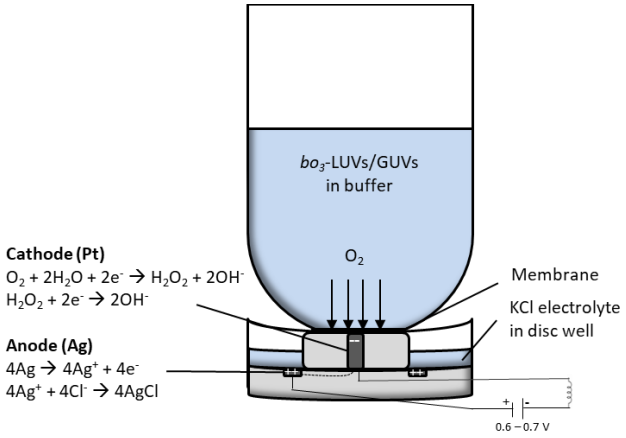

Scheme 3. Principle of oxygen concentration measurement. S1/MINI Clark-type oxygen electrode disc consists of a platinum cathode and silver anode set into an epoxy resin disc and it traps a layer of 50 % saturated KCl solution beneath an oxygen-permeable PTFE membrane. When a small voltage is applied across these electrodes, the electric current is at first negligible and the platinum becomes polarized (i.e., it adopts the externally applied potential). As this potential is increased to 700 mV, oxygen is reduced at the platinum surface, initially to hydrogen peroxide H_2O_2, so that the polarity tends to discharge as electrons are donated to oxygen. The electric current flows is stoichiometrically related to the oxygen consumed at the cathode.

Activity lifetime of lipid, hybrid and polymer bo₃-LUVs. Steady state activity of reconstituted *bo₃* oxidase was determined as described by (21, 195), with slight modifications. Total measurement volume was 1000 µl. The volume of *bo₃*-LUVs was adjusted to achieve theoretically the same molar concentration of *bo₃* oxidase, i.e., ~ 13.5 nM. *bo₃* oxidase was activated by addition of DTT (final concentration 8 mM) and Q_1 (final concentration 40 µM). The samples were measured for 11–13 days every 24 h and kept at 4 °C at all time. The oxygen consumption rates were reported as the average of 2–3 measurements, with standard deviation. All measurements were done at 22 °C while stirring.

Activity of polymer bo₃-LUVs during mechanical fusion. The samples were measured directly after reconstitution and after agitation at 1200 rpm at different time points. Briefly, 14 µl *bo₃*-LUVs were mixed with 210 µl buffer (1 mM Tris-HCl (pH 7.5), 250 mM KCl) in 1.5-ml Eppendorf tube to obtain final polymersomes concentration of 1.25 mg ml^{-1}. Next, diluted *bo₃*-LUVs were agitated for 1 or 3 h at 1200 rpm at room temperature, and protein activity was measured directly after that. Since protein activity decreases over time (faster at room temperature and slower at 4 °C), also activity of *bo₃*-LUVs was measured after 1 and 3 h of incubation at room temperature in absence of agitation (as a control). The total measurement volume in the Oxytherm system was 500 µl and final *bo₃* oxidase concentration was ~ 20.7 nM. *bo₃* oxidase was activated by addition of DTT (final concentration 8 mM) and Q_1 (final concentration

40 µM). The average oxygen consumption rates were determined from 2–3 measurements. All measurements were carried out at 22 °C while stirring.

Activity of aggregated bo_3 oxidase. To obtain aggregated *bo_3* oxidase, all the steps as for the reconstitution were repeated, with the exception that the vesicles were replaced by a buffer (1 mM Tris-HCl (pH 7.5), 250 mM KCl). Activity of aggregated *bo_3* oxidase was measured as described in paragraph above.

Retention of enzymatic activity in GUVs and sample homogeneity. For *bo_3*-hybrid-LUVs and *bo_3*-polymer-LUVs (starting with 0.65 µM *bo_3* oxidase in the reconstitution mixture), the baseline (210–230 nmol ml^{-1} O_2) was recorded with 492.5 µl of 1 mM Tris-HCl (pH 7.5), 100 mM sucrose buffer solution containing 1.5 µl of *bo_3*-SUVs and 4 µl of 1 M DTT (8 mM final concentration). To keep approximately the same amount of *bo_3* oxidase in the final measurement volumes, the baseline for *bo_3*-GUVs was recorded with 478 µl of 1 mM Tris-HCl (pH 7.5), 100 mM sucrose buffer solution containing 16 µl of *bo_3*-GUVs and 4 µl of 1 M DTT. For *bo_3* oxidase in liposomes (starting with 2.7 µM *bo_3* oxidase in reconstitution mixture), the baseline was measured with 0.4 µl of *bo_3*-lipid-SUVs in 493.6 µl of buffer, and 21 µl of *bo_3*-lipid-GUVs in 473 µl of buffer. In all cases, the reaction was initiated by the addition of 2 µl of 10 mM ubiquinone Q_1 (40 µM final concentration) and the enzyme turnover was recorded for 10–20 min. In the control experiments, the activity of *bo_3* oxidase in micelles after the purification was determined as well as the activity of aggregated *bo_3* oxidase (negative control). The average values and the standard deviations of the oxygen consumption rates were determined from 3–4 repeated measurements. All measurements were carried out at 22 °C while stirring.

2.9.6.2 Monitoring pH change in bo_3-polymer-GUVs

The proton pumping rate of *bo_3* oxidase, reconstituted in polymer GUVs, was monitored through the fluorescence change of the encapsulated pH-sensitive dye pyranine (8-hydroxypyrene-1,3,6-trisulfonic acid trisodium salt, HPTS). *bo_3*-polymer-GUVs in buffer (100 mM sucrose, 1 mM Tris-HCl (pH 7.5)) with 10 µM pyranine were loaded into the chip reservoir and flown through the channels to occupy the traps. After trapping 30–60 µm *bo_3*-polymer-GUVs, the outer pyranine was flushed away by exchanging the outer solution with pyranine-free buffer. Proton pumping was then activated by introducing a solution of 8 mM DTT and 40 µM Q_1. Pyranine was excited at 405 nm and 458 nm, and the emission intensity in a region inside the GUV was measured in the range 499–551 nm. The ratio of intensities emitted when exciting at the two wavelengths correlates with pyranine deprotonation and thus pH, which was quantified with a calibration curve for intravesicular pyranine (equation shown below, calibration curve shown in Figure 14). A control experiment was performed with protein-free GUVs, exposed to the same conditions as *bo_3*-GUVs

(buffer solution containing DTT/Q_1). For GUVs equipped with the reconstituted protein as well as for control experiments 5–6 GUVs were evaluated.

Calibration of the intravesicular fluorescence of pyranine to pH. The pH vs. fluorescence calibration curve (6.5–8.5) was obtained with confocal image analysis (excitation = 458 nm, 405 nm and emission = 499–551 nm) of five samples of polymer GUVs containing 10 μM pyranine and 100 mM sucrose in different buffering solutions (1 mM MES (pH 6.5), 1 mM MOPS (pH 7.0) and 1 mM Tris (pH 7.5, 8.0, 8.5)). For each pH 8 samples were analyzed. The calibration curve (Figure 14) was generated by taking a ratio of fluorescence intensity at 499–551 nm with 458 and 405 nm excitation (I_{458}/I_{405}). Comparing this ratio with the measured pH the data was fitted to the following equation, using OriginPro:

$$\frac{I_{458}}{I_{405}} = a\,pH + b$$

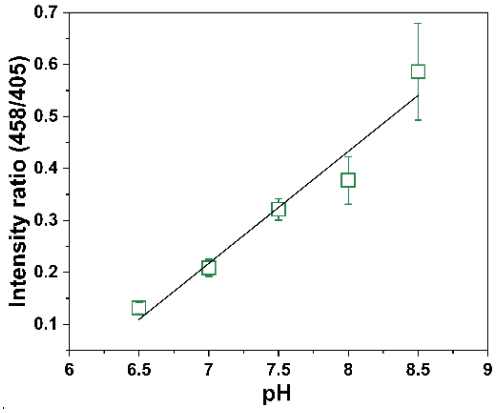

Figure 14. Standard curve for intravesicular pyranine. Protein-free polymer GUVs were prepared in 10 μM pyranine and 100 mM sucrose in different buffering solutions (1 mM MES (pH 6.5), 1 mM MOPS (pH 7.0), and 1 mM Tris (pH 7.5, 8.0, 8.5). Squares represent average of eight samples and their standard deviation. Pyranine was excited at 458 and 405 nm, and the emission was monitored at 499–551 nm. Linear fitting was applied.

2.9.6.3 Monitoring pH change in F_1F_O-hybrid-GUVs

Monitoring intravesicular pyranine fluorescence in microscopy chamber. F_1F_O-ATPase H^+ pumping was monitored via fluorescence change of encapsulated pyranine with Leica SP8 confocal laser scanning microscopy equipped with an oil immersion 63× objective. ATP synthesis was triggered by the addition of the selective K^+ transported valinomycin. In the presence of valinomycin, K^+ ions from the outer medium ($[K^+]_{out}$ = 50 mM) enter the lumen of vesicles ($[K^+]_{in}$ = 1 mM) and produce an electrical transmembrane potential (ψΔ), positive inside, which triggers the ATP synthesis by the F_1F_O-ATPases. The vectorial proton transport across the membrane eventually leads to the luminal basification of the GUV and promotes the synthesis of ATP by the F_1 subunit that binds ADP and inorganic phosphate (Pi) on the external side of the

GUV. 25 µl of F_1F_O-hybrid-GUVs were mixed with 75 µl outer buffer (1 mM Tris-HCl (pH 7.5), 20 mM KCl, 20 mM H_3PO_4, ~ 40 mM glucose) and incubated for 10 min at room temperature. Next 2.4 µl 7.5 mM ADP were added and incubated another 2 min. 50 µl of vesicle suspension were deposited on glass slide and the intraveiscular pyranine fluorescence was monitored (baseline). ATP synthesis was initiated by adding valinomycin and the fluorescence was monitored for another ~ 40 min. Different concentrations (5–20 µM) of valinomycin were tested: 20 µM valinomycin was shown to be too high (membrane permeability substantially increased); at 5 µM one did not observe any change in intraveiscular pyranine fluorescence; meanwhile, 10 µM was shown to be an appropriate concentration for the F_1F_O-hybrid-GUVs.

Monitoring intravesicular pyranine fluorescence in microfluidic device. The proton pumping by F_1F_O-ATPase reconstituted into hybrid GUVs was monitored through the fluorescence change of the encapsulated pyranine. F_1F_O-GUVs in buffer (1 mM Tris-HCl (pH 7.5), 1 mM KCl, 200 mM sucrose) supplemented with 10 µM pyranine were incubated with 10 µM valinomycin for 10 min (to achieve homogenous distribution of ionophore, Eppendorf tube was gently tapped all the time of incubation). Next, valinomycin-F_1F_O-GUVs were loaded into the chip reservoir and flown through the channels to occupy the traps. After trapping 15–45 µm valinomycin-F_1F_O-GUVs, the outer pyranine was flushed away by exchanging the outer solution with pyranine-free buffer. Proton pumping outwards was then activated by introducing a buffer containing 400 µM mM ADP and a higher concentration of K^+ (1 mM Tris-KOH (pH 7.5), 20 mM KCl, 20 mM H_3PO_4, ~ 50 mM sucrose). Pyranine was excited at 405 nm and 458 nm, and the emission intensity in a region inside the GUV was measured in the range 499–551 nm. The ratio of intensities emitted when exciting at the two wavelengths correlates with pyranine deprotonation and thus pH, which was quantified with a calibration curve for intravesicular pyranine (Figure 15). A control experiment was performed on protein-free valinomycin-GUVs, exposed to the same conditions as valinomycin-F_1F_O-GUVs. For GUVs with reconstituted protein as well as for the control experiment 10–20 GUVs were evaluated.

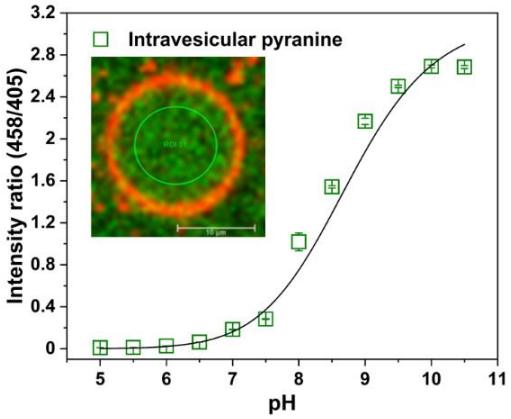

Figure 15. Standard curve for intravesicular pyranine. Protein-free hybrid GUVs were prepared in 10 µM pyranine and 200 mM sucrose in different buffering solutions (1 mM acetate buffer (pH 5.0), 1 mM MES (pH 5.5, 6.0, 6.5), 1 mM MOPS (pH 7.0), 1 mM Tris (pH 7.5, 8.0, 8.5, 9.0) and 1 mM glycine-NaOH (pH 9.5, 10.0, 10.5)). Squares represent average of three samples and their standard deviation. Pyranine was excited at 458 and 405 nm, and emission was monitored at 499–551 nm. Exponential fitting (ExpGro1) was applied.

Measurements of pyranine fluorescence with fluorescence spectrophotometer. Pyranine fluorescence in bulk was determined at five different concentrations of KCl and five different concentration of hybrid LUVs in pH range 5.5–10.5. Measurements were performed in fluorescence spectrophotometer Varian Cary Eclipse (Agilent) at excitation 405 and 458 nm and emission 511 nm (2.5/2.5 nm, 0.1 s), in a quartz cuvette at constant stirring. To 995 µl of buffer, containing different amounts of KCl or hybrid LUVs, 5 µl of 2 mM pyranine were added (final concentration 10 µM). As blank, a buffer lacking pyranine was used. Each measurement was repeated three times and presented as average with standard deviation. The pH level of each solution was determined with the help of a pH electrode.

2.9.6.4 Monitoring respiratory-driven ATP synthesis in luminometer

Activity of bo_3-F_1F_O-LUVs. Measurements of respiration-driven ATP production were performed as described previously (21), with a slight modification. To a solution containing 112.8 µl of measurement buffer (20 mM Tris-PO_4 (pH 8.0), 2.26 µl of luciferin/luciferase assay (CLSII, prepared according to manufactures protocol) and 5.4 µl of ADP (6.96 mM stock, ultra-pure), 2.26 µl of proteo-LUVs were added and a baseline was recorded. Next, 2.26 µl of ATP (2 µM stock) was added to normalize the signal against a defined ATP amount. The reaction was started by the addition of 1.5 µl of DTT/Q_1 (prepared from 6 µl 1 M DTT and 0.25 µl 80 mM Q_1) and the synthesis of ATP was recorded. The ATP production rates were reported as the average of 2 separate reconstitutions (each measured in 4 replicates) combined with the corresponding standard deviation.

Activity of bo_3-F_1F_O-GUVs. Measurements of respiration-driven ATP production were performed by monitoring the luminescence of the luciferin/luciferase assay in bulk-vesicle solution. 31.3 µl of *bo_3*-F_1F_O-

GUVs were added to 93.8 µl of reaction buffer (20 mM Tris (pH 7.5), 20 mM H_3PO_4, 114 mM sucrose; ~ 200 mOsmol kg^{-1}), and the 1.5 ml Eppendorf tube containing the sample was gently mixed (500 rpm) for 10 min at room temperature to equilibrate pH. Next, 2.26 µl of luciferin/luciferase reagent CLSII and 5.4 µl of 6.96 mM ADP (ultra-pure) (final concentration ~ 300 µM) were added, and the sample was gently mixed (500 rpm) for another 2 min. Before each measurement, the sample was vortexed in three short burst and the baseline was recorded for ~ 2 min. As standard, 2.26 µl of 2 µM ATP (final concentration 36.6 nM) were added and recorded for another ~ 2 min. To start the reaction, 1.5 µl freshly mixed DTT/Q_1 (6 µl 1 M DTT mixed with 0.25 µl 80 mM Q_1) were added. When adding ATP and DTT/Q_1, the sample was vortexed in three short bursts before continuing the measurement. ATP synthesis was recorded for around 15 min. The ATP production rates were reported as an average of 2–3 replicates.

2.9.6.5 Monitoring respiratory-driven ATP synthesis in microscopy chamber

Respiratory-driven ATP synthesis was monitored via luciferin fluorescence at an excitation wavelength of 405 nm (40 % laser power) and emission wavelength of 510–550 nm at 200 Hz speed with a Leica SP8 confocal laser scanning microscopy equipped with an oil immersion 63× objective. *bo*$_3$-F_1F_O-hybrid-GUVs were prepared in 1 mM Tris-HCl (pH 7.5) buffer containing 200 mM sucrose (inner buffer, 227 mOsmol kg^{-1}). For the ATP synthesis measurement in the microscopy chamber, *bo*$_3$-F_1F_O-hybrid-GUVs were diluted 1:4 (v/v) into a 20 mM Tris-HCl (pH 7.5) buffer containing 20 mM H_3PO_4 and ~ 114 mM glucose (outer buffer, osmolarity was adapted with glucose to reach osmolarity of inner buffer). 25 µl of *bo*$_3$-F_1F_O-hybrid-GUVs was mixed with 75 µl outer buffer and incubated for 20 min at room temperature. Next, 2.4 µl 7.5 mM ADP, 0.5 µl CLSII and 3 µl 1 M DTT was added. 50 µl of diluted *bo*$_3$-F_1F_O-hybrid-GUVs were deposited on the glass slide and the luciferin fluorescence around *bo*$_3$-F_1F_O-hybrid-GUVs was monitored for around 3 min (in close proximity to the membrane). To initiate proton pumping by *bo*$_3$ oxidase, 0.13 µl 80 mM Q_1 were added.

2.9.6.6 Monitoring fusion of syb-GUVs and ΔN-LUVs

The activity of reconstituted SNARE proteins was determined by monitoring content mixing between ΔN-GUVs and syb-LUVs (see Chapter 2.12.4.2 for details).

2.10 Vesicles mechanical characterization

2.10.1 Determination of LUVs size distribution

The size and dispersity of LUVs were evaluated before and after fusion, and also before and after reconstitution by dynamic light scattering (DLS). The DLS experiments were performed using a Zetasizer

Nano ZS (Malvern, Worcestershire, UK) with a 633 nm helium-neon laser with back-scattering detection. For polymersome growth analysis, 100 µl of polymersomes (5 mg ml^{-1}) mixed with 300 µl of salt solution was measured at a fixed 173° scattering angle in 500-µl quartz cuvette. The size distribution by intensity was determined at time t=0 and then hourly after start of agitation. Samples were agitated at 500–1500 rpm. For a negative control, samples were prepared in Milli-Q or sucrose and diluted in the same solution. Meanwhile, for size analysis of liposomes, hybrids and polymersomes before and after reconstitution of membrane proteins, 45 µl were transferred into 45-µl quartz cuvette and measured.

2.10.2 Determination of LUVs concentration

The LUV concentration was analyzed by Tunable Resistive Pulse Sensing (TRPS) with a qNano device (Izon Science, UK). Electrolyte used was KCl solution (130 mOsmol kg^{-1}) supplemented with 0.01 % Triton X-100. The Nanopore device used was NP 100 (50–330 nm). The calibration was performed with CPC 100 calibration particles (diluted 1:1001) with a mean diameter of 110 nm. Hybrid and polymer LUVs (10 mg ml^{-1}) were diluted 1:1000 and lipid LUVs 1:3000 (to obtain particle rate of ~ 2000/min at the highest operating pressure), applied on top of a stretchable pore (NP 100) and traces were recorded. Data analysis was performed with the Izon Control Suite (Izon Science).

2.10.3 Determination of zeta potential

Zeta potential measurements were done with Zetasizer Nano ZS (Malvern, Worcestershire, UK). 900 µl of Milli-Q, 200 mM sucrose, buffer (20 mM Tris-PO_4, pH 8.0 or 5 mM Tris-HCl, pH 7.5, 100 mM sucrose) or salt solution (250 mM KCl, 250 mM NaCl or 125 mM $MgCl_2$) was transferred with glass syringe into a disposable folded capillary cell DTS 1070. Next, ~ 100 µl of liposomes (10/60 mg ml^{-1}), hybrids (20/60 mg ml^{-1}) or polymersomes (40/60 mg ml^{-1}) was transferred to the bottom of the cell and directly after the zeta potential was measured. The zeta potential was measured with the following settings: model Smoluchowski, temperature 23 °C, equilibration time 0 s, data processing monomodal analysis (for salt solution)/auto mode (for Milli-Q, sucrose or buffer solution), number of measurements 1, runs 10–400. Each sample was measured 3–8 times.

2.10.4 Cryo-TEM

Cryo-TEM was performed on lipid (soy PC), hybrid (PDMS-*g*-PEO:soy PC) and polymer (PDMS-*g*-PEO) LUVs and *bo*$_3$-LUVs. 3.5 µl droplet of the LUVs colloidal suspension were applied on a glow-discharged R2/1 type 200 Mesh Quantifoil holey carbon grid. The vitrification of the samples was carried out using Vitrobot Mark IV System (Thermo Fisher Scientific) and standard Vitrobot Filter Paper (i.e., Ø55/20mm, Grade 595). The chamber of Vitrobot was held at 4 ºC and 95 % relative humidity. For vitrification, a blot

force of 2 and blotting time of 6 sec were applied. The grid was mounted onto a Thermo FEI Glacios 200 kV autoloader under cryo conditions. Images were acquired using Falcon 3EC direct electron detector in linear mode and a total dose of 50 $e^{-}/Å^2$.

Cryo-TEM was performed by Dr. Fotis L. Kyrilis and Dr. Farzad Hamdi under the supervision of Prof. Panagiotis Kastritis at Martin Luther University Halle-Wittenberg.

2.10.5 Membrane order analysis by Laurdan

To study the disorder of the membranes a polarity-sensitive fluorescent probe Laurdan (6-dodecanoyl-2-dimethylaminonaphthalene), which shows that a phase-dependent emission spectral shift (196) was used. The relationship between the emission intensities obtained on the blue and red side of the Laurdan emission spectra is called generalized polarization (GP) (196):

$$GP = \frac{I_{blue} - I_{red}}{I_{blue} + I_{red}} = \frac{I_{440} - I_{490}}{I_{440} + I_{490}}$$

The respective emission spectra were monitored in fluorescence spectrophotometer Varian Cary Eclipse (Agilent) at an excitation wavelength of 530 nm and an emission wavelength of 400–600 nm (10/10 nm). First, fluorescence was blanked with LUVs suspension in 200 mM sucrose, Milli-Q, 250 mM NaCl, 250 mM KCl, 125 mM $MgCl_2$ or 100 mM sucrose, 1 mM Tris-HCl (pH 7.5) (final lipid/polymer concentration was 200 µM). Next, a small amount of Laurdan (working stock solution 100 µM in DMSO) was added to the LUV suspension (final concentration of Laurdan was 600 nM), well-mixed by vortex and incubated for 1 h at room temperature. After 1 h, the sample was mixed again and the spectrum of Laurdan was recorded in triplicates. Measurements were done in 700-µl quartz cuvettes. The GPs values were calculated from the emissions determined at 440 and 490 nm, according to the equation given above and the average values are presented with standard deviation.

2.10.6 Analysis of interbilayer and transbilayer transport of M-NBD-phospholipids

Preparation of donor and acceptor LUVs. Donor neutral lipid LUVs contained 3 mol% M-NBD-PE (or M-NBD-PC), 6 mol% Egg PE-Rho, and 91 mol% DOPC. Donor cationic or anionic lipid LUVs contained 3 mol% M-NBD-PE (or M-NBD-PC), 6 mol% egg PE-Rho, 10 mol% DOTAP or soy PS, and 81 mol% DOPC. Donor neutral hybrid LUVs contained 3 mol% M-NBD-PE (or M-NBD-PC), 6 mol% egg PE-Rho, 10 mol% DOPC, and 81 mol% PDMS-*g*-PEO. Donor cationic or anionic hybrid LUVs contained 3 mol% M-NBD-PE (or M-NBD-PC), 6 mol% egg PE-Rho, 10 mol% DOTAP or soy PS, and 81 mol% PDMS-*g*-PEO. Acceptor LUVs contained 100 or 90 mol% DOPC or PDMS-*g*-PEO, 0 or 10 mol% of anionic or

cationic lipids, and no lipid dye. LUVs were prepared in 200 mM sucrose by freeze-thaw cycles and extrusion, as described above.

Transport assay using fluorescent phospholipids. To 1 ml of 200 mM sucrose (blank) in 1.5-ml quartz cuvette, 2.5 µl donor vesicles (0.8 mM lipid/polymer) were added and baseline was recorded in fluorescence spectrophotometer Varian Cary Eclipse (Agilent) at excitation 460 nm and emission 533 nm for M-NBD-PE and at excitation 464 nm and emission 531 nm for M-NBD-PC (10/20 nm slit width) at constant stirring. To initiate the transport, 5 µl acceptor vesicles (0.8 mM or 1.6 mM lipid/polymer) were added and the fluorescence was monitored for ~ 6 min. The introduction of the acceptor vesicles prompted a sharp increase in fluorescence followed by a second slower increase (hybrids) or a plateau (liposomes). The fluorescence increase was fitted to single or double exponential equations. The thereby obtained rate constants, k_1 and k_2, describe the fast and the slow phase, respectively. Curve fitting was performed by use of the commercial software Origin 2018.

2.10.7 Fluctuation (flickering) spectroscopy

2.10.7.1 Fluctuation spectroscopy of GUVs with reconstituted largely hydrophobic membrane protein

Polymer *bo*$_3$-GUVs for fluctuation analysis were prepared from fused *bo*$_3$-LUVs in lipid/polymer-to-protein molar ratio 9540:1. Protein-free GUVs were prepared by typical electroformation (not from fused LUVs) and proteoGUVs by prolonged overnight electroformation protocol. Here, 60 µl of outer solution (1 mM Tris-HCl (pH 7.5), 70 mM sucrose, 30 mM glucose; 119 mOsmol kg^{-1}) were deposited on glass slide of the observation chamber and 5 µl of *bo*$_3$-GUVs (in 1 mM Tris-HCl (pH 7.5), 100 mM sucrose; 121 mOsmol kg^{-1}) were pipetted directly into the droplet of outer solution and gently mixed with the pipette. To deflate the vesicles, the chamber was left open for 7–10 min (7 min for liposomes, 10 min for hybrids and polymersomes).

Fluctuation analysis was performed following the protocol described earlier (197). The data was acquired at room temperature (~ 23 °C). The acquisition of 1800 snapshots was done by high-resolution camera (pco.edge, PCO AG, Kelheim, Germany) with 200 µs exposure time and 15 fps frame rate (in phase contrast mode and 40× objective on inverted microscope Zeiss Observer.D1). Vesicle fluctuations were analyzed using a custom-built software as previously reported (197). Vesicles that had inclusions, large buds or tubes or did not significantly fluctuate were excluded from the analysis.

2.10.7.2 Fluctuation spectroscopy of GUV with reconstituted fusogenic proteins

Syb-GUVs and ΔN-GUVs for fluctuation analysis were prepared at polymer/lipid-to-protein molar ratio 500:1 and 1000:1, respectively. The Syb-GUVs did not contain membrane dye, while the ΔN-GUVs contained 1.5 mol% PE-Rho and 1.5 mol% PE-NBD. Here, 60 µl of outer solution (5 mM HEPES (pH 7.4), 5 mM KCl, 67 mM glucose; 85 mOsmol kg^{-1}) was deposited on glass slide of the observation chamber and 3–5 µl of GUVs (in 5 mM HEPES (pH 7.4), 5 mM KCl, 30 mM sucrose; 48 mOsmol kg^{-1}) were pipetted directly into the droplet of outer solution and gently mixed with the pipette.

Fluctuation analysis of SNARE-GUVs was performed in the similar manner as for *bo*$_3$-GUVs (Chapter 2.10.7.1), with only next difference: 2400 snapshots were acquired with 200 µs exposure time and 20 fps frame rate.

2.10.8 Protein and lipid/polymer diffusion coefficients determination by fluorescence recovery after photobleaching (FRAP)

FRAP was performed on protein-free GUVs and *bo*$_3$-GUVs, and diffusion coefficients of lipid dye (Rho-PE), polymer dye (PDMS-*g*-PEO-Rho) and labeled protein (*bo*$_3$ oxidase-ATTO 514) were determined. Lipid GUVs contained 0.05 mol% Rho-PE, and *bo*$_3$-lipid-GUVs contained 0.016 mol% Rho-PE. Hybrid and polymer GUVs contained 0.5 mol% PDMS-*g*-PEO-Rho, and *bo*$_3$-hybrid-GUVs and *bo*$_3$-polymer-GUVs contained 0.45 mol% PDMS-*g*-PEO-Rho. The maximum amount of dye was decided based on the quality of obtained GUVs (homogenous distribution of the dye, unilamellar, no internal structures); GUVs containing more than 0.5 mol% polymer dye contained smaller vesicles inside and the dye was not uniformly distributed. FRAP experiments were performed using the FRAP booster mode in a Leica TCS SP8 (Wetzlar, Germany) microscope with a 63× (1.2 NA) water immersion objective and at 1 Airy unit, as described in detail in (198) and (161). Imaging and photobleaching were performed with a 561 nm diode-pumped solid-state laser. Images were acquired with 128×128 format at a speed of 1400 Hz, with no line averaging. In this configuration, the time period between frames was 54 ms. Ten pre-bleach images at low laser intensity were recorded and used as a reference, and then the laser intensity was increased to maximum for another 4 frames for photobleaching, after which the laser intensity was again decreased to record photobleaching recovery. The nominal (user-defined) photobleaching radius (r_n) was set as 1.5 µm. The obtained curves were pre-analyzed using the Leica LAS X (Wetzlar, Germany) software and the FRAP curves were exported to Origin Pro 2015. The FRAP data was analyzed taking into account the diffusion that occurs during photobleaching (150). In short, due to the diffusion that occurs during the photobleaching, the measured effective bleaching radius (r_e) is larger than r_n. To obtain r_e, the line profile intensity on the first image after photobleaching was fitted using the equation

$$f(x) = 1 - Kexp\frac{-2x^2}{{r_e}^2}$$

where x is length of the profile and K is the photobleaching depth. The diffusion coefficient was hence obtained from

$$D = \frac{{r_n}^2 + {r_e}^2}{8t_{1/2}}$$

where $t_{1/2}$ is the half-time of fluorescence recovery (i.e., the time to reach $F_{1/2}= (F_o+ F_\infty)/2$, where F_o and F_∞ are the fluorescence intensities in the first post-bleach image and after full recovery, respectively. The first frame after photobleaching was normalized to $t = 0$.

To facilitate FRAP, the GUVs were immobilized in an agarose 0.2 wt% solution (final concentration) prepared in buffer (1 mM Tris-HCl (pH 7.5), 100 mM sucrose) using a method described in ref. (198). In short, the vesicles were mixed with previously heated agarose solution in the liquid phase and cooled down at room temperature for ~ 10 min, until the polymer solution jellified, after which the vesicles were ready for experiments.

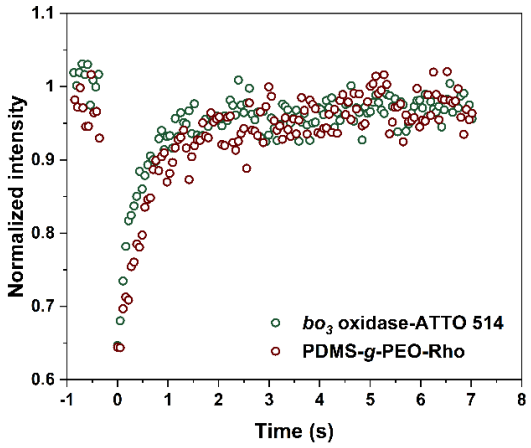

Figure 16. Typical FRAP curve for polymer dye and labeled protein in membrane of *bo*$_3$-polymer-GUV.

FRAP was performed by Dr. Rafael B. de Lira and Dr. Ziliang Zhao under the supervision of Dr. Rumiana Dimova at Max Planck Institute of Colloids and Interfaces in Potsdam/Golm.

2.10.9 Analysis of membrane passive proton permeability

2.10.9.1 Passive proton permeability of protein-free and protein-functionalized microcompartments

The passive proton permeability of protein-free GUVs and *bo*$_3$-GUVs was monitored for 60 min via the changes in the luminal pyranine fluorescence. The lipid/polymer-to-protein molar ratio in *bo*$_3$-GUVs was 9560:1, 9550:1 and 9540:1 for liposomes, hybrids and polymersomes, respectively. To achieve those molar ratios, the following concentrations of *bo*$_3$ oxidase were used in the reconstitution mixture: 0.35 µM for polymersomes, 0.45 µM for hybrids and 1.35 µM for liposomes. *bo*$_3$-polymer-GUVs and *bo*$_3$-hybrid-GUVs were prepared from dehydrated film of mixture of *bo*$_3$-LUVs and LUVs (1:1, v/v). GUVs and *bo*$_3$-GUVs in buffer (100 mM sucrose, 1 mM Tris-HCl (pH 7.5), 10 µM pyranine) were flushed into the microfluidic chip with a flow speed of 1 µl min^{-1} and GUVs > 10 µm were trapped. Next, non-encapsulated pyranine was washed away with 60 µl of the same buffer, lacking pyranine with a flow speed of 2 µl min^{-1}. In the last step, the outer solution was exchanged with 60 µl of isotonic solution ~ 100 mM sucrose, 1 mM MES (pH 6.0) with a flow speed of 1 µl min^{-1} and started the monitoring of proton transport. For data analysis images were taken every 15 s.

Proton permeability experiments were performed together with Dr. Ziliang Zhao and Dr. Rafael B. de Lira in the Dimova lab (Max Planck Institute of Colloids and Interfaces, Potsdam/Golm).

2.10.9.2 Determination of proton permeability coefficients from intravesicular pyranine fluorescence

In the absence of diffusion potentials, the permeability coefficient can be calculated through the flux (199, 200), while accounting for the surface-to-volume ratio and the buffering capacity of all species, including the phospholipids (201). In the present case however, the buffering capacity of the buffer and of the phospholipids was neglected because of its low ionic strength (1 mM) and the lower surface-to-volume ratio of the GUVs, respectively. In addition, two mechanisms have been proposed for treatment of the experimental data: transient pore and solubility-diffusion mechanism (200). The initial fast change of pH has been attributed to the stochastic nature of pore formation showing a Poisson distribution of the decay rates, while the following slower phase corresponded to a solubility-diffusion pathway (170). Since in the present case the pH changes were more accurately described by such a two-stage process, the data was fitted with a biexponential curve ($y = A_1 e^{-tk_1} + A_2 e^{-tk_2} + y_0$), where A is the amplitude of fluorescence signal, *k* is the first order rate constant of proton influx and y_0 the offset; the second (smaller) rate constant k_2 was used to calculate the permeability coefficient through the reported relation $P_{H^+} = k\frac{R}{3}$ (170), where

R was the vesicle radius. It should be noted that in some cases of (*bo*$_3$-)GUVs the data could be fitted with a single exponential function, which resulted in similar k_1 and k_2 values.

The solubility-diffusion rate, characterized by k_2, has been shown to reflect the limiting counter flux of charge-compensating co-ions such as K^+ (170, 202). Here, an ionophore was not introduced to the GUVs to counteract the potential build-up of $\Delta\psi$ because its homogeneous partitioning could not be ensured and its loading in the membrane calculated (valinomycin can become a protonophore at high concentration (168)). The lower surface-to-volume ratio should prolong the establishment of the electrochemical potential.

2.10.10 Monitoring leakage of carboxyfluorescein from nanocompartments

Vesicle leakage after exposure to ascorbate and ascorbyl radicals was monitored via the dequenching of encapsulated carboxyfluorescein (CF). LUVs were prepared in buffer (1 mM Tris-HCl (pH 7.5), 100 mM sucrose) supplemented with 20 mM CF. To remove the non-encapsulated CF, the vesicle suspension was first run through a Sephadex G-25 column and additionally purified with Nycodenz gradient separation. The vesicle suspension at the top of the Nycodenz gradient was carefully collected. Fluorescence of CF was monitored at an excitation wavelength of 492 nm and an emission wavelength of 517 nm (2.5/2.5 nm, 0.1 s) in a fluorescence spectrophotometer Varian Cary Eclipse (Agilent) at constant stirring. The fluorescence was blanked with a buffer (1 mM Tris-HCl (pH 7.5), 100 mM sucrose) and the baseline was monitored with a vesicle suspension diluted 1:2 (v/v). After around 10 min, ascorbate solution was added and after around 40 min $FeSO_4$ solution was added, which initiated the formation of ascorbyl free radicals. To obtain 100% fluorescence (complete dequenching), vesicles were solubilized with Triton X-100 (at concentration that we previously determined as solubilization point).

Table 2. Size of different LUVs used for CF leakage experiments. LUVs were prepared in buffer (100 mM sucrose, 1 mM Tris-HCl, pH 7.5) with 20 mM carboxyfluorescein in subsequent preparation and purification steps, and after vesicle solubilization with Triton X-100.

	Extrusion (100 nm)		**Gel filtration (Sephadex G-25)**		**Gradient separation (Nycodenz)**		**Solubilization**	
	Average size (nm)	PDI	Average size (nm)	PDI	Average size (nm)	PDI	Average size (nm)	PDI
Liposomes	116	0.080	126	0.228	126	0.186	16	0.257
Hybrids	85	0.222	86	0.232	98	0.243	9	0.333
Polymersomes	107	0.105	104	0.113	107	0.145	7	0.253

2.11 Analysis of membrane mixing during fusion

2.11.1 Analysis of membrane mixing of LUVs via fluorescence resonance energy transfer (FRET)

2.11.1.1 Membrane mixing of charged liposomes and hybrids

Vesicle preparation for membrane mixing assay. Liposomes (5 mg ml^{-1}) were prepared from DOPC, DOPC:DOTAP (70–95:30–5, mol%) or DOPC:soy PS (70–95:30–5, mol%). Hybrid vesicles were prepared from PDMS-*g*-PEO:soy PS (70–95:30–5, mol%), PDMS-*g*-PEO:DOTAP (70–95:30–5 molar ratio) or PDMS-*g*-PEO:DOPC (90:10, mol%). Anionic liposomes and hybrids were supplemented with 0.5/1.5 mol% PE-Rho and 0.5/1.5 mol% PE-NBD. 100 nm sized LUVs were prepared in 200 mM sucrose or Tris-PO_4 buffer (20 mM Tris (pH 8.0), 20 mM H_3PO_4) as described in Chapter 2.7.

Measurement setup. Membrane mixing was monitored via FRET between donor NBD and acceptor Rho by exciting NBD and measuring its emission (460/535 nm) in 1.5-ml quartz cuvettes at constant stirring at room temperature. The final measurement volume was 800 µl. The baseline was recorded with tagged LUVs, diluted at concentration 50 µM. Next, non-tagged LUVs were added (at final concentration 50, 100 or 250 µM) and NBD fluorescence dequenching was monitored for 4–10 min. To obtain 100 % NBD dequenching, Triton X-100 (10 %) was added in 5 µl steps until reaching maximum NBD fluorescence. Data is presented as average of three repeats with the corresponding standard deviation.

2.11.1.2 Membrane mixing of polymersomes

Preparation of LUVs for FRET. 200 nm polymersomes (5 mg ml^{-1}) were prepared from PDMS-*g*-PEO in 250 mM KCl, 250 mM NaCl or 125 mM $MgCl_2$ solution as described in Chapter 2.7. Tagged polymersomes for FRET measurements contained 0.6 mol% of PDMS-*g*-PEO-Rho and 0.6 mol% PDMS-*g*-PEO-FITC or 1.5 mol% PE-Rho and 1.5 mol% PE-NBD.

Kinetics. The fluorescence was monitored via excitation and emission of FITC or NBD (460/535 nm; 5/10 nm, 0.1 s) in a fluorescence spectrophotometer Cary Eclipse. To this end, 937.5 µl of 250 mM KCl were transferred in a quartz cuvette and blank/reference (zero) was measured. Next, 12.5 µl of tagged polymersomes (20 mg ml^{-1}) were added and the baseline was monitored while stirring. To dilute the tagged polymersomes, 50 µl of dye-free polymersomes (20 mg ml^{-1}) were added and FRET was monitored for ~ 20 h while stirring. To obtain total dequenching, vesicles were lysed by adding 10 % Triton X-100 (TTX) in 10 µl steps until reaching maximal fluorescence.

Time points. To 937.5 µl of 250 mM KCl in 1.5 ml Eppendorf tube, 50 µl of dye-free polymersomes (20 mg ml^{-1}) and 12.5 µl of tagged polymersomes (20 mg ml^{-1}) were added and agitated at 1200 rpm. As reference, diluted dye-free polymersomes were used. The fluorescence was measured via excitation/emission of NBD/NBD (460/535 nm) or excitation/emission of FITC/Rho (460/583 nm) every 10 min.

2.11.2 Analysis of membrane mixing of polymer LUVs via hydrophobic dye dequenching

Preparation of DiR-LUVs. For testing polymersomes fusion via membrane dye dequenching, polymersomes with and without hydrophobic dye DiR were prepared. DiR is weakly fluorescent in water, but highly fluorescent and quite photostable when incorporated into membranes. For preparation of polymersomes without DiR, 1 ml of PDMS-*g*-PEO (5 mg ml^{-1}) in chloroform:MeOH (2:1, v/v) was transferred into glass vial, solvent was evaporated under N_2 (~ 30 min) and polymer film was resuspended in 1 ml of 250 mM KCl. MLVs were extruded 11× through a 200 nm pore-size polycarbonate filter membrane. For polymersomes containing DiR in the membrane, 100 µl of 1.2 mM solution of DiR in EtOH were added to 1 ml PDMS-*g*-PEO (5 mg ml^{-1}) in chloroform:MeOH (2:1, v/v), resulting mixture contained dye:polymer ratio 0.025/0.00625 (mg DiR/mg polymer), i.e., 2.5/0.625 % DiR. DiR is light sensitive, therefore was always kept in dark.

Kinetics. Fluorescence was monitored at an excitation wavelength of 750 nm and an emission wavelength of 782 nm (5/5 nm, 0.1 s) in the fluorescence spectrophotometer Varian Cary Eclipse (Agilent). When measuring the DiR fluorescence over time, to 600 µl of 250 mM KCl, 150 µl of dye-free polymersomes and 50 µl polymersomes with DiR (2.5 %) were added. Measurement was done at constant stirring in fluorescence spectrophotometer.

Time points. To 300 µl 250 mM KCl in quartz cuvette, 75/150 µl of dye-free polymersomes and 25/50 µl of polymersomes with DiR were added. When exposed to agitation (vortex) diluted polymersomes were transferred in 1.5 ml Eppendorf tube.

2.11.3 Analysis of membrane mixing via epifluorescence microscopy

2.11.3.1 Membrane mixing during charge-mediated GUV-LUV fusion

For charge-mediated fusion of GUVs with LUVs, 50 µl of anionic (PDMS-*g*-PEO:soy PS:PE-NBD = 79.5:20:0.5, mol%) or neutral (PDMS-*g*-PEO:DOPC:PE-NBD = 79.5:20:0.5, mol%) hybrid GUVs were mixed with 10 µl of cationic (PDMS-*g*-PEO:DOTAP:PE-Rho = 79.5:20:0.5, mol%) or neutral (PDMS-*g*-PEO:DOPC:PE-Rho = 79.5:20:0.5, mol%) 200 nm hybrid LUVs (0.5 mg ml^{-1}) and incubated at room

temperature for 5 min. 10 µl of GUV/LUV mixture were deposited on poly-L-lysine-coated glass slides and membrane mixing was analyzed with the help of epifluorescence microscopy, as described in Section 2.14.

2.11.3.2 Membrane mixing during charge-mediated GUV-GUV fusion

For GUV-GUV charge-mediated fusion 10 µl of anionic hybrid (PDMS-*g*-PEO:soy PS:PE-Rho = 69.5:30:0.5, mol%) GUVs were mixed with 10 µl of cationic hybrid (PDMS-*g*-PEO:DOTAP:PE-NBD = 69.5:30:0.5, mol%) or lipid (DOPC:DOTAP:PE-NBD = 69.5:30:0.5, mol%) GUVs and incubated at room temperature for 5 min. 10 µl of GUVs mixture were deposited on poly-L-lysine-coated glass slides and membrane mixing was analyzed with epifluorescence microscopy, as described in Section 2.14.

2.11.3.3 Salt-mediated GUV-LUV membrane mixing/docking in microscopy chamber

PDMS-*g*-PEO GUVs were grown by agitation (1200 rpm) of PDMS-*g*-PEO LUVs (5 mg ml^{-1}) tagged with 0.6 mol% PDMS-g-PEO-Rho. PDMS-g-PEO LUVs, tagged with 0.6 mol% PDMS-g-PEO-FITC were added to GUVs (final concentration of LUVs was 1 mg ml^{-1}) and incubated for 5 min at room temperature without agitation. The docking events of vesicles were analyzed directly after incubation via epifluorescence microscopy.

2.11.3.4 Salt-mediated GUV-LUV membrane mixing/docking in microfluidic traps

Preparation of GUVs. GUVs could not be formed in 250 mM KCl (despite application of various techniques, such as electroformation and phase transfer). Only GUVs with a diameter < 5 µm were obtained in 250 mM KCl by electroformation or phase transfer, and those GUVs would escape through the gaps in traps of the microfluidic device. Therefore, PDMS-*g*-PEO GUVs were prepared with electroformation in ~ 500 mM sucrose. Beforehand, it was tested if the fusion between LUVs occurs when only the outer solution contained a salt. The LUVs prepared in 500 mM sucrose were diluted with isosmotic 250 mM KCl and agitated at 1200 rpm. Although it was hard to estimate from size distribution if it was less efficient or not, polymersomes definitely grew in size: a peak around 1 µm appeared at DLS, therefore, high K^+ concentration solely in the outer solution is likely to be sufficient for mediated fusion of PDMS-*g*-PEO polymersomes.

GUVs trapping and monitoring of potential docking events. PDMS-*g*-PEO GUVs prepared in ~ 500 mM sucrose via electroformation were trapped in the microfluidic device. Next, 200 nm polymersomes prepared in isosmotic 250 mM KCl were flushed into the chip. GUVs were tagged with PDMS-*g*-PEO-FITC and LUV were tagged with PDMS-*g*-PEO-Rho. Accumulation of LUVs signal on the trapped GUVs was monitored for ~ 30 min.

The microfluidics-based experiment above was performed by Dr. Ziliang Zhao in the Dimova lab.

2.11.3.5 Membrane mixing during SNARE-mediated GUV-LUV fusion

For GUV-LUV SNARE-mediated fusion 5 µl of syb-LUVs (PDMS-*g*-PEO:PE-NBD = 99.5:0.5, mol%; 5 mg ml^{-1}) were mixed with 0.3 µl 50 mM DTT. Next, syb-LUVs/DTT suspension was added to 10 µl of ΔN-GUVs (PDMS-*g*-PEO:PE-Rho = 99.5:0.5, mol%) and incubated at room temperature for 10 min (1 mM final DTT concentration). 10 µl of ΔN-GUV/syb-LUV mixture were deposited on poly-L-lysine-coated glass slides and membrane mixing was analyzed with epifluorescence microscopy, as described in Section 2.14.

2.11.3.6 Membrane mixing during SNARE-mediated GUV-GUV fusion

For GUV-GUV SNARE-mediated fusion, 10 µl of syb-GUVs (PDMS-*g*-PEO:PE-NBD = 99.5:0.5, mol%; 5 mg ml^{-1}) was mixed with ΔN-GUVs (PDMS-*g*-PEO:PE-Rho = 99.5:0.5, mol%) and 0.4 µl 50 mM DTT (1 mM final DTT concentration), and incubated at room temperature for 10 min. 10 µl of ΔN-GUV/syb-GUV mixture were deposited on poly-L-lysine-coated glass slides and membrane mixing was analyzed with epifluorescence microscopy, as described in Section 2.14.

2.12 Analysis of content mixing during fusion

2.12.1 Analysis of content mixing via Co^{2+}-calcein/EDTA assay

A Co^{2+}-calcein/EDTA assay was utilized to monitor the content mixing during the charge-mediated fusion of lipid and hybrid LUVs.

Vesicle preparation for Co^{2+}-calcein/EDTA assay. Lipid and hybrid LUVs for the content mixing assay were prepared as described in Chapter 2.7; the only difference was the rehydration buffer used. Cationic or neutral lipid/polymer film was rehydrated in buffer A (1 mM calcein, 1 mM $CoCl_2$, 90 mM NaCl, 10 mM HEPES (pH 7.4)) and anionic lipid/polymer film was rehydrated in buffer B (10 mM EDTA, 80 mM NaCl, 10 mM HEPES (pH 7.4)) at a final lipid/polymer concentration of 5 mg ml^{-1} by vortexing. The outer vesicle buffer was exchanged with buffer C (0.2 mM $CoCl_2$, 80 mM NaCl, 10 mM HEPES (pH 7.4)) by size exclusion chromatography with Sephadex G-25 resin. The prepacked G-25 column was not sufficient for complete outer calcein removal. A column with a height of 7.4 cm or 10.4 cm (and diameter 1.5 cm) was required for removal of the outer calcein for neutral LUVs or cationic LUVs, respectively.

Monitoring content mixing via Co^{2+}-calcein/EDTA assay. Measurements were performed in stirring quartz cuvettes in fluorescence spectrophotometer Cary Eclipse and fluorescence was monitored at calcein

excitation/emission (495/515 nm). The final measurement volume was 800 µl and the polymer/lipid concentration was 100 µM. Anionic and cationic LUVs were mixed in 1:1 molar ratio. As blank, buffer C was used. The baseline was recorded with cationic or neutral LUVs containing calcein. Fusion was initiated by addition of anionic LUVs, and Co^{2+}-free calcein was measured at constant stirring.

2.12.2 Analysis of content mixing in microscopy chamber

2.12.2.1 SRB dequenching during charge-mediated GUV-LUV fusion

PDMS-*g*-PEO:soy PS GUVs were prepared as described in Chapter 2.6.1. PDMS-*g*-PEO:DOTAP and PDMS-*g*-PEO:DOPC LUVs were prepared as described in Chapter 2.7 in 200 mM sucrose supplemented with 100 mM Sulforhodamine B (SRB). LUVs were extruded through a 400 nm membrane, resulting in an average vesicle size (determined by DLS) of 247 nm. The outer SRB was removed via size exclusion chromatography with a Sephadex G-25 resin (length 10 cm, diameter 1 cm). A prepacked G-25 column (3 cm) was not sufficient for SRB-LUVs and non-encapsulated SRB bend separation. For later experiments, the SRB concentration was decreased to 50 mM for more facile extrusion through membranes having a smaller pore size and for better separation effect on the column.

For content mixing analysis, 10 µl of anionic GUVs were mixed with 1 µl of cationic or neutral LUVs (~ 1 mg ml^{-1}), incubated for 5 min at room temperature and directly after observed under microscope (see Chapter 2.14).

2.12.3 Analysis of content mixing in microfluidics

Preparation of LUVs containing SRB. LUVs were prepared by polymer film rehydration with 250 mM KCl (10 mg ml^{-1}) containing 0.5 mM SRB and subsequent extrusion via 100 nm pore-size membrane. The LUV suspension was diluted to 0.2 mg ml^{-1} prior to use in the microfluidic experiments.

GUVs trapping and monitoring of potential fusion events. PDMS-*g*-PEO GUVs prepared in ~ 500 mM sucrose were trapped in the microfluidics device. Next, 200 nm polymersomes prepared in isosmotic 250 mM KCl were flashed into the chip. Two setups were tested to monitor potential content mixing:

i. non-tagged GUVs and LUVs tagged with PDMS-*g*-PEO-FITC and content marker sulforhodamine B (SRB);
ii. non-tagged GUVs and LUV tagged with PDMS-*g*-PEO-Rho and content marker calcein.

The microfluidics experiments above were performed by Dr. Ziliang Zhao in the Dimova lab.

Testing detachment of FITC from PDMS-g-PEO. To eliminate the option that the green fluorescence inside the GUVs (Figure S53) comes from ripped off FITC from PDMS-*g*-PEO molecules it was tested if there is any free-floating FITC in the polymersomes' sample in 250 mM KCl. Two hundred µl of 200 nm polymersomes labeled with PDMS-*g*-PEO-FITC (in 250 mM KCl) were ultracentrifuged (200,000 × *g*, 2 h) and the fluorescence of the supernatant and the pellet (polymersomes), resuspended in 200 µl of 250 mM KCl was measured at excitation/emission wavelengths of FITC (494/518 nm).

2.12.4 Functional coupling of membrane proteins

2.12.4.1 Content mixing during LUV-LUV charge-mediated fuson

Lipid and hybrid *bo*$_3$-LUVs and F_1F_O-LUVs were prepared via detergent-mediated reconstitution (Chapter 2.9.1). To fuse charged proteoliposomes or proteohybrids, 20 µl of cationic *bo*$_3$-LUVs was mixed with 20 µl anionic F_1F_O-LUVs and vortexed at 500 rpm for 10 min. For a control, neutral *bo*$_3$-LUVs were mixed with anionic F_1F_O-LUVs, and cationic *bo*$_3$-LUVs with neutral F_1F_O-LUVs. The content mixing efficiency was determined from the enzymes coupled activity (respiratory-driven ATP synthesis, see Chapter 2.9.6.5).

2.12.4.2 Content mixing during GUV-LUV SNARE-mediated fuson

Polymer LUVs with co-reconstituted synaptobrevin and *bo*$_3$ oxidase or synaptobrevin and F_1F_O-ATPase and LUVs with reconstituted ΔN complex were prepared via co-micellization (Chapter 2.9.2.2). The ΔN-GUVs were prepared from ΔN-LUVs via fusion/electroformation (Chapter 2.9.3.4). To 82.9 µl of reaction buffer (20 mM HEPES (pH 8.0/KOH), 5 mM KCl, 20 mM KH_2PO_4; 103 mOsmol kg^{-1}), 30 µl of ΔN-GUVs, 0.13 µl 1 M DTT, 2.2 µl luciferin/luciferase reagent (CLSII, reconstituted in Milli-Q at 10 mg ml^{-1} according to manufactures protocol) and 5.4 µl 6.96 mM ADP were added. Next, syb-*bo*$_3$-LUVs and syb-F_1F_O-LUVs were added at three different volumes: 1.45 µl, 2.9 µl or 5.8 µl of each, corresponding to synaptobrevin:ΔN complex molar ratio of 2:1, 4:1 and 8:1, and mixed in two short vortex bursts. For 2.9 µl and 5.8 µl, the difference in volume to the sample where 1.45 µl of each proteoLUVs were added, was substracted from reaction buffer. The baseline was recorded with mixture above and after ~ 2 min, proton pump was activated by addition of 1.5 µl DTT/Q_1 mixture (6 µl 1 M DTT was mixed with 0.25 µl 80 mM Q_1) and mixted in two short bursts. ATP synthesis was recorded at 22 °C without stirring for 35–40 min. At the end of the measurements, the signal was calibrated with the known amount of ATP (2.2 µl 2 µM ATP; final concentration was 34.6 nM).

2.13 Delivery of membrane proteins into hybrid GUVs

Preparation of lipid and hybrid LUVs. 100 nm LUVs were prepared via freeze-thaw and extrusion as described in 2.7. The composition of the lipid LUVs was DOPC:DOTAP (70:30, mol%). In case of the hybrid LUVs, the composition was PDMS-*g*-PEO:DOTAP (70:30, mol%).

Reconstitution of bo_3 oxidase into cationic LUVs. *bo_3* oxidase-ATTO 425 was reconstituted into cationic lipid (10 mg ml^{-1}) and hybrid (30 mg ml^{-1}) LUVs at lipid/polymer molar ratio of 8000:1. For reconstitution into lipid LUVs 0.348 % Triton X-100 (saturation point, R_{sat}) and for reconstitution into hybrid LUVs 0.074 % sodium cholate (R_{sat}) was used.

Preparation of anionic GUVs. GUVs were prepared by electroformation as described 2.6.1. To increase GUVs yield, electroformation chamber was placed in the oven at 50 ºC.

Monitoring fusion between bo_3-LUVs and GUV. Anionic hybrid GUVs (PDMS-*g*-PEO:soy PS = 70:30, mol%) in 200 mM sucrose were loaded into the chip reservoir and flow through the channels to occupy the traps. After trapping GUVs, *bo_3*-ATTO425-LUVs were flushed into the chip at a flow rate of 0.5 µl min^{-1} and vesicle fusion was monitored via fluorescence of ATTO 425 (ex 439, em 450–510 nm). After ~ 20 min non-fused *bo_3*-LUVs were flushed away with 200 mM sucrose.

2.14 Growth observation of charged hybrid microcompartments

For fusion between microcompartments, 10 µl of anionic hybrid GUVs were mixed with 10 µl of cationic hybrid or lipid GUVs, incubated for 5 min at room temperature (500 rpm), and evaluated by fluorescence microscopy. Meanwhile, for fusion between nano- and microcompartments, 10 µl 200 nm cationic or neutral hybrid LUVs (0.5 mg ml^{-1}) were mixed with 50 µl anionic or neutral hybrid GUVs, incubated for 5 min at room temperature (500 rpm), and evaluated for LUVs docking/membrane mixing by fluorescence microscopy.

Micrographs of hybrid GUVs were recorded on Zeiss Axio Imager M1 equipped with a digital AxioCam MRm camera (FireWire 1394a). The vesicles were observed with ×100/1.3 objective lens. Excitation is provided by a HBO 100 short-arc 100 W mercury lamp. Two different filter sets (Zeiss) were used to detect a signal from PDMS-*g*-PEO-Rho/PE-Rho/SRB (ex = 540 nm, em = 580 nm), PDMS-*g*-PEO-FITC/PE-NBD (ex = 490 nm, em = 525 nm) or both.

2.15 Morphology, size and encapsulation evaluation of grown polymer microcompartments via epifluorescence microscopy

Polymersomes, exposed to agitation in KCl solution, were evaluated for size, membrane dye distribution and structural integrity by use of the fluorescence microscope Axio Imager.M1 (Zeiss) with 100× oil objective in the Axio Vision Rel. 4.8 software. To visualize membrane dyes and encapsulated fluorescently labeled molecules, rhodamine and FITC filter sets were used. To decrease vesicle rapture, poly(lysine)-coated glass slides were used.

Encapsulation of cytosolic solutes. To PDMS-*g*-PEO LUVs (5 mg ml−1), tagged with 0.6 mol% PDMS-*g*-PEO-Rho, calcein/FITC-dextran/FITC-12-dUTP were added at a final concentration of 10 μM each, and agitated at 1200 rpm for 24 h. The encapsulation efficiency was qualitatively analyzed by epifluorescence microscopy.

2.16 Statistical analysis

Statistical hypothesis test (Student's t-test) was applied, in which the difference between two samples is not significant (ns) for a p-value >0.05, significant for a p-value ≤0.05 (*), very significant for a p-value ≤0.01 (**) and extremely significant for a p-value ≤0.001 (***). For a p-value ≤0.05, the null hypothesis was rejected. p-values were determined in Excel with the t-test, considering a two-tailed distribution and a two-sample assuming unequal variances.

3 Results and Discussion

Chapters 3.1, 3.4.2.3, 3.4.2.4 were reprinted (adapted) from Marušič et al., Constructing artificial respiratory chain in polymer compartments: Insights into the interplay between bo_3 oxidase and the membrane. *Proceedings of the National Academy of Sciences* 117 (26): 15006-15017 (2020) (1), licensed under CC BY 4.0 (https://creativecommons.org).

Chapters 3.2.1, 3.2.2, 3.2.3, 3.2.4.2, 3.2.5 were reprinted (adapted) with permission from Marušič et al., Increased efficiency of charge-mediated fusion in polymer/lipid hybrid membranes. *Proceedings of the National Academy of Sciences* (in press) (2), licensed under CC BY 4.0 (https://creativecommons.org).

Chapter 3.3 was reprinted (adapted) with permission from Marušič et al., Fusion-induced growth of biomimetic polymersomes: Behavior of poly(dimethylsiloxane)-poly(ethylene oxide) vesicles in saline solutions under high agitation. *Macromolecular Rapid Communications* 43 (5): 2100712 (2022) (3), licensed under CC BY 4.0 license (https://creativecommons.org).

3.1 Characteristic of hybrid and polymer compartments making them favorable for growth module

The current chapter focuses on the biophysical characterization of PDMS-*g*-PEO and PDMS-*g*-PEO:soy PC compartments. Prior to undertake the investigation of growth mechanism, the goal was to understand the behavior of those polymer and hybrid compartments alone and their interplay with membrane proteins. Furthermore, the biophysical characterization was performed also for soy PC compartments (benchmark), and the rationale of replacing lipid compartments with hybrid or polymer ones was postulated.

3.1.1 Favorable properties of PDMS-*g*-PEO membranes for fusion

3.1.1.1 Bending rigidity: How soft/rigid are PDMS-g-PEO and hybrid membranes and what happens after protein insertion?

As mentioned above (Section 1.3.5.1), bending rigidity is an important membrane characteristic for cell mimetics, and has in particular important role during fusion and fission involved in growth and division, respectively. To unveil how susceptible to bending are PDMS-*g*-PEO and hybrid membranes, the membrane fluctuations in GUVs was tracked by means of flickering spectroscopy (203) as described in (197). To allow for visible membrane fluctuations, GUVs were exposed to gentle hypertonic conditions (Section 2.10.7.1). A large fraction of the lipid and polymer GUVs exhibited tubes and buds (possibly resulting from buffer asymmetry, see (204)) and these vesicles were not analyzed, while the hybrid GUVs

appeared less tubulated. PDMS-*g*-PEO GUVs exhibited twice lower rigidity than soy PC (Figure 17). Rather than showing intermediate softening, hybrids exhibited lower bending rigidity than liposomes, comparable to that of pure polymersomes (i.e., 11.6 ± 2.4 k_BT), which indicates that this property is largely determined by the prevailing membrane component.

Previous studies report lipid membrane softening upon membrane protein insertion in the case of Ca^{2+}-ATPase (149), while in other cases softening occurred only after protein activation: bR (148, 205, 206), Na^+/K^+-ATPase (207) and F_1F_O-ATPase (76) (summarized in Table 3). Since membrane softening would have beneficial role during membrane fusion, possible changes induced by membrane proteins can be found as an important characteristic for the growth module. To check the influence of membrane proteins on the lipid and graft copolymer membranes, a largely hydrophobic membrane protein, the proton pump *bo*$_3$ oxidase, was reconstituted and a fluctuation analysis was performed. *bo*$_3$ oxidase was chosen as a model protein mainly due to its moderate size (144 kDa (208)) and its high hydrophobicity, leading to occupying large space in the membrane, which could potentially have a larger effect on the bending rigidity of the membrane than smaller proteins featuring a less hydrophobic character. Polymer GUVs and *bo*$_3$-polymer-GUVs were on average tenser than protein-free and protein-functionalized hybrids and liposomes, which suppressed fluctuation. Therefore, further deflation was necessary (additional ~ 5 min with open chamber to allow water evaporation). In addition, upon further deflation of the *bo*$_3$-polymer-GUVs, the excess area almost exclusively formed tubes instead of enhancing fluctuation, enabling only a narrow window for analysis. We speculated that the reason for this phenomenon was the protein-induced asymmetry, as it is known that transiently bound or constitutively inserted membrane proteins can alter the spontaneous curvature (149) and cause invaginations or tubulations (146). *bo*$_3$ oxidase introduces a slight asymmetry through its shape (predominantly hydrophobic truncated cone and small cytosolic fragment (209), Figure S1). Reconstitution of the proton pump caused membrane softening in all three types of membranes (20 % for polymer, 26 % for hybrid and 30 % for lipid membrane; Figure 17 and Table 3). This indicates that the graft copolymer membrane responds to the inserted proton pump in the same manner as lipid membranes and no undesirable rigidification is taking place. Retention of the membrane softness after protein insertion is crucial for the reconstitution of additional membrane proteins as well as for the integration of functional modules of artificial cells such as energy supply, motility, cell division and growth. Because it was previously demonstrated that non-active integral membrane proteins only slightly change the bending rigidity of lipid membranes, and to a considerable extent only when they were active (76, 149, 210), a larger influence of pumping *bo*$_3$ oxidase (in presence of activators) would be expected. In addition, we speculated that the asymmetry will be enhanced by the unidirectional proton pumping if the proteins have adopted a

preferred orientation. However, the assessment of activated membranes was not feasible due to very short time window available for analysis during which DTT was already oxidized.

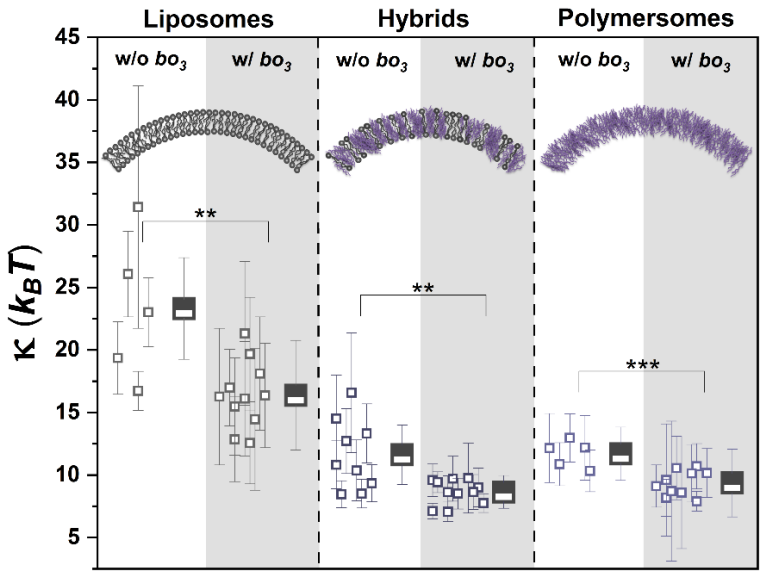

Figure 17. Bending rigidity (κ) for protein-free (w/o *bo*$_3$; white area) and protein-functionalized (w/ *bo*$_3$; gray area) liposomes, hybrids and polymersomes. Each square represents a measurement on a single GUV and its SD (result of the fitting). Half-filled squares represent the average of all evaluated GUVs and the average SD. Adapted from (1), licensed under CC BY 4.0.

Table 3. Bending rigidity of protein-free and protein-functionalized membranes of different compositions. Passive protein denotes the absence of the respective triggers. Adapted from (1), licensed under CC BY 4.0.

Type of membrane	Type of reconstituted protein	Lipid/polymer-to-protein molar ratio	Bending rigidity κ (k_BT)				Source
			Protein-free membrane ($\kappa_{lipid/polymer}$)	Protein-free membrane in presence of activators ($\kappa_{lipid/polymer}$)	Passive membrane (κ_{pass})	Active membrane (κ_{active})	
Egg PC	-	-	10 ± 1	-	-	-	Niggemann 1995 (211)
	bR	1000–60	-	-	~ 10	~ 5	Manneville 2007 (205)
	Ca^{2+}-ATPase	1300	10.2 ± 1.5	10.4 ± 1.1	9.4 ± 1.0	4.1 ± 0.8	Girard 2005 (149)
SOPC		1300	11.6 ± 0.7	11.2 ± 1.0	10.2 ± 1.1	4.4 ± 1.0	
DOPC:Chol	Na^+/K^+-ATPase	2698	22.93 ± 0.6	23.80 ± 0.63	26.40 ± 0.75	19.45 ± 1.02	Bouvrais 2012 (207)
DOPC:DOPS:Chol		2128	-	-	28.88 ± 0.97	20.40 ± 0.60	

E. coli TLE (total lipid extract)	F_1F_O-ATPase	$n_o = 10^{14}$ proteins per m^2	13 ± 2	-	14 ± 3	2 ± 1	Almendro-Vedia 2017 (76)
Soy PC	*bo3* oxidase	9560	23.3 ± 4.1 (n = 5)	-	16.4 ± 4.4 (n = 11)	-	This study
$PDMS_{26}$-*g*-$(PEO_{12})_2$:soy PC		9550	11.6 ± 2.4 (n = 9)	-	8.6 ± 1.3 (n = 11)	-	
$PDMS_{26}$-*g*-$(PEO_{12})_2$		9540	11.7 ± 2.1 (n = 5)	-	9.4 ± 2.7 (n = 10)	-	

The difference in the bending rigidity arises not only from the chemistry of the constituents, but also from the arrangement they adopt in those membranes. Cryo-TEM analysis indicated that the protein-free membrane thickness slightly increased with increasing amount of polymer: 4.40 ± 0.16 nm for lipid, 4.86 ± 0.17 nm for hybrid and 5.25 ± 0.17 nm for polymer membranes. Furthermore, distinct structural differences between all three types of membranes were observed. Lipid LUVs had a bilayer structure with sharp outer boundaries, while polymer membranes appeared as fuzzy monolayers (Figure 18). Meanwhile, two populations of hybrid vesicles were observed: ⅓ resembled polymersomes, while lipid nanodomains of different sizes (discussed in more detail in Section 3.1.2.3) were observed in the rest ⅔ of the hybrid LUVs (Figure 19).

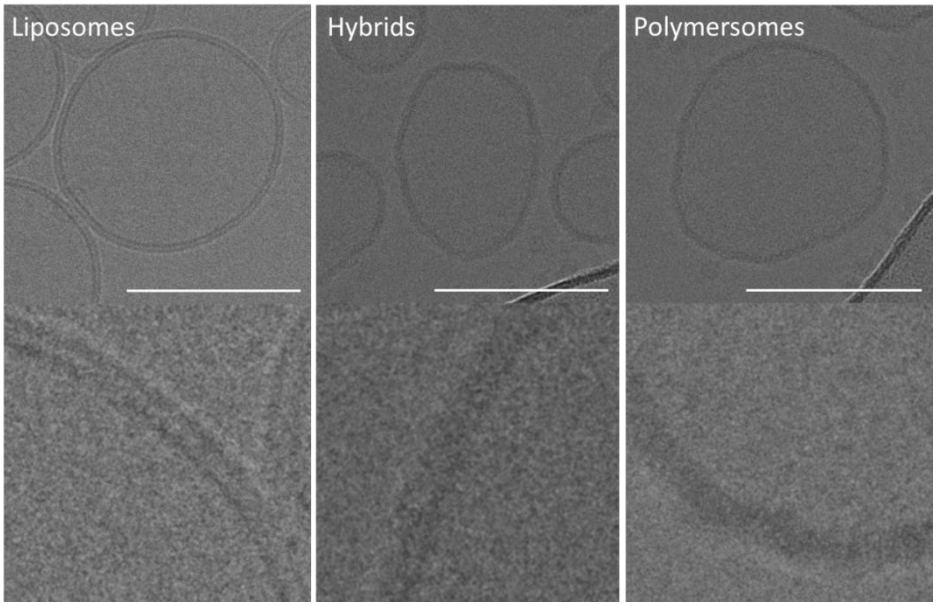

Figure 18. Cryo-TEM micrographs of lipid (soy PC), hybrid (PDMS-*g*-PEO:soy PC) and polymer (PDMS-*g*-PEO) LUVs. LUVs were prepared in 1 mM Tris (pH 7.5), 100 mM sucrose. Scale bar: 100 nm; defocus: ca. −2 µm. Adapted from (1), licensed under CC BY 4.0.

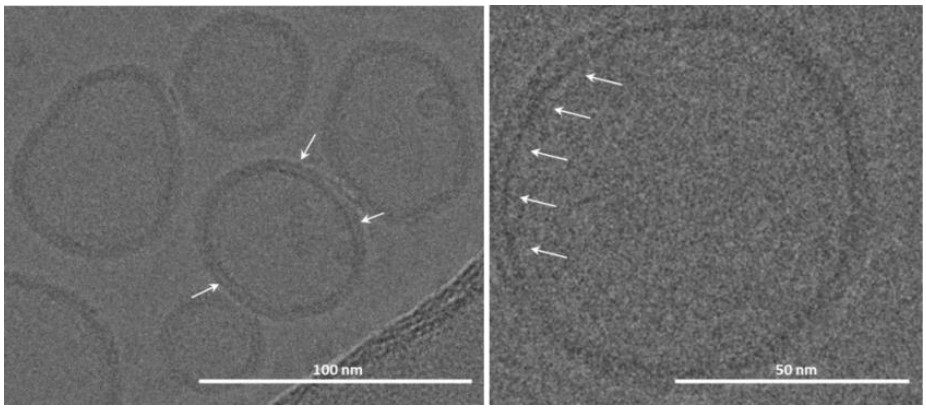

Figure 19. Cryo-TEM micrographs of PDMS-*g*-PEO:soy PC LUVs. LUVs were prepared from polymer:lipid mixture 70:30, mol%. The white arrows show lipid nanodomains. Defocus: ~ −2 µm. Adapted from (1), licensed under CC BY 4.0.

3.1.1.2 Lateral diffusion and membrane disorder: Changes in fluidity of the polymer membrane upon protein insertion

Membrane proteins can confer biological functionalities to synthetic membranes only when the former retain structural and functional integrity upon reconstitution. Key factors for this are the flexibility and fluidity of the membrane, which largely determine the lateral mobility of the protein (212, 213). In the case of the model protein used here, bo_3 oxidase, it is also important that the ubiquinone shuttle can readily diffuse to the active sites of the enzyme. Therefore, it was checked whether PDMS-*g*-PEO provided similar fluidity to the natural environment. To this end, the lateral diffusion of protein, polymer and lipid was determined by measuring the fluorescence recovery after photobleaching (FRAP). Lipid and polymer were labeled with rhodamine (Rho) and bo_3 oxidase with ATTO 514.

The soy PC membrane, used as a benchmark in this study, has a similar fluidity to the commonly used POPC and DOPC membranes (Table 4). In hybrids and polymersomes, the diffusion coefficients of the polymer dye decreased to approximately ½ and ⅓ of the diffusion coefficient of the lipid dye measured in natural membrane, respectively. Fluidity of the PDMS-*g*-PEO membrane was in line with previous reports for the same polymer (214) and in fact, similar to that of SOPC (3.8 ± 0.2 µm^2 s^{-1}) (215). The high fluidity of the graft copolymer can be partially attributed to the relatively low molecular weight of PDMS-*g*-PEO (MW 3000 g mol^{-1}) and the PDMS backbone (153).

Insertion of bo_3 oxidase led to a ~ 20 % decrease of the diffusion coefficients of the labeled lipids in liposomes and the labeled polymers in hybrids (Figure 20A and Table 4), while the diffusion coefficients of labeled lipids in hybrids and polymersomes decreased by 32 %. Similar decrease in fluidity upon reconstitution of the *E. coli* outer membrane proteins FhuA, LamB, NanC, OmpA and OmpF was

demonstrated in POPE:POPG bilayers (216). The latter effect was explained by the less smooth surface and the presence of concave regions in the membrane proteins that trapped phospholipids, resulting in an overall steric hindrance, which scenario should apply in the present case as well. Interestingly, this phenomenon was not observed in the case of the polymer dye in polymer membranes. On the contrary, the diffusion coefficient increased by 23 %. This can be attributed to the partitioning of the enzyme into the intertwined PDMS chains, which loosened their assembly and increased the diffusion of the tagged polymer (discussed below). In contrast, the repositioning of lipid molecules in the lipid and hybrid membranes could compensate for the structural disorder, caused by the insertion of *bo*$_3$ oxidase. The lower mobility of labeled lipids (0.3 mol%) in polymersomes (Figure 20A) supported such a repositioning around the protein. The diffusion coefficients of proteins and lipids are known to decrease linearly with increasing protein concentration (216, 217). However, an excessive decrease of the membrane fluidity could potentially hinder the conformational changes of membrane proteins. Therefore, the preserved fluidity of polymer membranes upon protein reconstitution may prove valuable for applications, which require higher protein density.

In the case of lipid and hybrid membranes, the lateral diffusion of *bo*$_3$ oxidase was faster than the diffusion of lipid and polymer dye, while in pure polymer vesicles the opposite was observed. Altogether, the protein diffusion slowed down from liposomes to polymersomes, which was analogous to the trend for the fluidity of protein-free membranes. The superimposition of properties of natural and synthetic materials resulted in the intermediate values observed for hybrid vesicles. The diffusion coefficient of labeled *bo*$_3$ oxidase in soy PC (9.9 ± 1.3 μm^2 s^{-1}) was identical to the previously determined by fluorescence correlation spectroscopy in DOPC and similar to the diffusion coefficients of smaller membrane proteins in POPC (Table 4). On the other hand, the protein diffusion in PDMS-*g*-PEO (3.5 ± 0.9 μm^2 s^{-1}) was at least two times higher than the diffusion of porins and channels in a triblock copolymer membrane. For instance, the diffusion coefficient of KcsA decreased nearly seven-fold upon transition from lipid to polymer (PMOXA$_7$-*b*-PDMS$_{49}$-*b*-PMOXA$_7$) environment (212), while for *bo*$_3$ oxidase in PDMS-*g*-PEO the decrease was less than three-fold. The favorable properties of the graft copolymer can be ascribed to the membrane thickness and the sufficient fluidity. In thicker membranes, the hydrophobic size mismatch between the membrane and the membrane protein is more pronounced and the polymer molecules compress the membrane protein stronger, which reduces its lateral mobility (212). In fact, the hydrophobic matching and slight compression of the PDMS-*g*-PEO membrane around the enzyme can be seen in cryo-TEM (see Chapter 3.1.2.3, Figure 28).

Since this work is embedded under the overarching aim of construction of an artificial cell, involving reconstitution of various types of membrane proteins (differing in functionality, size, hydrophobicity, and asymmetry), it was checked whether the increase of the polymer membrane fluidity upon protein insertion

is *bo*$_3$ oxidase-specific or a general phenomenon. Towards this end, *E. coli* F_1F_O-ATPase was labeled with ATTO 620 and reconstituted in hybrid and polymer GUVs by the same tailored fusion/electroformation protocol used for the proton pump, which demonstrated its utility for larger (F_1F_O-ATPase > 500 kDa (218)) and highly asymmetric membrane proteins (Figure 20B). Because of the lower reconstitution efficiency, which resulted in lower fluorescence signal we were unable to obtain reliable data for the protein diffusion. Nevertheless, the analysis of the labeled lipids and polymers demonstrated that the loosening of PDMS-*g*-PEO after protein insertion is not protein-specific: the diffusion of the polymer dye in polymersomes increased by 25 % upon reconstitution of F_1F_O-ATPase (Figure 20A).

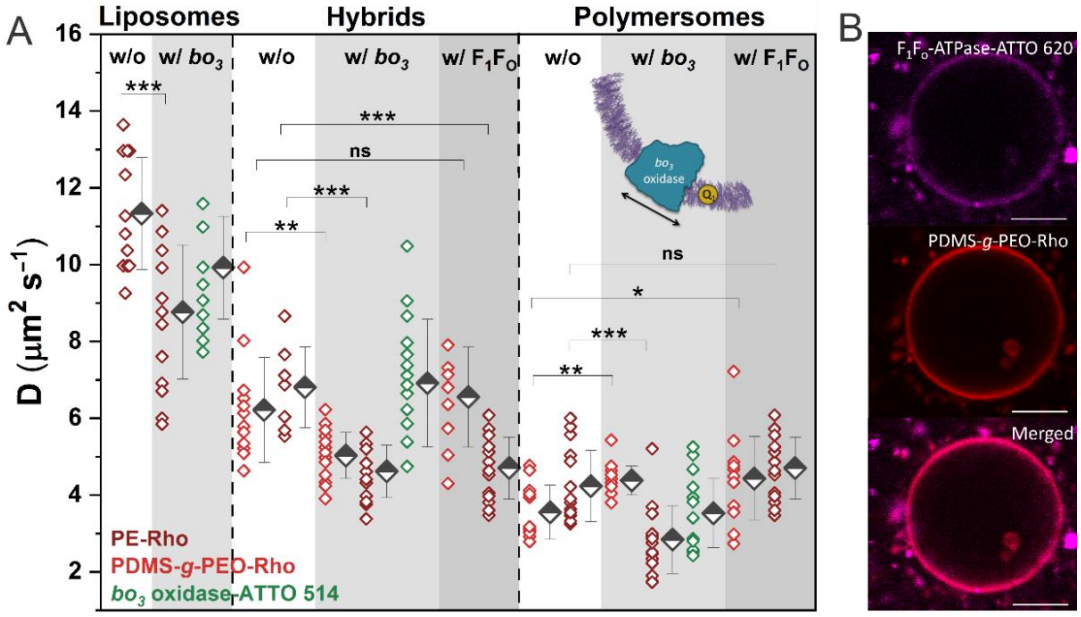

Figure 20. Lateral diffusion of membrane components and reconstituted proteins. (**A**) Diffusion coefficients for protein-free (w/o; white area) and protein-functionalized (w/ *bo*$_3$, light gray area; w/ F_1F_O, dark gray area) GUVs. Diffusion coefficients of lipid and polymer dyes are presented with red diamonds (PE-Rho, dark red; PDMS-*g*-PEO-Rho, light red); diffusion coefficients of *bo*$_3$ oxidase-ATTO 514 are presented with green diamonds. (**B**) Successful insertion of F_1F_O-ATPase-ATTO 620 (magenta) in F_1F_O-polymer-GUVs. Polymer dye PDMS-*g*-PEO-Rho (red) was used to visualize the membrane. Scale bar: 10 µm. Adapted from (1), licensed under CC BY 4.0.

Table 4. Comparison of the diffusion coefficients of protein-free and protein-functionalized membranes of different compositions, and diffusion coefficients of the reconstituted proteins. Adapted from (1), licensed under CC BY 4.0.

Type of membrane	Molecular weight (g mol^{-1})	Membrane thickness (nm)	Membrane diffusion coefficient (µm^2 s^{-1})		Reconstituted protein		Source
			Protein-free	Protein-functionalized	Type of protein	Diff. coeff. (µm^2 s^{-1})	
DMPC	677.933	5.0	8.8 ± 1.3 (36 °C)	-	Rhodopsin (37 kDa)	3.3 ± 0.3 (36 °C)	Vaz 1982 (219)

TLE (total lipid extract)			14 ± 0.1 (37 °C)	-	SR-ATPase (100 kDa)	1.8 ± 0.3 (36 °C)	
Soybean lipids			11 ± 0.1 (37 °C)	-	AchR (250 kDa)	2.4 ± 0.8 (36 °C)	
DMPC	677.933		6.9 (32 °C)	4.3 (32 °C)	bR (26 kDa)	2.3 (32 °C)	Peters 1982 (220)
DOPC:DOPG (75:25, mol/mol)	788.841	-	11.3 ± 0.6	11.4 ± 0.7	LacY (monomer, 45 kDa)	4.3 ± 0.4	Ramadurai 2009 (217)
DOPC:DOPS (75:25, w/w)	792.091	-	7.7 ± 0.8	-	LasS (dimer, ~140 kDa)	3.0 ± 0.3	Doeven 2005 (70)
				-	MscL (pentamer, ~70 kDa)	3.9 ± 0.3	
POPC	760.076	5.0 ± 0.4	9.8 ± 1.7 (154) 12.5 ± 0.5 (153)	-	KcsA-OG488 (tetramer)	8.5 ± 0.8 (212)	Itel 2015 (212)
					AqpZ-OG488 (tetramer)	7.9 ± 0.5 (212)	
DOPC	786.113	3.87 ± 0.05 (221)	10.0 ± 0.4 (222)	-	*bo*$_3$ oxidase-ATTO647N	~9.5 (79)	Sjöholm 2017 (79)
					bo$_3$ oxidase-ATTO594	~10.5 (79)	
Soy PC	775.037	3.49 ± 0.03 (223)	11.3 ± 1.5	8.8 ± 1.7	*bo*$_3$ oxidase-ATTO514	9.9 ± 1.3	This study
PDMS$_{26}$-*g*-(PEO$_{12}$)$_2$:soy PC	2333	-	6.2 ± 1.4	5.0 ± 0.6	*bo*$_3$ oxidase-ATTO514	6.9 ± 1.7	
				6.6 ± 1.3	F_1F_O-ATPase-ATTO620	-	
PDMS$_{26}$-*g*-(PEO$_{12}$)$_2$	3000	5 (224) – 5.4 (225)	3.6 ± 0.7	4.4 ± 0.4	*bo*$_3$ oxidase-ATTO514	3.5 ± 0.9	
				4.4 ± 1.1	F_1F_O-ATPase-ATTO620	-	
PMOXA$_{6-12}$-*b*-PDMS$_{34-63}$-*b*-PMOXA$_{6-12}$	3800 – 6900	9.2 ± 0.5 – 13.4 ± 0.9 (153)	2.4 ± 0.2 – 1.0 ± 0.1 (153)	-	AqpZ-OG488 (tetramer)	1.7 ± 0.1 – 0.8 ± 0.1 (212)	Itel 2015 (212)
PMOXA$_7$-*b*-PDMS$_{49}$-*b*-PMOXA$_7$	5100	12.1 ± 1.0 (153)	1.6 ± 0.2 (153)	-	KcsA-OG488 (tetramer)	1.3 ± 0.1 (212)	

Finally, the protein-induced loosening of the polymer membrane was inspected in more detail by analyzing the degree of disorder by a fluorescent probe in LUVs. Laurdan exhibited a red shift when set into more polar environment (presence of water in the membrane) (196) and the resulting generalized polarization (GP) values (for more details see Section 2.10.5) ranging from +1 (most ordered membranes) to −1 (most disordered membranes) (226). Soy PC membranes exhibited similar order to DOPC membranes (GP of soy PC was −0.26 ± 0.01 *vs.* −0.24 ± 0.00 for DOPC (226)), while polymer membranes displayed significantly higher disorder or water content (about 50 % lower GP values) (Figure 21B). Meanwhile, intermediate GP values were determined for hybrid membranes. The reconstitution of bo_3 oxidase caused a slight decrease only in the case of PDMS-*g*-PEO, which was in line with the hypothesis of loosened polymer architecture. High membrane disorder and sufficient fluidity, in combination with increase in lateral diffusion of membrane components upon protein insertion, plays in important role during vesicle fusion, in particular during membrane mixing (e.g., high disorder facilitated membrane mixing – discussed in Section 3.2.2).

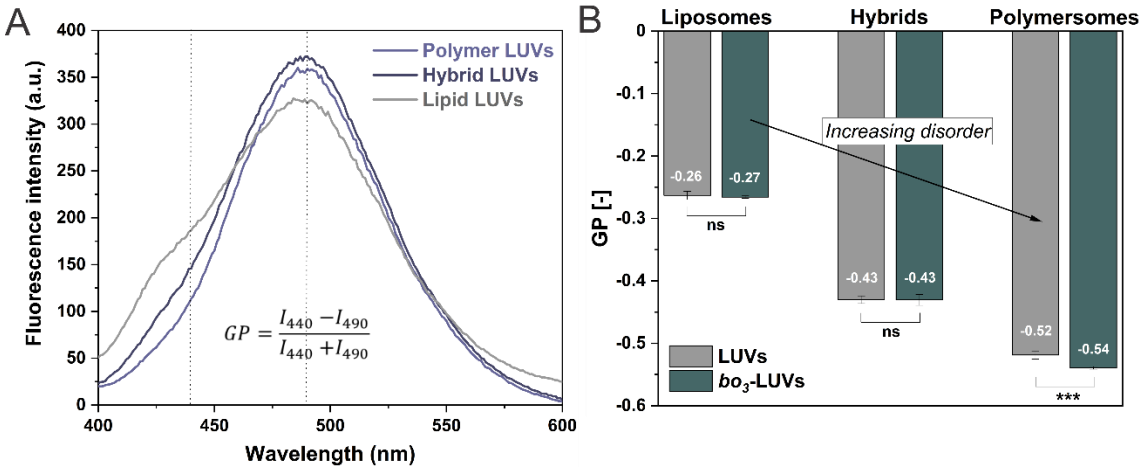

Figure 21. Membrane disorder. (**A**) Fluorescence emission spectra of Laurdan in lipid, hybrid and polymer membranes. (**B**) Generalized polarization (GP) values of protein-free and protein-functionalized LUVs. The black arrow shows the increasing exposure to water indicating increasing membrane disorder. Error bars represent SD from n = 3. Adapted from (1), licensed under CC BY 4.0.

3.1.2 Enhanced compartments – novel beneficial characteristic in interplay with membrane proteins

3.1.2.1 Can PDMS-g-PEO extend the activity lifetime of membrane proteins?

Reconstituted complex membrane proteins are known to drastically lose activity with time, whereby the rate of the loss depends on the protein type and the environment. While block copolymers have been shown to increase the functional stability (22), graft copolymers are still largely unexplored in this context. Since

the graft copolymer PDMS-*g*-PEO was considered to be used as the main membrane constituent for compartments involved in the growth module, its interplay with membrane proteins is crucial for its future integration with other modules that require membrane proteins. To test if PDMS-*g*-PEO can enhance the stability, detergent-mediated reconstitution by slightly modifying our previous protocol (21) was applied and the same model protein as above, bo_3 oxidase, was inserted in ~ 100 nm nanocompartments made of soy PC, PDMS-*g*-PEO:soy PC (70:30 molar ratio) and PDMS-*g*-PEO at a constant lipid/polymer-to-protein molar ratio of 9550:1. Then, intermittently the protein activity in all three systems over 13 days was measured. The assessment was based on oxygen reduction, which is coupled to proton pumping (169, 227). Oxygen consumption was measured using a Clark-type electrode (Section 2.9.6.1). The protein was activated with the electron shuttle ubiquinone 1 (Q_1) and dithiothreitol (DTT) under non-limiting concentration of the sacrificial electron donor (Figure 22A, inset).

Interestingly, when keeping the same lipid/polymer-to-protein molar ratio, bo_3 oxidase had the highest activity in hybrids, while its activity in polymersomes and liposomes was virtually the same (day 1, Figure 22A). The superior properties of hybrids were reflected in stability tests as well. On day 2 they retained 90 % of the initial activity, while liposomes and polymersomes decreased to 63 % and 69 %, respectively (Figure 22B). Similar relation was present towards the end of the measurements. On day 11 the activity of liposomes decreased to 4 %, while hybrids and polymersomes retained 25 % and 15 %, respectively (Figure 22A). Despite the scattering of the data, the qualitative trend (hybrids > polymersomes > liposomes) was maintained throughout the test. This was clearly evident also from the respective time constants of exponential decay (4.1 > 1.5 > 0.7), which reflected the days until the vesicles lost roughly ⅓ of their initial activities, even though the fit of liposome data might have led to some underestimation of the stability (Figure S2). The loss of activity was ascribed to the protein due to the similar behavior in micelles but the detailed mechanism of preservation should be clarified in a more detailed study. It is worth noting that the blending with graft copolymer resulted in a similar improvement (~ 20 %) of the stability in comparison to pure lipids as in the case of PBd-*b*-PEO:POPC (75:25) hybrid vesicles after one week (22). As previously emphasized (64), hybrids hold a great promise for the reconstitution of membrane proteins, whereby the enhanced durability, stability and shelf-life will be essential for application. PDMS-*g*-PEO:PC hybrids in particular may not only have a stabilizing effect but also increase the activity (presumably via higher reconstitution efficiency, yet to be determined). On the other hand, PDMS-*g*-PEO seems to be the only polymer so far, which enables fully retained bo_3 oxidase activity in addition to stabilization.

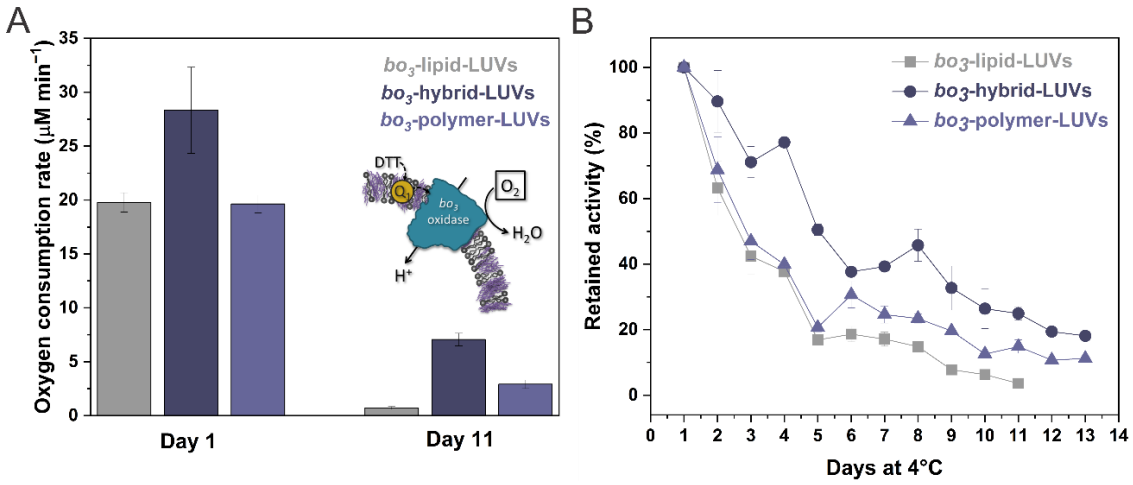

Figure 22. Activity of *bo*$_3$ oxidase reconstituted in LUVs over time at 4 °C, determined via oxygen consumption. (**A**) Enzyme activity in lipid hybrid and polymer LUVs on 1st and 2nd day. (**B**) Activity over time, measured every 24 h (each symbol represents the average of 2–3 repeats with SD). The shelf-life measurements of *bo*$_3$ oxidase, reconstituted in lipid, hybrid and polymer LUVs, alongside the controls in micelles, were terminated until the oxygen consumption of the liposomes activity dropped close to zero (after day 11 there was no significant difference with baseline, i.e. ± 0.5 μM min^{-1}). Adapted from (1), licensed under CC BY 4.0.

3.1.2.2 PDMS-g-PEO membranes resistivity against ROS

In addition to the shelf-life of individual membrane proteins, collateral damage caused by other enzymes may present an issue in more complex systems, e.g., oxidative stress in ETC assemblies. Since multiple artificial nano-organelles (one of them being reconstituted ETC) are planned to be encapsulated in larger polymer or hybrid microcompartment with ability to grow, reactive oxygen species (ROS) causing damage to membrane compartments and to all reconstituted membrane proteins should be considered. To study ROS damage on the reconstituted proton pump, the *bo*$_3$-LUVs were exposed to oxidative stress by incubation with ascorbyl free radicals following established protocols (228, 229). The incubation with ascorbate and ascorbyl radicals did not cause a change in the size distribution but it decreased the enzyme activity (1). However, PDMS-*g*-PEO shielded the proteins against oxidative stress; after 30 min of exposure to radicals polymersomes retained 73 ± 6 % activity, while liposomes only 10 ± 4 % (1). In addition, it should be noted that the activity decrease in polymersomes was statistically non-significant. The chemical resistance of the graft copolymer substantiates its suitability to accommodate the complete ETC and to counteract the detrimental influence of ROS (produced by Complex I in particular). The activity loss upon ROS exposure can be caused either by a direct attack to the reconstituted membrane proteins or by indirect deactivation via membrane disruption and enzyme delipidation. Since the vesicle size did not change, subtle changes associated with surface modifications and/or compromised tightness were sought for. Therefore, the surface charge of the vesicles without reconstituted *bo*$_3$ oxidase was measured and the leakage of encapsulated carboxyfluorescein (CF) by its dequenching (230) was tested. The different conditions did not

significantly alter the zeta potential results within the instrument accuracy (1). On the other hand, while liposomes were permeabilized upon radical exposure (Figure 23C,D), no leakage was detected in polymersomes and hybrids (Figure 23A,B), indicating the absence of membrane defects. In addition, protein-functionalized vesicles after oxidative treatment by cryogenic transmission electron microscopy (cryo-TEM) were inspected. A portion of the liposomes exhibited bilayer defects manifested as either visible pores or irregular surface (1). Such membrane disruptions by ROS likely lead to the delipidation of *bo*$_3$ oxidase and consequently to enzyme aggregation and deactivation (complete loss of activity in the absence of stabilizing amphiphiles is shown in Figure S3). On the contrary, no difference between the cryo-TEM images of ROS-treated and untreated samples was observed in both hybrids and polymersomes (1).

Finally, the effect of ROS on the enzyme alone was tested (i.e., *bo*$_3$ oxidase, which was not reconstituted in a membrane but stabilized in detergent micelles) and no loss of activity was observed (1). In fact, the oxygen consumption slightly increased, presumably due to direct reduction of hemes by ascorbate (25.5 ± 3.4 *vs.* 20.8 ± 3.5 µM min^{-1}). These observations further emphasize the importance of a stable scaffold even when the integrated membrane proteins are otherwise resistant to ROS. Furthermore, the structural integrity of the membrane is imperative for reaction compartmentalization or cargo delivery.

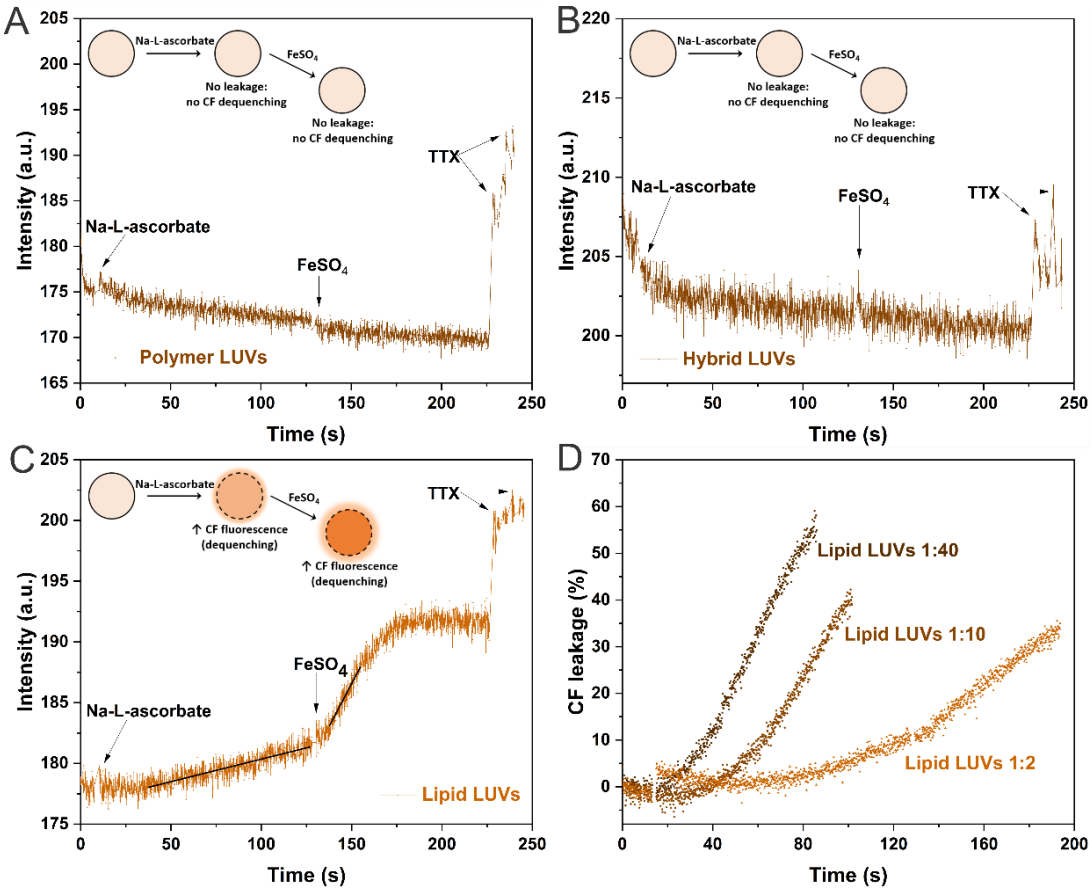

Figure 23. Changes in fluorescence intensity of carboxyfluorescein (CF) encapsulated in LUVs. CF was encapsulated in poymersomes (**A**), hybrids (**B**) and liposomes (**C**), (**D**). At the end of the measurement vesicles were solubilized with Triton X-100 (TTX) to achieve 100% dequenching of CF. Dye leakage with two different permeation rates was observed for liposomes: initial slower rate after the addition of Na-L-ascorbate and faster second rate after the addition of $FeSO_4$. No dye leakage was observed for polymersomes and hybrids after addition of Na-L-ascorbate or $FeSO_4$. (**D**) Dequenching of carboxyluorescein (CF) encapsulated in lipid LUVs at different dilutions (1:40, 1:10 and 1:2). The higher amount of vesicles results in higher CF concentration and dequenching is delayed. Adapted from (1), licensed under CC BY 4.0.

3.1.2.3 Passive proton permeability and membrane reorganization

The passive proton permeability is arguably the most important membrane characteristic with respect to the reconstitution of proton pumps, because it is fundamental for the establishment and sustainment of pH gradient. The insertion of bR has been shown to alter the tightness with respect to proton transport (168) but altogether, the systematic studies on the influence of membrane proteins are scarce and to the best of our knowledge have never been done for synthetic membranes in particular. Therefore, here, the passive proton permeability of the pristine and protein-functionalized membranes was determined by direct monitoring of GUVs. GUVs with reconstituted proton pump were prepared via fusion/electroformation approach, optimized for specific type of membrane. The latter approach is in detail described in Chapter 3.4, as it was considered as one of the approaches toward growth of membranous systems.

Thus far, the passive proton permeability of various membranes was predominantly measured in large vesicles (174, 202, 231, 232). While these bulk LUV studies enable the measurements of large populations at once, liposome intactness is occasionally questionable and the obtained values might not accurately depict the heterogeneity of the sample (170). In this regard, the convenience and the higher confidence of observations in the micrometer range could be potentially extended to account for individual attributes such as membrane curvature or compositional differences. Efforts in this direction have already been made: the permeability of lipid membranes with reconstituted bR was checked in GUVs but not quantified in detail (78). In the present study, microfluidic trapping was used in order to assess the permeability of individual GUVs (Figure 24). Luminal pH changes in a microfluidic device (see Section 2.2), which contained multiple rectangular traps similar to those in (185), with a gap size of about 5 µm between the posts forming the trap was followed (Section 2.10.9.1). This enabled entrapment of multiple GUVs with diameters > 10 µm and did not compromise their structural and functional integrity. The ΔpH was evaluated by encapsulation of the established ratiometric pH-sensitive dye pyranine (176, 233). Ratiometric measurements are advantageous as they are virtually insensitive to differences in pyranine encapsulation and photobleaching. First, the GUVs, suspended in the electroformation buffer (1 mM Tris-HCl, pH 7.5, containing 100 mM sucrose and 10 µM pyranine) were trapped in the microfluidic chip. Next, non-encapsulated pyranine was flushed away with dye-free buffer and finally, transmembrane pH gradient was induced by changing the external solution for isosmotic 1 mM MES, pH 6.0, containing ~ 100 mM sucrose (Figure 25A, inset). Upon acidification in the microfluidic device, the luminal pH of the different types of GUVs decreased differently (Figure S4).

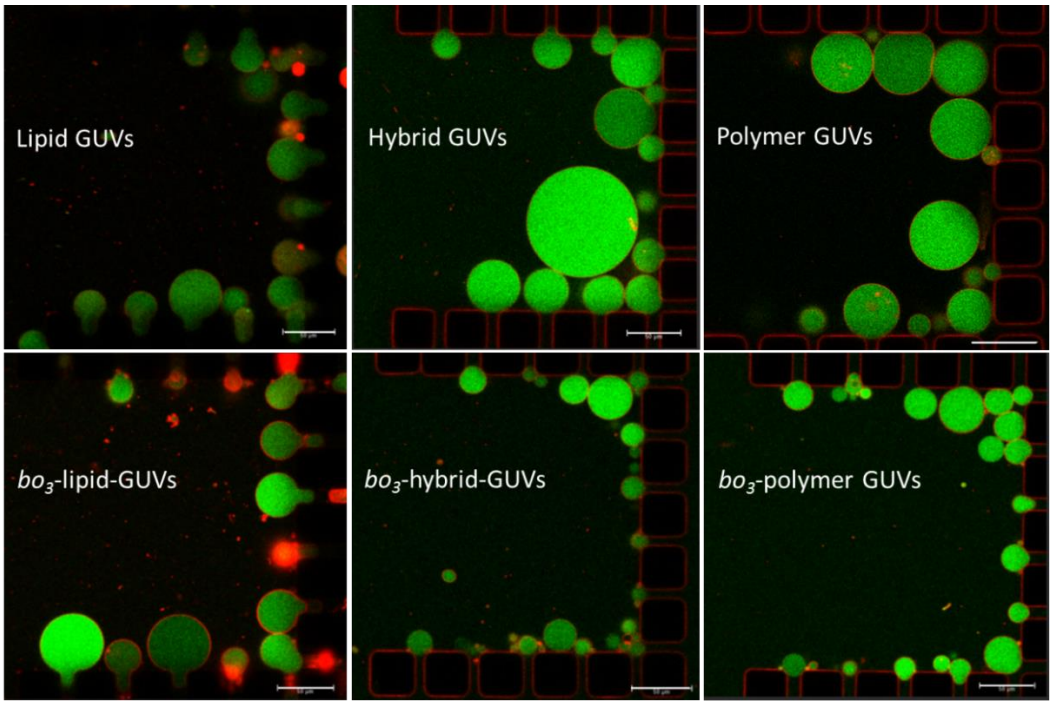

Figure 24. Examples of trapped GUVs and *bo*$_3$-GUVs evaluated for proton permeability. GUVs of 6 traps were evaluated for each system, one trap for each type of GUVs is shown as an example. All GUVs (including protein-free ones) were prepared by fusion/electroformation from LUVs. Scale bar: 50 µm. Adapted from (1), licensed under CC BY 4.0.

The reported values for proton permeability, which is more accurately denoted as net proton-hydroxyl permeability (199), vary over several orders of magnitude in liposomes (234). This discrepancy partially arises from different setups (pH dye, magnitude of pH gradient, temperature, etc.) and the calculation approaches; for details on the current data analysis, please see Section 2.10.9.2. The permeability coefficients at the micrometer scale slightly differed from the ones determined at nanometer scale (Table 5), but the values did not vary by more than an order of magnitude (×5 at most), which is the range of usually reported precision. This variance may be attributed first to the fact that in the bulk assay the integrity of the LUVs is not always guaranteed, and second to the differences in curvature and packing density, which accompany the size variance. This second assumption was supported by the minor difference in passive proton permeability (~ 9 %) in the case of protein-free polymersomes, in which the structure of the disorganized membrane with interdigitated PDMS chains (not a clear bilayer structure) should be largely preserved, regardless of the size. In the case of *bo*$_3$ oxidase-functionalized vesicles the difference in proton permeability on nano- and microscopic level may also arise from different membrane rearrangement and resealing after detergent removal (in the first case detergent was removed by gel filtration, while in the second by Bio-Beads). Altogether, with respect to the comparison between different membranes, the trends at different scales were remarkably reproducible.

In the case of protein-free vesicles the proton permeability of polymersomes (~ 2×10^{-7} cm s^{-1}) was slightly higher than that of liposomes in GUVs and 3.4× lower in LUVs (Table 5). In protein-free hybrids, different populations of vesicles were found; some exhibited a slightly higher permeability than liposomes and polymersomes, while others exceeded them many times over, which influenced the resulting mean values correspondingly (Figure 25B). This could obviously not be explained by the superimposition of properties of both membrane constituents, which would result in intermediate values. Instead, we hypothesize that the higher permeability to protons resulted from nanoscale phase separation. At 70 mol% polymer and 30 mol% lipid contents, the hybrid GUVs were exclusively homogeneous under the microscope. Only a single GUV with observable microdomains was found in the entire population (500–600) of all sample preparations (Figure S5) and no phase separation over time was observed (hybrids stayed microscopically homogeneous for over a week). Therefore, we speculate that the permeability may be increased because of heterogeneity at the nanoscale, caused by slight size mismatches and different molecular architectures. This would make the membranes more prone to spontaneous pore formation, especially at the phase interfaces. Increased permeability of hybrid membranes in comparison with pure lipid or polymer vesicles was already reported for DOPC:PEO-*b*-PBD blends (202), while nanodomain formation has been recently demonstrated for blends of PDMS-*g*-PEO and DPPC (200) and further confirmed in PDMS-*g*-PEO:soy PC hybrids with the help of cryo-TEM (this work). As mentioned in Section 3.1.1.1, in larger portion of the hybrid vesicles, nanodomains with lipid bilayer structure and surrounding fuzzy membrane resembling the structure of the polymer membrane were observed (Figure 18). Although the hybrids were prepared from 70 mol% polymer and 30 mol% lipid, the composition cannot be perfectly controlled as vesicles are out-of-equilibrium objects, which leads to the formation of hybrids with disperse lipid content, and consequently lipid domains (235). Our observations of nanodomains (Figure 19) and their size are in agreement with the previous report on PDMS-*g*-PEO:DPPC LUVs (3–7 nm, determined via SANS and FRET (200)). Importantly, lipid nanodomains in PDMS-*g*-PEO:PC were previously shown to be stable (no budding was observed in LUVs with nanodomains, while the budding occurred in phase-separated GUVs with microdomains) (235). Interestingly, despite the ~ 0.9 nm difference in the membrane thickness between the lipid and polymer membranes in the present case, the hybrid membrane had intermediate thickness and therefore no visible size mismatch was detected. A matching thickness between the lipid domains and the surrounding polymer membrane stabilizes the hybrid system by minimizing the line tension (235). Furthermore, the amphiphile mixing was previously shown to be more efficient for graft copolymer than for triblock with the same chemical composition and membrane thickness (PEO-*b*-PDMS-*b*-PEO) (200), giving an additional reason for preferably utilizing PDMS-*g*-PEO for preparation of stable hybrid vesicle systems.

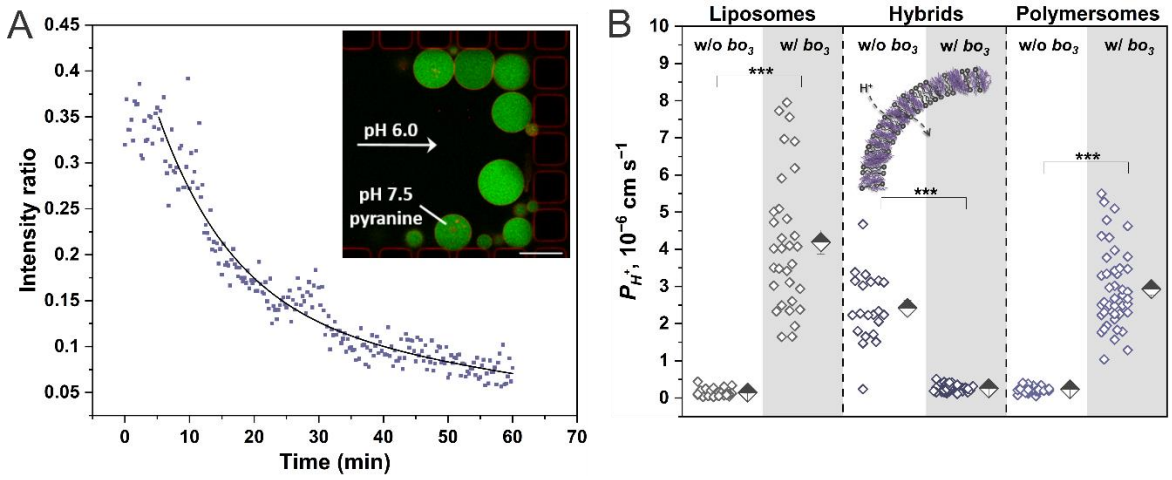

Figure 25. Passive proton permeability of GUVs and LUVs. (**A**) Fluorescence intensity ratio (excitation 458/405 nm, emission 499–551 nm) inside a single *bo*$_3$-polymer-GUV over time after exchange of external solution with more acidic buffer. Data was fitted with a biexponential decay function ($y = y_0 + A_1 e^{-tk_1} + A_2 e^{-tk_2}$). Scale bar: 50 µm. (**B**) Permeability coefficients (P_H^+) of protein-free GUVs (w/o *bo*$_3$; white area) and protein-functionalized GUVs (w/ *bo*$_3$; gray area). Individual GUV-related data are shown as diamonds. Average values are presented with half-filled diamonds and the corresponding mean error. Adapted from (1), licensed under CC BY 4.0.

Table 5. Summary of proton permeability for different protein-free and protein-functionalized membranes. For reconstituted bR is stated lipid-to-protein weight ratio and for *bo*$_3$ oxidase and F_1F_O-ATPase lipid/polymer-to-protein molar ratio. Adapted from (1), licensed under CC BY 4.0.

Type of membrane	Type of protein	Lipid/ polymer-to-protein ratio	Proton permeability – GUVs (cm s^{-1}) × 10^{-7}		Proton permeability – LUVs (cm s^{-1}) × 10^{-7}		Source
			Protein-free membrane	Protein-functionalized membrane	Protein-free membrane	Protein-functionalized membrane	
Egg PC/PA (9:1, mol/mol)	bR	160–40	-	-	~ 60	~ 120	Seigneuret 1986 (168)
		5	-	-		~ 600	
Soy PC	*bo*$_3$ oxidase / F_1F_O-ATPase	9560	1.4 ± 0.2 (n = 28)	41.9 ± 3.2 (*bo*$_3$) (n = 34)	7.1 ± 1.9	10.0 ± 2.6 (*bo*$_3$) 3.8 ± 0.4 (F_1F_O)	This study (GUVs), Marušič 2020 (1) (LUVs)
$PDMS_{26}$-*g*-$(PEO_{12})_2$:soy PC		9550	24.2 ± 2.0 (n = 21)	2.6 ± 0.2 (*bo*$_3$) (n = 38)	11.1 ± 1.4	7.9 ± 2.5 (*bo*$_3$) 5.7 ± 1.0 (F_1F_O)	
$PDMS_{26}$-*g*-$(PEO_{12})_2$		9540	2.3 ± 0.1 (n = 46)	29.3 ± 1.6 (*bo*$_3$) (n = 45)	2.1 ± 1.1	11.9 ± 3.0 (*bo*$_3$) 6.4 ± 1.5 (F_1F_O)	

To further assess the influence of phase separation in hybrids, microscopically heterogeneous GUVs (Figure 26) were deliberately formed, because we expected that if nanodomains were the cause of increased permeability microdomains should, due to their lower stability, cause similar or even higher proton

permeability. To obtain hybrids with microdomains, the classical electroformation procedure was employed, in which the hybrid amphiphile mixture was deposited on ITO-slides in organic solvent and not in the form of pre-formed vesicles (Section 2.6.1). The permeability of phase-separated hybrid GUVs (with polymer-to-lipid molar ratio of 40:60) was about three-fold higher than for homogenous hybrid GUVs (7.1 ± 1.9 × 10^{-6} cm s^{-1}) (Figure 27), which confirmed that the proton permeability correlated with the dynamics of phase separation.

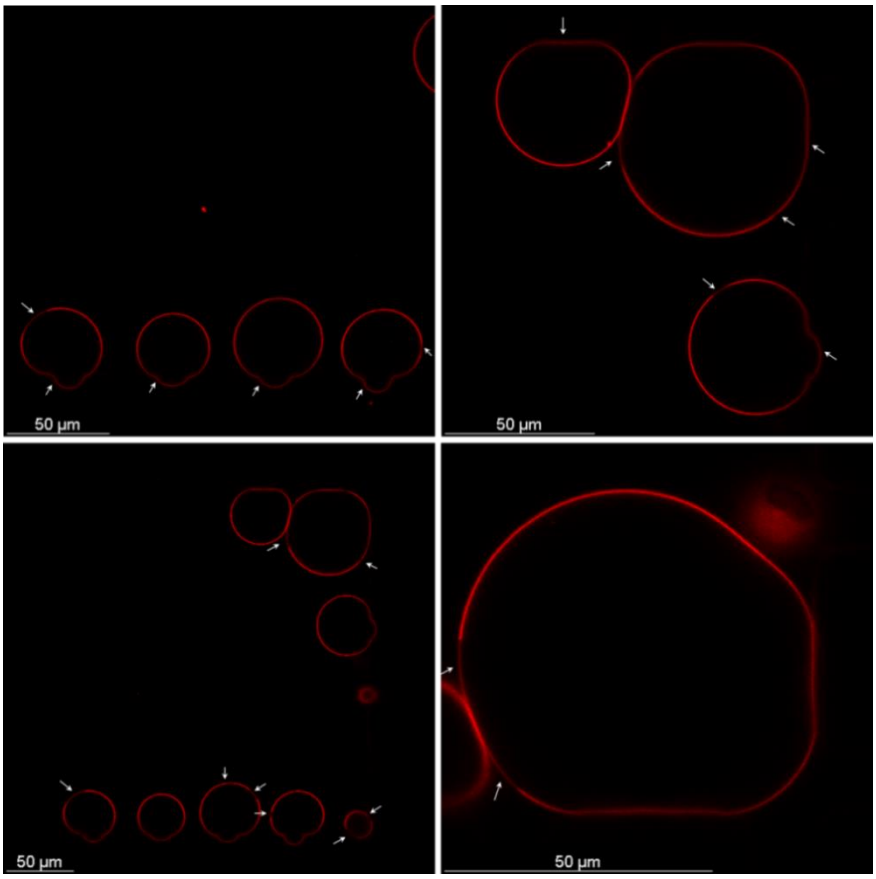

Figure 26. Phase-separated hybrid GUV evaluated for proton permeability of heterogeneous hybrids. GUVs composition was PDMS-*g*-PEO:soy PC = 40:60, mol%. GUVs were prepared by the classical electroformation procedure (in which hybrid mixture is deposited on ITO-slides in organic solvent and not in the form of pre-formed vesicles). The membrane is labeled with PDMS-*g*-PEO-Rho, which partitions primarily into polymer domains. White arrows show lipid domains (darker part, lower presence of polymer dye). Adapted from (1), licensed under CC BY 4.0.

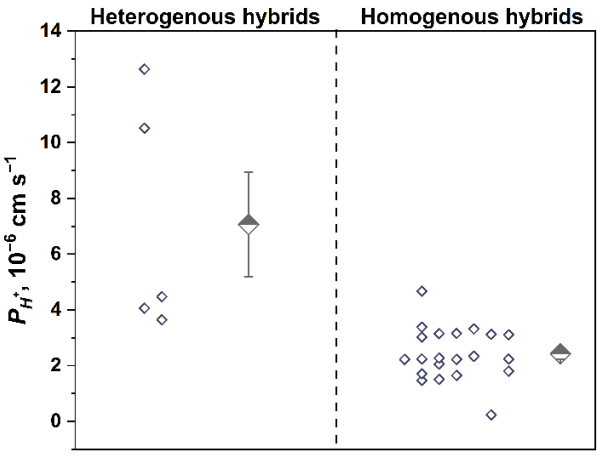

Figure 27. Permeability coefficients (P_{H^+}) of protein-free homogenous and heterogeneous hybrid GUV. GUVs were prepared by classical electroformation from a dry film. Composition of homogenous hybrids was PDMS-*g*-PEO:soy PC = 70:30, mol% and of heterogeneous PDMS-*g*-PEO:soy PC = 40:60, mol%. Adapted from (1), licensed under CC BY 4.0.

The reconstitution of *bo*$_3$ oxidase increased the proton permeability of the polymer GUVs, which was supported at the LUV scale (Table 5). The scattered data for *bo*$_3$ oxidase-functionalized polymersomes and liposomes likely results from the different reconstitution efficiency (GUVs with lower permeability have likely lower protein density). The decreased tightness of PDMS-*g*-PEO may be ascribed to the loosening of the polymer structure, as discussed in the case of the increased lateral diffusion (Figure 20) and membrane disorder (Figure 21). Permeability coefficients in the order of 10^{-5} cm s^{-1} at much lower lipid-to-protein weight ratios (40–160:1) were determined in egg PC:PA membranes with reconstituted bR (168). One can anticipate an increase of permeability at higher protein loadings in the present system as well; however, it is not expected that such loadings will be required for efficient bioenergetics.

In contrast to single component membranes, in hybrids *bo*$_3$ oxidase caused an unexpected decrease of the permeability for both GUVs and LUVs. To check if this phenomenon was protein-specific, the proton permeability at the LUV scale after insertion of *E. coli* F_1F_O-ATPase was additionally tested and the same behavior was observed (1). The permeability of polymer membranes increased, while the permeability of hybrids decreased (Table 5), whereby it should be noted that the type of detergent (sodium cholate for *bo*$_3$ oxidase, octyl glucoside for F_1F_O-ATPase) used in the reconstitution apparently did not play a role either.

A plausible explanation for the decreased proton permeability of proteohybrid membranes relates to the reorganization of the membrane by protein insertion; lipid molecules rearrange to fill the protein insertion spots and thus counteract the loosening of the polymer chains. To explore the latter hypothesis in greater detail, the partitioning of either lipid (PE-Rho) or polymer dye (PDMS-*g*-PEO-Rho) with respect to *bo*$_3$ oxidase-ATTO 514 in hybrid LUVs was analyzed (1). The intensity and dynamics of the FRET experiment

between the donor ATTO 514 and the acceptor rhodamine were strong indicators of random localization of the labeled polymer with respect to the enzyme and unrestricted mobility unlike the sustained intimate localization of lipids (1). This distinct positioning of the membrane constituents around the enzyme in hybrid membranes may be also the reason for the preserved activity of *bo₃* oxidase over time (Section 3.1.2.1). Nevertheless, this arrangement likely results in susceptibility to ROS exposure and lower stability compared to proteopolymersomes (1) because the delipidation of its tight surrounding is exposing the protein to aggregation. Furthermore, the entrapment of lipids is in line with their slower diffusion in the polymer membrane after protein insertion (Figure 20) in contrast to the increased overall membrane fluidity.

It was previously proposed that block copolymer membranes can adjust their thickness to the size of membrane protein, whereby in the case of hydrophobic mismatch between smaller membrane proteins (channels) and thicker PMOXA-*b*-PDMS-*b*-PMOXA membrane (9–13 nm) hydrophobic domains around the inserted MPs showed significant compression, explainable by the flexibility and low viscosity of PDMS (212). Cryo-TEM revealed that the PDMS-*g*-PEO membrane also compressed in the proximity of the protein (Figure 28). Meanwhile, the opposite behavior was observed in the hybrid membrane: the thickness around the integrated protein increased (average thickness changed from 4.9 ± 0.17 to 5.3 ± 0.54 nm), which was due to lipid accumulation in the protein surrounding. This rearrangement is most likely the reason behind the resealing of hybrids upon insertion of *bo₃* oxidase. In contrast, lipid membranes did not demonstrate adaptation of the thickness to the protein insertion (Figure 28), which was reflected by an increased proton permeability. The apparent sealing of the hybrid membrane by the membrane protein can be considered as a beneficial phenomenon, because it could help sustaining pH gradients across the membrane, while making use of the hybrid membrane chemistry.

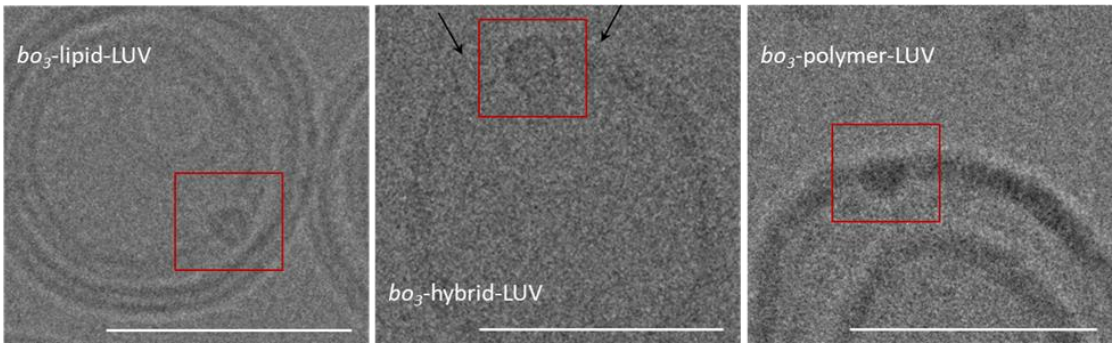

Figure 28. Cryo-TEM images of lipid, hybrid and polymer *bo₃*-LUVs. *bo₃* oxidase is marked with a red square. On the left and right image inward orientation of the cytosolic part (pump in) can be observed; see Figure S1 for *bo₃* oxidase dimensions and structure. The black arrows (middle image) show increased membrane thickness around the protein (from 4.9 nm to ~ 7.5 nm) in *bo₃*-hybrid-LUVs. Lipid bilayer thickness did not change after protein insertion (Table 6). In *bo₃*-polymer-LUVs (right) the membrane compressed in the vicinity of the protein (~ 4.4 nm) and expanded at further distance (~ 6.3 nm), leading to increase in the average thickness (~ 5.8 nm). LUVs were prepared

in 1 mM Tris (pH 7.5), 100 mM sucrose. Scale bar: 50 nm; defocus: ~ −2 µm. Adapted from (1), licensed under CC BY 4.0.

Table 6. Size distribution and membrane thickness of LUVs and *bo₃*-LUVs extruded through 100 nm-pore size membrane. For cryo-TEM, vesicle diameter and membrane thickness were analyzed in ImageJ (Fiji). Adapted from (1), licensed under CC BY 4.0.

Type of membrane	**DLS**				**Cryo-TEM**			
	Diameter (nm)		PDI		Diameter (nm)		Membrane thickness (nm)	
	w/o *bo₃*	w/ *bo₃*	w/o *bo₃*	w/ *bo₃*	w/o *bo₃*	w/ *bo₃*	w/o *bo₃*	w/ *bo₃*
Soy PC	106	96	0.066	0.053	80.7 ± 29.4 (n = 138)	70.2 ± 23.1 (n = 138)	4.4 ± 0.16 (n = 30)	4.5 ± 0.14 (n = 30)
$PDMS_{26}$-*g*-$(PEO_{12})_2$:soy PC	101	71	0.077	0.160	86.0 ± 39.6 (n = 91)	61.0 ± 23.9 (n = 158)	4.9 ± 0.17 (n = 30)	5.3 ± 0.54 (n = 66)
$PDMS_{26}$-*g*-$(PEO_{12})_2$	103	85	0.108	0.107	97.4 ± 34.7 (n = 36)	81.9 ± 39.0 (n = 61)	5.3 ± 0.17 (n = 30)	5.8 ± 0.42 (n = 47)

3.2 Charge-mediated growth: mixing natural and synthetic fusion mediators

First growth mechanisms investigated in this work were based on electrostatic interactions between the membranes. Utilizing anionic lipids (soy L-α-phosphatidylserine, soy PS), composing natural membranes, and synthetic cationic lipids (1,2-dioleoyl-3-trimethylammonium-propane, DOTAP), oppositely charged vesicles were formed and their fusion was explored. Furthermore, replacement of natural soy PS by synthetic PDMS-*g*-PEO was investigated.

3.2.1 Membrane mixing during charge-mediated fusion of nanocompartments

The hybrid vesicles used in this study were composed of PDMS-*g*-PEO and 5–40 mol% of anionic soy PS or cationic 1,2-dioleoyl-3-trimethylammonium-propane (DOTAP). For control experiments, zwitterionic (i.e., neutral) 1,2-dioleoyl-*sn*-glycero-3-phosphocholine (DOPC) was used instead of charged lipids or synthetic polymers. The size evolution and membrane mixing were monitored in ~ 100 nm sized unilamellar vesicles (LUVs), prepared by freeze-thaw cycles and subsequent extrusion, as described in Chapter 2.7. The size distribution was assessed by dynamic light scattering (DLS), while the membrane mixing assay was based on the fluorescence resonance energy transfer (FRET) between the donor 7-nitro-2-1,3-benzoxadiazol-4-yl (NBD) and the acceptor lissamine rhodamine B sulfonyl (Rho). Thereby, anionic vesicles contained both dyes, whereas cationic ones remained dye-free, and total NBD dequenching was obtained by solubilization with Triton X-100 (TTX). To confirm that both lipid dyes were homogenously distributed in the anionic hybrid membrane, optically accessible giant unilamellar vesicles (GUVs) were prepared by electroformation and analyzed by fluorescence microscopy (Figure S6).

Targeting primarily a single round of fusion, first oppositely charged LUVs (tagged with 1.5 mol% of each dye) were mixed in a 1:1 molar ratio and rapid dynamics in all tested amphiphile compositions was observed. In the benchmark liposomes, increasing the amount of charged lipids from 5 to 40 mol% led to a higher membrane mixing efficiency, as expected from the higher driving force. However, this was surprisingly not the case for hybrids, in which the highest score (49 ± 1 %) was obtained with 10 mol% of PS/DOTAP and decreased upon further charging (Figure 29A). This effect was ascribed to trapping and screening of PE-Rho and PE-NBD by the charged lipids, which skewed the FRET readout. Therefore, a higher membrane dilution was used to facilitate the diffusion of the tagged lipids. Indeed, increasing the amount of non-tagged LUVs led to more dequenching (Figure 29C). Since PDMS-*g*-PEO membranes are slightly negative (1) (and PE-Rho and PE-NBD further increase their negativity (3, 106)), whether the intrinsic charge of the polymer would suffice for membrane mixing was tested. This hypothesis was confirmed upon mixing of tagged polymersomes with non-tagged hybrids containing 5–40 mol% cationic

lipids, whereby the highest degree (about 20 %) of membrane mixing was again at 10 mol% DOTAP loading (Figure S7).

However, the membrane mixing did not always correspond to complete vesicle fusion, as evidenced by the absence of DLS changes in hybrids containing 5–10 mol% of charged lipids (Figure 30, volume distribution in Figure S8). The size increased only when electrostatic attraction was promoted by higher (20–40 mol%) amounts of PS/DOTAP, resulting in doubling of the vesicle areas roughly. For example, the mean diameter of hybrids containing 30 mol% of charged lipids increased to 173 nm upon fusion, which roughly corresponded to the expected value of 185 nm, calculated by adding the mean vesicle areas. Slightly lower experimental diameters in comparison to the theoretical ones have been also previously observed after SNARE-mediated liposome fusion (236). In parallel, using the volume constraint to calculate the theoretical diameters upon fusion leads to a better agreement with DLS data. However, an additional low-intensity peak at ~ 5 μm (pronounced in the volume distribution, Figure S8) suggested that hybrids with the latter compositions did not undergo only binary fusion; therefore, neither type of theoretical values may be used for precise quantification.

To minimize the trapping effect, the lipid dye concentration was reduced to 0.5 mol% in another set of FRET experiments. The dilution indeed improved the assay sensitivity for both, hybrids and liposomes, resulting in nearly twice as high intensity of mixing of the membrane in all tested systems (Figure 29B). However, the trends in liposomes and hybrids remained the same and 10 mol% loading of charged lipids in the latter membranes resulted in the highest response (79 ± 3 %) upon equimolar mixing. This substantiated the hypothesis that increasing the lipid amount beyond a certain threshold led to some form of membrane rearrangement and heterogeneity. Furthermore, the latter compositions required a higher amount of surfactant to obtain the maximal NBD fluorescence, even beyond the solubilization point.

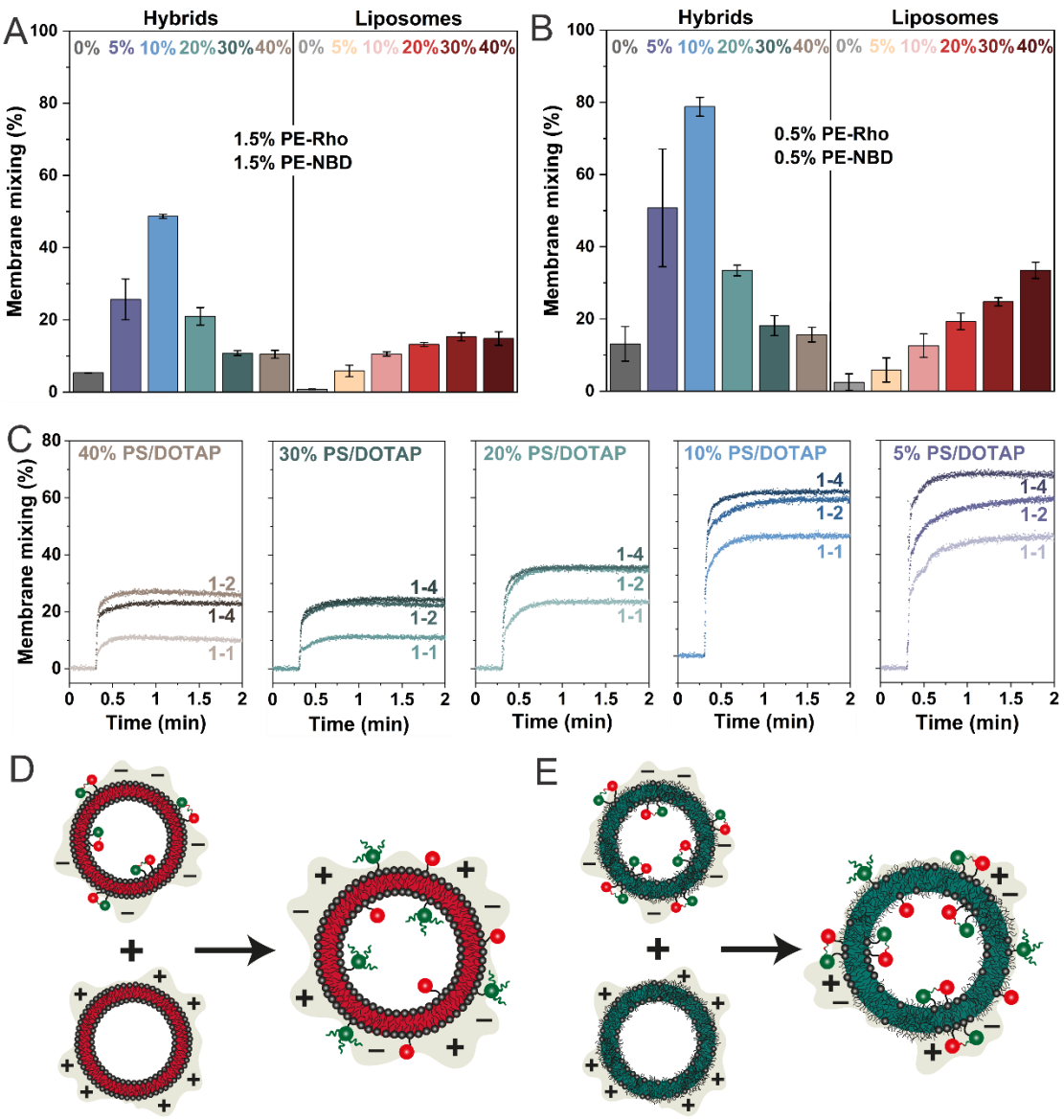

Figure 29. Charge-mediated membrane mixing of hybrid and lipid LUVs with different amounts of charged lipids. Hybrid LUVs were composed of 60–100 mol% PDMS-*g*-PEO and 0–40 mol% DOTAP/soy PS, while lipid LUVs contained 60–100 mol% DOPC and 0–40 mol% DOTAP/soy PS. (**A**), (**B**) Membrane mixing degree (after 3 min) of hybrid and lipid LUVs, containing different amounts of charged lipids (0–40 mol%), mixed in molar ratio 1:1; the final concentration of LUVs was 100 µM. Soy PS-LUVs were tagged with PE-Rho and PE-NBD at two different concentrations. The corresponding time courses are shown in Figure S9 and S10. (**C**) Membrane mixing kinetics of differently charged hybrid LUVs at three different molar ratios (1:1, 1:2, 1:4) between the tagged and non-tagged populations; the final concentrations of LUVs were 100, 150 or 250 µM, respectively. Soy PS-containing LUVs were tagged with 1.5 mol% PE-Rho and PE-NBD. (**D**) Mechanism of the FRET assay in liposomes. Upon fusion, the lipid dyes are homogenously distributed in the membrane and NBD is dequenched. (**E**) Proposed mechanism for the unusual behavior in hybrid LUVs. The lipid dyes are trapped in lipid nanodomains, leading to incomplete NBD dequenching upon vesicle fusion. Adapted from (2), licensed under CC BY 4.0.

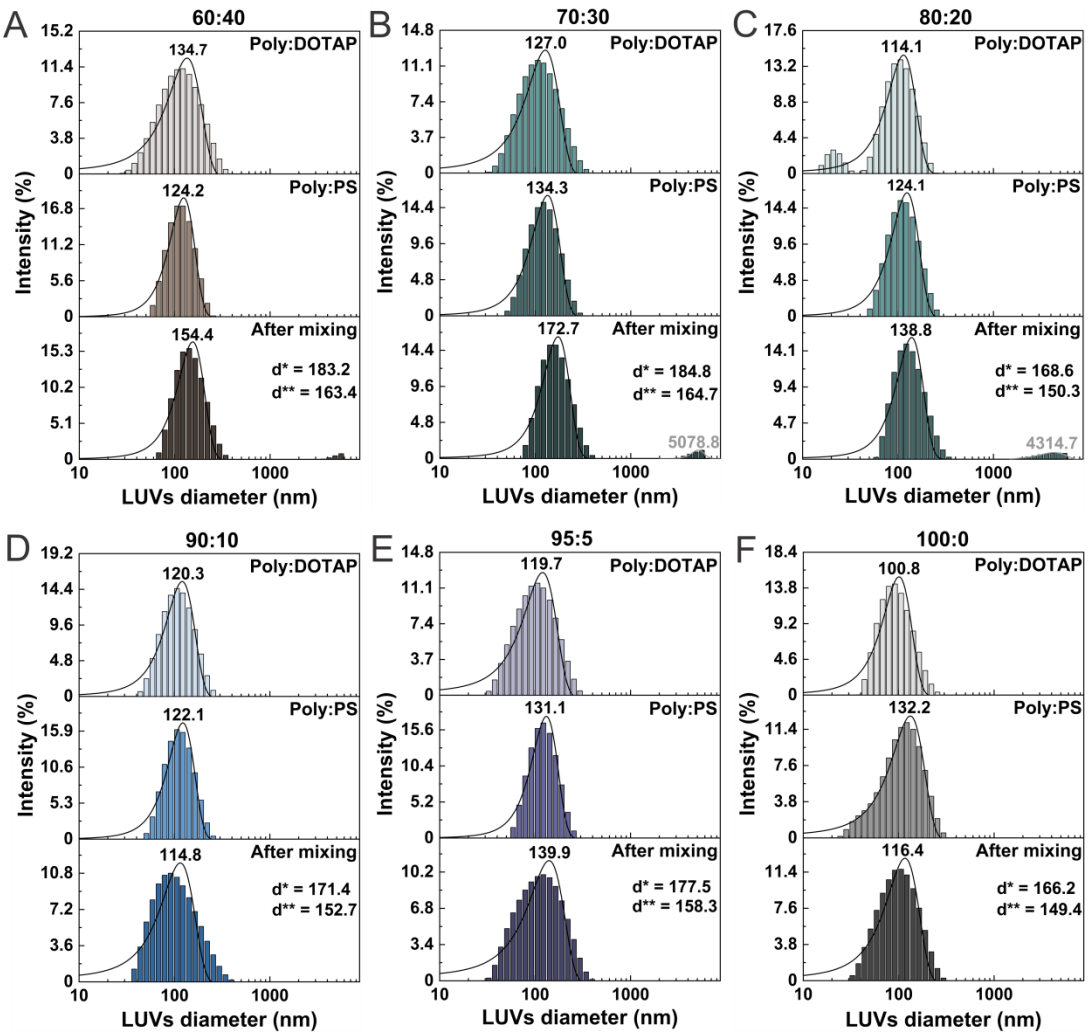

Figure 30. Size changes in differently charged hybrid LUVs upon fusion. The membrane compositions correspond to the ones in Figure 29A and the term "Poly" denotes PDMS-*g*-PEO. The respective intensity distribution before and after mixing (10 min at 500 rpm) was determined by DLS. The curves show fitted Gaussian distributions and the mean diameter is indicated above the curves. The mean diameter expected after binary fusion was calculated according to: $d^{*} = ({d_1}^2 + {d_2}^2)^{\frac{1}{2}}$ and $d^{**} = ({d_1}^3 + {d_2}^3)^{\frac{1}{3}}$ for the area and volume constraints, respectively. Adapted from (2), licensed under CC BY 4.0.

The effect of the surfactant (at 0.5 mol% dye loading) by replacing TTX with octyl glucoside (OG) was also probed, which led to a slower solubilization and required higher concentrations (34–42 µl of 10 % OG vs. 2–4 µl of 10 % TTX). This was likely due to the lower partitioning coefficient of OG in the membrane (58–75 M^{-1} vs. 6200 vs. M^{-1} for TTX in egg PC vesicles (237)). Apart from that, the different detergent did not influence the FRET dependence on the charged lipid loading and only slightly increased the readout magnitude (Figure 31).

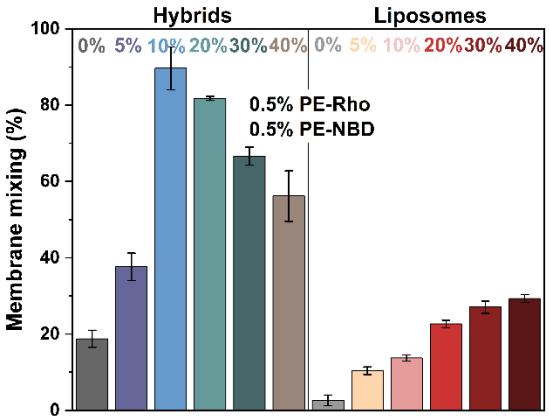

Figure 31. Charge-mediated membrane mixing of lipid and hybrid LUVs with different amount of charged lipids. Hybrid LUVs were composed of 60–100 mol% PDMS-*g*-PEO and 0–40 mol% DOTAP or soy PS, and lipid LUVs of 60–100 mol% DOPC and 0–40 mol% DOTAP or soy PS. Anionic and cationic LUVs were mixed in molar ratio 1:1; final concentration of LUVs was 100 µM. Anionic LUVs (DOPC:soy PS) were tagged with 0.5 mol% PE-Rho and 0.5 mol% PE-NBD. 100 % was obtained by solubilizing LUVs with octyl glucoside. The corresponding membrane mixing over time is shown in Figure S11. Adapted from (2), licensed under CC BY 4.0.

Due to the partial discrepancy between the FRET and DLS results, the effect of the charge sign on the membrane mixing efficiency was further explored. Despite the fact that 10 mol% charged lipids might not suffice for complete fusion (Figure 30), this ratio was used because it provided the highest sensitivity in FRET. For liposomes, it was previously shown that fusion required oppositely charged membranes, whereas the combination of neutral and negative LUVs did not promote membrane or content mixing due to the absence of sufficient electrostatic attraction forces (80). Here, this finding was confirmed only in part by testing three different charge combinations – the membrane mixing between neutral and cationic liposomes (Figure 32B) was much slower (and fairly linear) but still reached about 10 % after prolonged observation (Figure S12). In the case of hybrids vesicles though, mixing of tagged neutral LUVs with non-tagged cationic LUVs resulted in a measurable degree of membrane mixing in the first minute of the experiment (Figure 32A). On the other side, the low changes in the size distributions of both liposomes and hybrids corresponded to the comparatively low loadings of charged lipids (Figure S13 and S14).

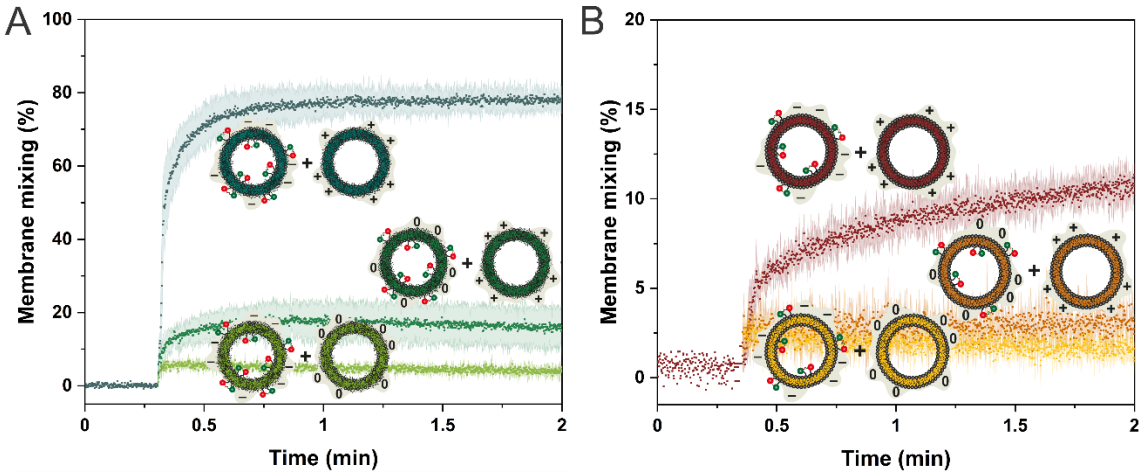

Figure 32. Charge-mediated membrane mixing of anionic (10 mol% soy PS), cationic (10 mol% DOTAP) and neutral (10 mol% DOPC) LUVs. Three combinations were tested: anionic/cationic, neutral/cationic, and anionic/neutral vesicles and the lipid dyes for FRET were incorporated either in anionic or neutral vesicles at 0.5 mol% loading. LUVs were mixed in the molar ratio 1:1 and the final concentration of LUVs was 100 µM. (**A**) Hybrid LUVs and (**B**) lipid LUVs in 200 mM sucrose. Adapted from (2), licensed under CC BY 4.0.

Although the hybrid membrane appears macroscopically homogeneous when the synthetic polymer predominates (21, 49), heterogeneities might be observable on smaller scale. In this regard, different techniques, including small-angle neutron scattering (SANS) indicated the presence of nanodomains in hybrid LUVs composed of PDMS-*g*-PEO and 2-dipalmitoyl-sn-glycero-3-phosphocholine (DPPC) (235). Here, nano-scale phase separation in PDMS-*g*-PEO:soy PC LUVs was also observed by cryo electron microscopy (cryoEM), where the heterogeneity was manifested by interchanging fuzzy (corresponding to the polymer) and clearly visible bilayer domains (Chapter 3.1.1.1 and ref(1)). To reveal if nanodomains were present in the charged hybrids, cryoEM was performed on PDMS-*g*-PEO:DOTAP and PDMS-*g*-PEO:soy PS:PE-Rho:PE-NBD LUVs containing 5 or 30 mol% of charged lipids. Nanodomains with sizes between 3 and 40 nm (2) were found in all four samples, but LUVs with smaller loading of charged lipids exhibited lower amount of nanodomains; the difference was in particular pronounced in the anionic LUVs containing dyes (for 30 mol% charged lipids 79 % cationic and 78 % anionic, and for 5 mol% charged lipids 71 % cationic and 53 % anionic hybrids contained nanodomains). Moreover, cryoEM data suggested that SNARE-mediated fusion (i.e., pore formation) of such hybrid LUVs often occurred between the lipid and polymer nanodomains (106). Therefore, fusion in hybrids was facilitated by the intrinsic negative charge of PDMS-*g*-PEO (compared to DOPC) on the one side, and the formation of lipid nanodomains when the ratio of charged lipids surpassed a certain threshold (~ 10 mol%) on the other. However, the latter phase separation also seems to prevent the full FRET loss, because the tagged lipids preferentially partition in the charged lipid phase, whereas the diffusion of PE-Rho and PE-NBD in liposomes is not affected and the dequenching scales only with the number of (hemi)fusion events (i.e., degree of membrane mixing). In

fact, similar phenomenon was observed when ubiquinol bo_3 oxidase was reconstituted in hybrids, which enzyme also sequestered lipids in its vicinity (Chapter 3.1.2.3 and ref(1)).

After fusion, cryoEM of hybrid LUVs containing 5 mol% of charged lipids manifested only early intermediates (referred to as point contact and hemifusion), while later fusion intermediates (referred to as pore opening and final configuration) dominated when the charged lipid loading was increased to 30 mol% (2). This observation is in agreement with the DLS data and the prospective pore opening snapshots (2) indicated the involvement of lipid nanodomains in the fusion process, similar to our previous observations (106).

3.2.2 Synergy between charge and mechanical properties promotes fusion of hybrid vesicles

To elucidate the reasons behind the more efficient membrane mixing in hybrids several relevant membrane characteristics were quantified. First, the most apparent cue for charge-mediated fusion was assessed by measuring the zeta potentials of LUVs with different membrane compositions in sucrose and in 20 mM Tris-phosphate buffer. The latter was chosen as a model solution with respect to enzyme requirements in the context of cell mimicking.

In sucrose, the effect of the charged lipid loading in hybrids and liposomes was fairly identical, although the negative charge contribution of the polymer was superimposed – it overall lowered the positive charge of hybrid LUVs and increased the negative one in comparison to liposomes (Figure 33A). The buffer partially neutralized the surface charge of all vesicles as expected, however, its influence was more prominent in the case of hybrids (Figure 33B). This screening was likely facilitated by better penetration of ions in the expanded hydrophilic layer, which hypothesis is based on the fact that the membrane thickness increased (from 5.8 ± 0.3 nm to 6.4 ± 0.3 nm for cationic hybrid LUVs (n = 100) and from 5.8 ± 0.4 nm to 6.5 ± 0.4 nm for anionic hybrid LUVs (n = 100)) as revealed by cryoEM data. In parallel, KCl caused a decrease in the bending rigidity (from 11.6 $\kappa_B T$ (1) to 6.6 $\kappa_B T$ (106)) of PDMS-*g*-PEO-containing membranes, which are in any case softer than DOPC ones (19.05 $\kappa_B T$ (238)). The latter property (i.e., membrane softness) decreases the energy needed for fusion pore opening, as discussed in the case of SNARE-mediated fusion (106), and apparently acts in synergy with the effect of the charge.

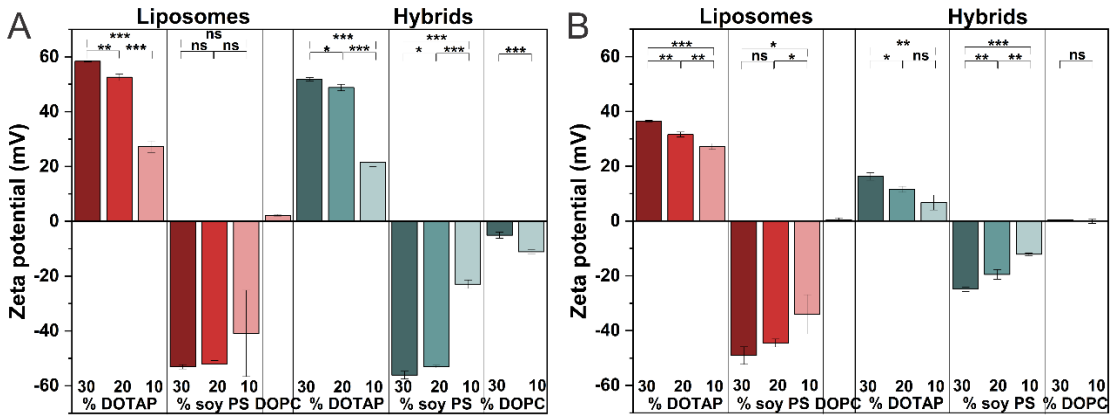

Figure 33. Zeta potential of lipid (red shades) and hybrid (green shades) LUVs, containing different amounts of cationic (DOTAP), anionic (soy PS), or neutral (DOPC) lipids. Zeta potential was determined in (**A**) 200 mM sucrose and (**B**) 20 mM Tris-phosphate buffer (pH 8.0). Bars show the average of two samples, each measured three times, and the average standard deviations. Ns = not significant for $P > 0.05$; *$P \leq 0.05$; **$P \leq 0.01$; ***$P \leq 0.001$. Adapted from (2), licensed under CC BY 4.0.

Next, the packing influence of charged and neutral lipids on the hybrid and lipid membranes in 200 mM sucrose was estimated by the generalized polarization (GP) value of Laurdan (196). The latter probe is a hydrophobic dye, sensitive to solvent polarity, and its exposure to the aqueous phase in less ordered membranes leads to changes in its fluorescent spectrum. Interestingly, whereas DOTAP had little effect on the membrane order in liposomes likely due to the matching fatty acids, PS progressively packed the latter membranes (Figure 34). This outcome is in part counterintuitive, because the major component (68 %) of the soy PS mixture is diunsaturated and it could be generalized that unsaturation is related to lesser order. For instance, replacement of one of the acyl chains in DOPC with a saturated one (POPC) caused considerable ordering of the liquid disordered (L_d) phase in pure membranes (226). However, the negatively charged lipid mixture also contained 10 % palmitic chains and blending of the amphiphiles can potentially amend some irregularities and thus tighten the bilayer. Similar outcome has been demonstrated in the case of PC, whereby natural PC mixtures from liver or brain exhibited higher order than DOPC (239). In parallel, the headgroup in all probability also exercises a packing effect, as shown by the ordering of DOPC:POPC by phosphoethanolamine (PE) (240). On the other side, the impact of charged lipids in hybrids was fairly similar and DOTAP resulted in roughly the same GP as DOPC (Figure 34). Furthermore, the individual impact of the main components of the soy PS mixture scaled with the degree of saturation – hybrids containing 18:2 PS exhibited higher disorder than the ones with 18:1 PS, and the palmitic chains further ordered the membranes (-0.27 ± 0.01, -0.23 ± 0.01, -0.17 ± 0.01, respectively). However, the final soy PS mixture did not behave like a weighted average, which suggests that a complex interplay with the polymer dictates the disorder of hybrid membranes. In summary, all types of hybrid mixtures exhibited higher degree of disorder in comparison to the lipid ones and the packing influence of PS was less pronounced in total.

Interestingly, DOPC caused relatively small but yet statistically significant ordering of the hybrid membranes, whereas PS did not produce a uniform trend. The latter could be potentially related to enhanced nano-scale phase separation above certain PS threshold, as discussed in the previous chapter. At 30 mol% charged lipids, replacement of sucrose with buffer did not exercise considerable effect (Figure S15) but the differences can explain the small deviations from previous data on the GP (e.g., −0.29 in this study *vs.* −0.24 (226) for DOPC, or −0.46 in this study *vs.* −0.43 (1) for hybrids containing 30 mol% neutral lipids). Altogether, the overall looser packing of hybrid membranes in comparison to DOPC apparently promotes membrane mixing. Moreover, it can be speculated that the more similar membrane arrangement of anionic and cationic hybrids, manifested by closer GP values, is another factor that facilitates the miscibility in conjunction with the electrostatic attraction.

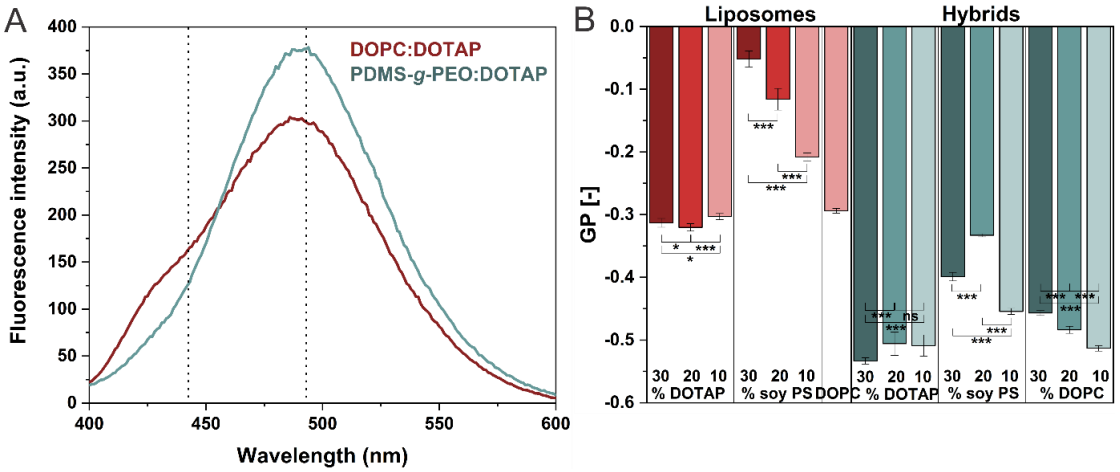

Figure 34. Membrane disorder of lipid and hybrid LUVs. (**A**) Fluorescence emission spectra of Laurdan in lipid (DOPC:DOTAP = 70:30 mol%, red shades) and hybrid (PDMS-*g*-PEO:DOTAP = 70:30 mol%, green shades) membranes in 200 mM sucrose. Dotted lines indicate wavelengths used to calculate GP values. (**B**) Generalized polarization (GP) values of lipid and hybrid LUVs with different amounts of anionic (PS) or cationic (DOTAP) lipids in 200 mM sucrose. Error bars represent SD from n = 3–6. *** for $P \leq 0.001$. Ns = not significant for $P > 0.05$; *$P \leq 0.05$; **$P \leq 0.01$; ***$P \leq 0.001$. Adapted from (2), licensed under CC BY 4.0.

During fusion, the rate and extent of membrane mixing is also determined by the interbilayer (i.e., between the outer layers of separate vesicles) and the transbilayer (i.e., between the outer and inner layers of the same vesicles; also known as flip-flop) transport of the membrane building blocks. Therefore, the kinetics of both processes in liposomes and hybrids was studied by using fatty acid-labeled phospholipids (M-NBD-PE and M-NBD-PC), as previously done for POPC and *Bacillus megaterium* vesicles (241). Due to their shorter acyl chains and consequently increased water solubility, these probes rapidly equilibrate between the outer leaflets of different vesicle populations. Addition of acceptor vesicles ("empty") to the donor vesicles (containing PE-Rho and the transport probes) resulted in NBD dequenching profiles that reflected the different behavior of both types of membranes (Figure 35A). For liposomes, the single exponential

profile implied only interbilayer exchange at this timescale. Meanwhile, the biphasic kinetics of hybrids indicated that the transbilayer exchange took place at the expected slower rate (Figure 35A, black trace). The respective rate constants for inter- (k_1) and transbilayer (k_2) transport are shown in Figure 35B. Thereby, changing the donor/acceptor molar ratio from 0.25 to 0.5 did not have a significant effect on k_1 (Figure 35C). Moreover, no transbilayer transport occurred in hybrids stained with M-NBD-PC (Figure 35D), suggesting that the size of the headgroup played a role in the flip-flop too. Altogether, cationic vesicles exhibited comparatively faster transport, which correlated to their increased disorder in both natural and hybrid membranes (Figure 35B). In this regard, the lesser packing of the latter corresponded to shorter half-times [$t_{1/2}$ = (ln 2)/k_1] of interbilayer exchange (0.03 s for M-NBD-PE and 0.02 s for M-NBD-PC) than for liposomes (0.08–0.13 s for M-NBD-PE and 0.04–0.05 s for M-NBD-PC). The amphiphile transport dictates the membrane mixing primarily during the vesicle docking and hemifusion stages but may influence the full fusion too. Since there is disparity between the inner and outer leaflets (e.g., in liposomes with an outer dimeter of 100 nm and membrane thickness of 5 nm the lipids in the outer leaflet are 1.5 fold more than those in the inner leaflet), this imbalance has to be compensated by lateral diffusion and flip-flop of membrane building blocks when the vesicles fuse (242). Apparently, the transmembrane mass transport barrier is less pronounced in the case of hybrid membranes in comparison to the intrinsically low rate of leaflet exchange in liposomes, leading to more efficient fusion.

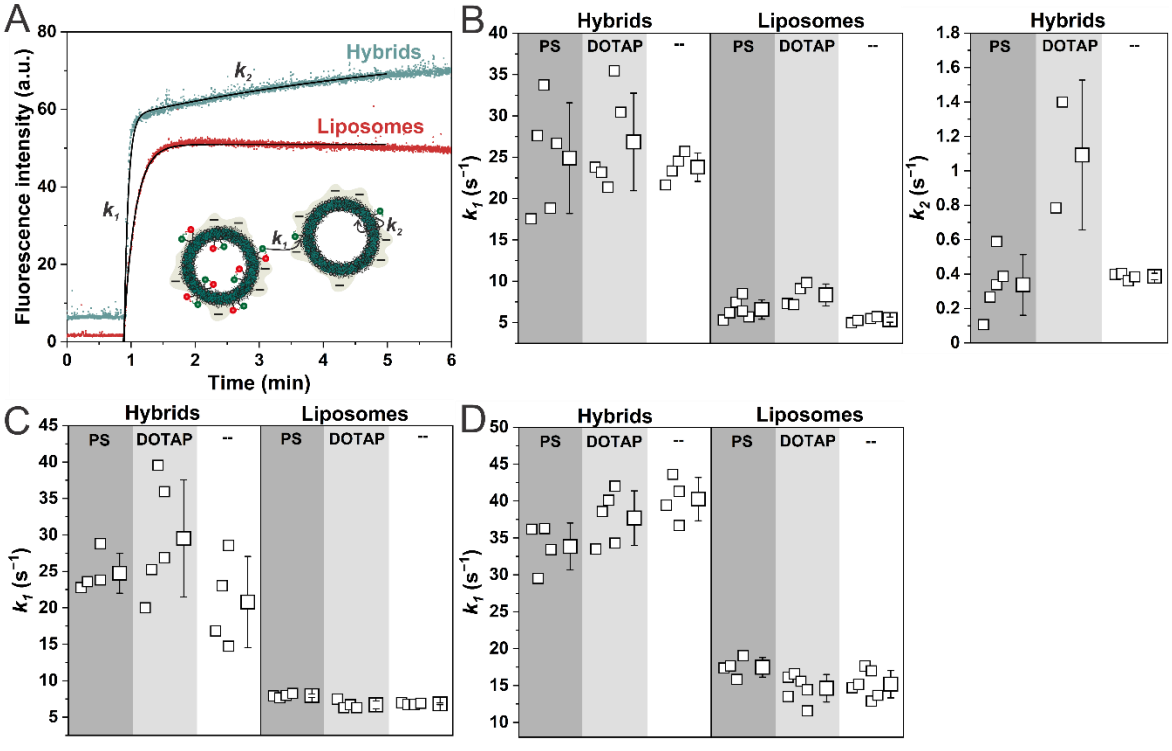

Figure 35. Interbilayer and transbilayer transport of M-NBD-phospholipids. (**A**) Transport of M-NBD-PE from donor to acceptor anionic LUVs. (**B**) Rate constants for M-NBD-PE obtained by fitting. LUVs contained 10 mol%

soy PS, DOTAP or DOPC (--); in the case of liposomes (--) represents 100 mol% DOPC. The values correspond to donor/acceptor molar ratio of 0.25. Only two of five samples of cationic hybrids could be fitted with double exponential function, indicating high sample heterogeneity. (**C**) Rate constants for M-NBD-PE. The values correspond to donor/acceptor molar ratio of 0.5. (**D**) Rate constants for M-NBD-PC. The values correspond to a donor/acceptor molar ratio of 0.25. Experimental data was fitted by single exponential equation. Adapted from (2), licensed under CC BY 4.0.

3.2.3 Fusion of nano- and microcompartments – snapshots at visible scale

As discussed above, vesicle fusion is a ubiquitous natural phenomenon, underpinning processes like communication and trafficking. With regard to the latter aspect, directed fusion can be deliberately employed for the assembly of artificial organelles and artificial cells, for example to deliver membrane proteins into giant unilamellar vesicles (GUV) (80) or to form loaded GUVs via fusion of small vesicles to droplets (243). Therefore, the fusion of hybrid LUVs to hybrid GUVs in different charge combinations was investigated next. Thereby, anionic (PDMS-*g*-PEO:PS) and neutral (PDMS-*g*-PEO:DOPC) GUVs were prepared by electroformation as described in the chapter "Materials and methods", and their membranes were tagged with PE-NBD; meanwhile, the membranes of cationic (PDMS-*g*-PEO:DOTAP) and neutral LUVs were tagged with PE-Rho. In control experiments, in which LUVs or GUVs were imaged separately, it was found that the NBD or Rho signals did not overlap and the two populations were not cross-contaminated (Figure 36), and anionic GUVs exhibited a homogenous distribution before starting the fusion experiments (Figure 37).

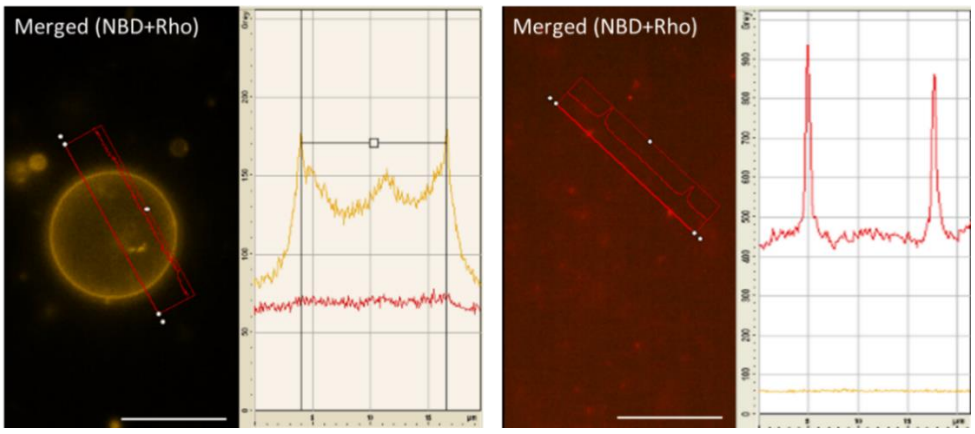

Figure 36. Micrographs of NBD-GUVs (left) and Rho-LUVs (right). PDMS-*g*-PEO:PS (70:30, mol%) GUVs were labeled with PE-NBD (yellow). PDMS-*g*-PEO:DOTAP (70:30, mol%) LUVs were labeled with PE-Rho (red). Scale bar: 10 µm. Adapted from (2), licensed under CC BY 4.0.

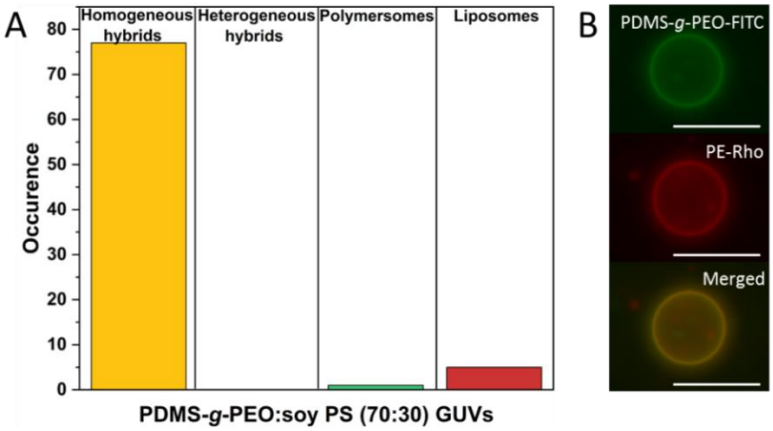

Figure 37. Analysis of phase separation in anionic hybrid GUVs. Hybrids were made by electroformation from PDMS-*g*-PEO:soy PS:PE-Rho:PDMS-*g*-PEO-FITC (69.5:29.7:0.3:0.5). Presence of two membrane dyes reduced yield and size of GUV (in comparison when only one dye was used); majority of GUVs had diameter 4–5 µm. Large majority of GUVs had homogenous distribution. GUVs were evaluated directly after formation. (**A**) Number of GUVs with homogeneous and heterogeneous lipid and polymer distribution, and number of GUVs containing only lipid or only polymer. (**B**) Example of homogenous lipid (red) and polymer (green) distribution in hybrid GUV. Scale bar: 10 µm. Adapted from (2), licensed under CC BY 4.0.

After 10-min incubation at 500 rpm of anionic GUVs and cationic LUVs, the red signal of the latter colocalized with the GUV surface, which indicated that full fusion or hemifusion took place (Figure 38A and Figures S16, S17). In particular, vesicle docking was likely succeeded by some form of fusion, since the latter was previously correlated with the homogeneity of the fluorescence signal (as in the present case) on the one side (17), and the demonstrated readiness of hybrids for membrane mixing (Figure 29) on the other. In addition, some (approximately a quarter) of the anionic GUVs were multivesicular upon formation but after mixing with cationic LUVs, a red signal was detected only on the outer membrane. This showed that vesicle engulfment, which was previously observed for cationic LUVs in POPC GUVs (17), did not occur here. In parallel, incubation of neutral GUVs with cationic LUVs also resulted in colocalization of the two dyes (Figure 38B and Figure S18), whereas mixing anionic GUVs with neutral LUVs did not lead to accumulation of the latter on the GUV membrane (Figure 38C and Figure S19). The PE-Rho signal intensity varied between the GUVs, likely due to uneven distribution of 1) the LUVs in the sample (only gentle mixing was applied in order to prevent GUV rupture) and 2) the charged lipids between different vesicles. However, quantitative analysis ascertained the trend observed between the different charge combinations and agreed with the membrane mixing results: the highest accumulation of PE-Rho signal from LUVs was detected for anionic GUV and cationic LUVs (49 ± 18 a.u., n = 42), lower for neutral GUVs and cationic LUVs (34 ± 15 a.u., n = 63) and almost negligible for anionic GUVs and neutral LUVs (13 ± 8 a.u., n = 69). This difference was even more pronounced when the background PE-Rho intensity (from non-hemifused/fused LUVs) was taken into account (45 ± 18 a.u., 6 ± 4 a.u., −12 ± 6 a.u., respectively).

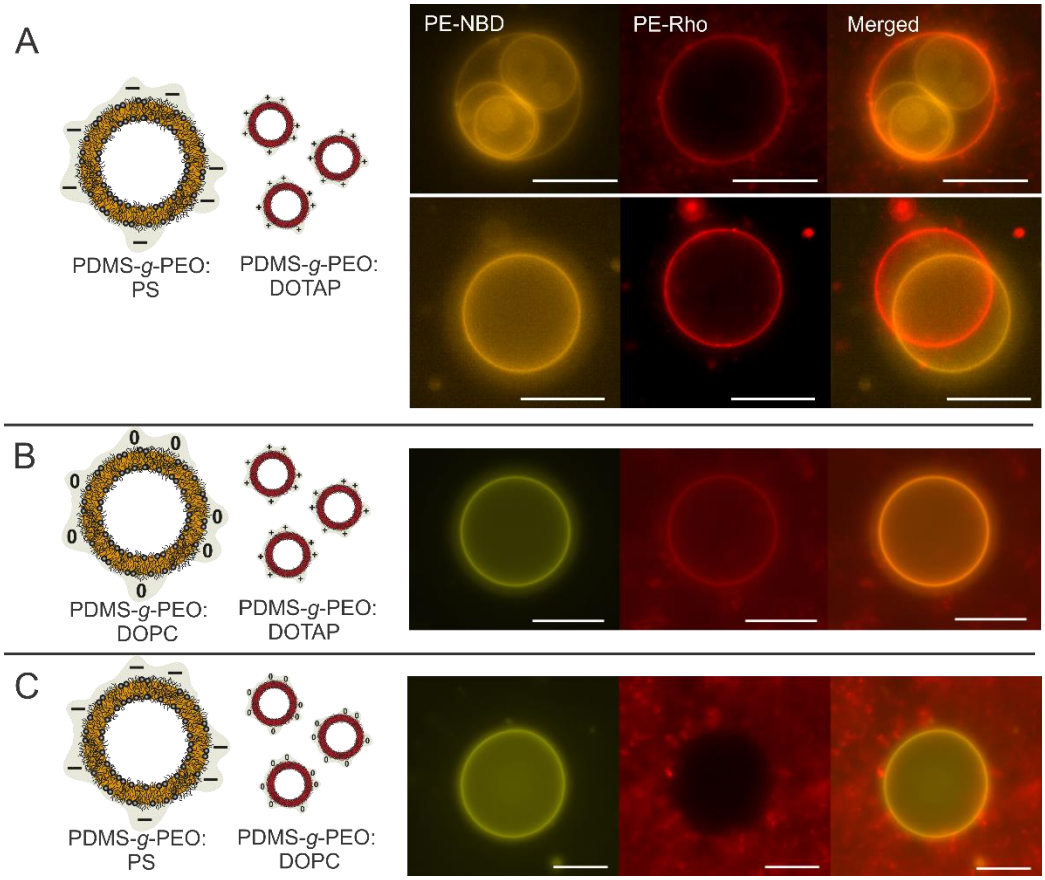

Figure 38. Membrane mixing upon fusion of nano- and microcompartments. Fluorescence microscopy of hybrid GUVs (yellow) mixed with hybrid LUVs (red), both containing 80 mol% PDMS-*g*-PEO. Both GUVs and LUVs were prepared in 200 mM sucrose. Images were taken after incubation at 500 rpm for 5 min at room temperature. (**A**) Anionic hybrid GUVs (20 mol% soy PS) tagged with PE-NBD (0.5 mol%) and cationic hybrid LUV (20 mol% DOTAP) tagged with PE-Rho (0.5 mol%). (**B**) Neutral hybrid GUVs (20 mol% DOPC) tagged with PE-NBD (0.5 mol%) and cationic hybrid LUV (20 mol% DOTAP) tagged with PE-Rho (0.5 mol%). (**C**) Anionic hybrid GUVs (20 mol% soy PS) tagged with PE-NBD (0.5 mol%) and cationic neutral LUV (20 mol% DOPC) tagged with PE-Rho (0.5 mol%). Scale bars: 10 µm. Adapted from (2), licensed under CC BY 4.0.

Next, the fusion between oppositely charged microcompartments was investigated in order to test whether the process would take place with less curved membranes. GUV-GUV fusion is in fact another promising tool in the context of bottom-up synthetic biology that has been used to, for instance, establish chemical communication between hemifused GUVs (244). To increase the driving force, hybrid GUVs containing 30 mol% charged lipids were used, and fusion was induced by mixing in 1:1 volumetric ratio of both populations and incubating them for 5 min at room temperature, prior to observation. Indeed, oppositely charged hybrid GUVs did fuse as evidenced by the dye colocalization in the newly formed vesicles (Figure 39A and Figure S20). Moreover, replacement of the lipid dye (PE-NBD) with a polymer dye (PDMS-*g*-PEO-FTIC) in cationic GUVs further substantiated the macroscopic membrane homogeneity (Figure 39A and Figure S21). In this regard, brighter spots in nearly all GUVs containing PE-NBD were detected prior to fusion (Figure S22), while the distribution of PDMS-*g*-PEO-FTIC remained uniform (Figure S23). This

aggregation may be ascribed to the formation of nanoscopic lipid domains, which sequestered the lipid dye. Another noteworthy observation was that in some cases the process was arrested in an intermediate state, evidenced by long contacts between several GUVs, which was ascribed to hemifusion in accordance with the pronounced ability for outer layer mixing in the hybrid membranes (Figures S21, S24).

Since certain membrane proteins require specific lipids to maintain their activity (like cardiolipin for complex I (245)), the fusion of giant liposomes as optimal protein vehicles with the hybrid GUVs was also explored. To this end, the fusion of positively charged lipid GUVs, tagged with PE-NBD, with negatively charged hybrid GUVs, tagged with PDMS-*g*-PEO-Rho, was tested. Upon mixing, colocalized signal from both dyes was observed, indicating successful fusion. Interestingly, large portion (~ 40 %) of the fused GUVs contained lipid and polymer domains (Figure 39B and Figure S25), which were stable during the time of observation (~ 3 h). Since it was demonstrated that membrane proteins may sequester lipids (Section 3.1.2.3), this lipid-hybrid fusion strategy may present a novel way for phase separation and concomitant formation of enzyme supercomplexes.

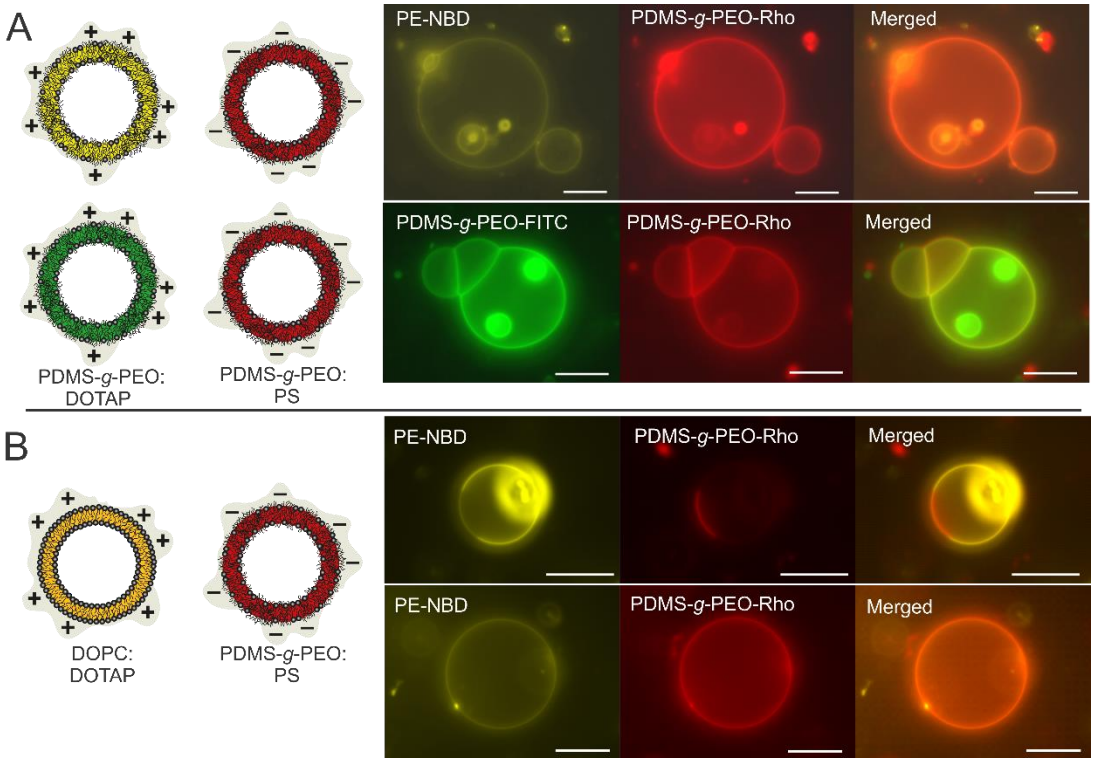

Figure 39. Membrane mixing upon fusion of microcompartments. (**A**) Cationic hybrid GUVs were labeled either with lipid dye (PE-NBD, yellow) or polymer dye (PDMS-*g*-PEO-FITC, green). Prior to fusion, no signal in Rho channel was observed for cationic hybrid GUVs (Figure S23). For additional micrographs, see Figure S20 and S21. (**B**) Two outcomes were observed upon fusion of cationic lipid GUV with anionic hybrid GUVs: fused GUVs had either homogenously distributed lipid and polymer or phase separation occurred and distinct polymer and lipid domains were observed (around 40 % of evaluated GUVs were heterogeneous). For additional micrographs, see Figure S25 and S26. Scale bar: 10 µm. Adapted from (2), licensed under CC BY 4.0.

Finally, it was investigated if cationic lipid GUVs can fuse with PDMS-*g*-PEO polymersomes, due to their low negative surface charge. Unfortunately, upon mixing of NBD-lipid-GUVs with Rho-polymer-GUVs, most of the GUVs ruptured during the observation, which made it impossible to obtain images. The rupture was assumingly associated with hemifusion and a membrane tension increase, which was previously observed upon introduction of cationic LUVs to pure POPC or POPC GUV with low (< 10 mol%) fraction of POPG (17). In a more similar (lipid) GUV-GUV system, it was proposed that strong adhesion can lead to lysis in the absence of weakened partitioning (double bilayer becomes a single bilayer in some areas) (97).

3.2.4 Content mixing during charge-mediated fusion

3.2.4.1 Content mixing analysis during charge-mediated fusion of nanocompartments via Co^{2+}/calcein-EDTA assay

FRET analysis of LUV populations corroborated more efficient membrane mixing in hybrids compared to liposomes, and optical observation at the GUV scale substantiated that the former membranes did undergo complete fusion. In order to fully quantify fusion, calcein-cobalt content mixing assay (98) was employed. First, ~ 100 nm anionic hybrid LUVs containing EDTA and cationic (or neutral) hybrid LUVs containing calcein complex with Co^{2+} via freeze-thaw steps and extrusion were formed. Non-encapsulated EDTA or Co^{2+}-calcein complex were removed via size expulsion chromatography with G-25 Sephadex resin. Fusion of vesicles is in this assay indicated by an increase of the fluorescence signal, as EDTA chelates Co^{2+}, calcein is dequenched. For complete separation of two bands, i.e., Co^{2+}-calcein and Co^{2+}-calcein-LUVs, column with height of 10.4 cm was required. Nevertheless, by monitoring calcein fluorescence, it was observed that outer Co^{2+}-calcein was not completely removed, indicating that it binds to the hybrid membrane. Increasing the length of the column from 7.4 to 10.4 cm helped to remove the outer complex, apparent from the decrease of the initial calcein fluorescence (Figure 40A,B). Interestingly, only slightly lower retention of complex on the membrane of hybrids with 10 mol% charged lipids was observed, but almost none for hybrids with 10 mol% of neutral lipids (Figure 40C,D).

The dequenching of calcein observed upon addition of EDTA-LUVs was more pronounced for hybrids with 30 mol% then 10 mol% charged lipids, but in both cases it barely reached 1 % of total calcein dequenching. Similar observations were previously obtained on lipid LUVs fusion, where LUVs containing 25 % charged lipids reached only around 0.5 % content mixing and less than 0.5 % leakage (98). Meanwhile, for 75 % charged anionic and cationic SUVs 8–11 % fusion was achieved, but with increased fraction of charged lipids, content leakage increased drastically (for 100 % charged vesicles content leakage was ~ 80 % (98)). In a different study, ~ 20 % vesicle fusion and ~ 4 % content leakage for anionic lipid

LUVs containing 25 mass% POPA and cationic ones containing 50 mass% E-PC or DOTAP was reported in diluted buffer (1 mM MOPS, pH 7.4) (104). For PC GUVs with 20 % charged lipids it was demonstrated ~ 23 % fusion and when content of charged lipids was increased to 40 %, ~ 37 % fusion was obtained (97). The systems in above mentioned studies substantially varied regarding the amount of charged lipids and measuring conditions (vesicle concentration and size, media), which is expressed in different content mixing values.

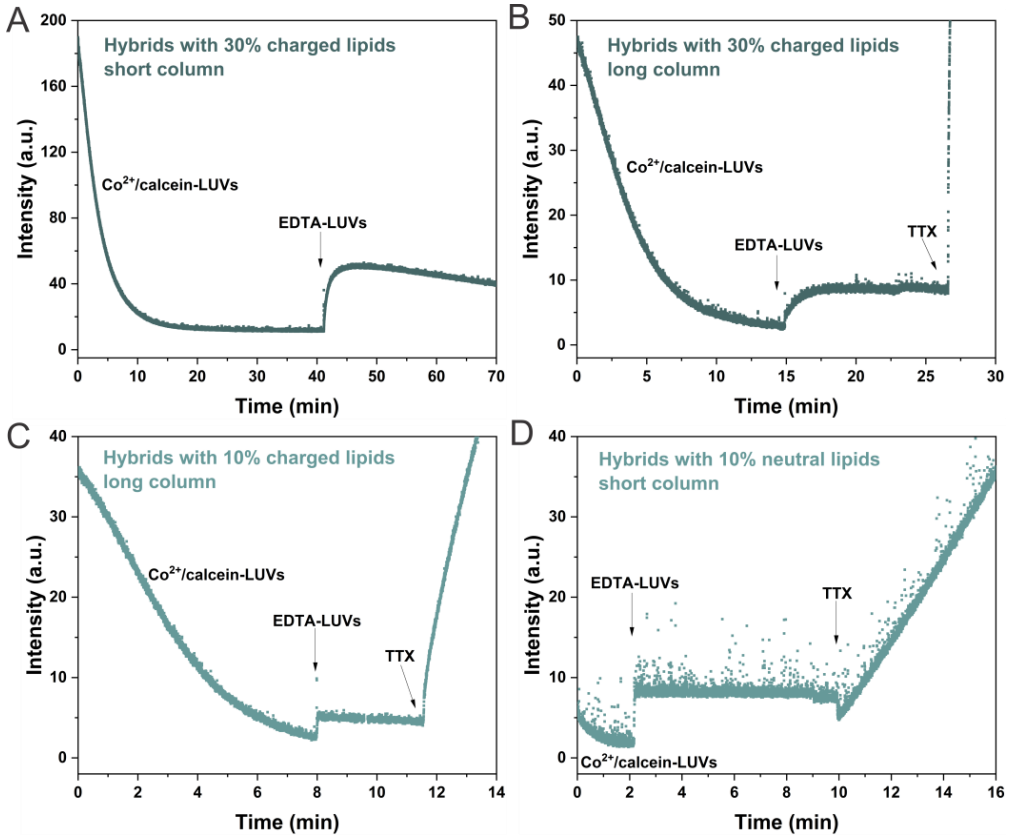

Figure 40. Content mixing during charge-mediated fusion via Co^{2+}/calcein-EDTA assay. Content mixing between PDMS-*g*-PEO:DOTAP (70:30, mol%) LUVs containing Co^{2+}/calcein complex and PDMS-*g*-PEO:PS (70:30, mol%) LUVs containing EDTA. Co^{2+}/calcein-LUVs were purified with 7.4 cm (**A**) or 10.4 cm (**B**) long column with diameter 1.5 cm, filled with G-25 Sephadex. Initial decrease in calcein fluorescence is due to its quenching by Co^{2+} in outer buffer. (**C**) Content mixing between hybrid LUVs containing 10 mol% charged lipids (DOTAP or PS). Co^{2+}/calcein-LUVs were purified with 10.4 cm long column with diameter 1.5 cm, filed with G-25 Sephadex. (**D**) Content mixing between PDMS-*g*-PEO:DOPC (90:10) LUVs containing Co^{2+}/calcein complex and PDMS-*g*-PEO:PS (90:10) LUVs containing EDTA. Co^{2+}/calcein-LUVs were purified with 7.4 cm long column with diameter 1.5 cm, filed with G-25 Sephadex.

3.2.4.2 Enzymatic coupling via fusion of nanocompartments

Since a complete removal of the outer Co^{2+}-calcein complex was not possible for charged hybrids, which led to highly underestimated content mixing, the next functional content mixing assay, which we previously used to probe SNARE-mediated fusion (106) was employed. To this end, two membrane proteins with

coupled activity were used – a proton pump (ubiquinol *bo*$_3$ oxidase) and a proton consumer (F_1F_O-ATP synthase) – which were reconstituted into separate compartments and brought together upon fusion. Only if both proteins are present in the membrane and the fused vesicle is proton-tight, ATPase may use the proton gradient generated by *bo*$_3$ oxidase to synthesize ATP. Thereby, proton pumping was activated by addition of the electron shuttle ubiquinone 1 (Q_1), which was in turn continuously reduced by dithiothreitol (DTT), while the ATP synthesis was monitored via the luciferin/luciferase assay (CLSII) (Figure 41A). Since by DLS, no size increase at lower amounts of charged lipids (Figure 30) was observed, hybrid proteoLUVs containing 30 mol% PS/DOTAP were used, next to DOPC as neutral control. To accommodate the membrane proteins, the sucrose solution was replaced by a Tris-phosphate buffer (20 mM Tris (pH 8.0), 20 mM H_3PO_4). Since the latter media considerably screened the surface charge, the influence on the membrane mixing efficiency was checked and only about 20 % decrease compared to sucrose (Figure S27) was observed. In these experiments, *bo*$_3$ oxidase was reconstituted in cationic or neutral hybrids and ATPase in anionic or neutral ones (Figure 41A). This particular setup was chosen because it was previously demonstrated that the ATP synthesis rate was ~ 2.5 times lower when the proton consumer was reconstituted in cationic liposomes (104). In addition, the size of the LUVs before/after reconstitution and upon fusion was analyzed by DLS.

Fusion of oppositely charged hybrids resulted in higher ATP synthesis rates than the case when *bo*$_3$ oxidase was present in neutral LUVs but remarkably, the highest activity was measured when ATPase was reconstituted in neutral LUVs, while the proton pump resided on cationic vesicles (representative measurements shown in Figure 41B). In these first measurements, *bo*$_3$ oxidase was inserted into liposomes by TTX and in hybrids by sodium cholate (SC), while for the reconstitution of ATPase in liposomes we used sodium deoxycholate (SDC), all at the respective saturation points (R_{sat}). In this regard, the influence of the reconstitution protocol for ATPase due to the known fragility of the latter enzyme was checked. This was done by testing four detergents at two different concentrations: at R_{sat} and at the solubilization points (R_{sol}), which were determined by titration (Figures 42–43). Overall, detergents at R_{sat} resulted in higher ATP synthesis rates upon fusion of oppositely charged proteoLUVs, thereby OG performing best, with the exception of SDC at R_{sol} (Figure 41C). The latter concentration was also associated with larger variability but despite the negative effect on the reproducibility, it enabled to reach considerably higher activities. Under these conditions, ATP synthesis rates as high as 35 ATP min^{-1} $enzyme^{-1}$ were measured when fusing neutral hybrids with ATPase and cationic ones with *bo*$_3$ oxidase (Figure 41D). Meanwhile, mixing cationic proteoliposomes with either neutral or anionic ones produced a similar response.

The behavior in content mixing corresponds to the FRET results shown above with respect to the fact that a positive charge on one of the vesicle populations suffices to induce fusion. This was also confirmed by

DLS analysis of hybrid proteoLUVs, which revealed a size increase only if cationic LUV populations functionalized with the proton pump were employed (Figure 41E–G and Figure S28). However, the functional coupling between the enzymes was also affected by the reconstitution of ATPase, which was in turn governed by the lipids and the protocol. It can be generalized that all membrane proteins sequester lipids in their vicinity (the so-called first-shell or annular lipids (246)) and this was demonstrated also for bo_3 oxidase in hybrid membranes (Section 3.1.2.3). However, the molecular rotor ATPase is known to exhibit even stronger and more specific interactions with certain lipids, which are buried in the c subunit of the F_O ring (247, 248). Therefore, it can be extrapolated that in the present hybrid system, DOPC provided a more suitable environment for the proton consumer than PS, which is in line with the composition of the *E. coli* membrane (i.e., the source of the protein), dominated by zwitterionic lipids like phosphatidylethanolamine (249). This was further confirmed by the fact that reconstitution of ATPase in hybrids containing 10 mol% soy PS and 20 mol% DOPC and subsequent fusion with cationic bo_3-LUVs led to higher ATP synthesis rates than in the case when 30 mol% soy PS was used (Figure S31; DLS can be found in Figure S32). Furthermore, the multimodal distribution of the activity could be related to the nearly complete vesicle dissolution at the solubilization point R_{sol}, which would enable two distinct orientations in different combinations. Thus, it appears that the final ATP synthesis rates result from the interplay between the electrostatic driving force and the membrane properties on the one side, and the matching protein environment and orientation on the other.

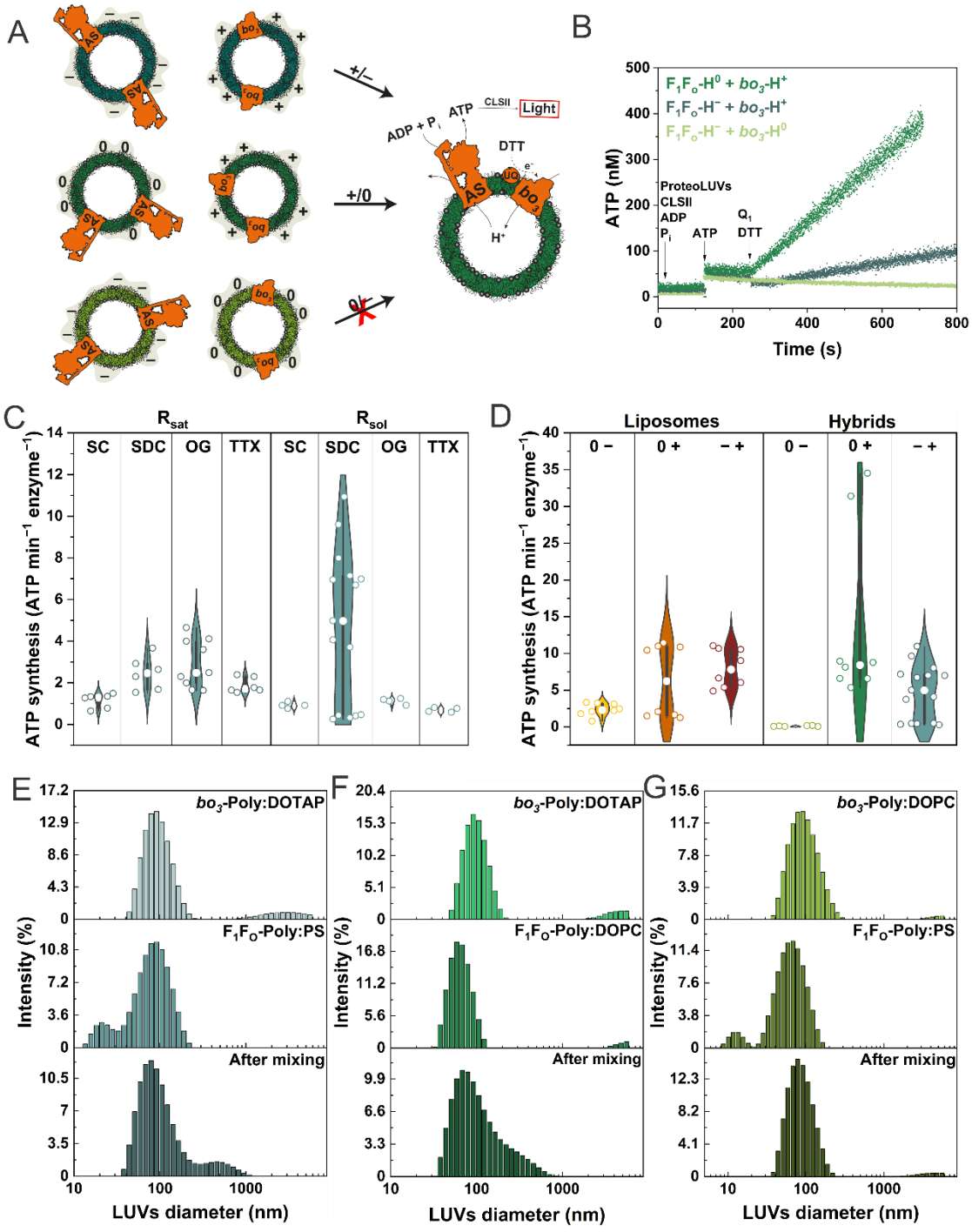

Figure 41. Content mixing during charge-mediated fusion via enzymatic coupling. (**A**) Scheme of the charge-mediated coupling of *bo*$_3$ oxidase and F_1F_O-ATPase. Liposomes were composed of DOPC:DOTAP (70:30), DOPC:PS (70:30) or DOPC, and hybrids of PDMS-*g*-PEO:DOTAP, PDMS-*g*-PEO:PS or PDMS-*g*-PEO:DOPC (all at 70:30). (**B**) Representative kinetics of ATP synthesis in hybrids. For liposomes see Figure S29. (**C**) ATP synthesis rates in hybrid LUVs upon variation of the reconstitution conditions for ATPase. *bo*$_3$ oxidase was reconstituted into PDMS-*g*-PEO:DOTAP LUVs by SC at R_{sat} (n = 4–15). (**D**) ATP synthesis rates in lipid and hybrid LUVs. ATPase was reconstituted by SDC at R_{sol} (n = 6–15). (**E**), (**F**) and (**G**) Size distributions (DLS) of differently charged hybrid proteoLUVs before and after fusion. Poly denotes PDMS-*g*-PEO. For liposomes see Figure S30. Adapted from (2), licensed under CC BY 4.0.

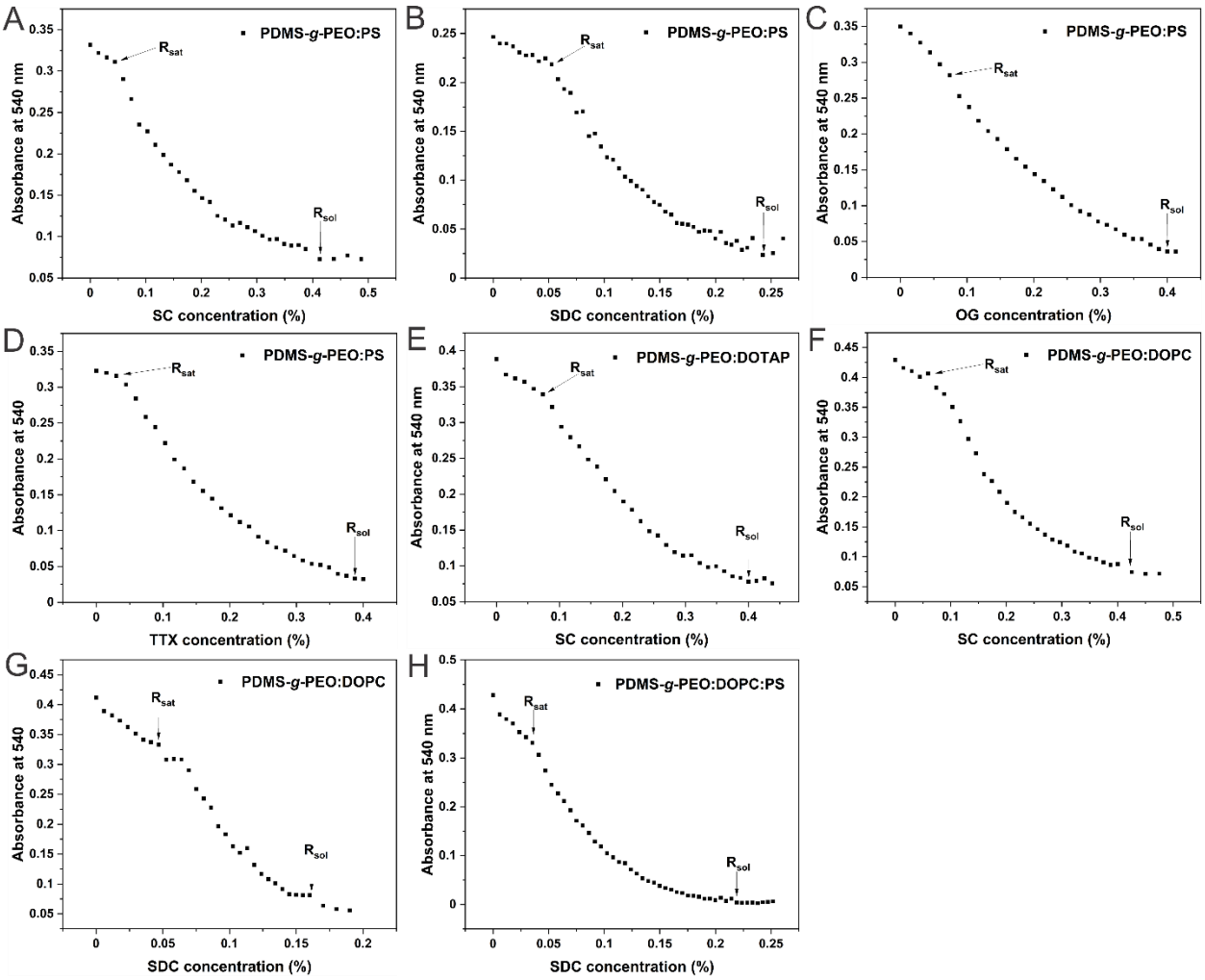

Figure 42. Solubilization of ~ 100 nm hybrid LUVs. Solubilization of PDMS-*g*-PEO:PS (70:30, mol%) LUVs by sodium cholate (SC) (**A**), sodium deoxycholate (SDC) (**B**), octyl glucoside (OG) (**C**) and Triton X-100 (TTX) (**D**). (**E**) Solubilization of PDMS-*g*-PEO:DOTAP (70:30, mol%) LUVs by sodium cholate (SC). Solubilization of PDMS-*g*-PEO:DOPC (70:30, mol%) LUVs by sodium cholate (SC) (**F**) and sodium deoxycholate (SDC) (**G**). (**H**) Solubilization of PDMS-*g*-PEO:DOPC:PS (70:20:10, mol%) LUVs by sodium deoxycholate (SDC). Arrows indicate saturation (R_{sat}) and solubilization point (R_{sol}). Adapted from (2), licensed under CC BY 4.0.

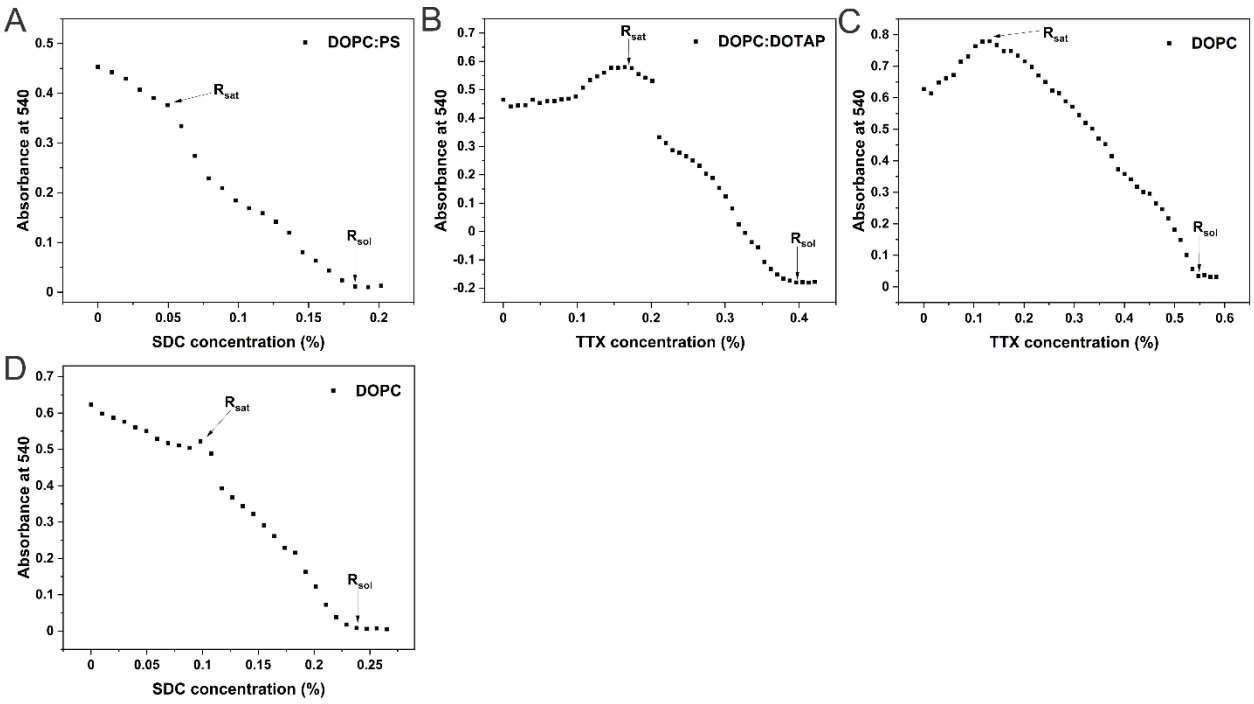

Figure 43. Solubilization of ~ 100 nm lipid LUVs. (**A**) Solubilization of DOPC:PS (70:30, mol%) LUVs by sodium deoxycholate cholate (SDC). (**B**) Solubilization of DOPC:DOTAP (70:30, mol%) LUVs by Triton X-100 (TTX). Solubilization of DOPC LUVs by Triton X-100 (TTX) (**C**) and sodium deoxycholate (SDC) (**D**). Arrows indicate saturation (R_{sat}) and solubilization point (R_{sol}). Adapted from (2), licensed under CC BY 4.0.

3.2.4.3 Content mixing analysis during charge-mediated fusion of nano and microcompartments via SRB assay

To analyze the content mixing in a conceptually more growth-relevant system (i.e., fusion of nano and microcompartments), water-soluble dye Sulforhodamine B (SRB) was encapsulated at self-quenched concentration in cationic hybrid LUVs. Its dequenching upon fusion with anionic hybrid LUVs was analyzed via epifluorescence microscopy. Fusion pore opening and content mixing for hybrids containing charged lipids indeed occurred (indicated by relatively high florescence observed inside GUV), but the exact quantification was not possible due to limitations of the epifluorescence microscopy (the signal above and below GUVs can be detected as well). The later was expressed in the SRB signal obtained in/above/below GUVs with neutral lipids. Nevertheless, a significantly higher signal was obtained for hybrids containing 30 rather than 10 mol% charged lipids (Figure 44), which implies that 10 mol% is not sufficient for efficient content mixing. Exact content mixing analysis on GUV-LUV should be performed upon availability of confocal microscope, where the plane focus enabled detection only inside the GUVs.

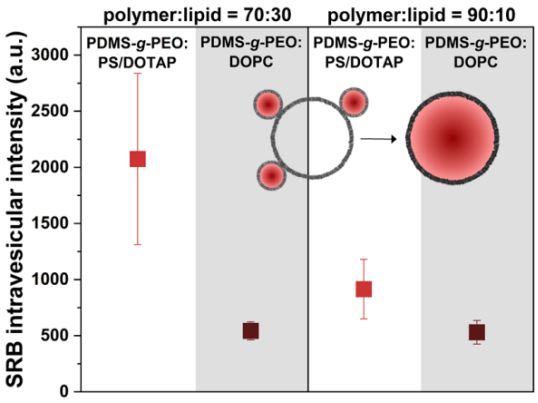

Figure 44. Content mixing during charge-mediated fusion of anionic GUVs and cationic 400 nm LUVs. Content mixing was determined via Sulforhodamine B (SRB) fluorescence: self-quenched SRB encapsulated in LUVs was transferred into GUVs upon fusion and due to its dilution dequenched. The gray area represents a control with neutral hybrids. Evaluated GUVs had a diameter of 10–50 µm.

3.2.5 Charge-mediated delivery of membrane proteins in hybrid GUVs

The charge-mediated fusion of hybrids was not only compatible with membrane proteins but was also used for their functional coupling at LUV scale. In addition, it was demonstrated that LUVs fused to GUVs. Therefore, as a final step, these two aspects were integrated, aiming at automated assembly of artificial cells and organelles. To this end, rectangular microfluidic traps (185) with a gap size of about 5 µm between the posts (for trap image see Chapter 2.2, Scheme 2) were employed. This setup enabled hydrodynamic control over the LUV delivery, fast exchange of the outer solution, and immobilization of the GUVs. Anionic hybrid GUVs (PDMS-*g*-PEO:PS = 70:30), stained with 0.1 mol% PE-Rho, were prepared via electroformation in 200 mM sucrose and trapped in the microfluidic device. Next, cationic hybrid LUVs (PDMS-*g*-PEO:DOTAP = 70:30), functionalized with ATTO 425-labeled bo_3 oxidase, were flushed into the chip. The latter protein tag was chosen to avoid overlap with the Rho channel. Finally, proteohybrids that did not fuse were washed away with 200 mM sucrose. As a result, the green signal from the protein accumulated on the outer GUV membrane, which indicated successful delivery to the microcompartment in the timescale of a few minutes (Figure 45A and Figure S33). Interestingly, ATTO 425 was detected also in the inner membranes of multivesicular GUVs, which suggested LUV uptake into the outer GUV lumen. It should be noted that the concentration of the introduced bo_3-LUVs played an imporant role in the fusion process and the stability of GUVs: at higher concentration (10 mg ml^{-1} vs. 0.3 mg ml^{-1}) most of the GUVs ruptured (Figure 46), which has likely to do with a significant increase of the membrane tension. With regard to the generally better suitability of natural lipids for protein reconstitution, we also used cationic lipid LUVs (DOPC:DOTAP = 70:30) as delivery vehicles, which resulted in the colocalization of bo_3 oxidase with the GUV membrane too (Figure 45B and Figure S34).

These preliminary experiments do not allow to deduce the prevailing orientation of the proton pump in the GUV membrane or to unequivocally corroborate complete fusion, although the latter is implied by the homogeneous distribution of the enzyme on the one side, and the DLS and content mixing observations at the LUV scale on the other. In this regard, we believe that the proposed strategy for automated assembly of membrane machinery can be applied to a variety of proteins, especially with respect to the fact that multiple reconstitution protocols for liposomes exist, whereas the functionality will need additional assessment in every particular case.

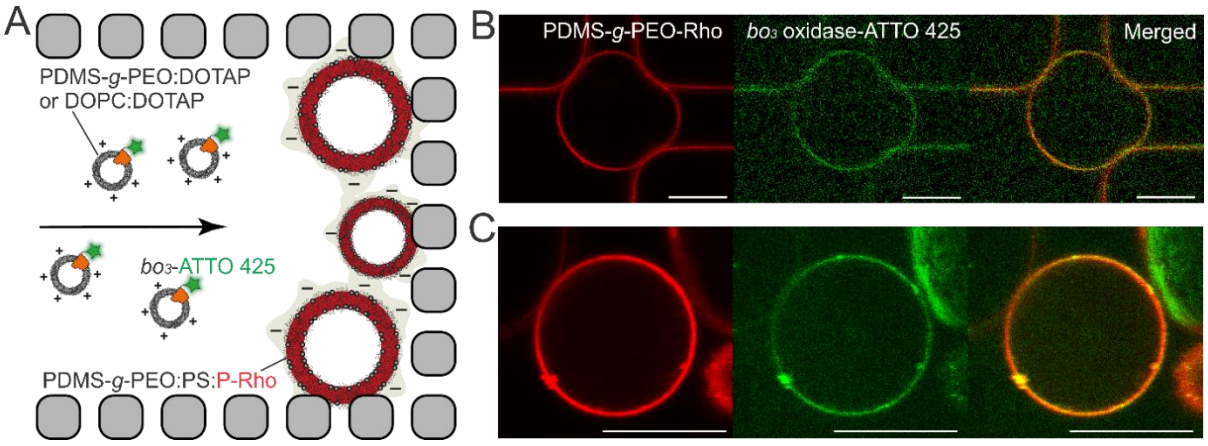

Figure 45. Delivery of *bo*$_3$ oxidase into anionic hybrid GUVs trapped in microfluidic device. (**A**) Schematic representation of the experiment. *bo*$_3$ oxidase was labeled with ATTO 425 (green) and reconstituted into cationic hybrid (**B**) or lipid (**C**) LUVs containing 30 mol% DOTAP. Hybrid GUVs were tagged with 0.1 mol% PDMS-*g*-PEO-Rho (P-Rho, red). Scale bar: 10 µm. Micrographs of hybrid GUVs before flushing with proteoLUVs are shown in Figure S35 and S36. Adapted from (2), licensed under CC BY 4.0.

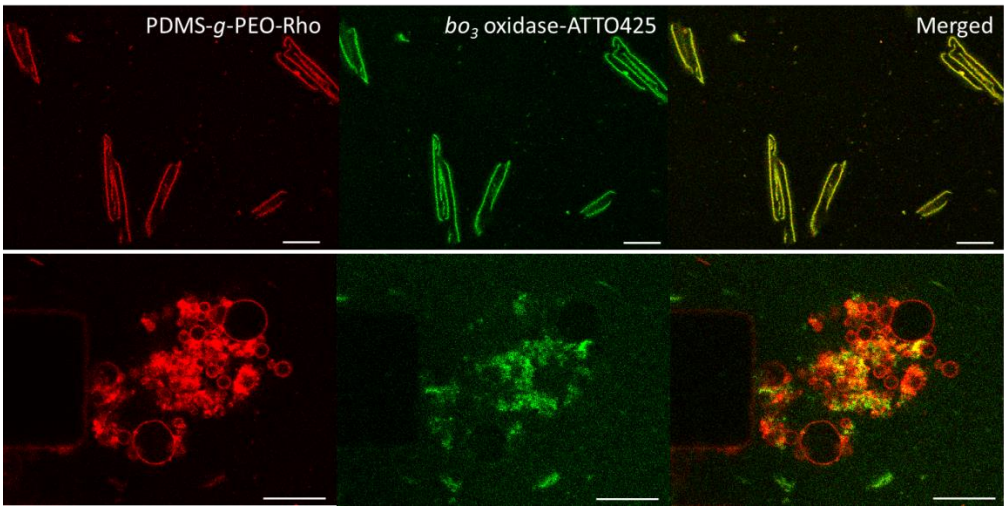

Figure 46. Delivery of *bo*$_3$ oxidase into anionic hybrid GUVs trapped in microfluidic device. *bo*$_3$ oxidase-ATTO 425 (green) (10 mg ml^{-1}) was delivered into anionic GUVs upon GUV-LUV fusion. High *bo*$_3$-LUVs concentration led to increase in membrane tension and GUVs rupture. *bo*$_3$ oxidase was reconstituted into cationic hybrid LUVs

containing 30 mol% DOTAP. Hybrid GUVs were tagged with 0.1 mol% PDMS-*g*-PEO-Rho (P-Rho, red). Scale bar: 20 µm.

3.2.6 Charge-mediated fusion of modified polymersomes with liposomes

Mixing PDMS-*g*-PEO polymer GUVs with cationic lipid GUVs led to vesicle rupture (Chapter 3.2.3). Nevertheless, non-negligible membrane mixing between polymer LUVs and cationic lipid LUVs was observed (Chapter 3.2.1). In this context, we were next interested in increasing the negative surface charge of polymersomes in order to undergo more efficient fusion with cationic liposomes. As expected, the surface charge of polymersomes became more negative at increasing pH, reaching −14.7 mV at pH 10 (Figure 47A). Although such a surface charge might be sufficient for fusion with cationic lipid LUVs, such a high pH level is incompatible with most of the enzymes that we used for artificial organelles. To circumvent this issue, a different approach was tackled next: utilizing cationic polymersomes and anionic liposomes instead. Cationic polymersomes were formed from a mixture of PDMS-*g*-PEO and PDMS-*g*-PEO with modified side groups (– OH groups were replaced by NH_2 ones). Polymersomes containing 40 mol% modified cationic polymer had a zeta potential of 35 mV at pH 7.5 (Figure 47B), which made them a good candidate for fusion with anionic liposomes with a zeta potential of –54 mV (Figure 47C).

Growth of cationic polymer GUVs upon fusion with anionic lipid LUVs was planned to be observed in a microfluidic device, similar as in Chapter 3.2.5. Unfortunately, the GUVs formed via electroformation had a maximum diameter of 5 µm, and such small GUVs would go through the post in microfluidic traps. Furthermore, the yield of those GUVs was low. The difficulty of formation of cationic GUVs seems to hold true regardless of the membranous system (lipid or polymer). In bulk experiments, accumulation of the fluorescence signal from anionic lipid LUV (tagged with PE-Rho) was observed on cationic polymer LUVs (tagged with PDMS-*g*-PEO-FITC). But due to the small size of cationic GUVs, no concluding experiments in a more controlled environment (microfluidics) could be made. This mechanism was therefore omitted as growth mechanism (growing GUVs), and should be explored in the future mainly on LUVs in the context of fusion with negatively charged membranes of living cells and their transfection.

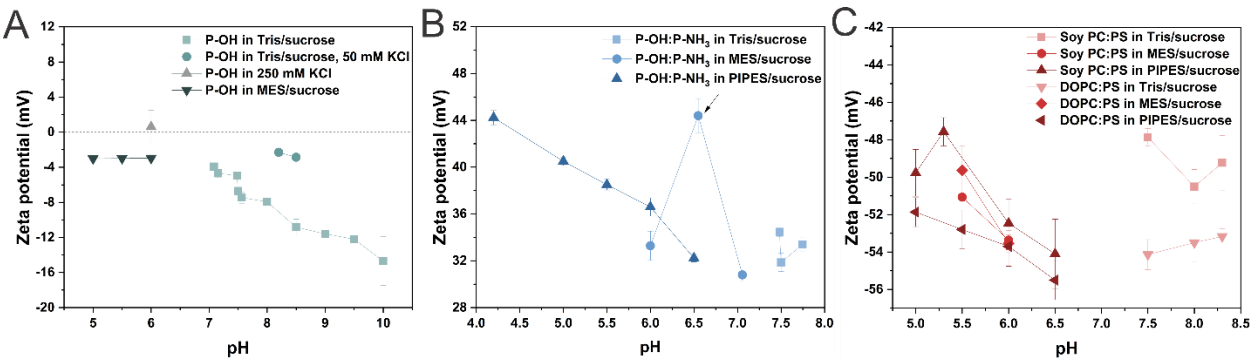

Figure 47. Change in zeta potential (mV) of lipid and polymer LUVs with pH. (**A**) Zeta potential of PDMS-*g*-PEO LUVs. (**B**) Zeta potential of polymer LUVs containing modified cationic polymer (PDMS-*g*-PEO:PDMS-*g*-PEO-NH_3 = 60:40, mol%). (**C**) Zeta potential of soy PC:soy PS (80:20) and DOPC:soy PS (80:20) LUVs. Tris/sucrose: 1 mM Tris, 200 mM sucrose; MES/sucrose: 1 mM MES, 200 mM sucrose; PIPES/sucrose: 1 mM PIPES, 200 mM sucrose.

Fusion between liposomes and polymersomes has an application potential beyond the growth module, thus presenting a novel way for the formation of hybrid vesicles, which can be applied in research of phase separation in the absence or presence of membrane proteins, and their partitioning. Although further studies are required in order to predict the behavior of such system, this opens a new branch of charge-mediated fusion research – fusing natural and synthetic vesicles, which can be applied also on fusion between cells and polymersomes. Furthermore, charge modification of membrane components opens opportunity for better control over the orientation of reconstituted membrane proteins, similarly as was previously demonstrated that charged lipids influence orientation of bacteriorhodopsin (250) and proteorhodopsin (251) in liposomes, and asymmetric polymersomes orientation of proteorhodopsin (23).

3.2.7 Ca^{2+}-mediated fusion of anionic hybrids

Based on electrostatic interactions, fusion can occur in addition to oppositely charged vesicles also between vesicles with the same (negative) surface charge in presence of divalent cations (such as Mg^{2+} or Ca^{2+}) (94-96). It was suggested that the role of phospholipids in membrane fusion is related to their ability to form dehydrated intermembrane complexes with divalent cations (108). Since in most biological membranes the percentage of PS among total phospholipids is significant, but lower than 50 % (108), we decided to prepare vesicles containing only 20 mol% of PS to avoid exceeding the natural PS contribution. It was previously shown that liposomes containing only 10–20 % PS are able to fuse extensively in the presence of Ca^{2+}; and furthermore, the presence of Mg^{2+} lowered the concentration of Ca^{2+} required to induce fusion (108). Here, Ca^{2+} as fusion mediator was studied.

To induce fusion of anionic hybrid (PDMS-*g*-PEO:PS = 80:20, mol%) LUVs, $CaCl_2$ was added at a final concentration of 10 mM. Vesicle aggregation and potential fusion was monitored via DLS and change in

absorbance at 272 nm. Upon addition of $CaCl_2$ a drastic increase of the absorption was observed for liposomes and slower but steady increase for hybrids (Figure 48), indicating pronounced vesicle aggregation for both systems. Similarly, DLS showed a peak shift toward larger diameters, which again confirmed the successful vesicle aggregation (and potentially fusion) in both systems (Figure 49).

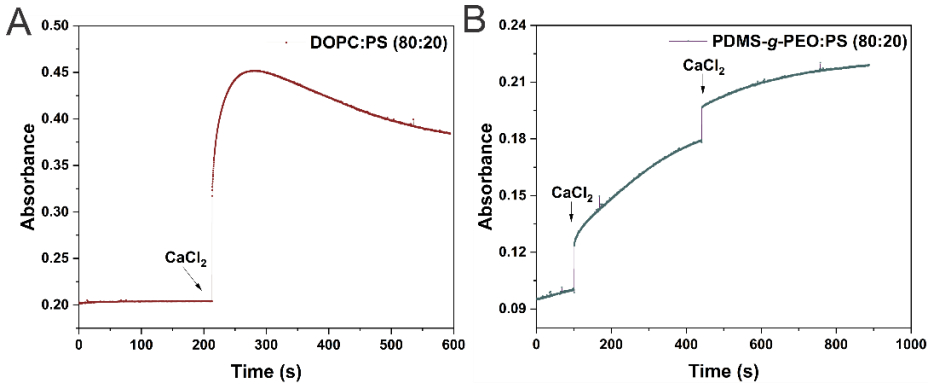

Figure 48. Ca^{2+}-induced anionic LUVs aggregation. Aggregation of anionic lipid LUVs (**A**) and anionic hybrid LUVs (**B**) was monitored via change in absorbance at 272 nm. LUVs contained 20 mol% soy PS.

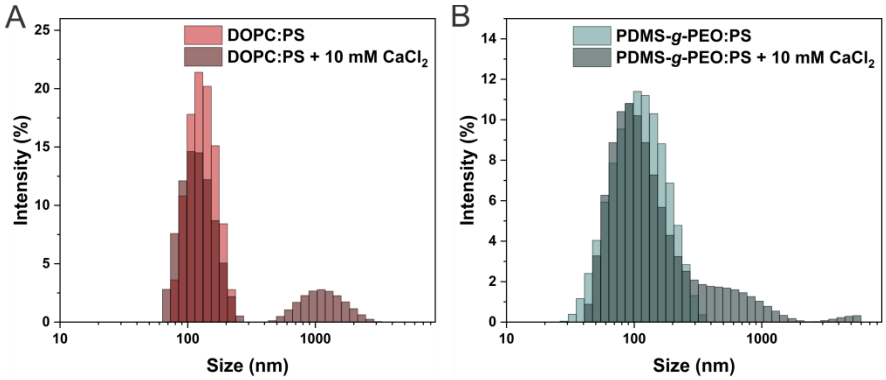

Figure 49. Size distribution by intensity of anionic LUVs before and after addition of $CaCl_2$. To anionic lipid (**A**) or hybrid (**B**) LUVs 10 mM $CaCl_2$ was added. LUVs were incubated with $CaCl_2$ for 10 min at 500 rpm. LUVs contained 20 mol% soy PS.

Since DLS cannot distinguish between docked and fused vesicles, membrane mixing was monitored next. FRET results revealed that the majority of membrane mixing between liposomes occured in the first 60 min and reached around 40 % (Figure 50A). Similar as slower aggregation demonstrated via absorbance, hybrid membrane mixing occurred slightly slower, but continued even after 60 min and did not reach a plateau even after 350 min duration of the measurement (Figure 50B). A slower rate of docking/membrane mixing for hybrids has likely to do with Ca^{2+} partially binding to polymer (PEO side groups) (see Chapter 3.3.4 for discussion on intercations between PEO and salts), and therefore a smaller amount is free for interactions with PS. For a block copolymer, poly(ethylene oxide)-*b*-poly(propylene oxide)-*b*-poly(ethylene oxide)

(PEO-PPO-PEO), it was previously observed that divalent cations, including Ca^{2+}, do indeed bind to it (252).

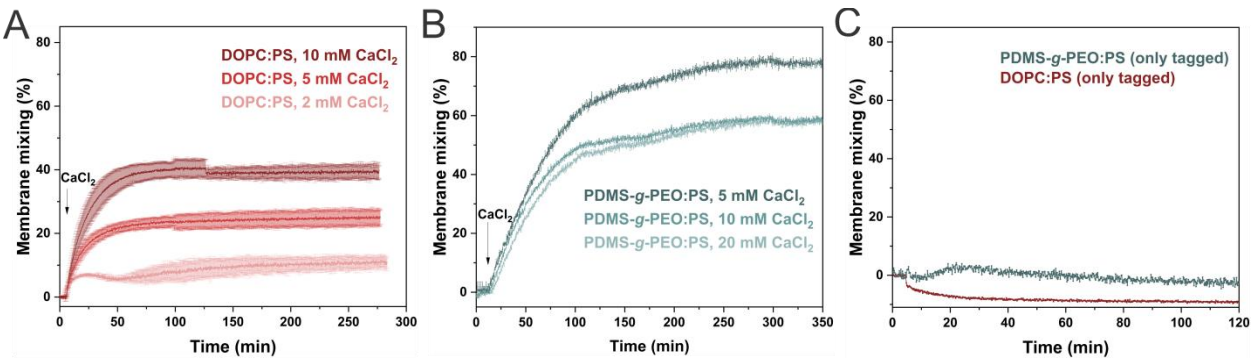

Figure 50. Membrane mixing of anionic LUVs in presence of $CaCl_2$. Membrane mixing of anionic lipid (DOPC:soy PS = 70:30, mol%) (**A**) and hybrid (PDMS-*g*-PEO:soy PS = 70:30, mol%) (**B**) LUVs was initiated by addition of $CaCl_2$ (final concentration of $CaCl_2$ was 2, 5, 10 or 20 mM). (**C**) Negative control: tagged vesicles (containing NBD and Rho dye) while stirring, in the absence of empty vesicles and $CaCl_2$.

Due to significantly slower kinetics of Ca^{2+}-mediated fusion of anionic hybrid LUVs in comparison to fusion of oppositely charged hybrid LUVs (80 % membrane mixing reached in ~ 300 min vs. < 1 min), as well as more random fusion mechanics for the former, Ca^{2+}-mediated growth mechanism was not further investigated on GUVs.

3.3 Mechanically-induced salt-mediated fusion: shift from natural mechanisms to achieve more efficient growth

Despite the high efficiency and fast rate of charge-mediated vesicle growth as discussed in the previous chapter, the process is limited by charge depletion. In order to achieve potentially unlimited growth and substantial increase in vesicle size, we next explored the fusion of vesicles with the same composition induced by external factors. In the present chapter, vesicles were composed of PDMS-*g*-PEO and the external factor was mechanical stress under moderate (physiological) concentration of salt.

3.3.1 Polymer nanocompartments grow to microns

PDMS-*g*-PEO vesicles were prepared by extrusion through 200 nm pores, according to the reported protocol (21). By the use of DLS, the effect of $MgCl_2$ and KCl was tested, next to NaCl that was previously used for fusion of PBd-*b*-PEO LUVs. No size change was observed in 5–250 mM divalent or monovalent salts upon incubation at room temperature for up to one week. Salts might destabilize the vesicle suspensions but even the highest concentrations did not induce polymersome aggregation (Figure 51A). The size did not change with agitation (0–1200 rpm) in Milli-Q water, sucrose or 5–50 mM salt solutions either. In contrast, 200 nm PBd-*b*-PEO polymersomes were shown to fuse at low salt concentration (10 mM NaCl) after 1 h at 20 Hz (1200 rpm) (126). Larger PDMS-*g*-PEO vesicles were only found after 8 h agitation at 1200 rpm in 250 mM NaCl when additional small peak appeared at ~ 5 μm (Figure 51B). Further agitation (24 h) resulted in more micron-sized structures, though another new peak at ~ 30 nm reflected concomitant fission and/or lysis. $MgCl_2$ exhibited similar behavior but the two new populations appeared sooner (Figure 51C). In the presence of 250 mM KCl, the monodisperse polymersome suspension nearly doubled its size only after 3 h, and after 7–8 h the intensity of the ~ 5 μm peak substantially increased (Figure 51D). Increasing the concentration of KCl to 350 mM did not improve the aggregation/fusion efficiency and neither did faster agitation at 1300 rpm. The latter merely caused the appearance of smaller vesicles (Figure 51E) as in the presence of $MgCl_2$, which effect was further substantiated at 1500 rpm due to the higher shear stress. Unlike salts, agitation at 1300 rpm in Milli-Q did not cause fission of polymersomes; their size remained unchanged even after 24 h vigorous vortexing (Figures S38–S39). The influence of different salts and agitation speed is summarized in Figure 52 and Table S1.

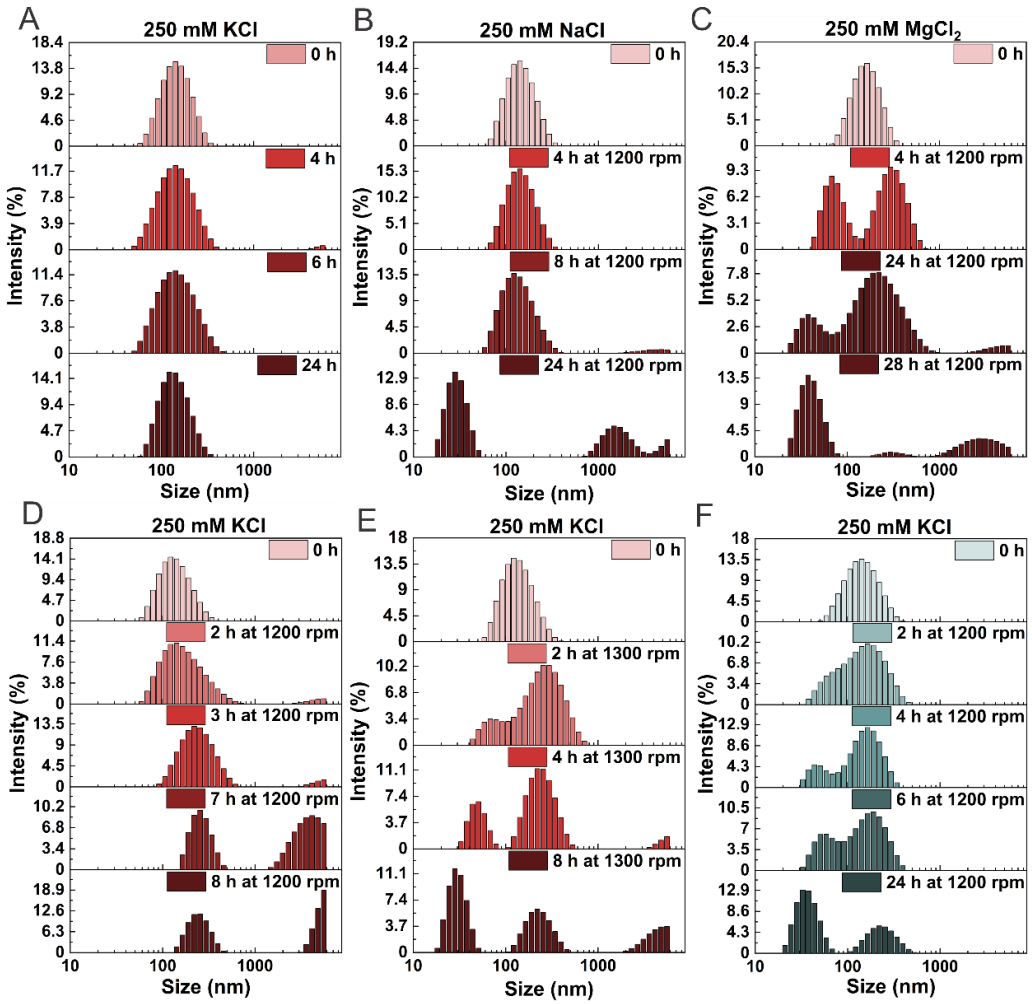

Figure 51. Time-resolved size distribution of vesicles (1.25 mg ml^{-1}) with salt and agitation. Salt-to-polymer molar ratio is 600:1 and the measurement volume is 400 µl. (**A**) Polymersomes in 250 mM KCl in absence of agitation. (**B**) Polymersomes in 250 mM NaCl agitated at 1200 rpm. (**C**) Polymersomes in 250 mM $MgCl_2$ agitated at 1200 rpm. (**D**) Polymersomes in 250 mM KCl agitated at 1200 rpm. (**E**) Polymersomes in 250 mM KCl agitated at 1300 rpm. (**F**) Hybrids in 250 mM KCl agitated at 1200 rpm. Adapted from (3), licensed under CC BY 4.0.

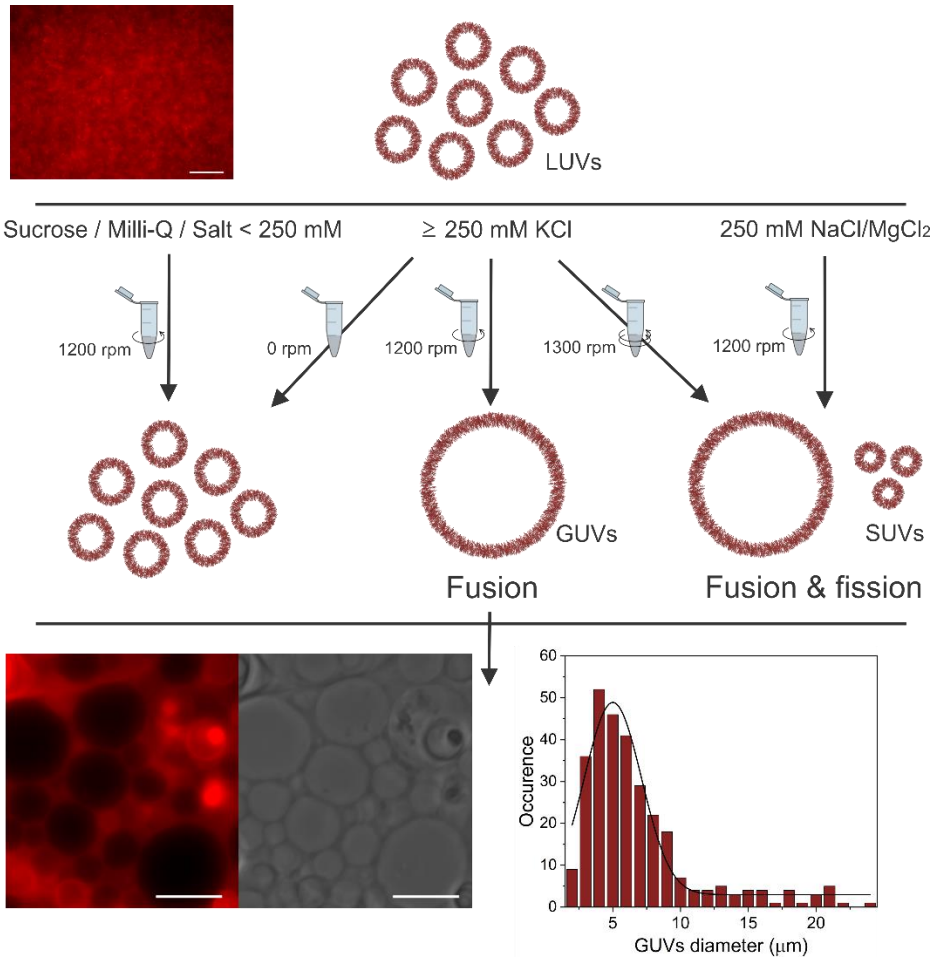

Figure 52. Scheme summarizing the influence of salts and agitation on PDMS-*g*-PEO polymersomes. LUVs (5 mg ml^{-1}) in 250 mM KCl before agitation are shown in the upper micrograph, while the resulting GUVs after 24 h at 1200 rpm are shown in the lower one. Scale bars: 10 µm. Membrane was tagged with labeled polymer (1.2 mol% PDMS-*g*-PEO-Rho, red). The right lower panel shows the respective size distribution of GUVs (n = 300). Adapted from (3), licensed under CC BY 4.0.

As DLS cannot distinguish between aggregated and fused vesicles and suffers from a limited upper range, it was confirmed by microscopy that the micrometer structures were giant unilamellar vesicles (GUVs); agitation at 1200 rpm for 3 h in 250 mM KCl resulted in diameters of 4–20 µm and some of the polymersomes were apposed (Figures S40). While cryo-TEM revealed that PDMS-*g*-PEO formed exclusively unilamellar vesicles (Chapter 3.1.1.1), agitation of PBd-*b*-PEO led to mixtures of uni- and multilamellar ones (253). To increase the yield and potentially the size of the GUVs, the initial concentration of polymer was increased from 1.25 to 5 mg ml^{-1} and the time of agitation from 3 to 24 h. In addition, the microscopic analysis was facilitated by incorporation of tagged polymer (PDMS-*g*-PEO-Rhodamine) at 1.2 mol% loading. Indeed, the amount of GUVs substantially increased, but the size did not exceed 25 µm and a smaller portion of the vesicles became multivesicular (Figure S42). With the same agitation, any > 1 µm vesicles were not found in 250 mM NaCl and 125 mM $MgCl_2$.

The > 20 µm GUVs contained a lower amount of labeled polymer compared to the smaller ones, which corresponded to our previous observations on polymersomes, formed by partial dehydration of LUVs and electroformation (1). Both occurrences suggest that the dye hampers fusion, which might be associated with steric or charge effects, even though the difference between the nearly neutral zeta potentials of labeled and non-labeled polymersomes was rather small in 250 mM KCl due to charge screening (Figure 53). Since higher amphiphile loading improved the yield of GUVs, we further doubled the LUV amount to 10 mg ml^{-1} and reduced the amount of labeled polymer twice (to 0.6 mol%). Those two factors had a positive effect on the growth and GUVs with diameter of 40 µm could be found in the sample (Figure 54).

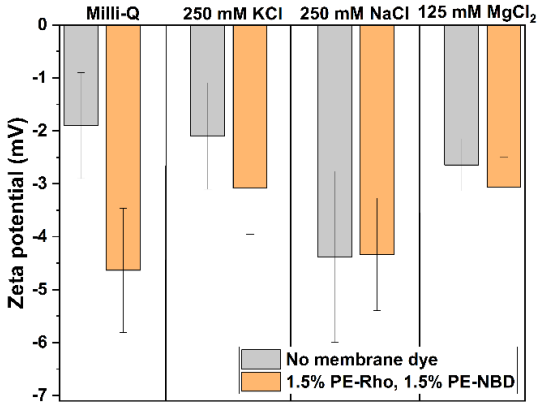

Figure 53. Zeta potential of PDMS-*g*-PEO LUVs without and with lipid dye in Milli-Q and in salt solutions. Three salt solutions were tested: 250 mM KCl, 250 mM NaCl and 125 mM $MgCl_2$. Bars represent average of 6–8 measurements with standard deviation. Adapted from (3), licensed under CC BY 4.0.

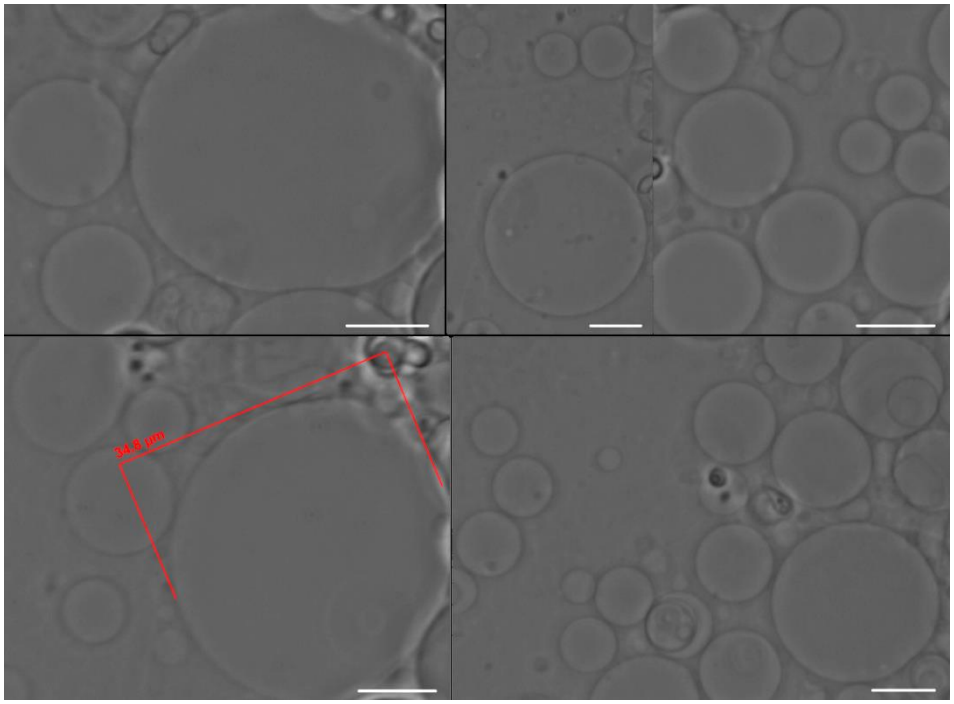

Figure 54. PDMS-*g*-PEO GUVs grown in 250 mM KCl. GUVs were grown from 200 nm polymersomes (10 mg ml^{-1}) by agitation at 1200 rpm for 24 h. Increased initial concentration of LUVs from 5 to 10 mg ml^{-1} increased maximum size of GUVs obtained. Scale bar: 10 µm. Adapted from (3), licensed under CC BY 4.0.

Next, PDMS-*g*-PEO were benchmarked against natural lipids. No apparent change in the size distribution of DOPC liposomes was observed in 250 mM KCl at 1200 rpm. Furthermore, agitation of hybrid vesicles composed of 80 mol% PDMS-*g*-PEO and 20 mol% DOPC (an amphiphile ratio that ensures homogenous distribution (49)) caused only a decrease of the vesicle size (Figure 51F). The mechanical stress apparently destabilized the hybrids, via either rupture/fission or phase separation and budding, thus the presence of lipids prevented fusion at the given conditions.

Finally, membrane defects were induced via hypotonic shocks since pores may act as nucleation sites for fusion and also applied hypertonic conditions. The osmotic difference >150 mOsmol kg^{-1} was previously demonstrated to induce fusion of adjacent lipid membranes (vesicles in contact with a planar bilayer) (254, 255), while on the other hand, rigid block polymersomes may explode when exposed to osmotic shock (256). Neither hypertonic incubation nor hypotonic conditions in presence or absence of agitation changed the vesicle size (no swelling/shrinking or aggregation/fusion) (Figures S44, S45). We ascribed the intactness to the regulation of osmotic stress by transient pore opening (257), which released the membrane tension and counteracted fusion.

In all examples above, fusion and growth were investigated, starting from LUVs extruded by 200-nm filter. To test if extrusion can be circumvented, we also tried to grow GUVs from polymer film under the same

conditions. After 24 h at 1200 rpm mixed population of LUVs and small GUVs (with diameters of 1–2 μm) (Figures S46, S47) was obtained. This indicated that the optimal starting material for the current procedure is a population of relatively small LUVs. Apparently, an increased positive membrane curvature accelerates the fusion process (previously demonstrated for charge-mediated liposome fusion (80)), which was likely the case for the present system, too.

3.3.2 Membrane mixing during mechanically-induced fusion

When a small portion of vesicles fuse, the scattering peak may not be detectable by DLS, while only micrometer-sized polymersomes can be optically accessed. To further assess fusion, membrane mixing was monitored via the dequenching of a hydrophobic dye 1,1'-dioctadecyl-3,3,3',3'-tetramethylindotricarbocyanine iodide (DiR), which was previously used for PBd-*b*-PEO vesicles (139), and also measured the decreasing FRET signal between 7-nitrobenz-2-oxa-1,3-diazol-4-yl (NBD) and fluorescein (FITC) or lissamine rhodamine B sulfonyl (Rho). Membrane mixing of DiR-LUVs and dye-free LUVs results in dilution of the dye, which restores its fluorescence (Figure S48A). Indeed, the intermittently measured DiR fluorescence increased with agitation at 1200 rpm and the continuous dequenching could be followed directly in the spectrophotometric cuvette (Figure S49). Though, the newly formed micron-sized structures did not resemble the previously observed GUVs and appeared as polymer beads (Figure 55). Similar structures were observed in populations of PEO_{16}-*b*-PBO_{22} vesicles upon addition of 20 kDa PEO (258). Higher DiR concentrations have been also shown to promote the fusion of liposomes to cells for staining purposes (259) and the weak size control of DiR-DOPC liposomes (139) may be also related to similar interactions.

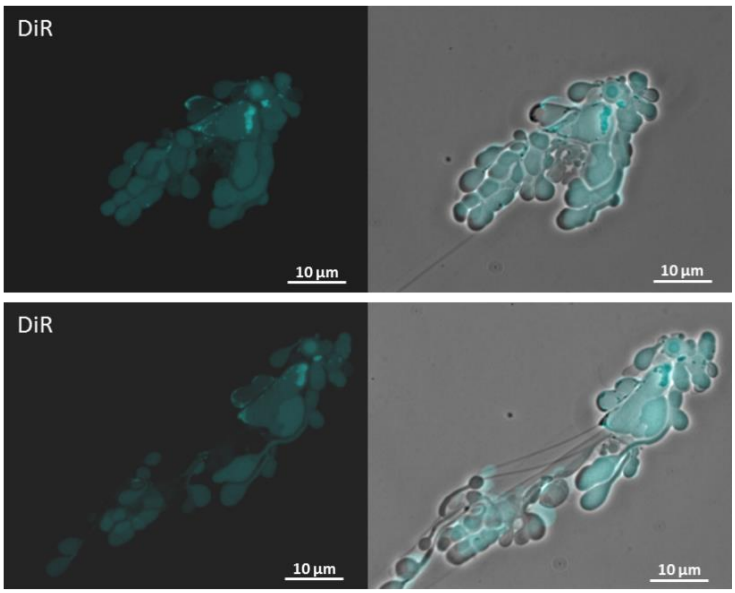

Figure 55. Epifluorescence microscopy of connected DiR/PDMS-*g*-PEO structures. The microsized structures (polymer beads) were formed upon agitation (1200 rpm) of polymer LUVs for 5 h in presence of 250 mM KCl. Adapted from (3), licensed under CC BY 4.0.

To circumvent the unfavorable effect of DiR, two FRET pairs were employed next in a similar assay based on dilution. Labelled 1,2-dipalmitoyl-sn-glycero-3-phosphoethanolamine (PE) was used first and the NBD emission was monitored upon its excitation (Figure 56A). Membrane mixing occurred fairly linearly and leveled off after about 2 h. By a shorter experiment and lysis with Triton X-100, it was confirmed that at this point the arbitrary 100 % (full FRET loss) was achieved (Figure 56B). Under the gentle stirring in the spectrophotometer, the fusion efficiency was lower as expected; in 20 h it barely exceeded 30 % (Figure 56C). Under these conditions, the initial transient response was ascribed to vesicle docking and subsequent disaggregation, while steady membrane mixing started after 2 h. Micrographs of the resulting suspensions revealed homogeneous GUVs (Figure 57), which indicates that 1.5 mol% labelled lipids did not suppress the vesicular growth as in the case of the hybrids containing 20 mol% DOPC. The occasional brighter spots may be due to aggregated LUVs or accumulation of tagged lipids.

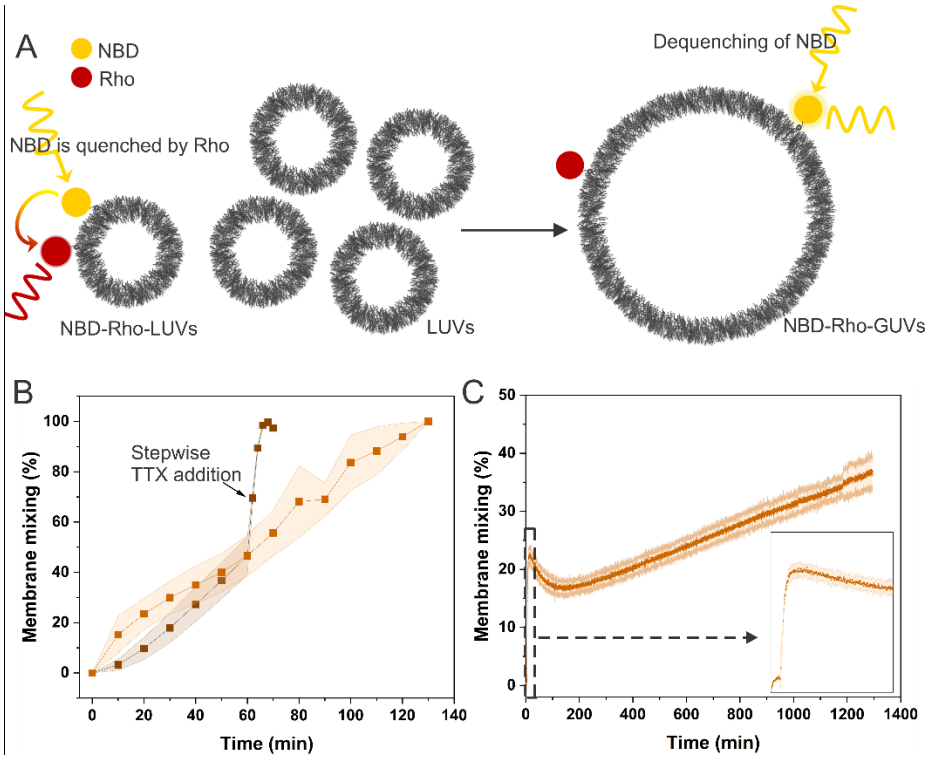

Figure 56. Membrane mixing via FRET between labeled lipids (PE-NBD and PE-Rho). Membrane mixing was determined by monitoring of the NBD fluorescence (ex/em = 460/535 nm). (**A**) Scheme representing the FRET setup. Tagged (1.5 mol% PE-Rho and PE-NBD) and bare polymersomes are mixed in volume ratio 1:4. Upon their fusion, NBD is dequenched and its fluorescence increased. (**B**) Intermittent membrane mixing at 1200 rpm. Points represent the averages of four samples and shaded area shows the standard deviation. 100% FRET signal was obtained by lysis with Triton X-100 (TTX). (**C**) Membrane mixing during stirring in the spectrophotometric cuvette. The inset shows magnification of the initial kinetics. The amount of LUVs corresponds to 1.25 mg ml^{-1} amphiphile concentration, KCl is 250 mM. Adapted from (3), licensed under CC BY 4.0.

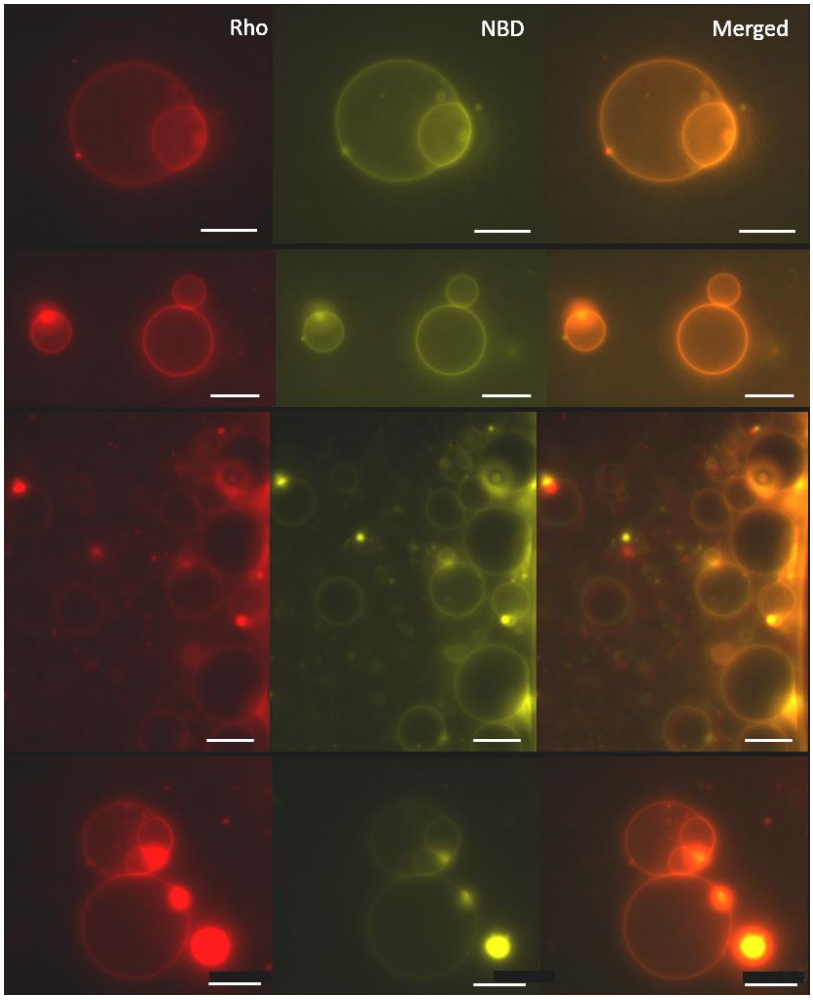

Figure 57. Epifluorescent microscopy of polymer GUV. Polymer GUVs, with 0.6 mol% PE-NBD and 0.6 mol% PE-Rho, were grown from 200 nm polymersomes (1.25 mg ml^{-1}) by agitation at 1200 rpm for 3 h, in 250 mM KCl. Shiny spots are tagged-LUVs aggregated on the surface of GUVs. Scale bar: 10 µm. Adapted from (3), licensed under CC BY 4.0.

Even though labeled lipids were a small fraction of the total amphiphiles and apparently did not affect growth, the experiment was repeated with labeled polymers, whereby the FRET donor was FITC. Under the same salt and agitation conditions, the intermittently measured Rho fluorescence decreased to zero within about 20 min and the course was nearly identical in all three samples (Figure 58A). In parallel, the effect of the reporter dye was checked and the FITC excitation/emission was monitored under constant stirring in the spectrophotometer; the mixing efficiency was again lower, as expected (Figure 58B). Altogether, the variable courses in different assays suggest that an absolute kinetic quantification is virtually impossible and highly dependent on the chosen assay. Nevertheless, comparative analysis within the same setups clearly indicated that the vesicles undergo some form of fusion within the first minutes of agitation, before any detectable change in size distribution, and that milder stirring has a smaller effect than vortexing.

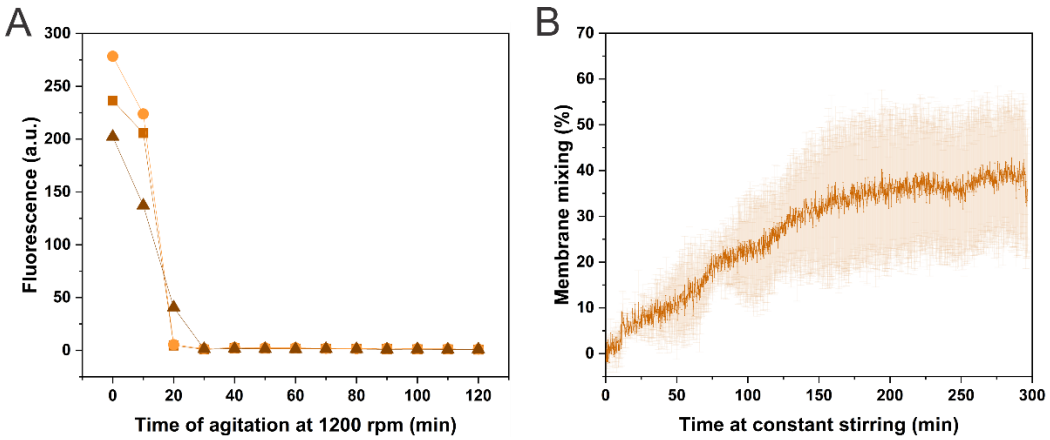

Figure 58. Membrane mixing via FRET between labeled polymers (PDMS-*g*-PEO-FITC and PDMS-*g*-PEO-Rho). (**A**) Change in FRET signal (FITC/Rho = excitation/emission = 460/583 nm) during constant stirring in thefluorescence spectrophotometer for three samples. (**B**) Membrane mixing, calculated from FRET signal (FITC emission) during constant stirring in fluorescence spectrophotometer. The line presents average and standard deviation of two samples. Adapted from (3), licensed under CC BY 4.0.

As shown in the previous section by DLS, the agitation at 1200 rpm in presence of NaCl and $MgCl_2$ simultaneously stimulated growth and fission. FRET data with labeled lipids demonstrated that all salts had a similar effect on the membrane mixing during stirring in the spectrophotometric cuvette, but the process slowed down after about 5 h in the case of 250 mM NaCl and 125 mM $MgCl_2$ (Figure 59). In both NaCl and $MgCl_2$ no visible structures were found when 1.25 mg ml^{-1} polymersomes were agitated for 24–48 h. Increasing the polymersome concentration to 5 mg ml^{-1} did not help to form GUVs after 48 h at 1200 rpm either. 1–3 µm multilamellar (Figure S50) and larger multivesicular vesicles (Figures S51) were rarely detected, while the majority of the polymer constituted long multilamellar tubes (Figure 60) and polymer beads (Figure 61). Such an increase in lamellarity with increasing NaCl concentration was previously observed for DOPC vesicles (26) and multilamellar tubes were formed upon contact with water (260).

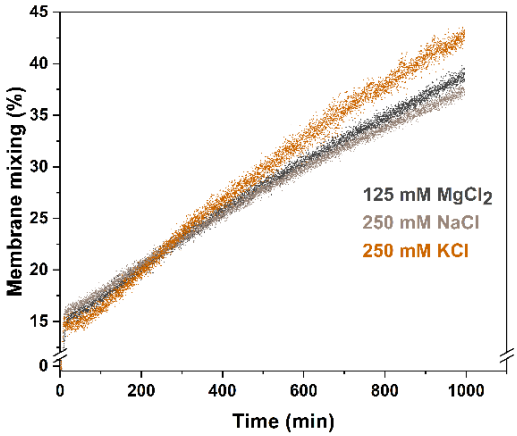

Figure 59. Membrane mixing of polymersomes in three different salt solutions during constant stirring in fluorescence spectrophotometer. Membrane mixing was monitored via NBD emission. Stirring was set at maximum

available in Cary Eclipse spectrophotometer. Baseline was recorder with tagged LUVs, a jump was noticed upon addition of non-tagged LUVs, which we prescribe to LUVs docking. Concentration of LUVs in cuvette was 1.25 mg ml^{-1}. Adapted from (3), licensed under CC BY 4.0.

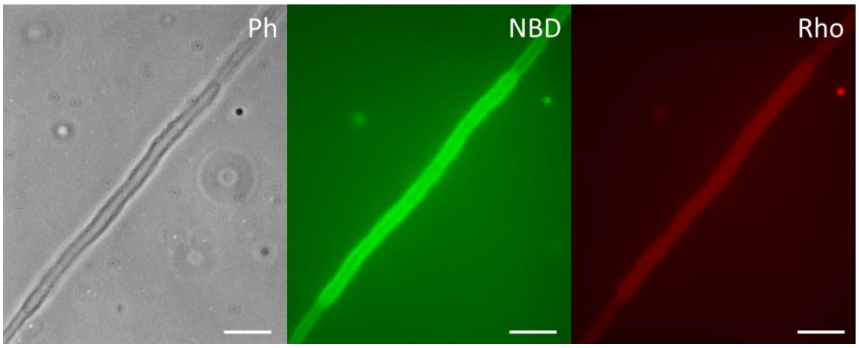

Figure 60. PDMS-*g*-PEO multilamellar tubes formed in NaCl upon agitation. Tubular structures were formed from 200 nm polymersomes (5 mg ml^{-1}), tagged with 1.5 mol% PE-Rho (red) and 1.5 mol% PE-NBD (green), by agitation at 1200 rpm for 48 h, in 250 mM NaCl. Scale bar: 10 µm. Adapted from (3), licensed under CC BY 4.0.

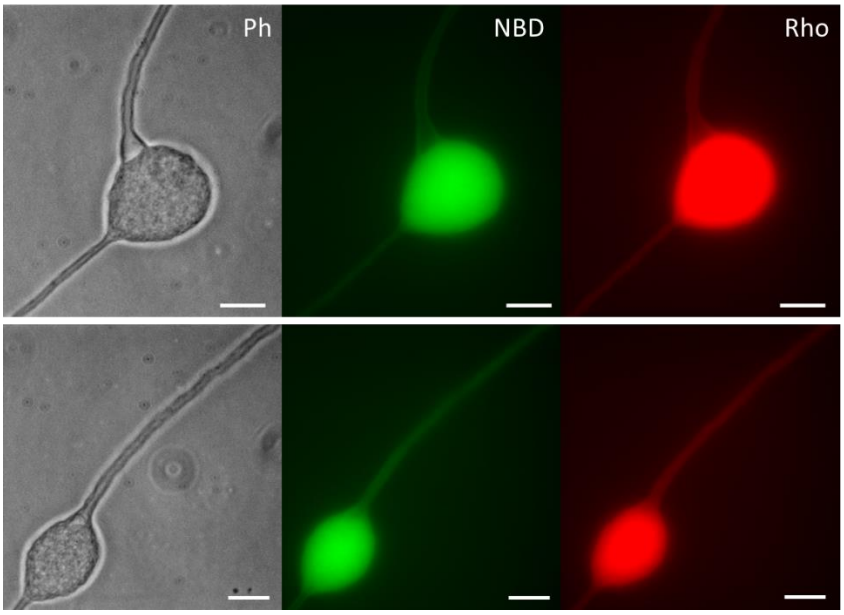

Figure 61. PDMS-*g*-PEO beads formed in NaCl upon agitation. The structures were formed from 200 nm polymersomes (5 mg ml^{-1}), tagged with 1.5 mol% PE-Rho (red) and 1.5 mol% PE-NBD (green), by agitation at 1200 rpm for 48 h, in 250 mM NaCl. Images show membrane junctions with tubular branches and bead on multilamellar tubes. Similar morphologies were previously observed for lipid multilamellar tubes (260). In image below, axially symmetric bead is attached on a multilamellar tube. Scale bar: 10 µm. Adapted from (3), licensed under CC BY 4.0.

3.3.3 Analysis of individual compartments

The current protocol resulted in multiple fusion events leading to a size increase of two orders of magnitude. To further analyze this process, LUVs docking on newly grown GUVs were monitored by tagging them with different dyes (LUVs with PDMS-*g*-PEO-FITC and GUVs with PDMS-*g*-PEO-Rho) (Figure 62A). Indeed, the green signal of LUVs colocalized with the red membrane of preformed GUVs (Figure 62B) but

its intensity varied (Figure S52) likely due to a varying LUV distribution within the sample (no extensive mixing was introduced in order not to break the GUVs; instead the Eppendorf tube was only gently tapped upon mixing of both suspensions).

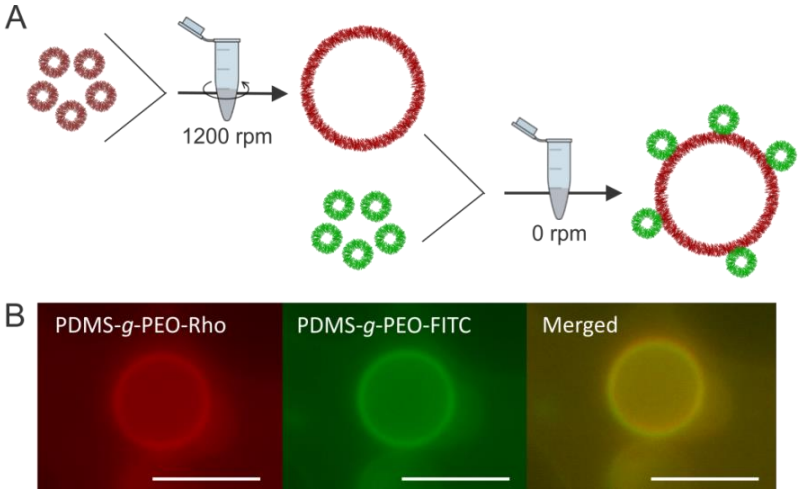

Figure 62. Mixing of PDMS-*g*-PEO LUVs and GUVs in 250 mM KCl. (**A**) Schematic representation of the docking assay. (**B**) Representative micrograph. LUVs were tagged with PDMS-*g*-PEO-FITC (green) and GUVs with PDMS-*g*-PEO-Rho (red). Scale bar: 5 µm. Adapted from (3), licensed under CC BY 4.0.

In order to control the mass transport of the LUVs the docking process in a microfluidic setup with confocal microscopy (185) was analyzed next. To this end, polymer FTIC-tagged GUVs were prepared by electroformation in ~ 500 mM sucrose, trapped, and Rho-tagged LUVs in 250 mM KCl were introduced at a flow rate of 1 µl min^{-1} (Figure 63). Due to asymmetric ion distribution across the membrane, the GUVs exhibited limited stability (Figure 64), which was slightly improved by coating the chip with BSA (bursting decreased). After 30 min of flushing, the Rho signal accumulated on the GUV membrane, which confirmed the docking (Figure 63 and 65).

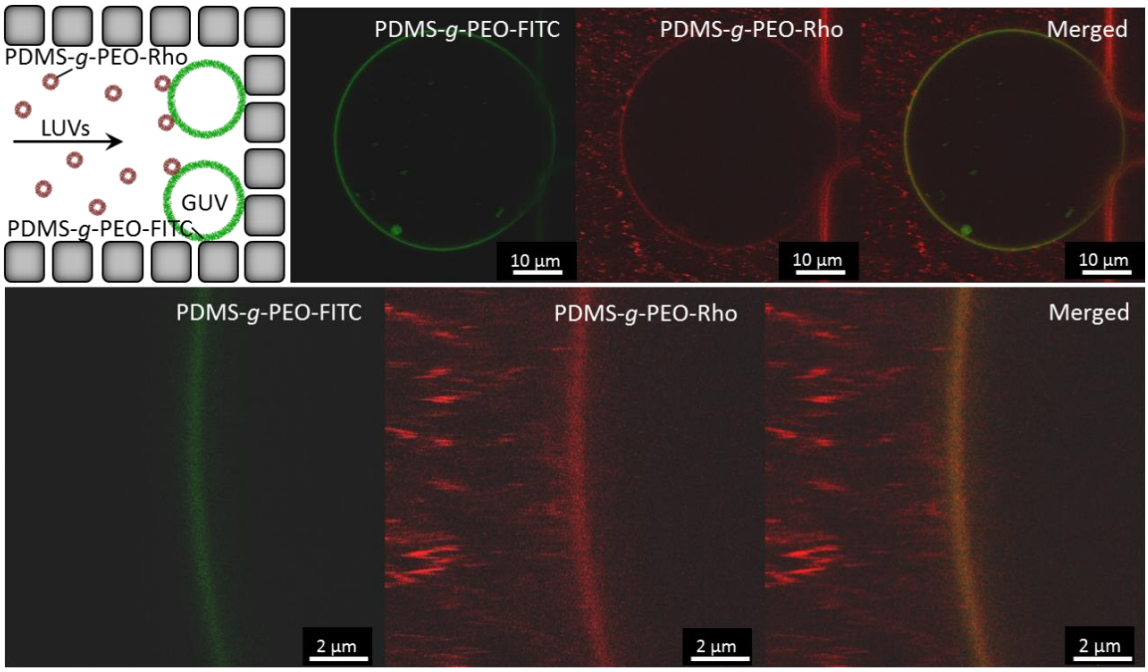

Figure 63. Membrane mixing experiment in microfluidics. GUVs were trapped in a microfluidic chip with multiple rectangular traps similar to those in (185), with a gap size of about 10 µm between the posts forming the trap. GUVs prepared in ~ 500 mM sucrose and labelled with PDMS-*g*-PEO-FITC (green), were exposed to a flow of LUVs, labelled with PDMS-*g*-PEO-Rho (red) in isosmotic 250 mM KCl. Adapted from (3), licensed under CC BY 4.0.

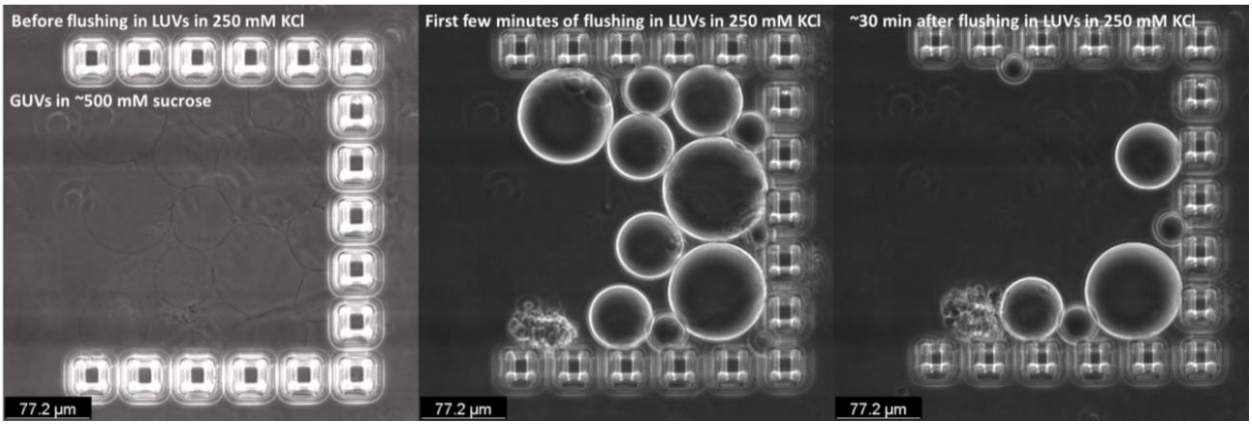

Figure 64. PDMS-*g*-PEO GUVs trapped in microfluidics. After flushing in LUVs in 250 mM KCl, the majority of GUVs burst (left – before flushing in LUVs, inside and outside GUVs is ~ 500 mM sucrose; middle and right – after flushing in LUVs). Adapted from (3), licensed under CC BY 4.0.

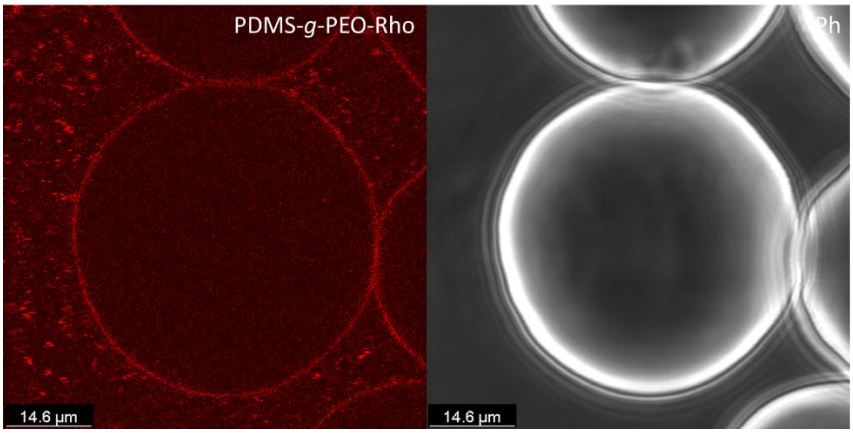

Figure 65. Membrane mixing of polymersomes in microfluidics. PDMS-*g*-PEO GUVs (in ~ 500 mM sucrose) trapped in microfluidics after rinsing with PDMS-*g*-PEO LUVs tagged with PDMS-*g*-PEO-Rho (red) in 250 mM KCl. An accumulation of red signal from tagged polymer was observed, indicating LUVs docking and potential membrane mixing. Adapted from (3), licensed under CC BY 4.0.

To discriminate between docking and fusion, a content mixing experiment was performed next. FITC-tagged LUVs in 250 mM KCl in presence of sulforhodamine B (SRB) were prepared and the resulting suspension was flushed to non-labeled GUVs. After 30 min, the microfluidic chips were washed with 250 mM KCl to remove the free LUVs. Upon this, LUVs did not collocate with the GUV membrane, but apparently entered in the GUV lumen as both the SRB and FTIC signals were observed there (Figure 66A and Figures S53, S54). Thereby, the possibility of non-covalently bound FTIC, released from the polymer, was excluded by analyzing the supernatant after ultracentrifugation of LUVs. Since any Rho signal inside the vesicles in the experiments with differently labeled LUVs and GUVs (Figure 63) was not observed, calcein was encapsulated next in the Rho-tagged LUVs and the microfluidic test was repeated. The LUVs collocated with the GUV membrane but neither Rho, nor calcein signal was observed in the GUV lumen. This indicates that the observed membrane interactions were mediated by the membrane and content mixing dyes and are likely associated with their charges (Figure 66B), which needs to be explored in more detail in the future. Since no content mixing was observed between GUVs and LUVs labelled with Rho, it can be assumed that the observed dye accumulation at the GUV membrane resulted from mere docking and possibly hemifusion. Provided that the driving force was not dissipated as in the case of SNARE- (106) or charge-mediated fusion (17) and that mild agitation in the spectrophotometric cuvette did not suffice to induce growth, we can ascribe the limited fusion in the microfluidic setup to the different hydrodynamic conditions. This hypothesis could be tested by variation of the flow rate once the stability of the GUVs will be improved.

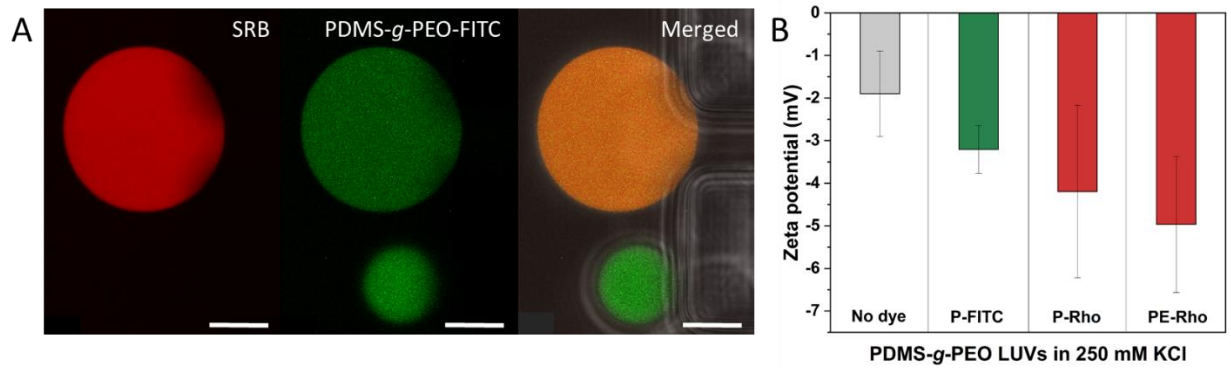

Figure 66. Content mixing experiment and charge of labeled polymersomes. (**A**) Content mixing experiments in microfluidics. Trapped GUVs (no membrane or content dye) were flushed with polymer LUV solution containing water-soluble sulforhodamine B (SRB) (red) and 250 mM KCl. The membrane of the LUVs was doped with PDMS-*g*-PEO-FITC (green). Scale bar: 15 µm. (**B**) Zeta potentials of LUVs doped with different dyes (1.2 mol% PDMS-*g*-PEO-FITC (P-FITC), 1.2 mol% PDMS-*g*-PEO-Rho (P-Rho) or 1.2 mol% PE-Rho) in 250 mM KCl. Bars represent average of 4 measurements with standard deviation. Adapted from (3), licensed under CC BY 4.0.

3.3.4 The role of salts in the fusion of polymersome

Unlike the more sophisticated orchestration of fusion by protein pores, the proximity model postulates that a close apposition of membranes and small perturbations suffice to induce fusion. Although this mechanism has been developed for liposomes (128), it was recently extended to the fusion of polymer vesicles (261), and is likely valid for the current case. The strong agitation facilitates the contacts between PDMS-*g*-PEO polymersomes and destabilizes their membranes, whereby these effects could be possibly implemented by other mechanical means such as ultrasound treatment (261). 1200 rpm appears to be a sweet spot between the sufficient agitation to ensure multiple vesicle collisions on the one side and the comparatively high shear stress in the vortex mixer, resulting in rupture and fission, on the other. However, aggregation and growth was not observed in the absence of salts at and beyond physiological levels (262-264) despite that the zeta potential in Milli-Q water was close to zero (-2 ± 1 mV). In theory, values in this range suggest colloidal instability and the polymersomes would be expected to aggregate readily, but the size distribution did not change in a week, as discussed above. On the other side, even if some charge was introduced to the membrane via the dyes, it was neutralized in the presence of salts (Figure 53). However, we refrain from electrostatic interpretation due to the low magnitude of the latter change and the potential inaccuracy arising from different ionic strengths and aggregation (163), and the nearly neutral zeta potential in the absence of salts.

The association between PEO chains and Mg^{2+} should be even stronger than with Na^+ or K^+ due to the smaller ionic radius and higher electronegativity (252). The effectiveness of salts, however, does not follow the ionic strength – equal salting out power of K_2SO_4 and $MgSO_4$ (265), and of KCl and NaCl (266) was previously observed. The salting out effect reduces the steric resistance between vesicles (266) and enables

docking, which is a prerequisite to vesicle fusion. GUV aggregation was observed multiple times, as exemplified in Figures S40 and S42 and discussed above.

The cations in this study can partition between four environments: (1) free in water, (2) bound to the Cl^- anions, (3) bound to the PEO oxygen atoms, or (4) bound to the lipid headgroup oxygen atoms in the case when tagged lipids were used. Molecular dynamic simulations previously showed that Na^+ ions were predominately bound to PEO but also to a lesser degree to the headgroup (267). K^+ ions were also found in the PEO layer, though a larger portion of them remained in the solution outside the membrane than in the case of Na^+ cations, which indicated weaker interaction. The rationale for the latter lies in the natural curvature of PEO chain that fits more comfortably around Na^+ than K^+ ions (268). It can be speculated that under the present conditions, the stronger association led to fission events in addition to fusion, and the formation of multilamellar tubes (Figure 60) instead of spherical giant vesicles.

Molecular dynamic simulations also showed that the thickness of the PEO layer was slightly expanded in the presence of salt, which can be explained by the greater number of bound cations, which increase the electrostatic repulsion within the layer (267). To inspect if such changes in the hydrophilic portion of the polymer membrane cause changes of the overall packing, the salt effect was analyzed by the polarity-sensitive fluorescent probe Laurdan (196). PDMS-*g*-PEO membranes exhibited similar disorder in Milli-Q water and in mono- and divalent salt solutions (Figure 67B), thus the PDMS phase apparently remained intact. Meanwhile, we observed that salt had an effect on the membrane bending rigidity: even 5 mM KCl softened PDMS-*g*-PEO membranes (bending rigidity decreased from 11.7 $\kappa_B T$ to 6.1 $\kappa_B T$ (see Chapter 3.1.1.1 and Chapter 3.5.2)), which in turn positively affected the SNARE-mediated polymersome fusion. Similarly, an anionic DPPG bilayer with substantially higher bending rigidity than the PDMS-*g*-PEO monolayer (~ 110 $k_B T$) was previously shown to soften upon increasing NaCl concentration with a slope of $-0.13 \pm 0.02\ k_B T\ \mathrm{mM}^{-1}$ (269). Furthermore, the combined effect of NaCl and Tris buffer was stronger than their individual contributions, giving rise to 40 % reduction of the bending rigidity of POPC GUVs (270). Meanwhile though, zwitterionic DOPC vesicles were shown to rigidify in presence of NaCl and the bilayer thickness increased, as evidenced by small-angle X-ray scattering (26). In regard to the present case, we recently observed increase in the membrane thickness of PDMS-*g*-PEO/phosphatidylcholine (70:30 molar ratio) mixtures in presence of KCl via cryo electron microscopy: in the absence of salt the thickness was 4.9 nm (Chapter 3.1.2.3, Table 6), while in a buffer containing 150 mM KCl it was 6.1 nm (106). Thus, the fusion in the present case can be attributed to the PEO expansion upon interaction with salts, contrary to the previously assumed corona contraction in the case of PBd-*b*-PEO (126), the expansion of which in turn softens the membrane and thus lowers the energetic barriers during fusion-related deformations. A similar

effect of the size of the headgroup on the bending rigidity was observed via simulations in the case of phospholipids (271).

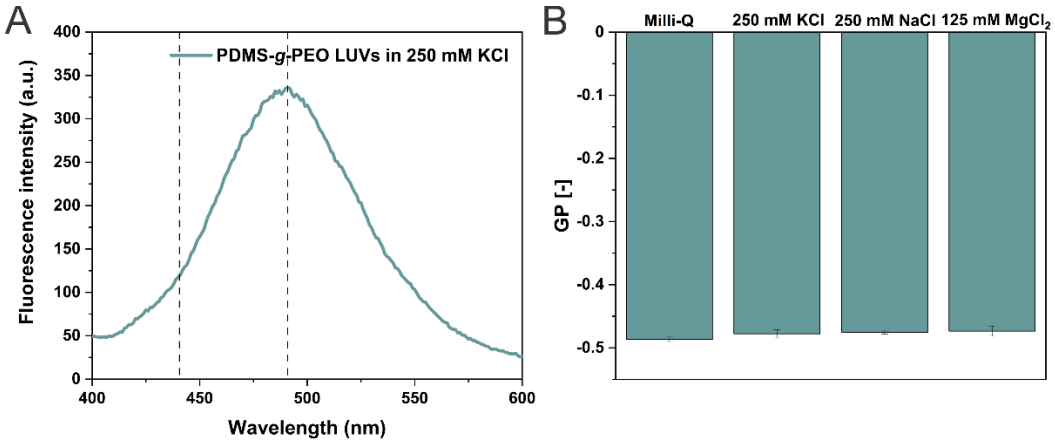

Figure 67. Disorder of polymer membranes in salt solutions. (**A**) Fluorescence emission spectra of Laurdan in PDMS-*g*-PEO membrane in 250 mM KCl. (**B**) Generalized polarization values (GPs) of polymer LUVs. Error bars represent SD from n = 3. Adapted from (3), licensed under CC BY 4.0.

Principally, the whole fusion process includes four successive steps: membrane contact, formation of a hemifusion diaphragm, expansion of the fusion pore, and complete fusion. For the majority of observed polymer GUVs only long contact was observed; in only rare cases we saw a hemifusion diaphragm (Figure 68). This confirms that agitation is necessary to open the fusion pore, and therefore, the polymer GUVs growth stopped in the absence of agitation. The energy barriers related to curvature deformation during hemifusion-stalk and fusion-pore formation and expansion must be overcome. Recently, we utilized a combination of salt and SNARE proteins to lower those barriers (106). Here, an increased salt concentration was used to decrease those barriers by softening the membranes, and agitation to increase membrane lateral tension, which is very important for the fusion pore. Lateral tension, mainly concentrated on the fusion neck, likely leads to an enlargement of the fusion pore. Overall, the fusion process was observed between GUVs of different sizes, and the simultaneous fusion of three or more polymersomes was also observed. This indicated that membrane fusion is not restricted to polymer LUVs and that the vesicle size is not a severe limitation to membrane fusion.

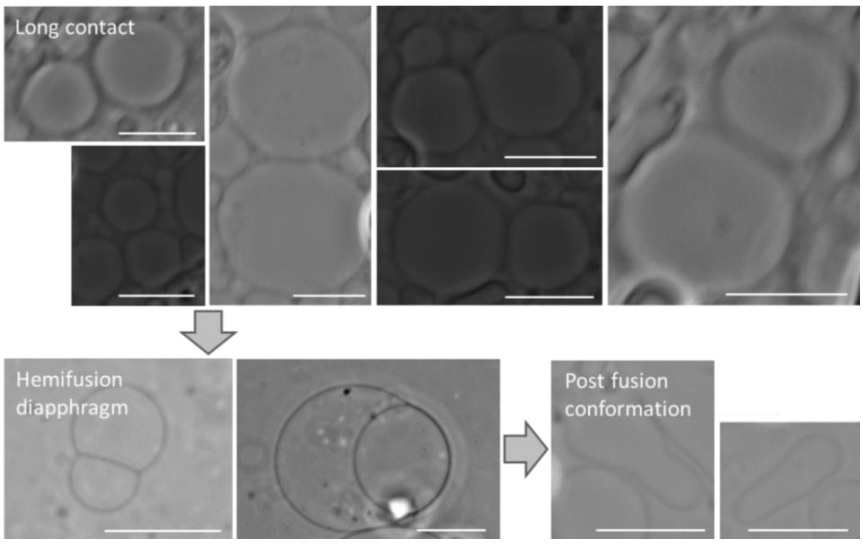

Figure 68. Proposed fusion progression of PDMS-*g*-PEO vesicles in 250 mM KCl as suggested by captured micrographs. Scale bar: 10 µm.

3.3.5 Compatibility of the protocol with essential artificial cell features

Finally, we investigated whether this simple procedure to grow optically accessible polymer compartments can be integrated with the encapsulation of cytosolic components and the reconstitution of membrane machinery. This practical rationale is in line with the reductionistic view of the cell as a functionalized, closed membrane, which accommodates water-soluble machinery and metabolites in its lumen. This was approached by introducing different hydrophilic molecules (at 10 µM final concentration) to the LUVs in 250 mM KCl, and after 24 h of agitation at 1200 rpm, their partitioning was analyzed via fluorescence microscopy (Figure 69A). First, calcein was tested – a small fluorescent dye (MW = 623 g mol^{-1}), which is commonly used to monitor vesicle leakage and content mixing during fusion. The size of the GUVs was overall smaller than in the absence of the dye but calcein was distributed fairly homogenously (Figures 69B and S55). To test if larger molecules also entered the polymersomes, labeled dextran (MW = 20,000 g mol^{-1}) was employed next. The resulting varying distribution was likely a result from the stochasticity of the growth process and the slower dextran mass transport (Figures 69C and S56, S57). Finally, a model nucleotide (FITC-12-dUTP) was added to probe the encapsulation of information carriers. Interestingly, when LUVs were agitated in the presence of FITC-12-dUTP, much larger GUVs were formed (reaching diameters of ~ 50 µm). We assume that growth was facilitated by FITC-12-dUTP due to stronger attractive forces between the vesicles. This could be explained by K^+ bridging between PEO and the phosphate group of dUTP since it was shown that ATP associates with DOPC bilayers (272). These membrane interactions led to heterogeneous distribution of FITC-12-d-UTP (Figures 69D and S58, S59) and often resulted in tight contacts between the GUVs and the formation of tissue-like structure (Figure S60).

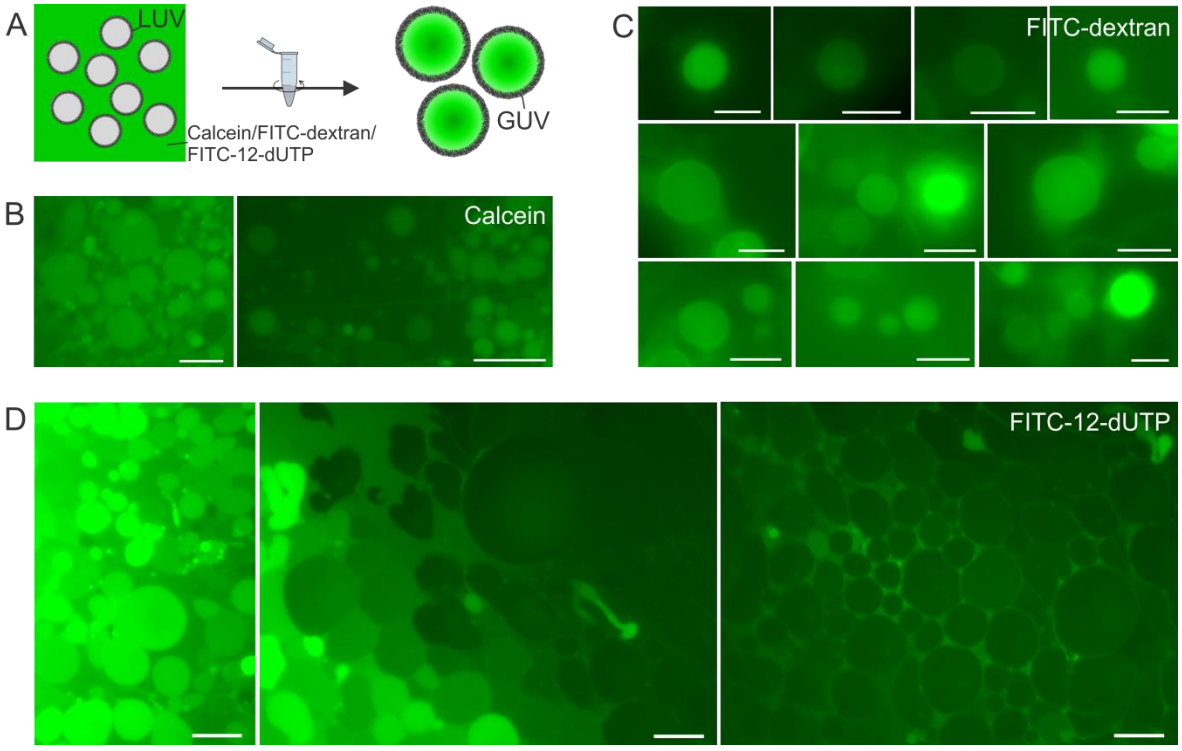

Figure 69. Uptake of cytosolic load during growth of GUVs from LUVs. (**A**) Scheme representing the encapsulation experiment. Representative micrographs of PDMS-*g*-PEO GUVs with encapsulated (**B**) calcein. Scale bar: 10 µm. (**C**) FITC-dextran. Scale bar: 5 µm. (**D**) FITC-12-dUTP. Scale bar: 10 µm. Adapted from (3), licensed under CC BY 4.0.

The harsh agitation may in parallel turn harmful to sensitive membrane proteins due to e.g., membrane destabilization and subsequent protein delipidation. To test for such a potential detrimental effect, the 144 kDa four-subunit bacterial proton pump ubiquinol *bo*$_3$ oxidase (208) was reconstituted in polymer LUVs and its enzymatic activity was measured via oxygen consumption upon agitation at 1200 rpm. Since it was observed that the activity of *bo*$_3$ oxidase dropped even at 4 ºC (~ 30 % decrease after one day (Chapter 3.1.2.1)), the behavior was also tested at room temperature. As a negative control, aggregated *bo*$_3$ oxidase was obtained by removing the stabilizing detergent (n-dodecyl β-D-maltoside) via Bio-Beads to mimic the detrimental influence of delipidation (Figure 70A). In parallel, whether protein-functionalized membranes were still prone to fusion was tested. Up to 4 h after reconstitution, we did not measure a decrease in protein activity at room temperature, regardless if the sample was agitated or not (Figure S61), which gives a reasonable time window for experimentation. No difference was observed also between the activity at room temperature and at 4 ºC either (Figure 70B). Furthermore, the size of the polymersomes with reconstituted protein increased (Figure 70C), which indicated that the protocol was compatible with the sensitive protein.

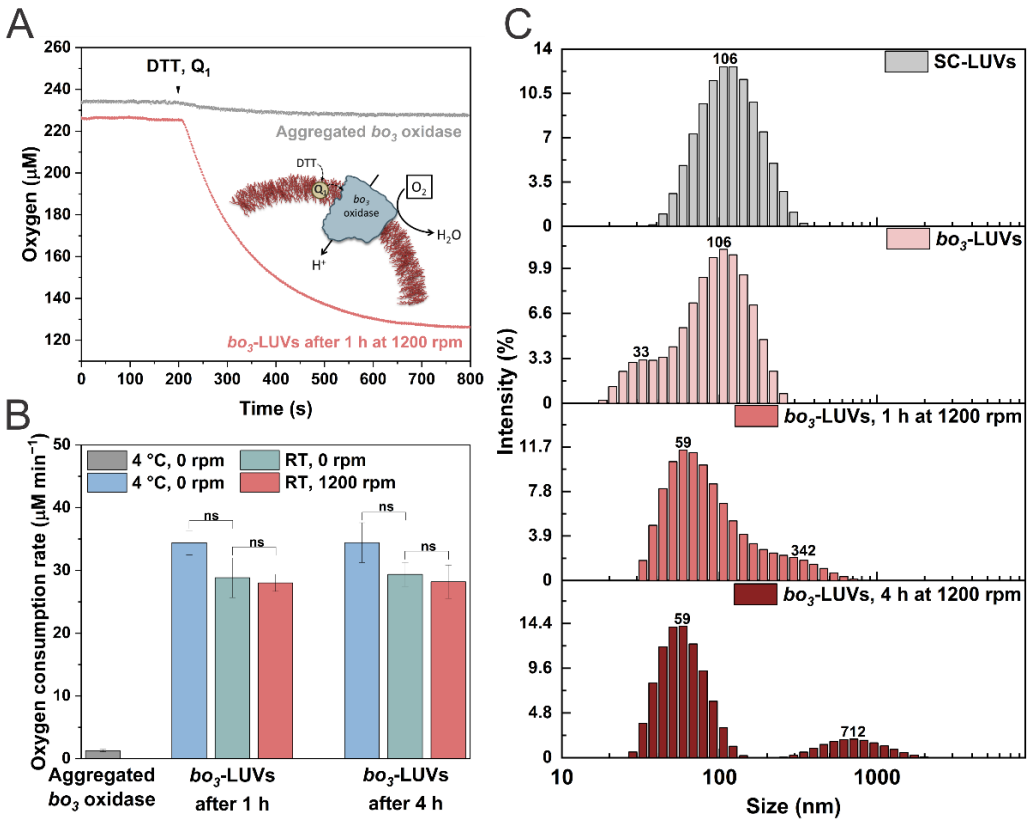

Figure 70. Activity and size distribution of *bo*$_3$-LUVs. (**A**) Oxygen consumption by *bo*$_3$ oxidase reconstituted in PDMS-*g*-PEO LUVs and aggregated *bo*$_3$ oxidase (negative control in absence of stabilizing amphiphiles (detergent/polymer)). At ~ 200 s mark, the enzyme reaction was initiated by dithiothreitol (DTT) and ubiquinol 1 (Q_1). (**B**) Oxygen consumption rates by aggregated (n = 2) and reconstituted *bo*$_3$ oxidase (n = 3) upon incubation at 4 °C or room temperature (RT) in absence (0 rpm) and presence of agitation (1200 rpm). Statistical hypothesis test (Student's t-test) was applied, according to which the difference between two samples is not significant (ns) for a *p*-value > 0.05. (**C**) Size distribution of LUVs with sodium cholate (SC) and *bo*$_3$-LUVs before and after agitation. Adapted from (3), licensed under CC BY 4.0.

3.4 Fusion/electroformation: growth with high utility in bottom-up synthetic biology

Continuing with vesicle fusion induced by external factors, in the next step, membrane dehydration was studied as another possible mechanism to fuse the membranes of LUVs. Dehydration of membrane surface, which enables approximation and mixing of apposing membranes, was here achieved by water evaporation. The latter destabilized the membranes of LUVs, which induced their fusion and formation of lipid/polymer film. Note that this fusion mechanism did not form larger vesicles, but instead a thin membranous film. To form micro-sized vesicles from initial nano-sized ones, the fused LUVs film was in the next step rehydrated in the presence of an alternating current (AC, electroformation). Vesicle growth occurs during swelling of fused LUVs film. Although membranous system with significantly larger final size (from nano- to micrometer scale) indeed grows in this approach, it should be noted, that conceptually this is a different approach than other mechanisms described in this thesis – as mentioned above, there is a middle step involving membranous film that is not involved in other mechanisms. Nevertheless, due to the high relevance of this approach for bottom-up synthetic biology, it was included in our growth study of hybrid and polymer compartments.

3.4.1 Key factors in growing polymer and hybrid proteoGUVs via fusion/ electroformation

Fusion/electroformation or dehydration/electroformation is typically used for the preparation of membrane protein-functionalized GUVs (proteoGUVs), whereby the starting material is the membrane protein-functionalized LUV (proteoLUVs). In the present study, the initial fusion/electroformation experiments were performed with protein-free LUVs. Once the protocol to obtain high yield of GUVs with appropriate size (> 10 µm) was established, protein-free LUVs were replaced by proteoLUVs (or a mixture of both), and proteoGUVs were grown. The model membrane protein was a largely hydrophobic proton pump bo_3 oxidase, and in later steps also a highly asymmetric F_1F_O-ATPase. Those two membrane proteins were chosen due to their distinct structure, different size, shape and hydrophobicity. Nevertheless, it should be noted, that this growth mechanism is not limited solely to those two types of membrane proteins – with some modifications, it can be applied to other membrane proteins and media as well (as discussed in Chapter 3.5).

The proteoGUV formation process involves three successive steps: 1) protein incorporation in LUVs through detergent-mediated reconstitution, 2) partial dehydration of proteoLUVs on ITO-coated glass slides, and 3) hydration under electric field (Figure 71). The respective setup for steps 2 and 3 is shown in

Figure 11. Overall, amphiphile-tailored optimization (see Chapter 2.9.3.1) of the fusion/electroformation approach resulted in > 10 µm GUVs, the successful insertion of *bo*$_3$ oxidase, and its co-reconstitution with F_1F_O-ATPase. Starting with LUVs enabled better control over protein orientation and reconstitution efficiency, while fine tuning was possible because PDMS-*g*-PEO LUVs could be readily solubilized with a wide concentration range of various detergents. Notably, lower detergent concentrations were required for the solubilization of PDMS-*g*-PEO in comparison to PC or block copolymer ones (see Chapter 1.3.3.1), which diminishes the probability of denaturation and the amount of detergent to be removed. After hybrid or polymer proteoLUVs were deposited on ITO-coated glass slides, they were fused to form a thin lipid/polymer film after 40 min dehydration at room temperature. The fusion was assessed by analyzing the size distribution of vesicles after electroformation via dynamic light scattering (DLS); the presence of starting material (LUVs with approx. size of 100 nm) indicated poor dehydration and fusion (Figure 72).

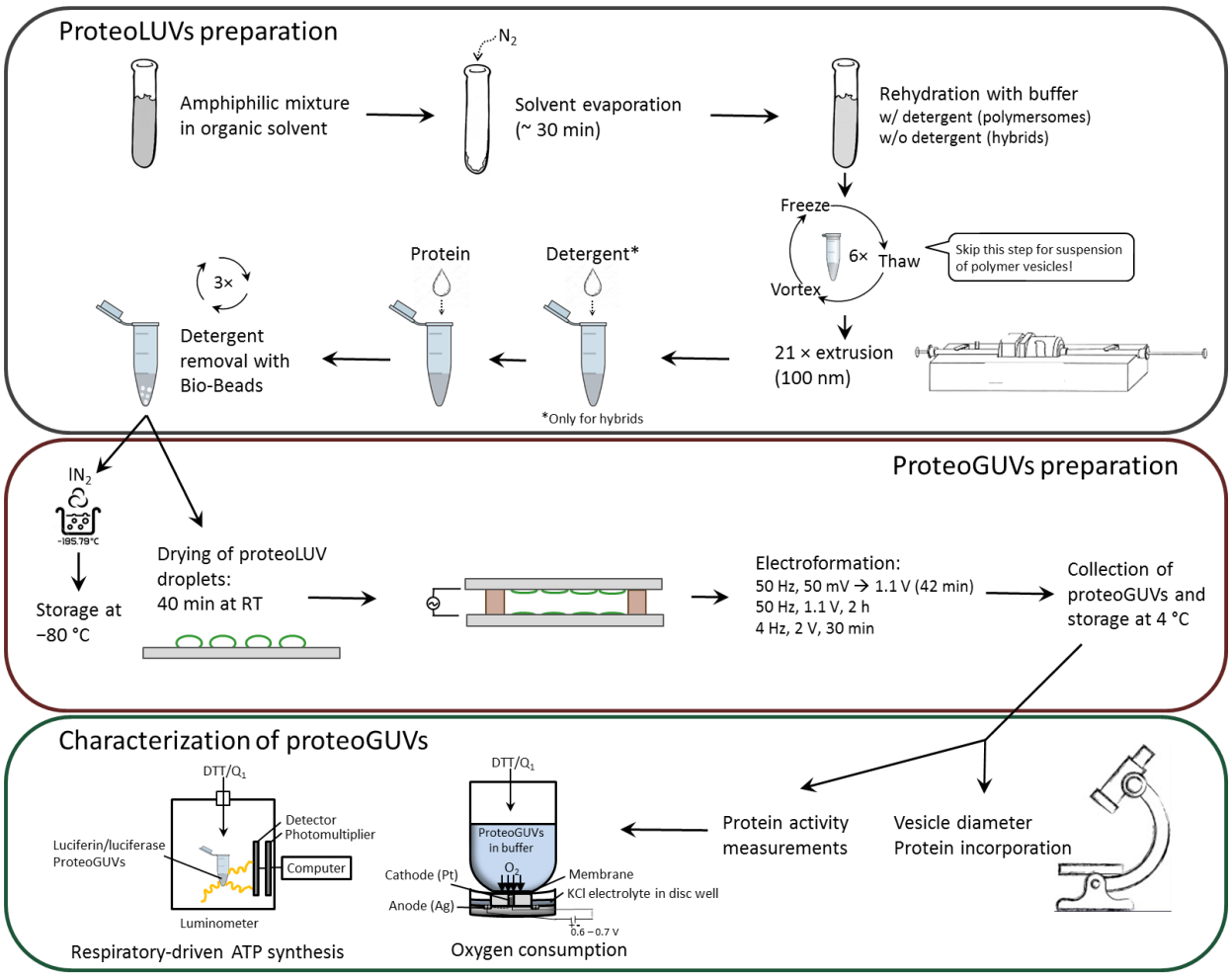

Figure 71. Scheme of the preparation and characterization of polymer and hybrid proteoGUVs. LUVs were prepared by rehydration of amphiphile film and extrusion to unify their size. *bo*$_3$ oxidase and F_1F_O-ATPase were reconstituted or co-reconstituted in LUVs with the help of detergent. Droplets of proteoLUV suspensions were

deposited on ITO-coated glass slides, partially dehydrated, and proteoGUVs were grown by electroformation. The latter were analyzed with respect to size, protein incorporation and distribution, alongside biological activity.

It should be noted that a sufficiently high (> 5 mg ml^{-1}) concentration of proteoLUVs was necessary for achieving successful electroformation (for details on vesicle deposition please see Chapter 2.9.3.1). On the other side, we observed that proteoLUVs deposited at 10 mg ml^{-1} successfully fused but only in part as DLS indicated significant presence of residual LUVs. In all cases, the majority (> 95 %) of hybrid and polymer GUVs was unilamellar and without intravesicular structures judged by their morphological appearance. Importantly, when proteoLUVs were prepared with a low amount of salt, longer dehydration was necessary (~ 40 min), while with increasing salt concentration, a shorter dehydration time was sufficient (~ 30 min). For comparison, lipid LUVs fused with greater difficulty in buffers without salts, and special conditions had to be provided: saturated NaCl environment in desiccator for 24 h at 4 ºC and a much higher (100 mg ml^{-1}) LUVs concentration, whereby some of the proteoGUVs were multilamellar or multivesicular. Meanwhile, for block copolymers, proteoGUVs formation attempts via fusion/ electroformation are still extremely rare. The only one (to the best of our knowledge) report used a stepwise deposition of LUVs, and was accompanied by protein aggregation upon the partial dehydration (212).

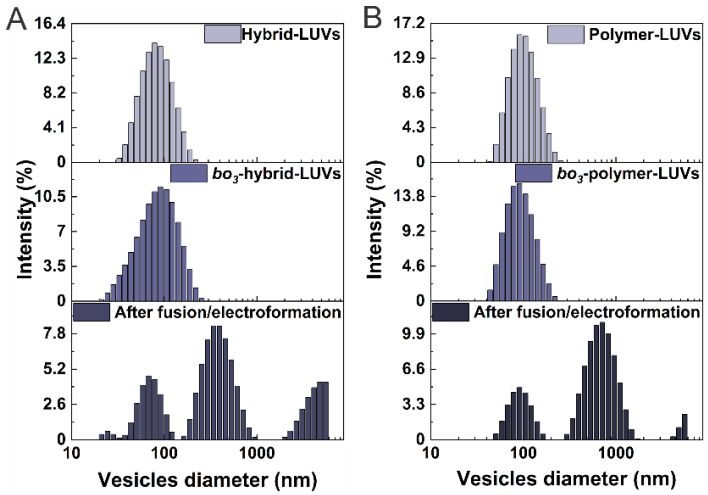

Figure 72. Vesicles size distribution. PDMS-*g*-PEO:PC (70:30, molar ratio) hybrids (**A**) and PDMS-*g*-PEO polymersomes (**B**): size distribution by intensity before and after reconstitution of *bo*$_3$ oxidase and after dehydration and electroformation, determined by DLS. Time of dehydration was only 30 min, which was insufficient, and thus a large portion of LUVs remained unfused.

Next, some common one-step electroformation protocols used for lipids (for details please see Chapter 2.9.3.1) were tested, which altogether resulted in *bo*$_3$-GUVs with a diameter of only ~ 1 µm (Figure 73, left). Therefore, the final electroformation protocol in the current study combines three steps. The first one was the most critical to obtain GUVs with a diameter > 5 µm, whereby we assumed that slower initial swelling prevented the early LUV film detachment. Meanwhile, in the second step, vesicles continued to

swell and grew to the final size of GUVs; 2 h at least were required to obtain 10–40 µm GUVs. By extending the duration from 2 to 12 h, the size increased further and GUVs with a diameter of ~ 100 µm formed, but the majority of vesicles did not detach. For the prolonged protocol, it was crucial that the chamber was moved to 4 ºC to retain the enzymatic activity of the membrane proteins. In the third step, the GUVs detached at elevated voltage and decreased frequency. Overall, the final optimized protocol resulted in GUVs with a median size > 10 µm (Figure 74), a homogenous protein distribution (Figure 75) and the absence of LUVs in the lumen.

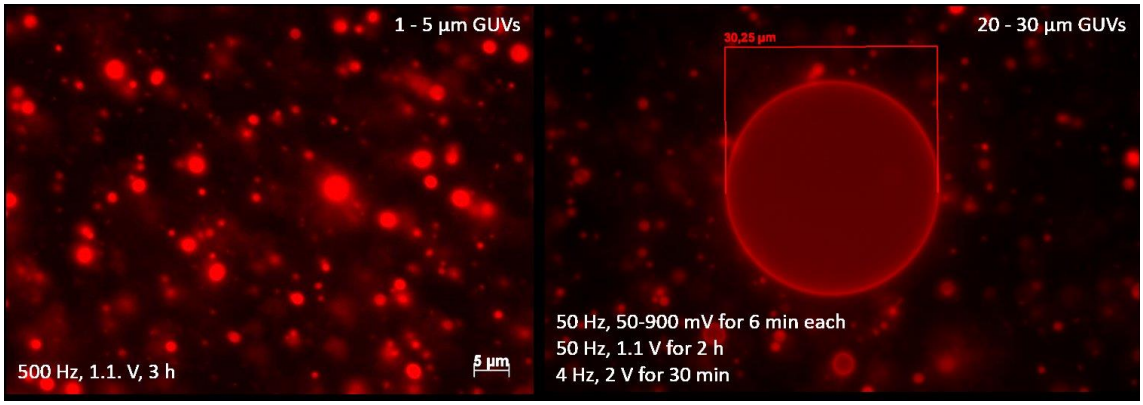

Figure 73. Micrographs of protein-free polymer GUVs after fusion/electroformation. PDMS-*g*-PEO GUVs (0.05 mol% PDMS-*g*-PEO-Rho) prepared by rehydrating the fused LUVs film under two different electroformation protocols (right: final protocol).

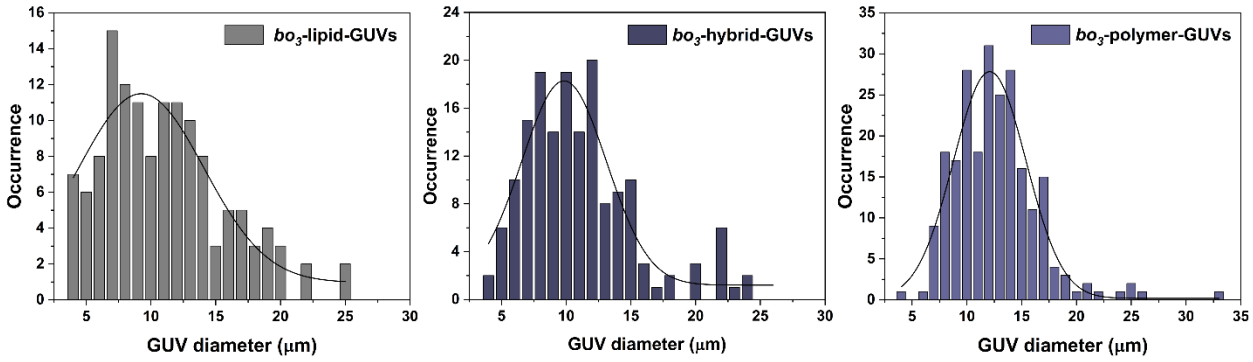

Figure 74. Typical size distribution of *bo*$_3$-GUVs prepared by the fusion/electroformation technique. Vesicles with a diameter lower than 4 µm were not counted, along with a small fraction of 40–60 µm GUVs that was occasionally observed. From left to right: *bo*$_3$-lipid-GUVs, *bo*$_3$-hybrid-GUVs, and *bo*$_3$-polymer-GUVs. The protocol for *bo*$_3$ oxidase-functionalized PDMS-*g*-PEO membranes could be applied also to PDMS-*g*-PEO:soy PC ones and resulted in similar size distribution, which has likely to do with the high polymer content (70 mol%). Meanwhile, the protocol did not work for soy PC membranes. Concentration of deposited LUVs had to be substantially increased and dehydration conditions had to be changed (as discussed above, for details see Chapter 2.9.3.1).

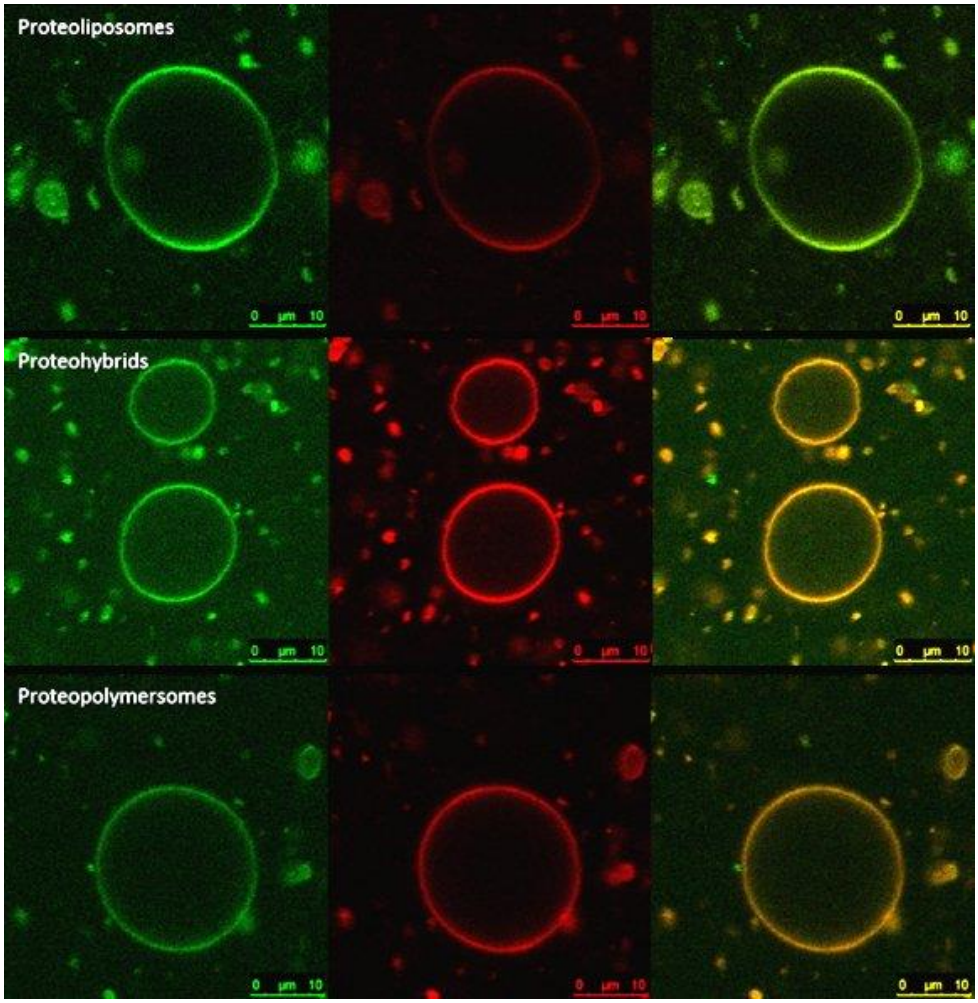

Figure 75. Micrograph of protein-functionalized polymer GUV. Successful insertion and homogenous distribution of *bo*$_3$ oxidase-ATTO 514 (green) in *bo*$_3$-GUVs. Typical soy PC (top), PDMS-*g*-PEO:soy PC (middle) and PDMS-*g*-PEO (bottom) *bo*$_3$-GUVs. The lipid dye PE-Rho for liposomes or the polymer dye PDMS-*g*-PEO-Rho (red) for polymersomes and hybrids were used to visualize the membrane. From left to right: ATTO 514 channel (green), rhodamine channel (red), overlay of both channels.

3.4.2 Model reconstitution of largely hydrophobic membrane protein

3.4.2.1 Vesicle size and membrane thickness

Biological membranes are crowded and the lipid-to-protein weight ratios range from ~ 0.35 (inner mitochondrial membrane) to ~ 1 (plasma membrane) and > 1 (secretory vesicles) (273). Meanwhile, membrane proteins can be reconstituted in man-made vesicles at various protein densities, depending on the protein type and function, and the intended application. Thus, protein densities in bottom-up energy supply modules range from comparatively high (lipid-to-bR = 160–1,350 (71)) to moderate (lipid-to-reaction center = 2,200 (68), lipid-to-bR = 2,200 ± 700 (78)) and low (~ 30 *bo*$_3$ oxidase/µm^2 (79)). Thereby, lower densities are typically used for chemically-driven proton pumps in comparison to light-driven ones,

due to the higher turnover rate of the former (274). This effect correlates with the ATPase-normalized ATP synthesis rates found in the literature: 280 nmol min^{-1} if combined with bR (275) versus 1280 nmol min^{-1} if combined with *bo₃* oxidase (195). In parallel, membrane protein detection by fluorescence microscopy requires a sufficiently strong signal, which further depends on the fluorophore and the degree of protein labeling. In the present case, *bo₃* oxidase could be detected in polymer GUVs even at relatively high polymer-to-protein molar ratios (~ 50,000), whereas obtaining $\Delta pH \geq 1$ across the membrane required about 15 times higher protein loading (see Section 3.4.2.4).

Here, we checked how changing the polymer-to-*bo₃* oxidase molar ratio influenced the size of the GUVs. Towards this end, we started with protein-free vesicles and increased the ratio to 1,500(:1), while analyzing the size distribution by optical microscopy. Different protein densities were achieved in one of the following two ways: either by varying the protein concentration in the starting LUVs or by mixing protein-free LUVs with *bo₃*-LUVs in different volume ratios, prior to the dehydration step. The average diameter of polymer GUVs negatively correlated with the protein loading. In addition, their mean size was similar in buffer and sucrose solution, but in the latter a larger number of GUVs with a diameter 20–30 µm (Figures S62–64) was noticed. At polymer-to-protein molar ratios lower than ~ 4,000, the average size of *bo₃*-GUVs decreased and *bo₃*-GUVs with a diameter larger than 25 µm occurred rarely. A similar correlation was noticed for hybrids (Figure S65). In parallel, the higher protein loadings resulted in lower polydispersity for both amphiphiles (Figures 76 and S65).

These scaling effects may not have a similar magnitude for other enzymes with a different hydrophobic region and asymmetry, and the charge distribution in their tertiary structure should play a role as well (we observed a similar decrease of the GUV size with an increasing concentration of membrane dyes from 0.05 to 0.5 mol%).

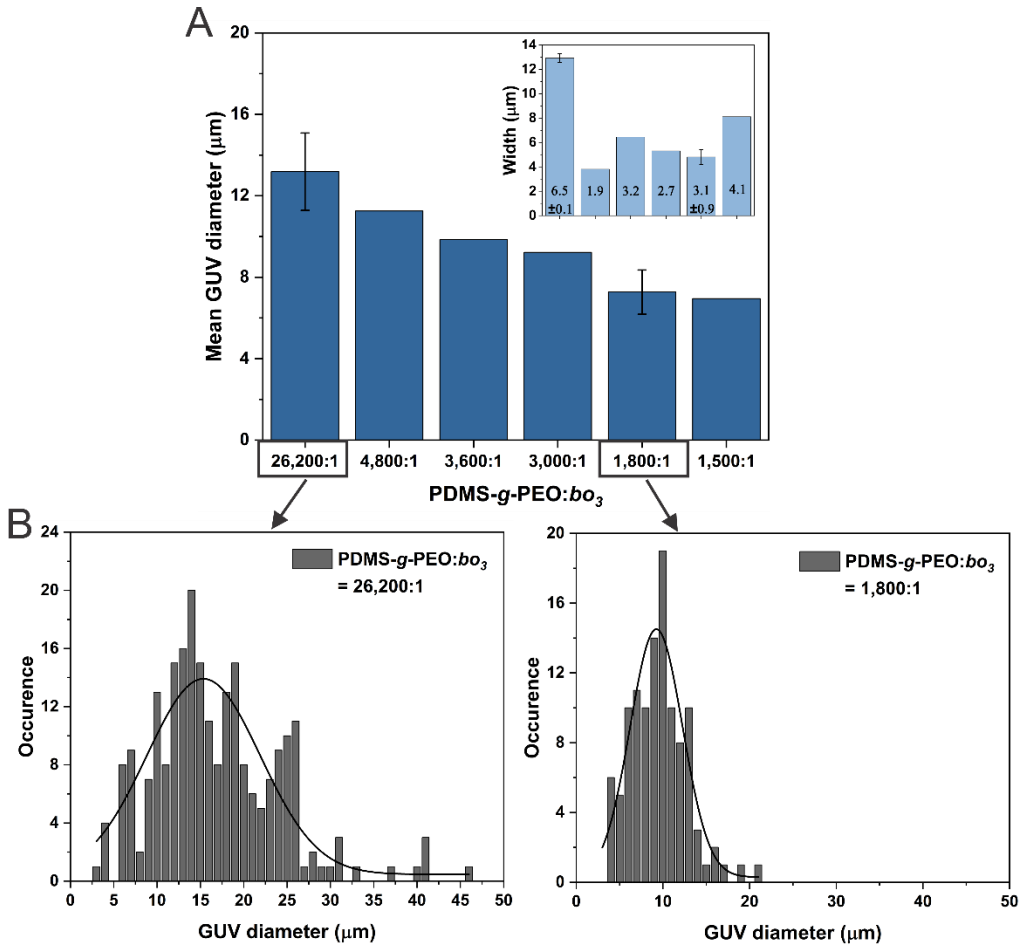

Figure 76. *bo*$_3$-GUVs size distribution at different protein densities. (**A**) Mean size variation at different protein loadings. Inset shows the half-maximum widths and the standard deviations (σ) of the respective normal distributions. Buffer: 1 mM Tris-HCl, pH 7.5, 100 mM sucrose. Molar ratios 26,200 and 1,800 were analyzed from three different preparations to assess reproducibility. (**B**) Representative size distributions of *bo*$_3$-polymer-GUVs at two polymer-to-protein molar ratios. The black lines represent fitted normal distributions. See Figure S62 for other molar ratios.

Finally, *bo*$_3$-GUVs were analyzed for their membrane thickness and lamellarity. As observed by cryo-TEM (Chapter 3.1.2.3), the thickness of polymer and hybrid membrane increased for 8.6 and 7.5 % upon *bo*$_3$ oxidase insertion, respectively. That data was collected on *bo*$_3$-LUVs, meanwhile, here, a different approach was applied for *bo*$_3$-GUVs in order to compare the distribution of the membrane thickness on nano and microscale. Since the membrane thickness is below the microscope resolution, the most often used standard method for lamellarity determination, i.e., measuring the of membrane fluorescence and plotting it against the GUVs' diameter (276), was applied. Figure 77 shows the membrane fluorescence intensity plotted against the GUVs' diameter for lipid, hybrid and polymer *bo*$_3$-GUVs. In many cases, *bo*$_3$-GUVs with the same diameter exhibited more than 2× higher fluorescence intensity, which could indicate their multilamellarity. Although this might be the case for *bo*$_3$-lipid-GUVs, it is likely not the case for *bo*$_3$-hybrid-GUVs and *bo*$_3$-polymer-GUVs. In cryo-TEM micrographs of *bo*$_3$-LUVs (Chapter 3.1.2.3) not a single

multilamellar *bo*$_3$-hybrid-LUVs and *bo*$_3$-polymer-LUVs was found; meanwhile, there were a few multilamellar *bo*$_3$-lipid-LUVs (Figure S73). However, the range of thicknesses in between hybrid and polymer *bo*$_3$-LUVs (and even inside the same vesicle) substantially increased upon protein insertion: from 4.9–5.6 nm to 5.0–6.9 nm for polymer LUVs and from 4.5–5.3 nm to 4.4–7.0 nm for hybrid LUVs. We assume, that the deviation in membrane fluorescence intensity of hybrid and polymer *bo*$_3$-GUVs arises also from the difference in the membrane thickness, and not from the multilamellarity. Furthermore, the difference in membrane florescence intenisty for *bo*$_3$-GUVs with the same diameter is particularly pronounced in hybrids, which could be caused by polymer dye partitioning in hybrids containing a higher amount of polymer (composition 70:30 polymer-to-lipid cannot be completely retained in between GUVs).

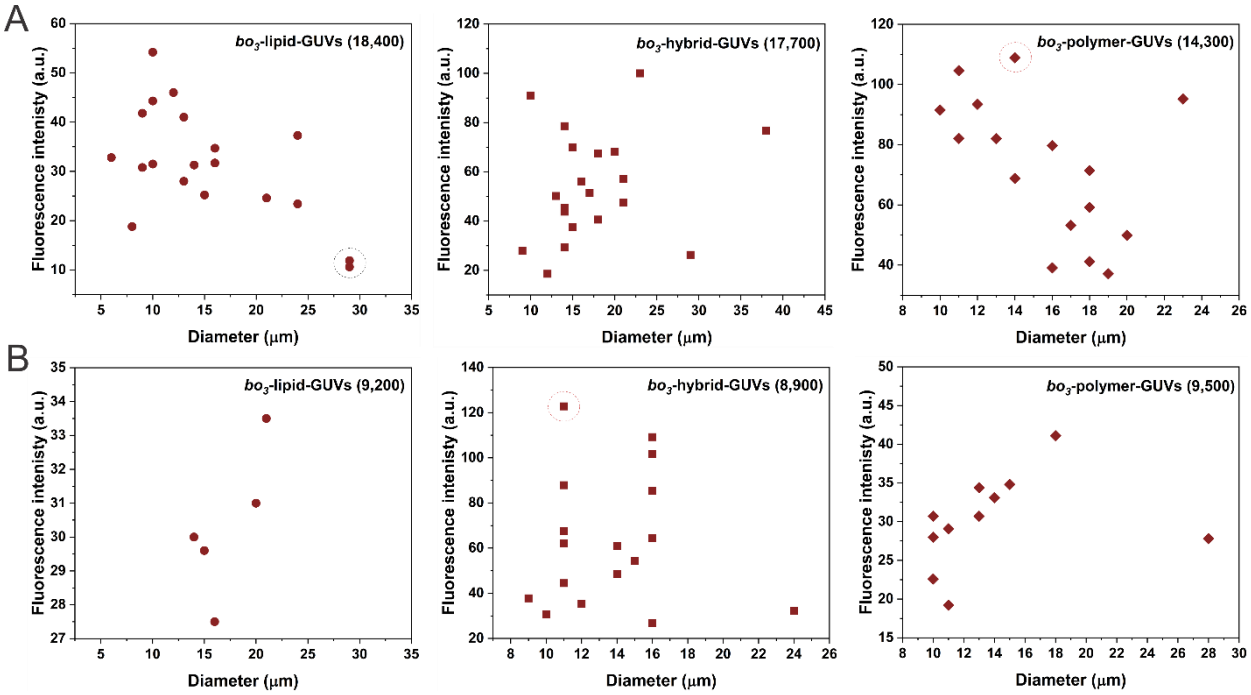

Figure 77. Membrane thickness of *bo*$_3$-GUVs. Scatter plots represent membrane fluorescence intensity (0.05 mol% PE-Rho or PDMS-*g*-PEO-Rho) of lipid, hybrid and polymer *bo*$_3$-GUV with two different polymer/lipid-to-protein molar ratios (higher (**A**) and lower (**B**)) against their diameter. *bo*$_3$-lipid-GUV with a larger diameter (29 µm) contained less membrane dye (dotted black circle). *bo*$_3$-GUV in red dotted circles likely have a larger membrane thickness.

3.4.2.2 Protein distribution and concentration

Next, we tested if higher protein densities could be achieved, while avoiding a decrease in size. For this purpose, a proportionately smaller volume of *bo*$_3$-LUVs with a high protein loading with a larger volume of protein-free LUVs (up to 1:10 v/v) was mixed. This yielded a heterogeneous population of *bo*$_3$-GUVs with diameters in the range 5–30 µm and varying protein content (Figures 78), but the membrane distribution of *bo*$_3$ oxidase in each vesicle was uniform, regardless of the mixing ratio (1:1–10, v/v). Indeed, it was observed that mixing the protein-loaded with the protein-free LUVs allowed for larger *bo*$_3$-GUVs

than the ones formed only from LUVs highly loaded with protein (Figures S62 and S63). Thus, the current protocol allows forming *bo*$_3$-GUVs with various protein densities and the ratio between protein-free LUVs and *bo*$_3$-LUVs affects the homogeneity of the final population (Figure 79). Even though this mixing approach does not fully maintain the desired protein density, the latter could be determined by calibration, if required (69, 79), and higher loadings of *bo*$_3$ oxidase could still be obtained.

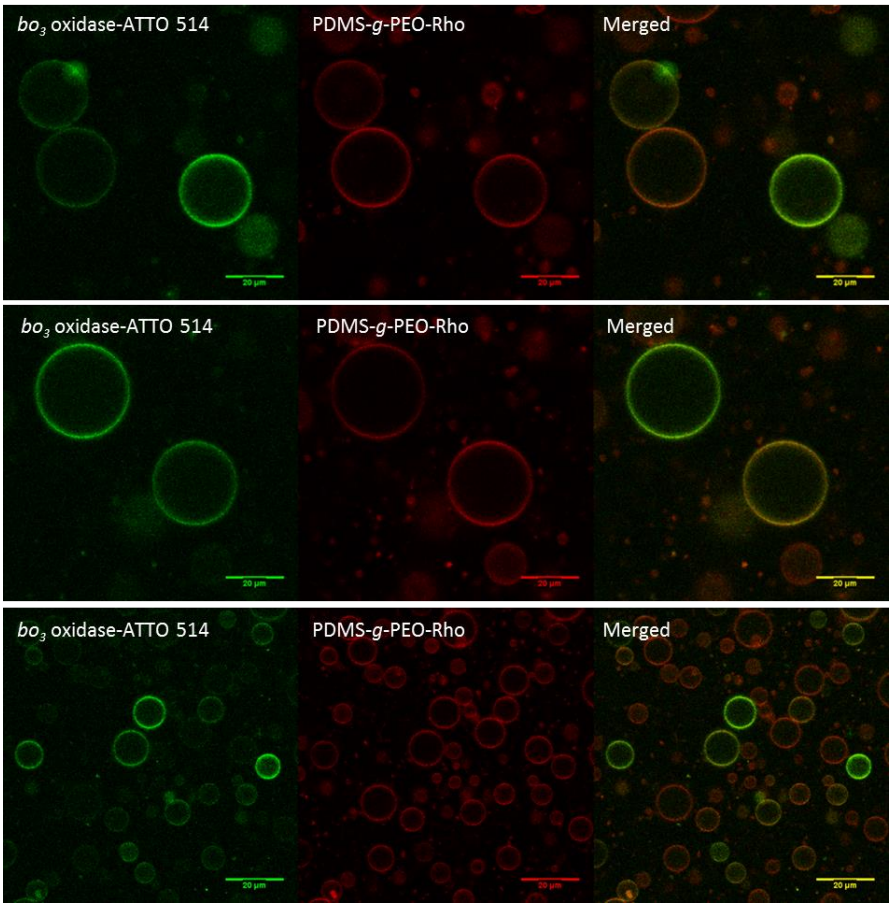

Figure 78. Micrograph of a heterogeneous population of *bo*$_3$-GUV. Heterogeneous distribution of *bo*$_3$ oxidase (green) in between polymersomes, prepared from *bo*$_3$-LUVs(0.7 μM *bo*$_3$ oxidase):LUVs = 1:10, v/v). In each GUV *bo*$_3$ oxidase is homogenously distributed within the membrane.

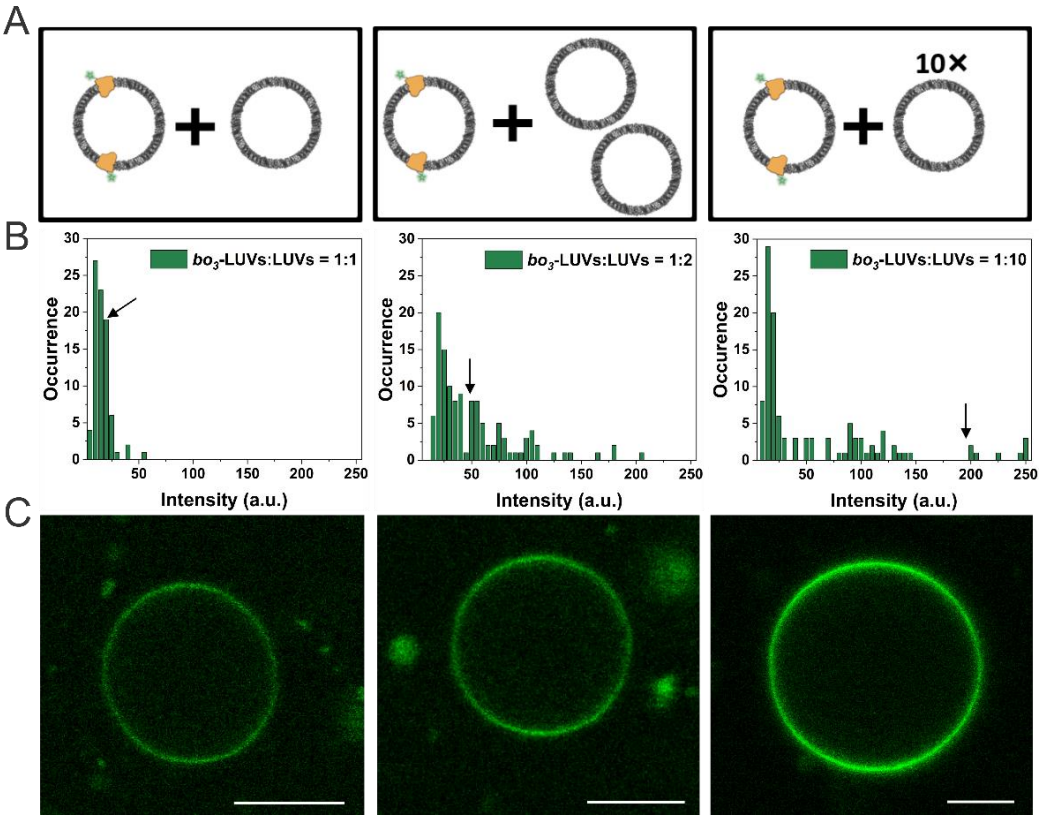

Figure 79. Protein distribution in *bo*$_3$-GUVs upon "dilution" of *bo*$_3$-LUVs with protein-free polymer LUVs in the electroformation film. (**A**) Schemes of the mixing of *bo*$_3$-LUVs and protein-free LUVs at volume ratios 1:1, 1:2 and 1:10 (all at 5 mg ml^{-1}). (**B**) Fluorescence intensity distribution of *bo*$_3$ oxidase-ATTO 514 in polymer GUVs. For *bo*$_3$-GUVs prepared from a 1:1 mixture, the protein distribution was fairly homogenous, while for 1:2 and 1:10 higher variation was observed (see Figure 78). The latter two setups also yielded portions of GUVs with relatively high protein density. Arrows indicate the intensities that correspond to *bo*$_3$-polymer-GUVs shown in the micrographs in panel (**C**); scale bar: 10 µm.

Finally, to estimate the reconstitution efficiency and the concentration of *bo*$_3$ oxidase in the GUVs' membrane, calibration with vesicles containing a labeled lipid (DOPE-ATTO 520) with similar emission/excitation spectra as ATTO 514 was performed (for details see Chapter 2.9.5). Figure 80 shows a histogram of the protein concentration in the polymer and hybrid *bo*$_3$-GUVs at two different polymer/lipid-to-protein molar ratios. The distribution was fairly broad for higher ratios (14,300 and 17,700); meanwhile, for lower ratios (9,500 and 8,900) a narrower peak was observed. While the distribution at different molar ratios was quite different, the average concentration for hybrids was nearly identical (0.0025 vs. 0.0024 mol%) and very similar for polymersomes (0.0424 vs. 0.0544 mol%). For *bo*$_3$-polymer-GUVs higher protein concentrations were obtained than theoretically expected. *bo*$_3$-polymer-GUVs formed at polymer-to-protein molar ratio of 9,500:1 and at 14,300 would have a theoretical concentration at 100 % incorporation efficiency 0.0105 and 0.0070 mol%, which is 4.0× and 7.8× lower than the experimentally determined values. It can be speculated that there was a change in protein and lipid composition during the

formation of *bo*$_3$-GUVs due to the large portion of non-detached polymer from the ITO surface. Polymer LUVs film retention was observed with naked eye (as discussed above), but only current results on protein concentration revealed that the lost material was merely the polymer and likely not the protein (or at least to much lesser extent). Meanwhile, for *bo*$_3$-hybrid-GUVs a protein concentration lower than the theoretically expected concentration was observed: *bo*$_3$-hybrid-GUVs formed at polymer/lipid-to-protein molar ratios of 8,900:1 and 17,700:1 would have theoretically concentrations at 100 % incorporation efficiency of 0.0123 and 0.0056 mol%, respectively. This is 4.9× and 2.4× higher than the experimentally determined values. The decrease of the molar ratio for proteo-hybrid-GUVs could be due to protein precipitation. While salt screening was observed for polymer membranes as a reason for a change in bending rigidity (discussed in Chapter 3.5.2) and as the edge of the polymer LUVs droplets was becoming milky during dehydration, this might not be the case to such extent for zwitterionic lipids. Longer dehydration was needed to observe milky edge on droplets containing hybrid LUVs deposited on ITO slides. Due to lipid partitioning around the protein in the hybrid membrane (demonstrated in Chapter 3.1 and in ref. (1)), the protein is not protected from dehydration (and consequently from precipitation) by the polymer salt screening, as it is the case in a pure polymer membrane. Those results make clear that one should be careful when assessing the polymer- or polymer/lipid-to-protein ratio in proteoGUVs, and have in mind that it does not directly reflect the ratio from proteoLUVs. Furthermore, the data on protein concentration revealed another protective characteristic of the PDMS-*g*-PEO – protein protection against the dehydration by salts.

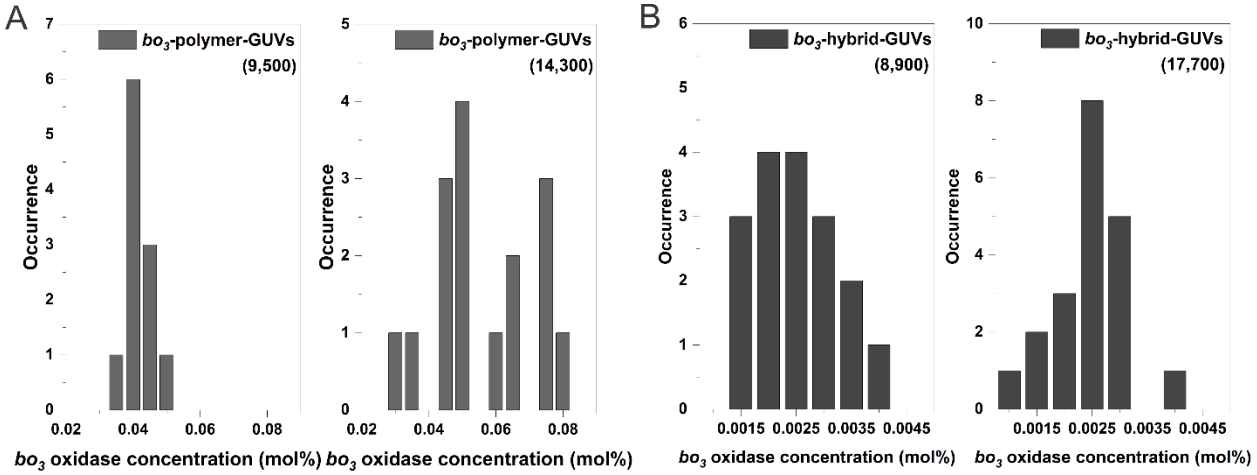

Figure 80. Histograms showing distribution of *bo*$_3$ oxidase in the membrane of GUVs. *bo*$_3$-polymer (**A**) and *bo*$_3$-hybird (**B**) GUVs were formed via fusion/electroformation using a low salt buffer (1 mM Tris-HCl (pH 7.5), 100 mM sucrose). Histograms were obtained by comparing membrane fluorescence intensity at the equator of GUVs containing labeled proton pumps with GUVs containing known concentration of labeled lipids (DOPE-ATTO 520) (for details see Chapter 2.9.5).

3.4.2.3 Population activity testing: oxygen consumption by bo_3-GUVs

The mechanism addressed in this chapter enables the growth of micro-sized membranous systems that already include membrane proteins. In this aspect, the retention of their functionality is crucial for the functional construction of artificial organelles. Therefore, *bo₃* oxidase activity retention after dehydration and electroformation was tested next. The oxygen consumption of different *bo₃*-GUVs and *bo₃*-LUVs was determined from bulk samples (population study) using a Clark-type electrode (Chapter 2.9.6.1), whereby we always applied the same amount of protein (~ 1.95 nM) in order to avoid the accumulation of errors from rescaling. For this purpose, the sample volumes to the final volume were adapted, under the assumption that no enzyme was lost during the formation of *bo₃*-GUVs from *bo₃*-LUVs. In the case of small vesicles, the initial oxygen consumption rates were 3.2 ± 0.2 µM min^{-1} for liposomes, 5.3 ± 1.1 µM min^{-1} for hybrids and 4.0 ± 0.6 µM min^{-1} for polymersomes. The reconstitution protocol for hybrid and polymer LUVs differed from the protocol for lipid LUVs (see Chapter 2.9.1.1): liposomes required higher concentrations of phospholipid and protein, which may have led to a less efficient reconstitution. This could explain the lower activity of the latter, while in the case of polymer-containing vesicles the rates were comparable (non-significant difference, *p*-value = 0.0949), as it was previously reported (21). When referred to the respective *bo₃*-LUVs, the conversion to *bo₃*-GUVs resulted in a decrease of the initial rates. We found that 82 ± 8 % of the activity was retained in liposomes, 74 ± 5 % in hybrids, and 57 ± 6 % in polymersomes after the scale-up. During the dehydration step, the hybrid and polymer *bo₃*-LUV films adhered more strongly to the ITO slides than the lipid ones and during the electroformation only lipid GUVs detached completely (polymer/hybrid residue could be seen with the naked eye). Thus, we believe that the apparent decrease of the protein activity is largely due to overestimation of the protein amount rather than due to the enzyme deactivation. Potentially, the loss during the electroformation could be reduced by decreasing the drying duration. However, insufficient drying negatively affected the GUV formation, and therefore, trying to find a compromise was unavoidable.

By correlating the increase in oxygen consumption rates with incremental volumes of the vesicle suspensions, i.e., by proportional increase of the protein amount in a constant reaction volume, the homogeneity of the protein distribution was assessed. The average oxygen consumption rates of lipid and polymer *bo₃*-GUVs increased by a factor of roughly 0.6 (see below), while the *bo₃*-hybrid-GUVs exhibited lower proportionality (Figure 81). The deviations may be attributed to the rather wide size range of formed *bo₃*-GUVs and the less homogenous distribution of *bo₃* oxidase in hybrid GUVs. The characterization of the latter membranes led to substantial scattering also with respect to other properties.

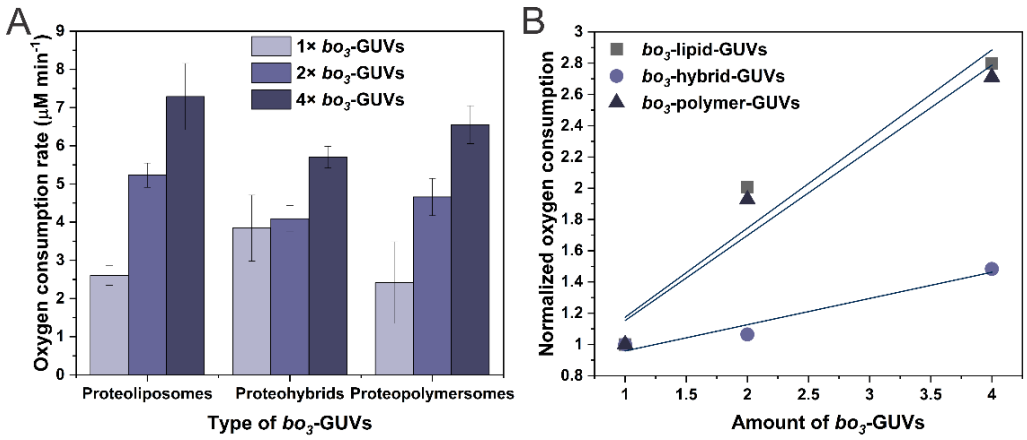

Figure 81. Homogeneity of the *bo*$_3$-GUVs suspension. (**A**) Increase of oxygen consumption with increased amount of protein (concentration of *bo*$_3$-GUVs), starting with ~ 2 nM *bo*$_3$ oxidase in the measurement chamber. (**B**) Oxygen consumption (normalized to the first aliquot) of *bo*$_3$-GUVs with increasing concentration of *bo*$_3$-GUVs in the total measurement volume. Slopes: 0.57 (R^2 > 0.93), 0.17 (R^2 > 0.96), 0.54 (R^2 > 0.94) for *bo*$_3$-lipid-GUVs, *bo*$_3$-hybrid-GUVs and *bo*$_3$-polymer-GUVs, respectively.

3.4.2.4 Single vesicle activity testing: proton pumping by bo$_3$*-GUVs*

Following the populational activity characterization of the *bo*$_3$-GUVs via oxygen consumption, the proton translocation on a single-vesicle level was probed next. Characterization of individual vesicles provides additional information, which could be overlooked and averaged in bulk tests due to vesicle rupture and size variance. Here, we were able to directly deduce the enzyme orientation by observing the net ΔpH upon chemical activation. Since it was previously shown that the orientation of a complex membrane protein such as Ca^{2+}-ATPase is retained upon the fusion/electroformation approach (71), we focused solely on the novel system, namely *bo*$_3$ oxidase reconstituted in PDMS-*g*-PEO GUVs.

Similar observations were made only for bR (71, 78) and a RC (68) in conventional observation chambers. The downside of the latter setup is that the vesicles could move out of the focus if not deliberately immobilized at the surface (which in turn can alter the membrane tension and local composition) and the external solution cannot be exchanged completely; instead, the samples are being diluted. While this effect is irrelevant for light-activated proton pumps, we preferred that oxygen and Q_1/DTT were supplied in a defined manner. For that purpose, similar microfluidic setup as in Chapter 3.1.2.3 was applied. Briefly, *bo*$_3$-GUVs were prepared in weakly buffered solution (100 mM sucrose, 1 mM Tris-HCl, pH 7.5) in the presence of 10 µM pyranine, then trapped and washed by flushing pyranine-free buffer in the microfluidic chip. Next, proton pumping was initiated by flushing in 40 µM Q_1 and 8 mM DTT (Figure 82A).

The luminal pH decreased upon activation and the established ΔpH correlated with the increasing amount of *bo*$_3$ oxidase per vesicle, while the pH in protein-free polymersomes stayed fairly constant. *bo*$_3$-GUVs

with a molar ratio of 9540:1 polymer-to-protein acidified by nearly 0.3 pH units in the first 3 min and tripling the protein content (2980:1) increased ΔpH to 0.5 in roughly the same time (Figure 82B). After that, the pH in GUVs with higher protein loading continued to decrease at a much lower rate: ~ 0.2 units over 25 min and overall ΔpH after 30 min exceeded 1 unit. The ΔpH and time scales for *bo*$_3$ oxidase in the synthetic membrane were comparable with light-induced proton pumping in lipid membranes. bR reconstituted in lipid GUVs was observed to lower the intravesicular pH by 0.8 pH units in 30 min (78), while RC was shown to cause an increase by approximately 0.8 pH units in 15 min (68). The lipid-to-protein molar ratios of reconstituted bR (2200 ± 700) and RC (2200) were slightly higher than the polymer-to-protein molar ratio (2980) used in this study. The similarity in performance is a good indicator for the viability and biocompatibility of the PDMS-*g*-PEO membranes towards complex membrane proteins.

At higher protein loading, the increased pumping rate was sustained for about 3 min and was followed by a more moderate decrease. The initial fast rate took more than a minute to fully develop, which we ascribed to partitioning of Q_1 into the membrane and diffusion to the enzyme (the latter is a rate-limiting step in the mitochondrial ETC (233)). Interestingly, the rate did not decrease progressively but very sharply. Note that the traces are averaged and the scattering is due to the size variance. However, the high protein loading data was very reproducible, therefore a changing rate could be clearly identified: 0.35 pH min^{-1} and 0.64×10^{-2} pH min^{-1}. A decrease of the pumping rate has been observed also in the case of bR-liposomes (reaching a steady-state after about 3 min (171) or 5–6 min (71) of illumination), which was ascribed to a retroinhibition by the established ΔpH (back-pressure effect) (171).

The magnitude of the pH gradient directly depends on the type and amount of reconstituted membrane proteins. While light-driven proton pumps, such as bR provide the virtue of orthogonality with respect to the energy source, chemically-driven pumps such as *bo*$_3$ oxidase have higher turnovers (300–341 s^{-1} *vs.* 37–50 s^{-1}) (274) and introduce additional means for coupling with metabolic reactions. With respect to the reconstitution of the energy machinery, the enzyme orientation in the membrane plays a pivotal role as well. The latter can be controlled by the type of detergent and the experimental conditions, but it is largely determined by the membrane. Prevailing inward orientation of *bo*$_3$ oxidase was previously deduced in DOPC SUVs (172) and later on in PDMS-*g*-PEO LUVs (21) from the respiratory-driven ATP synthesis (possible only with favorable gradient direction). Here, we confirmed the utility of the reconstitution method and the synthetic membrane, alongside the scale-up procedure through direct visual observation of the pH change. In addition, it can be anticipated that an even higher ΔpH could be established at the interface, where protons might accumulate before diffusing into the vesicle lumen. This has been postulated in phospholipid membranes at distances between *bo*$_3$ oxidase and F_1F_O-ATPase shorter than 80 nm, in which the lateral proton transfer along the surface was faster than the equilibration with the bulk water (79).

With respect to the synthetic interface, *bo*$_3$ oxidase has been previously reconstituted in PBd-*b*-PEO but the protein was functional only in combination with POPC, i.e., in hybrid LUVs (64). The latter showed increased durability, but the random (symmetrical) orientation resulted in subtle pH changes (no data shown). The activity in the present study substantiates the choice of the graft copolymer for *bo*$_3$ oxidase and provides the potential to extend this synthetic platform to other complex membrane proteins, beyond the ones comprising ETC.

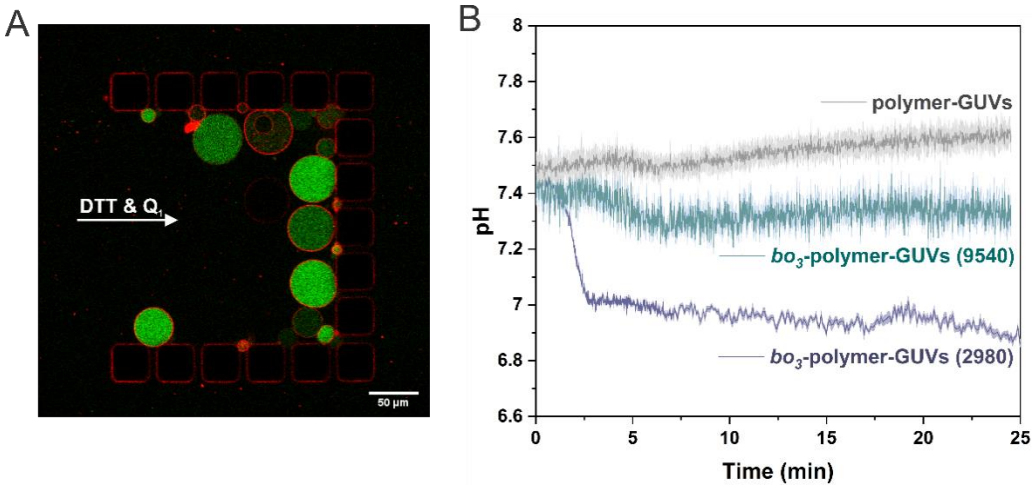

Figure 82. Proton pumping by *bo*$_3$ oxidase reconstituted in polymer GUVs. (**A**) *bo*$_3$-polymer-GUVs (PDMS-*g*-PEO:*bo*$_3$ oxidase = 2980:1 mol/mol) with encapsulated pH-sensitive pyranine (green) trapped in microfluidic chip. Membrane was stained with 0.05 mol% PDMS-*g*-PEO-Rho (red). Scale bar: 50 µm. (**B**) Intravesicular pH change for negative control (protein-free vesicles; gray trace), and two types of GUVs with different polymer-to-protein molar ratios; 2980:1 (purple trace) and 9540:1 (green trace) upon activation with DTT/Q_1 reached *bo*$_3$-polymer-GUVs trapped in the microfluidic chip. Each trace represents the mean of 5–7 individual vesicles and their SD.

3.4.3 Model reconstitution of highly asymmetric membrane proteins

3.4.3.1 Single vesicle activity test in microscopy chamber: proton pumping by F_1F_O-ATPase

In Chapter 3.4.2 it was demonstrated that optimized fusion/electroformation approach can be applied to hybrid and polymer membranous nanosystems with inserted largely hydrophobic membrane proteins, in order to grow protein-functionalized microcompartments. In this chapter, a different type of membrane protein, a highly asymmetric F_1F_O-ATPase, was tested for its compatibility with the above mentioned growth approach. F_1F_O-ATPases does not only have different shape than *bo*$_3$ oxidase, but is also larger in size (750 kDa vs. 144 kDa) and sensitive to temperature (drastic loss in activity was observed at room temperature).

Utilizing protocol optimized for PDMS-*g*-PEO and PDMS-*g*-PEO:soy PC membranes, polymer and hybrid microcompartments with inserted F_1F_O-ATPase (F_1F_O-GUVs) were successfully grown. Protein insertion

was confirmed with confocal microscopy of fluorescently labeled F_1F_O-ATPase (F_1F_O-ATPase-ATTO 620) (Figure S67 and S68). Activity of F_1F_O-ATPase reconstituted in hybrid GUVs was tested via proton pumping by F_1F_O-ATPase induced by potassium gradient, as was previously done for F_1F_O-lipid-GUVs (76). A change of the intravesicular pH level was monitored via fluorescence of encapsulated pyranine, as described above (see Chapter 3.1.2.3 and 3.4.2.4). F_1F_O-ATPase was activated with an electrochemical gradient established by the higher concentration of the outer K^+ ($[K^+]$in = 1 mM, $[K^+]$out = 20 mM) in the presence of the K^+ ionophore valnomycin (Figure 83A). Initial experiments were performed in microscopy chamber by diluting 1:4 (v/v) F_1F_O-GUVs into a buffer containing higher concentrations of K^+, ADP and Pi. The optimal concentration of valinomycin, to avoid an increasing membrane permeability and to transport enough K^+ in the GUVs interior to activate F_1F_O-ATPases, had to be determined. With valinomycin in concentration above 10 µM, the membrane of F_1F_O-GUVs appeared permeable for pyranine (change in intravesicular pyranine concentration was observed), while for concentrations below 10 µM no intravesicular pH change was observed, which likely indicated a limiting K^+ transfer rate. At 10 µM valnomycin, pH increase in F_1F_O-GUVs was observed, but the vesicles could be monitored only until they went out of focus. Furthermore, the outer solution was not exchanged completely, therefore the pumping rate was limited by the diffusion of K^+, ADP and Pi. Nevertheless, a substantial change of the intravesicular pyranine fluorescence was observed (Figure 83B). The pH change was determined from the intensity ratio vs. the pH standard curves for intravesicular pyranine (Figure 15). PEO groups on PDMS-*g*-PEO have a high capacity to bind water; this affects the water activity and introduces artifacts into the pyranine pH-dependence determination (277). To take the influence of the polymer (different amount of PEO groups changes pyranine p*Ka* differently) into account, a standard curve was recorded with GUVs (and not buffer alone). Upon activation of F_1F_O-ATPases the maximum observed pH difference was ΔpH = 1.5 pH units (from pH ~ 8.0 to ~ 9.5) and the minimum observed was ΔpH = 0.5 pH units (from pH ~ 9.0 to ~ 9.5). In a similar study, where F_1F_O-ATPase was reconstituted in lipid GUVs, the average increase of fluorescence corresponded to a ΔpH of 1.5 to 2 units (76).

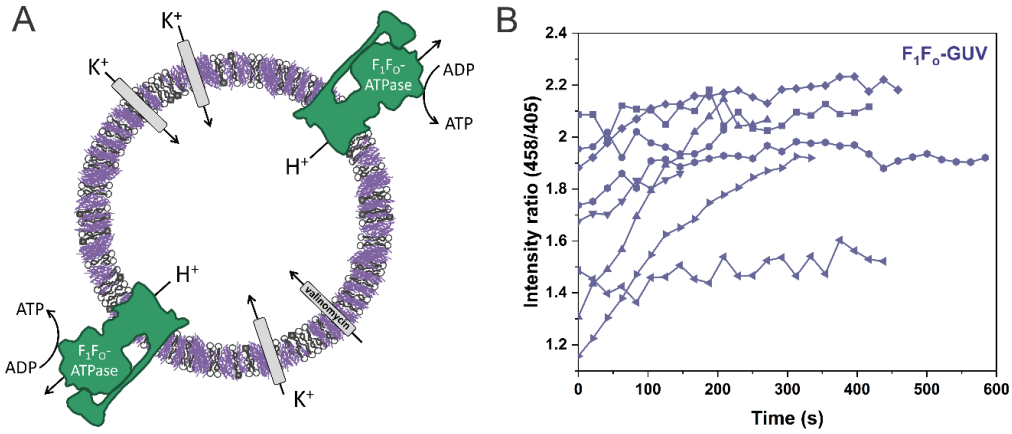

Figure 83. Monitoring intravesicular pyranine fluorescence in a microscopy chamber. (**A**) Scheme of F_1F_O-ATPase reconstituted in hybrid GUVs upon activation by a K^+ gradient. GUVs were prior to activation incubated with the K^+ ionophore valinomycin. (**B**) Change in intravesicular fluorescence intensity ratio of F_1F_O-valinomycin-hybrid-GUVs.

3.4.3.2 Single vesicle activity test in microfluidic chip: proton pumping by F_1F_O-ATPase

To reduce GUVs movement and completely exchange the outer solution, the experiment from Chapter 3.4.3.1 was repeated in a microfluidic setup. F_1F_O-GUVs, prepared in the inner buffer (1 mM Tris-HCl (pH 7.5), 1 mM KCl, 200 mM sucrose) supplemented with 10 µM pyranine, were trapped in a microfluidic device (Figure 84A). Next, non-encapsulated pyranine was washed away, and finally F_1F_O-ATPases were activated by flushing with the outer buffer containing a higher concentration of K^+ (1 mM Tris-KOH (pH 7.5), 20 mM H_3PO_4, 50/20 mM KCl, 600 µM ADP, sucrose). The increase in intravesicular pH upon activation of F_1F_O-ATPases was monitored via pyranine fluorescence. As a control, the same experiment was repeated with protein-free GUV.

Intravesicular pH substantially increased after flushing F_1F_O-GUVs with an outer buffer containing a higher K^+ concentration ($\Delta[K^+]$ = 49 mM) (Figure S74). But the apparent pH increased above the linear range for pyranine, and therefore the experiment was next repeated by applying a lower potassium gradient ($\Delta[K^+]$ = 19 mM). The intravesicular pH level again appeared to rapidly increase, reaching a plateau at pH ≈ 8.4 (Figure 84B), which likely indicated the time when the potassium concentration inside and outside of GUVs were equilibrated. Surprisingly, the intravesicular pH increased also for protein-free GUVs (Figure 84C). This results indicate that to a certain extent a false positive pH change was likely observed for F_1F_O-GUVs. Surprisingly, the artifact in pyranine fluorescence due to the K^+ concentration appear to occur only under constant replenishment of K^+ (in microfluidics), but not when only diluting GUVs in a microscopy chamber (76); therefore, in some studies a control with valinomycin but without H^+-pumping membrane protein is left out (78). Nevertheless, it seems that pyranine behaves differently in the presence and absence of

potassium ions and responds to a change of the K^+ concentration. The latter phenomenon was further investigated in the following chapter.

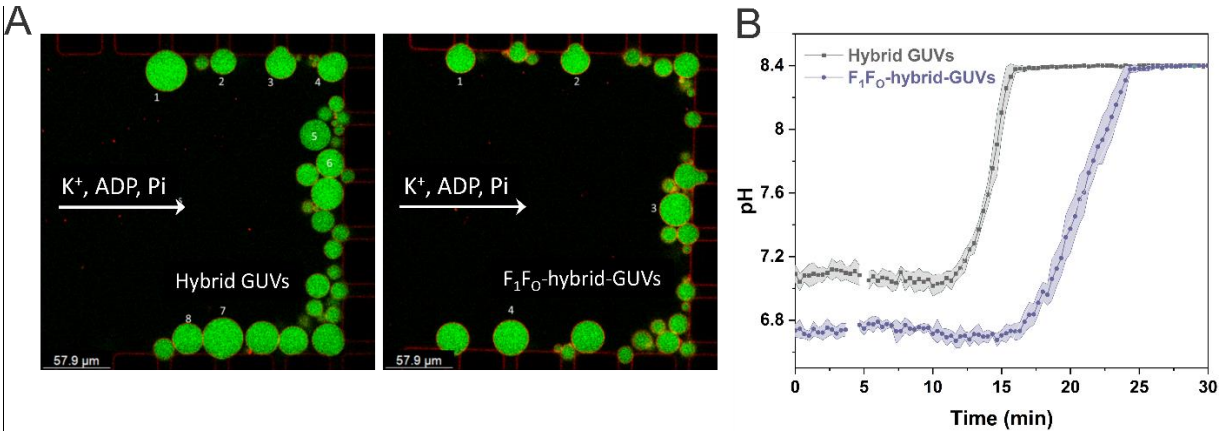

Figure 84. **Monitoring intravesicular pyranine fluorescence in microfluidic traps.** (**A**) Micrograph of evaluated (F_1F_O-)GUVs, with encapsulated pyranine, trapped in a microfluidic device. The membrane was doped with 0.05 mol% PDMS-*g*-PEO-Rho. (**B**) Assuming a change of the intravesicular pH after flushing with a buffer supplemented with K^+ and ADP. pH was calculated from the intensity ratio from the standard curve in Figure 15. According to the pyranine dependence on the K^+ concentration (Figure 85), we observed an increase of the intravesicular K^+ concentration or a combination of increased K^+ and decreased H^+ concentrations, but not just a decreasing H^+ concentration (i.e., a changeof the pH).

3.4.3.3 Pyranine fluorescence artifacts caused by potassium ions

To study the effect of potassium on pyranine fluorescence, its dependence on the KCl concentration was tested in bulk in the absence of vesicles. The ratio of fluorescence intensities significantly increased with increasing KCl concentration (Figure 85), which confirmed that the apparent change of pH for protein-free GUVs (Figure 84B) was indeed not due to a change of the proton concentration, but instead due to the entering of potassium ions through valinomycin into the GUVs lumen.

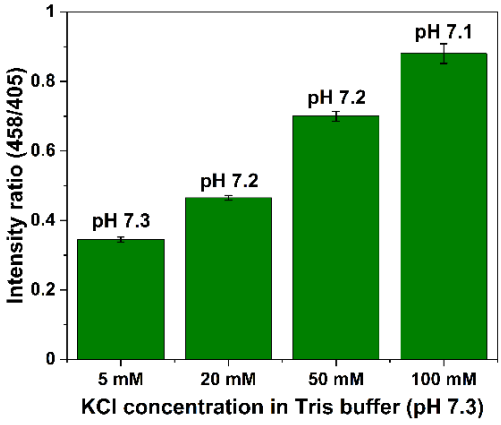

Figure 85. Change in fluorescence intensity ratio of pyranine as a function of KCl concentration. Pyranine was added to the buffer (1 mM Tris-HCl, pH 7.3) at a final concentration of 10 µM. the pyranine fluorescence intensity

ratio increased with increasing concentration of KCl at almost constant pH (pH slightly decreases). pH values given above the bars were measured with a pH meter.

The pK_a of pyranine is reported to be approximately 7.3, but several studies have shown that this value varies with medium composition (277-279). Here, the influence of KCl on the pK_a of pyranine was investigated. In presence of KCl, the pK_a was shifted downward to lower values; therefore, the calculated pH shifted upward relative to the actual pH (as determined by a pH meter) (Figure 86A). A similar shift was previously observed for NaCl and $CaCl_2$, and the authors concluded that the shift is a consequence of both the type and the concentration of anions and cations that form the salt (278). This shift explains the increase in the fluorescence intensity ratio of pyranine upon K^+ entering the GUVs lumen (Figure 84B). Furthermore, salts are not the only species that affect the pK_a of pyranine. It was previously observed that PEO induced an effect opposite to that of the salt (i.e., an upward pK_a shift) (277), which is expressed as pH being more acidic than that measured by a pH meter. The hybrid membrane is composed of 70 mol% of PDMS-*g*-PEO and therefore, the vesicles might have an impact on pyranine pK_a value. To see to what extent the fluorescence intensity of pyranine changes in presence of PDMS-*g*-PEO, fluorescence of pyranine was measured in the presence of different concentrations of hybrid LUVs. As predicted, a pK_a shift upward was observed (Figure 86B). Nevertheless, the tested hybrid LUVs concentration was much higher than of the hybrid GUVs utilized in Chapter 3.4.3.2 (~ 0.23 mM), and therefore, the effect of PEO can be neglected in case of GUVs. To ensure reproducibility, a curve for 20 mM hybrids was repeated with new set of samples and demonstrated very low deviation (Figure S75). The shift of the pyranine pK_a value can be explained by the change in structure of water by both ions and PEO, and water interaction with pyranine, thereby changing pyranine's apparent pK_a value (277).

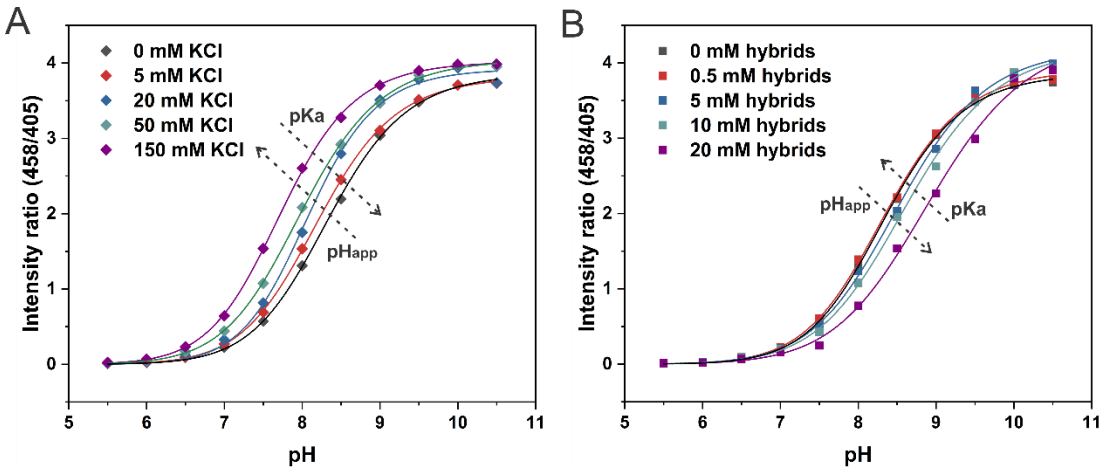

Figure 86. Plot of the fluorescence intensities ratios of pyranine as a function of pH. (**A**) Change in fluorescence intensities ratios of pyranine at five different KCl concentrations (0–150 mM) or (**B**) in the presence of five concentrations of hybrid LUVs (0–20 mM) as a function of pH (5.5–10.5). The fluorescence intensity ratio was measured by use of a fluorescence spectrophotometer. The curves were fitted to the Langmuir EXT1 equation using

Origin. The apparent pH (pH_{app}) increased with the concentration of KCl and decreased with the concentration of hybrid LUVs in comparison to the pH determined with the pH meter.

The data in Figure 86 shows that at a fixed pH, the I_{458}/I_{405} ratio is elevated by salt and decreased by PDMS-*g*-PEO:soy PC LUVs in a concentration-dependent manner. This result confirms that pyranine is subjected to medium composition-induced changes, and a correction of the fluorescence measured pH values should be applied (279). Nevertheless, the correction is more difficult when media composition ($\Delta[K^+]$) is dynamically changing during the experiment, as for example during monitoring of proton pumping by the F_1F_O-ATPsynthase (current study and (76)) or by bR (78)). Other pH-sensitive probes should be tested in order to avoid fluorescence artifacts caused by salts, but this is out of the scope of this work. Successful growth and activity of microcompartments functionalized with largely asymmetric membrane protein was rather tested via coupled activity tests, as discussed in Chapter 3.4.4.4.

3.4.4 Growth of proteoGUVs with two types of membrane proteins

3.4.4.1 Mixing as a strategy for bypassing co-reconstitution in LUVs

In relation to the mixing approach discussed in the Chapter 3.4.2.2, hybrid and polymer GUVs containing *bo₃* oxidase and F_1F_O-ATPase were formed in two ways: from LUVs with separately reconstituted enzymes (approach I) and from LUVs with co-reconstituted enzymes (approach II) (Figure 87). Different membrane proteins require different protocols in order to achieve an optimal reconstitution efficiency and orientation, and it is therefore often difficult to find the best conditions for simultaneous co-reconstitution. For instance, we previously screened various detergents (and concentrations) and found that sodium cholate was optimal for *bo₃* oxidase in polymer LUVs at partial solubilization, while octyl glucoside at saturation gave better results for F_1F_O-ATPase (21). In this respect, approach I allows the definition of optimal protocols for the individual membrane proteins. Using both approaches, a labeled proton pump (*bo₃* oxidase-ATTO 514) and a labeled proton consumer (F_1F_O-ATPase-ATTO 620) were successfully co-reconstituted in polymer and hybrid GUVs, as well as in soy PC that served as a benchmark, and the protein distribution by confocal microscopy was assessed (see Figures 89 and 90 in Chapters 3.4.4.2 and 3.4.4.3, respectively). Interestingly, a relatively low difference in protein insertion between the two approaches was observed. For instance, in polymer proteoGUVs formed by approach II (at polymer-to-*bo₃* oxidase-to-F_1F_O-ATPase molar ratio of 8,900:1:1) the average fluorescence intensity of *bo₃* oxidase-ATTO 514 was 10.6 ± 2.8 (a.u.) and of F_1F_O-ATPase-ATTO 620 was 10.5 ± 2.7 (n = 27). Meanwhile, approach I led to similar intensities for the proton pump (11.3 ± 1.9) and higher ones for the ATPase (15.3 ± 3.7) (n = 27), while both ways enabled a homogenous protein distribution in the polymer GUVs. Note that only the signal of either dye between the two approaches under identical imaging parameters was compared.

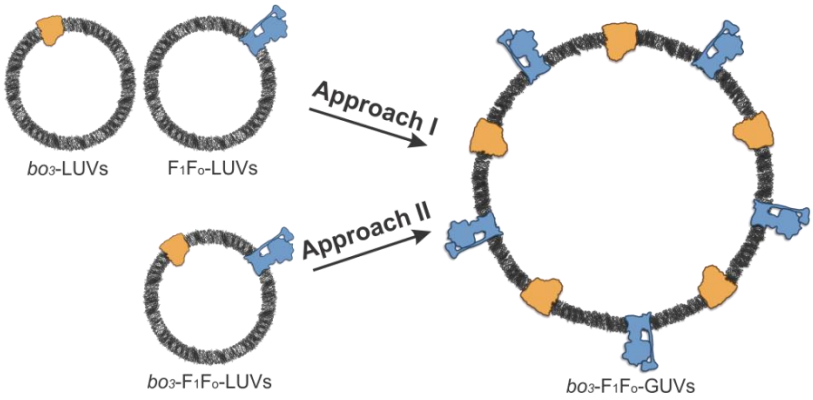

Figure 87. Scheme of the two approaches explored for growth of proteoGUVs with two types of membrane proteins. Approach I is based on the mixing LUVs with separately reconstituted *bo*$_3$ oxidase (*bo*$_3$) and ATP synthase (F_1F_O), while approach II uses LUVs with two co-reconstituted enzymes (*bo*$_3$-F_1F_O).

Overwhelmingly more reconstitution protocols are available for the reconstitution of membrane proteins into lipids – after all, the membrane proteins have evolved together with the natural amphiphiles towards optimal integration and activity. Therefore, another variation of approach I was also tested in order to increase the reconstitution efficiency of F_1F_O-ATPase in hybrid GUVs, because the latter enzyme was apparently more sensitive to the environment, as evidenced by the lower ATP synthesis rates in hybrids (21). Towards this end, protein-free polymersomes containing 0.1 mol% PDMS-*g*-PEO-FITC and protein-free liposomes containing 0.05 mol% PE-Rho were first mixed to probe whether hybrid membranes could be obtained (Figure 88A). These LUVs (both at 5 mg ml^{-1}) were combined in such volumes to achieve a final polymer-to-lipid molar ratio of 70:30, corresponding to the rest of the experiments in this study. Thereby, the LUV mixture was subjected to longer dehydration (~ 90 min) than either polymer or hybrid LUVs, in line with the necessary conditions for pure soy PC discussed above. However, the pronounced background signal from non-fused lipid LUVs (Figure S76) indicated that this dehydration was yet not sufficient and suggested that the final GUV composition comprised less lipid than intended. Nevertheless, relatively high GUV yield with colocalized lipid and polymer dyes was obtained (Figure 88B). Whereas further optimization of the dehydration duration may resolve this issue, in the following experiments we resorted to pre-formed hybrid membranes in order to maintain the desired membrane composition and limit the uncertainty.

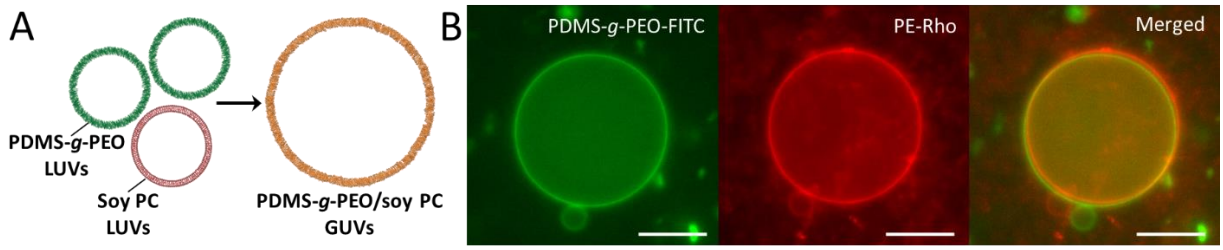

Figure 88. Protein-free hybrid GUVs. (**A**) Scheme showing polymer (green) and lipid (red) LUVs, and hybrid (orange) GUVs formed from those LUVs. Well-mixed lipid and polymer LUVs were fused by dehydration to form a hybrid film, from which hybrid GUVs were grown via electroformation. To obtain homogeneous distribution of polymer and lipid in GUVs membranes, > 60 mol% of PDMS-*g*-PEO was used. (**B**) Epifluorescence images of hybrid GUV formed from mixture of PDMS-*g*-PEO LUVs (100 nm) and soy PC LUVs (100 nm), mixed in molar ratio 70:30. Lipid LUVs contained 0.05 mol% PE-Rhodamine (red) and polymer LUVs contained 0.1 mol% PDMS-*g*-PEO-FITC (green). Lipid and polymer dye were homogeneously distributed in the membrane. The misalignment in merged images derives from GUV movement (GUVs were not fixed to the surface). Scale bar: 10 µm.

3.4.4.2 Lower co-reconstitution in polymersomes

Reconstitution of *bo*$_3$ oxidase alone in polymer GUVs resulted in comparatively high insertion as evident by the strong fluorescence from the labeled protein. Meanwhile, when *bo*$_3$ oxidase was co-reconstituted with F_1F_O-ATPase, the average ATTO 514 signal decreased from 46.6 ± 5.0 (n = 16) to 10.6 ± 2.8 (n = 27) (Figures S77 and S78). Furthermore, higher intensities from both labeled enzymes were detected in lipid GUVs under the same imaging parameters (Figure 89, lower panel). These results are in agreement with the decrease of the reconstitution efficiency from liposomes to polymersomes, suggested by the decreasing ATP synthesis rates (21). Interestingly, ATPase appears to prevent the insertion of *bo*$_3$ oxidase too, which is otherwise virtually unaffected by the type of the amphiphile.

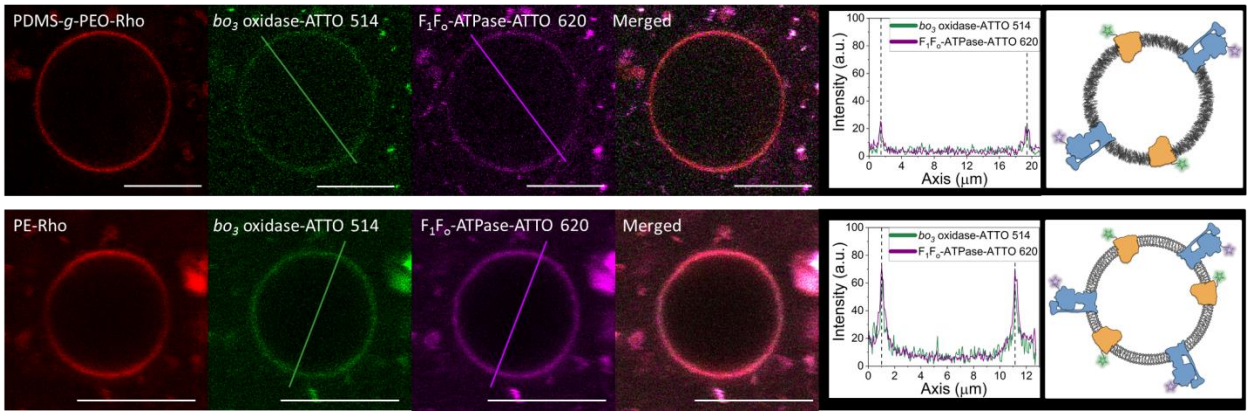

Figure 89. Representative images of respiratory-functionalized polymer (upper panel) and lipid (lower panel) GUVs. *bo*$_3$ oxidase-ATTO 514 (green) and F_1F_O-ATPase-ATTO 620 (magenta) were co-reconstituted in LUVs and *bo*$_3$-F_1F_O-GUVs were prepared by fusion/electroformation. Membrane was tagged with labeled polymer (PDMS-*g*-PEO-Rho) or lipid (PE-Rho) (red). The position of the membrane is indicated by dotted lines in the respective line profiles. The schemes reflect the higher amount of both proteins in lipid GUVs compared to polymer GUVs, but are not to actual scale. Scale bar: 10 µm.

3.4.4.3 Labeled membrane proteins and hybrid membrane remodeling

The majority of the hybrid proteoGUVs were optically homogeneous and both enzymes were uniformly distributed in the membrane (Figure 90, upper panel). However, in most of the larger vesicles (> 20 µm) separation to lipid and polymer-rich phases over the course of ~ 4 days was observed, whereby *bo*$_3$ oxidase and F_1F_O-ATPase preferentially partitioned in the lipid domains (Figure 90, lower panel and S73). No phase separation was optically detected in protein-free hybrids and neither in proteoGUVs containing individual enzymes (typical hybrid *bo*$_3$-GUV in Figure S80 and F_1F_O-GUVs in Figure S81). Therefore, we probed for the cooperative influence of the proteins and their tags since ATTO 514 bears a negative charge and ATTO 620 is positive. Interchangeable use of labeled enzymes (either *bo*$_3$ oxidase or F_1F_O-ATPase), while the other one was kept native, resulted in optically homogeneous proteoGUVs only. Therefore, the phase separation was ascribed to the respective protein dyes. Fluorescence labeling is known to modify the overall protein charge and the associated interactions, as demonstrated in surface adsorption and cell binding studies (280, 281). In parallel, we previously observed by fluorescence resonance energy transfer (FRET) that *bo*$_3$ oxidase induced local changes of the hybrid membrane composition and sequestered lipids in its vicinity (1). Thus, it appears that in some cases the cumulative electrostatic attraction between labeled proteins, which in turn caused membrane rearrangement and hauled lipids along, sufficed to overcome the critical line tension for macroscopic phase separation. A related phenomenon in the inverse direction was previously shown for peripheral proteins, whose equivalent charges resided on their side faces, and the resulting repulsion considerably diminished the propensity for demixing (282). These observations show in fact that the interplay of lipid- and protein-mediated formation of functional domains (283) can be mimicked in synthetic systems. Furthermore, the particular superstructural organization of the proton pump and the proton consumer may be exploited in the future for modulating the length of the proton diffusion pathway (and thus the activity) as protons have been suggested to traverse along the membrane (195). Furthermore, the local accumulation of proteins could mitigate the limited reconstitution efficiency of certain membrane proteins and potentially facilitate complexation with other respiratory enzymes.

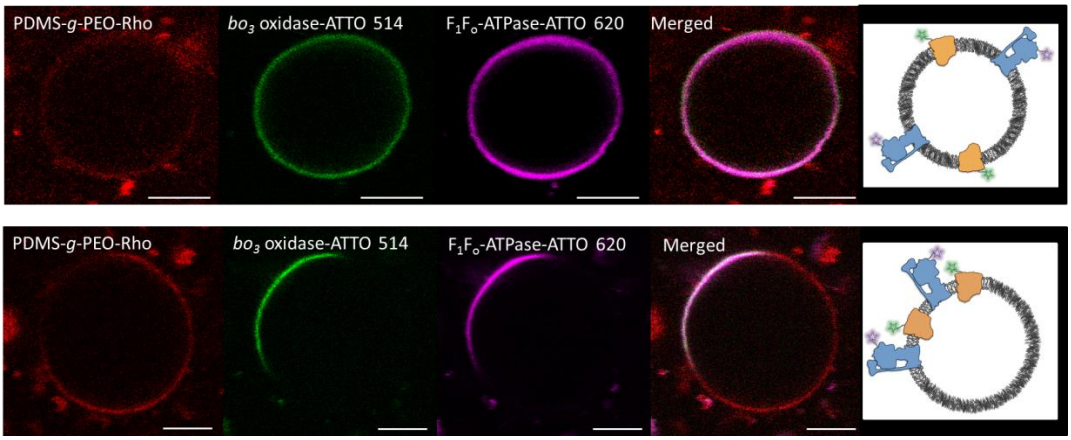

Figure 90. Representative images of respiratory-functionalized hybrid GUVs with homogeneous (upper panel) and heterogeneous (lower panel) distribution of proteins. Color codes correspond to Figure 89. The schemes show the phase separation and formation of functional protein domains. Scale bar: 5 µm.

3.4.4.4 Activity of hybrid proteoGUV with coupled membrane proteins

Hybrid polymer/lipid vesicles integrate the advantages of synthetic and natural materials (4) and may exhibit emergent properties as discussed above. In particular, integration of *bo₃* oxidase in PDMS-*g*-PEO:soy PC LUVs led to a higher functional stability and lower proton permeability, compared to both pure polymers and lipids (Chapter 3.1.2.1 and 3.1.2.3). Furthermore, the hybrid interface secured near-natural membrane fluidity as a prerequisite for unhindered activity (Chapter 3.1.1.2), next to lateral *bo₃* oxidase mobility within the diffusion coefficients of smaller membrane proteins in lipid membranes (1.8–10.5 $\mu m^2\ s^{-1}$). Here, the diffusion of F_1F_O-ATPase was assessed by FRAP and the mobility of the rotary engine in the hybrid membrane was confirmed by showing similar diffusion ($5.9 \pm 0.9\ \mu m^2\ s^{-1}$) to the proton pump ($6.9 \pm 1.7\ \mu m^2\ s^{-1}$) (Figure S82). These diffusion coefficients in the hybrid membrane corresponded to the ones observed in DOPC (~ $6\ \mu m^2\ s^{-1}$) upon ATTO labeling (79).

The dehydration step at room temperature can have a deleterious effect on membrane proteins (71). While we confirmed that this was not the case for *bo₃* oxidase (Chapter 3.4.2.3 and 3.4.2.4), here, we tested the activity of F_1F_O-ATPase upon its coupling with the proton pump in hybrid GUVs. In parallel, we probed whether the favorable protein orientation in LUVs (21) (*bo₃* oxidase pumping inwards and the hydrophilic F_1 facing outwards) was retained after the fusion/electroformation. Thereby, ATP was monitored via the luciferin/luciferase assay (Figure 91A) and non-labeled proteins were used to avoid phase separation. Hybrid proteoGUVs containing said respiratory enzymes were prepared via approaches I and II and in both cases ATP synthesis was successfully detected.

Starting with a molar ratio of mixed amphiphiles to proteins of 8,900, an anomalous decreasing of ATP production rates was observed upon doubling the overall protein loading, while the ratio (2:1) between *bo₃*

oxidase and F_1F_O-ATPase was kept constant (Figure S83). Furthermore, a twice as high proton pump density (4:1) also led to a lower activity. Therefore, it was assumed that the unexpected inverse correlation was due to the higher oxygen consumption by terminal oxidases. Thus, in absence of replenishment, oxygen was depleted in the system, which lowered the driving force for synthesis of ATP and in parallel, might have affected the luciferase assay (Figure 91B). This was also confirmed by the fact that short and mild vortex pulses temporarily restored the rates in all tested samples (Figure 91C). In order to decrease the oxygen consumption, the amphiphile proportion was increased to 17,700, which now lowered the activity approximately twice, corresponding to the doubly reduced protein loading (Figure 91D). It should be noted that these rates were normalized to the volume, whereas the exact concentration of the GUV suspensions could not be controlled. Nevertheless, we do not anticipate large variations of the latter as in all cases the same protocol was carefully followed, while the superimposition of the protein and oxygen effects provides a plausible explanation of the peak rate at intermediate enzyme loading. Notably, at identical protein densities higher rates were achieved when proteoGUVs were prepared via approach I (Figure 91D). We believe that this outcome upholds our initial intention to make use of tailored reconstitution protocols in separate LUVs and secure high reconstitution and favorable orientation.

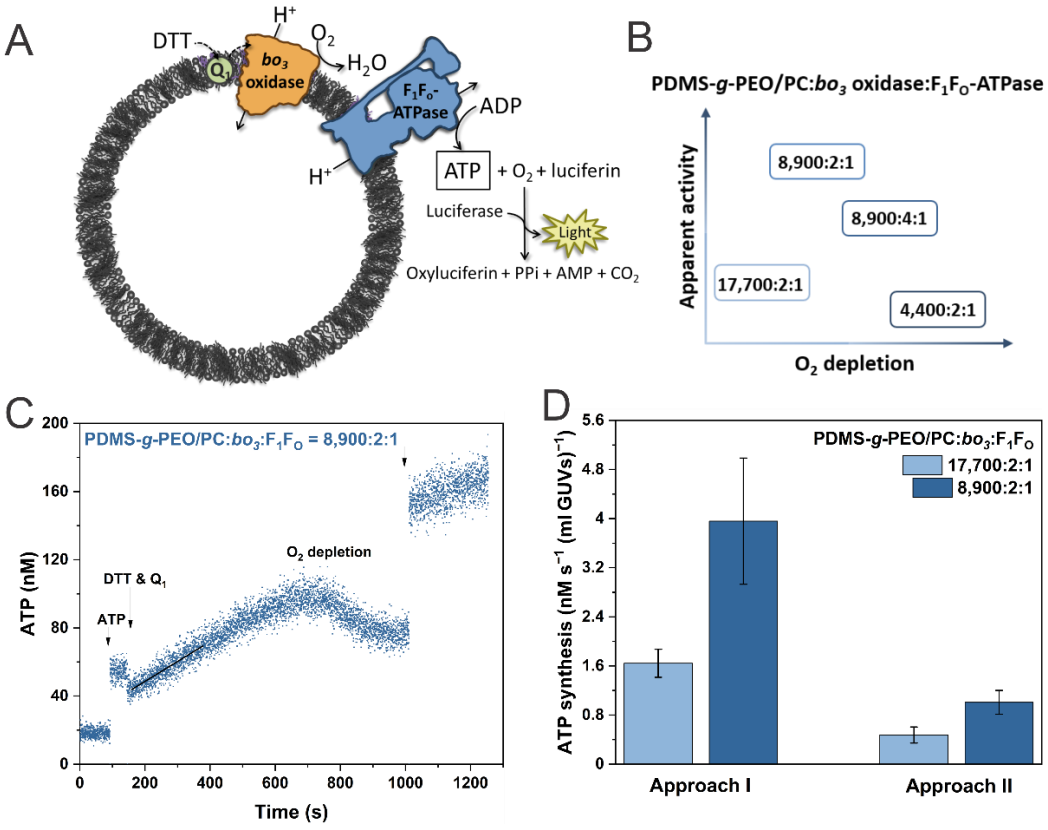

Figure 91. Activity of grown *bo*$_3$-F_1F_O-hybrid-GUV (respiratory-driven ATP synthesis). (**A**) Scheme of the functional coupling of enzymes via pH gradient and the ATP detection via luciferin/luciferase. (**B**) Change in the ATP

synthesis rate at four molar ratios of amphiphile-to-*bo*$_3$ oxidase-to-F_1F_O-ATPase. GUVs were prepared by approach I. **(C)** Typical ATP measurement in respiratory-functionalized hybrid GUVs: ATP standard added for internal calibration; proton pumping activated by DTT and Q_1; arrows indicate additions and vortexing. (**D**) Comparison of ATP synthesis rates via approach I and II at two amphiphile-to-protein molar ratios.

We also attempted to assess the ATP synthesis rates in phase-separated hybrid GUVs in line with the above hypothesis for enhanced performance due to enzyme proximity as a form of substrate channeling. However, preliminary evaluation of labeled *bo*$_3$ oxidase and ATPase in LUVs (i.e., before the electroformation) showed about 43 % decrease of the activity (Figure 92), compared to unlabeled membrane proteins, and therefore we did not proceed to GUV experiments. The ATTO dyes may affect the intrinsic activity of the enzymes, the reconstitution efficiency, and the orientation, alongside the subsequent electroformation. Once the negative effect of the dyes has been mitigated and the respective protein insertion has been optimized, the developed strategy for artificially formed functional domains can be explored further.

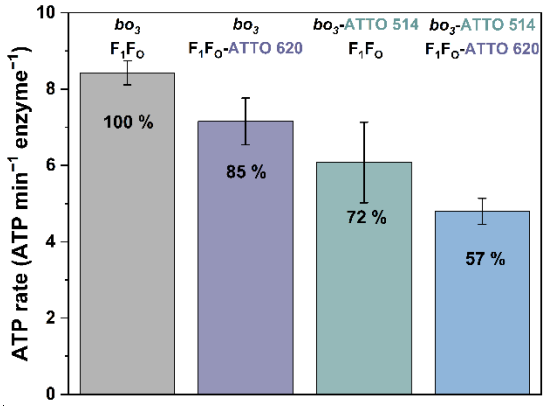

Figure 92. Respiratory-driven ATP synthesis rate in hybrid LUVs in dependence to protein label. Fluorescently labeled (with ATTO dye) or non-labeled *bo*$_3$ oxidase and F_1F_O-ATPase were co-reconstituted in ~ 100 nm hybrids. Only 57 % activity was retained when both proteins were ATTO-labeled. Since no decrease in oxygen consumption was observed by *bo*$_3$ oxidase-ATTO 514 reconstituted alone, decrease in activity in co-reconstituted system is assumable due to non-preferred orientation of the labeled proton pump.

A main drawback of bulk measurements in the luminometer is that the activity of *bo*$_3$-F_1F_O-GUVs with diameter varying from 1–40 µm is averaged out. To be able to monitor ATP synthesis by single *bo*$_3$-F_1F_O-GUV, an alternative setup in the microscopy chamber was tested next. Here, ATP was monitored via luciferin fluorescence, similar as was previously done for ATP release in pancreatic acini (284). An ATP standard curve (Figure 93A) was obtained by adding different amounts of ATP to a buffer (20 mM Tris-HCl (pH 7.5), 20 mM H_3PO4, ~ 114 mM glucose, 0.4 mM ADP) containing HSII reagent. The *bo*$_3$ oxidase embedded in the membrane of GUVs was activated with DTT and Q_1. Initially, the reaction was initiated by addition of DTT, while Q_1 was already present. But since DTT seemed to have an effect on luciferin fluorescence, the order was next changed – the sample was incubated first with DTT and afterwards Q_1 was added. Before addition of Q_1 (baseline) luciferin fluorescence was increasing, therefore, the ATP synthesis

slope after addition was corrected: slope baseline before Q_1 addition was 0.02916 fluorescence units s^{-1}, after addition of Q_1 was −0.00476 fluorescence units s^{-1}, and corrected slope after addition of Q_1 was −0.03392 fluorescence units s^{-1}. The decrease in luciferin fluorescence upon addition of Q_1 indicated that *bo*$_3$-F_1F_O-GUVs synthetized ATP, which was then with substrate luciferin used by luciferase. Using the luciferin standard curve, synthetized ATP could be calculated, which was 106.3 µM (Figure 93B). Adding Q_1 for the second time led to only slight increase in ATP concentration (123.6 µM). It should be noted that the luciferin fluorescence was monitored in close proximity to vesicles membrane; nevertheless, diffusion of newly synthetized ATP from surrounding vesicles cannot be completely dismissed. Despite the just mentioned drawback, this approach is more relevant to ATP producing GUVs than to luminometer measurements. The only issue that occurred was that when higher concentrations of HSII were added to *bo*$_3$-F_1F_O-hybrid-GUVs, the vesicles that were in contact with glass slide were destabilized and some of them burst. Therefore, a minimum concentration of HSII should be used to still detect the luciferin change (for details see Chapter 2.9.6.5).

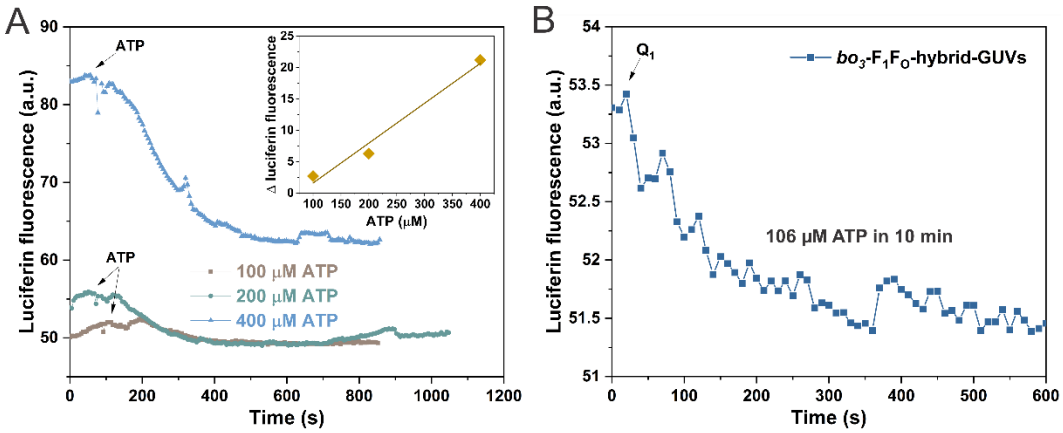

Figure 93. Monitoring respiratory-driven ATP synthesis in microscopy chamber. (**A**) ATP calibration curve determined from luciferin fluorescence. (**B**) ATP synthesis of *bo*$_3$-F_1F_O-hybrid-GUVs prepared in 1 mM Tris-HCl (pH 7.5) buffer containing 200 mM sucrose. Vesicles were mixed 1:4 (v/v) with 1 mM Tris-HCl (pH 7.5) buffer containing 200 mM sucrose, HSII, ADP and DTT. Proton pumping was initiated by addition of Q_1.

3.4.5 Fusion/electroformation extended: growth of multicompartmentalized vesicle systems

The construction of artificial cells requires the sub-compartmentalization of individual functional modules, especially in such cases where enzyme crowding, establishment of ion gradients, or interface for membrane proteins is required. Sub-compartmentalization prevents also potential inhibition of metabolic cascades and non-desired cross-reactions. In order to grow multicompartmentalized membrane systems, we utilized electroformation or fusion/electroformation. The encapsulated nanocompartments were either SUVs (~ 50 nm) or LUVs (~ 100 nm). The current growth protocol was tackled in order to integrate growth, energy

supply, metabolism and transport related functionalities, in collaboration with Dr. Lado Otrin and Dr. Olivier Biner. In such artificial organelles, GUVs would contain a lactate transporter in the membrane, meanwhile the GUV lumen would contain a short metabolic cascade and an ATP-generating SUVs/LUVs (one of the two types of reconstituted artificial respiratory chain comprising complex I, oxidase and F_1F_O-ATPase: one with alternative oxidase constructed by Dr. Olivier Biner and another with transmembrane proton pumping oxidase constructed by Dr. Lado Otrin). The composition of LUVs was chosen to be DOPC:DOPE:TOCL:PE-Rho (82.85:11.4:5.7:0.05, mol%) in order to retain the highest activity of the short respiratory chain comprising complex I and F_1F_O-ATPase (245). While the composition of the nanocompartments was dictated by membrane proteins, the outer microcompartment was chosen to be made solely of PDMS-*g*-PEO, due to its chemical resistivity to ROS (see Chapter 3.1.2.2). In order to evaluate the encapsulation efficiency by the use of fluorescence microscopy, GUVs were tagged with a polymer dye (PDMS-*g*-PEO-FITC) and SUV/LUVs with a lipid dye (PE-Rho).

As mentioned above, the growth of multicompartmentalized vesicular system was tackled in two ways: either by growing them from a polymer film (electroformation) or from a fused polymer LUVs film (fusion/electroformation). The latter would enable simultaneous growth and integration of transporter into the GUV membrane. In the first step, growth from a polymer film was tackled; whereby three different electroformation protocols were tested (see Chapter 2.6.2). A two-step protocol starting with 1.2 V, 10 Hz for 8 h, and followed by application of 2 V, 4 Hz for 30 min led to the growth of GUVs with the largest diameter. The LUV concentration in the electroformation media was varied from 1 to 3 mg ml^{-1} and was observed to have an impact on the growth of GUVs. Only 1 mg ml^{-1} led to GUVs with a sufficiently large diameter (> 10 µm), a size being suitable for future studies in microfluidic traps.

While growing GUVs with encapsulated LUVs, one should be careful on electrostatic interactions between their membranes. In particular, too strong repulsive forces will inhibit efficient encapsulation of LUVs, meanwhile, too strong attractive forces will induce fusion between outer and inner membranes. Here, fusion of the outer membrane and the LUVs was interrupted by electrostatic repulsive interactions between moderately negatively charged PDMS-*g*-PEO:PDMS-*g*-PEO-FITC ($\zeta = -25.9 \pm 1.8$, n = 5) and strongly negatively charged DOPC:DOPE:TOCL:PE-Rho LUVs ($\zeta = -55.72 \pm 1.89$, n = 5), which enabled encapsulation of SUVs/LUVs (Figures 94 and S87). Meanwhile, in a control experiment, anionic LUVs were replaced with cationic (DOPC:DOTAP:PE-Rho) LUVs. In the latter case, strong accumulation of the signal from LUVs (red) was observed on the membrane of GUVs (green) (Figures 95 and S85). A high positive surface charge of the LUVs made from the cationic lipid ($\zeta = 52.5 \pm 1.2$, n = 3) led to their fusion with the outer polymer membrane. It appears, that fusion occurred already during swelling of GUVs (before their detachment), as seen from parts of the polymer film and GUVs that were unnaturally detached from

ITO slides (sucked by pipette) (Figure S86). Although the control experiment with cationic LUVs led to a novel way for growth of (mainly) monocompartmentalized hybrid GUVs, it is undesirable for growth of multicompartentalized membranous systems. Nevertheless, it shows once again that the surface charge should be always considered, independent of the growth mechanism under the investigation. Attractive interaction between polymer GUVs and cationic lipid LUVs are in agreement with the observed non negligible membrane mixing between polymer LUVs and cationic lipid LUVs (Chapter 3.2.1, Figure S7). In future studies, such a growth mechanism of hybrid GUVs (conceptually similar to the one discussed in Chapter 3.2.5, but achieved in different manner) could be utilized for the delivery of membrane proteins into a GUV (starting with a proteo-lipid-LUVs and a polymer film). This might hold in particular promise for membrane proteins where reconstitution protocols into liposomes are already developed and where difficulties in reconstitution into hybrids arise. Perhaps such growth mechanism would enable functionalization with complex membrane proteins also of more rigid polymer membranes, which was so far a struggle.

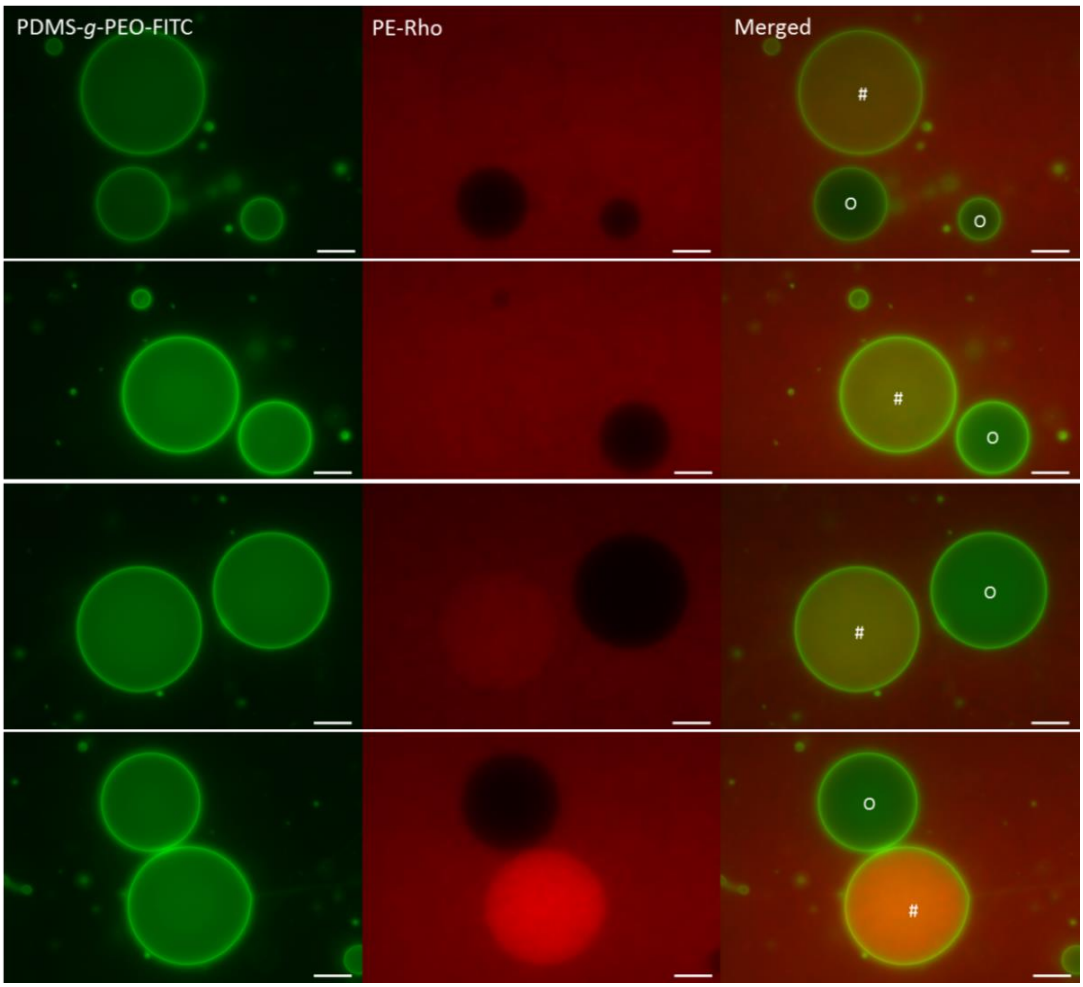

Figure 94. Encapsulation of anionic LUVs in polymer GUVs. Epifluorescence images of PDMS-*g*-PEO GUVs (membrane tagged with 0.5 mol% PDMS-*g*-PEO-FITC, green) with encapsulated 100 nm DOPC:DOPE:TOCL LUVs (membrane tagged with 0.05 mol% PE-Rho, red) after electroformation. #: LUVs encapsulated GUVs, O: empty GUVs. Scale bar: 10 µm.

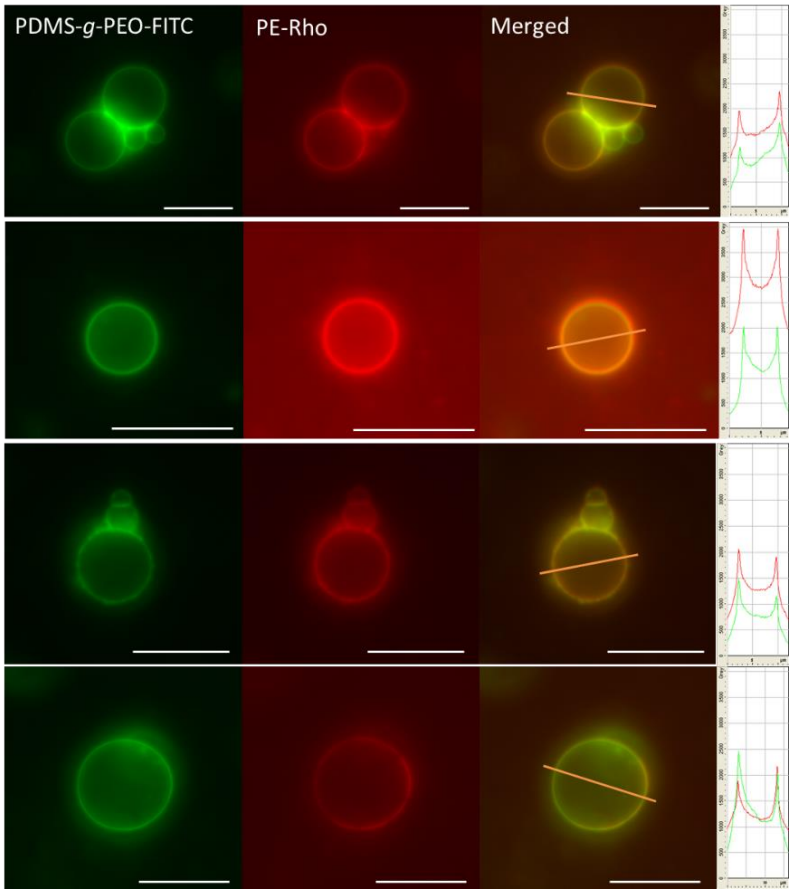

Figure 95. Encapsulation of cationic LUVs in polymer GUVs. Epifluorescence images of PDMS-*g*-PEO GUVs (membrane tagged with 0.5 mol% PDMS-*g*-PEO-FITC, green) formed with electroformation in the presence of 100 nm DOPC:DOTAP LUVs (membrane tagged with 0.05 mol% PE-Rho, red) after electroformation. The majority of LUVs fused with the membrane of GUVs (accumulation or red signal – see line profiles on the right). Scale bar: 10 µm.

While the majority of cationic LUVs (~ 100 nm in size) fused with the outer membrane, and only a low amount was successfully encapsulated in GUVs (relatively low red signal), anionic LUVs were observed only in the GUVs lumen and in their exterior. The encapsulation efficiency of anionic LUVs varied significantly between the GUVs. Although all GUVs contained at least a very low amount of anionic LUVs, the majority of GUVs contained a lower LUV concentration than the outer solution. Those GUVs were considered as empty (although this was not exactly the case), because only GUVs with a high LUVs content would be utilized in future experiments (selection can be done by microfluidic trapping). Nevertheless, 35.3 % of the GUVs contained the same or a higher amount of LUVs as the outer solution. Given that only GUVs with successful encapsulation can be chosen for later studies, having more than ⅓ of GUVs to choose from, electroformation can be considered as a suitable encapsulation technique. Nevertheless, the encapsulation efficiency could be potentially increased by reducing the LUVs and GUVs membranes repulsion, by replacing strongly anionic LUVs for moderately anionic or neutral LUVs (such as for example

DOPC LUVs). Another factor determining the encapsulation efficiency is the size of the encapsulated nanocompartments. To test the latter, encapsulation of ~ 50 nm SUVs was investigated next. Not surprisingly, the encapsulation efficiency indeed increased with the decreased size of the nanocompartments (Figure 96, upper panel). In a previous study, where anionic (PG) liposomes were encapsulated into anionic (PS) liposomes, 85 % encapsulation efficiency was obtained for 50 nm liposomes and 75 % for 100 nm ones (72). The lower encapsulation efficiency in the current study mainly arises from the different composition of membranes. In addition, the evaluation with epifluorescence microscopy (current study) or confocal microscope (previous study) might also have a certain artifact contribution (for example due to lower signal detection with epifluorescence microscopy).

In the next step, we combined the methodology to grow microcompartments from Chapter 3.4.1 (fusion/electroformation) with the here-discusssed technique for encapsulation of nanocompartments. Polymer GUVs were formed from fused polymer LUVs, with encapsulated anionic lipid SUVs or LUVs (Figure 96, lower panel). Surprisingly, the three-step electroformation protocol utilized for fused LUVs film (see Chapter 3.4.1) was shown to yield less multicompartmentalized GUVs than the two-step protocol used in the present chapter. Nevertheless, to obtain an even higher yield of GUVs, the duration of the first step of the electroformation protocol was increased from 8 to 24 h, and the ITO-coated glass slides had to be always plasma cleaned before use. Interestingly, encapsulation efficiency did not correspond to the decrease in liposome size. With 1 mg ml^{-1} of liposomes in the electroformation solution, the size of grown GUVs via fusion/electroformation was smaller than when grown via conventional electroformation. A decreased liposomes concentration by a half led to an increase of the GUVs size, but to a decrease of the encapsulation efficiency (Figure 96, lower panel). To the best of our knowledge, this is the first successful attempt so far to grow multicompartmentalized vesicular system via fusion/electroformation. The method holds great promise for the growth of membrane protein-functionalized multicompartmentalized vesicles.

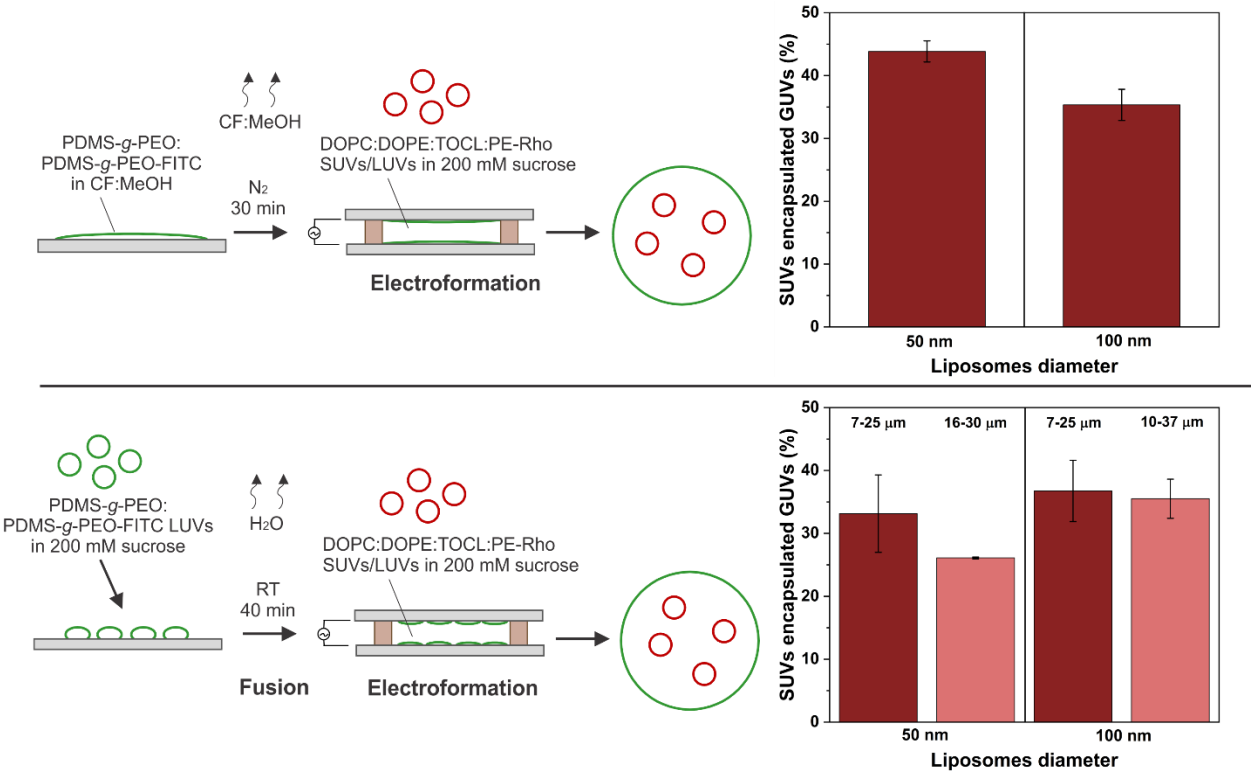

Figure 96. Encapsulation efficiency of 50 and 100 nm anionic liposomes in polymer GUVs. *Upper panel*: Multicompartmentalized vesicle systems were grown via electroformation from a polymer film. The polymer film was formed by depositing the polymer solution in chloroform:methanol (CF:MeOH) on an ITO-coated glass slides, followed by solvent removal under a gentle stream of nitrogen. *Lower panel*: Multicompartmentalized vesicles were grown via fusion/electroformation from a fused polymer LUVs film. Droplets of LUVs were deposited on ITO-coated glass slides and fused by dehydration at room temperature (RT). Intensity of bars indicates SUVs/LUVs concentration: 1 mg ml^{-1} (dark red) and 0.5 mg ml^{-1} (light red). The encapsulation decreased with increased size of encapsulated vesicles, when GUVs were grown via electroformation, but not when they were grown via fusion/electroformation. Lower SUVs/LUVs concentration led to slightly lower encapsulation efficiency, but larger GUVs size. Error bars indicate the mean ± s.d. of three (for upper panel) or two (for lower panel) independent experiments. For each preparation 90–200 GUVs were evaluated.

3.5 Returning to nature – SNARE-mediated vesicle growth

Final growth mechanisms explored in this thesis utilized SNARE proteins, which are recognized as key drivers of membrane fusion in nature as discussed in Chapter 1.3.4.1. As a step towards SNARE-mediated growth, fusion between nano- and microcompartments and between microcompartments was explored. The membrane of each type of compartment contained one half of SNARE complex: ΔN complex or synaptobrevin. ΔN complex constituted syntaxin-1A, SNAP-25 and synaptobrevin-2 fragment.

3.5.1 Preparation of syb-GUVs and ΔN-GUVs

For reconstitution of SNAREs into LUVs, the previously developed protocol via co-micellization (Chapter 2.9.2) was utilized, which was demonstrated to give prevailingly (> 85 %) correct orientation of SNAREs in lipid, hybrid and polymer LUVs (106). For scale-up to the size of several micrometers, the fusion/electroformation growth approach (Chapter 3.4) was applied. The protocol optimized for largely hydrophobic membrane proteins in a low salt buffer, had to be slightly modified for SNAREs and the different buffer composition, containing higher amounts of salt. In particular, the polymer/lipid-to-protein molar ratios, 500:1 for synaptobrevin and 1,000:1 for ΔN complex, were much lower than the ones used for bo_3 oxidase (9,500:1). In order to obtain a high protein density, SNARE-GUVs had to be directly grown from SNARE-LUVs, and not from a mixture of proteoLUVs and protein-free LUVs. Furthermore, the starting material in the current case were SNARE-LUVs prepared with co-micellization, which had a different concentration and size than the proteo-LUVs prepared by extrusion and detergent-mediated reconstitution (e.g., bo_3-LUVs). We modified all the steps of our previous protocol by increasing the concentration of deposited proteoLUVs, decreasing the dehydration time (the presence of salt accelerated the dehydration process), and by increasing the time and voltage applied during electroformation (Chapter 2.9.3.4).

The size of syb-polymer-GUVs was observed to decrease with increasing concentration of salt in the electroformation solution. In low salt buffer (5 mM HEPES (pH 7.4), 5 mM KCl, 100 mM sucrose) syb-polymer-GUVs had a mean diameter of 6.5 µm, and a few syb-polymer-GUVs with 20–35 µm size were found (Figure 97B). Meanwhile, in high salt buffer (20 mM HEPES (pH 7.4), 150 mM KCl, 100 mM sucrose) the mean diameter decreased to 5.3 µm and no syb-polymer-GUVs with diameter > 20 µm were found (Figure 97C). Similar observations were made for ΔN-polymer-GUVs, where the mean diameter decreased from 8.7 to 6.0 µm from low to high salt buffer (Figure 97E–F). Interestingly, there was no large difference in size for either syb-polymer-GUVs or ΔN-polymer-GUVs in sucrose solution or low salt buffer. Overall, the average diameter of ΔN-polymer-GUVs was larger than of previously ITO slides grown ΔN-lipid-GUVs and slightly smaller than of ΔN-lipid-GUVs grown on Pt wires (5.8 and 13.5 µm,

respectively (73). Nevertheless, the largest observed ΔN-polymer-GUVs (d = 40 μm) were larger than the largest ΔN-lipid-GUVs (d = 33 μm) (73).

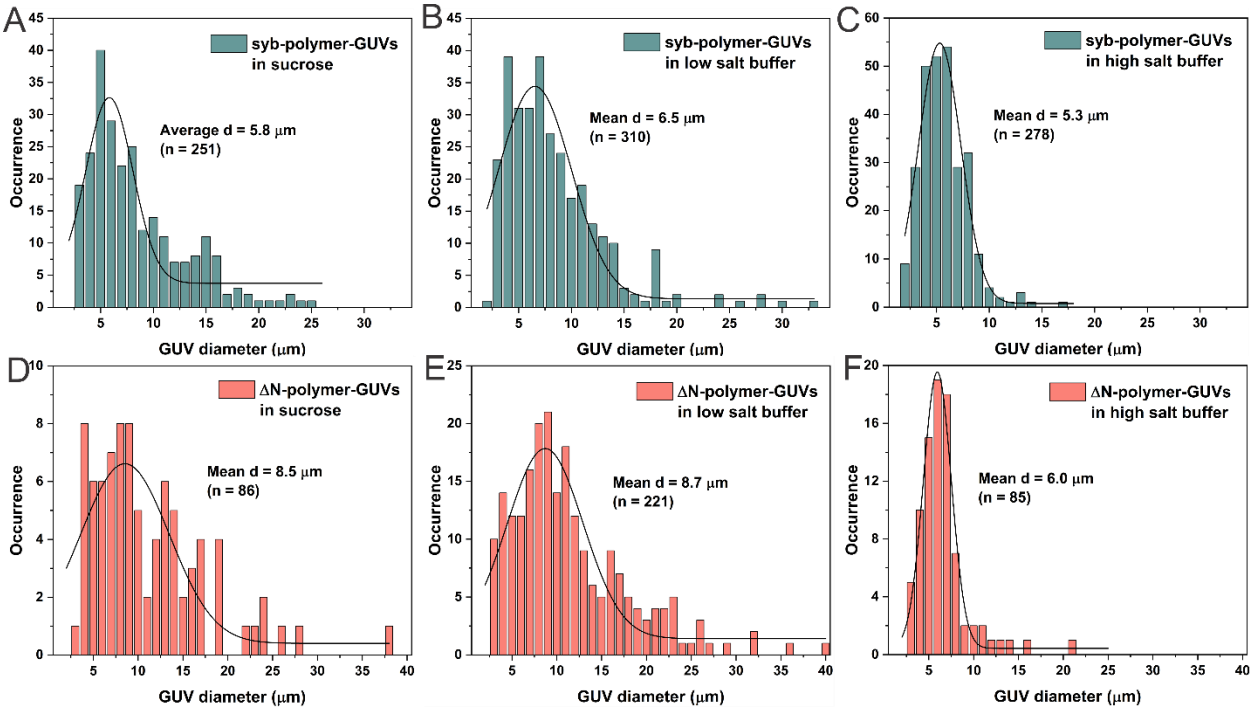

Figure 97. Size distribution of SNARE-polymer-GUVs. Synaptobrevin and ΔN complex were reconstituted in PDMS-*g*-PEO polymersomes at polymer-to-protein molar ratio of 500:1 and 1000:1, respectively. Histograms present SNARE-polymer-GUVs size distribution in three different media: 100 mM sucrose (**A**) and (**D**), 5 mM HEPES (pH 7.4), 5 mM KCl, 100 mM sucrose (**B**) and (**E**), and 20 mM HEPES (pH 7.4), 150 mM KCl, 100 mM sucrose (**C**) and (**F**). The mean diameter did not substantially change in between three different solutions, but the width of the distribution substantially decreased in high salt buffer. Furthermore, the rare larger GUVs observed in high salt buffer burst during observation (due to contact with glass slide) and could not be evaluated.

3.5.2 Bending rigidity of syb-GUVs and ΔN-GUVs

In order to measure the membrane bending rigidity with fluctuation analysis, the GUVs should have a size > 10 μm, in order to detect membrane fluctuations (i.e., by following the contour) by means of our in-house software (197). Therefore, we aimed at obtaining GUVs with a diameter of 15–20 μm, which meant to avoid using buffers with high concentration of salt (Figure 97C). Since the presence of different salts is known to influence the bending rigidity of vesicles (144, 285), we decided to keep the conditions (with respect to salt concentration and pH) similar to the ones previously used for the membrane mixing experiments on LUVs (106), although the salt concentration had to be reduced, so that vesicles with desired diameter would still form. Therefore, vesicles for bending rigidity evaluation were formed in 5 mM HEPES (pH 7.4) and 5 mM KCl. Furthermore, for vesicle deflation and sedimentation, sucrose and glucose were utilized (for details please see Chapter 2.10.7.2).

Remarkably, even at a reduced salt concentration the effect was still significant: 47.8 % and 43.2 % decrease in bending rigidity of polymersomes and hybrids, respectively (see Figure 98 and Chapter 3.1.1.1, Figure 17 for comparison). Similar membrane softening in the presence of salt was previously observed for POPC (144) and POPC:POPG liposomes (285). Furthermore, we recently observed by cryo-TEM that the presence of 5 mM KCl caused a polymer membrane thickening by 0.82 nm (106). Combined results clearly indicate that monovalent cations bind to the polymer and induced changed in the membrane biophysical properties. Interestingly, lipid dyes (PE-NBD and PE-Rho) further soften the membranes (Figure 98). Presumably this was due to the increased salt screening via the additional membrane charge introduced by Rho and NBD (285, 286). Meanwhile, the opposite effect was observed upon protein insertion: synaptobrevin and ΔN rigidified polymer and hybrid membrane (Figure 98), but the effect was not so pronounced as the effect of salt or lipid dyes. This indicated that SNAREs have an opposite effect on the membrane bending rigidity, different from multidomain transmembrane proteins with a larger hydrophobic region (such as bo_3 oxidase) (Chapter 3.1.1.1, Figure 17). Meanwhile, a similar increase in the bending rigidity was previously reported for DNA, anchored in lipid membranes (287).

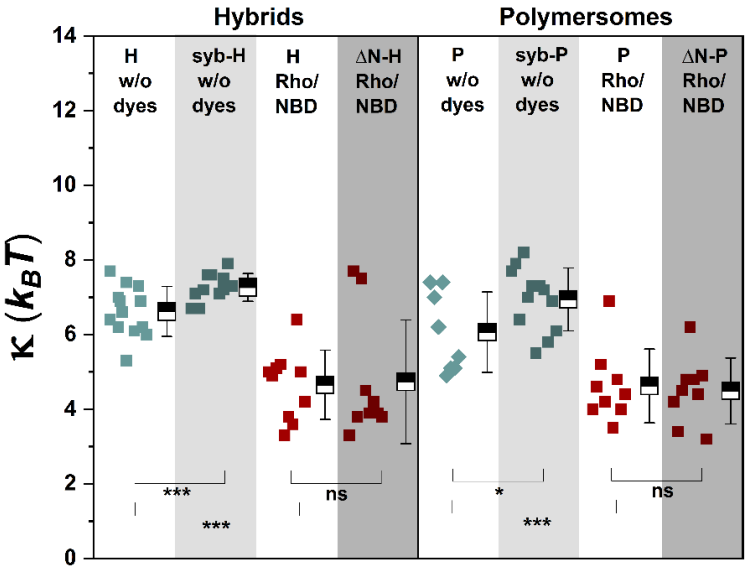

Figure 98. Bending rigidity of SNARE-free and SNARE-functionalized hybrid and polymer GUVs. GUVs were prepared via fusion/electroformation in 5 mM HEPES (pH 7.4), 5 mM KCl, 30 mM sucrose. The bending rigidity was determined by fluctuation analysis. Adapted from (106), licensed under CC BY 4.0.

3.5.3 Membrane mixing during syb-LUVs/GUVs and ΔN-GUVs

Growth of microcompartments via SNARE-mediated fusion can be achieved via fusion of GUVs with reconstituted ΔN complex and LUVs with reconstituted synaptobrevin, where upon vesicle docking, a *trans*-SNARE complex is assembled, followed by pore opening and vesicle fusion (Figure 99). Upon

fusion, newly grown GUVs contain in their membrane a *cis*-SNARE complex. Fusion can proceed until all ΔN complexes are assembled with synaptobrevin in *cis*-SNARE complexes.

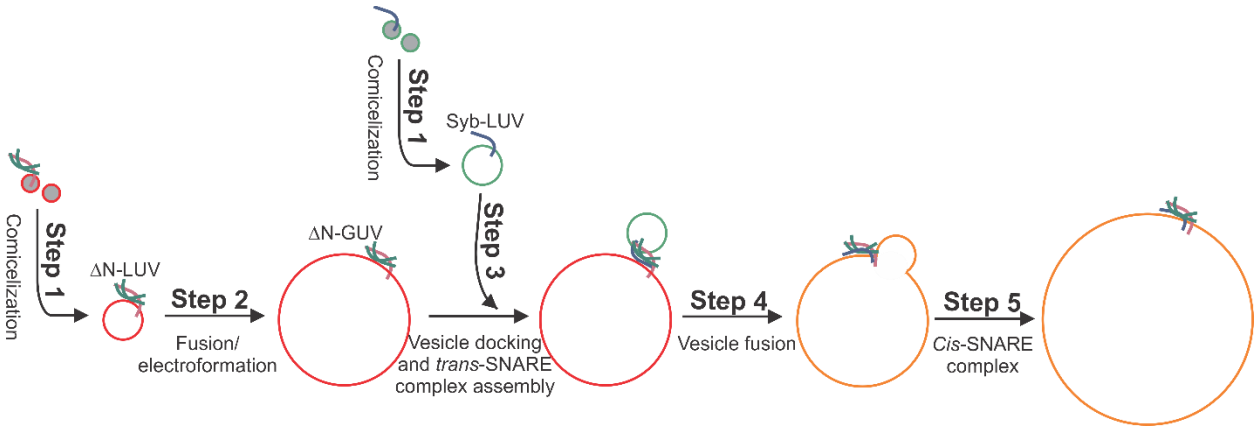

Figure 99. Scheme for SNARE-mediated growth of microcompartments. Step 1: ΔN-LUVs and syb-LUVs are prepared via comicellization from mixed polymer/protein micelles. SNARE-LUVs are formed during size exclusion chromatography upon detergent removal. ΔN complex consists of syntaxin-1A, SNAP-25 and synaptobrevin-2 fragment. **Step 2:** ΔN-GUVs are grown via fusion/electroformation. **Step 3:** Syb-LUVs are added to ΔN-GUVs, dock on their membrane and *trans*-SNARE complex is assembled. **Step 4**: Syb-LUVs undergo membrane mixing with ΔN-GUV, following by pore opening and fusion. **Step 5:** Membrane surface of SNARE-GUV is increased. SNAREs are found in the membrane in *cis* conformation.

We previously demonstrated that membrane mixing occurred between hybrid and polymer syb-LUVs and ΔN-LUVs and slightly surpassed the membrane mixing in liposomes (~ 20 %, ~ 25 % and ~ 22 % in 2 h for liposomes, hybrids and polymersomes, respectively) (106). Nevertheless, GUVs are known to be less fusogenic due to their decreased membrane curvature, and therefore the fusion efficiency from nanocompartments cannot be directly translated to microcompartments. Furthermore, the curvature of the opposing membranes (i.e., vesicle diameter) dictates also the size of t-/v-SNARE complex forming the pore and its size: the smaller the vesicles, the smaller the size of the SNARE complex and of the pore formed (288). It was previously observed that SNARE-ring complexes ranging in diameter from approx. 15 to 300 nm are formed when t-SNARE-LUVs and v-SNARE-LUVs, with a diameter of 40–800 nm, met (288).

To analyze if membrane mixing between PDMS-*g*-PEO nano- and microcompartments occurs, syb-LUVs were tagged with PE-NBD (green) and ΔN-GUVs with PE-Rho (red), mixed and incubated for 10 min at room temperature in presence of 1 mM DTT (for details see Section 2.11.3.5). Epifluorescence microscopy revealed docking/membrane mixing between polymer syb-LUVs and ΔN-GUVs (apparent from green signal accumulation on the GUVs membrane) (Figure 100). This confirmed that there are indeed attractive interactions between SNARE-functionalized compartments, but to what extent fusion occurs (docking/hemifusion/fusion) could not be extracted solely from images. Due to low intensity of mixing (gentle tapping on Eppendorf tube) not all ΔN-GUVs obtained signal from syb-LUVs. The later could be

also related to a non-homogenous SNARE density between vesicles. Interestingly, micrographs of ΔN-GUVs alone revealed that there are some non-specific interactions between ΔN-complexes in opposing GUVs (portion of vesicles was aggregated and in rare cases hemifused, Figure 101). The latter has likely to do with the interactions between truncated synaptobrevin-2 from ΔN complex in one GUVs with syntaxin-1A/SNAP-25a from ΔN complex in opposing GUV.

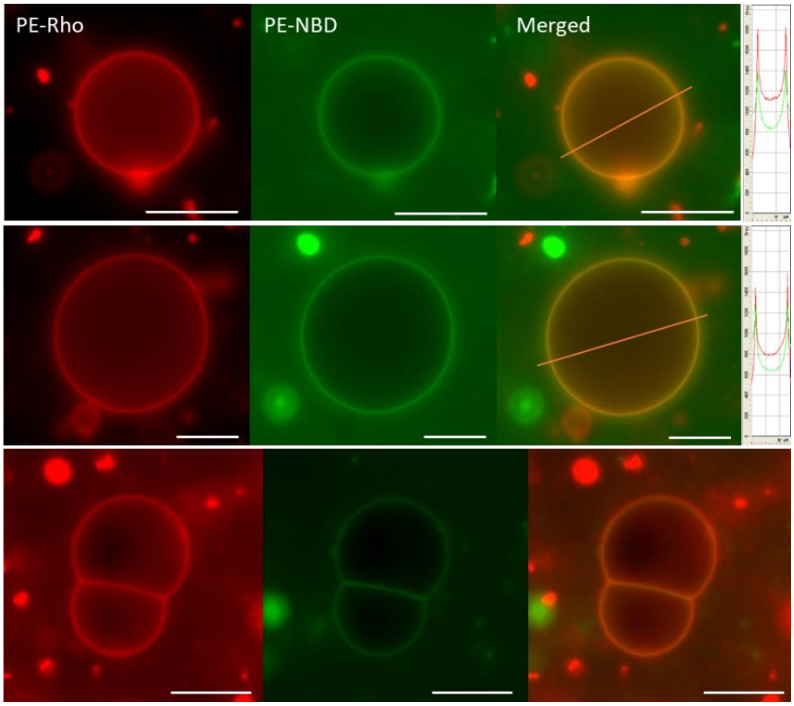

Figure 100. Membrane mixing of ΔN-polymer-GUVs with syb-polymer-LUVs. (**A**) Epifluorescence microscopy images of ΔN-polymer-GUVs tagged with 0.5 mol% PE-Rho (red) after incubation with syb-polymer-LUVs tagged with 0.5 mol% PE-NBD (green) and 1 mM DTT for 5 min. Long contact between two SNARE-GUVs can be observed in the lower image. (**B**) Epifluorescence microscopy images of polymer-GUVs tagged with 0.5 mol% PE-Rho (red) after incubation with syb-polymer-LUVs tagged with 0.5 mol% PE-NBD (green) and 1 mM DTT for 5 min. Scale bar: 10 µm.

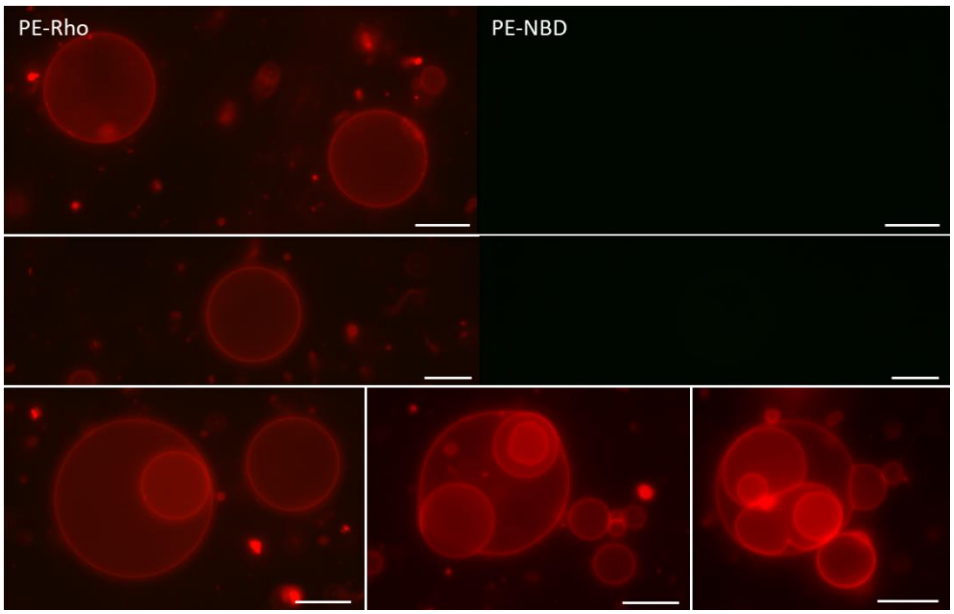

Figure 101. Micrographs of ΔN-polymer-GUVs. No fluorescence signal contribution was observed in NBD channel. Occasionally, aggregated ΔN-polymer-GUVs were observed and in rare cases two ΔN-polymer-GUVs in long contact phase and hemifusion, which indicated on nonspecific interaction between the ΔN complex in proximate GUVs.

To be able to optically observe the behavior of SNARE-polymer-GUVs and potentially see intermediates, ΔN-GUVs were next mixed with syb-GUVs (for details see Section 2.11.3.6). Observed intermediates were related to the initial stages of fusion (see Chapter 1.3.4.3) (Figure 102), while no post-fusion conformations (semi-spherical GUVs containing both signals) were observed. A number of docked syb-GUVs and ΔN-GUVs (Figure 102I) were detected, some GUVs established point contact (Figure 102II), narrow hemifusion (Figure 102III), or even diaphragm was observed (Figure 102IV). Interestingly, observed intermediates of polymer fusion on the micrometer scale resemble the ones we previously observed on the nanometer scale with a cryo-TEM (106). The difference was that in the latter study we observed also later stage intermediates, such as membrane thinning on part of the diaphragm and pore opening at the extremity. Presumably, this can be ascribed to lower energy of GUVs and a fusion process arrested in the hemifusion state, while LUVs have more energy for complete fusion. Due to the observed membrane mixing in the GUV-GUV system (red and green signal observed in membrane of SNARE-GUVs (Figure 102II–IV), we assume that the observed accumulation signal for GUV-LUV system (Figure 100) is indeed membrane mixing and not solely syb-LUVs docked on ΔN-GUV.

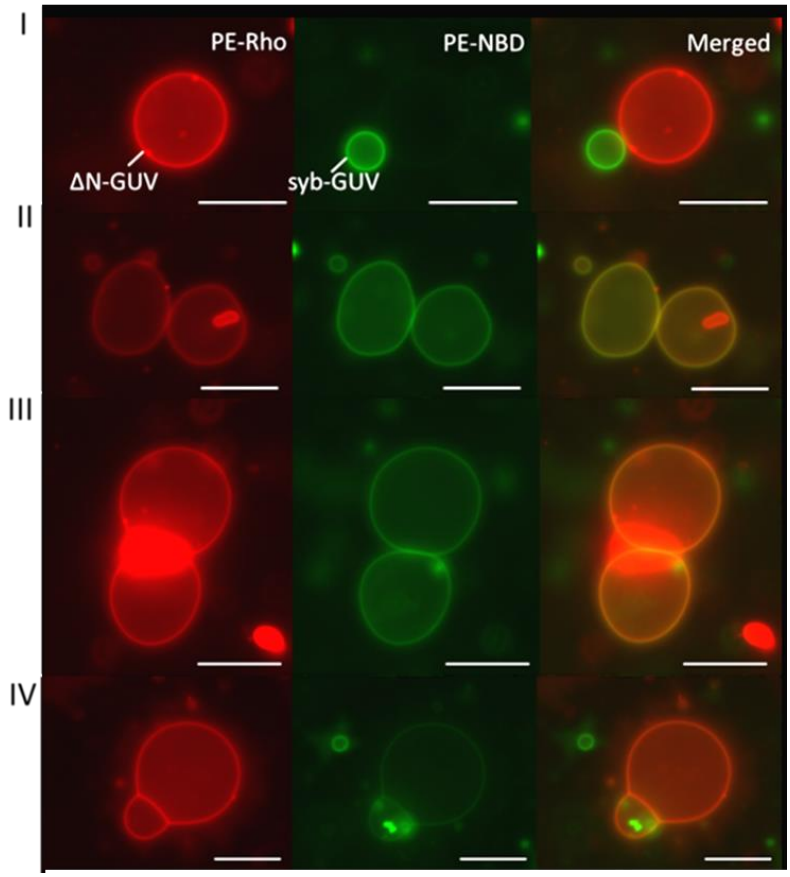

Figure 102. Membrane mixing during syb-polymer-GUV and ΔN-polymer-GUV fusion. SNARE-GUVs were formed via fusion/electroformation in 5 mM Tris-HCl (pH 7.4), 5 mM KCl, 100 mM sucrose. Syb-polymer-GUVs were tagged with 0.5 mol% PE-NBD, and ΔN-polymer-GUVs with 0.5 mol% PE-Rho. Observed fusion intermediates: docking (**I**), point contact (**II**), narrow hemifusion (**III**), hemifusion diaphragm expansion (**IV**). Scale bar: 10 µm.

3.5.4 Content mixing during syb-LUVs and ΔN-GUVs fusion

In order to determine if ΔN-polymer-GUVs and syb-polymer-LUVs undergo only membrane mixing or full fusion, content mixing was analyzed next. Content mixing during SNARE-mediated ΔN-lipid-GUV and syb-lipid-LUV fusion is typically analyzed via a self-quenched dye (e.g., calcein or sulforhodamin B (138)) encapsulated in LUVs. Upon fusion, the dye is released into the GUV lumen, which leads to rapid dilution of the dye and increase of the fluorescence intensity. For the latter analysis, confocal microscope, total internal reflection fluorescence microscopy (TIRFM) or similar is required in order to analyze fluorescence intensity only in the focal plane (GUVs cross section), so that environmental (background) fluorescence can be avoided. Due to unavailability of such equipment at the time of experiment, a different approach was applied. Similarly as we previously analyzed the content mixing in charge-mediated [Chapter 3.2.4.2] and SNARE-mediated (106) LUV-LUV fusion via enzymatic coupling of two membrane proteins (*bo*$_3$ oxidase and F_1F_O-ATPase), here, the content mixing between ΔN-GUV and syb-LUV was analyzed. In the current setup F_1F_O-ATPase was co-reconstituted with synaptobrevin in one population of LUVs, *bo*$_3$

oxidase was co-reconstituted with synaptobrevin in another population of LUVs, and ΔN-complex was reconstituted alone in GUVs (Figure 103A). If complete fusion occurred, ATPase and a proton pump would be delivered into the GUVs, where upon activation of the proton pump with DTT and Q_1, ATP synthesis would initiate. For a negative control, the experiment was repeated without SNARE proteins (with protein-free GUVs, *bo*$_3$-LUVs and F_1F_O-LUVs). While ΔN-GUVs and GUVs were grown overnight due to the long preparation procedure, syb-*bo*$_3$-LUVs and syb-F_1F_O-LUVs were prepared on the day of the activity measurements. To avoid activity loss of respiratory enzymes, proteoLUVs were kept on ice at all times.

Three different molar ratios of synaptobrevin:ΔN complex were tested: 2:1, 4:1, and 8:1. Different ratios were achieved by changing the volume of syb-*bo*$_3$/F_1F_O-LUVs added to ΔN-GUVs (for details see Chapter 2.12.4.2). For all three tested ratios, ATP synthesis was higher than in the control setup used without SNAREs (Figure 103B). The latter indicates that the delivery of respiratory enzymes was significantly more efficient when mediated by SNARE proteins. For the molar ratio synaptobrevin:ΔN complex = 2:1, where the lowest volume of syb-*bo*$_3$/F_1F_O-LUVs was added, the two measurements greatly differed. The latter can be ascribed to an uneven delivery of the respiratory enzymes into the ΔN-GUVs. Interestingly, a ratio of 8:1 gave a lower ATP synthesis rate than a ratio of 4:1. This indicates that the amount of respiratory enzymes in GUVs was so high that it significantly increased the membrane proton permeability (see Chapter 3.1.2.3) and consequently decreased the available proton gradient for ATP synthesis. The latter speculations should be in detail studied in the future. Furthermore, the density of fluorescently labeled SNAREs as well as respiratory enzymes in the GUVs can be analyzed via confocal microscopy. Nevertheless, the current populational study demonstrated that polymer ΔN-GUVs and syb-LUVs can successfully undergo complete fusion.

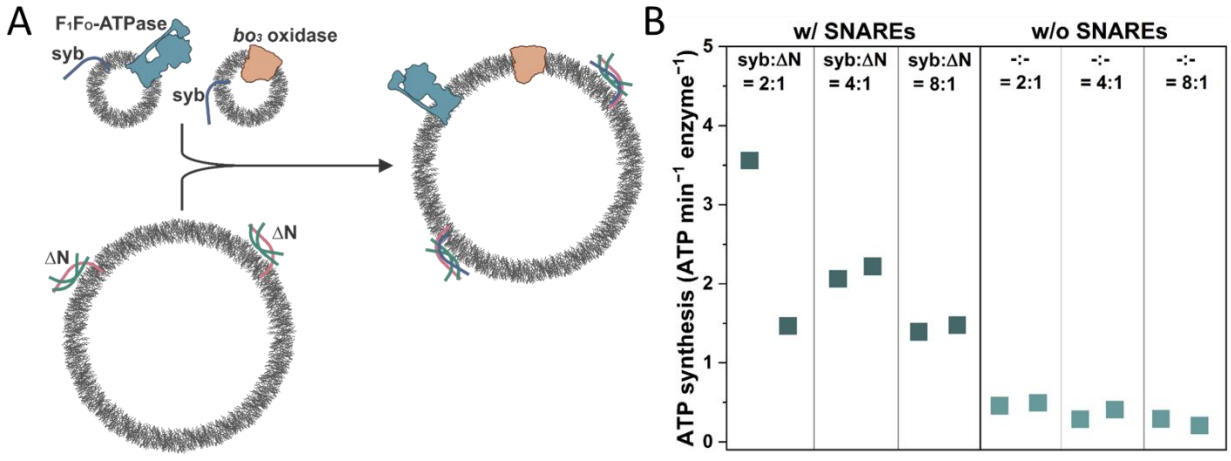

Figure 103. Content mixing analysis of SNARE-mediated polymersome fusion. (**A**) Schematic representation of content mixing analysis determined via respiratory-driven ATP synthesis. ΔN-polymer-GUVs were mixed with syb-*bo*$_3$-polymer-LUVs and syb-F_1F_O-polymer-LUVs and ATP synthesis was determined directly after. (**B**) ATP synthesis

rate for vesicles with (w/) and without (w/o) reconstituted SNAREs. Three different synaptobrevin:ΔN complex molar ratio were tested: 2:1, 4:1 and 8:1. For a negative control, the experiment was repeated in the absence of SNARE proteins, using the same ratios of mixed GUVs and proteoLUVs.

4 Conclusions and Outlook

A modular platform for the growth of polymer and polymer/lipid hybrid membranous systems by vesicle fusion was developed in order to facilitate the construction of artificial cells. Membrane fusion is a two-step process. First, the membranes are brought into close proximity, whereby repulsive electrostatic forces need to be overcome before the membrane constituents (lipids or polymers) can interact. Second, the boundary between the hydrophilic and hydrophobic portion of the membrane is destabilized and transition states are generated, culminating in the formation of an aqueous fusion pore. In this thesis, four different mechanisms (Figure 104) were investigated and utilized to trigger those two steps, and consequently the growth of compartments:

- electrostatic attraction between oppositely charged membranes (charge-mediated growth),
- membrane softening and charge neutralization by salt in combination with agitation to increase the vesicle collision probability and the formation of membrane defects acting as fusion nucleation sites (mechanically-induced salt-mediated growth),
- membrane dehydration by water evaporation (fusion/electroformation-mediated growth),
- bringing the membranes in close proximity by fusogenic proteins (SNARE-mediated growth).

Unlike the other three mechanisms, the fusion/electroformation-mediated growth involves two distinct experimental steps, where electroformation is needed to grow microcompartments from fused LUVs film. The rationale behind choosing this conceptually different mechanism lies in the next three facts: 1) fusion and growth potential of hybrid compartments was until now completely unexplored and of polymer compartments limited to only a few examples (PDMS-*g*-PEO compartments not being one of them), 2) developing a platform that includes various mechanisms for growth of PDMS-*g*-PEO and PDMS-*g*-PEO:lipid compartments opens more possibilities for future integration with other functional modules (not each growth mechanism is compatible with all other functional modules), 3) fusion and growth of protein-functionalized compartments has application beyond membrane expansion (discussed below) and a versatile stepwise platform is in this regard highly convenient.

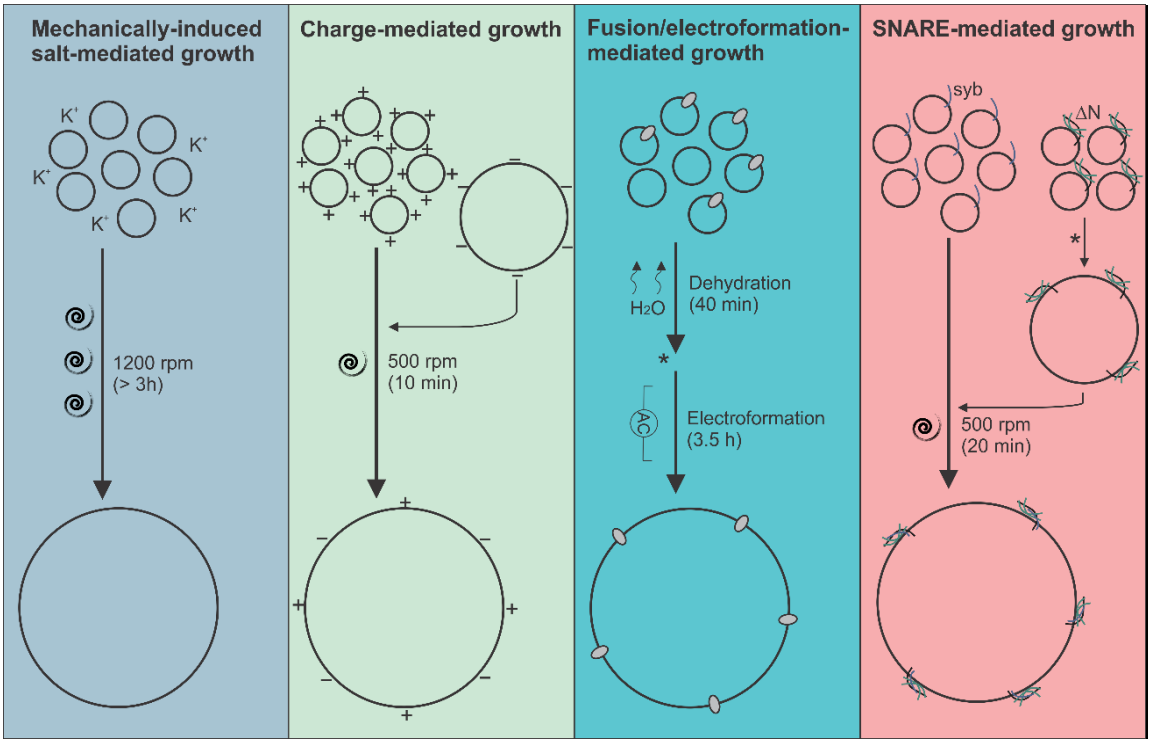

Figure 104. Growth mechanisms utilized in the thesis. Mechanically-induced salt-mediated growth is based on membrane charge neutralization and softening by salt, and membrane destabilization in combination with increased vesicle collision by agitation. Charge-mediated growth is based on electrostatic attractive interactions between anionic and cationic compartments. Fusion/electroformation-mediated growth is a two-step process where in the first step nanocompartments fuse by dehydration and form a thin polymer/lipid film, and in the second step microcompartments grow via electroformation. SNARE-mediated growth is mediated by SNARE complex formation between nanocompartments with reconstituted synaptobrevin (syb) and microcompartments with reconstituted ΔN complex (ΔN). For charge-mediated fusion scheme represents fusion between cationic LUVs and anionic GUVs, but LUVs-LUVs and GUV-GUV fusion was explored as well. Similarly, for SNARE-mediated fusion GUV-LUVs and GUV-GUV fusion was also explored.

The development of said modular platforms was achieved in several stages:

1. biophysical characterization of compartments (emphasis on the characteristics relevant for the growth module) and their interplay with membrane proteins,
2. identification of growth mechanisms that could be potentially applied to PDMS-*g*-PEO and PDMS-*g*-PEO:lipid compartments,
3. development/optimization of growth protocols,
4. analysis of fusion (size distribution, membrane and content mixing analysis) and growth efficiency (epifluorescence microscopy),
5. study of the compatibility of growth mechanisms with membrane proteins.

First, bending rigidity, lateral diffusion, membrane disorder, proton permeability, durability, and stability against ROS of PDMS-*g*-PEO, PDMS-*g*-PEO:soy PC and soy PC compartments was analyzed.

Furthermore, as a model, the largely hydrophobic membrane protein *bo*$_3$ oxidase was reconstituted in GUVs and its interplay with polymer and hybrid membrane was studied. Lateral diffusion of graft copolymer membrane constituents was slightly lower than in lipid membranes, but higher than in common block copolymer membranes. It was found that the studied membranes interacted differently with the reconstituted protein: While insertion of *bo*$_3$ oxidase in soy PC decreased the fluidity, it exercised the opposite effect on the polymer presumably by loosening its structure. Membrane fluidity retention upon protein insertion is in particular beneficial when higher protein loadings are required. The lateral diffusion of *bo*$_3$ oxidase decreased with increasing polymer content (liposomes > hybrids > polymersomes), but was still in the range of other membrane proteins in lipid membranes. The remarkable finding is that the characteristics of hybrid membranes are not always intermediate between lipid and polymer ones – blending the membrane led to increased proton permeability and broad distribution, but after proton pump insertion the compartments were surprisingly resealed, which was attributed to the rearrangement of the hybrid membrane. On the other side, the bending rigidity of the hybrid membranes appeared to scale with the ratio of the constituents – the prevailing component (polymer) dictated the membrane softness. Both hybrid and polymer membranes were shown to further soften upon insertion of a largely hydrophobic membrane protein. The later softening is in particular favorable for the fusion of protein-functionalized compartments. Furthermore, PDMS-*g*-PEO increases the functional lifetime of membrane proteins and their resistance to ROS. For example, 25 % of *bo*$_3$ oxidase activity was retained after 11 days when reconstituted in polymersomes, and only 4 % when reconstituted in liposomes. While both polymer and hybrid membranes have shown some promising characteristics as compartments of artificial cells, they were also exhibiting the highest performance in other aspects: for example, polymersomes when durability of the system is the main factor, or hybrids when low proton permeability is required upon membrane protein insertion. Therefore, both types of compartments were included into the current growth study.

Comparision of different fusion/growth mechanisms

Membrane fusion can vary in space and time. When micron-sized organelles such as yeast vacuoles fuse, the area of contact is ~ 10,000-fold larger than when synaptic vesicles undergo exocytosis, and the time of fusion – minutes for vacuoles, miliseconds for synaptic vesicles – is ~ 10,000-fold longer (89). Large difference in the rates of fusion was observed also between the different mechanisms in the current study, the fastest being for charge-mediated growth and the slowest for mechanically-induced growth. In addition to the rate of fusion kinetics, the extent of fusion progression for GUV-GUV charge- and SNARE-mediated fusion vary substantially: while for the first system full fusion occurred (pore opening), in the second case fusion was arrested in hemifusion. This can be attributed to different fusion mechanisms (attractive electrostatic interactions between the membranes vs. mechanical pulling the membranes together).

Noteworthy, the difference between growth mechanisms lies also in the membrane composition: while for charge-mediated growth charged lipids are a prerequisite (at least in one compartment population) and for mechanically-induced fusion one is limited to polymer membranes, for fusion/electroformation and SNARE-mediated growth membrane composition can vary. The main requirements, advantages and drawbacks of each growth mechanism are summarized in Table 7. Meanwhile, summarized results, possible future studies and applications of each growth mechanism are discussed below.

Table 7. Overview of requirements, advantages and drawbacks of growth approaches utilized in the thesis.

Growth approach	Charge-mediated growth	Mechanically-induced growth	Fusion/electroformation-mediated growth	SNARE-mediated growth
Equipment	None	Vortex	ITO-coated glass slides, voltage generator	None
Duration of samples preparation	~ 2 h (LUVs) ~ 9 h (GUVs)	~ 1.5 h (LUVs)	~ 6.5 h (GUVs)	~ 2 h (syb-LUVs) ~ 23.5 h (ΔN-GUVs)
Growth duration	Very short (< 1 min)	Long (hours)	Long (hours)	Short (~ 10 min)
Essential requirements(s)	Charged lipids	Salt, agitation	None	SNARE proteins
Required types of compartments	Two (anionic and cationic)	One	One	Two (ΔN-GUVs and syb-LUVs)
Salt concentration	Low/no (salts neutralize charge)	High	Low to moderate	Low to moderate
Main advantage	Fast rate of fusion; highly efficient fusion; works well for different-sized vesicles	Does not require any specific modification of vesicles; multiple rounds of fusion are enabled	Compatible with different membrane and buffer compositions; enables multicompartmentaliza-tion	Highly compatible with different membrane and buffer compositions; SNAREs can be regenerated thus enabling multiple rounds of fusion
Main drawback	Limited rounds of fusion (charge neutralization); formation of charged vesicles can be very challenging	Works only for polymersomes; slow rate of fusion	Delicate handling; protocol optimization required for each type of membrane	Preparation of SNARE-LUVs/GUVs demanding (protocol optimization)
Membrane proteins compatibility	Limited (incompatibility with charged lipids)	Moderate (reconstitution difficulties; high salt concentration	High (universal approach to grow proteoGUVs)	High (possible co-reconstitution with SNAREs)

		potentially incompatible with MPs)		

Interplay between different growth mechanisms

Although these growth mechanisms are conceptually different, they have some common repeating mediators. For example, the interplay between a charged membrane and its neutralization by salt has a similar role in all four fusion mechanisms. During the fusion of oppositely charged compartments, salt (partially) neutralized the surface charge, which decreased the fusion efficiency of those compartments. Meanwhile, in all three other mechanisms, salt (in particular monovalent cations) neutralized the slightly negatively charged lipid, hybrid or polymer compartments, which enabled their apposition. In particular for mechanically-induced fusion, the membrane charge neutralization in combination with its softening was a prerequisite for vesicle fusion. Meanwhile, for fusion/electroformation, salt presence accelerated the fusion process (as seen from decreased dehydration time when buffer was supplemented with 5 mM KCl). Furthermore, salt did not only accelerate the growth of ΔN-GUVs, but also their fusion with syb-LUVs.

Mechanically-induced growth of interconnected polymer microcompartments

Polymersomes grown by mechanical stress in presence of salt represents a facile approach toward the growth of an artificial cell, and its compatibility with essential artificial cell functions, such as encapsulation of cytosolic components and the reconstitution of membrane machinery, was demonstrated in this work. The advantage and drawback of such an approach lies in particular in the integrity of growing compartments – on one side compartments are able to uptake cytosolic components, while on the other side they might lose initially encapsulated material (depended on its size and charge). Furthermore, the significantly decreased polymer membrane bending rigidity in presence of K^+ makes them adjustable to barriers, such as channels in microfluidic devices (facile formation of elongated worm-like structures), but difficult to manipulate in microfluidic traps, where they squeeze in-between the posts. It was observed that via the type of salt one could control what type of polymer structures grow upon agitation (for example, GUVs in KCl and long tubes and polymer beads in NaCl). An interesting aspect of those mechanically grown polymersomes, which might show as promising in mimicking intercellular communication, are the tightly connected PDMS-*g*-PEO GUVs, forming tissue-like structures in presence of dUTP (highly resembling cork cells).

Charge-mediated fusion and its broad utility

As mentioned above, growth achieved by fusing two (or more) oppositely charged compartments represents the fastest mechanisms of the ones studied in this thesis (< 1 min). It was demonstrated that partially replacing the lipids with synthetic polymer PDMS-*g*-PEO led to significantly increased fusion efficiency. Furthermore, it was revealed that charged lipids are not required in both fusion-intended vesicles populations during hybrid membrane fusion; neutral hybrids can be utilized instead of anionic ones, which also led to higher content mixing. Meanwhile, the limitation of charge-mediated vesicle fusion is manifested in particular in the reconstitution of membrane proteins that are incompatible with anionic or cationic lipids. In particular cationic lipids, which are not appearing in nature, but are synthetically synthetized, are problematic. Cationic fatty acid amines and alcohols exist in some eukaryotic membranes (289, 290), but eubacterial cationic phospholipids have not been discovered so far. Due to lipid rearrangement around the proteins in hybrid membranes, replacing cationic lipids with cationic polymer, while keeping low amount of neutral lipids, might show as a highly promising way to circumvent incompatibility of cationic lipids with membrane proteins.

Charge-mediated fusion is a convenient tool beyond the potential growth module and assembly of artificial organelles, it has a relevant role also outside bottom-up synthetic biology – cationic DNA transfection agents that form bilayers can undergo fusion with anionic bilayers (291). Cationic lipids form complexes with DNA (lipoplexes) that are taken up by the cell and, because some of the DNA makes its way to the nucleus, these compounds have been widely used in nonviral gene therapy applications (292-295). Furthermore, cationic vesicles have a potential to be utilized in cancer therapies – cancer cells differ from normal ones by exhibiting abnormal negative surface charge (296). In the context of bottom-up synthetic biology, the charge-mediated fusion between artificial and live cells provides opportunities for the rapid screening of diverse membrane proteins, and polymer material-cell interactions. An example of the latter is fusion between cationic hybrid GUVs and microalgae with anionic membrane (Figure 105, *left*). One step further could be integration of bottom-up and top-down synthetic biology for charge-mediated microalgae transfection (Figure 105, *right*).

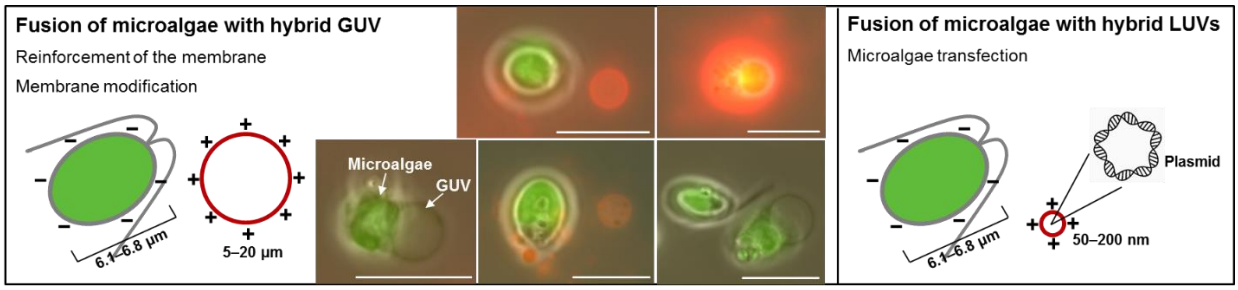

Figure 105. Communication between synthetic constructs and microalgae. *Left:* Micrographs show microalgae *Dunaliella Salina* and its interactions with hybrid GUVs. *Dunaliella Salina* has no cell wall and negatively charged

membrane (ζ = −15.4 ± 0.9 mV at pH 10 (297)), which enables attractive interactions with cationic hybrid GUVs. Images were obtained by epifluorescence microscopy 10 min after incubation of cationic hybrid GUVs (PDMS-*g*-PEO:DOTAP:PE-Rho = 69.9:30:0.1, mol%) with microalgae. Scale bar: 10 µm. *Right:* Encapsulation of plasmid into cationic hybrid LUVs, delivery into microalgae and its transfection.

Moreover, the combination of hemifusion/fusion and microfluidic trapping is relevant for research in bottom-up synthetic biology, including the assembly of synthetic prototissues, and the design of vesicle-mediated chemical communication pathways. Finally, newly fused and phase separated functionalized hybrid microcompartments could be implemented in directed inter-cellular communication. The latter could be achieved via fusion/fission cycles; such example is presented in Figure 106.

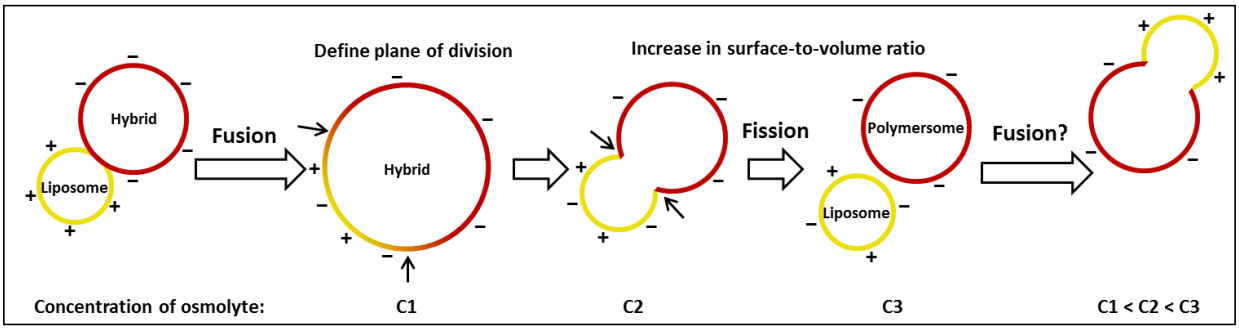

Figure 106. Communication between compartments via fusion/fission. Following fusion between anionic hybrid and cationic lipid GUVs and formation of new phase separated hybrid GUVs, fission could be achieved via osmotic shock, similarly as was previously done for phase separated liposomes containing cholesterol (121). In the latter study, one phase was disordered and one ordered, while in the example in the figure both phases are disordered. Second round of fusion could be implemented by fusing newly formed anionic polymersomes with cationic polymersomes. Each compartment would contain a metabolic cascade, which would be coupled via fusion.

Fusion/electroformation-mediated growth and its application in bottom-up synthetic biology

Fusion/electroformation was optimized for PDMS-*g*-PEO, PDMS-*g*-PEO:soy PC and soy PC membranes, and protein-functionalized microcompartments were successfully grown. Due to efficient formation of membrane protein-functionalized microcompartments, the approach is highly relevant for the construction of cell-sized artificial organelles. Importantly, optimization of said approach enabled biophysical study of the interplay between the membrane and inserted membranes proteins (not feasible on nano scale). Moreover, it was demonstrated that the optimized approach could be utilized for different types of membrane proteins – transmembrane peptides or complex largely hydrophobic or asymmetric proteins. The method resulted in active enzymes:

- Activity and orientation of reconstituted largely hydrophobic model protein bo_3 oxidase was extracted on single vesicle level by monitoring directional proton pumping. bo_3 oxidase had predominantly inward orientation, which in combination with a well-sealed membrane, acidified the lumen of the synthetic compartments.

- Activity of reconstituted F_1F_O-ATPase was monitored via respiratory-driven ATP synthesis in bulk.
- Activity of reconstituted SNAREs was confirmed via membrane and content mixing during ΔN-GUV/syb-LUV fusion.

Finally, the approach was extended to the growth of multicompartmentalized microcompartments. Such a platform will enable the integration of artificial organelles into artificial cell.

SNARE-mediated fusion – arguably the most promising growth approach in artificial cell context

Utilizing know-how for the formation of protein-functionalized microcompartments (obtained by optimizing fusion/electroformation growth approach), in the final study, 2–40 µm SNARE-functionalized GUVs were formed. This was the first time that SNAREs were successfully reconstituted into polymer or hybrid GUVs. Interestingly, SNAREs had an opposite effect on membrane bending rigidity than the largely hydrophobic membrane protein (*bo*$_3$ oxidase) – SNAREs rigidified both polymer and hybrid membrane. Next, fusion of ΔN-GUVs/syb-GUVs and ΔN-GUVs/syb-LUVs was explored. While epifluorescent microscopy revealed membrane mixing for both systems, ΔN-GUVs and syb-GUVs did not undergo full fusion. Meanwhile, hemifusion of ΔN-GUVs and syb-LUVs continued into pore opening, as confirmed by content mixing experiment.

Comparing the two growth mechanisms where two types of compartments are required, there are some obvious advantages of charge- in comparison to SNARE-mediated growth. First, preparation of anionic or cationic GUVs is more facile and less time-consuming than preparation of SNARE-GUVs. And second, fusion rate for charge-mediated growth is significantly faster. Therefore, the next question arises: Why even exploring SNARE-mediated fusion as a growth mechanism? The main drawback of charge-mediated growth are the limited rounds of fusion (therefore, limited growth), due to charge neutralization and exhaustion of driving force. On the other hand, this is not the case for SNARE-mediated growth, where SNARE complex can be disassembled by NSF/α-SNAP (298), which would enable another round of fusion (Figure 107). Potentially, SNARE-complex assembly/disassembly could undergo multiple rounds, until desired size is achieved (growth module of 2nd generation). Furthemore, such growth module could be integrated with an energy module: since NSF is an ATPase, ATP could be generated by light- or chemically-driven energy module. Due to highly promising growth potential via multiple SNARE-mediated fusion cycles, in the future studies, it would be important to understand and control the assembly/disassembly of the SNARE complex in hybrid and polymer compartments. We are looking with excitement how those natural machineries will perform in cell-growth mimetics. Furthermore, we are interested in exploring also other cell-mimicking phenomena, such as lipid rafts; in particular we are inspired to further explore the phenomena occurring at interface between lipid, polymer and membrane proteins in hybrid GUVs, and how

to utilize phase separation for targeted protein partitioning. Finally, our hope is that the obtained knowledge of fusion mechanisms and optimized techniques can be utilized for functional modules integration and inter-cellular communication, which will bring us closer to construction of a functional artificial tissue.

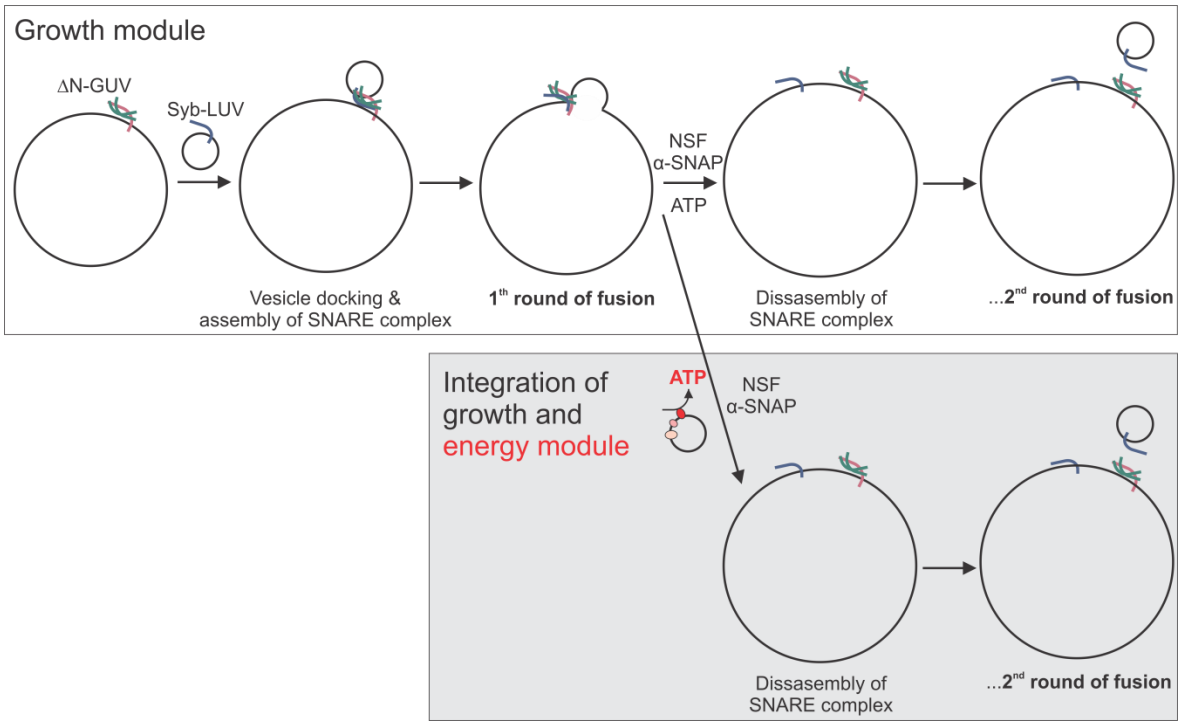

Figure 107. Growth module of 2nd generation. *Upper panel*: Construction of vesicle fusion-based growth module with unlimited growth potential (multiple successive steps of SNARE complex assembly and disassembly). First round of fusion and disassembly of SNARE complex is followed by synaptobrevin-LUVs docking and SNARE complex assembly (heterotypic fusion). *Lower panel*: Integration of growth module with energy module. ATP (required for ATPase NSF) is generated by the artificial respiratory chain.

5 References

1. Marušič N, Otrin L, Zhao Z, Lira RB, Kyrilis FL., Hamdi F, Kastritis LP, Vidaković-Koch T, Ivanov I, Sundmacher K, Dimova R (2020) Constructing artificial respiratory chain in polymer compartments: Insights into the interplay between bo_3 oxidase and the membrane. *Proc. Natl. Acad. Sci. U.S.A.* 117(26):15006–15017.
2. Marušič N, Otrin L, Rauchhaus J, Zhao Z, Kyrilis FL, Hamdi F, Kastritis PL, Dimova R, Ivanov I, Sundmacher K (2022) Increased efficiency of charge-mediated fusion in polymer/lipid hybrid membranes. *Proc. Natl. Acad. Sci. U.S.A.* (in press)
3. Marušič N, Zhao Z, Otrin L, Dimova R, Ivanov I, Sundmacher K (2021) Fusion-induced growth of biomimetic polymersomes: behavior of poly(dimethylsiloxane)-poly(ethylene oxide) vesicles in saline solutions under high agitation. *Macromol. Rapid Commun.* 43(5): 2100712.
4. Le Meins JF, Schatz C, Lecommandoux S, Sandre O (2013) Hybrid polymer/lipid vesicles: state of the art and future perspectives. *Mater. Today* 16(10):397-402.
5. Thingholm B, Schattling P, Zhang Y, Städler B (2016) Subcompartmentalized Nanoreactors as Artificial Organelle with Intracellular Activity. *Small* 12(13):1806-1814.
6. Belluati A, Thamboo S, Najer A, Maffeis V, von Planta C, Craciun I, Palivan CG, Meier W (2020) Multicompartment Polymer Vesicles with Artificial Organelles for Signal-Triggered Cascade Reactions Including Cytoskeleton Formation. *Adv. Funct. Mater.* 30(32):2002949.
7. Hindley JW, Zheleva DG, Elani Y, Charalambous K, Barter LMC, Booth PJ, Bevan CL, Law RV, Ces O (2019) Building a synthetic mechanosensitive signaling pathway in compartmentalized artificial cells. *Proc. Natl. Acad. Sci. U.S.A.* 116(34):16711-16716.
8. Elani Y, Law RV, Ces O (2014) Vesicle-based artificial cells as chemical microreactors with spatially segregated reaction pathways. *Nat. Commun.* 5(1):5305.
9. Guertin DA, Sabatini DM (2008) Chapter 12 - Cell Growth. *The Molecular Basis of Cancer (Third Edition)*, eds Mendelsohn J, Howley PM, Israel MA, Gray JW, & Thompson CB (W.B. Saunders, Philadelphia), pp 169-175.
10. Blom T, Somerharju P, Ikonen E (2011) Synthesis and biosynthetic trafficking of membrane lipids. *Cold Spring Harb. Perspect. Biol.* 3(8):a004713-a004713.
11. Kohlwein SD, Daum G, Schneiter R, Paltauf F (1996) Phospholipids: synthesis, sorting, subcellular traffic - the yeast approach. *Trends Cell Biol.* 6(7):260-266.
12. Gánti T (2003) *The Principles of Life* (Oxford University Press).
13. Cheng Z, Luisi PL (2003) Coexistence and Mutual Competition of Vesicles with Different Size Distributions. *J. Phys. Chem. B* 107(39):10940-10945.
14. Exterkate M, Caforio A, Stuart MCA, Driessen AJM (2018) Growing Membranes In Vitro by Continuous Phospholipid Biosynthesis from Free Fatty Acids. *ACS Synth. Biol.* 7(1):153-165.
15. Blanken D, Foschepoth D, Serrão AC, Danelon C (2020) Genetically controlled membrane synthesis in liposomes. *Nat. Commun.* 11(1):4317.
16. Ivanov I, Lira RB, Tang T-YD, Franzmann T, Klosin A, da Silva LC, Hyman A, Landfester K, Lipowsky R, Sundmacher K, Dimova R (2019) Directed Growth of Biomimetic Microcompartments. *Adv. Biosyst.* 3(6):1800314.
17. Lira RB, Robinson T, Dimova R, Riske KA (2019) Highly Efficient Protein-free Membrane Fusion: A Giant Vesicle Study. *Biophys. J.* 116(1):79-91.
18. Deshpande S, *et al.* (2019) Membrane Tension–Mediated Growth of Liposomes. *Small* 15(38):1902898.
19. Seredyuk VA, Menger FM (2004) Membrane-bound protein in giant vesicles: induced contraction and growth. *J. Am. Chem. Soc.* 126(39):12256-12257.
20. Rideau E, Dimova R, Schwille P, Wurm FR., Landfester K (2018) Liposomes and polymersomes: a comparative review towards cell mimicking. *Chem. Soc. Rev.* 47:8572-8610.

21. Otrin L, Marušič N, Bednarz C, Vidaković-Koch T, Lieberwirth I, Landfester K, Sundmacher K (2017) Toward Artificial Mitochondrion: Mimicking Oxidative Phosphorylation in Polymer and Hybrid Membranes. *Nano Lett.* 17(11):6816-6821.
22. Khan S, Li M, Muench SP, Jeuken LJ, Beales PA (2016) Durable proteo-hybrid vesicles for the extended functional lifetime of membrane proteins in bionanotechnology. *Chem. Commun.* 52(73):11020-11023.
23. Gaitzsch J, Hirschi S, Freimann S, Fotiadis D, Meier W (2019) Directed Insertion of Light-Activated Proteorhodopsin into Asymmetric Polymersomes from an ABC Block Copolymer. *Nano Lett.* 19(4):2503-2508.
24. Varlas S, Keogh R, Xie Y, Horswell SL, Foster JC, O'Reilly RK (2019) Polymerization-Induced Polymersome Fusion. *J. Am. Chem. Soc.* 141(51):20234-20248.
25. Kurisu M, Aoki H, Jimbo T, Sakuma Y, Imai M, Serrano-Luginbühl S, Walde P (2019) Reproduction of vesicles coupled with a vesicle surface-confined enzymatic polymerisation. *Commun. Chem.* 2(1):117.
26. De Mel JU, Gupta S, Perera RM, Ngo L, Zolnierczuk P, Bleuel M, Pingali SV, Schneider GJ (2020) Influence of External NaCl Salt on Membrane Rigidity of Neutral DOPC Vesicles. *Langmuir* 36(32):9356-9367.
27. Steinkühler J, De Tillieux P, Knorr RL, Lipowsky R, Dimova R (2018) Charged giant unilamellar vesicles prepared by electroformation exhibit nanotubes and transbilayer lipid asymmetry. *Sci. Rep.* 8(1):11838.
28. Veatch SL, Keller SL (2003) Separation of liquid phases in giant vesicles of ternary mixtures of phospholipids and cholesterol. *Biophys. J.* 85(5):3074-3083.
29. Onaca O, Enea R, Hughes DW, Meier W (2009) Stimuli-Responsive Polymersomes as Nanocarriers for Drug and Gene Delivery. *Macromol. Biosci.* 9(2):129-139.
30. Palivan CG, Goers R, Najer A, Zhang X, Car A, Meier W. (2016) Bioinspired polymer vesicles and membranes for biological and medical applications. *Chem. Soc. Rev.* 45(2):377-411.
31. Choi H-J, Montemagno CD (2005) Artificial Organelle: ATP Synthesis from Cellular Mimetic Polymersomes. *Nano Lett.* 5(12):2538-2542.
32. Kleineberg C, Wölfer C, Abbasnia A, Pischel D, Bednarz C, Ivanov I, Heitkamp T, Börsch M, Sundmacher K, Vidaković-Koch T (2020) Light-Driven ATP Regeneration in Diblock/Grafted Hybrid Vesicles. *Chembiochem* 21(15):2149-2160.
33. Lee JS, Feijen J (2012) Polymersomes for drug delivery: design, formation and characterization. *J. Control Release* 161(2):473-483.
34. Discher DE, Ortiz V, Srinivas G, Klein ML, Kim Y, Christian D, Cai S, Photos P, Ahmed F (2007) Emerging applications of polymersomes in delivery: From molecular dynamics to shrinkage of tumors. *Prog. Polym. Sci.* 32(8):838-857.
35. Meng F, Zhong Z, Feijen J (2009) Stimuli-Responsive Polymersomes for Programmed Drug Delivery. *Biomacromolecules* 10(2):197-209.
36. Egli S, Nussbaumer MG, Balasubramanian V, Chami M, Bruns N, Palivan C, Meier W (2011) Biocompatible Functionalization of Polymersome Surfaces: A New Approach to Surface Immobilization and Cell Targeting Using Polymersomes. *J. Am. Chem. Soc.* 133(12):4476-4483.
37. Lee Y, Chang J-B, Kim HK, Park TG (2006) Stability studies of biodegradable polymersomes prepared by emulsion solvent evaporation method. *Macromol. Res.* 14(3):359-364.
38. Mata A, Fleischman AJ, Roy S (2005) Characterization of Polydimethylsiloxane (PDMS) Properties for Biomedical Micro/Nanosystems. *Biomed. Microdevices* 7(4):281-293.
39. Poschenrieder ST, Schiebel SK, Castiglione K (2018) Stability of polymersomes with focus on their use as nanoreactors. *Eng. Life Sci.* 18(2):101-113.
40. Rodríguez-García R, Mell M, López-Montero I, Netzel J, Hellweg T, Monroy F (2011) Polymersomes: smart vesicles of tunable rigidity and permeability. *Soft Matter* 7(4):1532.
41. Le Meins JF, Sandre O, Lecommandoux S (2011) Recent trends in the tuning of polymersomes' membrane properties. *Soft matter* 34(2):14.

42. Xiao M, Liu J, Yang J, Wang R, Xie D. (2013) Biomimetic membrane control of block copolymer vesicles with tunable wall thickness. *Soft Matter* 9(8):2434-2442.
43. Petit J, Thomi L, Schultze J, Makowski M, Negwer I, Koynov K, Herminghaus S, Wurm FR, Bäumchen O, Landfester K (2018) A modular approach for multifunctional polymersomes with controlled adhesive properties. *Soft Matter* 14(6):894-900.
44. Kadenbach B (2003) Intrinsic and extrinsic uncoupling of oxidative phosphorylation. *Biochim. Biophys. Acta 1604* 1604(2):77–94.
45. Murphy MP (2009) How mitochondria produce reactive oxygen species. *Biochem.* 417(1):1-13.
46. Girotti AW (1985) Mechanisms of lipid peroxidation. *Free Radic. Biol. Med.* 1(2):87-95.
47. Schnitzer E, Pinchuk I, Lichtenberg D (2007) Peroxidation of liposomal lipids. *Eur. Biophys. J.* 36(4-5):499-515.
48. Hu A, Cui Y, Wei X, Lu Z, Ngai T (2010) Hydrogen-Bonding-Induced Complexation of Polydimethylsiloxane-graft-poly(ethylene oxide) and Poly(acrylic acid)-block-polyacrylonitrile Micelles in Water. *Langmuir* 26(18):14502-14508.
49. Chemin M, Brun P-M, Lecommandoux S, Sandre O, Le Meins J-F (2012) Hybrid polymer/lipid vesicles: fine control of the lipid and polymer distribution in the binary membrane. *Soft Matter* 8(10):2867.
50. Jukarainen HJ, Clarson SJ, Seppälä JV, Retzinger GS, Ruohonen JK (2012) Block and Graft Copolymers of Poly(ethylene glycol) and Poly(dimethylsiloxane) for Blood Contacting Biomedical Materials Applications. *Silicon* 4(4):231-238.
51. Ranjan A, Townsley BT, Ichihashi Y, Sinha NR, Chitwood DH (2015) An Intracellular Transcriptomic Atlas of the Giant Coenocyte Caulerpa taxifolia. *PLoS Genet.* 11(1):e1004900.
52. Foulon E, Not F, Jalabert F, Cariou T, Massana R, Simon N (2008) Ecological niche partitioning in the picoplanktonic green alga Micromonas pusilla: evidence from environmental surveys using phylogenetic probes. *Environ. Microbiol.* 10(9):2433-2443.
53. Chien A-C, Hill Norbert S, Levin Petra A (2012) Cell Size Control in Bacteria. *Current Biology* 22(9):R340-R349.
54. Jesorka A, Orwar O (2008) Liposomes: technologies and analytical applications. *Annu. Rev. Anal. Chem.* 1:801-832.
55. Kita-Tokarczyk K, Grumelard J, Haefele T, Meier W (2005) Block copolymer vesicles—using concepts from polymer chemistry to mimic biomembranes. *Polymer* 46(11):3540-3563.
56. Karamdad K, Law RV, Seddon JM, Brooks NJ, Ces O (2015) Preparation and mechanical characterisation of giant unilamellar vesicles by a microfluidic method. *Lab Chip* 15(2):557-562.
57. Altamura E, Albanese P, Marotta R, Milano F, Fiore M, Trotta M, Stano P, Mavelli F (2021) Chromatophores efficiently promote light-driven ATP synthesis and DNA transcription inside hybrid multicompartment artificial cells. *Proc. Natl. Acad. Sci. U.S.A.* 118(7):e2012170118.
58. van Swaay D, deMello A (2013) Microfluidic methods for forming liposomes. *Lab Chip* 13(5):752-767.
59. Dao TPT, Fauquignon M, Fernandes F, Ibarboure E, Vax A, Prieto M, Le Meins JF (2017) Membrane properties of giant polymer and lipid vesicles obtained by electroformation and pva gel-assisted hydration methods. *Colloids Surf. A: Physicochem. Eng. Asp.* 533:347-353.
60. Lira RB, Dimova R, Riske KA (2014) Giant unilamellar vesicles formed by hybrid films of agarose and lipids display altered mechanical properties. *Biophys. J.* 107(7):1609-1619.
61. Rideau E, Wurm FR, Landfester K (2019) Self-Assembly of Giant Unilamellar Vesicles by Film Hydration Methodologies. *Adv. Biosyst.* 3(6):1800324.
62. Kim S-H, Shum HC, Kim JW, Cho J-C, Weitz DA (2011) Multiple Polymersomes for Programmed Release of Multiple Components. *J. Am. Chem. Soc.* 133(38):15165-15171.
63. Rigaud JL, Pitard B, Levy D (1995) Reconstitution of membrane proteins into liposomes: application to energy-transducing membrane proteins. *Biochim. Biophys. Acta* 1231(3):223-246.

64. Seneviratne R, Khan S, Moscrop E, Rappolt M, Muench SP, Jeuken LJC, Beales PA (2018) A reconstitution method for integral membrane proteins in hybrid lipid-polymer vesicles for enhanced functional durability. *Methods* 147:142-149.
65. Chung D-w, Lim JC (2009) Study on the effect of structure of polydimethylsiloxane grafted with polyethyleneoxide on surface activities. *Colloids Surf. A: Physicochem. Eng. Asp.* 336(1):35-40.
66. Althoff T, Davies KM, Schulze S, Joos F, Kühlbrandt W (2012) GRecon: a method for the lipid reconstitution of membrane proteins. *Angew. Chem. Int. Ed.* 51(33):8343-8347.
67. Rigaud J-L, Lévy D (2003) Reconstitution of Membrane Proteins into Liposomes. *Meth. Enzymol.* 372:65-86.
68. Altamura E, Milano F, Tangorra RR, Trotta M, Omar OH, Stano P, Mavelli F (2017) Highly oriented photosynthetic reaction centers generate a proton gradient in synthetic protocells. *Proc. Natl. Acad. Sci. U.S.A.* 114(15):3837-3842.
69. Aimon S, Manzi J, Schmidt D, Poveda Larrosa JA, Bassereau P, Toombes GE (2011) Functional reconstitution of a voltage-gated potassium channel in giant unilamellar vesicles. *PLoS One* 6(10):e25529.
70. Doeven MK, Folgering JH, Krasnikov V, Geertsma ER, van den Bogaart G, Poolman B (2005) Distribution, lateral mobility and function of membrane proteins incorporated into giant unilamellar vesicles. *Biophys. J.* 88(2):1134-1142.
71. Girard P, Pecreaux J, Lenoir G, Falson P, Rigaud JL, Bassereau P (2004) A new method for the reconstitution of membrane proteins into giant unilamellar vesicles. *Biophys. J.* 87(1):419-429.
72. Lee KY, Park SJ, Lee KA, Kim SH, Kim H, Meroz Y, Mahadevan L, Jung KH, Ahn TK, Parker KK, Shin K (2018) Photosynthetic artificial organelles sustain and control ATP-dependent reactions in a protocellular system. *Nat. Biotechnol.* 36(6):530-535.
73. Witkowska A, Jablonski L, Jahn R (2018) A convenient protocol for generating giant unilamellar vesicles containing SNARE proteins using electroformation. *Sci. Rep.* 8(1):9422.
74. Tareste D, Shen J, Melia TJ, Rothman JE (2008) SNAREpin/Munc18 promotes adhesion and fusion of large vesicles to giant membranes. *Proc. Natl. Acad. Sci. U.S.A.* 105(7):2380-2385.
75. Bacia K, Schuette CG, Kahya N, Jahn R, Schwille P (2004) SNAREs prefer liquid-disordered over "raft" (liquid-ordered) domains when reconstituted into giant unilamellar vesicles. *J. Biol. Chem.* 279(36):37951-37955.
76. Almendro-Vedia VG, Natale P, Mell M, Bonneau S, Monroy F, Joubert F, Lopez-Montero I (2017) Nonequilibrium fluctuations of lipid membranes by the rotating motor protein F1F0-ATP synthase. *Proc. Natl. Acad. Sci. U.S.A.* 114(43):11291-11296.
77. Wijekoon CJ, Udagedara SR, Knorr RL, Dimova R, Wedd AG, Xiao Z (2017) Copper ATPase CopA from Escherichia coli: Quantitative Correlation between ATPase Activity and Vectorial Copper Transport. *J. Am. Chem. Soc.* 139(12):4266-4269.
78. Dezi M, Di Cicco A, Bassereau P, Lévy D (2013) Detergent-mediated incorporation of transmembrane proteins in giant unilamellar vesicles with controlled physiological contents. *Proc. Natl. Acad. Sci. U.S.A.* 110(18):7276-7281.
79. Sjoholm J, Bergstrand J, Nilsson T, Sachl R, Ballmoos CV, Widengren J, Brzezinski P (2017) The lateral distance between a proton pump and ATP synthase determines the ATP-synthesis rate. *Sci. Rep.* 7(1):2926.
80. Biner O, Schick T, Muller Y, von Ballmoos C (2016) Delivery of membrane proteins into small and giant unilamellar vesicles by charge-mediated fusion. *FEBS Lett.* 590(14):2051-2062.
81. Garni M, Thamboo S, Schoenenberger CA, Palivan CG (2017) Biopores/membrane proteins in synthetic polymer membranes. *Biochim. Biophys. Acta* 1859(4):619-638.
82. Dimova R, Seifert U, Pouligny B, Förster S, Döbereiner H-G (2002) Hyperviscous diblock copolymer vesicles. *Eur. Phys. J. E* 7(3):241-250.
83. Goers R, Thoma J, Ritzmann N, Di Silvestro A, Alter C, Gunkel-Grabole G, Fotiadis D, Müller D. J, Meier W (2018) Optimized reconstitution of membrane proteins into synthetic membranes. *Commun. Chem.* 1(1):35.

84. Graff A, Fraysse-Ailhas C, Palivan CG, Grzelakowski M, Friedrich T, Vebert C, Gescheidt G, Meier W (2010) Amphiphilic Copolymer Membranes Promote NADH:Ubiquinone Oxidoreductase Activity: Towards an Electron-Transfer Nanodevice. *Macromol. Chem. Phys.* 211(2):229-238.
85. Grigorieff N, Ceska TA, Downing KH, Baldwin JM, Henderson R (1996) Electron-crystallographic Refinement of the Structure of Bacteriorhodopsin. *J. Mol. Biol.* 259(3):393-421.
86. Jahn R, Scheller RH (2006) SNAREs — engines for membrane fusion. *Nat. Rev. Mol. Cell Biol.* 7(9):631-643.
87. Söllner T, Whiteheart SW, Brunner M, Erdjument-Bromage H, Geromanos S, Tempst P, Rothman JE (1993) SNAP receptors implicated in vesicle targeting and fusion. *Nature* 362(6418):318-324.
88. Weber T, Zemelman BV, McNew JA, Westermann B, Gmachl M, Parlati F, Söllner TH, Rothman JE (1998) SNAREpins: Minimal Machinery for Membrane Fusion. *Cell* 92(6):759-772.
89. Jahn R, Lang T, Südhof TC (2003) Membrane Fusion. *Cell* 112(4):519-533.
90. Leabu M (2006) Membrane fusion in cells: molecular machinery and mechanisms. *J. Cell Mol. Med.* 10(2):423-427.
91. Huppertz B, Bartz C, Kokozidou M (2006) Trophoblast fusion: fusogenic proteins, syncytins and ADAMs, and other prerequisites for syncytial fusion. *Micron* 37(6):509-517.
92. Harrison SC (2015) Viral membrane fusion. *Virology* 479-480:498-507.
93. Kendall DA, MacDonald RC (1982) A fluorescence assay to monitor vesicle fusion and lysis. *J. Biol. Chem.* 257(23):13892-13895.
94. Wilschut J, Duzgunes N, Fraley R, Papahadjopoulos D (1980) Studies on the mechanism of membrane fusion: kinetics of calcium ion induced fusion of phosphatidylserine vesicles followed by a new assay for mixing of aqueous vesicle contents. *Biochemistry* 19(26):6011-6021.
95. Dfizgtine N, Nir S, Wilschut J, Bentz J, Newton C, Portis A, Papahadjopoulos D (1981) Calcium- and Magnesium-Induced Fusion of Mixed Phosphatidylserine/Phosphatidylcholine Vesicles: Effect of Ion Binding. *J. Membr. Biol.* (59):115-125.
96. Papahadjopoulos D, Poste G, Schaeffer BE, Vail WJ (1974) Membrane fusion and molecular segregation in phospholipid vesicles. *Biochim. Biophys. Acta* 352(1):10-28.
97. Pantazatos DP, MacDonald RC (1999) Directly Observed Membrane Fusion Between Oppositely Charged Phospholipid Bilayers. *J. Membr. Biol.* (170):27–38.
98. Pantazatos DP, Pantazatos SP, MacDonald RC (2003) Bilayer mixing, fusion, and lysis following the interaction of populations of cationic and anionic phospholipid bilayer vesicles. *J. Membr. Biol.* 194(2):129-139.
99. Koike S, Jahn R (2019) SNAREs define targeting specificity of trafficking vesicles by combinatorial interaction with tethering factors. *Nat. Commun.* 10(1):1608.
100. Ungermann C, Langosch D (2005) Functions of SNAREs in intracellular membrane fusion and lipid bilayer mixing. *J. Cell Sci.* 118(17):3819–3828.
101. Floyd DL, Ragains JR, Skehel JJ, Harrison SC, van Oijen AM (2008) Single-particle kinetics of influenza virus membrane fusion. *Proc. Natl. Acad. Sci. U.S.A.* 105(40):15382-15387.
102. Kim IS, Jenni S, Stanifer ML, Roth E, Whelan SP, van Oijen AM, Harrison SC (2017) Mechanism of membrane fusion induced by vesicular stomatitis virus G protein. *Proc. Natl. Acad. Sci. U.S.A.* 114(1):E28-e36.
103. Nordlund G, Brzezinski P, von Ballmoos C (2014) SNARE-fusion mediated insertion of membrane proteins into native and artificial membranes. *Nat. Commun.* 5(1):4303.
104. Ishmukhametov RR, Russell AN, Berry RM (2016) A modular platform for one-step assembly of multi-component membrane systems by fusion of charged proteoliposomes. *Nat. Commun.* 7:13025.
105. Weiss M, Frohnmayer JP, Benk LT, Haller B, Janiesch J-W, Heitkamp T, Börsch M, Lira RB, Dimova R, Lipowsky R, Bodenschatz E, Baret J-C, Vidakovic-Koch T, Sundmacher K, Platzman I, Spatz JP (2018) Sequential bottom-up assembly of mechanically stabilized synthetic cells by microfluidics. *Nat. Mater.* 17(1):89-96.

106. Otrin L, Witkowska A, Marušič N, Zhao Z, Lira RB, Kyrilis FL, Hamdi F, Ivanov I, Lipowsky R, Kastritis PL, Dimova R, Sundmacher K, Jahn R, Vidaković-Koch T (2021) En route to dynamic life processes by SNARE-mediated fusion of polymer and hybrid membranes. *Nat. Commun.* 12(1):4972.
107. Mondal Roy S, Sarkar M (2011) Membrane fusion induced by small molecules and ions. *J Lipids* 2011:528784.
108. Düzgüneş N, Wilschut J, Fraley R, Papahadjopoulos D (1981) Studies on the mechanism of membrane fusion. Role of head-group composition in calcium- and magnesium-induced fusion of mixed phospholipid vesicles. *Biochim. Biophys. Acta* 642(1):182-195.
109. Wagle S, Georgiev VN, Robinson T, Dimova R, Lipowsky R, Grafmüller A (2019) Interaction of SNARE Mimetic Peptides with Lipid bilayers: Effects of Secondary Structure, Bilayer Composition and Lipid Anchoring. *Sci. Rep.* 9(1):7708.
110. Marsden HR, Elbers NA, Bomans P, Sommerdijk N, Kros A (2009) A reduced SNARE model for membrane fusion. *Angew. Chem. Int. Ed.* 48 13:2330-2333.
111. Lygina AS, Meyenberg K, Jahn R, Diederichsen U (2011) Transmembrane Domain Peptide/Peptide Nucleic Acid Hybrid as a Model of a SNARE Protein in Vesicle Fusion. *Angew. Chem. Int. Ed.* 50(37):8597-8601.
112. Wehland J-D, Lygina AS, Kumar P, Guha S, Hubrich BE, Jahn R, Diederichsen U (2016) Role of the transmembrane domain in SNARE protein mediated membrane fusion: peptide nucleic acid/peptide model systems. *Mol. Biosyst.* 12(9):2770-2776.
113. Chan YH, van Lengerich B, Boxer SG (2009) Effects of linker sequences on vesicle fusion mediated by lipid-anchored DNA oligonucleotides. *Proc. Natl. Acad. Sci. U.S.A.* 106(4):979-984.
114. Löffler PMG, Ries O, Rabe A, Okholm AH, Thomsen RP, Kjems J, Vogel S (2017) A DNA-Programmed Liposome Fusion Cascade. *Angew. Chem. Int. Ed.* 56(43):13228-13231.
115. Haluska CK, Riske KA, Marchi-Artzner V, Lehn JM, Lipowsky R, Dimova R (2006) Time scales of membrane fusion revealed by direct imaging of vesicle fusion with high temporal resolution. *Proc. Natl. Acad. Sci. U.S.A.* 103(43):15841-15846.
116. Marchi-Artzner V, Gulik-Krzywicki T, Guedeau-Boudeville M-A, Gosse C, Sanderson JM, Dedieu J-C, Lehn J-M (2001) Selective Adhesion, Lipid Exchange and Membrane-Fusion Processes between Vesicles of Various Sizes Bearing Complementary Molecular Recognition Groups. *ChemPhysChem* 2(6):367-376.
117. Richard A, Marchi-Artzner V, Lalloz M-N, Brienne M-J, Artzner F, Gulik-Krzywicki T, Guedeau-Boudeville M-A, Lehn J-M (2004) Fusogenic supramolecular vesicle systems induced by metal ion binding to amphiphilic ligands. *Proc. Natl. Acad. Sci. U.S.A.* 101(43):15279-15284.
118. Suzuki Y, Nagai KH, Zinchenko A, Hamada T (2017) Photoinduced Fusion of Lipid Bilayer Membranes. *Langmuir* 33(10):2671-2676.
119. Rørvig-Lund A, Bahadori A, Semsey S, Bendix PM, Oddershede LB (2015) Vesicle Fusion Triggered by Optically Heated Gold Nanoparticles. *Nano Lett.* 15(6):4183-4188.
120. Kulin S, Kishore R, Helmerson K, Locascio L (2003) Optical Manipulation and Fusion of Liposomes as Microreactors. *Langmuir* 19(20):8206-8210.
121. Dreher Y, Jahnke K, Bobkova E, Spatz JP, Göpfrich K (2021) Division and Regrowth of Phase-Separated Giant Unilamellar Vesicles**. *Angew. Chem. Int. Ed.* 60(19):10661-10669.
122. Rikken RSM, Engelkamp H, Nolte RJM, Maan JC, van Hest JCM, Wilson DA, Christianen PCM (2016) Shaping polymersomes into predictable morphologies via out-of-equilibrium self-assembly. *Nat. Commun.* 7(1):12606.
123. Sanson C, Le Meins J-F, Schatz C, Soum A, Lecommandoux S (2010) Temperature responsive poly(trimethylene carbonate)-block-poly(L-glutamic acid) copolymer: polymersomes fusion and fission. *Soft Matter* 6(8):1722-1730.
124. Litschel T, Ganzinger KA, Movinkel T, Heymann M, Robinson T, Mutschler H, Schwille P (2018) Freeze-thaw cycles induce content exchange between cell-sized lipid vesicles. *New J. Phys.* 20(5):055008.

125. Su W, Luo Y, Yan Q, Wu S, Han K, Zhang Q, Gu Y, Li Y (2007) Photoinduced Fusion of Micro-Vesicles Self-Assembled from Azobenzene-Containing Amphiphilic Diblock Copolymers. *Macromol. Rapid Commun.* 28(11):1251-1256.
126. Henderson IM, Paxton WF (2014) Salt, shake, fuse--giant hybrid polymer/lipid vesicles through mechanically activated fusion. *Angew. Chem. Int. Ed.* 53(13):3372-3376.
127. Chernomordik LV, Kozlov MM (2008) Mechanics of membrane fusion. *Nat. Struct. Mol. Biol.* 15(7):675-683.
128. Martens S, McMahon HT (2008) Mechanisms of membrane fusion: disparate players and common principles. *Nat. Rev. Mol. Cell Biol.* 9(7):543-556.
129. Lentz BR, Malinin V, Haque ME, Evans K (2000) Protein machines and lipid assemblies: current views of cell membrane fusion. *Curr. Opin. Struct. Biol.* 10(5):607-615.
130. Chanturiya A, Chernomordik LV, Zimmerberg J (1997) Flickering fusion pores comparable with initial exocytotic pores occur in protein-free phospholipid bilayers. *Proc. Natl. Acad. Sci. U.S.A.* 94(26):14423-14428.
131. Chernomordik LV, Kozlov MM (2003) Protein-Lipid Interplay in Fusion and Fission of Biological Membranes. *Annu. Rev. Biochem.* 72(1):175-207.
132. Yang L, Huang HW (2003) A Rhombohedral Phase of Lipid Containing a Membrane Fusion Intermediate Structure. *Biophys. J.* 84(3):1808-1817.
133. Malinin VS, Frederik P, Lentz BR (2002) Osmotic and Curvature Stress Affect PEG-Induced Fusion of Lipid Vesicles but Not Mixing of Their Lipids. *Biophys. J.* 82(4):2090-2100.
134. Chernomordik LV, Melikyan GB, Chizmadzhev YA (1987) Biomembrane fusion: a new concept derived from model studies using two interacting planar lipid bilayers. *Biochim. Biophys. Acta - Biomembr.* 906(3):309-352.
135. Luo L, Eisenberg A (2001) Thermodynamic Size Control of Block Copolymer Vesicles in Solution. *Langmuir* 17(22):6804-6811.
136. Lin Y-L, Chang H-Y, Sheng Y-J, Tsao H-K (2014) Self-assembled polymersomes formed by symmetric, asymmetric and side-chain-tethered coil–rod–coil triblock copolymers. *Soft Matter* 10(11):1840-1852.
137. Lin Y-L, Chang H-Y, Sheng Y-J, Tsao H-K (2014) The fusion mechanism of small polymersomes formed by rod–coil diblock copolymers. *Soft Matter* 10(10):1500-1511.
138. Witkowska A, Jahn R (2017) Rapid SNARE-Mediated Fusion of Liposomes and Chromaffin Granules with Giant Unilamellar Vesicles. *Biophys. J.* 113(6):1251-1259.
139. Henderson IM, Collins AM, Quintana HA, Montaño GA, Martinez JA, Paxton WF (2016) Lights on: Dye dequenching reveals polymersome fusion with polymer, lipid and stealth lipid vesicles. *Polymer* 83:239-245.
140. Liu X, Seven AB, Xu J, Esser V, Su L, Ma C, Rizo J (2017) Simultaneous lipid and content mixing assays for in vitro reconstitution studies of synaptic vesicle fusion. *Nat. Protoc.* 12(9):2014-2028.
141. Kyoung M, Zhang Y, Diao J, Chu S, Brunger AT (2013) Studying calcium-triggered vesicle fusion in a single vesicle-vesicle content and lipid-mixing system. *Nat. Protoc.* 8(1):1-16.
142. Pantazatos DP, MacDonald RC (1999) Directly Observed Membrane Fusion Between Oppositely Charged Phospholipid Bilayers. *J. Membr. Biol.* 170(1):27-38.
143. Meleard P, Gerbeaud C, Bardusco P, Jeandaine N, Mitov MD, Fernandez-Puente L (1998) Mechanical properties of model membranes studied from shape transformations of giant vesicles. *Biochimie* 80(5-6):401-413.
144. Dimova R (2014) Recent developments in the field of bending rigidity measurements on membranes. *Adv. Colloid Interface Sci.* 208:225-234.
145. Manca F, Pincet F, Truskinovsky L, Rothman JE, Foret L, Caruel M (2019) SNARE machinery is optimized for ultrafast fusion. *Proc. Natl. Acad. Sci. U.S.A.* 116(7):2435-2442.
146. Bassereau P, Sorre B, Lévy A (2014) Bending lipid membranes: Experiments after W. Helfrich's model. *Adv. Colloid Interface Sci.* 208:47-57.

147. Lin LC, Gov N, Brown FL (2006) Nonequilibrium membrane fluctuations driven by active proteins. *J. Chem. Phys.* 124(7):74903.
148. Manneville J-B, Bassereau P, Lévy D, Prost J (1999) Activity of Transmembrane Proteins Induces Magnification of Shape Fluctuations of Lipid Membranes. *Phys. Rev. Lett.* 82:4356.
149. Girard P, Prost J, Bassereau P (2005) Passive or active fluctuations in membranes containing proteins. *Phys. Rev. Lett.* 94(8):088102.
150. Kang M, Day CA, Kenworthy AK, DiBenedetto E (2012) Simplified equation to extract diffusion coefficients from confocal FRAP data. *Traffic* 13(12):1589-1600.
151. Mueller F, Mazza D, Stasevich TJ, McNally JG (2010) FRAP and kinetic modeling in the analysis of nuclear protein dynamics: what do we really know? *Curr. Opin. Cell Biol.* 22(3):403-411.
152. Day CA, Kenworthy AK (2009) Tracking microdomain dynamics in cell membranes. *Biochim. Biophys. Acta Biomemb*. 1788(1):245-253.
153. Itel F, Chami M, Najer A, Lörcher S, Wu D, Dinu IA, Meier W (2014) Molecular Organization and Dynamics in Polymersome Membranes: A Lateral Diffusion Study. *Macromolecules* 47(21):7588-7596.
154. Nam J, Beales PA, Vanderlick TK (2011) Giant Phospholipid/Block Copolymer Hybrid Vesicles: Mixing Behavior and Domain Formation. *Langmuir* 27(1):1-6.
155. Heinemann F, Betaneli V, Thomas FA, Schwille P (2012) Quantifying Lipid Diffusion by Fluorescence Correlation Spectroscopy: A Critical Treatise. *Langmuir* 28(37):13395-13404.
156. Granek R, Pierrat S (1999) Enhanced Transverse Diffusion in Active Biomembranes. *Physical Review Letters* 83(4):872-875.
157. Howell JI, Ahkong QF, Cramp FC, Fisher D, Tampion W, Lucy JA (1972) Membrane fluidity and membrane fusion. *Biochem.* 130(1):44P.
158. Prives J, Shinitzky M (1977) Increased membrane fluidity precedes fusion of muscle cells. *Nature* 268(5622):761-763.
159. Noutsi P, Gratton E, Chaieb S (2016) Assessment of Membrane Fluidity Fluctuations during Cellular Development Reveals Time and Cell Type Specificity. *PLoS One* 11(6):e0158313.
160. Miyawaki A (2011) Proteins on the move: insights gained from fluorescent protein technologies. *Nat. Rev. Mol. Cell Biol.* 12(10):656-668.
161. Poojari C, Wilkosz N, Lira RB, Dimova R, Jurkiewicz P, Petka R, Kepczynski M, Róg T (2019) Behavior of the DPH fluorescence probe in membranes perturbed by drugs. *Chem. Phys. Lipids* 223:104784.
162. Harris FM, Best KB, Bell JD (2002) Use of laurdan fluorescence intensity and polarization to distinguish between changes in membrane fluidity and phospholipid order. *Biochim. Biophys. Acta Biomembr.* 1565(1):123-128.
163. Lowry GV, Hill RJ, Harper S, Rawle AF, Hendren CO, Klaessig F, Nobbmann U, Sayre P, Rumble J (2016) Guidance to improve the scientific value of zeta-potential measurements in nanoEHS. *Environ. Sci. Nano* 3(5):953-965.
164. Midekessa G, Godakumara K, Ord J, Viil J, Lättekivi F, Dissanayake K, Kopanchuk S, Rinken A, Andronowska A, Bhattacharjee S, Rinken T, Fazeli A (2020) Zeta Potential of Extracellular Vesicles: Toward Understanding the Attributes that Determine Colloidal Stability. *ACS Omega* 5(27):16701-16710.
165. Nelson DA, Shiveshwarkar P, Lim B, Rojas G, Abure I, Shrestha A, Jaworski J (2020) Tuning the Surface Charge of Self-Assembled Polydiacetylene Vesicles to Control Aggregation and Cell Binding. *Biosensors* 10(10):132.
166. Ho JCS, Rangamani P, Liedberg B, Parikh AN (2016) Mixing Water, Transducing Energy, and Shaping Membranes: Autonomously Self-Regulating Giant Vesicles. *Langmuir* 32(9):2151-2163.
167. Paula S, Volkov AG, Van Hoek AN, Haines TH, Deamer DW (1996) Permeation of protons, potassium ions, and small polar molecules through phospholipid bilayers as a function of membrane thickness. *Biophys. J.* 70(1):339-348.

168. Seigneuret M, Rigaud JL (1986) Analysis of passive and light-driven ion movements in large bacteriorhodopsin liposomes reconstituted by reverse-phase evaporation. 1. Factors governing the passive proton permeability of the membrane. *Biochemistry* 25(21):6716-6722.
169. Li M, Jørgensen SK, McMillan DGG, Krzemiński Ł, Daskalakis NN, Partanen RH, Tutkus M, Tuma R, Stamou D, Hatzakis NS, Jeuken LJC (2015) Single Enzyme Experiments Reveal a Long-Lifetime Proton Leak State in a Heme-Copper Oxidase. *J. Am. Chem. Soc.* 137(51):16055-16063.
170. Kuyper CL, Kuo JS, Mutch SA, Chiu DT (2006) Proton Permeation into Single Vesicles Occurs via a Sequential Two-Step Mechanism and Is Heterogeneous. *J. Am. Chem. Soc.* 128(10):3233-3240.
171. Seigneuret M, Rigaud JL (1986) Analysis of passive and light-driven ion movements in large bacteriorhodopsin liposomes reconstituted by reverse-phase evaporation. 2. Influence of passive permeability and back-pressure effects upon light-induced proton uptake. *Biochemistry* 25(21):6723-6730.
172. von Ballmoos C, Biner O, Nilsson T, Brzezinski P (2016) Mimicking respiratory phosphorylation using purified enzymes. *Biochim. Biophys. Acta* 1857(4):321-331.
173. Beard DA (2005) A biophysical model of the mitochondrial respiratory system and oxidative phosphorylation. *PLoS Comput. Biol.* 1(4):e36.
174. Wiedenmann A, Dimroth P, von Ballmoos C (2008) $\Delta\psi$ and ΔpH are equivalent driving forces for proton transport through isolated F0 complexes of ATP synthases. *Biochim. Biophys. Acta Bioenerg.* 1777(10):1301-1310.
175. Lande MB, Donovan JM, Zeidel ML (1995) The Relationship between Membrane Fluidity and Permeabilities to Water, Solutes, Ammonia, and Protons *J. Gen. Physiol.* Volume 106, 67-84
176. Clement NR, Gould JM (1981) Pyranine (8-hydroxy-1,3,6-pyrenetrisulfonate) as a probe of internal aqueous hydrogen ion concentration in phospholipid vesicles. *Biochemistry* 20(6):1534-1538.
177. Kano K, Fendler JH (1978) Pyranine as a sensitive pH probe for liposome interiors and surfaces. pH gradients across phospholipid vesicles. *Biochim. Biophys. Acta Biomembr.* 509(2):289-299.
178. Gan BS, Krump E, Shrode LD, Grinstein S (1998) Loading pyranine via purinergic receptors or hypotonic stress for measurement of cytosolic pH by imaging. *Am. J. Physiol. Cell Physiol.* 275(4):C1158-1166.
179. Wu J, Eisenberg A (2006) Proton Diffusion across Membranes of Vesicles of Poly(styrene-b-acrylic Acid) Diblock Copolymers. *J. Am. Chem. Soc.* 128:2880-2884.
180. Peña A, Ramírez J, Rosas G, Calahorra M (1995) Proton pumping and the internal pH of yeast cells, measured with pyranine introduced by electroporation. *J. Bacteriol. Res.* 177(4):1017-1022.
181. Giuliano KA, Gillies RJ (1987) Determination of intracellular pH of BALB/c-3T3 cells using the fluorescence of pyranine. *Anal. Biochem.* 167(2):362-371.
182. Damiano E, Bassilana M, Rigaud JL, Leblanc G (1984) Use of the pH sensitive fluorescence probe pyranine to monitor internal pH changes in Escherichia coli membrane vesicles. *FEBS Lett.* 166(1):120-124.
183. Wang M, Weber A, Hartig R, Zheng Y, Krafft D, Vidaković-Koch T, Zuschratter W, Ivanov I, Sundmacher K (2021) Scale up of Transmembrane NADH Oxidation in Synthetic Giant Vesicles. *Bioconjugate Chem*. 32(5):897–903.
184. Deshpande S, Caspi Y, Meijering AEC, Dekker C (2016) Octanol-assisted liposome assembly on chip. *Nat. Commun.* 7:10447.
185. Yandrapalli N, Robinson T (2019) Ultra-high capacity microfluidic trapping of giant vesicles for high-throughput membrane studies. *Lab Chip* (19):626-633.
186. Frericks HL, Zhou DH, Yap LL, Gennis RB, Rienstra CM (2006) Magic-angle spinning solid-state NMR of a 144 kDa membrane protein complex: E. coli cytochrome bo3 oxidase. *J. Biomol. NMR* 36(1):55-71.

187. Ishmukhametov RR, Galkin MA, Vik SB (2005) Ultrafast purification and reconstitution of His-tagged cysteine-less Escherichia coli F1Fo ATP synthase. *Biochim. Biophys. Acta Bioenerg*. 1706(1):110-116.
188. Stein A, Weber G, Wahl MC, Jahn R (2009) Helical extension of the neuronal SNARE complex into the membrane. *Nature* 460(7254):525-528.
189. Pobbati AV, Stein A, Fasshauer D (2006) N- to C-Terminal SNARE Complex Assembly Promotes Rapid Membrane Fusion. *Science* 313(5787):673-676.
190. Schuette CG, Hatsuzawa K, Margittai M, Stein A, Riedel D, Küster P, König M, Seidel C, Jahn R (2004) Determinants of liposome fusion mediated by synaptic SNARE proteins. *Proc. Natl. Acad. Sci. U.S.A.* 101(9):2858-2863.
191. Fasshauer D, Antonin W, Margittai M, Pabst S, Jahn R (1999) Mixed and non-cognate SNARE complexes. Characterization of assembly and biophysical properties. *J. Biol. Chem.* 274(22):15440-15446.
192. Yavuz H, Kattan I, Hernandez JM, Hofnagel O, Witkowska A, Raunser S, Walla PJ, Jahn R (2018) Arrest of trans-SNARE zippering uncovers loosely and tightly docked intermediates in membrane fusion. *J. Biol. Chem.* 293(22):8645-8655.
193. Hernandez JM, Stein A, Behrmann E, Riedel D, Cypionka A, Farsi Z, Walla PJ, Raunser S, Jahn R (2012) Membrane fusion intermediates via directional and full assembly of the SNARE complex. *Science* 336(6088):1581-1584.
194. Garten M, Aimon S, Bassereau P, Toombes GE (2015) Reconstitution of a transmembrane protein, the voltage-gated ion channel, KvAP, into giant unilamellar vesicles for microscopy and patch clamp studies. *J. Vis. Exp.* (95):52281.
195. Nilsson T, Lundin CR, Nordlund G, Adelroth P, von Ballmoos C, Brzezinski P (2016) Lipid-mediated Protein-protein Interactions Modulate Respiration-driven ATP Synthesis. *Sci. Rep.* 6:24113.
196. Bagatolli LA (2006) To see or not to see: Lateral organization of biological membranes and fluorescence microscopy. *Biochim. Biophys. Acta Biomembr.* 1758(10):1541-1556.
197. Gracià RS, Bezlyepkina N, Knorr RL, Lipowsky R, Dimova R (2010) Effect of cholesterol on the rigidity of saturated and unsaturated membranes: fluctuation and electrodeformation analysis of giant vesicles. *Soft Matter* 6(7):1472-1482.
198. Lira RB, Steinkuhler J, Knorr RL, Dimova R, Riske KA (2016) Posing for a picture: vesicle immobilization in agarose gel. *Sci. Rep.* 6:25254.
199. Nichols JW, Deamer DW (1980) Net proton-hydroxyl permeability of large unilamellar liposomes measured by an acid-base titration technique. *Proc. Natl. Acad. Sci. U.S.A.* 77(4):2038-2042.
200. Dao TPT, Brûlet A, Fernandes F, Er-Rafik M, Ferji K, Schweins R, Chapel JP, Fedorov A, Schmutz M, Prieto M, Sandre O, Le Meins JF (2017) Mixing Block Copolymers with Phospholipids at the Nanoscale: From Hybrid Polymer/Lipid Wormlike Micelles to Vesicles Presenting Lipid Nanodomains. *Langmuir* 33(7):1705-1715.
201. Grzesiek S, Dencher NA (1986) Dependency of delta pH-relaxation across vesicular membranes on the buffering power of bulk solutions and lipids. *Biophys. J.* 50(2):265-276.
202. Paxton WF, McAninch PT, Achyuthan KE, Shin SHR, Monteith HL (2017) Monitoring and modulating ion traffic in hybrid lipid/polymer vesicles. *Colloids Surf. B* 159:268-276.
203. Meleard P, Pott T, Bouvrais H, Ipsen JH (2011) Advantages of statistical analysis of giant vesicle flickering for bending elasticity measurements. *Soft matter* 34(10):116.
204. Karimi M, Steinkühler J, Roy D, Dasgupta R, Lipowsky R, Dimova R (2018) Asymmetric Ionic Conditions Generate Large Membrane Curvatures. *Nano Lett.* 18(12):7816-7821.
205. Manneville JB, Bassereau P, Lévy D, Prost J (1999) Magnification of Shape Fluctuations of Active Giant Unilamellar Vesicles. *Perspectives in Supramolecular Chemistry* 6.
206. Faris MDEA, Lacoste D, Pecreaux J, Joanny JF, Prost J, Bassereau P (2009) Membrane tension lowering induced by protein activity. *Phys. Rev. Lett.* 102(3):038102.

207. Bouvrais H, Cornelius F, Ipsen JH, Mouritsen OG (2012) Intrinsic reaction-cycle time scale of Na^+,K^+-ATPase manifests itself in the lipid-protein interactions of nonequilibrium membranes. *Proc. Natl. Acad. Sci. U.S.A.* 109(45):18442-18446.
208. Musatov A, Ortega-Lopez J, Demeler B, Osborne JP, Gennis RB, Robinson NC (1999) Detergent-solubilized Escherichia coli cytochrome bo 3 ubiquinol oxidase: a monomeric, not a dimeric complex. *FEBS Lett.* 457(1):153-156.
209. Berman HM, Westbrook J, Feng Z, Gilliland G, Bhat TN, Weissig H, Shindyalov IN, Bourne PE (2000) The Protein Data Bank. *Nucleic Acids Res.* 28(1):235-242.
210. Manneville JB, Bassereau P, Ramaswamy S, Prost J (2001) Active membrane fluctuations studied by micropipet aspiration. *Phys. Rev. E Stat. Nonlin. Soft Matter Phys.* 64(2 Pt 1):021908.
211. Niggemann G, Kummrow M, Helfrich W (1995) The Bending Rigidity of Phosphatidylcholine Bilayers: Dependences on Experimental Method, Sample Cell Sealing and Temperature. *J. Phys. II France* 5(3):413-425
212. Itel F, Najer A, Palivan CG, Meier W (2015) Dynamics of Membrane Proteins within Synthetic Polymer Membranes with Large Hydrophobic Mismatch. *Nano Lett.* 15(6):3871-3878.
213. Lee AG (2004) How lipids affect the activities of integral membrane proteins. *Biochim. Biophys. Acta* 1666(1-2):62-87.
214. Dao TPT, Fernandes F, Fauquignon M, Ibarboure E, Prieto M, Le Meins JF (2018) The combination of block copolymers and phospholipids to form giant hybrid unilamellar vesicles (GHUVs) does not systematically lead to "intermediate" membrane properties. *Soft Matter* 14(31):6476-6484.
215. Lee JCM, Santore M, Bates FS, Discher DE (2002) From Membranes to Melts, Rouse to Reptation: Diffusion in Polymersome versus Lipid Bilayers. *Macromolecules* 35:323-326.
216. Goose JE, Sansom MSP (2013) Reduced Lateral Mobility of Lipids and Proteins in Crowded Membranes. *PLoS Comput Biol.* 9(4).
217. Ramadurai S, Holt A, Krasnikov V, van den Bogaart G, Killian JA, Poolman B (2009) Lateral Diffusion of Membrane Proteins. *J. Am. Chem. Soc.* 131(35):12650-12656.
218. Okuno D, Iino R, Noji H (2011) Rotation and structure of FoF1-ATP synthase. *J. Biochem.* 149(6):655-664.
219. Vaz WLC, Criado M, Madeira VMC, Schoellmann G, Jovin TM (1982) Size dependence of the translational diffusion of large integral membrane proteins in liquid-crystalline phase lipid bilayers. A study using fluorescence recovery after photobleaching. *Biochemistry* 21(22):5608-5612.
220. Peters R, Cherry RJ (1982) Lateral and rotational diffusion of bacteriorhodopsin in lipid bilayers: experimental test of the Saffman-Delbrück equations. *Proc. Natl. Acad. Sci. U.S.A.* 79(14):4317-4321.
221. Pokorna S, Jurkiewicz P, Cwiklik L, Vazdar M, Hof M (2013) Interactions of monovalent salts with cationic lipid bilayers. *Faraday discuss.* 160:341-358; discussion 389-403.
222. Heinemann F, Betaneli V, Thomas FA, Schwille P (2012) Quantifying lipid diffusion by fluorescence correlation spectroscopy: a critical treatise. *Langmuir* 28(37):13395-13404.
223. Rawicz W, Olbrich KC, McIntosh T, Needham D, Evans E (2000) Effect of chain length and unsaturation on elasticity of lipid bilayers. *Biophys. J.* 79(1):328-339.
224. Lin Z, Hill RM, Davis HT, Scriven LE, Talmon Y (1994) Cryo transmission electron microscopy study of vesicles and micelles in siloxane surfactant aqueous solutions. *Langmuir* 10(4):1008-1011.
225. Salva R, Le Meins J-F, Sandre O, Brûlet A, Schmutz M, Guenoun P, Lecommandoux S (2013) Polymersome Shape Transformation at the Nanoscale. *ACS Nano* 7(10):9298-9311.
226. Kaiser H-J, Lingwood D, Levental I, Sampaio JL, Kalvodova L, Rajendran L, Simons K (2009) Order of lipid phases in model and plasma membranes. *Proc. Natl. Acad. Sci. U.S.A.* 106(39):16645-16650.
227. Pereira MM, Santana M, Teixeira M (2001) A novel scenario for the evolution of haem–copper oxygen reductases. *Biochim. Biophys. Acta Bioenerg.* 1505(2):185-208.

228. Khailova LS, Dedukhova VI, Mokhova EN (2008) Cations SkQ1 and MitoQ accumulated in mitochondria delay opening of ascorbate/FeSO4-induced nonspecific pore in the inner mitochondrial membrane. *Biochemistry* 73(10):1121-1124.
229. Schaffazick SR, Pohlmann AR, de Cordova CAS, Creczynski-Pasa TB, Guterres SS (2005) Protective properties of melatonin-loaded nanoparticles against lipid peroxidation. *Int. J. Pharm.* 289(1):209-213.
230. Mui BL, Cullis PR, Evans EA, Madden TD (1993) Osmotic properties of large unilamellar vesicles prepared by extrusion. *Biophys. J.* 64(2):443-453.
231. Elferink MGL, de Wit JG, Driessen AJM, Konings WN (1994) Stability and proton-permeability of liposomes composed of archaeal tetraether lipids. *Biochim. Biophys. Acta - Biomembr.* 1193(2):247-254.
232. Gensure RH, Zeidel ML, Hill WG (2006) Lipid raft components cholesterol and sphingomyelin increase H+/OH− permeability of phosphatidylcholine membranes. *Biochem.* 398(3):485-495.
233. Gupte S, Wu ES, Hoechli L, Hoechli M, Jacobson K, Sowers AE, Hackenbrock CR (1984) Relationship between lateral diffusion, collision frequency, and electron transfer of mitochondrial inner membrane oxidation-reduction components. *Proc Natl. Acad. Sci. U.S.A.* 81(9):2606-2610.
234. Deamer DW, Nichols JW (1983) Proton-hydroxide permeability of liposomes. *Proc Natl. Acad. Sci. U.S.A.* 80(1):165-168.
235. Dao TPT, Fernandes F, Er-Rafik M, Salva R, Schmutz M, Brûlet A, Prieto M, Sandre O, Le Meins J. F (2015) Phase Separation and Nanodomain Formation in Hybrid Polymer/Lipid Vesicles. *ACS Macro Lett.* 4(2):182-186.
236. Kong B, Yang Y, Kweon DH (2019) Dynamic Light Scattering Analysis to Dissect Intermediates of SNARE-Mediated Membrane Fusion. *Methods Mol. Biol.* 1860:53-69.
237. Lasch J (1995) Interaction of detergents with lipid vesicles. *Biochim. Biophys. Acta* 1241(2):269-292.
238. Chakraborty S, Doktorova M, Molugu TR, Heberle FA, Scott HL, Dzikovski B, Nagao M, Stingaciu L-R, Standaert RF, Barrera FN, Katsaras J, Khelashvili G, Brown MF, Ashkar R (2020) How cholesterol stiffens unsaturated lipid membranes. *Proc. Natl. Acad. Sci. U.S.A.* 117(36):21896-21905.
239. Sezgin E, Gutmann T, Buhl T, Dirkx R, Grzybek M, Coskun Ü, Solimena M, Simons K, Levental I, Schwille P (2015) Adaptive Lipid Packing and Bioactivity in Membrane Domains. *PLoS One* 10(4):e0123930.
240. Ballweg S, Sezgin E, Doktorova M, Covino R, Reinhard J, Wunnicke D, Hänelt I, Levental I, Hummer G, Ernst R (2020) Regulation of lipid saturation without sensing membrane fluidity. *Nat. Commun.* 11(1):756.
241. Hrafnsdóttir S, Nichols JW, Menon AK (1997) Transbilayer Movement of Fluorescent Phospholipids in Bacillus megaterium Membrane Vesicles. *Biochemistry* 36(16):4969-4978.
242. Gardner JM, Abrams CF (2018) Lipid flip-flop vs. lateral diffusion in the relaxation of hemifusion diaphragms. *Biochim. Biophys. Acta Biomembr.* 1860(7):1452-1459.
243. Göpfrich K, Haller B, Staufer O, Dreher Y, Mersdorf U, Platzman I, Spatz JP (2019) One-Pot Assembly of Complex Giant Unilamellar Vesicle-Based Synthetic Cells. *ACS Synth. Biol.* 8(5):937-947.
244. Wang X, Tian L, Du H, Li M, Mu W, Drinkwater BW, Han X, Mann S (2019) Chemical communication in spatially organized protocell colonies and protocell/living cell micro-arrays. *Chem. Sci.* 10(41):9446-9453.
245. Biner O, Fedor JG, Yin Z, Hirst J (2020) Bottom-up construction of a minimal system for cellular respiration and energy regeneration. *ACS Synth. Biol.*
246. Marsh D (2008) Protein modulation of lipids, and vice-versa, in membranes. *Biochim. Biophys. Acta Biomembr.* 1778(7):1545-1575.
247. Oberfeld B, Brunner J, Dimroth P (2006) Phospholipids Occupy the Internal Lumen of the c Ring of the ATP Synthase of Escherichia coli. *Biochemistry* 45(6):1841-1851.

248. Laage S, Tao Y, McDermott AE (2015) Cardiolipin interaction with subunit c of ATP synthase: Solid-state NMR characterization. *Biochim. Biophys. Acta Biomembr.* 1848(1, Part B):260-265.
249. Ames GF (1968) Lipids of Salmonella typhimurium and Escherichia coli: structure and metabolism. *J. Bacteriol.* 95(3):833-843.
250. Wang Z, Bai J, Xu Y (2008) The effect of charged lipids on bacteriorhodopsin membrane reconstitution and its photochemical activities. *Biochem. Biophys. Res. Commun.* 371(4):814-817.
251. Tunuguntla R, Bangar M, Kim K, Stroeve P, Ajo-Franklin CM, Noy A (2013) Lipid bilayer composition can influence the orientation of proteorhodopsin in artificial membranes. *Biophys. J.* 105(6):1388-1396.
252. Lutter JC, Wu T-y, Zhang Y (2013) Hydration of Cations: A Key to Understanding of Specific Cation Effects on Aggregation Behaviors of PEO-PPO-PEO Triblock Copolymers. *J. Phys. Chem.* 117(35):10132-10141.
253. Henderson IM, Paxton WF (2015) Control of mechanically activated polymersome fusion: Factors affecting fusion. *J. Polym. Sci. B Polym. Phys.* 53(4):297-303.
254. Woodbury DJ, Hall JE (1988) Role of channels in the fusion of vesicles with a planar bilayer. *Biophys. J.* 54(6):1053-1063.
255. Finkelstein A, Zimmerberg J, Cohen FS (1986) Osmotic swelling of vesicles: its role in the fusion of vesicles with planar phospholipid bilayer membranes and its possible role in exocytosis. *Annu. Rev. Physiol.* 48:163-174.
256. Peyret A, Ibarboure E, Tron A, Beauté L, Rust R, Sandre O, McClenaghan ND, Lecommandoux S (2017) Polymersome Popping by Light-Induced Osmotic Shock under Temporal, Spatial, and Spectral Control. *Angew. Chem. Int. Ed.* 56(6):1566-1570.
257. Carlsen A, Glaser N, Le Meins JF, Lecommandoux S (2011) Block copolymer vesicle permeability measured by osmotic swelling and shrinking. *Langmuir* 27(8):4884-4890.
258. Smart TP, Fernyhough C, Ryan AJ, Battaglia G (2008) Controlling Fusion and Aggregation in Polymersome Dispersions. *Macromol. Rapid Commun.* 29(23):1855-1860.
259. Kleusch C, Hersch N, Hoffmann B, Merkel R, Csiszar A (2012) Fluorescent lipids: functional parts of fusogenic liposomes and tools for cell membrane labeling and visualization. *Molecules* 17(1):1055-1073.
260. Bhatia T (2021) Tubules, beads, discs and junctions – Morphologies and dynamics of dispersed multilamellar lipid phases in excess water. *J. Colloid Interface Sci.* 584:706-713.
261. Zhou Y, Yan D (2005) Real-Time Membrane Fusion of Giant Polymer Vesicles. *J. Am. Chem. Soc.* 127(30):10468-10469.
262. Moore RD, Morrill GA (1976) A possible mechanism for concentrating sodium and potassium in the cell nucleus. *Biophys. J.* 16(5):527-533.
263. Naora H, Naora H, Izawa M, Allfrey VG, Mirsky AE (1962) Some observations on differences in composition between the nucleus and cytoplasm of the frog oocyte. *Proc. Natl. Acad. Sci. U.S.A.* 48(5):853-859.
264. Romani AMP (2011) Cellular magnesium homeostasis. *Arch. Biochem. Biophys.* 512(1):1-23.
265. Bailey Jr. FE, Callard RW (1959) Some properties of poly(ethylene oxide)1 in aqueous solution. *J. Appl. Polym. Sci.* 1(1):56-62.
266. Yu K, Eisenberg A (1998) Bilayer Morphologies of Self-Assembled Crew-Cut Aggregates of Amphiphilic PS-b-PEO Diblock Copolymers in Solution. *Macromolecules* 31(11):3509-3518.
267. Magarkar A, Karakas E, Stepniewski M, Róg T, Bunker A (2012) Molecular Dynamics Simulation of PEGylated Bilayer Interacting with Salt Ions: A Model of the Liposome Surface in the Bloodstream. *J. Phys. Chem.* 116(14):4212-4219.
268. Johansson P, Gejji SP, Tegenfeldt J, Lindgren J (1996) Local coordination and conformation in polyether electrolytes: Geometries of M-triglyme complexes (M = Li, Na, K, Mg and Ca) from ab-initio molecular orbital calculations. *Solid State Ion.* 86-88:297-302.

269. Lu B-S, Gupta SP, Belička M, Podgornik R, Pabst G (2016) Modulation of Elasticity and Interactions in Charged Lipid Multibilayers: Monovalent Salt Solutions. *Langmuir* 32(50):13546-13555.
270. Bouvrais H, Duelund L, Ipsen JH (2014) Buffers Affect the Bending Rigidity of Model Lipid Membranes. *Langmuir* 30(1):13-16.
271. Sreekumari A, Lipowsky R (2018) Lipids with bulky head groups generate large membrane curvatures by small compositional asymmetries. *J. Chem. Phys.* 149(8):084901.
272. Garcia A, Pochinda S, Elgaard-Jørgensen PN, Khandelia H, Clarke RJ (2019) Evidence for ATP Interaction with Phosphatidylcholine Bilayers. *Langmuir* 35(30):9944-9953.
273. Zinser E, Sperka-Gottlieb CD, Fasch EV, Kohlwein SD, Paltauf F, Daum G (1991) Phospholipid synthesis and lipid composition of subcellular membranes in the unicellular eukaryote Saccharomyces cerevisiae. *J. Bacteriol. Res.* 173(6):2026-2034.
274. Otrin L, Kleineberg C, Caire da Silva L, Landfester K, Ivanov I, Wang M, Bednarz C, Sundmacher K, Vidaković-Koch T (2019) Artificial Organelles for Energy Regeneration. *Adv. Biosyst.* 3(6).
275. Wagner N, Gutweiler M, Pabst R, Dose K (1987) Coreconstitution of bacterial ATP synthase with monomeric bacteriorhodopsin into liposomes. *Eur. J. Biochem.* 165(1):177-183.
276. Akashi K, Miyata H, Itoh H, Kinosita K (1996) Preparation of giant liposomes in physiological conditions and their characterization under an optical microscope. *Biophys. J.* 71(6):3242-3250.
277. Avnir Y, Barenholz Y (2005) pH determination by pyranine: Medium-related artifacts and their correction. *Anal. Biochem.* 347(1):34-41.
278. Barnadas-Rodríguez R, Estelrich J (2008) Effect of salts on the excited state of pyranine as determined by steady-state fluorescence. *J. Photochem. Photobiol.* 198(2):262-267.
279. Opitz N, Lübbers DW (1984) A Correction Method for Ionic Strength-Independent Fluorescence Photometric pH Measurement. *Oxygen Transport to Tissue-V*, eds Lübbers DW, Acker H, Leniger-Follert E, Goldstrick TK (Springer US, Boston, MA), 907-912.
280. Romanowska J, Kokh DB, Wade RC (2015) When the Label Matters: Adsorption of Labeled and Unlabeled Proteins on Charged Surfaces. *Nano Lett.* 15(11):7508-7513.
281. Yin L, Wang W, Wang S, Zhang F, Zhang S, Tao N (2015) How does fluorescent labeling affect the binding kinetics of proteins with intact cells? *Biosens. Bioelectron.* 66:412-416.
282. Mbamala EC, Ben-Shaul A, May S (2005) Domain Formation Induced by the Adsorption of Charged Proteins on Mixed Lipid Membranes. *Biophys. J.* 88(3):1702-1714.
283. Dwek RA, Butters TD, Platt FM, Cox TM, Harder T (2003) Formation of functional cell membrane domains: the interplay of lipid- and protein-mediated interactions. *Philos. Trans. R. Soc.* 358(1433):863-868.
284. Sørensen CE, Novak I (2001) Visualization of ATP Release in Pancreatic Acini in Response to Cholinergic Stimulus: Use of fluorescent probes and confocal microscopy. *Int. J. Biol. Chem.* 276(35):32925-32932.
285. Faizi HA, Frey SL, Steinkühler J, Dimova R, Vlahovska PM (2019) Bending rigidity of charged lipid bilayer membranes. *Soft Matter* 15(29):6006-6013.
286. Bouvrais H, Pott T, Bagatolli LA, Ipsen JH, Méléard P (2010) Impact of membrane-anchored fluorescent probes on the mechanical properties of lipid bilayers. *Biochim. Biophys. Acta Biomembr.* 1798(7):1333-1337.
287. Nikolov V, Lipowsky R, Dimova R (2007) Behavior of giant vesicles with anchored DNA molecules. *Biophys. J.* 92(12):4356-4368.
288. Cho WJ, Jeremic A, Jena BP (2005) Size of Supramolecular SNARE Complex: Membrane-Directed Self-Assembly. *J. Am. Chem. Soc.* 127(29):10156-10157.
289. Cravatt B, Prospero-Garcia O, Siuzdak G, Gilula N, Henriksen S, Boger D, Lerner R (1995) Chemical characterization of a family of brain lipids that induce sleep. *Science* 268(5216):1506-1509.
290. Hannun Y, Bell R (1989) Functions of sphingolipids and sphingolipid breakdown products in cellular regulation. *Science* 243(4890):500-507.

291. Hung M, Huang L, Wagner E (2001) *Nonviral Vectors for Gene Therapy* (Springer).
292. Felgner PL, Gadek TR, Holm M, Roman R, Chan HW, Wenz M, Northrop JP, Ringold GM, Danielsen M (1987) Lipofection: a highly efficient, lipid-mediated DNA-transfection procedure. *Proc. Natl. Acad. Sci. U.S.A.* 84(21):7413-7417.
293. Gao X, Huang L (1991) A novel cationic liposome reagent for efficient transfection of mammalian cells. *Biochem. Biophys. Res. Commun.* 179(1):280-285.
294. Leventis R, Silvius JR (1990) Interactions of mammalian cells with lipid dispersions containing novel metabolizable cationic amphiphiles. *Biochim. Biophys. Acta Biomembr.* 1023(1):124-132.
295. MacDonald RC, Rakhmanova VA, Choi KL, Rosenzweig HS, Lahiri MK (1999) O-ethylphosphatidylcholine: A metabolizable cationic phospholipid which is a serum-compatible DNA transfection agent. *J. Pharm. Sci.* 88(9):896-904.
296. Cook GMW, Jacobson W (1968) The electrophoretic mobility of normal and leukaemic cells of mice. *Biochem.* 107(4):549-557.
297. Besson A, Formosa-Dague C, Guiraud P (2019) Flocculation-flotation harvesting mechanism of Dunaliella salina: From nanoscale interpretation to industrial optimization. *Water Res.* 155:352-361.
298. Ryu J-K, Jahn R, Yoon T-Y (2016) Review: Progresses in understanding N-ethylmaleimide sensitive factor (NSF) mediated disassembly of SNARE complexes. *Biopolymers* 105(8):518-531.
299. Gilliland G, Berman HM, Weissig H, Shindyalov IN, Westbrook J, Bourne PE, Bhat TN, Feng Z (2000) The Protein Data Bank. *Nucleic Acids Res.* 28(1):235-242.

6 Acknowledgments

My deepest gratitude goes to Prof. Dr.-Ing. Kai Sundmacher for opportunity to do PhD in his group and be a part of exciting MaxSynBio project. I would also like to sincerely thank Dr. Ivan Ivanov for excellent mentorship, and for the most appreciated support on all my growth-related projects.

I would like to express large gratitude to Dr. Rumiana Dimova for warm welcome in her lab, enabling me to perform experiments not feasible in our lab, and for fruitful collaboration.

Many thanks to Prof. Panagiotis Kastritis for cryo-TEM support, providing insight into structure of our vesicles.

Appreciations go also to Prof. Christoph von Ballmoos and Prof. Reinhard Jahn for generous sharing of materials and methods.

For experimental collaboration and interesting discussions, I would like to thank Dr. Lado Otrin, Dr. Ziliang Zhao and Dr. Rafael B. Lira. Our work together was always a pleasure and I am looking forward to our future collaboration. Additional thanks goes to Lado for providing guidance of experimental path in our lab, and always-useful feedback, in particular for projects involving membrane proteins. For nice collaboration, I would also like to thank Dr. Fotis L. Kyrilis and Dr. Farzad Hamdi.

Special thanks go to my colleague Claudia Bednarz for timely proteins purification, and always pleasant discussions over coffee. Many thanks go also to our lab team – Anne Reichelt, Markus Ikert and Bianka Stein, to my students, our administration and IT.

Finally, I would like to thank my committee for reviewing my work and for their suggestions.

7 Supplementary Information

7.1 Additional data on characterization of hybrid and polymer compartments

7.1.1 Structure of ubiquinol *bo₃* oxidase

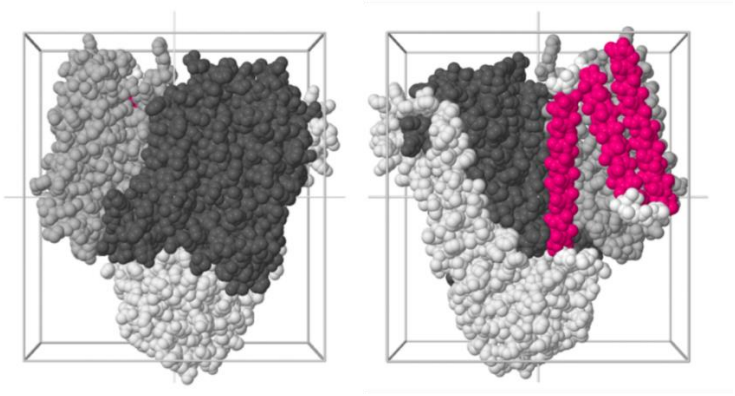

Figure S1. The structure of ubiquinol *bo₃* oxidase from *E. coli*, front (left) and back (right) (PDB (299)). The shape asymmetry originates from membrane part (size $L_1 \approx 8$ nm, $L_2 \approx 7.2$ nm) and cytosolic part (ranging ~3.8 nm out of the membrane).

7.1.2 Activity lifetime *bo₃*-LUVs and chemical stability of LUVs

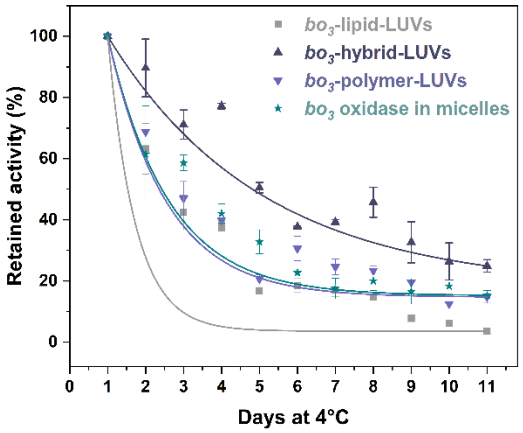

Figure S2. Activity of *bo₃* oxidase reconstituted in lipid, hybrid and polymer LUVs over 11 days. *bo₃* oxidase was reconstituted in all three types of vesicles at lipid/polymer-to-protein molar ratio 9550:1 and at ~ 13.5 nM protein in the measurement chamber. Exponential fitting (in OriginPro) of the experimental data on activity retention of *bo₃* oxidase in LUVs and n-dodecyl-β-D-maltoside micelles. The respective time constants were: 0.72 for *bo₃*-lipid-LUVs, 4.06 for *bo₃*-hybrid-LUVs, 1.54 for *bo₃*-polymer-LUVs and 1.6 for *bo₃* oxidase in micelles.

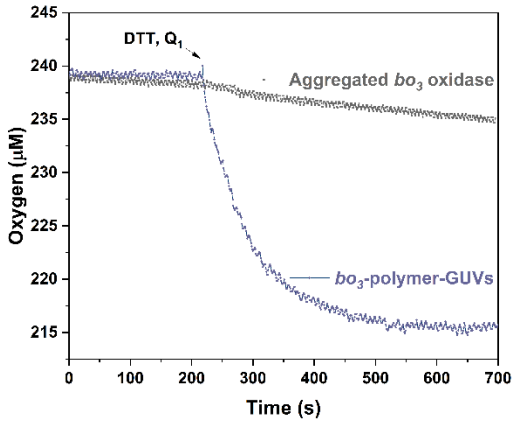

Figure S3. Oxygen consumption by *bo₃* oxidase reconstituted in GUVs (measured in population) and aggregated *bo₃* oxidase. Aggregated *bo₃* oxidase: negative control, absence of stabilizing amphiphiles (detergent/lipid/polymer). At ~ 220 s mark, the reaction was initiated by DTT and Q_1.

7.1.3 Passive proton permeability of GUVs

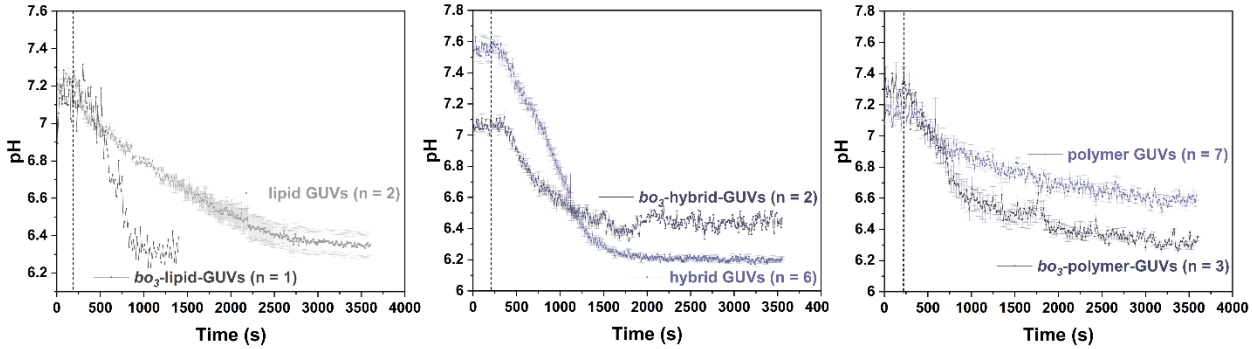

Figure S4. Fluorescence intensity ratio inside GUVs and *bo₃*-GUVs after external buffer exchange (from initial pH 7.5 to pH 6.0). Pyranine was excited at 405 nm and 458 nm, and the emission intensity measured in the range 499-551 nm. The ratio of intensities inside GUV correlates with pyranine deprotonation and thus pH. The curves present mean and standard deviation for 2–7 GUVs from single experiment (1 trap).

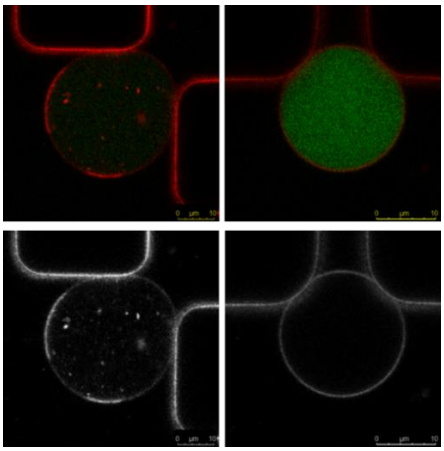

Figure S5. **Micrographs of protein-free hybrid GUVs traped in microfluidic device.** Hybrid with domains (left) and hybrid with homogenous distribution of lipid and polymer (right).

7.2 Additional data on charge-mediated growth

7.2.1 Lipid dyes distribution in anionic hybrid GUVs

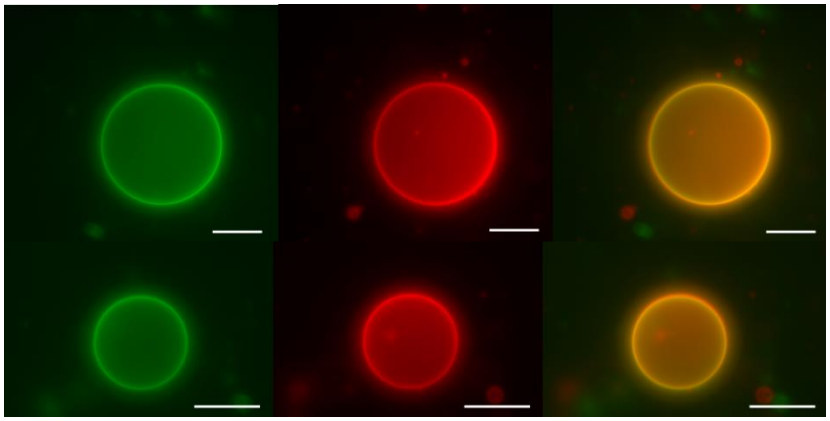

Figure S6. Micrographs of anionic hybrid GUVs. GUVs composition was PDMS-*g*-PEO:soy PS:PE-Rho:PE-NBD = 89:10:0.5:0.5, mol%. Channels from left to right: NBD (green), Rhodamine (red) and merged. Scale bar: 10 µm.

7.2.2 Membrane mixing of LUVs

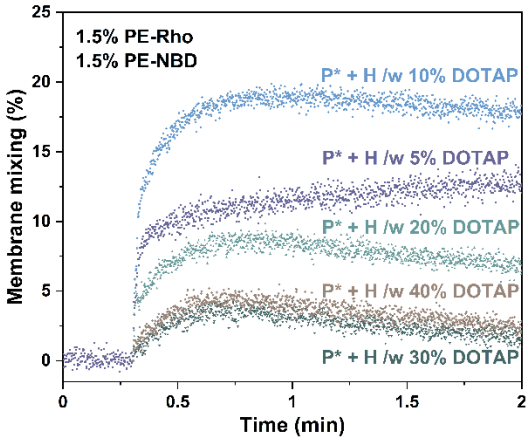

Figure S7. Membrane mixing of polymersomes with hybrids. Membrane mixing of ~ 100 nm PDMS-*g*-PEO LUVs ("P*"), containing 1.5 mol% PE-Rho and 1.5 mol% PE-NBD, and ~ 100 nm hybrid LUVs ("H"), containing different amount of cationic lipids (0–40 mol%), mixed in molar ratio 1:1.

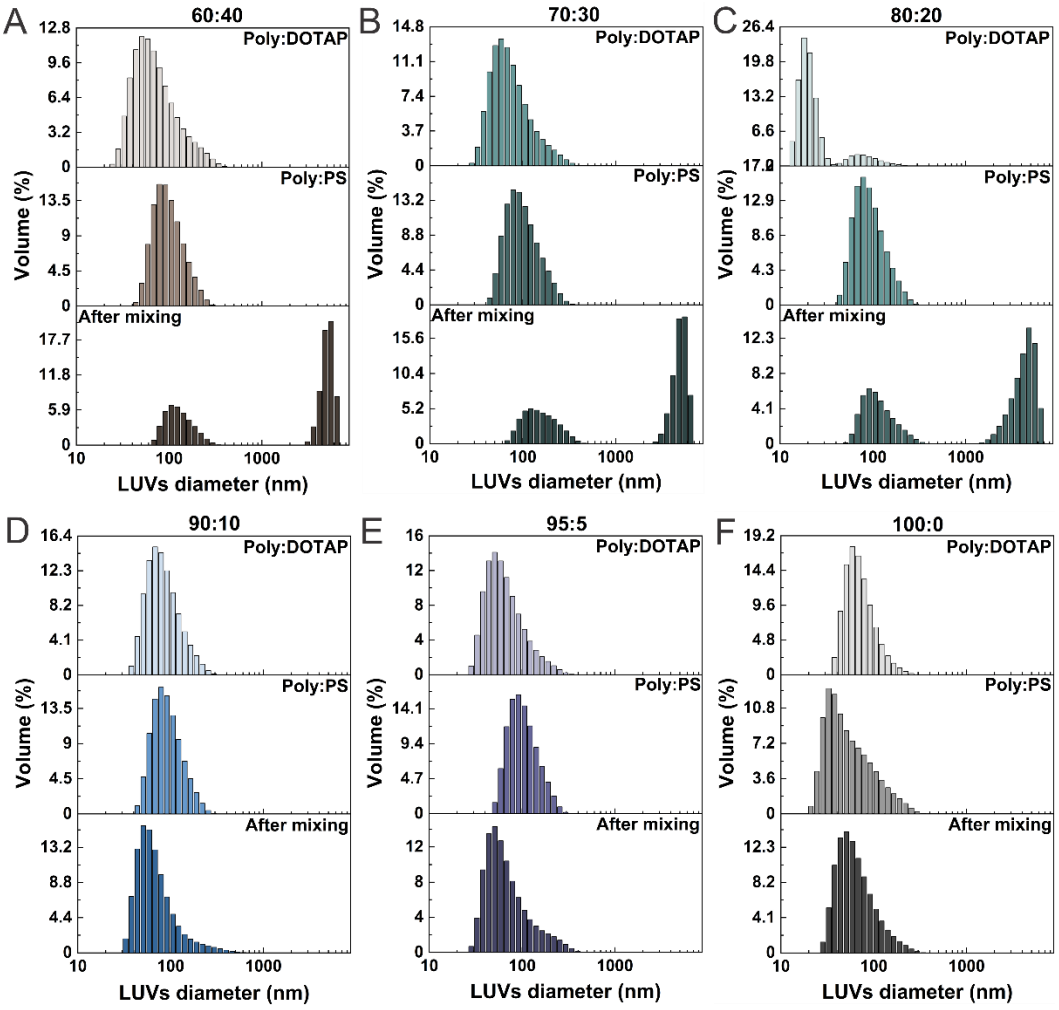

Figure S8. Size of hybrid LUVs with different amount of charged lipids (from FRET experiment). Size distribution by volume of PDMS-*g*-PEO:DOTAP, PDMS-*g*-PEO:PS and PDMS-*g*-PEO LUVs before and after mixing (10 min at 500 rpm), determined by DLS. LUVs were composed of 40 (**A**), 30 (**B**), 20 (**C**), 10 (**D**), 5 (**E**) or 0 mol% charged lipids (**F**). LUVs containing PS were supplemented with 1.5 mol% PE-NBD and 1.5 mol% PE-Rho.

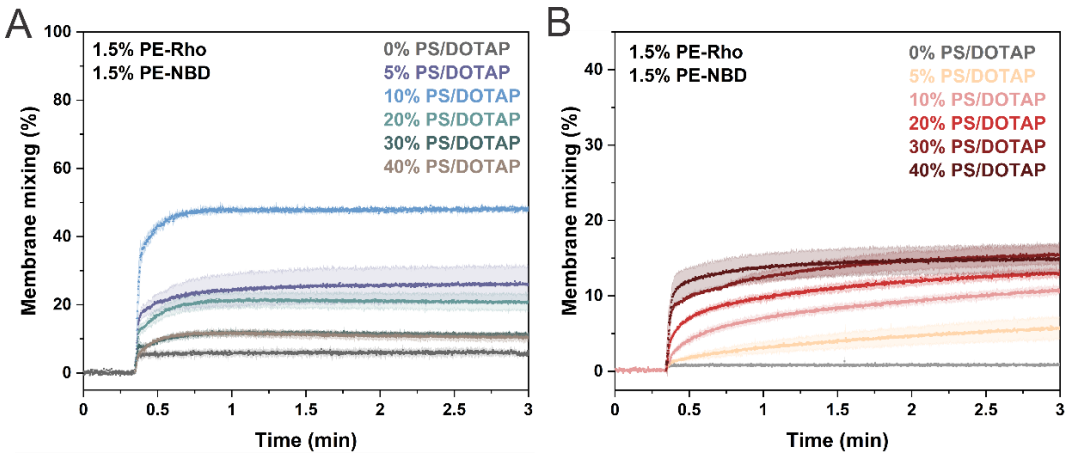

Figure S9. Charge-mediated membrane mixing of hybrid LUVs with different amount of charged lipids. Tagged hybrids contained 1.5 mol% PE-Rho and 1.5 mol% PE-NBD. 100 % was obtained by solubilizing LUVs with Triton X-100.

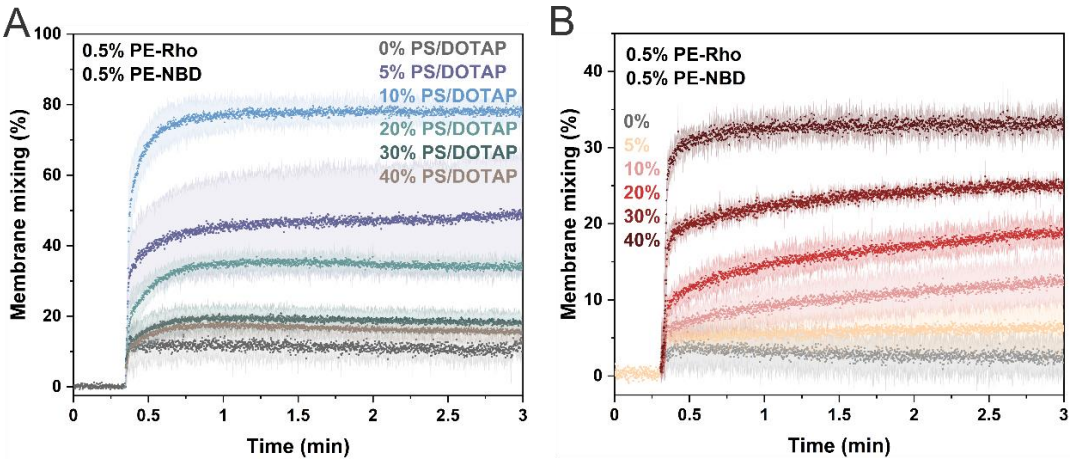

Figure S10. Charge-mediated membrane mixing of hybrid LUVs with different amount of charged lipids. Tagged hybrids contained 0.5 mol% PE-Rho and 0.5 mol% PE-NBD. 100 % was obtained by solubilizing LUVs with Triton X-100.

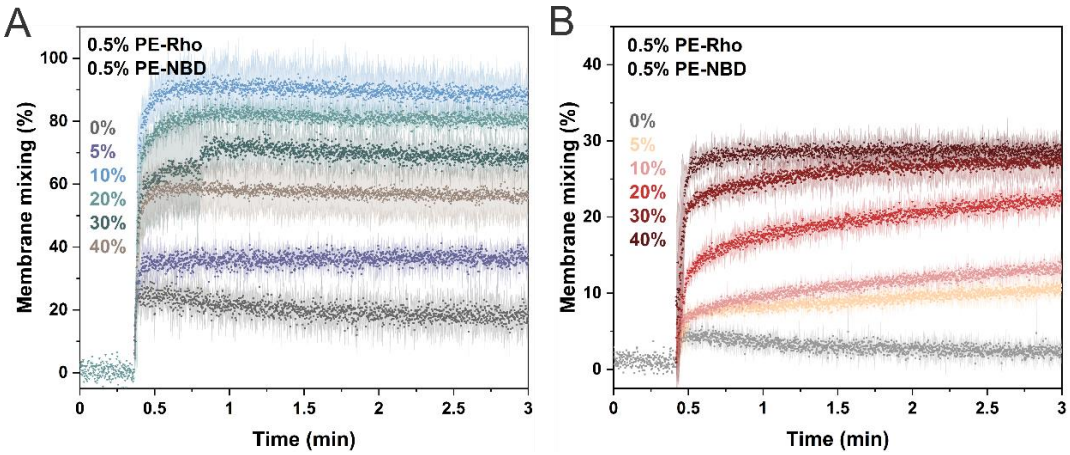

Figure S11. Charge-mediated membrane mixing of hybrid and lipid LUVs with different amount of charged lipids. LUVs were composed of 60–100 mol% PDMS-*g*-PEO and 0–40 mol% DOTAP or soy PS. Anionic and cationic LUVs were mixed in molar ratio 1:1; final concentration of LUVs was 100 μM. (**A**) Membrane mixing of ~ 100 nm hybrid LUVs. Anionic LUVs (PDMS-*g*-PEO:soy PS) were tagged with 0.5 mol% PE-Rho and 0.5 mol% PE-NBD. 100 % was obtained by solubilizing LUVs with octyl glucoside. (**B**) Membrane mixing of ~ 100 nm lipid LUVs. Anionic LUVs (DOPC:soy PS) were tagged with 0.5 mol% PE-Rho and 0.5 mol% PE-NBD. 100 % was obtained by solubilizing LUVs with octyl glucoside.

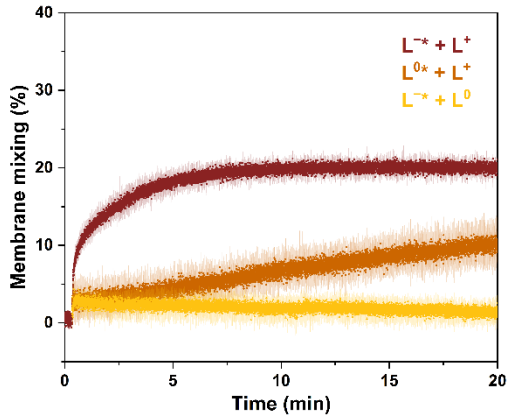

Figure S12. Membrane mixing of ~ 100 nm lipid LUVs in 200 mM sucrose over 20 min. Membrane mixing of neutral and cationic lipid LUVs increasing with slow rate can be observed.

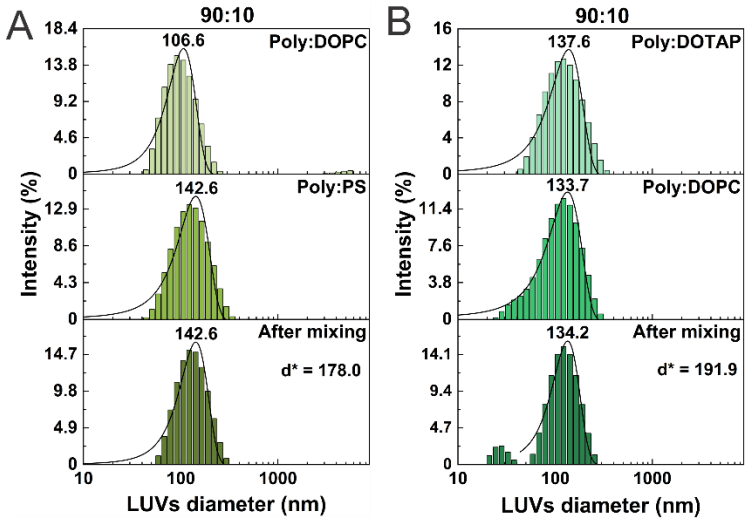

Figure S13. Size distribution by intensity of neutral and charged hybrid LUVs (from FRET experiment) determined by DLS. LUVs in middle panel were supplemented with 0.5 mol% PE-NBD and 0.5 mol% PE-Rho. (**A**) Cationic and anionic hybrid LUVs. (**B**) Neutral and anionic hybrid LUVs. (**C**) Cationic and neutral hybrid LUVs.

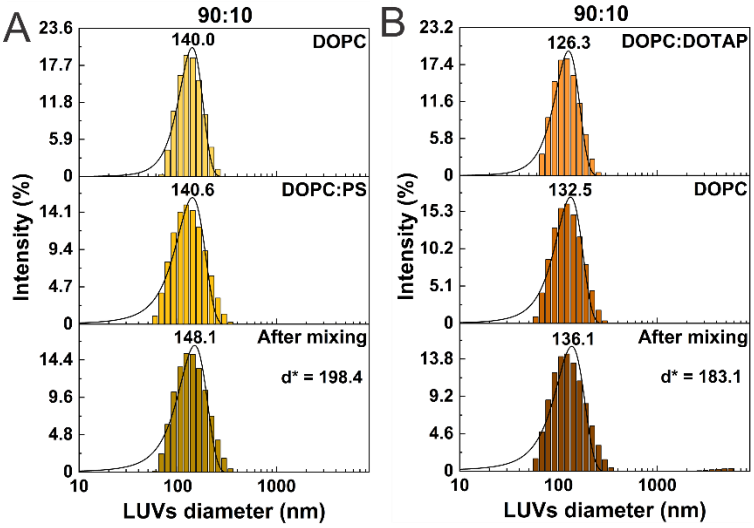

Figure S14. Size distribution by intensity of neutral and charged lipid LUVs (from FRET experiment) determined by DLS. LUVs in middle panel were supplemented with 0.5 mol% PE-NBD and 0.5 mol% PE-Rho. (**A**) Cationic and anionic lipid LUVs. (**B**) Neutral and anionic lipid LUVs. (**C**) Cationic and neutral lipid LUVs.

7.2.3 Membrane disorder

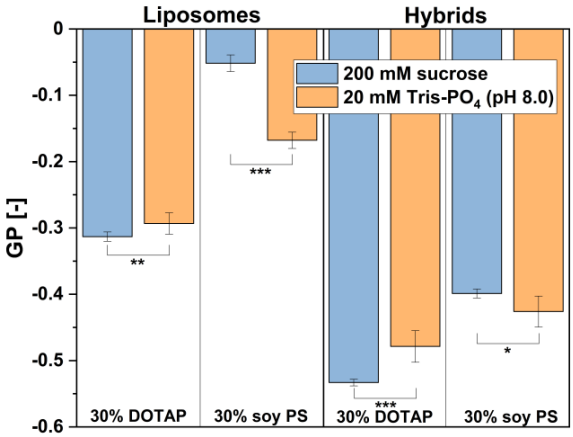

Figure S15. Membrane disorder of lipid and hybrid LUVs. Generalized polarization (GP) values of lipid and hybrid LUVs with 30 mol% anionic (PS) or cationic (DOTAP) lipids in 200 mM sucrose (blue) and in 20 mM Tris-PO_4 (pH 8.0) (orange). Error bars represent SD from n = 3–6. *** for $P \leq 0.001$. *$P \leq 0.05$; **$P \leq 0.01$; ***$P \leq 0.001$.

7.2.4 Hybrid GUV-LUV fusion

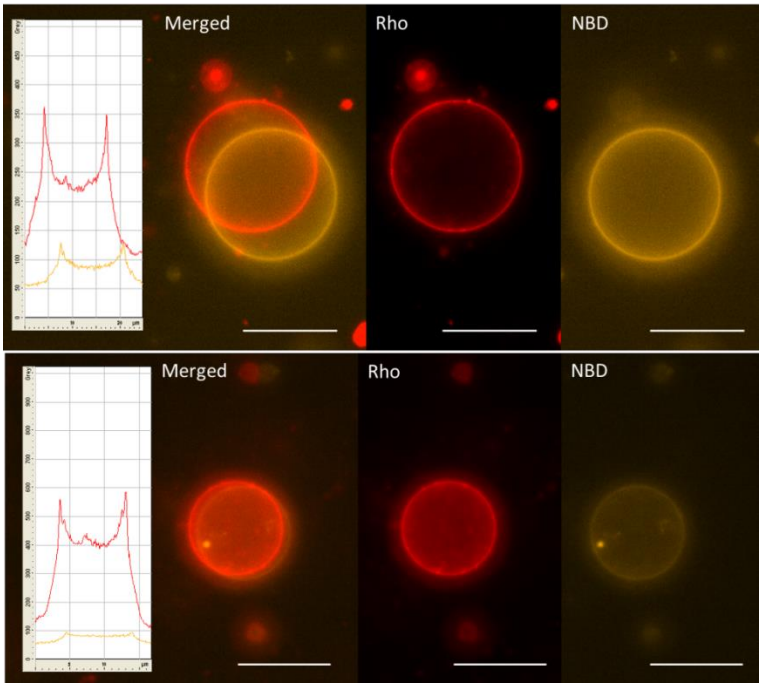

Figure S16. Micrographs of PDMS-*g*-PEO:PS GUVs, tagged with PE-NBD (yellow), upon incubation with PDMS-*g*-PEO:DOTAP LUVs, tagged with PE-Rho (red). Both, GUVs and LUVs were prepared in 200 mM sucrose. After incubation of Rho-LUVs with NBD-GUVs at 500 rpm for 10 min, both membrane dyes were observed in the membrane of GUVs. Scale bar: 10 µm.

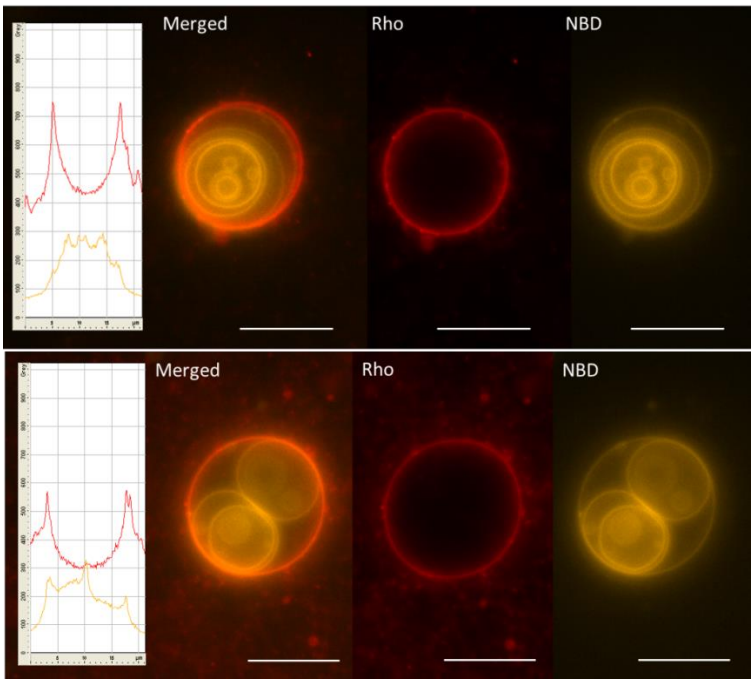

Figure S17. Micrographs of multivesicular PDMS-*g*-PEO:PS giant vesicles, tagged with PE-NBD (yellow), upon incubation with PDMS-*g*-PEO:DOTAP LUVs, tagged with PE-Rho (red). Both, GUVs and LUVs were prepared in 200 mM sucrose. After incubation of Rho-LUVs with NBD-GUVs at 500 rpm for 10 min, both membrane dyes were observed in the membrane of GUVs. Portion of hybrid giant vesicles was multivesicular; in those vesicle Rho-LUVs fused only with outer membrane. Scale bar: 10 μm.

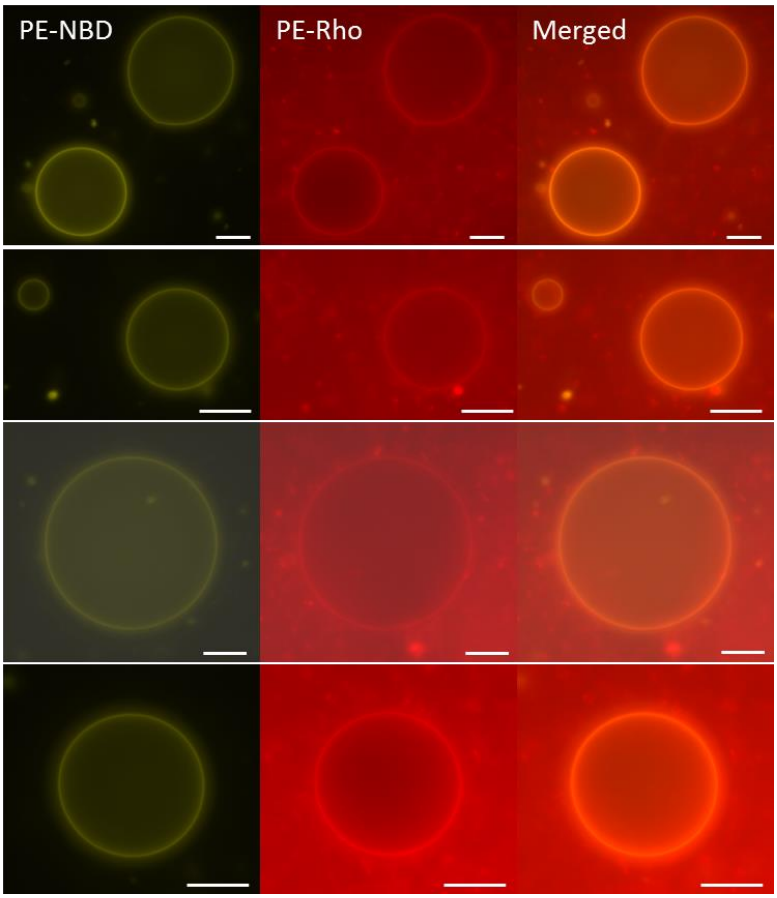

Figure S18. Fluorescent microscopy of neutral GUVs (PDMS-*g*-PEO:DOPC:PE-NBD = 79.5:20:0.5, mol%; yellow) and cationic LUVs (PDMS-*g*-PEO:DOTAP:PE-Rho = 79.5:20:0.5, mol%; red) upon their incubation for 5 min. Accumulation of red signal from LUVs was observed on the membrane of GUVs. Scale bar: 10 µm.

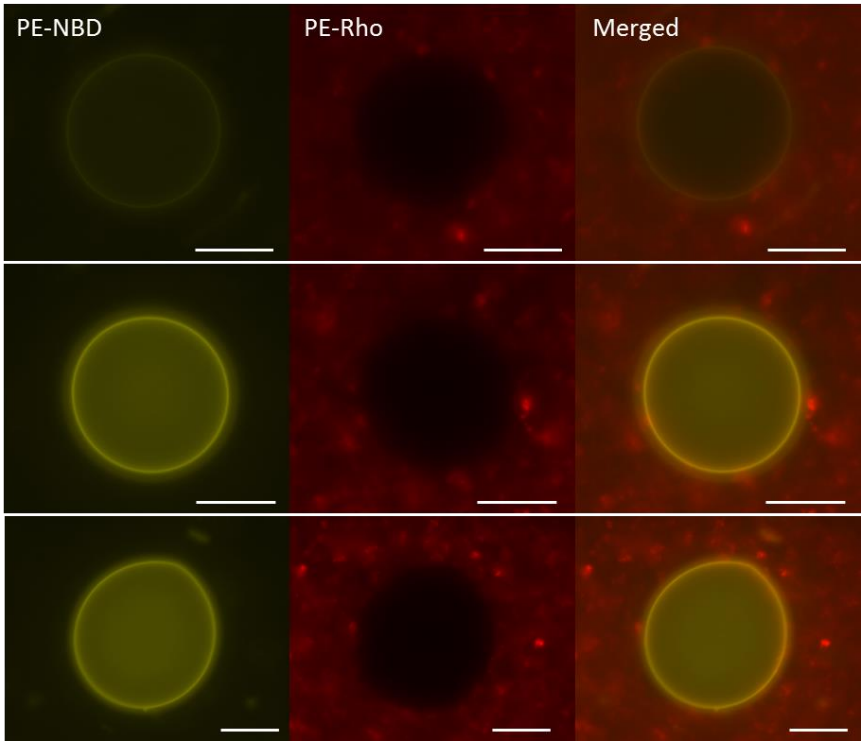

Figure S19. Fluorescent microscopy of anionic GUVs (PDMS-*g*-PEO:soy PS:PE-NBD = 79.5:20:0.5, mol%; yellow) and neutral LUVs (PDMS-*g*-PEO:DOPC:PE-Rho = 79.5:20:0.5, mol%; red) upon their incubation for 5 min. No accumulation of red signal from LUVs on the GUVs was observed. Scale bar: 10 μm.

7.2.5 Hybrid GUV-GUV fusion

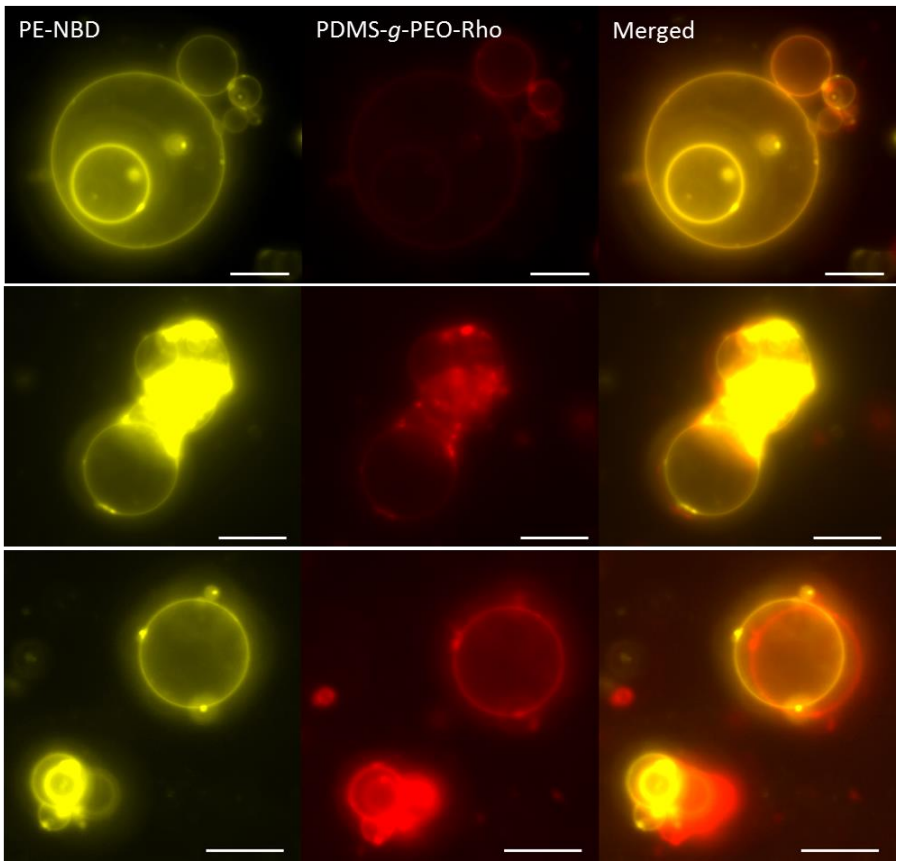

Figure S20. Micrographs of hybrid GUVs upon fusion of anionic and cationic hybrid GUVs. Cationic GUVs were tagged with lipid dye (PDMS-*g*-PEO:DOTAP:PE-NBD (69.1:30:0.9)) and anionic GUVs with polymer dye (PDMS-*g*-PEO:soy PS:PDMS-*g*-PEO-Rho (70:30:0.08)). Aggregated PE-NBD observed on cationic hybrids alone (Figure S22) was retained upon fusion with anionic hybrid GUVs. Difference in red and yellow signal indicates on asymmetric GUV-GUVs fusion in terms of their size. Scale bar: 10 µm.

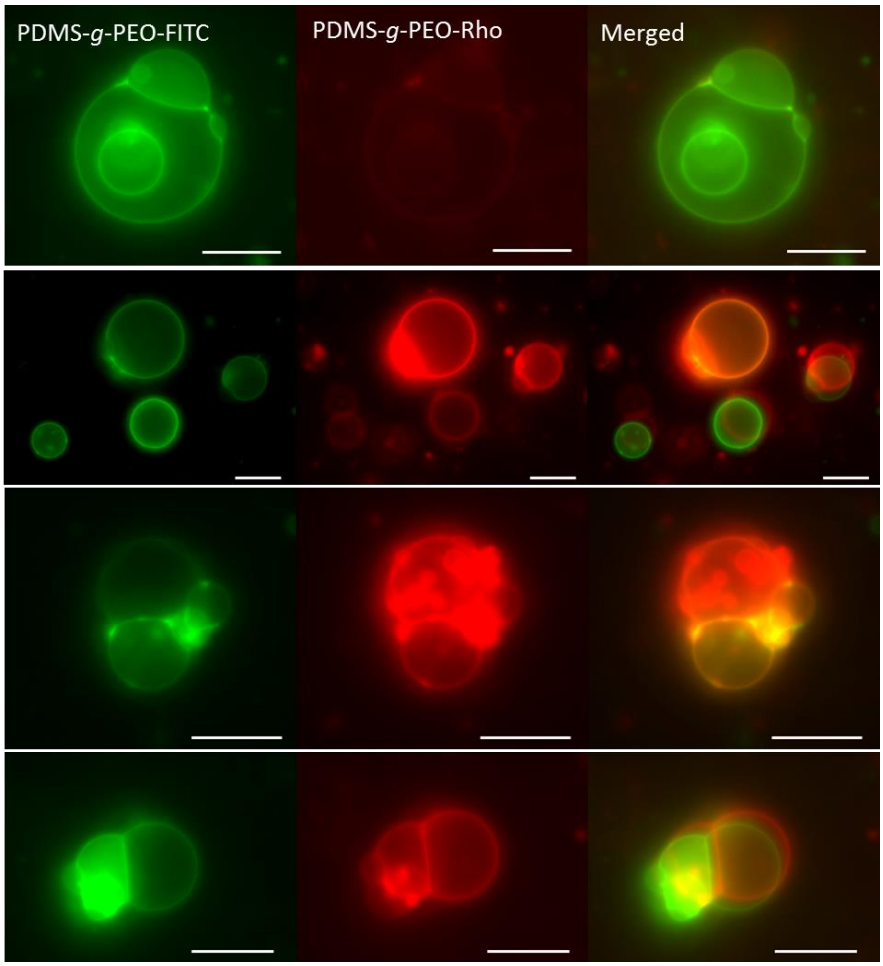

Figure S21. Micrographs of hybrid GUVs upon fusion of cationic and anionic hybrid GUVs. Cationic and anionic hybrids were both tagged with polymer dyes: PDMS-*g*-PEO:DOTAP:PDMS-*g*-PEO-FITC (69.5:30:0.5)) and PDMS-*g*-PEO:soy PS:PDMS-*g*-PEO-Rho (70:30:0.08), respectfully. Due to absence of mixing and different GUVs size, the contribution of material from anionic and cationic GUVs varied in-between newly grown (fused) GUVs. Scale bar: 10 µm.

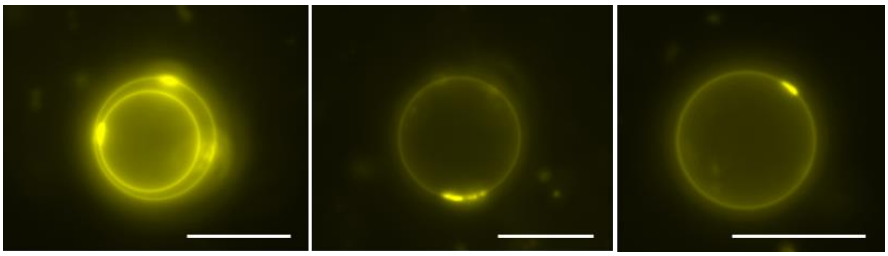

Figure S22. Cationic hybrid GUVs with lipid dye. GUVs composition: PDMS-*g*-PEO:DOTAP:PE-NBD (69.1:30:0.9, mol%). In majority of GUVs PE-NBD aggregation was observed (strong yellow signal). Scale bar: 10 µm.

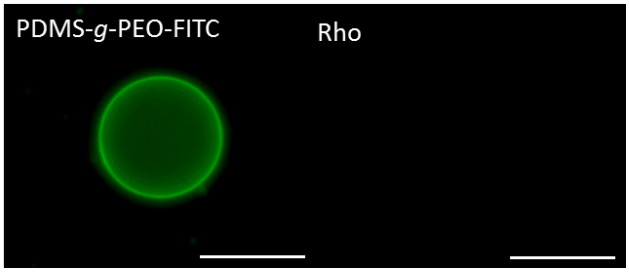

Figure S23. Cationic hybrid GUVs with polymer dye (green). GUVs composition: PDMS-*g*-PEO:DOTAP:PDMS-*g*-PEO-FITC (69.5:30:0.5). No signal was observed with Rhodamine filter set. Opposite to GUVs labeled with PE-NBD (Figure S12), no aggregation was observed here. Scale bar: 10 µm.

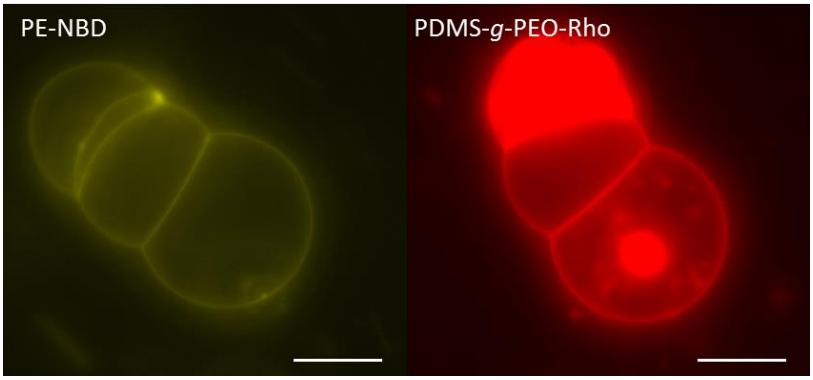

Figure S24. Micrograph of hybrid GUVs after fusion of anionic (polymer labeled, red) and cationic (lipid labeled, yellow) hybrid GUV. Long contact between newly grown GUVs was often observed. Scale bar: 10 µm.

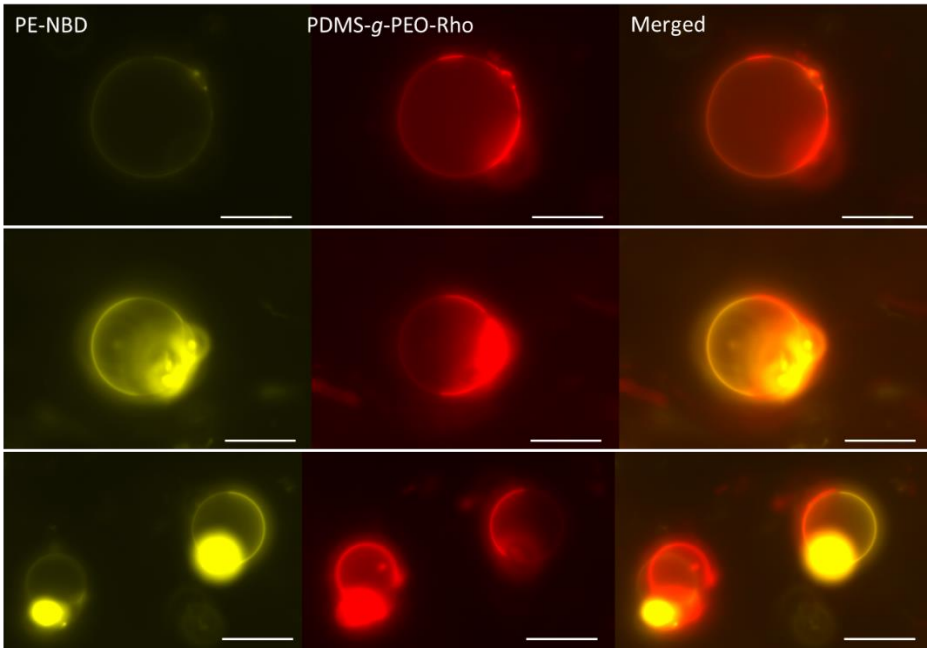

Figure S25. Micrographs of heterogeneous (phase separated lipid and polymer domain) hybrid GUVs upon fusion of cationic lipid and anionic hybrid GUVs. Scale bar: 10 µm.

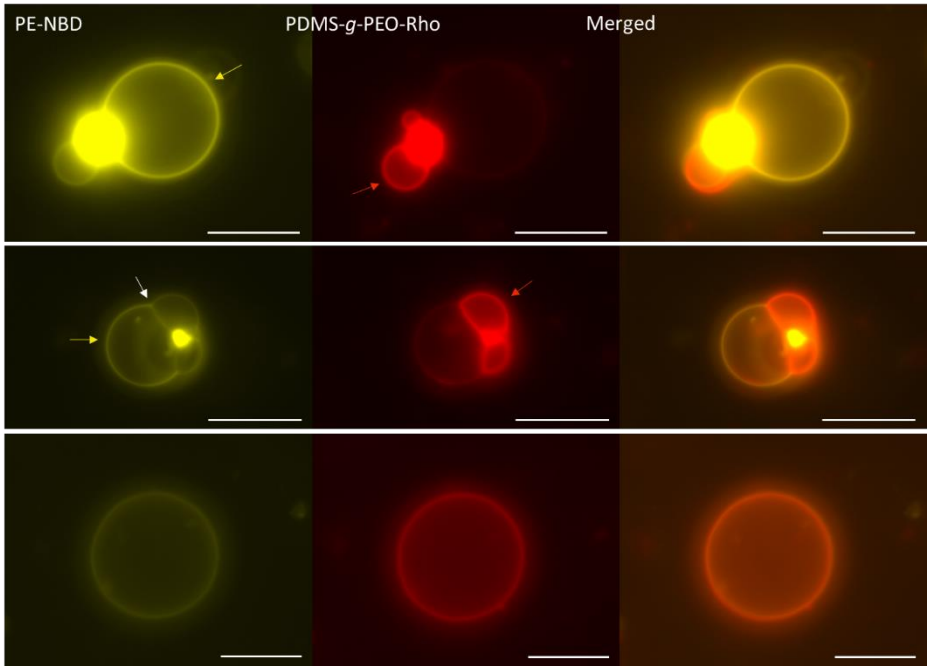

Figure S26. Micrographs of homogenous hybrid GUVs upon fusion of cationic lipid and anionic hybrid GUVs. Yellow arrows indicate higher presence of lipid and rad arrows higher presence of polymer. White arrows shows on long constant between the two GUVs, where higher amount of polymer then lipid is present. Scale bar: 10 µm.

7.2.6 Content mixing via enzymatic coupling

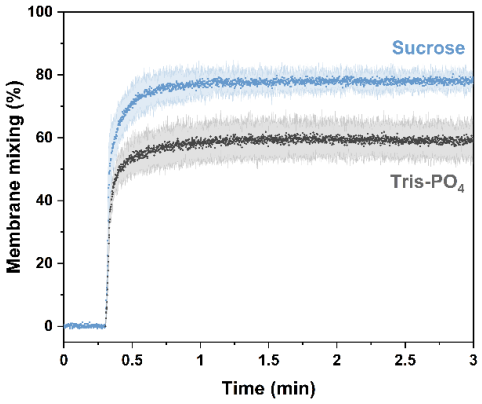

Figure S27. Charge-mediated membrane mixing of hybrid LUVs with 10 mol% of charged lipids in 200 mM sucrose (blue trace) and 20 mM Tris (pH 8.0), 20 mM H_3PO_4 (gray trace). LUVs were composed of 89–90 mol% PDMS-*g*-PEO and 10 mol% DOTAP or soy PS. Membranes of LUVs containing soy PS were tagged with 0.5 mol% PE-Rho and 0.5 mol% PE-NBD. Tagged and non-tagged LUVs were mixed in molar ratio 1:1; final concentration of LUVs was 100 µM. 100 % was obtained by solubilizing vesicles with Triton X-100.

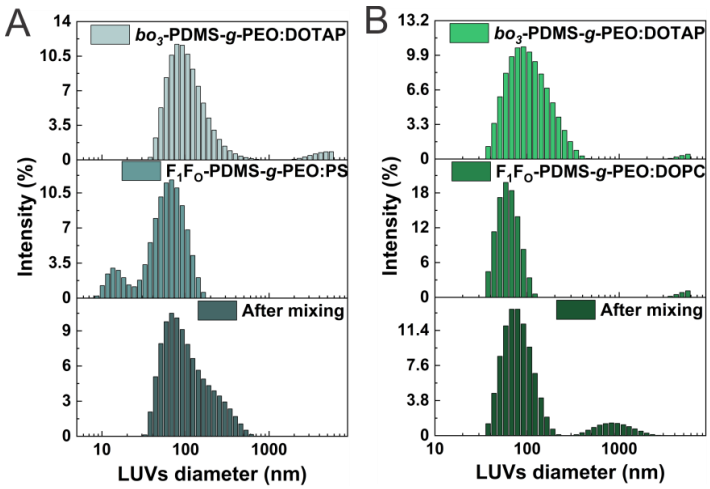

Figure S28. Hybrids size distribution by intensity, determined by DLS. *bo*$_3$ oxidase was reconstituted with SC R_{sat}, and F_1F_O-ATPase with SDC R_{sol}. The vesicles correspond to lower activity in Figure 41D. (**A**) *bo*$_3$ oxidase was reconstituted into PDMS-*g*-PEO:DOTAP (70:30, molar ratio) LUVs, and F_1F_O-ATPase into PDMS-*g*-PEO:PS (70:30, molar ratio) LUVs. (**B**) *bo*$_3$ oxidase was reconstituted into PDMS-*g*-PEO:DOTAP (70:30, molar ratio) LUVs, and F_1F_O-ATPase into PDMS-*g*-PEO:DOPC (70:30, molar ratio) LUVs.

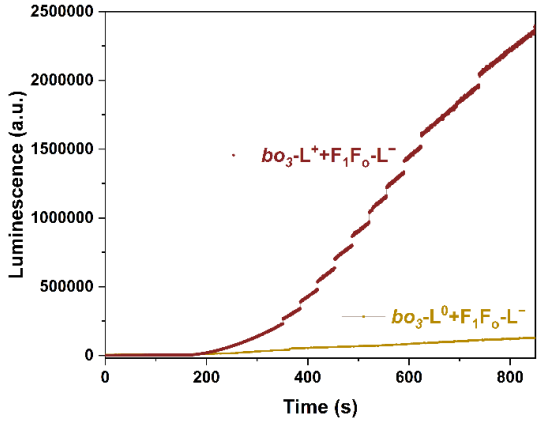

Figure S29. **Respiratory-driven ATP synthesis after charge-mediated fusion of neutral or cationic lipid LUVs with reconstituted *bo*$_3$ oxidase and anionic lipid LUVs with reconstituted F_1F_O-ATPase.** Charged liposomes were composed of DOPC:DOTAP or DOPC:PS (70:30, mol%). Change in luminescence over time corresponding to synthetized ATP. ATP can be synthetized by F_1F_O-ATPase only if both proteins are in the same vesicle, ΔpH is established by *bo*$_3$ oxidase and vesicles are proton tight.

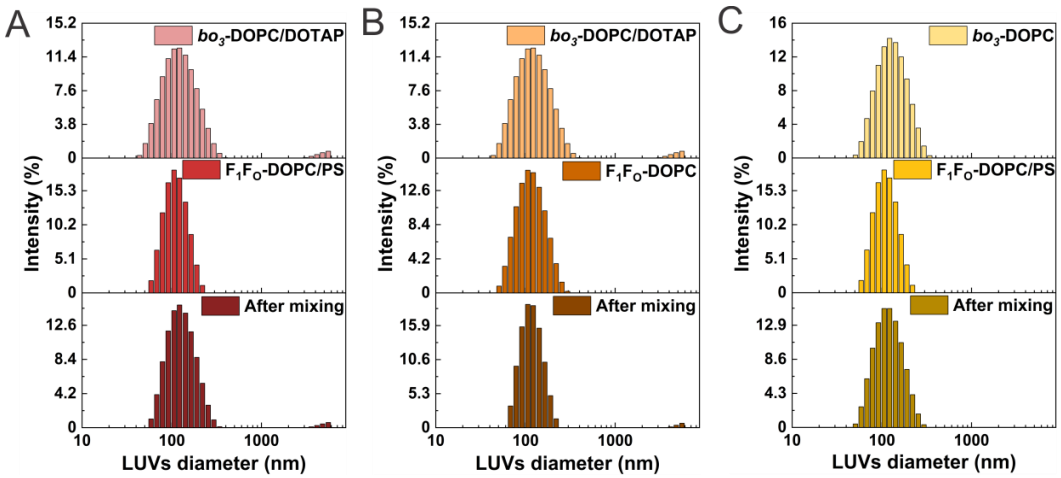

Figure S30. Liposomes size distribution by intensity, determined by DLS. Upon reconstitution of MPs, *bo*$_3$-lipid-LUVs and F_1F_O-lipid-LUVs were incubated together at room temperature for 10 min (at 500 rpm). (**A**) *bo*$_3$ oxidase was reconstituted into DOPC:DOTAP (70:30, molar ratio) LUVs, and F_1F_O-ATPase into DOPC:PS (70:30, molar ratio) LUVs. (**B**) *bo*$_3$ oxidase was reconstituted into DOPC:DOTAP (70:30, molar ratio) LUVs, and F_1F_O-ATPase into DOPC LUVs. (**C**) *bo*$_3$ oxidase was reconstituted into DOPC LUVs, and F_1F_O-ATPase into DOPC:PS (70:30, molar ratio) LUVs.

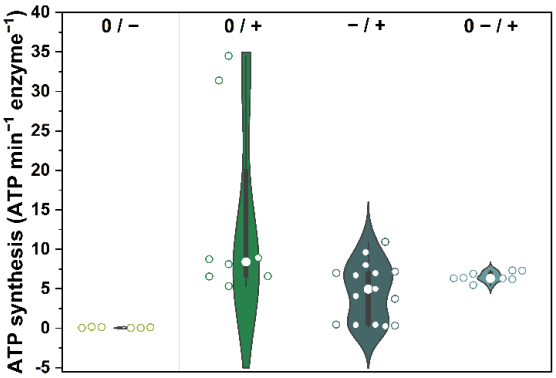

Figure S31. Respiratory-driven ATP synthesis in hybrid LUVs.

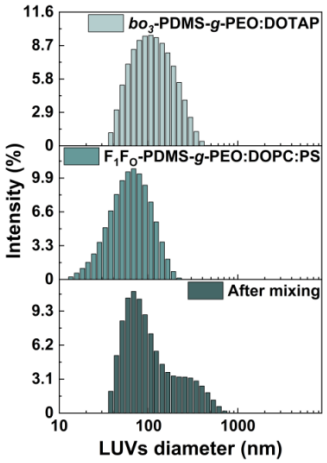

Figure S32. Proteo-hybrid-LUVs size distribution by intensity, determined by DLS (before and after fusion). *bo*$_3$ oxidase was reconstituted into cationic hybrids containing 30 mol% DOTAP and F_1F_O-ATPase into anionic hybrids containing 10 mol% soy PS.

7.2.7 Delivery of *bo₃* oxidase-ATTO 425 into hybrid GUVs

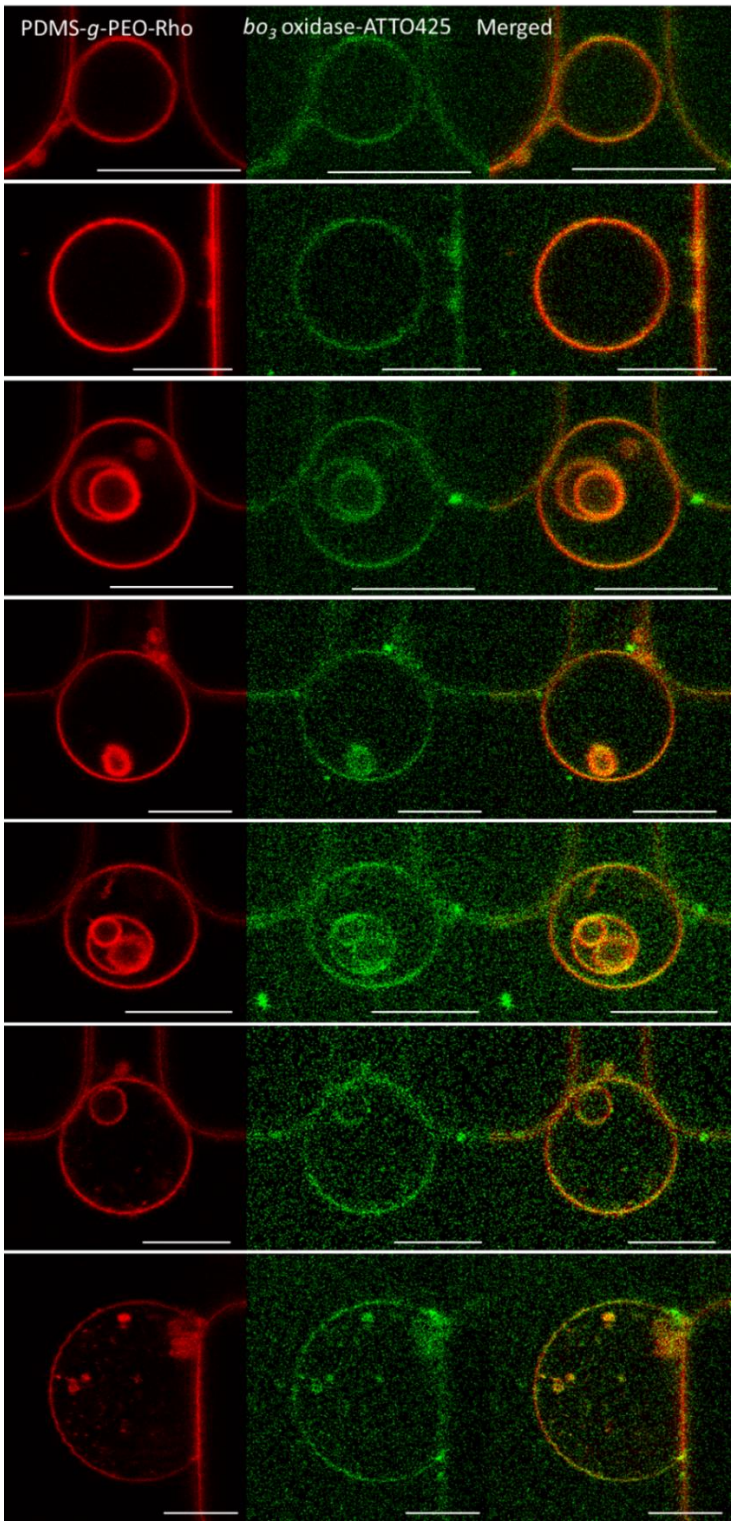

Figure S33. Delivery of *bo₃* oxidase from cationic hybrid LUVs into anionic hybrid GUVs trapped in microfluidic device. *bo₃* oxidase-ATTO 425 (green) was delivered into anionic GUVs upon GUV-LUV fusion. *bo₃* oxidase was reconstituted into cationic hybrid (PDMS-*g*-PEO:DOTAP = 70:30, mol%) LUVs. Scale bar: 10 µm.

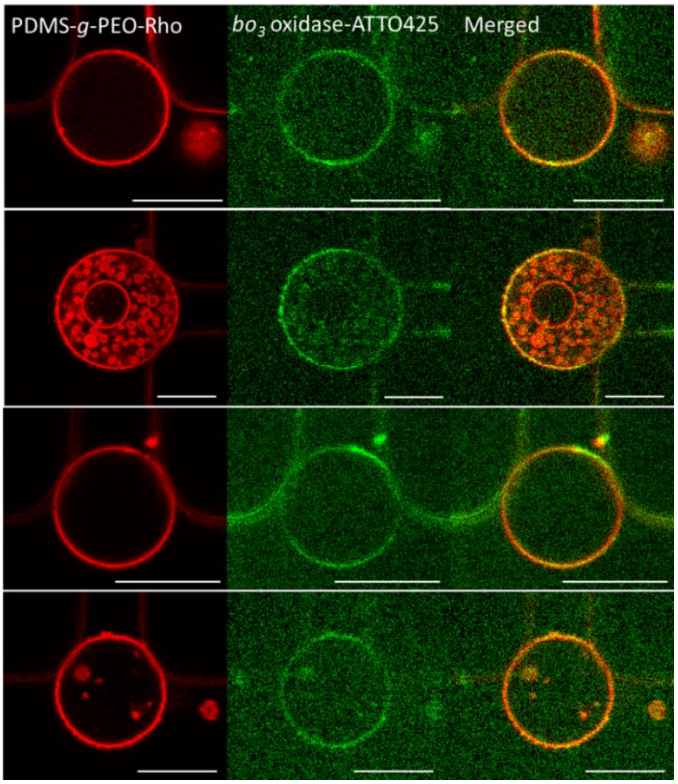

Figure S34. Delivery of *bo*$_3$ oxidase from cationic lipid LUVs into anionic hybrid GUVs trapped in microfluidic device. *bo*$_3$ oxidase-ATTO 425 (green) was delivered into anionic GUVs upon GUV-LUV fusion. *bo*$_3$ oxidase was reconstituted into cationic lipid (DOPC:DOTAP = 70:30, mol%) LUVs. Scale bar: 10 µm.

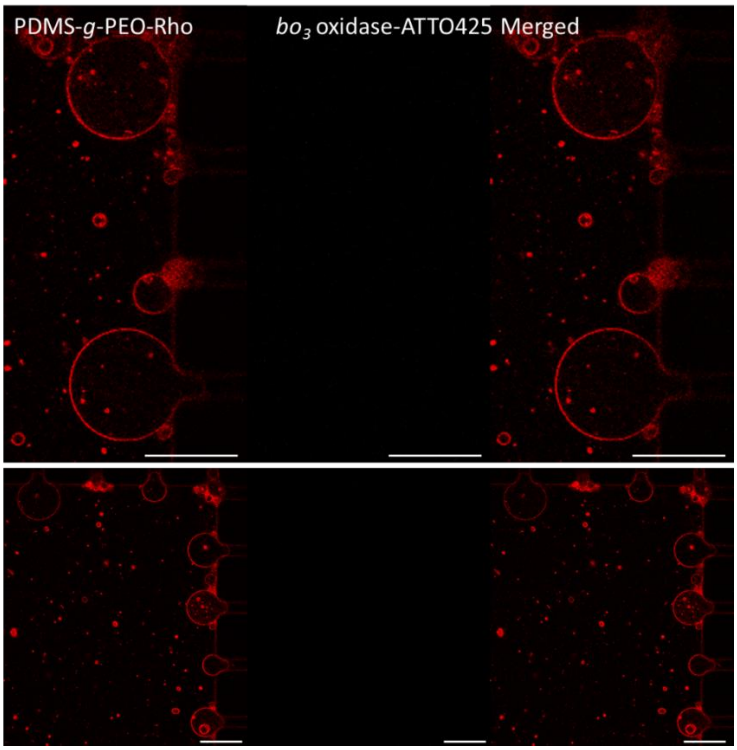

Figure S35. Cationic hybrid GUVs trapped in microfluidic device before flushing with *bo*$_3$-ATTO425-hybrid-LUVs. Hybrid GUVs were tagged with PDMS-*g*-PEO-Rho. Scale bar: 30 µm.

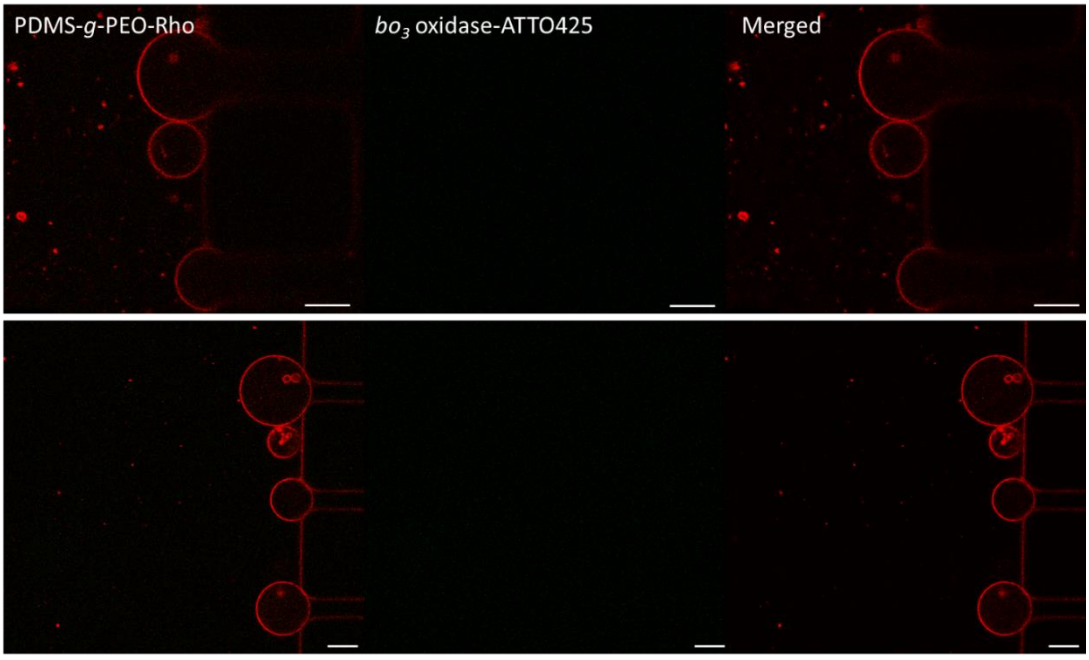

Figure S36. Cationic hybrid GUVs trapped in microfluidic device before flushing with *bo*$_3$-ATTO425-lipid-LUVs. Hybrid GUVs were tagged with PDMS-*g*-PEO-Rho. Scale bar: 10 µm.

7.3 Additional data on mechanically-induced growth

7.3.1 Size distribution of polymersomes in Milli-Q and isosmotic solution

Table S1. Table summarizing the influence of salts and agitation on PDMS-*g*-PEO polymersomes. Vesicles size distribution was determined by DLS. – indicates there was no change in vesicle size, ↑ portion of vesicles increased in size (fusion), ↑' portion of vesicles increased in size (fusion) but not observed with DLS, only with microscopy, ↓ portion of vesicles decreased in size (fission).

rpm	Milli-Q	KCl [mM]					NaCl [mM]				$MgCl_2$ [mM]				
		0	5	50	250	350	0	5	50	250	0	5	50	125	250
0	–	–	–	–	–	–	–	–	–	–	–	–	–	–	–
500	–	–	–	–	–	–	–	–	–	–	–	–	–	–	–
800	–	–	–	–	–	–	–	–	–	–	–	–	–	–	–
1100					↑'										
1200	–	–	–	–	↑	↑	–	–	–	↑↓	–	–	–	↑↓	↑↓
1300	–	–	–	–	↑↓	↑↓				↓				↓	↓
1500					↓	↓									

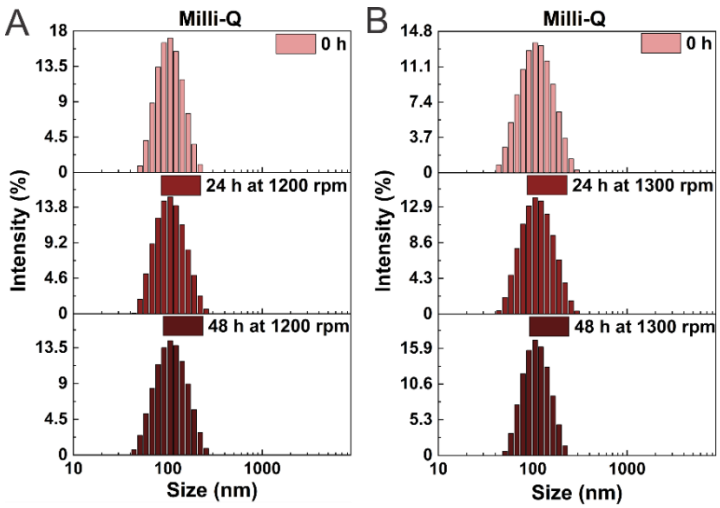

Figure S37. Size distribution by intensity (DLS) of polymersomes (5 mg ml^{-1}) in Milli-Q before and after agitation at 1200 and 1300 rpm. (**A**) Polymersomes without membrane dye (dye-free). (**B**) Dye-free polymersomes mixed with polymersomes containing 1.5 mol% PE-Rho and 1.5 mol% PE-NBD, in volume ratio 1:4.

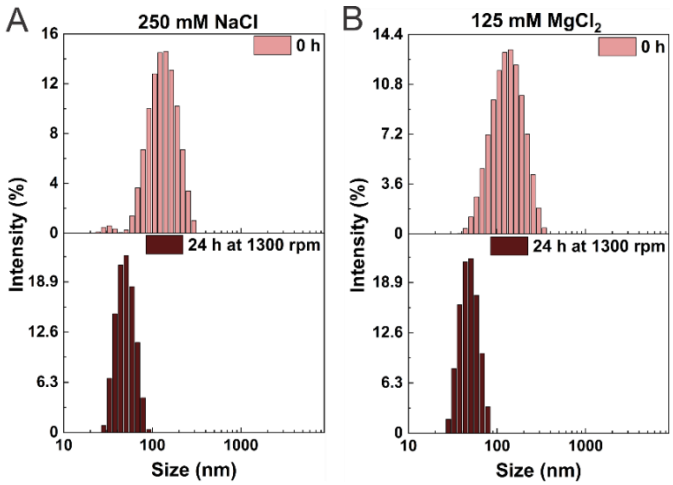

Figure S38. Size distribution by intensity (DLS) of polymersomes (5 mg ml^{-1}) in different salt solutions. (**A**) Polymersomes in 250 mM NaCl and (**B**) polymersomes in 125 mM $MgCl_2$ before and after agitation at 1300 rpm. Dye-free polymersomes were mixed with polymersomes containing 1.5 mol% PE-Rho and 1.5 mol% PE-NBD, in volume ratio 1:4.

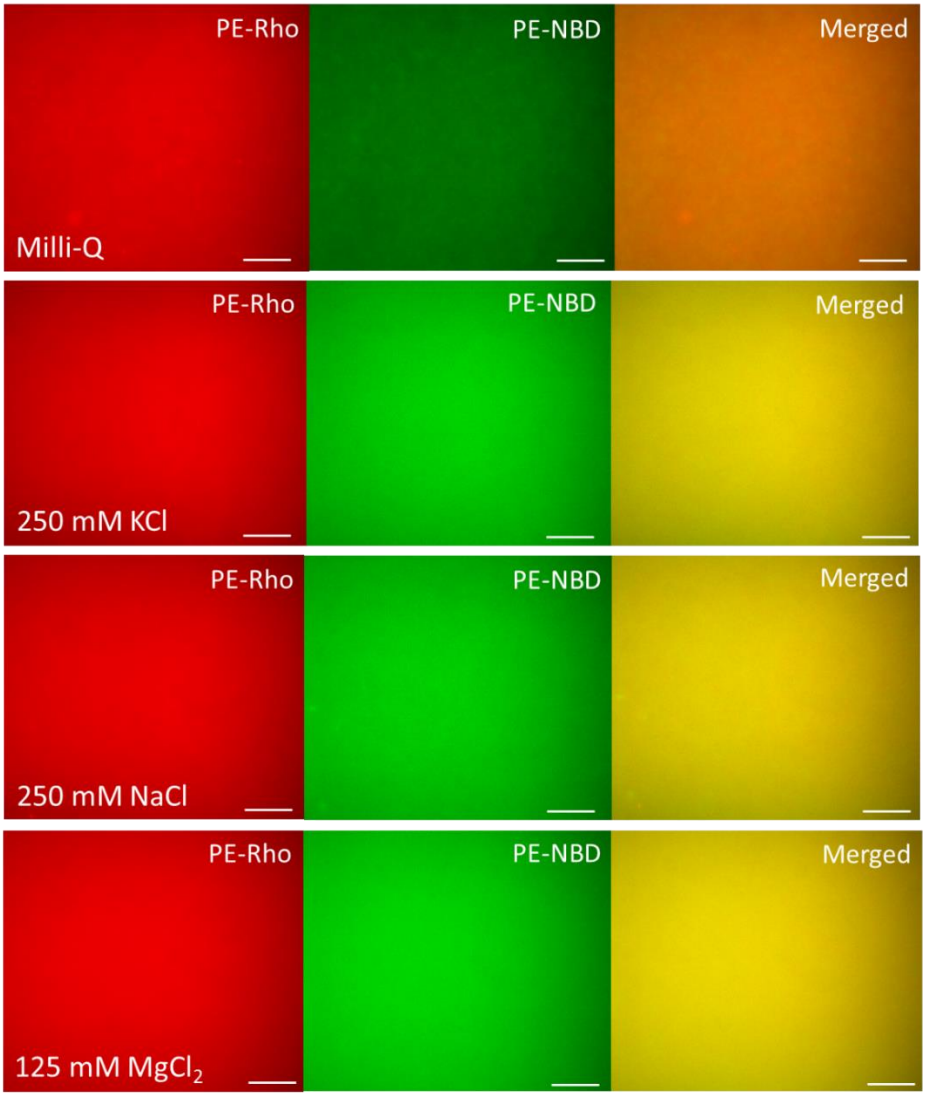

Figure S39. Fluorescence microscopy images of PDMS-*g*-PEO LUVs (5 mg ml^{-1}) after agitation at 1300 rpm for 24 h, in Milli-Q, 250 mM KCl, 250 mM NaCl and 125 mM $MgCl_2$. Dye-free polymersomes were mixed with polymersomes containing 1.5 mol% PE-Rho and 1.5 mol% PE-NBD, in volume ratio 1:4.

7.3.2 Microscopy of polymer GUVs grown from LUVs by agitation in KCl

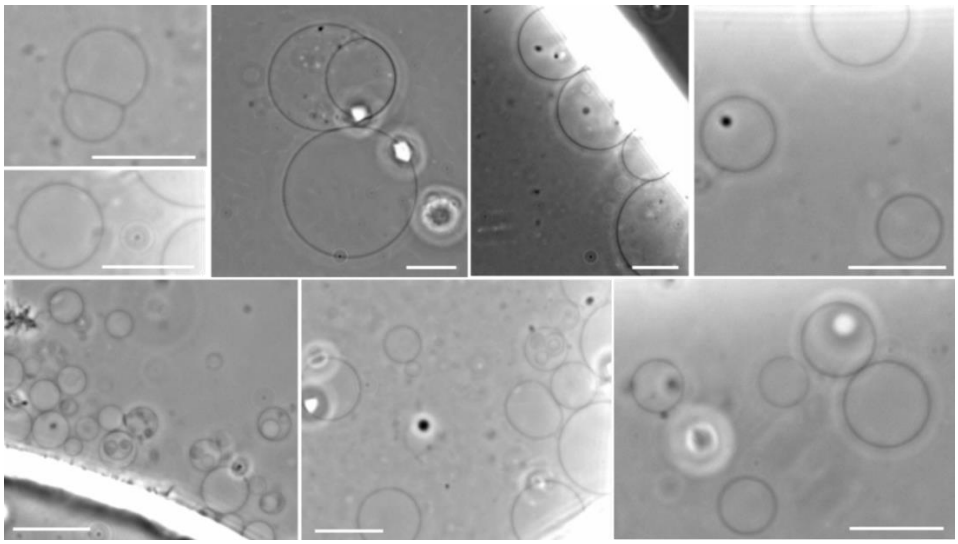

Figure S40. Phase contrast images of PDMS-*g*-PEO GUVs grown from LUVs (1.25 mg ml^{-1}) in 250 mM KCl by agitation at 1200 rpm. Majority of GUVs were found localized at the cover slip edges. Typically 2–3 GUVs were aggregated together. Scale bar: 10 µm.

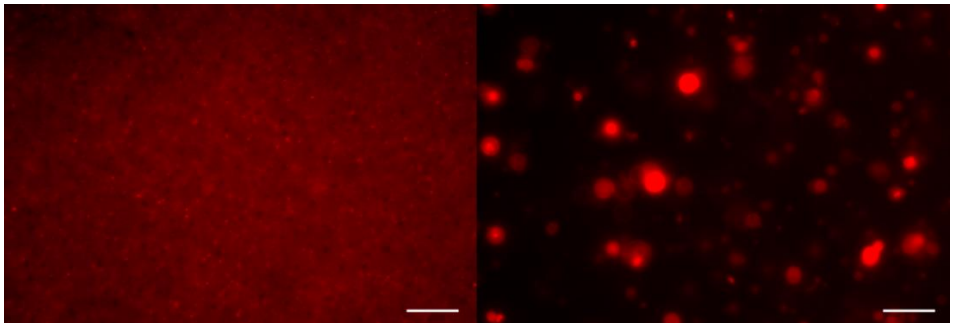

Figure S41. PDMS-*g*-PEO LUVs, tagged with 1.2 mol% PDMS-*g*-PEO-Rhodamine, (left) and PDMS-*g*-PEO GUVs grown from LUVs (1.25 mg ml^{-1}) by agitation at 1200 rpm for 3 h, in 250 mM KCl (right). Scale bar: 10 µm.

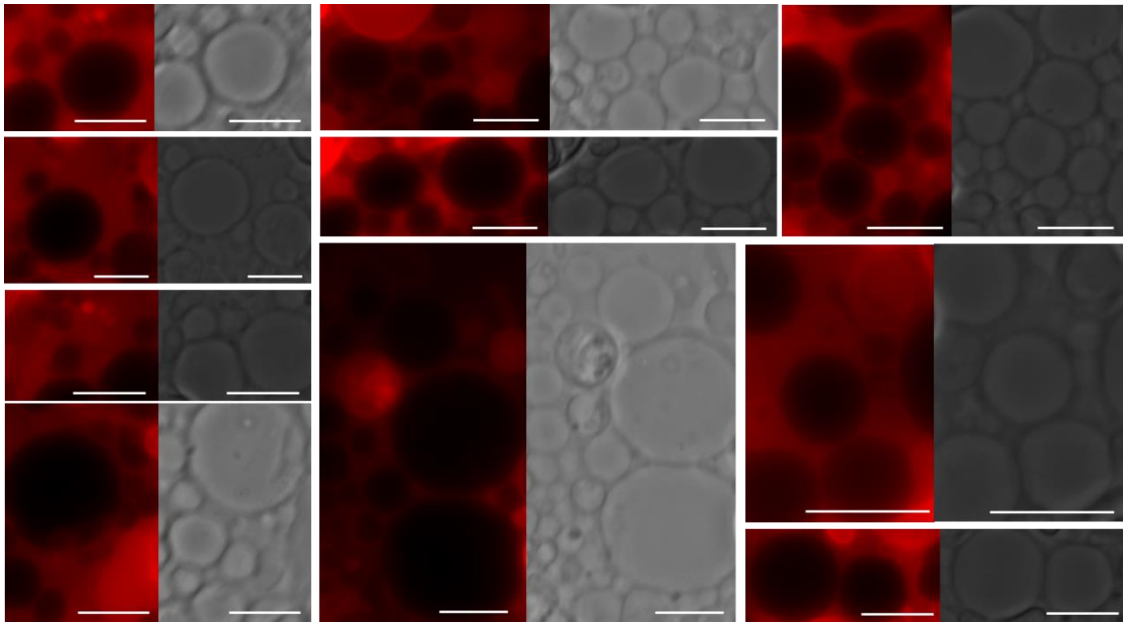

Figure S42. PDMS-*g*-PEO GUVs, tagged with 1.2 mol% PDMS-*g*-PEO-Rho, grown from 200 nm polymersomes (5 mg ml^{-1}) by agitation at 1200 rpm for 24 h, in 250 mM KCl. Scale bar: 10 µm. Increased initial concentration of LUVs and prolonged agitation substantially increased yield of GUVs.

7.3.3 Size distribution of hybrids in isosmotic KCl solution

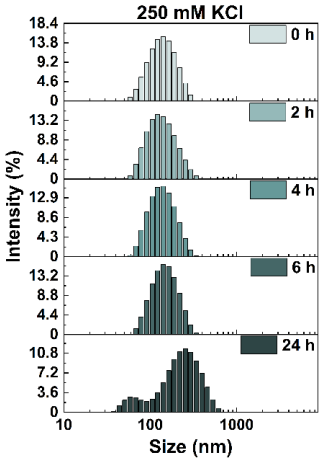

Figure S43. Change in size distribution by intensity (DLS) of hybrids in 250 mM KCl before and after agitation at 1200 rpm. Hybrids were composed of 80 mol% PDMS-g-PEO and 20 mol% DOPC. At > 60 mol% PDMS-*g*-PEO, polymer and lipid are homogenously distributed in the membrane.

7.3.4 Size distribution of polymersomes in hypertonic and hypotonic KCl solution

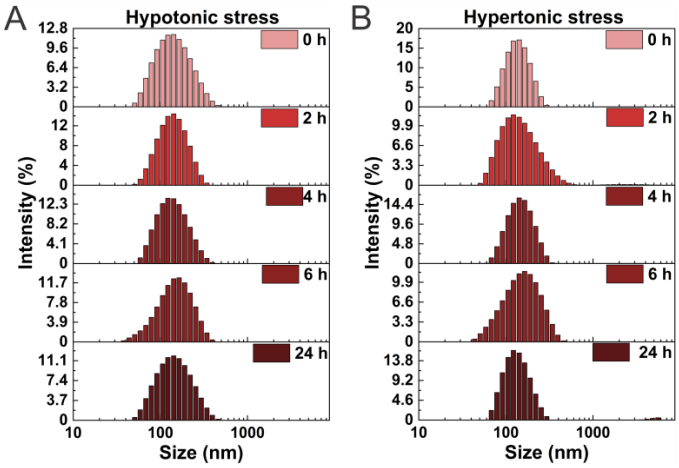

Figure S44. Polymersomes under osmotic stress in absence of agitation. (**A**) Hypotonic stress: 300 µl Milli-Q was mixed with 100 µl 200 nm polymersomes in 250 mM KCl (5 mg ml^{-1}). (**B**) Hypertonic stress: 300 µl 500 mM KCl was mixed with 100 µl 200 nm polymersomes in 250 mM KCl (5 mg ml^{-1}). Final polymersomes concentration was 1.25 mg ml^{-1}.

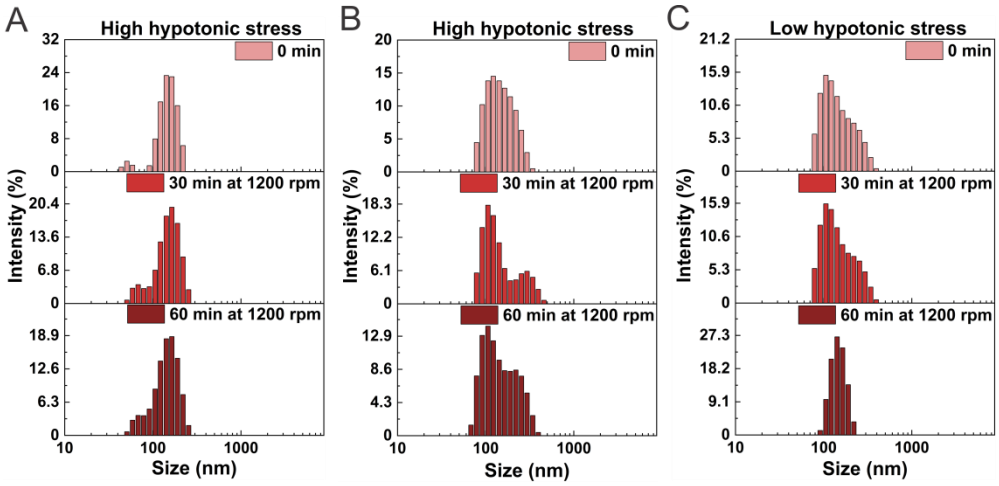

Figure S45. Polymersomes under hypotonic stress and agitation. Polymer LUVs, prepared in 250 mM KCl, exposed to high hypotonic stress (external solution Milli-Q) and agitation at 1200 rpm; final polymersomes concentration was 2 mg ml^{-1} (**A**) or 4 mg ml^{-1}(**B**). (**C**) Polymer LUVs, prepared in 250 mM KCl, exposed to low hypotonic stress (external solution 150 mM KCl) and agitation at 1200 rpm; final concentration was 4 mg ml^{-1}.

7.3.5 Agitation of polymer film

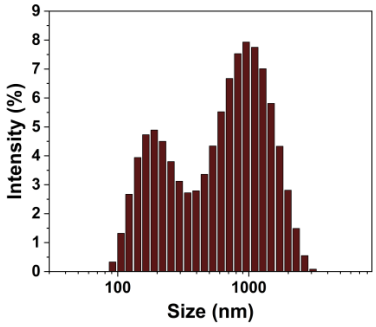

Figure S46. Size distribution by intensity of PDMS-*g*-PEO vesicles formed from polymer film. Polymersomes were agitated at 1200 rpm for 24 h.

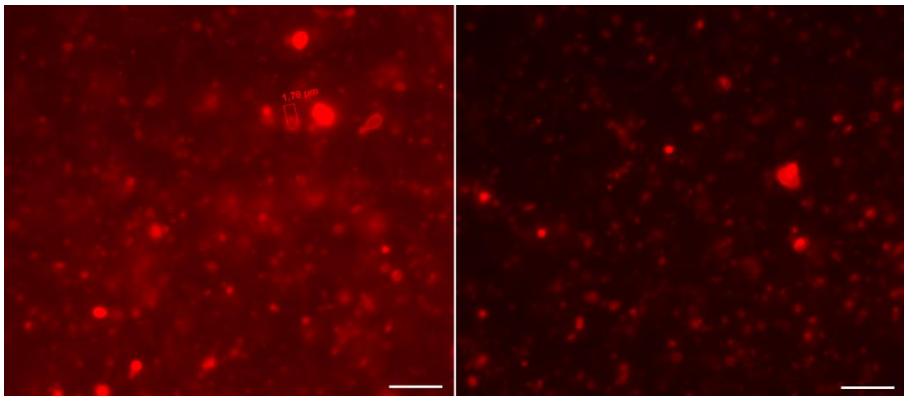

Figure S47. PDMS-g-PEO LUVs and small GUVs obtained by agitation at 1200 rpm for 24 h. Scale bar: 10 µm.

7.3.6 Membrane mixing in bulk

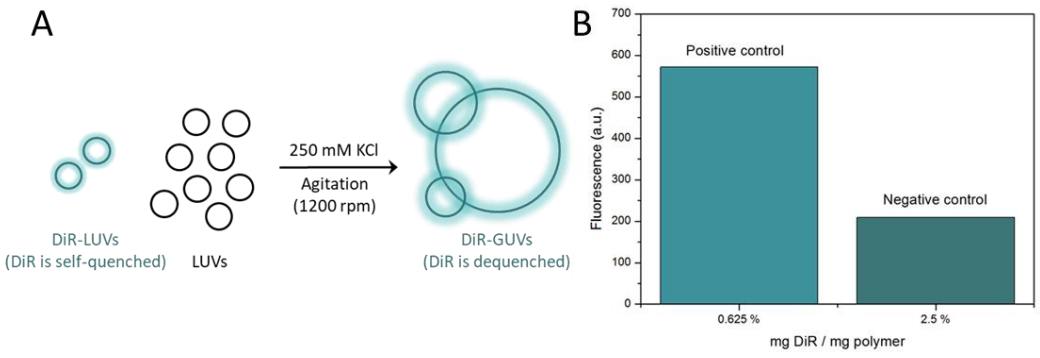

Figure S48. Membrane mixing analysis via DiR dequenching. (**A**) Scheme presenting DiR dequenching upon fusion of DiR-LUVs and dye-free LUVs, mixed in ratio 1:4, v/v. If fusion occurs, DiR is dequenched upon dilution in the membranes and newly formed larger LUVs and GUVs emmitted higher fluorescence intensity. (**B**) Positive (polymersomes with 0.625 % DiR, the concentration obtained upon complete fusion of vesicles) and negative control (polymersomes with 2.5 % DiR, high quenching) for membrane mixing.

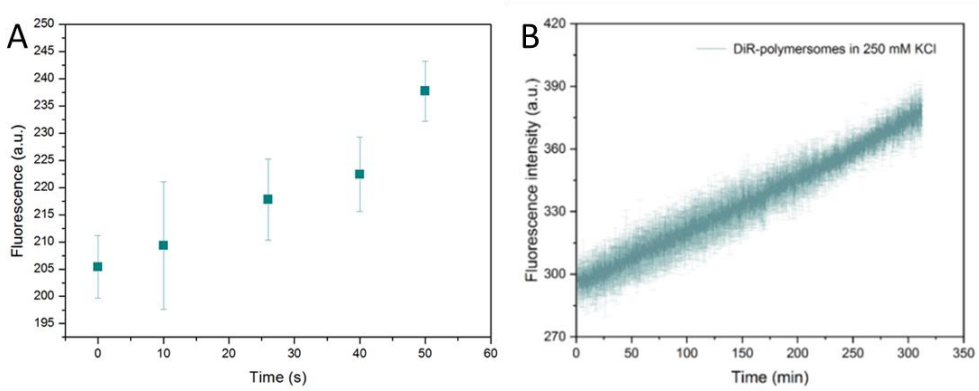

Figure S49. Membrane mixing of polymersomes in 250 mM KCl. (**A**) Change in florescence of DiR in the membrane of polymersomes (dye dilution and dequenching) upon agitation at 1200 rpm in 250 mM KCl. (**B**) Dequenching of DiR in the membrane of polymersomes in presence of 250 mM KCl at constant stirring.

7.3.7 Fluorescence microscopy of polymer structures grown from LUVs by agitation in NaCl

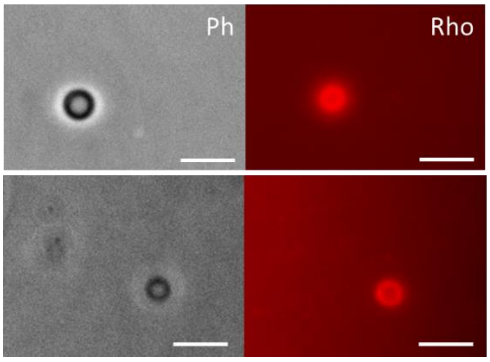

Figure S50. PDMS-*g*-PEO multilamellar giant vesicles formed in NaCl. Vesicles were formed from 200 nm polymersomes (5 mg ml^{-1}), tagged with 1.5 mol% PE-Rho (red) and 1.5 mol% PE-NBD, by agitation at 1200 rpm for 48 h, in 250 mM NaCl. Scale bar: 10 µm.

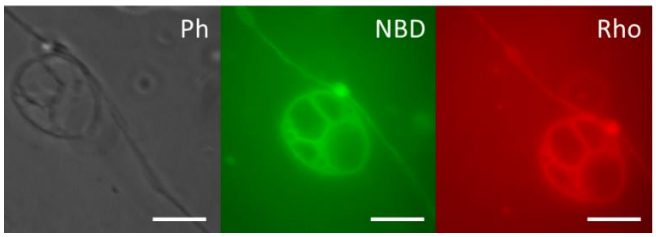

Figure S51. PDMS-*g*-PEO multivesicular giant vesicles formed in NaCl. Vesicle were formed from 200 nm polymersomes (5 mg ml^{-1}), tagged with 1.5 mol% PE-Rho (red) and 1.5 mol% PE-NBD, by agitation at 1200 rpm for 48 h, in 250 mM NaCl. Scale bar: 10 µm.

7.3.8 LUVs docking on GUVs

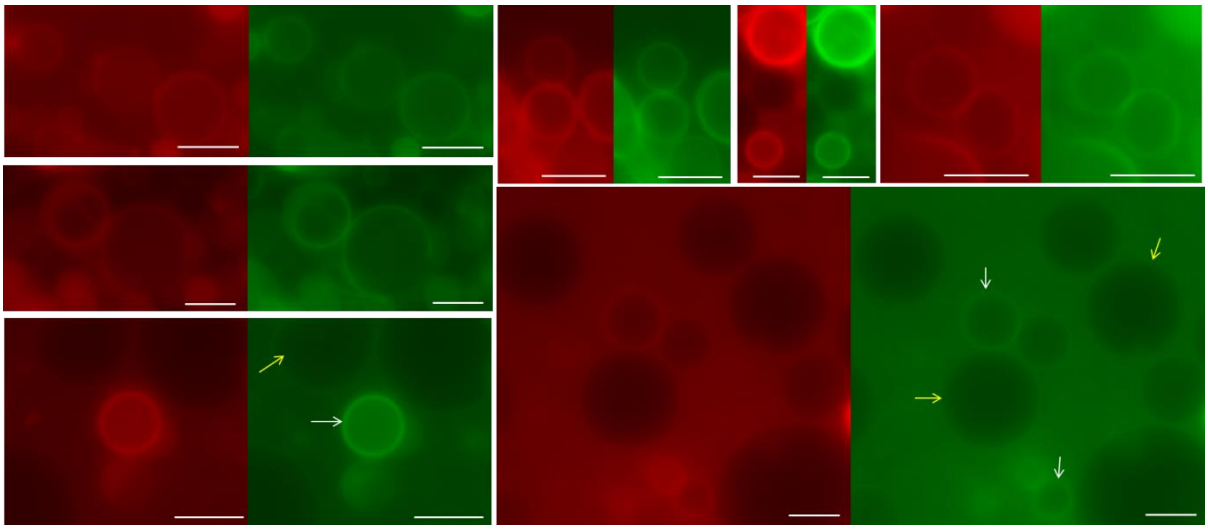

Figure S52. Docking of PDMS-*g*-PEO LUVs on GUVs. LUVs were tagged with 0.6 mol% PDMS-*g*-PEO-FITC (green), and GUVs with 0.6 mol% PDMS-*g*-PEO-Rhodamine (red). White arrows indicate GUVs with higher amount of docked LUVs, while yellow arrows indicate GUVs where only low amount of docked LUVs were observed. Scale bar: 5 µm.

7.3.9 Single vesicle content mixing experiments

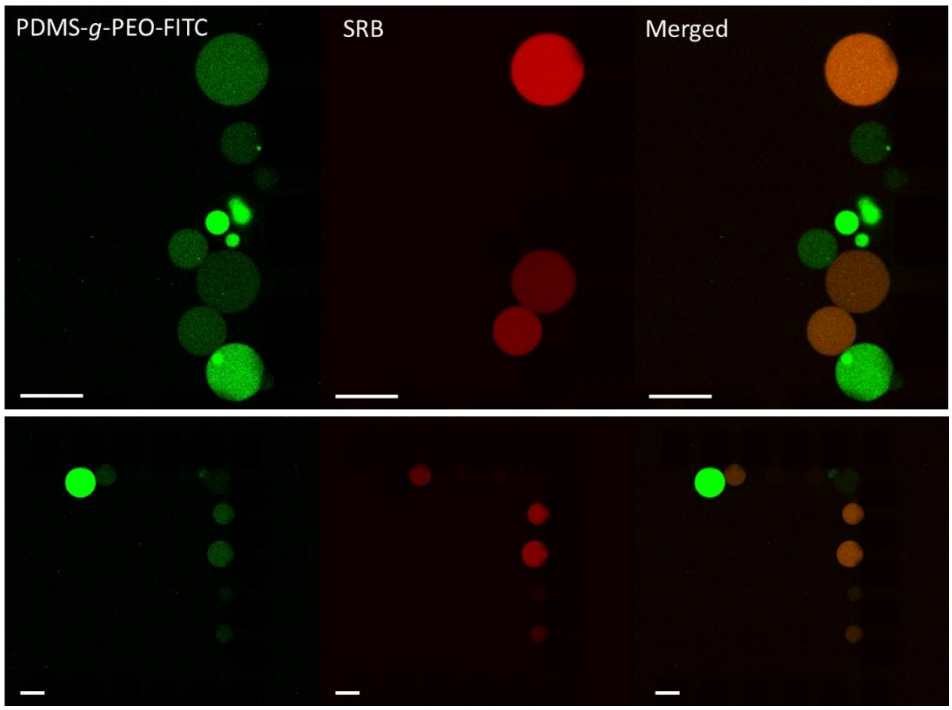

Figure S53. **Content mixing experiment in microfluidics.** GUVs, prepared in ~ 500 mM sucrose with electroformation, trapped in microfluidics after flushing into the chip LUVs tagged with PDMS-*g*-PEO-Fluorescein (green) and content marker SRB (red) in 250 mM KCl. The image was taken after flushing away non-fused or non-encapuslated LUVs with 250 mM KCl. Scale bar: 10 µm.

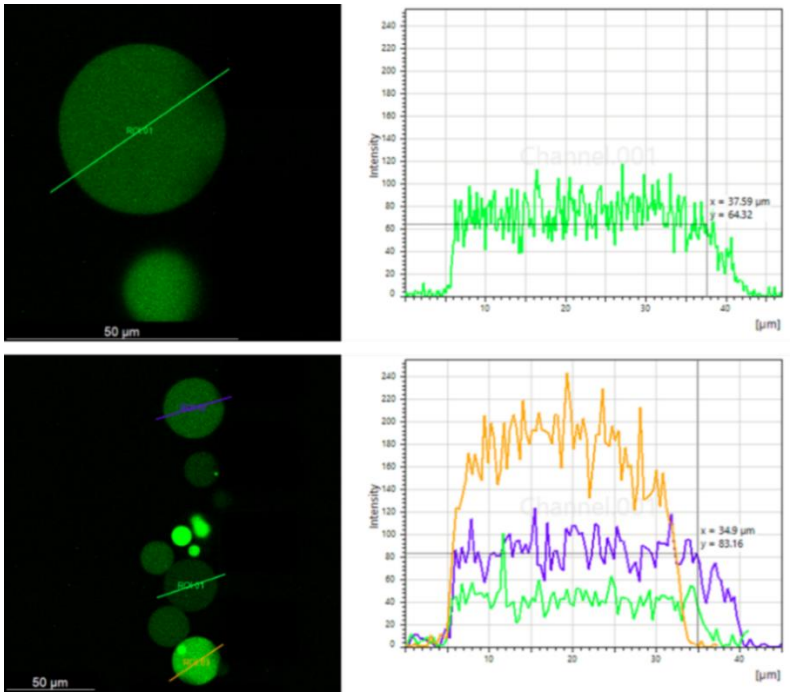

Figure S54. Analysis of FITC signal in GUVs cross section. GUVs, prepared in ~ 500 mM sucrose with electroformation, trapped in microfluidics after flushing into the chip LUVs tagged with PDMS-*g*-PEO-FITC (green) and content marker SRB (red) in 250 mM KCl. Line profile for fluorescein is shown on right side.

7.3.10 Encapsulation of cytosolic solutes

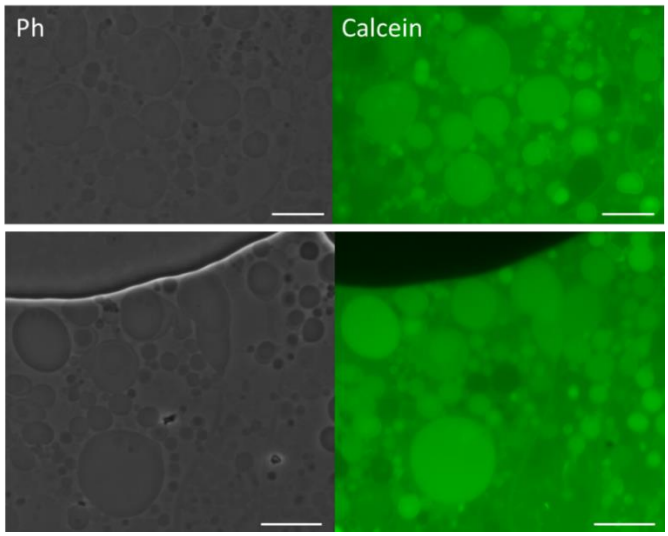

Figure S55. Micrographs of PDMS-*g*-PEO GUVs with encapsulated calcein (green). Scale bar: 10 µm.

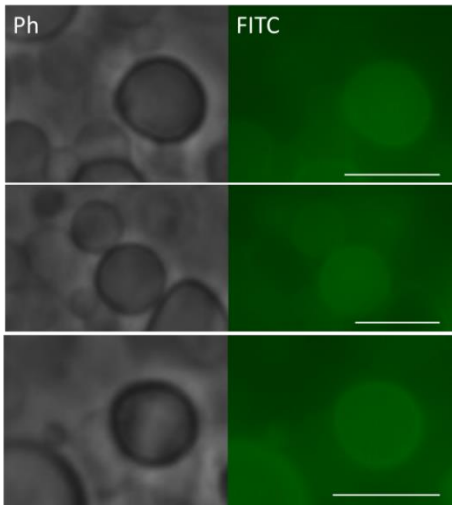

Figure S56. Micrographs of PDMS-*g*-PEO GUVs with encapsulated FITC-dextran. Ph: phase contrast; FITC: fluorescein channel. Scale bar: 5 µm.

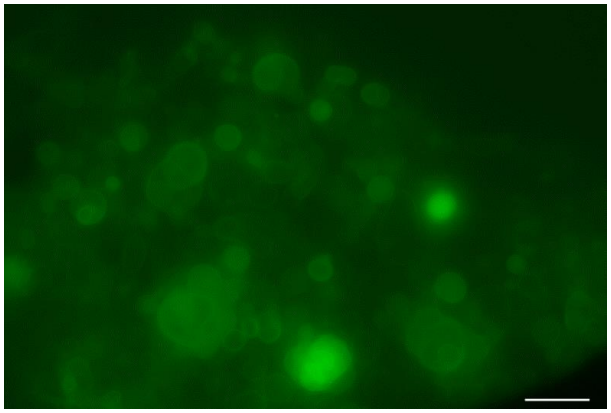

Figure S57. Micrograph of PDMS-*g*-PEO GUVs with encapsulated FITC-dextran. Scale bar: 10 µm.

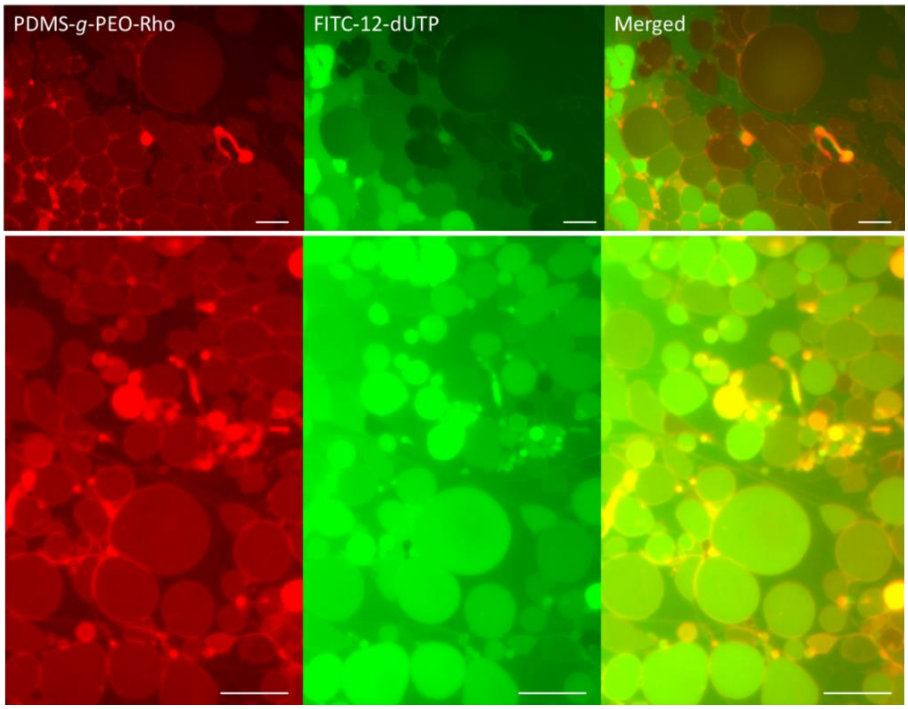

Figure S58. Micrographs of PDMS-*g*-PEO GUVs grown in presence of FITC-12-UTP. PDMS-*g*-PEO GUVs were grown from LUVs in 250 mM KCl by agitation. Polymersomes were labeled with PDMS-g-PEO-Rhodamine (red). FITC-12-dUTP (green) was added to LUVs before agitation and was encapsulated during growth of GUVs. The GUVs were larger than in absence of FITC-12-dUTP. Scale bar: 10 µm.

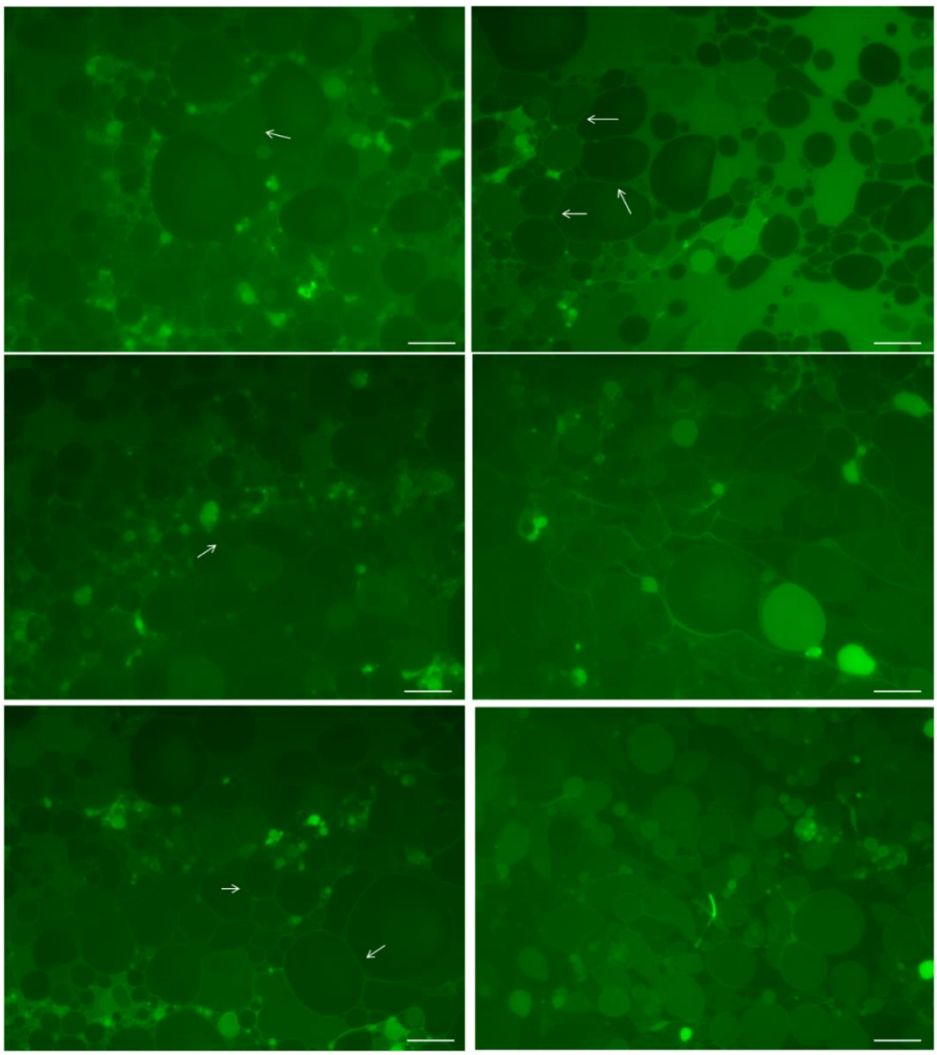

Figure S59. Micrographs of PDMS-*g*-PEO GUVs grown in presence of FITC-12-UTP. PDMS-*g*-PEO GUVs were grown from LUVs in 250 mM KCl by agitation. FITC-12-dUTP (green) was added to LUVs before agitation. Majority of GUVs contained only low amount of FITC-12-dUTP inside, its distribution was highly heterogonous in-between GUVs. For large amount of GUVs long contact was observed (a few examples are indicated with white arrow). Scale bar: 10 μm.

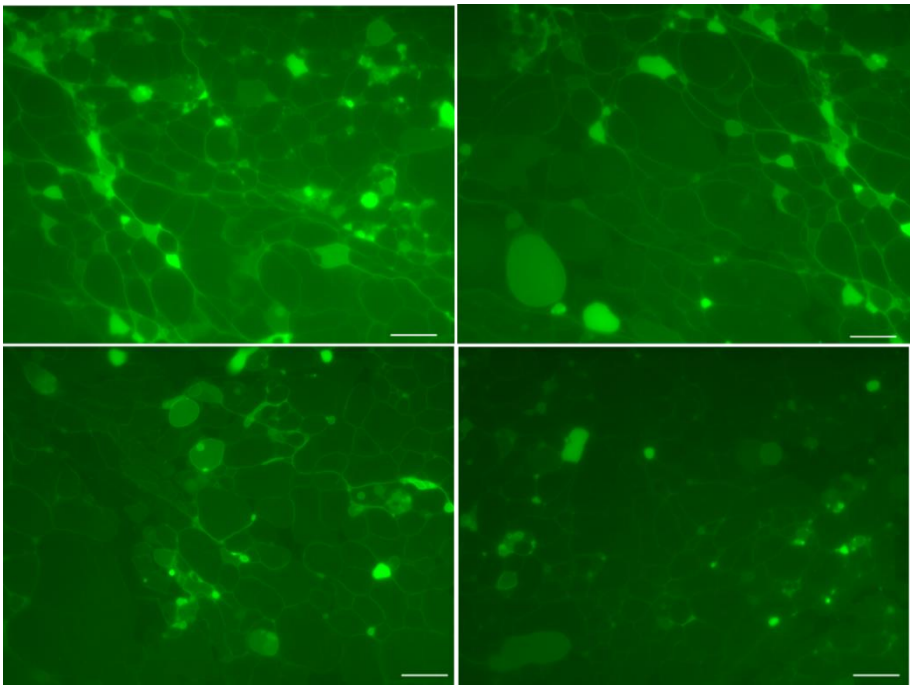

Figure S60. Micrograph of interconnected PDMS-*g*-PEO GUVs grown in presence of FITC-12-UTP. Interconnected GUVs were grown from LUVs in 250 mM KCl by agitation. FITC-12-dUTP (green) was added to LUVs before agitation. Elongated GUVs were connected by long contact and mimicking tissue structure; similar intracellular structure can be seen by cork cells. Scale bar: 10 µm.

7.3.11 Stability of reconstituted *bo₃* oxidase over time

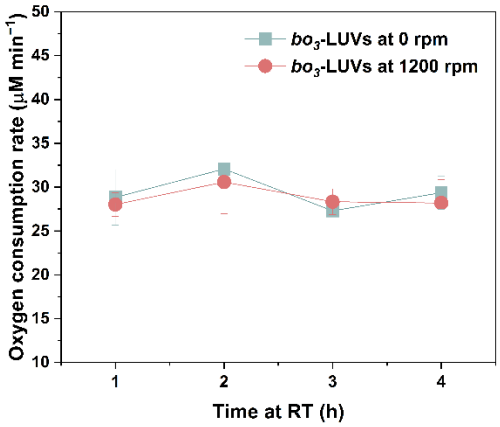

Figure S61. Change in activity of *bo₃* oxidase over time at room temperature (RT). *bo₃* oxidase was reconstituted in polymer LUVs. Activity was measured for the first time 1 h after reconstitution.

7.4 Additional data on fusion/electroformation-mediated growth

7.4.1 Size distribution of *bo*$_3$-GUVs

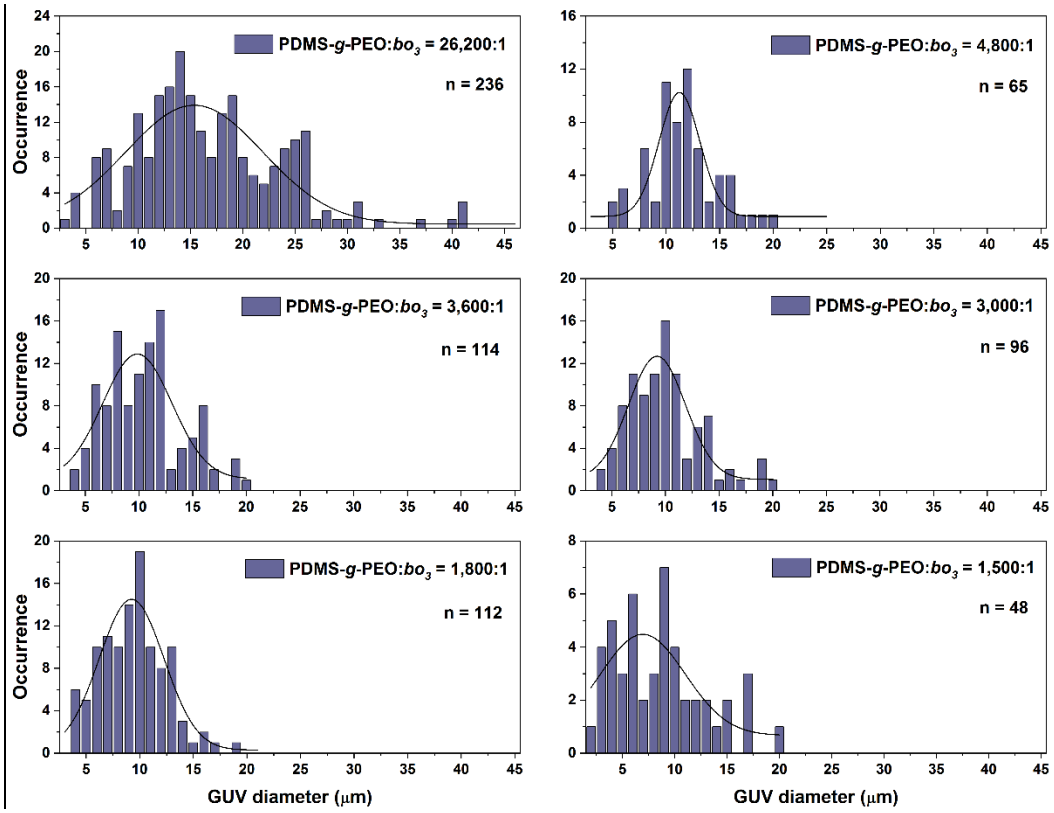

Figure S62. Size distribution of *bo*$_3$-polymer-GUVs in buffer (1 mM Tris-HCl, pH 7.5, 100 mM sucrose). *bo*$_3$-polymer-GUVs with molar ratio 1,800:1 and 1,500:1 were prepared from 1.4 µM *bo*$_3$ oxidase in LUVs, other samples were prepared from 0.7 µM *bo*$_3$ oxidase in LUVs, mixed with protein-free polymersomes accordingly; *bo*$_3$-LUV:LUV (v/v) (from top left to bottom right): 1:10, 1:1, 2:1, 4:1, 2:1, 4:1. Black lines represent Gauss distributions.

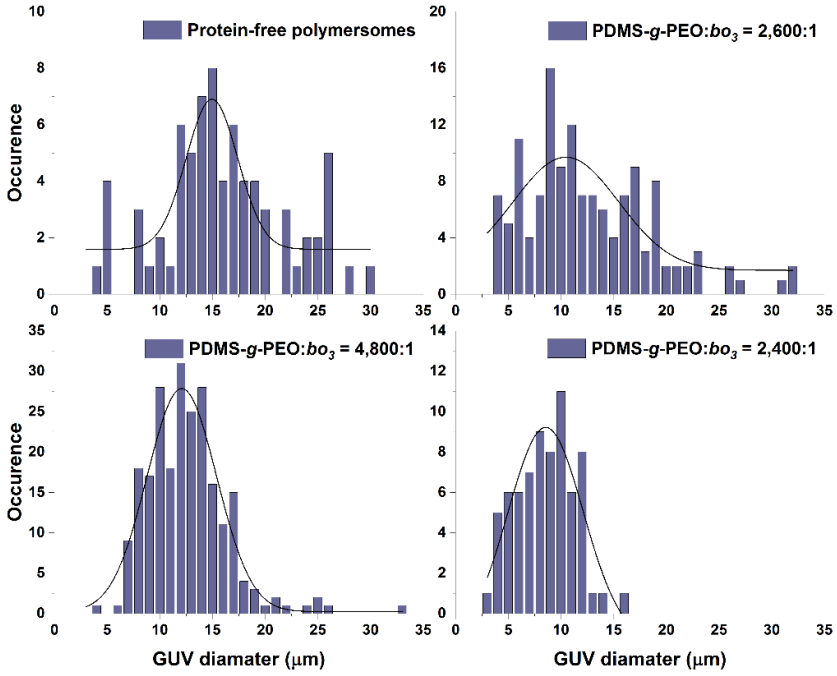

Figure S63. Size distribution of polymer *bo*$_3$-GUVs in 100 mM sucrose. For all the samples with protein *bo*$_3$ oxidase was reconstituted at 0.7 μM concentration in *bo*$_3$-LUVs suspension; *bo*$_3$-GUVs were formed from mixtures of *bo*$_3$-LUVs and protein-free LUVs (different volume ratios).

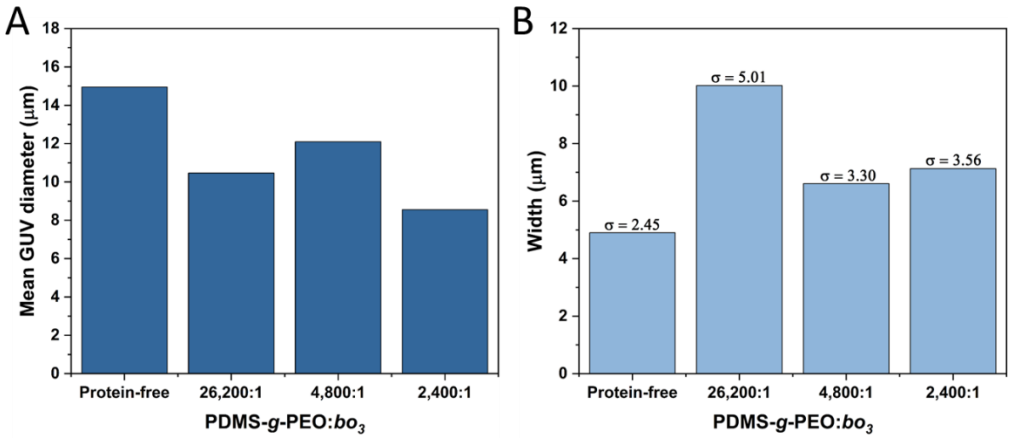

Figure S64. Size distribution of protein-free polymer GUVs and *bo*$_3$-polymer-GUVs in 100 mM sucrose. (**A**) Change in mean size of GUVs with decreasing polymer-to-proton pump molar ratio. (**B**) Half-width of the fitted Gaussian distributions of *bo*$_3$-polymer-GUVs at four different polymer-to-proton pump molar ratios.

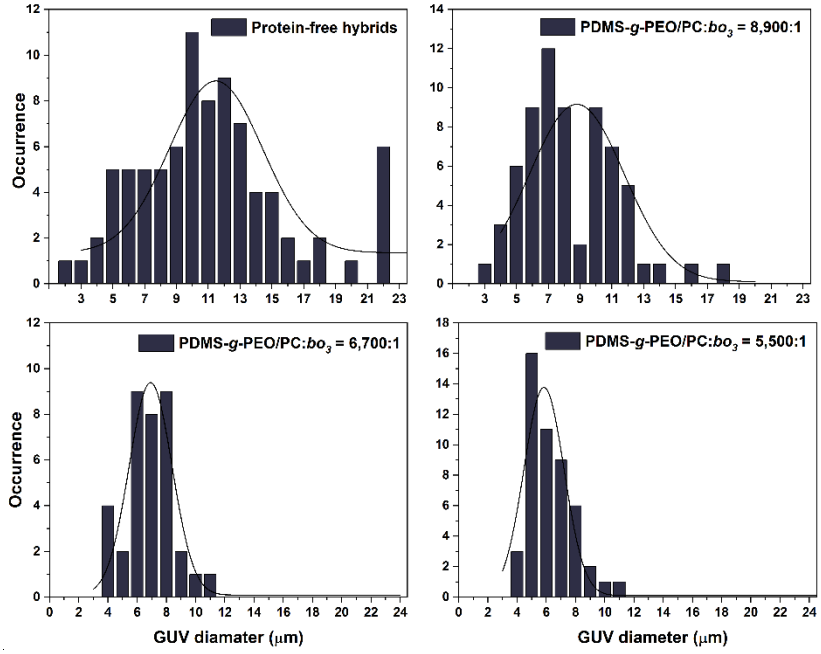

Figure S65. Size distribution of hybrid GUVs and *bo*$_3$-GUVs prepared by fusion/electroformation in buffer (1 mM Tris-HCl (pH 7.5), 100 mM sucrose). Hybrids composition was PDMS-*g*-PEO:PC = 70:30, mol%. Size of GUVs decreases with increasing protein density. *bo*$_3$ oxidase was reconstituted at 0.7 μM concentration in proteoLUVs suspension. For PDMS-*g*-PEO/PC:*bo*$_3$ oxidase = 8,900, proteoLUVs were mixed with protein-free LUVs in volume ratio 1:1, for 6,700 in ratio 2:1, and for 5,500 in ratio 4:1.

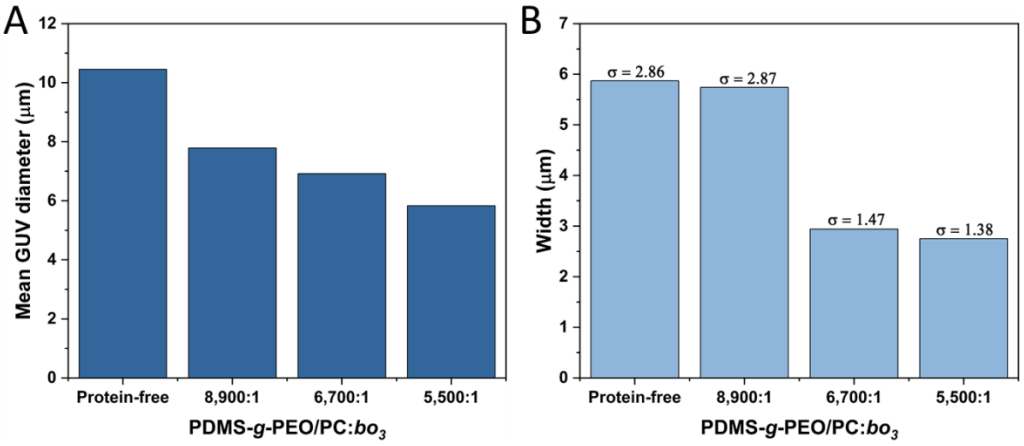

Figure S66. Size distribution of protein-free hybrid GUVs and *bo*$_3$-hybrid-GUVs in buffer (1 mM Tris-HCl (pH 7.5), 100 mM sucrose). (**A**) Change in mean size of GUVs with decreasing polymer/lipid-to-proton pump molar ratio. (**B**) Half-width of the fitted Gaussian distributions of *bo*$_3$-hybrid-GUVs at four different polymer/lipid-to-proton pump molar ratios.

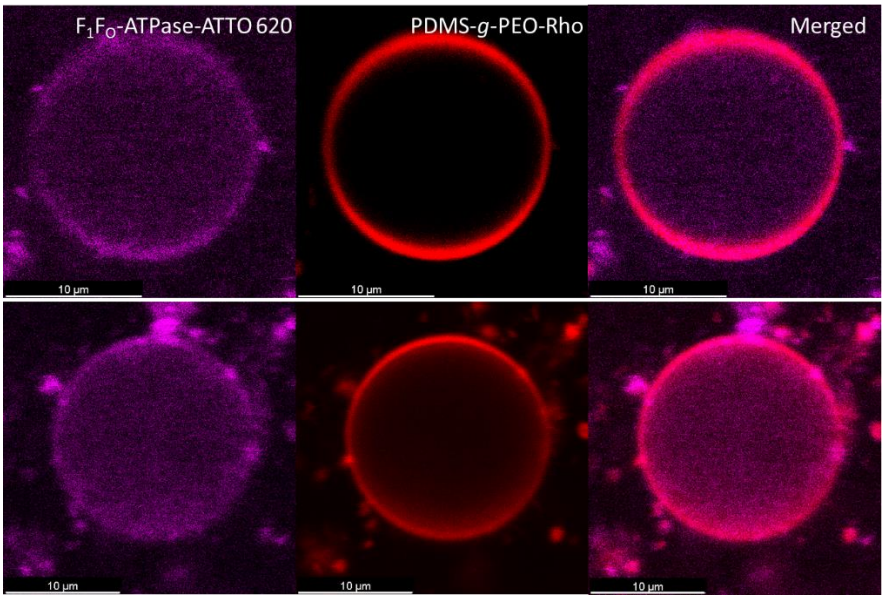

Figure S67. Successful insertion of F_1F_O-ATPase-ATTO 620 (magenta) in F_1F_O-hybrid-GUVs. Polymer dye PDMS-*g*-PEO-Rho (red) was used to visualize the membrane.

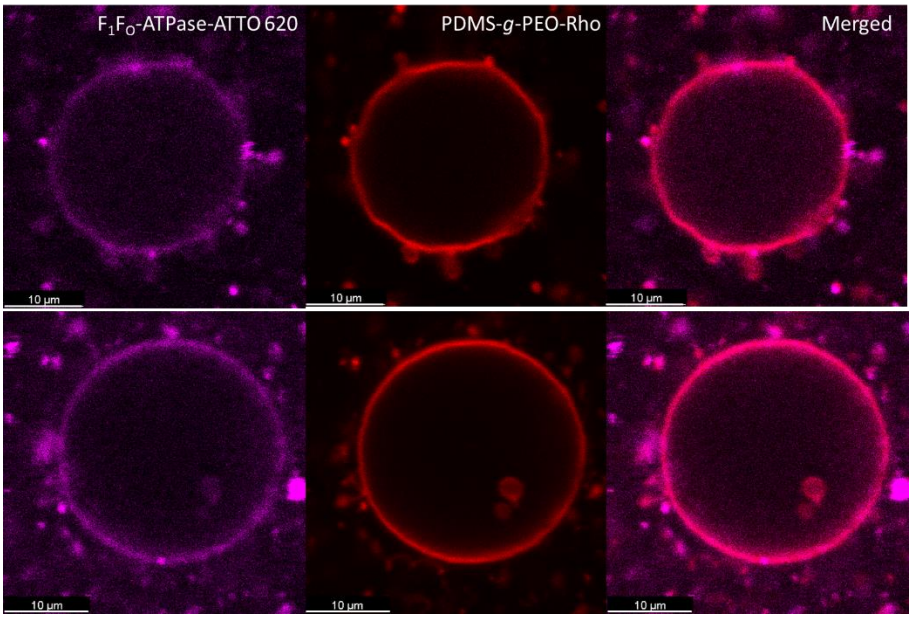

Figure S68. Successful insertion of F_1F_O-ATPase-ATTO 620 (magenta) in F_1F_O-polymer-GUVs. Polymer dye PDMS-*g*-PEO-Rho (red) was used to visualize the membrane.

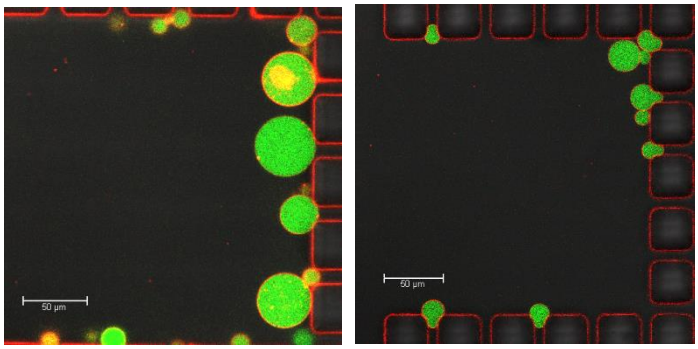

Figure S69. **Polymersomes evaluated for proton pumping.** *Left*: Protein-free polymersomes (negative control). *Right*: Polymersomes with reconstituted bo_3 oxidase (PDMS-*g*-PEO:bo_3 oxidase = 9540:1).

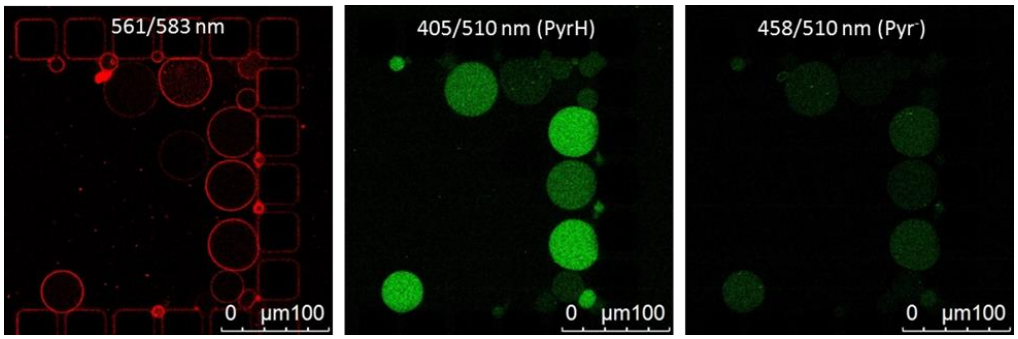

Figure S70. bo_3-polymer-GUVs with encapsulated pyranine trapped in microfluidic chip. Polymer-to-protein molar ratio was 2,980:1. Pyranine fluorescence (green) was monitored at two excitation wavelengths (405 nm and 458 nm). For better visualization, membrane of proteoGUVs was tagged with polymer dye (PDMS-*g*-PEO-Rho, red).

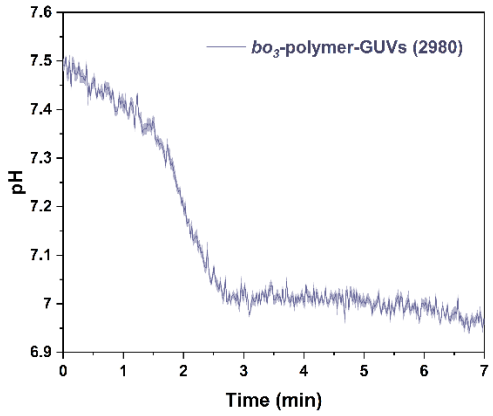

Figure S71. Intravesicular pH change for bo_3-polymer-GUVs in first 7 min. Polymer-to-protein molar ratio was 2,980:1.

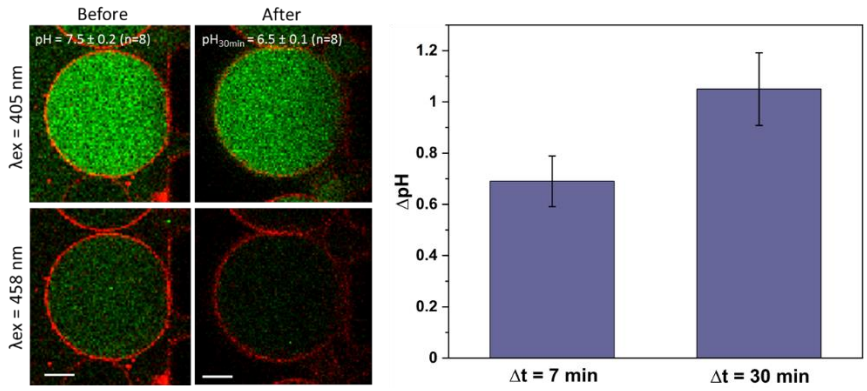

Figure S72. pH change in *bo*$_3$-polymer-GUVs after 30 min. Scale bar: 10 µm. Initial pH in *bo*$_3$-polymer-GUVs was 7.5 ± 0.2 (n = 8), 7 min after activation with DTT/Q_1 pH decreased to 6.8 ± 0.2 (n = 9) and after 30 min further decreased to 6.5 ± 0.1 (n = 8).

7.4.2 Cryo-TEM analysis of lipid LUVs

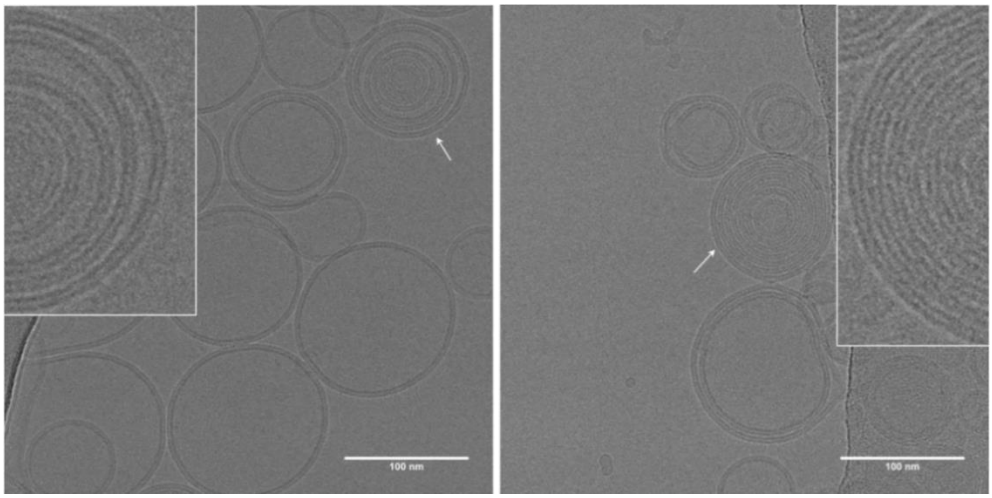

Figure S73. Cryo-TEM of large unilamellar and multilamellar soy PC vesicles. *Left*: protein-free vesicles, *right*: functionalized with *bo*$_3$ oxidase. White arrows indicate multilamellar vesicles (majority of vesicles was unilamellar). Defocus: ~ −2 µm.

7.4.3 Proton pumping by F_1F_O-GUVs and pyranine artifacts

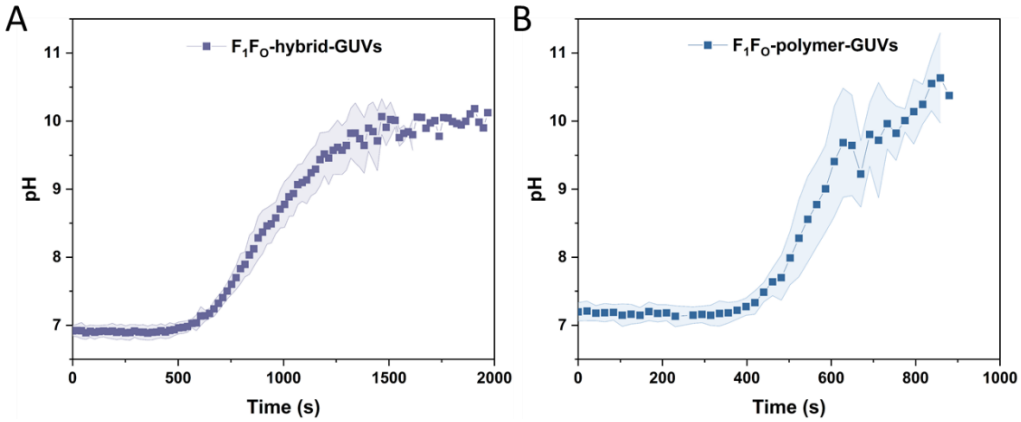

Figure S74. Monitoring intravesicular pyranine fluorescence in microfluidic traps. (**A**) Change in pH in lumen of F_1F_O-hybrid-GUVs. Purple squares represent average of 21 GUVs with standard deviation. (**B**) Change in pH in lumen of F_1F_O-polymer-GUVs. Blue squares represent average of 13 GUVs with standard deviation.

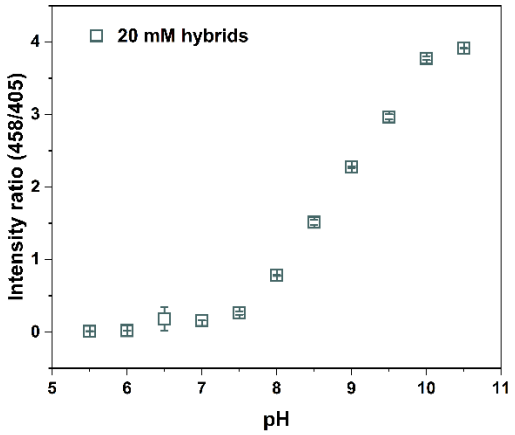

Figure S75. Plot of the ratio of fluorescence intensities of pyranine as a function of pH. 20 mM hybrid LUVs were present in the measurement buffer. Open squares represent measurements of two different samples with their standard deviation.

7.4.4 Growth of hybrid GUVs from lipid and polymer LUVs

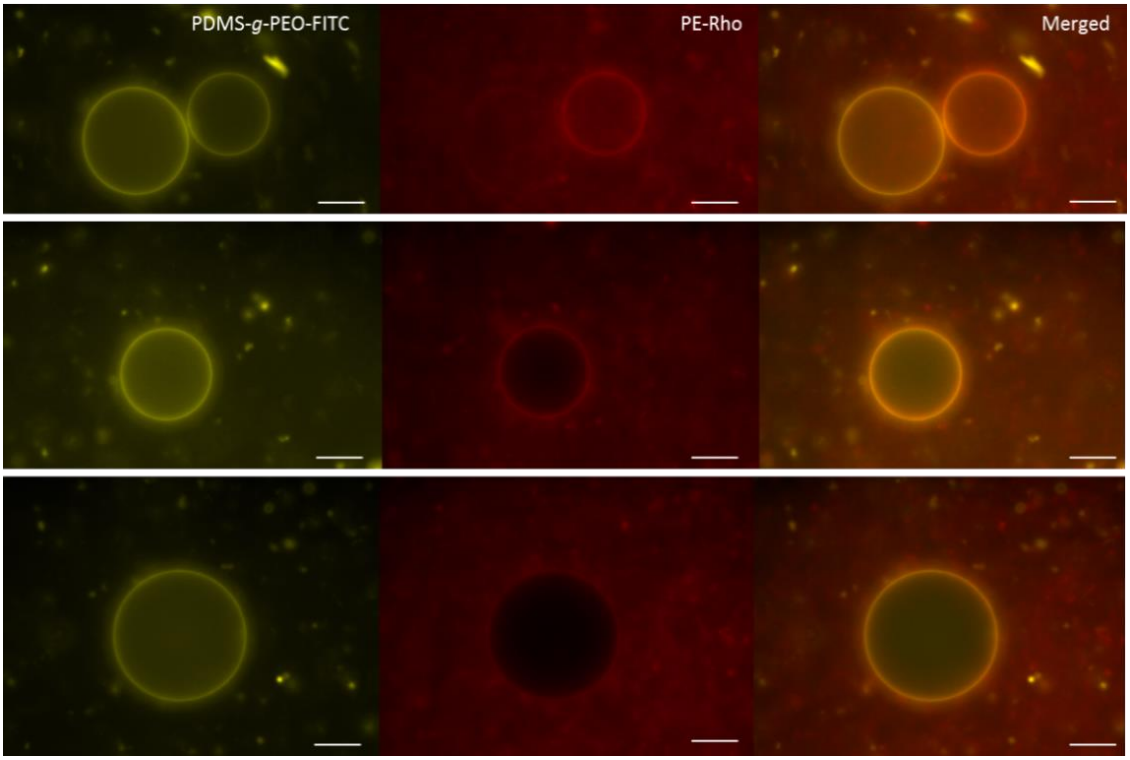

Figure S76. Epifluorescence images of hybrid GUVs formed from mixture of PDMS-*g*-PEO LUVs (100 nm) and soy PC LUVs (100 nm), mixed in molar ratio 70:30. Lipid LUVs contained 0.05 mol% PE-Rhodamine (red) and polymer LUVs contained 0.1 mol% PDMS-*g*-PEO-FITC (yellow). Lipid and polymer dye were homogenously distributed in the membrane. Non-fused lipid LUVs can be seen surrounding the GUVs (red channel). Scale bar: 10 µm.

7.4.5 *bo₃* oxidase and F_1F_O-ATPase in polymer GUVs

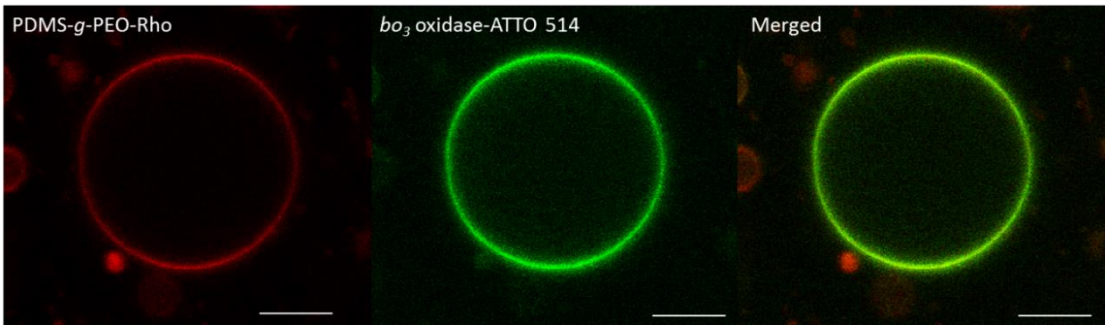

Figure S77. ***bo₃* oxidase-ATTO 514 (green) reconstituted in polymer GUV.** Membrane is doped with PDMS-*g*-PEO-Rho (red). Scale bar 20 µm.

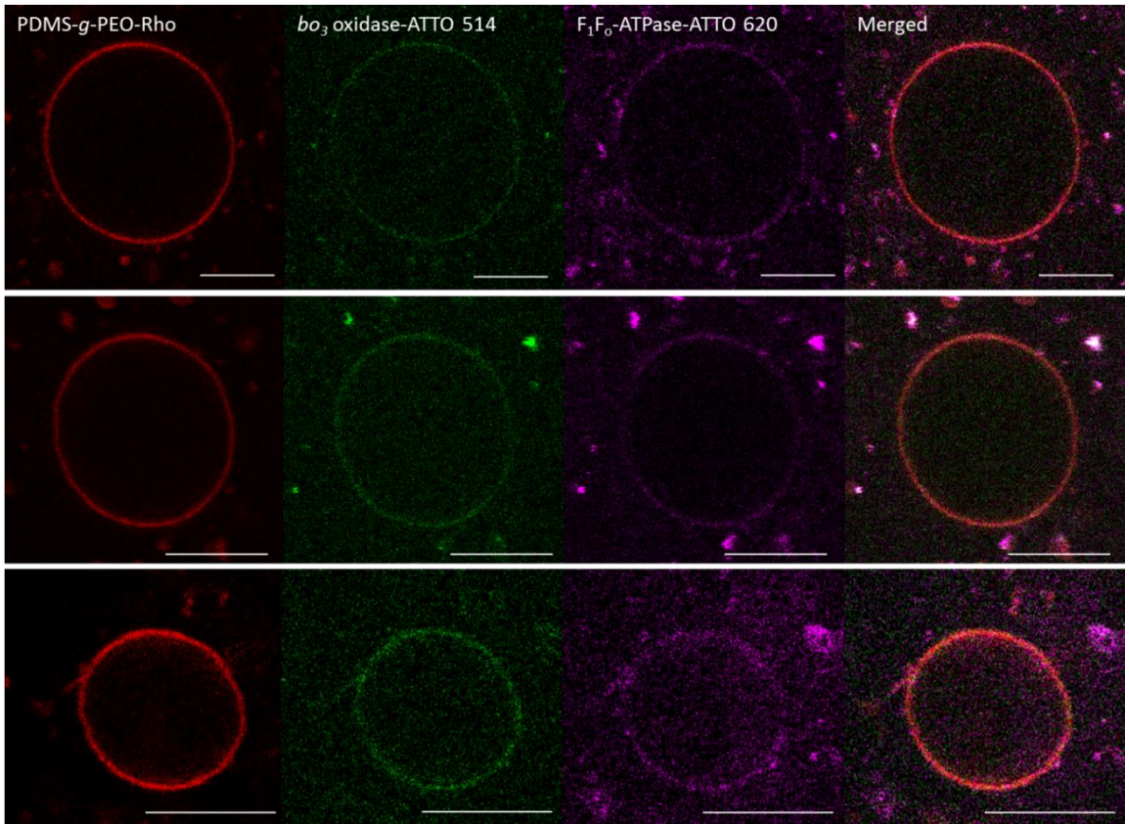

Figure S78. *bo*$_3$ oxidase-ATTO 514 (green) and F_1F_o-ATPase-ATTO 620 (magenta) co-reconstituted in polymersomes (*bo*$_3$-F_1F_o-polymer-GUVs). Membrane was doped with PDMS-*g*-PEO-Rho (red). Scale bar: 10 µm.

7.4.6 *bo*$_3$ oxidase and F_1F_O-ATPase in hybrid GUVs

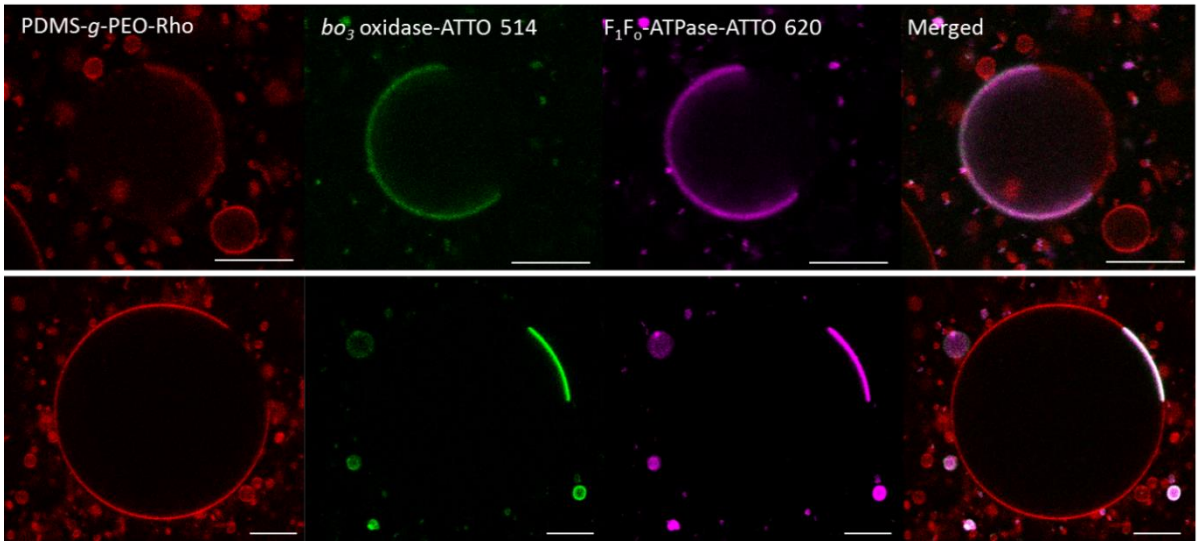

Figure S79. *bo*$_3$-F_1F_O-hybrid GUVs. Domain formation in hybrids with co-reconstituted *bo*$_3$ oxidase-ATTO 514 (green) and F_1F_o-ATPase-ATTO 620 (magenta). Membrane is doped with PDMS-*g*-PEO-Rho (red). Scale bar: 10 µm.

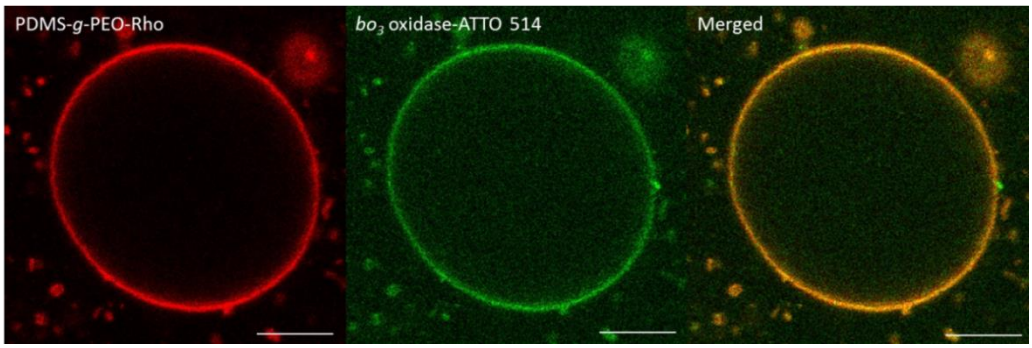

Figure S80. Hybrids with reconstituted *bo*$_3$ oxidase-ATTO 514 (green). Membrane is doped with PDMS-*g*-PEO-Rho (red). The GUV in the middle has a diameter of 36.64 μm. Scale bar: 10 μm.

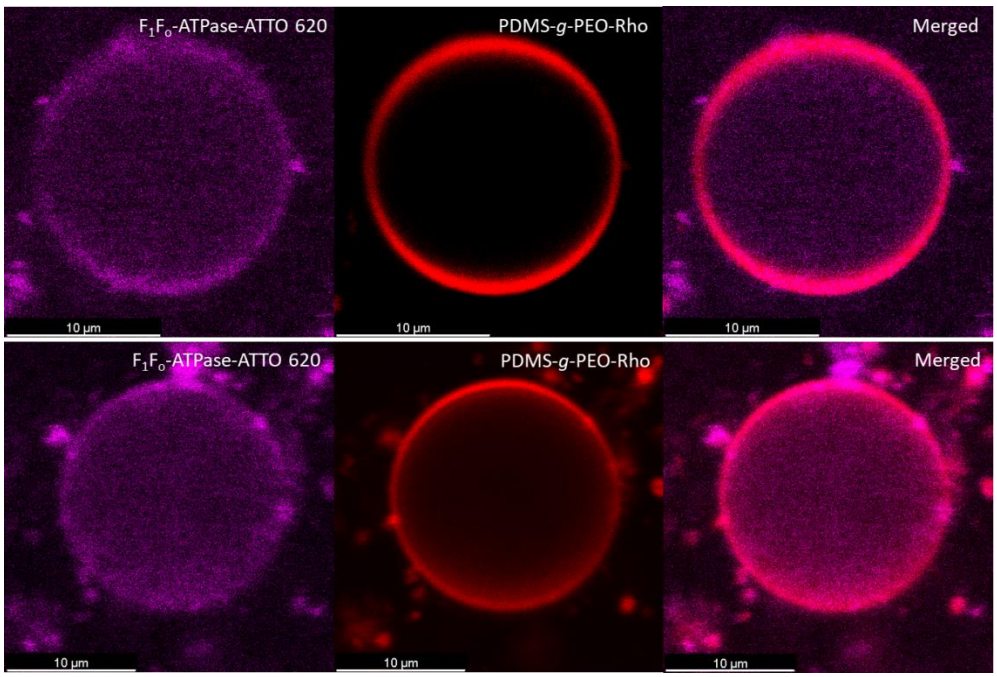

Figure S81. Successful insertion of F$_1$F$_O$-ATPase-ATTO 620 (magenta) in hybrid GUVs. Polymer dye PDMS-*g*-PEO-Rho (red) was used to visualize the membrane.

7.4.7 Lateral protein diffusion in hybrid GUVs

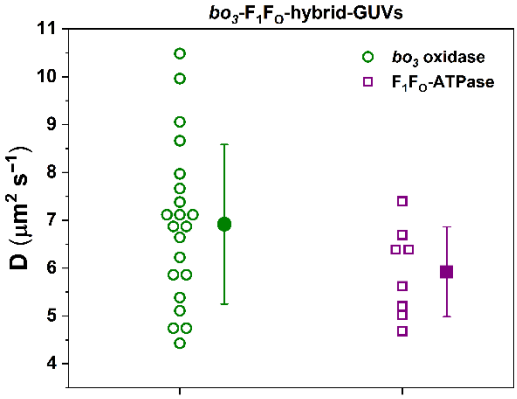

Figure S82. Diffusion coefficients of *bo*$_3$ oxidase-ATTO 514 and F_1F_O-ATPase-ATTO 620 in hybrid GUVs. Diffusion coefficients were determined by fluorescence recovery after photobleaching (FRAP).

7.4.8 Activity of hybrid proteoGUV

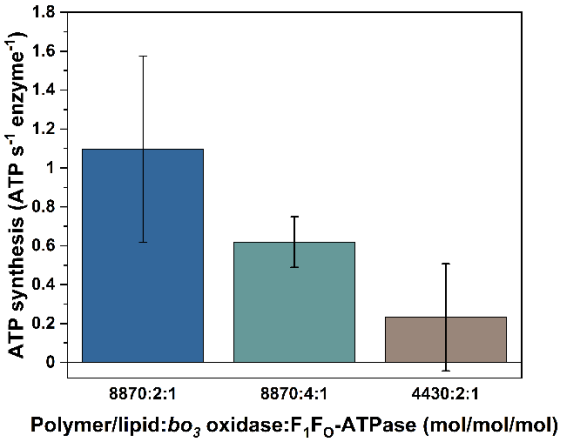

Figure S83. Respiratory-driven ATP synthesis by *bo*$_3$-F_1F_O-hybrid-GUVs. *bo*$_3$-F_1F_O-hybrid-GUVs were prepared by fusion/electroformation from *bo*$_3$-LUVs and F_1F_O-LUVs at three different polymer/lipid-to-protein molar ratio. ATP synthesis rates at different polymer/lipid-to-protein ratios.

7.4.9 Additional data on multicompartmentalized GUVs

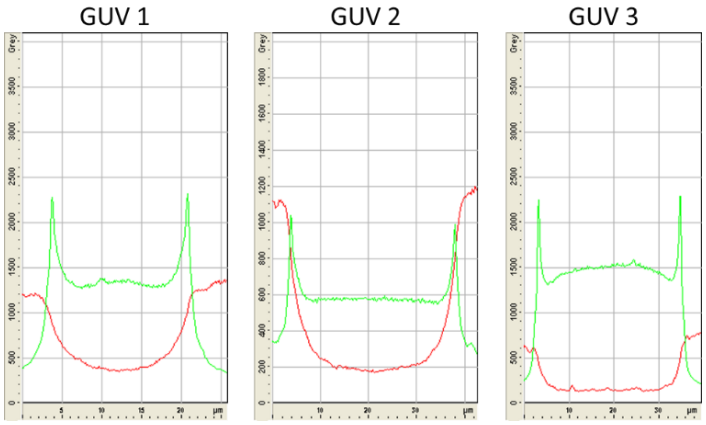

Figure S84. Line profiles of PDMS-*g*-PEO (green) GUVs with encapsulated lipid (red) LUVs. No signal from LUVs was found on the membrane on GUVs, indicating no fusion between LUVs and GUVs occurred.

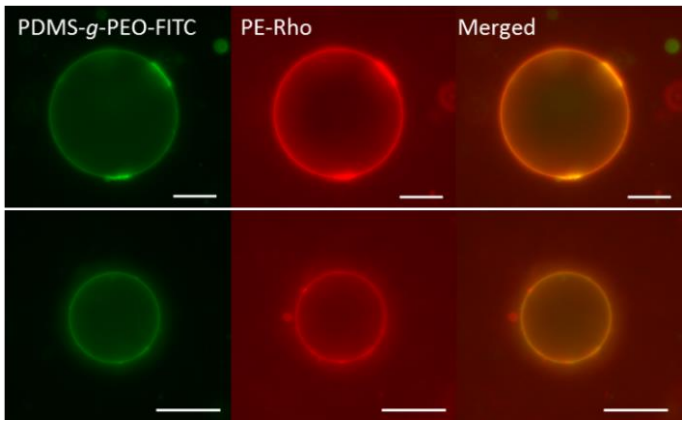

Figure S85. Encapsulation of cationic LUVs in polymer GUVs. Epifluorescence images of PDMS-*g*-PEO GUVs (membrane tagged with 0.5 mol% PDMS-*g*-PEO-FITC, green) formed with electroformation in presence of 100 nm DOPC:DOTAP LUVs (membrane tagged with 0.05 mol% PE-Rho, red) after electroformation. Majority of LUVs fused with the membrane of GUVs (accumulation or red signal). Scale bar: 10 µm.

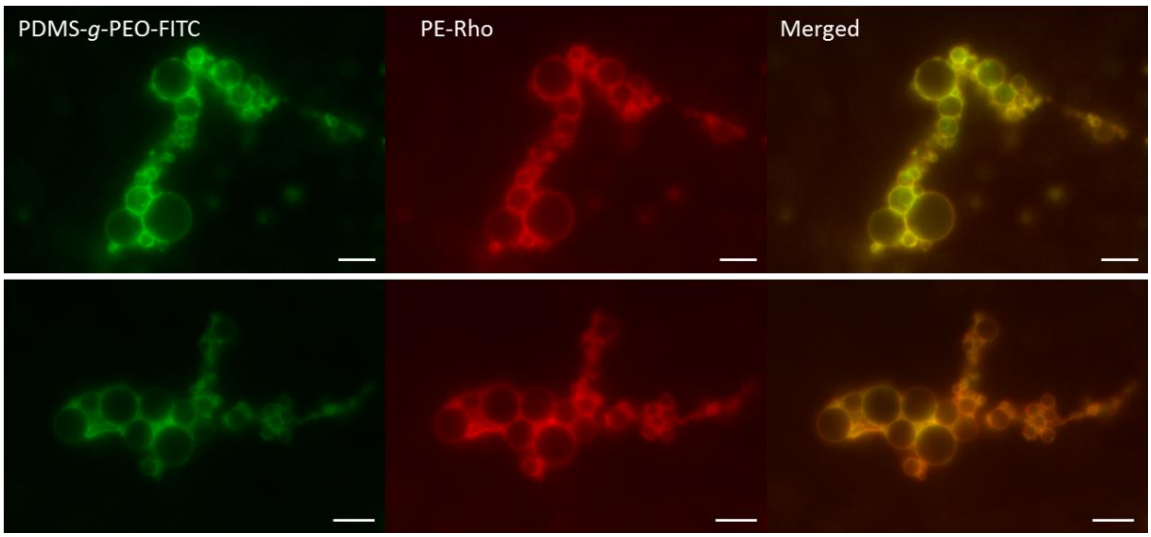

Figure S86. Encapsulation of cationic LUVs in polymer GUVs. Epifluorescence images of PDMS-*g*-PEO GUVs (membrane tagged with 0.5 mol% PDMS-*g*-PEO-FITC, green) formed with electroformation in presence of 100 nm DOPC:DOTAP LUVs (membrane tagged with 0.05 mol% PE-Rho, red) after electroformation. Majority of LUVs fused with the membrane of GUVs before their detachment from ITO slide. Scale bar: 10 μm.

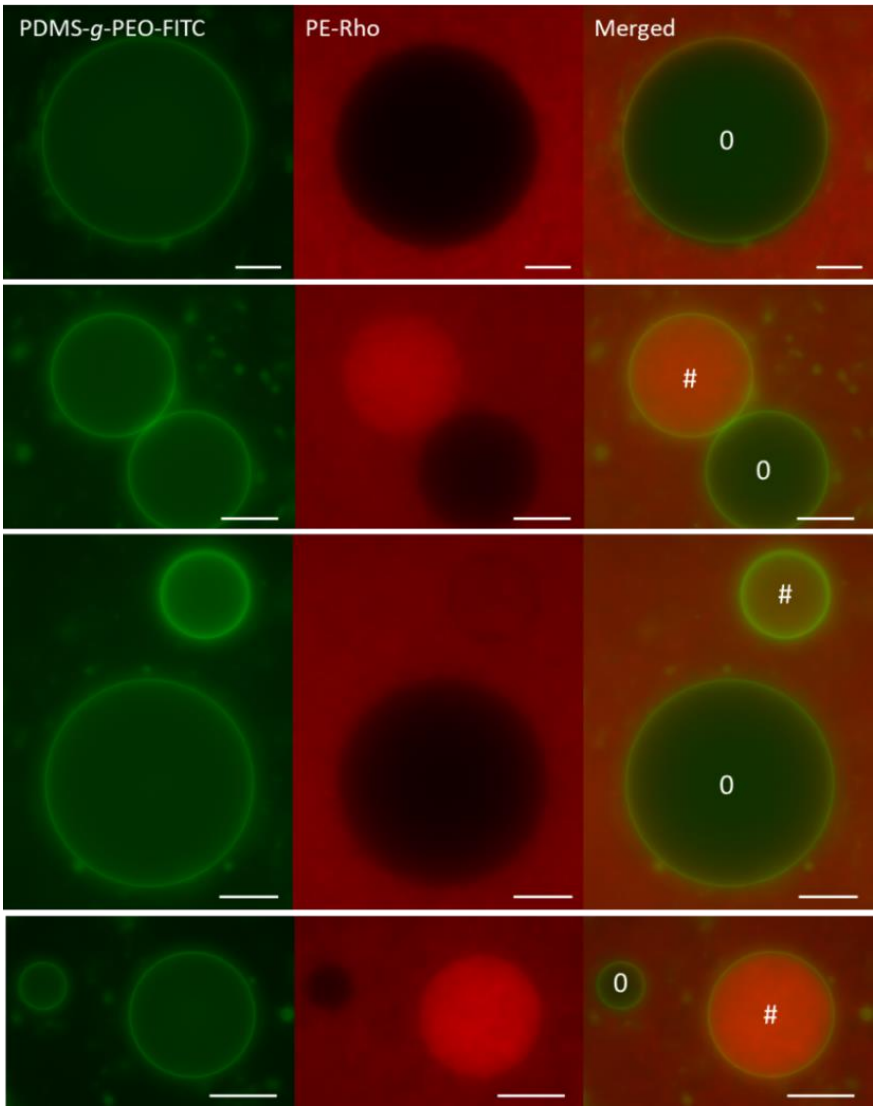

Figure S87. Encapsulation of 100 nm anionic LUVs in polymer GUVs. Epifluorescence images of PDMS-*g*-PEO GUVs (membrane tagged with 0.08 mol% PDMS-*g*-PEO-FITC, green) with encapsulated 100 nm DOPC:DOPE:TOCL LUVs (membrane tagged with 0.05 mol% PE-Rho, red) after fusion/electroformation. #: LUVs encapsulated GUVs, O: empty GUVs. Scale bar: 10 µm.

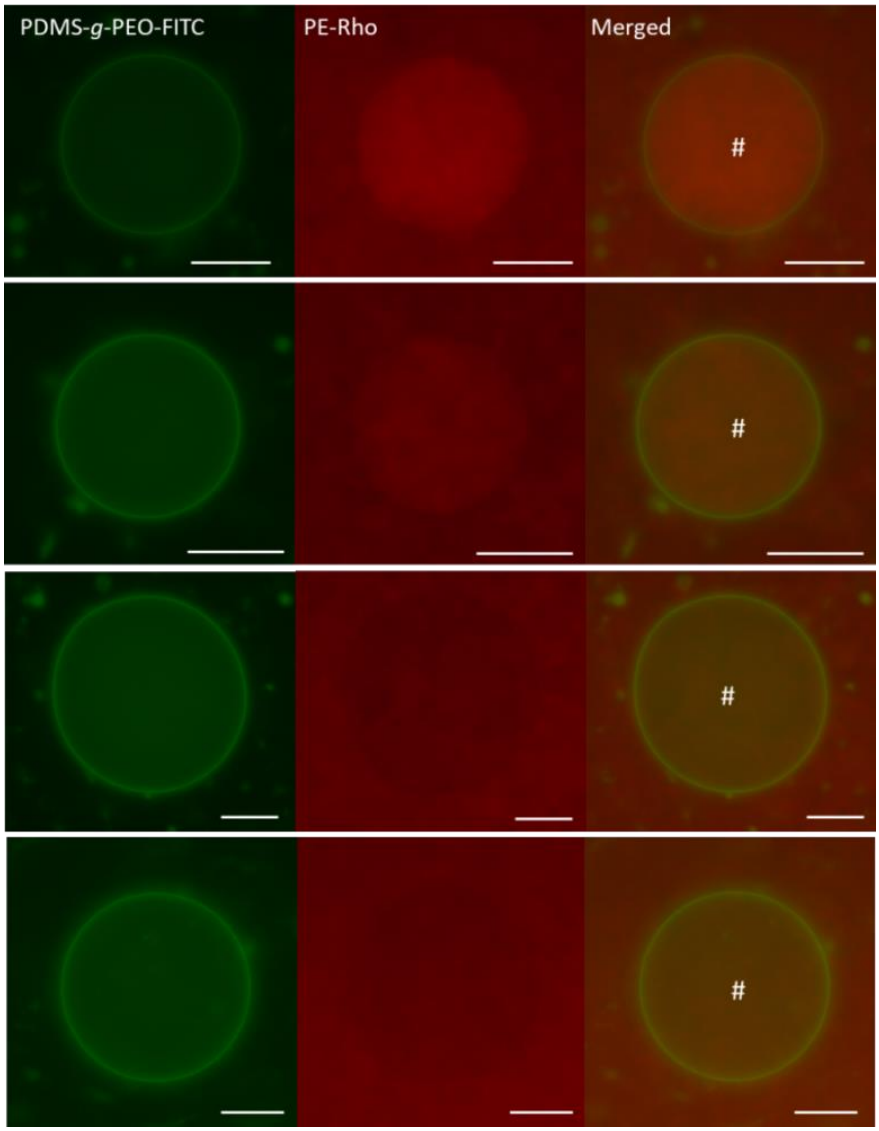

Figure S88. Encapsulation of 50 nm anionic SUVs in polymer GUVs. Epifluorescence images of PDMS-*g*-PEO GUVs (membrane tagged with 0.08 mol% PDMS-*g*-PEO-FITC, green) with encapsulated 100 nm DOPC:DOPE:TOCL LUVs (membrane tagged with 0.05 mol% PE-Rho, red) after fusion/electroformation. #: LUVs encapsulated GUVs, O: empty GUVs. Scale bar: 10 μm.

7.1 Additional data on SNARE-mediated GUV-LUV fusion

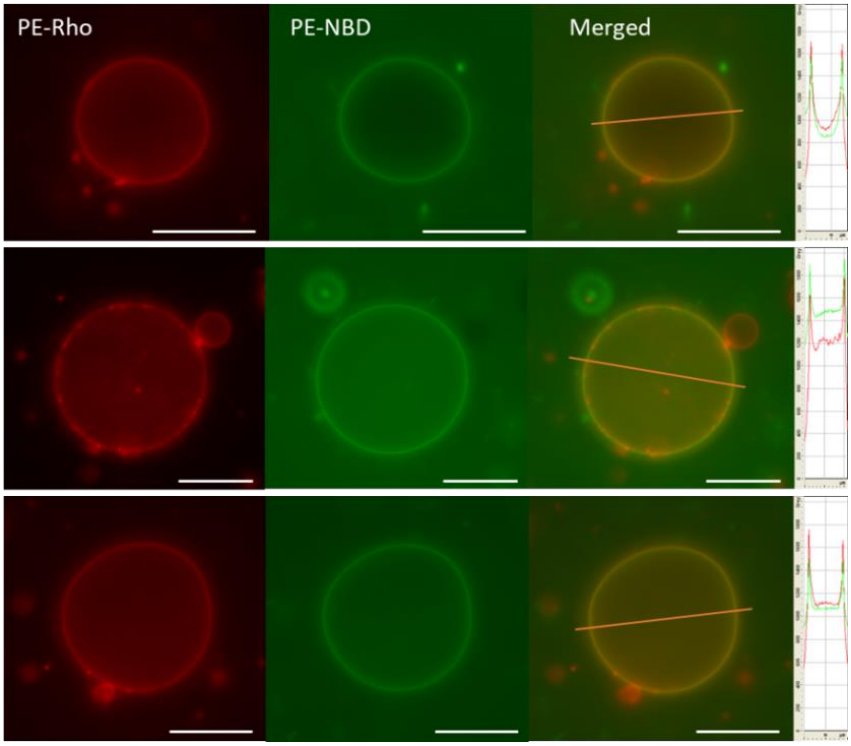

Figure S89. Membrane mixing of ΔN-polymer-GUVs with syb-polymer-LUVs. Epifluorescence microscopy images of ΔN-polymer-GUVs tagged with 0.5 mol% PE-Rho (red) after incubation with syb-polymer-LUVs tagged with 0.5 mol% PE-NBD (green) and 1 mM DTT for 5 min. Scale bar: 10 µm.

8 List of Publications

Nika Marušič, Lado Otrin, Jonas Rauchhaus, Ziliang Zhao, Fotis L. Kyrilis, Farzad Hamdi, Panagiotis L. Kastritis, Rumiana Dimova, Ivan Ivanov, Kai Sundmacher. Increased efficiency of charge-mediated fusion in polymer/lipid hybrid membranes. *Proceedings of the National Academy of Sciences of the United States of America* **2022**, 119 (20): e2122468119.

Contribution: conceptualized the study, design of experiments, performing the experiments (preparation of samples, performing membrane and content mixing analysis, flip-flop analysis, membrane disorder analysis, zeta potential analysis), data analysis, visualization of the data, and writing of the draft.

Nika Marušič, Ziliang Zhao, Lado Otrin, Rumiana Dimova, Ivan Ivanov, Kai Sundmacher. Fusion-induced growth of biomimetic polymersomes: behavior of poly(dimethylsiloxane)-poly(ethylene oxide) vesicles in saline solutions under high agitation. *Macromolecular Rapid Communications* **2022**, 43(5): 2100712.

Contribution: conceptualized the study, design of experiments, performing the experiments (optimization of growth conditions, encapsulation, fluorescence microscopy analysis, membrane protein reconstitution and activity measurements, membrane disorder analysis, zeta potential analysis), data analysis, visualization of the data, and writing of the draft.

This publication was selected for a back cover.

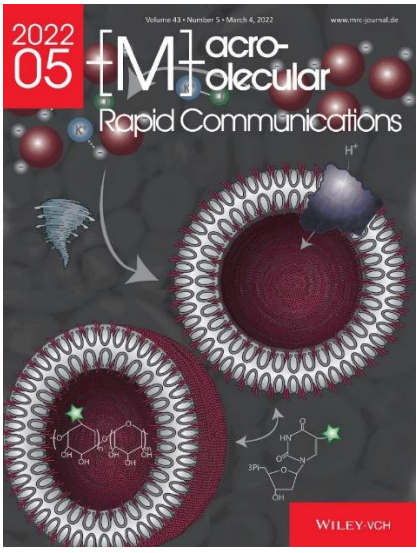

Lado Otrin, Agata Witkowska, Nika Marušič, Ziliang Zhao, Rafael B. Lira, Fotis L. Kyrilis, Farzad Hamdi, Ivan Ivanov, Reinhard Lipowsky, Panagiotis L. Kastritis, Rumiana Dimova, Kai Sundmacher, Reinhard

Jahn, Tanja Vidaković-Koch. En route to dynamic life processes by SNARE-mediated fusion of polymer and hybrid membranes. *Nature Communications* **2021**, 12(1): 4972.

Contribution: performing the experiments (optimization of fusion/electroformation protocol for SNARE-GUVs, preparation of GUVs and SNARE-GUVs, performing fluctuation analysis), data analysis (analysis of fluctuation data and membrane thickness), and coordination of the research.

Ivan Ivanov, Sebastián López Castellanos, Severo Balasbas III, Lado Otrin, Nika Marušič, Tanja Vidaković-Koch, Kai Sundmacher. Bottom-Up Synthesis of Artificial Cells: Recent Highlights and Future Challenges. *Annual Review of Chemical and Biomolecular Engineering* **2021**, 12: 287-308.

Contribution: writing of "Compartmentalization, growth and division" section.

Nika Marušič, Lado Otrin, Ziliang Zhao, Rafael B. Lira, Fotis L. Kyrilis, Farzad Hamdi, Panagiotis L. Kastritis, Tanja Vidaković-Koch, Ivan Ivanov, Kai Sundmacher, and Rumiana Dimova. Constructing artificial respiratory chain in polymer compartments: Insights into the interplay between bo_3 oxidase and the membrane. *Proceedings of the National Academy of Sciences of the United States of America* **2020**, 117 (26), 15006-15017.

Contribution: conceptualized the study, design of experiments, coordination of the research, performing the experiments (optimization of fusion/electroformation protocol, preparation of all samples, fluctuation analysis, partially proton permeability analysis on GUVs, CF leakage experiments, oxygen consumption measurements for functional lifetime analysis, membrane disorder analysis, zeta potential anaylsis), data analysis, visualization of the data, and writing of the draft.

Nika Marušič, Lado Otrin, Ziliang Zhao, Rafael B. Lira, Tanja Vidaković-Koch, Ivan Ivanov, Rumiana Dimova, Kai Sundmacher. Reconstitution of Respiratory Enzymes in PDMS-*g*-PEO Polymer and Polymer/Lipid Hybrid Vesicles. *Biophysical Journal* **2020**, 118 (3), 131a.

This work was presented on Biophysical Society 2020 Annual Meeting and published as an abstract in *Biophysical Journal*.

Other Contributions

Nika Marušič, Lado Otrin, Ziliang Zhao, Fotis L. Kyrilis, Farzad Hamdi, Panagiotis L. Kastritis, Rumiana Dimova, Tanja Vidaković-Koch, Ivan Ivanov, Kai Sundmacher. Charge vs. SNARE-mediated fusion of biomimetic polymer/lipid hybrid compartments: Which one is more efficient? *SynCell* **2021**, online event (poster presentation)

Nika Marušič, Lado Otrin, Ziliang Zhao, Rafael B. Lira, Claudia Bednarz, Jonas Rauchhaus, Tanja Vidaković-Koch, Rumiana Dimova, Ivan Ivanov, Kai Sundmacher. Fusion of biomimetic polymer and hybrid compartments and applications in bottom-up synthetic biology. *MaxSynBio Symposium* **2020**, online event (poster presentation)

Nika Marušič, Lado Otrin, Ziliang Zhao, Rafael B. Lira, Tanja Vidaković-Koch, Ivan Ivanov, Rumiana Dimova, Kai Sundmacher. Reconstitution of respiratory enzymes in PDMS-*g*-PEO polymer and polymer/lipid hybrid vesicles. *Biophysical Society Annual Meeting* **2020**, San Diego, US (poster presentation)

Nika Marušič, Lado Otrin, Ziliang Zhao, Rafael B. Lira, Tanja Vidaković-Koch, Ivan Ivanov, Rumiana Dimova, Kai Sundmacher. Integration of respiratory enzymes in PDMS-*g*-PEO polymer and polymer/lipid hybrid vesicles. *Biomembrane Days* **2019**, Berlin, Germany (poster presentation)

Nika Marušič, Lado Otrin, Ziliang Zhao, Rafael B. Lira, Tanja Vidaković-Koch, Ivan Ivanov, Rumiana Dimova, Kai Sundmacher. Reconstitution of respiratory enzymes in PDMS-*g*-PEO polymer and polymer/lipid hybrid vesicles. *BioSynSys & MaxSynBio* S*ymposium* **2019**, Bordeaux, France (talk)

Nika Marušič. Insights into the interplay between the bo_3 oxidase and (semi)synthetic compartments for membrane protein integration. **2019**, Potsdam/Golm, Germany (invited talk at Max Planck Institute of Colloids and Interfaces)

Nika Marušič, Lado Otrin, Rafael Lira, Ziliang Zhao, Claudia Bednarz, Rumiana Dimova, Tanja Vidaković-Koch, Ivan Ivanov, Reinhard Lipowsky, Kai Sundmacher. Growth of functional microcompartments. *MaxSynBio Symposium* **2018**, Magdeburg, Germany (talk)

Nika Marušič, Ivan Ivanov, Kai Sundmacher. Growth of microcompartments. *MaxSynBio Workshop* **2017**, Marburg, Germany (poster presentation)